Invariant Mechanical Properties of Calcium-Silicate-Hydrates (C-S-H) in Cement-Based Materials: Instrumented Nanoindentation and Microporomechanical Modeling

by

Georgios Constantinides

B.Eng., University College London (2000)
S.M., Massachusetts Institute of Technology (2002)

Submitted to the Department of Civil and Environmental Engineering
in partial fulfillment of the requirements for the degree of

Doctor of Philosophy in the field of Structures and Materials

at the

MASSACHUSETTS INSTITUTE OF TECHNOLOGY

February 2006

Signature of Author .....
Department of Civil and Environmental Engineering
21 September 2005

Certified by .....
Franz-Josef Ulm
Associate Professor of Civil and Environmental Engineering
Thesis Supervisor

Accepted by .....
Andrew J. Whittle
Chairman, Department Committee for Graduate Students

Invariant Mechanical Properties of Calcium-Silicate-Hydrates (C-S-H) in Cement-Based Materials: Instrumented Nanoindentation and Microporomechanical Modeling

by

Georgios Constantinides

Submitted to the Department of Civil and Environmental Engineering
on 21 September 2005, in partial fulfillment of the
requirements for the degree of
Doctor of Philosophy in the field of Structures and Materials

Abstract

Random porous solids such as bone and geomaterials exhibit a multiphase composite nature, characterized by water-filled pores of nm- to μm-scale diameter. The natural synthesis and operating environments of such materials significantly alters phase composition and multi-scale structural heterogeneities throughout the material lifetime, defining significant changes in macroscopic mechanical performance for applications ranging from multispan bridges to calcium-phosphate bone replacement cements. However, the nanoscale phases formed within the unique chemical environment of pores cannot be recapitulated ex situ in bulk form, and imaging of the composite microstructure is obfuscated by the size, environmental fragility, and nonconductive nature of such geomaterials and natural composites. Thus, there is an increasing drive to develop new approaches to image, quantify the mechanical contributions of, and understand the chemomechanical coupling of distinct phases in such composites.

In this thesis, we utilize recent advances in experimentation namely instrumented indentation, and micromechanical modeling namely homogenization techniques, in an attempt to quantify the mutli-phase, multi-scale heterogeneity observed in all cement-based materials. We report a systematic framework for mechanically enabled imaging, measuring and modeling of structural evolution for cement based materials (CBM), porous geocomposites, at length scales on the order of constituent phase diameters ($10^{-8} - 10^{-6}$ m), and thus identify two structurally distinct but compositionally similar phases heretofore hypothesized to exist. The presented experimental and modeling results culminated in micromechanical models for elasticity and strength that can predict the macroscopic mechanical behavior for a range of CBM systems. The models directly correlate the changes in chemical and mechanical state to predict the experimentally observed range of macroscopic mechanical properties. This general framework is equally applicable to other man-made and natural composites, and enables accurate prediction of natural composite microstructure and mechanical performance directly from knowledge of material composition.

Thesis Supervisor: Franz-Josef Ulm
Title: Associate Professor of Civil and Environmental Engineering

Contents

List of Tables

List of Figures

Acknowledgements

Firstly, I would like to thank my advisor Prof. F.-J. Ulm for providing me the opportunity to pursue this degree and for his continued financial support which allowed full-time work on this study – Thank you. Thanks are also due to the people that invested in this research and made it possible: the groups of Dr. Paul Acker from Lafarge and Dr. Russ Ewy from Chevron-Texaco. Your contribution is greatly appreciated. This work wouldn't have started if it wasn't for the unconditional financial support I was provided, during my first year of stay in MIT (2000 – 2001), by the Rosenblith and Presidential Fellowship – I am grateful for that! Furthermore, I would like to express my appreciation to the other three members of my committee: Prof. H. Jennings, for the interest and availability with which he followed this work and his inspiring comments and discussions; Dr. J. Germaine, for his availability and willingness to help on every aspect of this research; A special thanks goes to Prof. K. J. van Vliet for introducing me to the nanoindentation technique, following this work closely, and continuously supporting me over the years – Thank you for everything!

In addition to my committee-members, many other people helped in different ways to make this work possible. Among them are: Francois Ganneau for the computational implementation of the yield design problem presented in this thesis and the collaboration we had on converting hardness data into strength properties – Thank you Francois; Antoine Delafargue for the collaboration we had on modeling the elastic behavior of geological materials (shales) – Antoine, I had a great time; Alan Schwartzman for his guidance and support regarding the instrumentation situated in the Nanolab of the Department of Materials Science and Engineering at MIT – Thank you Alan; the support staff in the CEE department, particularly Alice, Cynthia, and Anthee – you made my life in MIT much easier; Furthermore, I would like to express my gratitude and admiration to Prof. J.J. Connor. Finally, a special thank you goes to Emilio Silva who has been answering my questions ever since I met him – I am thankful for your help and I am grateful for your friendship. You deserve the best and I am certain you will get it!

The main privilege of being in MIT is that you get the chance to meet all these extraordinary individuals gathered from all over the world. In particular, I would like to acknowledge my office-mates over the past five years: Franz, Dirk, Emilio-Nina, Hesson, JongMin-Eunkyung (keep up the good work Korea, you deserve the best!), Laetitia (thank you!), Francois, Matt-Cara, Chris,

Antoine, Gabriel, Sophie, Matthieu-Marina; other people in the CEE Karim, Rita, Jad. I have learned a lot from you and it has been a privilege to meet you all. Thank you for being next to me all these years and please do keep in touch.

Life in MIT wouldn't be the same without my Greek friends that provided me with countless memories: my buddies here in MIT, Costas[3] (Psallidas, Galanis, Pelekanakis), Gougou, Antono – life without you would be extremely boring; Thank you Christina, Noelle, Antonis, Mariakat, Thodoris-Anna, Babis, Fragkiskos, Giannag, Laura, Petros-Lia, Bletsas, Vasilis, Katsoufis, Aristos, Areti, Dora, Giwrgos-Dominiki, Antreas, Anna-Ramin for the many good times we had over the years! Thank you for the friendship and affection you have afforded me. I look forward in meeting you again here in the U.S. or at some other place on this globe.

I was fortunate enough to have additional support coming from my home country, Cyprus: I would like to thank Petros-Marina and more recently Athena (you have been a constant source of encouragement), Iakobos-Nikoletta, Stasinos-Anthi, Nikos, Elli, Persela, Nikolas, Christos, Theodoros, Elena for their transatlantic support and moral-boosting. Finally, my greatest appreciation goes to Angelina: "I would have never completed this thesis if not for you. I truly thank you for everything you have done. You are an angel!"

Last, but not least, I would like to express my deepest love and appreciation to my family: Dinos, Ianthi, Katia, Katina-Nikos, Lala-Giwrgos. "Little (if any) of what I have done would be posssible without your love, guidance and support"[1].

[1] I am almost certain I forget people that should be included in this acknowledgement. I am grateful to all, those mentioned above and those unintentionally not.

...

To my parents,

Dinos and Ianthi

Part I

GENERAL PRESENTATION

Chapter 1

Introduction

Natural solids such as bones, geomaterials, woods, and cement-based materials exhibit a multi-scale multi-phase composite nature[1]. The most prominent heterogeneity of these systems is the pore space which varies from a few Angstroms in diameter to micrometric dimensions. It is this multi-scale, environmentally coupled heterogeneity that ultimately defines the macroscopic mechanical performance of these materials. For example, consistent with trends in other natural composites (see Tab. 1.1), the elastic modulus (E) and uniaxial compressive strength (Σ_c) of a cementitious composite can range from $E = 10$ to 60 GPa and $\Sigma_c = 10$ to 200 MPa, respectively, depending on material composition and degree of hydration. From a structural design point of view this uncertainty in strength and elasticity constitutes a threat to possible damage and catastrophic failures of safety-critical applications ranging from multi-span bridges to calcium-phosphate cements currently being considered as bone replacement materials [231]. While most codes of practice in design account for this heterogeneity through safety factors to achieve macroscopic material properties with some certainty, current trends in materials science and engineering aim at a better representation of the microstructure at multiple length scales. Advances in experimental approaches such as instrumented nanoindentation and analytical approaches such as micromechanical homogenization present an opportunity to quantify structurally heterogeneous materials at length scales corresponding to individual chemical

[1] Virtually all natural solids are multiphase multiscale material systems, i.e., they are composed of several chemical constituents (multiphase) that manifest themselves in different length-scales (multiscale) creating in the process complicated hierarchical composites to deal with.

Material	*Elastic Modulus,* [GPa]	*Compressive Strength,* [MPa]	*References*
Bone	1-40	1-100	[163]
Cement-Based Material	10-60	10-200	[180]
Geomaterial	5-40	1-30	[142]
Wood	0.5-20	5-20	[99]

Table 1.1: Approximate mechanical properties ranges for selected natural composites.

phases, and then to upscale their mechanical response at the level of engineering applications. The development of such a framework would enable one to model and predict the mechanical performance of a multi-phase, multi-scale composite directly from knowledge of the material composition and a modest number of mechanical experiments. Here, in this thesis, we demonstrate this approach through the correlation of nanomechanical testing and micromechanical modeling of cementitious composites as a function of environmental exposure, and predict with high accuracy the macroscopic mechanical behavior of this multi-scale composite. The techniques and methodology proposed are quite general, and apply equally well to other man-made, geological, and biological composites.

1.1 Problem Statement

Is it possible to break down cement-based materials (or more generally, natural porous material systems) to a scale where solids no longer change from one material to another, and upscale ('nanoengineer') the behavior from the nanoscale to the macroscale of engineering applications? – This is the challenging question we want to address in this thesis through the use of some tools and methods of experimental and theoretical microporomechanics.

As it was elegantly stated by Scrivener and Van Damme in a recent special issue of Materials Research Society Bulletin [208] "...the application of concrete is largely based on empirical knowledge acquired through macroscopic testing, and the depth of our understanding of the chemical and physical processes that deliver the performance of concrete on a macroscopic scale is quite limited." The lack of knowledge can be attributed to the high complexity possessed by these materials. Understanding cement-based materials (CBM) requires knowledge from chemistry, geological sciences, materials science, granular media, porous media, colloidal physics, etc. In addition, the inability of certain experimental methods to be applied quantitatively

to CBM, have added further confusion. One can therefore reach the unfortunate conclusion that a conceptual framework for modeling the mechanical behavior of cement-based materials as elegant as that of metals, polymers, and ceramics does not currently exist [208]. It is therefore the intention of this thesis to provide such a framework by utilizing recent progress in experimental and theoretical nanomechanics. Figure 1-1 shows a schematic of the materials science approach adopted in this thesis. While significant progress has been made over the last 50 years on the link between synthesis, processing and microstructural evolution, very little is known on the link between structure-property relations. It is the intention of this thesis to bridge this gap and provide a direct link between physical chemistry and mechanics. Once such a coupling is established, predictions of the macroscopic mechanical behavior can be made based on knowledge of the material synthesis.

1.2 Research Objectives

A comprehensive approach is presented in this thesis to address the scientific challenge. It is composed of experimental investigation, theory and modeling, and finally experimental validation (see details in Section 1.3). This approach studies the effects of microstructural details on the multi-scale mechanical behavior of CBM materials ranging from the nanometer scale where a porous material exists, to the macroscopic scale where concrete is applied in engineering applications. To tackle this problem, we pose a series of objectives which, once met can lead to a solution to our problem. The four research objectives are now summarized:

Objective 1: *Develop a theoretical framework that allows application of indentation techniques to multi-phase, cohesive-frictional materials.* The nanoscale phases formed within the unique chemical environment of CBM pores, the Calcium Silicate Hydrates (C-S-H), cannot be recapitulated *ex-situ* in bulk form, and as a consequence their mechanical properties are essentially unknown. Nanoindentation provides a possibility for overcoming this problem. The knowledge of indentation analysis is currently restricted to homogeneous metallic materials, i.e., materials that follow a cohesive yield behavior independent of the hydrostatic pressure. As a prerequisite to the experimental investigation, a comprehensive framework that allows extracting mechanical properties from indentation on such complicated systems is developed.

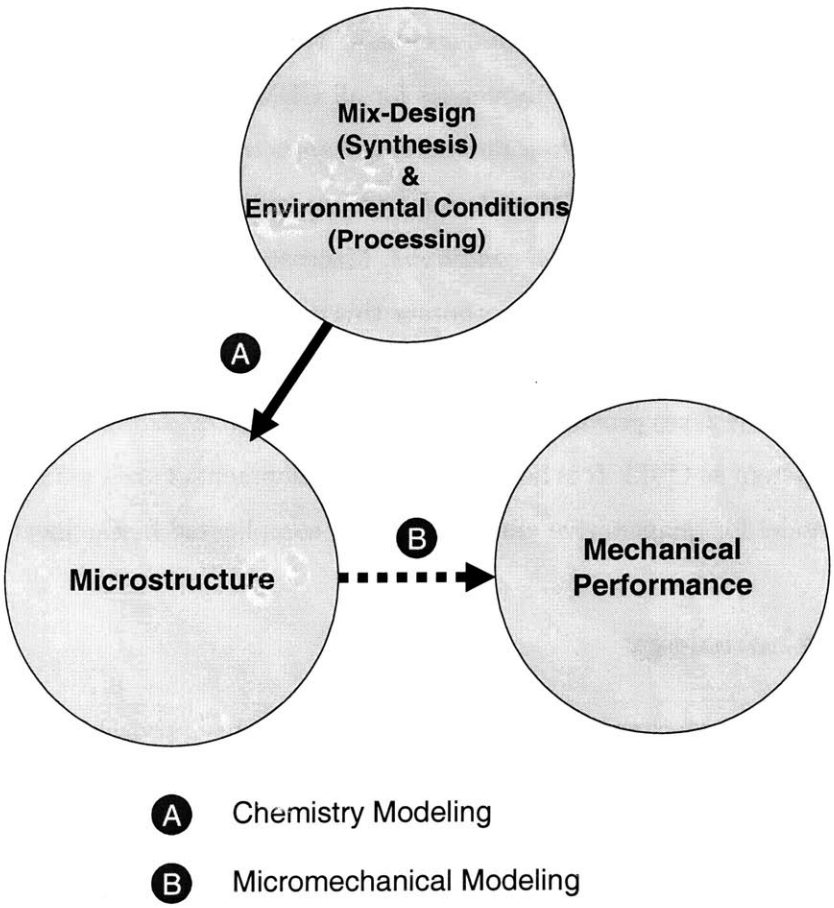

Figure 1-1: Materials science approach applied to mechanical behavior of solids.

Objective 2: *Validate the tools of indentation analysis on model materials.* The developed schemes for cohesive-frictional materials and multi-phase composites are validated on a series of tests performed on a bulk metallic glass (BMG) and a titanium-titanium boride.

Objective 3: *Study the multi-scale mechanical behavior of CBM materials and reconstruct quantitatively its microstructure.* The mechanical behavior of the individual constituents composing cement pastes microstructure are essentially unknown. In fact the exact nature of the main constituent, the C-S-H, is still under debate. We aim to decode the microstructural details and provide intrinsic mechanical properties for all CBM constituents.

Objective 4: *Develop a multi-scale micromechanics model that can predict the macroscopic mechanical behavior of any CBM material, independently of initial mix proportions, degree of hydration or applied environmental conditions.* Macroscopic mechanical behavior of CBM shows significant variability. We aim to incorporate this diversity in our micromechanical model and provide a direct link between synthesis and mechanics.

These four objectives provide an elegant framework for modeling a multi-scale, multi-phase mechanical system as CBM. It is hoped that the development of such a framework can therefore serve as a model for quantitative analysis of other complicated hierarchical composites.

1.3 Methodology

[2]Modeling the micromechanical behavior of concrete can be approached from several directions and at various degrees. Many of the formulas used in design rely on empirical expressions that seem to fit the extensive experimental data. Even though such approaches have been extensively used in cement-based modeling and proved to be useful and convenient, the results are limited to the conditions under which the data were obtained. The methods provide no physical understanding and restrict our predictive capabilities to the range on which the laboratory experiments were performed. In this thesis, we seek a more general approach, one that will give us the ability to predict and a refined understanding. In pursuing such a fundamental approach, we place a premium on this goal of predictive power. However, a goal of this magnitude requires

[2]The introduction of this section is motivated by the introduction given by R.M. Christensen in his book 'Mechanics of composite materials', Ref. [53].

significant effort and time. We aim here to lay the foundation and stimulate interest for further research.

1.3.1 Theoretical Modeling

Homogenization techniques developed within the framework of continuum micromechanics are arguably the most systematic methods to address the large heterogeneity observed in CBM. The underlying idea of continuum micromechanics is that it is possible to separate a heterogeneous material into phases with (on-average) constant mechanical and structural properties. Homogenization, which is based on volume averaging over the representative element volume (R.E.V.) of the constitutive relations defined at the scale of the phases, delivers the macroscopic elastic/poroelastic/strength properties of the R.E.V. as a function of the microscopic phase properties, volume fractions, and specific morphologies. Upscaling schemes for elasticity and poro-elasticity are well developed in the literature, whereas schemes for strength are still the subject of intense research. Application of these elements to CBM will be detailed in following chapters. It is instructive to note that special emphasis is placed on the representation of the material which masks the physics of the problem.

1.3.2 Experimental Investigation

The primary purpose of our experimental effort is to provide the necessary ingredients for the micromechanical modelling of our materials. We recall that the required information for a micromechanical modeling are a) the mechanical properties of each phase, b) their volume fractions, and c) their morphologies. Morphological characterization is primarily achieved via electron microscopy. Throughout this research Scanning Electron Microscopy (SEM), Environmental Scanning Electron Microscopy (ESEM), Atomic Force Microscopy (AFM), and Optical Microscopy have been extensively used. The morphological investigations culminate in the development of multi-scale think model that guided both our experimental and modeling program. It should be noted that the multi-scale model for CBM presented in Chapter 4 satisfies the separation of scales principle. That is, each level is separated from the next one by at least one order of magnitude, which is a prerequisite for the application of homogenization schemes. Volume fractions have been obtained through experimental chemical methods. In the case of

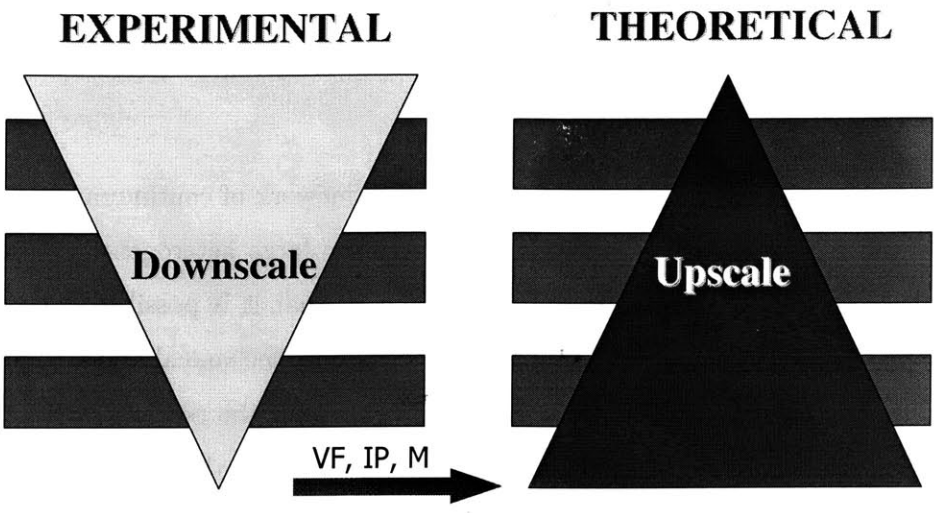

Figure 1-2: Proposed methodology. Microstructural break down (downscale) of natural material systems using experimental methods. Once volume fractions (VF), intrinsic mechanical properties (IP), and morphological characterestics (M) are obtained, upscaling is enabled via micromechanical models.

CBM, one can go a step further and provide predictions of volume fractions using advanced chemistry models, certain of which have been verified with the help of X-ray diffraction or indentation results. Instrumented indentation provided the mechanical properties of each phase. Its use has been the key feature that made this research possible.The proposed methodology is summarized in Fig. 1-2. In the presence of a new material system, one needs to downscale and reconstruct the multi-scale structure of the material using experimental methods. In particular the use of instrumented indentation will prove to be of utmost importance. Once the structure is understood and all necessary ingredients are in place, macroscopic properties can be predicted with the use of advanced homogenization schemes. These two complimentary approaches will prove to be of extreme importance. We show for the first time in this thesis that their coupling can be an invaluable tool for modeling natural composites.

1.4 Industrial and Scientific Motivation

Cement-based-materials are characterized by low cost and high availability. These two characteristics, coupled with excellent mechanical properties, are the primary reasons that concrete

is the leading construction material in the world. The five major elements that make up most of cements minerals, Si – O – Al – Ca – Fe, are the dominant elements in the Earth's crust. It is therefore reasonable to predict that no other material is expected to displace concrete from the construction industry in the years to come. Refining our understanding of the mechanisms responsible for the macroscopic mechanical response of the dominant construction material on Earth is essential and indispensable. The multi-scale materials science approach developed in this thesis has the promise to provide answers to questions concerning the mechanical origin and durability performance of natural composites, by bridging length scales between the microstructure of construction materials (materials science), the macroscopic mechanical material properties (mechanics of materials), and the engineering stiffness-, strength-, and deformation behavior of structures (structural engineering). Once this link is established, the relative significance of the individual chemical constituents comprising the materials microstructure can be quantified. Such an approach can provide some industrial and scientific benefits. They include:

- *Reduced macroscopic tests:* Macroscopic mechanical properties prediction can be made by the sole knowledge of the chemistry of the problem. This can significantly replace a large fraction of macroscopic mechanical tests with a few chemical tests, with significant economic benefits for the industrial world.

- *Quantification of the strength and elasticity at various length-scales:* The advent of nanoindentation allows access to the mechanical properties of materials at length scales where chemical constituents with intrinsic atomic structure and mechanical properties manifest themselves. It is for the first time that the mechanical response of the C-S-H component, the main constituent of all CBM systems, can be quantitatively investigated.

- *Material optimization and 'concrete à la carte':* Using advances in the materials science and manufacturing, it will be possible to rationally design the macroscopic mechanical behavior of cement-based materials for specific applications by tailoring their microstructure at different scales. The development of sustainable materials, which are dimensionally stable in space and time, becomes possible. From the knowledge thus acquired, a new generation of these materials might well become available.

- *Physical basis for understanding degradation mechanisms:* The approach adapted in this

research has its starting point at the level of the individual constituents, providing a fundamental understanding to the origins of elasticity and strength of cement-based materials. Since all chemical constituents are incorporated in our modeling procedure the same models can capture the effect of chemical reactions on mechanics, provided the chemistry is understood and mechanical testing of asymptotic behavior is obtained.

- *Provide a link between physical chemistry and mechanics:* The approach adapted in this thesis aims at bridging the gap between cement chemistry and concrete mechanics. It is hoped that results presented in this thesis will stimulate interest and bring the two communities closer together.

1.5 Thesis Outline

This thesis is divided into six major parts. The first part, Chapter 1, deals with the presentation of the topic. The second part of the thesis focuses on the experimental approach that made this research possible: instrumented indentation. Chapter 2 presents the technique and the theoretical tools that allow converting indentation data into meaningful mechanical properties. While most efforts in the literature concentrate on indentation on metals, we attempt to extend the method to non-metallic materials, in particular to materials that follow a pressure sensitive yield/failure criterion of the Mohr-Coulomb or Drucker-Prager type. For validation purposes, we then employ in Chapter 3 the tools developed in Chapter 2 on a model cohesive-frictional material, bulk metallic glass, an amorphous metal.

The third part of this thesis focuses on the multi-scale experimental investigation of CBM and comprises three chapters. Chapter 4 presents the proposed multi-scale model that guides both the experimental and theoretical developments. Chapter 5 extends the indentation methods to account for the multi-phase nature of cement-based materials. A new method which accounts for this complexity is presented and validated on a white cement paste. Chapter 6 then describes the experimental investigation performed on cement-based materials: materials tested include cement pastes and mortars with different compositions (w/c–ratios and cement composition), curing temperature (heat curing 20-60°C), and experienced environmental conditions (heat treated, calcium leached).

Parts IV and V of this thesis deal with the micromechanical modeling of CBM systems. Motivated by our experimental findings, we develop a multi-scale poroelastic model that depends on a few material-invariant properties and volumetric proportions. The model which is presented in Chapter 7 can predict mechanical properties over length scales spanning several orders of magnitude. The multi-scale poroelastic model is then validated in Chapter 8 for a variety of CBM and experimental conditions. The fifth part is then devoted to the strength behavior of CBM systems. Using the tools developed in Chapter 2 we present first order estimates of the C-S-H strength (Chapter 9). Potential routes for upscaling the mechanical behavior of CBM systems are then presented in Chapter 10 and compared with experimental data in Chapter 11.

Chapter 12 (Part VI) summarizes the main findings of this study, discusses current limitations, and proposes future perspectives. Additional information complementing the ideas and discussions put-forward in this thesis are presented in the Appendix.

Part II

INDENTATION ANALYSIS

Chapter 2

Instrumented Indentation on Cohesive-Frictional Materials

The use of indentation will play a prominent role in our multi-scale investigation of natural composite materials. Here, we introduce the experimental approach and present the theoretical background that will allow us to transform indentation data into meaningful mechanical properties. The advent of instrumented indentation techniques has provided the mechanics community with an unprecedented opportunity to explore mechanical properties of materials at multiple length and force scales. Indeed, thanks to the self-similarity possible in indentation tests[1] and the resulting mechanical response of the materials system, one single experimental technique is able to provide access to mechanical properties of materials from the nanoscale to the macroscale. Most of the developments in the last decade concentrated on indentation testing of metals, which are atomically cohesive materials. In contrast, natural composites, like cement-based materials, soils, bones, wood, etc., exhibit a pronounced cohesive-frictional behavior that will play an important role in our investigation. Starting from a dimensional analysis of the physical quantities involved in indentation testing, the aim of this chapter is to review recent developments in the field of indentation analysis, and to identify the tools required

[1] In the case of pyramidal or conical indentation, the ratio of the area of contact to the depth of indentation is independent of the magnitude of the applied load. This leads to a property of the indentation test called geometric similarity. For geometrically similar indentations the stresses and strain within the material are independent of the depth of penetration or load application. This is discussed in detail in Section 2.2 of this chapter.

to translate indentation data of cohesive-frictional materials into mechanical properties. These tools will be validated in Chapter 3 for a particular cohesive-frictional material: bulk metallic glass. In this chapter, we restrict ourselves to the analysis of indentations on homogeneous materials. The heterogeneous nature of natural composite materials will be addressed in Chapter 5.

2.1 Introduction

It has long been hypothesized that the localized contact response measured by an instrumented indentation experiment can serve to characterize the mechanical properties of materials as quantitatively as conventional testing techniques such as uniaxial compression and tension. This experimental approach provides a continuous record of the variation of the depth of penetration, h, as a function of the prescribed indentation load, P, into the indented specimen surface. Advances in hardware and software control currently enable maximum penetration depths on the nanometer scale, such that nanoscale instrumented indentation provides a convenient, relatively non-destructive means to evaluate the fundamental mechanical response (stiffness, strength, creep, etc.) of small material volumes of a bulk, thin film, or composite material. Commercially available indenters accommodate various indenter geometries, including sharp pyramidal, conical or spherical probes, so that elastic and inelastic mechanical properties can be estimated at any scale within the limits defined by the indenter dimensions and maximum penetration depth, as well as by the load and depth resolution/maxima of the specific instrument. Thus, instrumented indentation is a versatile tool for material characterization, particularly at scales where classical mechanical tests based on volume-averaged stresses are inadequate [50, 185, 98].

2.1.1 Historical Background

The very concept of 'hardness' can be found as early as in the 18th century in the works of several prominent mineralogists, Réaumur (1683–1757), Haüy (1743–1822) and Mohs (1773–1839) [245][2]. These scientists, however, were not fundamentally concerned with the hardness as

[2]The French scientist René Réaumur (1683–1757), was named by Williams [245] as the father of hardness measurements. The French mineralogist, René-Just Haüy is one of the founders of the science of crystallography. In 1812 the Mohs scale of mineral hardness was devised by the German mineralogist Frederich Mohs (1773–1839),

a mechanical property, but introduced 'hardness' as a means for the classification of materials and standardization of products. The application of indentation methods to assess material properties is more recent and can be traced back to the work of the Swedish metallurgist Brinell (1849–1925). Pushing a small sphere of hardened steel or tungsten carbide against the surface of the specimen, Brinell empirically correlated the shape of the resulting permanent impression (indentation) with the strength of metal alloys (steels). The first accessible work of this pioneering approach of the Swedish engineer can be found in a 1900 International congress in Paris [36]. The merits of Brinell's proposal were quickly appreciated by contemporaries: Meyer, O'Neill, and later Tabor [223] suggested empirical relations to transform indentation data into meaningful mechanical properties. These early studies concentrated on the evaluation of hardness of metals and on the link of hardness with strength properties. Hardness is defined as the maximum applied force divided by the projected residual imprint left on the material. Hardness measurements, therefore, do not require a continuous measurement of the indentation depth. In contrast, as we will see later on, an estimate of the elastic properties of the material requires information on the depth response of the material to the indentation force. More recently, due to progress in hardware and software control, depth sensing techniques were introduced that allow a continuous monitoring of the displacement of the indenter into the specimen surface during both loading and unloading. Depth sensing indentation techniques have been conceptualized by Tabor and coworkers [216, 223] and its implementation down to the nanoscale appears to have developed first in the former Soviet Union from the mid 1950s on throughout the 1970s. This instrumented indentation approach received considerable attention world-wide, ever since Doerner and Nix [70] and Oliver and Pharr [184] in the late 1980s and early 1990s, also identified this technique for analysis and estimation of mechanical properties of materials such as microelectronic thin films for which few other experimental approaches were available. While the chronology of events of discovery may still be in debate[3], there is little doubt, at least as far as the elastic behavior is concerned, that it is the Hertz-type contact

who selected ten common minerals and attributed hardness values from 1 to 10, 1 being Talcum Powder, 10 being diamond. The scale is not a linear scale, but somewhat arbitrary, and the hardness has no dimension. For a review of early contributions (prior to 1940) see Ref. [245] and references therein. For more recent reviews of modern indentation techniques and analysis, see Refs. [50,185,31].

[3]The chronology of events of discovery of depth-sensing indentation and indentation analysis is discussed by Borodich in several publications (see for instance Ref. [31]).

problem that forms much of the theoretical background of modern indentation analysis. The analytical solution of Heinrich Hertz (1882) [114] of the linear elastic contact problem of two spherical surfaces (with different radii and elastic constants) provides a means of evaluating the contact area of indentation, and forms the basis of much experimental and theoretical work in indentation analysis based on contact mechanics. In 1885, Boussinesq published a solution for the problem of contact between a solid of revolution and an elastic continuum [33], of which the flat punch solution is the best known. In the first half of the 20th century, the elastic solutions were extended to other shapes of indenters by Love [157], Galin [89], and Harding and Sneddon [107]. Subsequently, Sneddon [213] derived general relationships among load, displacement and contact area for a punch of arbitrary axisymmetric shape. Much of the later developments [137] rely on these general solutions and solution methods.

Incorporating plasticity phenomena in the indentation analysis is a much more complex problem. The nonlinear nature of the constitutive relations, as well as the increased number of material properties required to describe material behavior, complicate the derivation of analytical solutions. As a result, much of our knowledge of the importance of plasticity in indenter contact problems comes from experimentation, and more recently through finite element simulations. Various researchers have proposed semi-analytical procedures in which the experimental $P-h$ response is used to calculate elastic properties such as the Young's modulus E, pseudo-properties characterizing resistance to deformation such as hardness H, and plastic properties such as the yield strength σ_y and the strain hardening exponent n [70, 184, 98]. Experimental data has demonstrated that analysis of indentation response via elastic and rigid-plastic solutions provides reasonable estimates of the elastic modulus and hardness of the indented material, provided that the contact area is measured or calculated accurately [70, 184]. The validity of these concepts in the case of cohesive-frictional materials is reviewed below.

2.1.2 Indentation Test: Measured Quantities

An indentation test consists of establishing contact between a material of known properties, i.e. the indenter (typically diamond), and the indented material for which the mechanical properties are of interest. By monitoring the mechanical response of the system, i.e. the $P-h$ curve, and by applying a mechanical model to the data, the unknown mechanical properties of

the indented material are extracted. The technique has its origins in the original Mohs scale of mineral hardness developed to rank materials based on their ability to leave a permanent scratch on the surface of each other. The approach is still in use today, but the scale of observation has shifted by several orders of magnitude, from the macroscopic scale to the nanoscale. The ability of currently available equipment allows displacements to be monitored down to the Angstrom scale and forces down to nanoNewtons.

A typical indentation test consists of (at least) a loading and an unloading phase. The type of data presented in Fig. 2-1 is obtained when an indenter is brought in contact with the flat surface of a specimen under a constant loading (or displacement) rate. Both the loading and the indentation depth are recorded at each load increment. During loading, the material immediately below the rigid indenter undergoes elastoplastic deformation, whereas the material further away from the contact zone deforms elastically. Thus, a portion of the energy that is provided to the system is either stored in elastic deformation or dissipated by plastic deformation in the material below the indenter and along surfaces of discontinuity. Following the holding of load at maximum force $P_{\max}$ the load is steadily decreased until complete unloading. During unloading, the load-displacement follows a different path than during loading, until, at zero load, a permanent impression is left on the surface. Naturally, if only elastic deformation is imposed, the loading and unloading paths retrace. During this unloading process, the elastic energy is recovered and the contact stiffness, $S_{\max} = \frac{dP}{dh}|_{h_{\max}}$, gives a measure of the material elastic response. Often, a holding period at maximum load, during which the load is maintained approximately constant, is also employed and an increase of the indentation depth is indicative of some creep behavior of the material.

Provided the calibrations are performed properly and the factors affecting force and displacement are controlled, the $P - h$ response is recorded within the accuracies defined by the indentation equipment (see Tab. 3.1); typically load resolution in 100 nN and depth resolution in 0.1nm. Except for the projected area of contact, A_c, all measured quantities are directly obtained from the $P - h$ curves: the maximum applied force, $P_{\max}$, with the corresponding maximum depth $h_{\max}$ for the loading phase, and the unloading indentation stiffness $S_{\max}$, with the residual indentation depth h_f for the unloading phase. The contact area A_c at $P_{\max}$ is also extrapolated from $h_{\max}$. These measured quantities allow one to determine the hardness H and

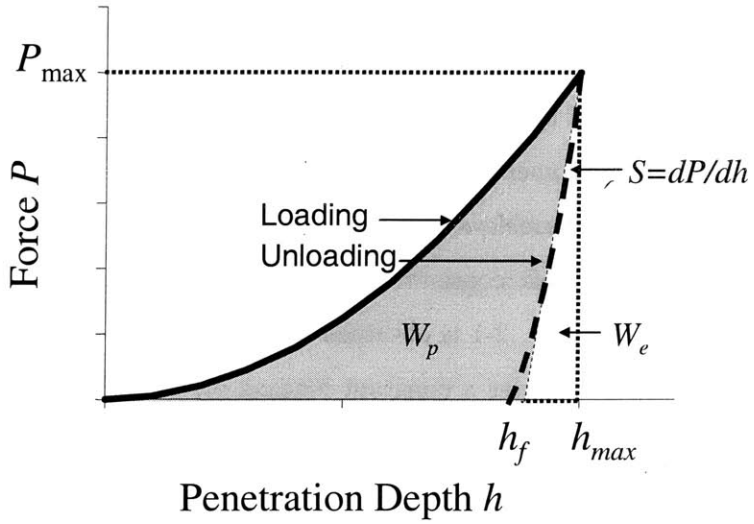

Figure 2-1: $P-h$ response of an indentation test. Measured quantities include the maximum load, $P_{\max}$, the maximum depth, $h_{\max}$, the residual depth, h_f, the contact stiffness at maximum load, $S_{\max} = \frac{dP}{dh}|_{h_{\max}}$, the plastic indentation work, W_p, and the elastic indentation work, W_e.

the indentation modulus M of the indented material from:

$$H \stackrel{def}{=} \frac{P_{\max}}{A_c} \tag{2.1}$$

$$S \stackrel{def}{=} \frac{2}{\sqrt{\pi}} M \sqrt{A_c} \tag{2.2}$$

Definition (2.2) is also known as Bulychev–Alekhin–Shoroshorov (BASh) equation [30], or Sneddon's solution [213].

Two alternative quantities that can be determined from the indentation curves, are the total work provided to the system W_t, and the elastic recoverable energy W_e (Fig. 2-1):

$$W_t = \int_{h=0}^{h_{\max}} P_{loading}(h)dh \; ; \; W_e = \int_{h=h_f}^{h_{\max}} P_{unloading}(h)dh \tag{2.3}$$

The ratios H/M, W_e/W_t or $h_f/h_{\max}$ all quantify the relative influence of elastic and plastic deformation in an indentation test. However, as we will see below, it is important to note that

the measured quantities H and M (as well as W_t and W_e) are not material properties, but rather snapshots of the strength and stiffness properties of the indented material system. In the following sections we investigate the very nature of the hardness (see Eq. (2.1)) and the indentation modulus (see Eq. (2.2)); and we propose ways to link them to true mechanical properties of cohesive-frictional materials. In other words, we aim at presenting the theoretical tools that allow us to link H and M to strength and elastic material properties of the indented material.

2.2 Self-Similarity of the Indentation Test

2.2.1 Indenter Geometries

Spherical, conical or pyramidal indenters are the most common shapes used in practice. Spherical indenters provide a smooth transition between elastic to elastic-plastic contact [132] and are commonly used for larger scales as the evolution of the contact area with depth is rapidly evolving. In this thesis, however, we are primarily concerned with sharp indentation testing with conical or pyramidal indenters. The Vickers indenter is a four-sided pyramid with a semi-vertical angle of 68° (Fig. 2-2). The Berkovich indenter which is commonly employed for small scale testing it is a three-sided pyramid and was constructed with a semi-vertical angle of 65.3°, such as to maintain the same area-to-depth ratio as the Vickers indenter. In contrast to the four-sided pyramids, Berkovich indenters have the advantage that their three edges are more easily manufactured to meet at a point. A cube corner indenter has the same geometry as a Berkovich indenter but with a sharper face angle of 90°.

2.2.2 Self-Similarity Properties

One key feature of the analysis of pyramidal or conical indentation is the self-similarity of Hertz-type contact problems. The conditions under which frictionless Hertz type contact problems possess classical self-similarity were stated by Borodich (see Ref. [30]); and include:

1. The shape of the indenter is described by a homogeneous function whose degree is greater or equal to unity. Using a Cartesian coordinate system $Ox_1x_2x_3$ whose origin O is at

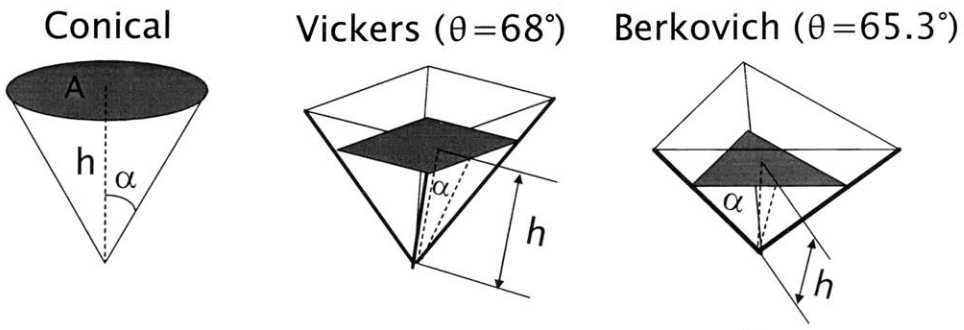

$A = \pi h^2 \tan^2 \alpha$

$A = 4h^2 \tan^2 \alpha$
$A = 24.5h^2$

$A = 3\sqrt{3}h^2 \tan^2 \alpha$
$A = 24.56h^2$

Figure 2-2: Geometrical characteristics of conical, Vickers, and Berkovich indenters.

the indenter tip and x_3 is the orientation of the indentation, the shape of the indenter (height) is defined by:

$$f(\lambda x_1, \lambda x_2) = \lambda^d f(x_1, x_2) \tag{2.4}$$

for arbitrary positive λ. Here d is the degree of the homogeneous function f; in particular $d = 1$ for a cone and $d = 2$ for the elliptic paraboloid considered by Hertz. Such axisymmetric indenters can be described by monomial functions of the form (first introduced by Galin, according to Borodich and Keer [31]):

$$f = f(x_1 = r\cos\theta, x_2 = r\sin\theta) = Br^d \tag{2.5}$$

where B is the shape function of the indenter at unit radius. For a conical indenter ($d = 1$), having a semi-vertical angle θ; $B = \cot\theta$. For a spherical indenter of radius R, $d = 2$ and $B = 1/(2R)$. The previous expression was recently extended to indenters of non-axi-symmetric shape, such as pyramidal indenters that are frequently employed in depth-sensing indentation tests [30]:

$$f = B(\phi)\, r^d \tag{2.6}$$

where $B(\phi)$ describes the height of the indenter at a point $(\phi, r = 1)$. For a three-sided pyramid, $d = 1$, and making use of the triple symmetry:

$$B(\alpha) = \cot\vartheta \sin(\pi/6 + \phi) \tag{2.7}$$

where ϑ is the angle in vertical cross-sections. For a Berkovich indenter, having a face angle of 115.13°, $\vartheta = 65.3°$; and for a cube corner indenter of 90° face angle, $\vartheta = 35.26°$ (see Tab. 2.1).

2. The operators of constitutive relations F for the indented material is a homogeneous function of degree κ with respect to the components of the strain tensor $\boldsymbol{\varepsilon}$ (respectively the strain rate-tensor $\mathbf{d}$):

$$F(\lambda\boldsymbol{\varepsilon}) = \lambda^{\kappa} F(\boldsymbol{\varepsilon}) \tag{2.8}$$

Evidently, a linear elastic law satisfies this relation since $\kappa = 1$; as does any nonlinear secant elastic formulation of the form $\boldsymbol{\sigma} = \mathbb{C}(\boldsymbol{\varepsilon}) : \boldsymbol{\varepsilon}$ for which the secant elastic stiffness tensor satisfies:

$$\mathbb{C}(\lambda\boldsymbol{\varepsilon}) = \lambda^{\kappa-1}\mathbb{C}(\boldsymbol{\varepsilon}) \tag{2.9}$$

A similar reasoning applies to the dissipation function $\pi(\lambda\mathbf{d}) = \lambda^{\kappa}\pi(\mathbf{d})$ applied in yield design solutions, as we will see in Section 2.3.2.

Then provided the homogeneity of material properties and that the stress-strain relation remains the same for any depth of indentation, the whole load-displacement curve in a depth-sensing test can be scaled by [30]:

$$\frac{P}{P_1} = \left(\frac{h}{h_1}\right)^{\frac{2+\kappa(d-1)}{d}} ; \frac{h}{h_1} = \left(\frac{A_c}{A_1}\right)^{d/2} \tag{2.10}$$

where A_c is the projected contact area, which appears to be not affected by the constitutive relation. In return, the hardness is scaled with the indentation depth by:

$$\frac{H}{H_1} = \left(\frac{h}{h_1}\right)^{\frac{\kappa(d-1)}{d}} \tag{2.11}$$

	Projected Area	Semi-vertical angle, ϑ	Equivalent cone angle θ
Berkovich	$3\sqrt{3}h^2\tan^2\vartheta$	65.3°	70.32°
Vickers	$4h^2\tan^2\vartheta$	68.0°	70.32°
Cube corner	$3\sqrt{3}h^2\tan^2\vartheta$	35.26°	42.28°
Cone	$\pi h^2\tan^2\vartheta$	θ	θ

Table 2.1: Geometrical relations between projected area and equivalent half-apex cone angle.

We note that the load-displacement relation is scaled by $P \propto h^2$ for conical and ideal (sharp) pyramidal indentation, for which $d = 1$, irrespective of the constitutive relation. As a consequence, the hardness is a constant over the loading process, which justifies Eq. (2.1). On the other hand, the constitutive relation power κ significantly affects the load-displacement relation for spherical or elliptic paraboloid indenter geometries, for which $d = 2$, and must be known in advance in order to analyze the load-displacement curve. For instance, for an elastic behavior, $P \propto h$ (which corresponds to $d \to \infty$) is indicative of flat indentation, and is described by Boussinesq's solution; $P \propto h^{3/2}$ is indicative of linear elastic spherical or paraboloids of revolution [213].

Finally, given the same $d = 1$ degree of the homogeneous shape function of three-sided pyramidal (Berkovich, corner cube) and conical indentation, it is common practice to consider, instead of the original three-dimensional pyramidal shape, an equivalent cone of revolution in sharp indentation analysis, such that the projected contact area with respect to indentation depth of the cone is the same as that for the real indenter, i.e. from Eq. (2.10):

$$A(h) = C_1 h^2 = \pi (h\tan\theta)^2 \Longrightarrow \tan\theta = \sqrt{\frac{C_1}{\pi}} \tag{2.12}$$

where C_1 is a constant characterizing the specific pyramidal indenter, and θ is the equivalent semi-apex cone angle (see Tab. 2.1). Using Eq. (2.12), the flat Berkovich indenter ($\vartheta = 65.3°$), for which $C_1 = 24.56$, can be assimilated to an equivalent cone of semi-apex angle $\theta = 70.32°$; and a cube corner indenter ($\vartheta = 35.26°; C_1 = 2.598$) to one with $\theta = 42.28°$. The area-to-depth relations for different sharp indenter shapes are summarized in Tab. 2.1.

SCANNING PROBE MICROSCOPY 'SPM'

Scanning probe microscopy is a technology for imaging and measuring surfaces on a fine scale, down to the level of molecules and groups of atoms. In this type of imaging, a cantilever sharp probe tip is moved in a raster scan pattern across a sample surface using a three-axis piezo positioner. The X-Y piezo tube moves the tip across the surface with very high resolution, while the Z-axis position is varied using a feedback loop. This feedback loop is controlled by some type of detector (typically a force detector) to measure spatial information about the sample (in our case height). Typical types of detectors include chemical, electrical, mechanical, thermal etc. and typical spatial information would be elasticity, capacitance, thermal characteristics, chemistry, but most often, height. In such a fashion a surface topology is obtained. Equipment that employ mechanical force detectors to measure the interaction force between the tip and investigated surface are the most commonly employed in practice and are often referred to by the name, Atomic Force Microscopes or simply 'AFM'. The resulting images can be viewed in several ways:

Topography images show change in elevation on the sample using a range of colors, light being high and dark being low.
Gradient images show change in slope on the sample using a range of colors.

Both indenters used in this study are capable of Scanning Probe microscopy.

Table 2.2: Scanning Probe Microscopy 'SPM' techniques.

2.2.3 Imperfect Indenter Geometry

In practice, the area-to-depth relations $A(h)$ often deviate from the ideal geometry parameters given in Tab. 2.1, as most indenters end in a spherical cup that has a radius R on the order of $R = 50 - 250$ nm. The indenter tip radius used in this study were ensured by the manufacturer to be in the range of $50 - 100$ nm. To account for non-ideal geometry (see Fig. 2-3) it is necessary to apply a correction factor to the ideal area-to-depth relations of Tab. 2.1. This correction factor can be found directly by SEM-AFM investigations (see Tabs. 2.2 and 2.3 for details) of the exact indenter tip geometry.

The approach is however time consuming and an indirect method is commonly employed in practice, by means of a corrected area function of the form:

$$A(h) = C_1 h^2 + C_2 h + C_3 h^{1/2} + C_4 h^{1/4} + ... \tag{2.13}$$

SCANNING ELECTRON MICROSCOPY 'SEM'
Scanning electron micrographs are direct ways to visualize materials microstructures. From a simplistic point of view they provide the tools for us to observe an invisible object (with naked eye) in a stereographic fashion with a magnified scale. SEM produces and scan a finely-focused beam of electrons across the specimen and measures signals resulting from the electron beam-specimen interaction. Common signals employed in SEM analysis include secondary electrons (SE) for imaging surface topology; backscatter electrons (BE) for highlighting compositional differences; and X-rays for determining elemental composition and imaging element spatial distribution. Images from an SEM are monochrome since they reflect the electron or X-ray flux resulting from the beam-specimen interaction. BE and X-ray modes are most useful for quantitative purposes.

Table 2.3: Details of Scanning Electron Microscopy, 'SEM', imaging technique.

where C_1 is the area-to-depth constant of the perfect pyramidal indenter (i.e. $C_1 = 24.6$ for Berkovich and $C_1 = 2.6$ for cube corner), while the constants $C_i\,(i = 2, 3, ...)$ are constants used for accounting for the curvature. These constants are determined from indentation tests on a reference material of known elastic properties (indentation modulus M), typically fused quartz. Assuming that the elastic properties do not change with the indentation depth, several indents at different load levels are performed, and using the BASh formula Eq. (2.2) the actual area-to-depth relation is determined and fitted to the function shown in Eq. (2.13). It is interesting to note that imperfect indenter geometry plays a significant role only for indentation depths comparable to the indenter radius, $h/R \sim 1$ The error tends to get very small as the indentation depth increases and the correction seems unnecessary.

2.3 Indentation Hardness

From its very start, the field of indentation technique concentrated on hardness measurements, a fundamental quantity which constitutes the vast majority of metallurgical tests. Despite its extensive long standing use, an exact physical interpretation is still a matter of debate [49, 50]. For a wide variety of metals, a proportionality of hardness to yield strength was found experimentally, on the order of $H/\sigma_y = 3$ [223]. This rule-of-thumb [206], however, is restricted to cohesive frictionless materials, and cannot be extrapolated for cohesive-frictional materials: Several researchers report hardness-to-compressive strength ratios for frictional materials on

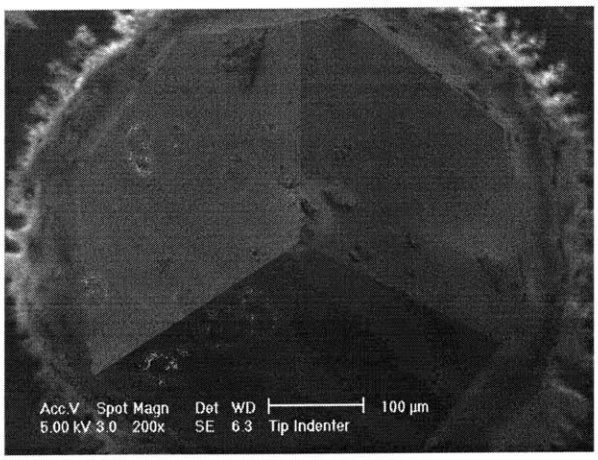

Figure 2-3: An SEM image, in the secondary electron mode (SE) – see Tab. 2.3, of a Cube Corner indenter showing the imperfect geometry of the tip. Dust particles on the surface are also visible.

the order of $H/\Sigma_c \simeq 20 - 30$ [125,136,59], which highlights the effect of internal friction on the hardness of cohesive-frictional materials. We start our presentation with a dimensional analysis of the indentation test and present a limit analysis approach that can provide, under certain restrictions, a link between hardness H and the fundamental mechanical properties characterizing the strength response of cohesive-frictional materials: cohesion c and friction angle φ.

2.3.1 Dimensional Analysis

To motivate the forthcoming developments, we consider a three-dimensional, rigid, conical indenter of a given half-angle θ, indenting normally into a homogeneous elastic perfectly plastic cohesive-frictional material half-space. The origin (O) of the Cartesian coordinate system is put at the point of the initial contact between the conical indenter and the half-space (Fig. 2-4). Conical indentation leads to geometrically self-similar indentation states. That is, for a given half-angle, the average pressure below the indenter is independent of the indentation load and the true contact area. Using the projected current contact area, which is proportional to the true contact area for geometrically self-similar indenters (i.e., $A_M = A_c/\sin\theta$ for conical

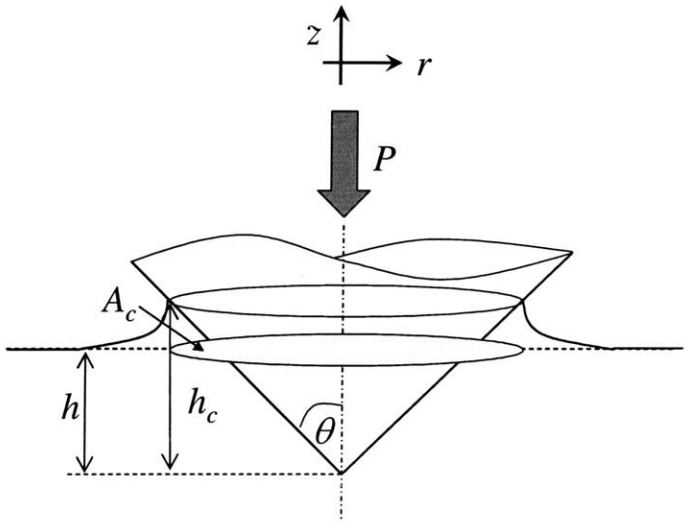

Figure 2-4: Schematic of a conical indentation test.

indenters), yields the classical definition of hardness H, presented in Eq. (2.1), which can be determined at any point along the $P - h$ curve for which the contact area is known:

$$H \overset{def}{=} \frac{P_1}{A_1} = \frac{P_2}{A_2} = ... = \frac{P}{A_c} \tag{2.14}$$

where $A_c = \pi a^2$ is the projected contact area, $a = h_c \tan\theta$ is the contact radius, and h_c is the contact depth (Fig. 2-4).

The main problem in the analysis is that the contact surface A_c (respectively the contact depth h_c) is not known *a priori*, but is a solution of a boundary value problem. In fact, the rigid displacement h of the indenter is generally not the contact depth, h_c (Fig. 2-4), corresponding to the maximum projected contact surface of the indenter with the deformed half-space surface: $h_c/h < 1$ corresponds to what is referred to, in the indentation literature, as sink-in; and $h_c/h > 1$ as pile-up (Fig. 2-4). Hence, there are *a priori* two independent measurements to be carried out: the force P and the projected contact surface A_c. It is instructive to perform

a dimensional analysis[4]: The two dependent quantities of interest that define the hardness (2.1), force P and contact area A_c (respectively the contact depth h_c), depend on the material properties (Young's modulus E, Poisson's ratio ν, cohesion c, friction angle φ), the indenter geometry (which in the case of conical indentation reduces to the semi-apex angle θ), and the indentation depth h:

$$P = f_L(E, \nu, c, \varphi, \theta, h) \tag{2.15a}$$

$$A_c = g(E, \nu, c, \varphi, \theta, h) \tag{2.15b}$$

Among the six governing parameters $E, \nu, c, \varphi, \theta$, and h two of them, namely c and h have independent dimensions. From a straightforward application of dimensional analysis (or more precisely the Pi-Theorem [12]) to relations (2.15), the two dimensionless relations are readily found:

$$\frac{P}{ch^2} = \Pi_\alpha\left(\frac{E}{c}, \nu, \varphi, \theta\right) \tag{2.16a}$$

$$\frac{A_c}{h^2} = \Pi_\beta\left(\frac{E}{c}, \nu, \varphi, \theta\right) \tag{2.16b}$$

Eqs. (2.16a) and (2.16b) demonstrate that the force of the indenter P and the contact area A_c are, for conical indenters, proportional to the square of indenter displacement h; and that the dimensionless numbers $\frac{P}{ch^2}$ and $\frac{A_c}{h^2}$ are independent of the indentation depth h. In fact, for a given semi-apex angle θ, they are only functions of three dimensionless material characteristics, $\frac{E}{c}, \nu, \varphi$. Hence, any deviation from the h^2–scaling relations would imply the presence of a length-scale that has not been considered in the sets (2.15) of independent quantities.

Furthermore, Eqs. (2.16a) and (2.16b) define a unique third dimensionless relation, the hardness-to-cohesion ratio as a function of the stiffness-to-cohesion ratio and the Poisson's ratio, the friction angle and the semi-apex angle:

$$\frac{H}{c} = \frac{\Pi_\alpha}{\Pi_\beta} = \mathcal{H}\left(\frac{E}{c}, \nu, \varphi, \theta\right) \tag{2.17}$$

[4]The dimensional analysis presented here is inspired by the one presented in a review paper by Cheng and Cheng, 2004 [50]. In contrast to Cheng and Cheng's presentation, our focus will be on the indentation response of cohesive-frictional materials.

We readily find that the hardness is independent of the depth of indentation h, which demonstrates the self-similarity of the problem as recognized by its definition (2.14). In turn, the hardness of a material, or the average pressure under the indenter tip, or its resistance to indentation, stems *a priori* from a combination of elastic, plastic and geometrical contributions[5]. Equation (2.17) has been extensively studied for elasto-plastic cohesive materials ($\varphi = 0$), with and without strain hardening (see review in Ref. [50]); in the case of a power-law strain hardening material, it suffices to add the power exponent n to the set of independent parameters on the right-hand-side of relations (2.15)). In particular, it has been shown, that the $H/c-$ratio for cohesive materials, for which $c/E \to 0$, comes close to Tabor's suggestion (noting that $\sigma_y = 2c$ for a Tresca material):

$$\frac{H}{\sigma_y} = \frac{H}{2c} = \frac{1}{2}\mathcal{H}\left(\frac{c}{E} \to 0, \varphi = 0, \theta\right) \simeq 2.8 \tag{2.18}$$

It is worthwhile to note that $c/E \to 0$ comes close to the assumption of yield design approaches which can be found early on in the indentation literature. For instance, Lockett [156] and Chitkara [51] developed yield design solutions for conical indentations in rigid-plastic solids. Later developments attempted to incorporate the elastic contribution into the model. In 1945, Bishop et al. [28] suggested that the stress distribution under a conical indenter can be approximated by that of a spherical cavity. Using this approximated stress field and assuming that the contact area was essentially the geometric contact projection, Johnson [132] derived the pressure distribution beneath a conical indenter of angle θ:

$$\frac{H}{\sigma_y} = \frac{2}{3}\left[1 + \ln\left(\frac{\cot(\theta)}{12c(1-\nu)}\frac{E}{2c} + \frac{2}{3}\left(\frac{1-2\nu}{1-\nu}\right)\right)\right] \tag{2.19}$$

Equation (2.19), which is commonly referred to as the 'cavity expansion model', is often used to analyze indentation data in elastic-perfectly plastic solids, though questions remain about the extend of its validity. More recently, Cheng and coworkers [46,47] showed by means of finite element simulations for a large range of material properties that H/σ_y is not a constant, but decreases with the strength-to-stiffness ratio σ_y/E (and to a lesser extent with the Poisson's ratio ν). Figure 2-5 displays the different results. However, for most metals for which $0.001 \leq$

[5] An additional contribution may come from the friction between indenter and indented material, which is not considered in this investigation.

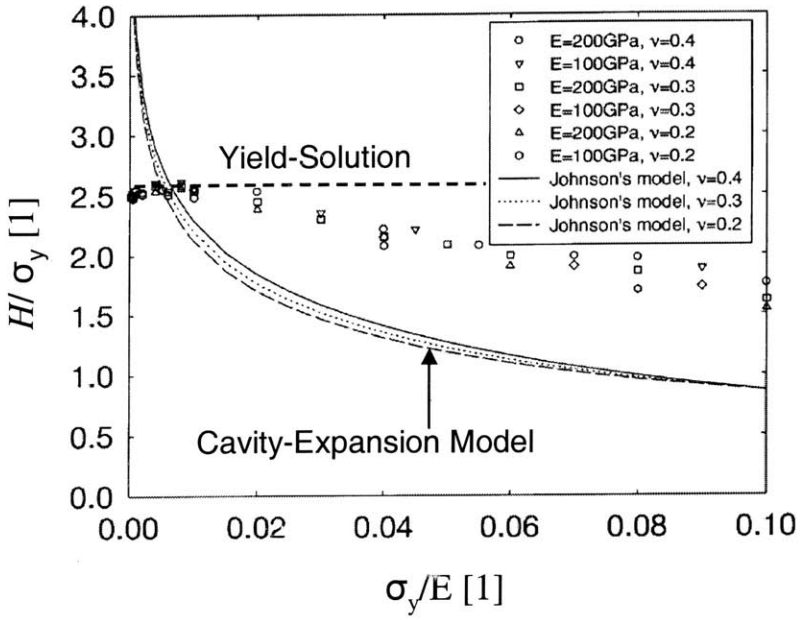

Figure 2-5: Finite element simulations of Cheng et al. [50] of frictionless conical indentation ($\theta = 68°$) on an elastic/Von Mises half-space. The dimensionless parameter H/σ_y is plotted against σ_y/E for different Poisson's ratios and Young's moduli. The cavity expansion model of Johnson [132] (see Eq. 2.19), and the rigid-plastic solution of Lockett [156] are also displayed for comparison.

$\sigma_y/E \leq 0.01$ [8], H/σ_y is between 2.5 and 2.6 [223, 132]; thus very close to the rigid-plastic solution of Lockett [156], which seems relevant for $\sigma_y/E < 0.01$.

It becomes apparent that yield design approaches are well suited for characterizing the hardness response of cohesive materials provided that the strength-to-stiffness ratio is very small. The same should hold true for cohesive-frictional materials. Indeed, for most geomaterials, for which typically $c/E \sim 10^{-3} - 10^{-6}$ it is most likely that yield design solutions are highly relevant; i.e. solutions of the form:

$$\frac{H}{c} = \mathcal{H}(\varphi, \theta) \tag{2.20}$$

However, a limit analysis result of the form (2.20) is still missing for conical indentation in cohesive-frictional materials, since –as Johnson notes in his classical book [132]– 'problems of axi-symmetrical plastic flow cannot, in general, be solved by the method of characteristics (slip

lines) as in plane strain (page 168)'. Indeed, to our knowledge, the only analytical slip-line solutions we found for cohesive-frictional materials in axi-symmetrical conditions are for flat punch indentation problems (the circular foundation problem), for which $\theta = \pi/2$ [121, 165]. Of course, like for pure cohesive materials, the finite-element method has been employed for the inverse analysis of indentation load vs. indentation depth curves for some particular cohesive-frictional materials, such as metallic glass [236]. Beside questions concerning the uniqueness of this inverse problem (see e.g., Ref. [50]), finite element analysis are computationally too intensive to be used for day-to-day applications in instrumented indentation analysis. Hence, a solution for conical indentation is highly desirable as a first engineering approach to the assessment of the cohesion and friction angle of cohesive-frictional materials.

2.3.2 Limit Analysis of Cohesive-Frictional Materials

In this section[6] we present the formulation of the indentation problem within the framework of limit analysis. To this end, we consider an indentation test of a rigid conical indenter into an infinite half-space oriented in the $-z$ direction (Fig. 2-4). The indenter is at an indentation depth h, the contact area A_c is assumed to be known, and a force P is applied. The work rate provided from the outside to the (half-space material) system is:

$$\delta W = P\mathring{h} = \int_{A_M} \underline{T}(\underline{n}) \cdot \underline{U}\, da \tag{2.21}$$

where $\mathring{h}$ is the rate of indentation, $A_M = A_c/\sin\theta$ is the contact area of the cone mantel with the material (A_c being the projection of this surface on the $z-$axis); $\underline{T}(\underline{n}) = \boldsymbol{\sigma} \cdot \underline{n}$ is the stress vector on A_M oriented by the unit outward normal $\underline{n}$ (positive outward to the material domain; i.e. in a cylinder coordinate frame $\underline{n} = -\cos\theta\, \underline{e}_r + \sin\theta\, \underline{e}_z$); and $\underline{U}$ is the velocity field of the material on A_M.

In elasto-plastic problems, a part of the external work rate shown in Eq. (2.21) is stored into recoverable elastic energy (including hardening) into the material system. In contrast, limit analysis is based on the assumption that a material system, at plastic collapse, has exhausted

[6] The limit analysis results presented in this and the next sections, which will lead to the proposition of a novel dual indentation technique, were achieved in co-operation with François Ganneau, during his Master Thesis at M.I.T. [93]. The results are also presented in a co-authored paper [92].

in response to the prescribed force P the capacities (i) to develop stress fields that are both statically compatible (i.e. in equilibrium) with the external loading and compatible with the local strength domain of the constitutive materials; and (ii) to store the externally supplied work rate (Eq. (2.21)) into recoverable elastic energy. As a consequence, the work rate δW is entirely dissipated in the material bulk and along surfaces of discontinuity; hence from an application of the generalized divergence theorem to Eq. (2.21):[7]

$$\delta W = \int_{\Omega} \pi(\mathbf{d})\, d\Omega + \int_{\Gamma} \pi([[\underline{U}]])\, d\Gamma \tag{2.22}$$

where $\pi(\mathbf{d}) = \sup \boldsymbol{\sigma} : \mathbf{d}$ and $\pi([[\underline{U}]]) = \sup \underline{T} \cdot [[\underline{U}]]$ is the maximum dissipation capacity the material can develop in the material bulk and along surfaces of discontinuity for the solution fields $(\boldsymbol{\sigma},\underline{U})$. The solution stress field $\boldsymbol{\sigma}$ is statically and plastically admissible, satisfying:

$$\boldsymbol{\sigma} = {}^{t}\boldsymbol{\sigma};\ \operatorname{div}\boldsymbol{\sigma} = 0;\ [[\underline{T}]] = [[\boldsymbol{\sigma} \cdot \underline{n}]] = 0 \tag{2.23a}$$

$$f(\boldsymbol{\sigma}) \leq 0;\ f(\underline{T}) \leq 0 \tag{2.23b}$$

where superscript t stands for transpose; and $f(\boldsymbol{\sigma})$ and $f(\underline{T})$ are the yield functions defining the strength domain of the material system in continuous material sub-domains and on surfaces of discontinuity, respectively, while $\mathbf{d}$ is the solution strain rate field in continuous material sub-domains, and $[[\underline{U}]]$ is the velocity jump over surfaces of discontinuity Γ, which are kinematically compatible with the velocity field $\underline{U}$, and compatible with the plastic flow rule of the material:

$$\mathbf{d} = \frac{1}{2}\left(\operatorname{grad}\underline{U} + {}^{t}\operatorname{grad}\underline{U}\right) = \mathring{\lambda}\frac{\partial f}{\partial \boldsymbol{\sigma}} \tag{2.24a}$$

$$[[\underline{U}]] = \underline{U}^{+} - \underline{U}^{-} = \mathring{\lambda}\frac{\partial f}{\partial \underline{T}} \tag{2.24b}$$

Here $\mathring{\lambda}$ stands for the plastic multiplier. Provided that $(\boldsymbol{\sigma},\underline{U})$ are related through Eq. (2.24) by

[7] For completeness, the generalized divergence theorem reads:

$$\int_{\partial\Omega} \mathbf{f} \cdot \underline{n}\, da = \int_{\Omega} \operatorname{div}\mathbf{f}\, d\Omega + \int_{\Gamma} [[\mathbf{f}]] \cdot \underline{n}\, d\Gamma$$

where Ω is the domain of boundary $\partial\Omega$ and $[[\mathbf{f}]] = \mathbf{f}^{+} - \mathbf{f}^{-}$ denotes the jump of $\mathbf{f}$ over the surface of discontinuity Γ.

the normality rule of plastic flow, the dissipation functions are unique functions of the strain rate (respectively velocity jump) only. For instance, for a Mohr-Coulomb material, for which the yield function is given by:

$$f(\boldsymbol{\sigma}) = \sigma_I(1+\sin\varphi) - \sigma_{III}(1-\sin\varphi) - 2c\cos\varphi \leq 0 \tag{2.25a}$$

$$f(\underline{T}) = |\underline{t}\cdot\underline{T}(\underline{n})| + \tan\varphi\,(\underline{n}\cdot\underline{T}(\underline{n})) - c \leq 0 \tag{2.25b}$$

the volume dissipation function $\pi(\mathbf{d})$ is [204, 232]:

$$\pi(\mathbf{d}) = \left\{ \begin{array}{c} \rho\,\mathrm{tr}\,\mathbf{d} \text{ if } \mathrm{tr}\,\mathbf{d} \geq \sin\varphi\,(|d_I| + |d_{II}| + |d_{III}|) \\ +\infty \text{ else} \end{array} \right\} \tag{2.26}$$

and the discontinuity dissipation function $\pi([[\underline{U}]])$ is:

$$\pi([[\underline{U}]]) = \left\{ \begin{array}{c} c\,|U_t| \text{ if } U_n \geq |U_t|\tan\varphi \\ +\infty \text{ else} \end{array} \right\} \tag{2.27}$$

where $\sigma_I \geq \sigma_{II} \geq \sigma_{III}$ are principal stresses; $d_I \geq d_{II} \geq d_{III}$ are principal strain rates; $U_t = \underline{t}\cdot[[\underline{U}]]$ and $U_n = \underline{n}\cdot[[\underline{U}]]$ are the tangential and normal velocity jump, respectively, and $\rho = c\cot\varphi$ is the cohesive pressure.

The limit theorems of yield design approach the actual dissipation capacity shown in Eq. (2.22) by a lower and an upper bound estimate. The lower estimate is based on statically and plastically admissible stress fields $\boldsymbol{\sigma}'$ and stress vectors $\underline{T}'$ satisfying Eq. (2.23); and the upper bound approach is based on kinematically and plastically admissible strain rate fields $\mathbf{d}'$ and velocity jumps $[[\underline{U}']]$, satisfying Eq. (2.24). Noting that $\mathrm{tr}\,\mathbf{d}' = \mathrm{div}\,\underline{U}'$ in Eq. (2.26) and making use of the generalized divergence theorem for the upper bound, the limit theorems for the conical indentation problem for a homogeneous Mohr-Coulomb material half-space can be written in the form:

$$-\int_{A_M} \underline{T}'(\underline{n})\cdot\underline{e}_z\,da\,\mathring{h} \leq P\mathring{h} \leq \rho\int_{\partial\Omega}\underline{U}'\cdot\underline{n}da \tag{2.28}$$

Herein, $P' = -\int_{A_M}\underline{T}'(\underline{n})\cdot\underline{e}_z\,da$ is a lower bound limit of the indentation load in equilibrium with statically and plastically admissible stress fields $\boldsymbol{\sigma}'$ in Ω, satisfying Eqs. (2.23) and (2.25);

while $\underline{U}' \cdot \underline{n}$ is the normal component of the velocity field at the surface $\partial\Omega$ of the half-space, which includes the cone mantel A_M oriented by $\underline{n} = -\cos\theta\,\underline{e}_r + \sin\theta\,\underline{e}_z$, and the stress-free surface outside the contact radius $r \geq a = \sqrt{A_c/\pi}$ oriented by $\underline{n} = \underline{e}_z$. In order for the dissipation to remain finite, this surface velocity field $\underline{U}'$ must locally satisfy the inequalities in Eqs. (2.26) and (2.27). Finally, since the contact area is assumed to be known, inequalities of Eq. (2.28) can be recast in the form of the dimensionless relation (2.20):

$$\frac{H^-}{c} \leq \frac{H}{c} = \mathcal{H}(\varphi,\theta) \leq \frac{H^+}{c} = \frac{\delta'(\varphi,\theta)}{\tan\varphi} \tag{2.29}$$

where $\delta'(\varphi,\theta) = \frac{1}{A_c}\int_{\partial\Omega} \overline{U}' \cdot \underline{n} da$ (with $\overline{U}' = \underline{U}'/\mathring{h}$ the normalized surface velocity field) represents a global dilatation coefficient. Hence, any statically admissible stress-strength solution provides a lower bound H^-/c to the sought dimensionless relation in Eq. (2.17); and it is the inverse of any velocity-flow rule solution.

Lastly, for either the lower or upper bound, we need to define the boundary conditions, or more precisely the contact conditions at the indenter-material interface. For a frictionless contact condition, all shear stresses at the interface are zero, i.e. $\forall \underline{t} \cdot \underline{n} = 0;\ \underline{t} \cdot \underline{T}'(\underline{n}) = 0 \Leftrightarrow \underline{T}'(\underline{n}) = \sigma'\underline{n}$:

$$\forall (r,z) \in A_M;\ \left\{ \begin{array}{l} \underline{t} \cdot \underline{T}'(\underline{n}) = \frac{1}{2}(\sigma'_{zz} - \sigma'_{rr})\sin 2\theta + \sigma'_{rz}\cos 2\theta = 0 \\ \\ \underline{n} \cdot \underline{T}'(\underline{n}) = \sigma'_{rr}\sin^2\theta + \sigma'_{zz}\cos^2\theta - \sigma'_{rz}\sin 2\theta \end{array} \right\} \tag{2.30}$$

$$\forall r \geq a; z = 0 : \underline{T}'(\underline{n} = \underline{e}_z) = 0$$

In the upper bound approach, a velocity field is kinematically admissible if it satisfies the zero-velocity boundary conditions at infinity. On the other hand, there is an additional interface condition, which arises from a frictionless contact condition, that *a priori* permits a tangential slip (without dissipation) while the normal velocity $\underline{U}' \cdot \underline{n}$ is the one of the rigid indenter:

$$\begin{array}{c} \forall (r,z) \in A_M;\ \underline{U}' \cdot \underline{n} = -\mathring{h}\sin\theta \\ (r,z) \to \infty;\ \underline{U}' = 0 \end{array} \tag{2.31}$$

2.3.3 Ganneau's Solution and Validation

The formulation of the indentation problem described in the previous section defines two formidable optimization problems: either to construct statically admissible stress fields $\boldsymbol{\sigma}'$ that maximize the indentation load (or the hardness); or to construct kinematically admissible velocity fields $\underline{U}'$ that minimize the maximum dissipation capacity the material can support. Given the limited possibilities for analytical solutions (such as slip-line solutions), the beneficial use of a continuum discretization into finite elements together with linear programming techniques was early on recognized for the implementation of both the lower bound theorem for plane stress conditions [162], [188] and the upper bound theorem for plane strain conditions [6], [87], [32]. The most advanced implementation is due to Sloan et al. combining (plane stress/plane strain) 2-D or 3-D linear finite element formulations with linear and non-linear programming [210], [211], [212], [160], [161]. Ganneau and Ulm [93] employed a similar strategy for the axi-symmetrical conditions of the indentation test, which to our knowledge have not been addressed in the open literature. The material domain is discretized by linear finite elements (triangles in 2-D, tetrahedra in 3-D). In the lower bound approach, stress discontinuities are *a priori* permitted for out-of-plane stresses provided that the stress vector continuity ($[[\boldsymbol{\sigma}' \cdot \underline{n}]] = 0$) is enforced as a constraint condition over common edges of adjacent elements. This is achieved by designing nodes of elements so that multiple nodes share the same set of coordinates. A similar strategy is employed to model velocity jumps in the upper bound approach.

In the lower bound approach, the stress field is discretized in the form:

$$\sigma'_{ij} = \sum_k N_k(r,z)\,\sigma^k_{ij} \tag{2.32}$$

where σ^k_{ij} are the nodal stresses and N_k are linear shape functions which in axi-symmetrical conditions depends only on r, z. Since most optimization algorithms are minimization algorithms, the lower bound optimization problem for the indentation test is formulated using the objective function $\max_{\sigma^k_{ij}}(H^-) = \min_{\sigma^k_{ij}}(-H^-)$ in the discretized form for a unit projected

contact area:

$$\left\{ \begin{array}{c} -H^- = -\min_{\sigma_{ij}^k} [C]^T [\sigma'] \\ \text{Subject to:} \\ [A_1][\sigma'] - [b_1] = 0 \\ F(\sigma') \simeq [A_2][\sigma'] - [b_2] \leqslant 0 \end{array} \right\} \tag{2.33}$$

Herein, $[C]$ assembles the objective function matrices for the nodes along the cone surface from a discretization of the lower bound integral in Eq. (2.28); $[A_1]$ and $[b_1]$ assemble the constraint coefficients arising from a discretization of the momentum balance $\operatorname{div} \boldsymbol{\sigma}' = 0$ per element of the stress vector continuity $[[\boldsymbol{\sigma}' \cdot \underline{n}]] = 0$ over shared edged of elements and of extension elements at the boundary of the discretized domain (which extend the statically admissible stress field beyond the limits of the domain discretized by finite elements). $F(\sigma')$ assembles the constraints arising from the yield criterion Eq. (2.25a) at all nodes (including the one of the extension elements situated at the boundary), which ensures that the stress field is plastically admissible throughout the entire half-space. In order to satisfy the strength criterion Eq. (2.25b) throughout the element, it suffices to enforce it at the element nodes since the stresses vary linearly according to the chosen shape or interpolation functions between the nodes [160]. This reduces the number of inequalities significantly. Furthermore, in order to employ the tools of linear programming (thus avoiding nonlinear constraints on the unknown nodal stresses), the Mohr-Coulomb criterion is linearized through a polygonal approximation of the principal stresses, which is expressed by the matrix $[A_2]$ and vector $[b_2]$ in Eq. (2.33). The derivation and expressions of the matrices and vectors for axi-symmetrical conditions can be found in Ref. [93].

In the upper bound approach, the velocity field is discretized in the form:

$$U_i' = \sum_k N_k (r, z)\, u_i^k \tag{2.34}$$

where u_i^k are the nodal velocities and N_k are linear shape functions. Using the classical notation of displacement-based finite element formulation (see e.g., Ref. [16]) which is here applied to the velocity formulation, the components of the strain rate tensor are given by $[d'] = [B_{ij}] \left[u_i^k\right]$, where $[B_{ij}]$ is the strain rate-velocity matrix (equivalent to the strain-displacement matrix in the

FEM), which allows a straightforward calculation of the maximum local dissipation capacity per element from (2.26) and along surfaces of discontinuities (i.e., joined edges between elements) from (2.27). Integrated over the discretized half-space domain, it is this dissipation capacity which is minimized in the upper bound implementation; i.e. formally:

$$\left\{ \begin{array}{c} H^{+} = \min_{u_i^k} \left[C'\right]^T \left[\bar{U}'\right] \\ \text{Subject to:} \\ \left[A_1'\right]\left[\bar{U}'\right] - \left[b_1'\right] = 0 \\ G(\bar{U}') \simeq \left[A_2'\right]\left[\bar{U}'\right] - \left[b_2'\right] \leqslant 0 \end{array} \right\} \tag{2.35}$$

where $\left[\bar{U}'\right] = u_i^k/\mathring{h}$ is the normalized nodal velocity vector and matrix $[C']$ assembles the (unit) element and discontinuity dissipation terms. The equality constraints arise from the contact condition in Eq. (2.31), while $G(\bar{U}') \leq 0$ assembles the constraints arising from the conditions $g(\mathbf{d}') = \sin\varphi\left(|d_I'| + |d_{II}'| + |d_{III}'|\right) - \operatorname{tr}\mathbf{d}' \leq 0$ and $g\left([[\underline{U}']]\right) = |U_t|\tan\varphi - U_n \leq 0$ in Eqs. (2.26) and (2.27) that ensure the finiteness of the (local) dissipation. In order to preserve the nature of these equations as a linear programming tool, these (nonlinear) inequality constraints were linearized (on similar lines as the Mohr-Coulomb criterion), in a series of linear inequalities. The derivations and expressions of the matrices and vectors can be found in Ref. [93].

This novel computational limit analysis of the indentation problem was validated for the two analytical solutions that exist in the literature. The first solution, which is due to Hopkins et al. [121], is for the 'smooth' punch corresponding to the frictionless boundary conditions (2.30) and (2.31):

$$\forall\,(r, z=0) \in A_M;\ \left\{ \begin{array}{c} \sigma' = -\sigma_{zz}';\sigma_{rz}' = 0 \\ \underline{U}' \cdot \underline{n} = -\mathring{h} \end{array} \right\} \tag{2.36}$$

It is based on kinematically admissible velocity fields $\underline{U}'$, i.e., an upper bound approach, which is shown to be compatible with a statically and plastically admissible stress field $\sigma_{ij}^{*}\left(\underline{U}'\right)$ in the bounded region below the footing and throughout the rest of the half-space satisfying the lower bound conditions (6.7). Hence, the slip-line solution for the smooth flat punch problem is the exact plastic collapse solution in the sense of Eqs. (2.21) to (2.24). The second benchmark solution is due to Matar and Salençon [165]: a perfectly rough punch on a Mohr-Coulomb half-space. The perfectly rough punch translates into a frictional interface stress condition and

a no-slip velocity condition of the form:

$$\forall (r, z = 0) \in A_M; \left\{ \begin{array}{c} f(\underline{T}') = |\sigma'_{rz}| + \tan\varphi\sigma'_{zz} - c \leq 0 \\ \underline{U}' \cdot \underline{n} = -\mathring{h};\ \underline{U}' \cdot \underline{t} = 0 \end{array} \right\} \tag{2.37}$$

Matar and Salençon's solution is based on statically and plastically admissible stress fields σ'_{ij}, i.e. a lower bound approach, constructed by the method of characteristics along characteristic lines in a zone spreading under the foundation and emerging at the stress-free surface. In this same zone a velocity field $\underline{U}^* \left(\sigma'_{ij}\right)$ is constructed that satisfies the compatibility conditions of Eqs. (2.24) and $(2.37)_2$; yielding a so-called 'incomplete solution' [28], as the stress field and the velocity fields have not been extended throughout the rest of the half-space. Both solutions employ the Haar-Karman hypothesis[8] which is *a posteriori* verified.

Figure 2-6 displays the lower and upper bounds of the hardness-to-cohesion relation $H/c = \mathcal{H}(\varphi, \theta = \pi/2)$, obtained with the yield design algorithm presented in Ref. [93] for the smooth punch problem and the rough punch problem together with the benchmark solutions. The upper bound solution comes remarkably close to the exact solution of Hopkins et al. [121], and also very close to the 'incomplete' (lower bound solution) of Matar and Salençon [165] (the maximum relative difference is consistently less than 6%); while the lower bound solution performs rather poorly. The reason for this poor performance of the lower bound is that the algorithm converges towards diagonal stress fields (no shear stress) due to the stress-free boundary condition on $r \geq a$, which propagates $\sigma'_{rz} = 0$ from the surface boundary into the entire domain [93]. Because of this restriction to diagonal stress fields, the lower bound approach is limited to a relative small range of possible stress solutions that appear too restrictive to come close to the actual stress fields in the punch tests. In contrast, the upper bound approach is free of such restrictions and is able to accommodate any collapse mechanism, converging towards the actual dissipation capacity. The observation that the upper bound solutions are much more realistic than the lower bound solutions does not only hold for the punch problem, but was verified for

[8] The Haar-Karman hypothesis assumes that the middle principle stress is equal either to the major or minor principal stress,

$$\sigma_{II} = \frac{1}{2}\left[(\sigma_I + \sigma_{III}) - \epsilon(\sigma_I - \sigma_{III})\right];\ \epsilon = \pm 1$$

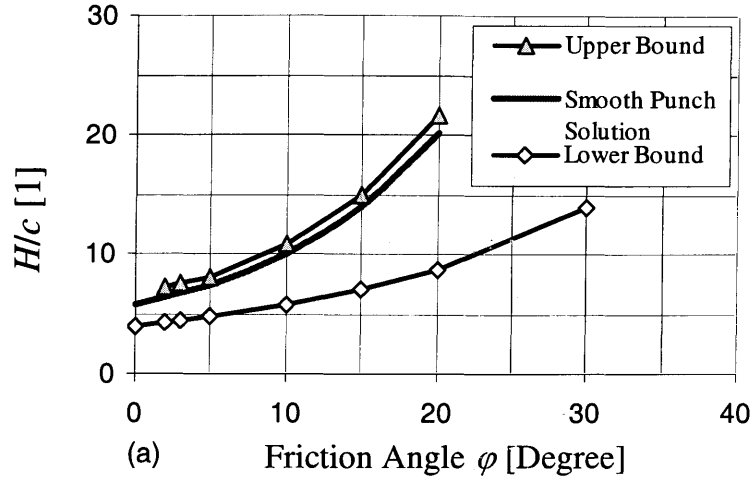

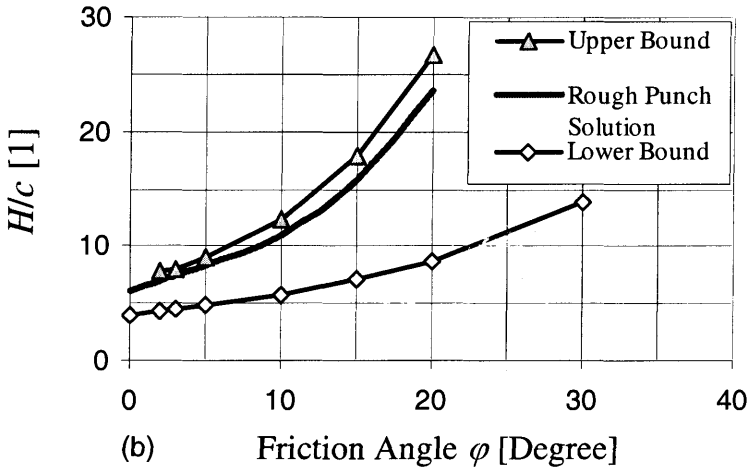

Figure 2-6: Hardness-to-cohesion solutions for the flat punch problem: (a) 'Smooth' punch solutions (benchmark solution of Hopkins et al. [121]); (b) 'Perfectly rough' punch solutions (benchmark solution of Matar and Salençon [165]), from Ref. [92].

all types of axisymmetric indentation tests: conical, spherical, etc. (for details, see Ref. [93]). This and the excellent agreement of the flat punch solutions with the reference solutions are very strong arguments in favor of the use of the upper bound solution for indentation analysis.

2.3.4 Dual Indentation Technique

It has very recently been recognized that the extraction of material properties from the reverse analysis of a single indentation test suffers from non-uniqueness (see e.g., Ref. [50]); and several multiple indenter approaches have been proposed to overcome this limitation for elasto-plastic cohesive materials (with or without strain hardening) using conical or pyramidal indenters [37, 52, 88, 221]. The key idea of the multiple indenter approach is to exploit the self-similarity of the indentation test with respect to the indenter geometry; i.e., for conical indentation with respect to the semi-apex angle θ. We follow a similar strategy here for the extraction of the cohesion and the friction angle from the hardness-to-cohesion relation (2.20), using the upper bound approach for conical indentation. It is readily understood, that the number of indentation results obtained with different semi-apex angles should equal the number of unknown constants in the constitutive model [88], i.e., two hardness measurements in the case of cohesive frictional materials, provided that $c/E \to 0$. However, the uniqueness of such a dual indentation procedure needs to be ensured.

Figure 2-7 shows the results of upper-bound simulations for different tip semi-apex angles (and frictionless contact conditions), while keeping the friction angle constant. The results are displayed in form of H/c vs. θ (Fig. 2-7), together with some velocity fields for selected semi-apex angles (Fig. 2-8). The resulting $H/c = \mathcal{H}(\varphi_0 = const, \theta)$ curve has a minimum around $\theta \simeq 45°$ and increases for both smaller and larger semi-apex angles. The increase for larger semi-apex angles can be attributed to the simple idea that a sharp cone ($\theta \geq 45°$) is easier to drive into a material half-space than a flat punch ($\theta = 90°$). This is evidenced from the velocity profiles shown in Fig. 2-8: the velocity profiles appear more concentrated for smaller semi-apex angle than for larger semi-apex angle. Hence, at plastic collapse, the amount of activated material volume that contributes to the overall dissipation decreases when the semi-apex angle is reduced and reaches a minimum around $\theta \simeq 45°$. Surprisingly, for very sharp cones ($\theta \leq 45°$) there is an inverse trend, an apparent increase of the hardness, which may be

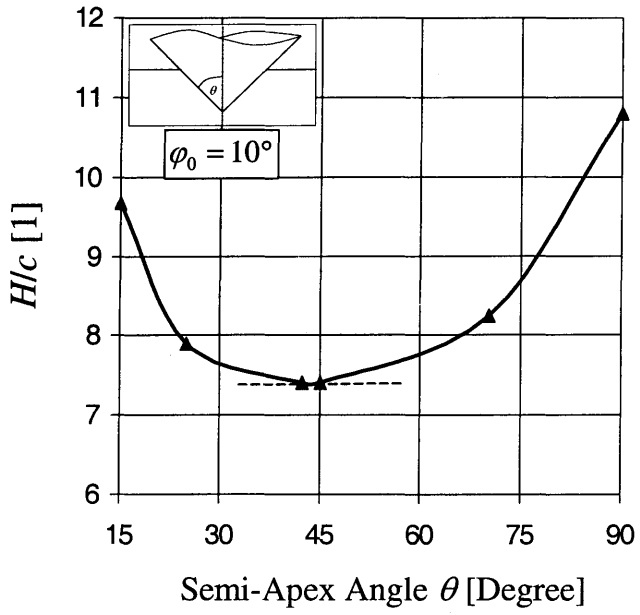

Figure 2-7: Influence of the apex angle on the hardness-to-cohesion ratio ($\varphi = 10°$). Evidence of the existence of a minimum, from Ref. [92].

due to the fact that the plastic zone concentrates into a material cone around the very sharp indenter whose volume increases quadratically compared to the volume of the conical indenter. A similar minimum phenomenon was reported by Houlsby and Wroth for the cone penetration test used in geotechnical applications, who reported a minimum of $\theta \simeq 50°$ from exploring a lower bound approach [122]. This minimum phenomenon is an important property regarding uniqueness of the inverse problem of the assessment of the cohesion and friction angle by two indentation tests. Indeed, provided that H/c for a given friction angle is a monotonic increasing (or decreasing) function of the semi-apex angle, the uniqueness of the dual indentation method can be ensured.

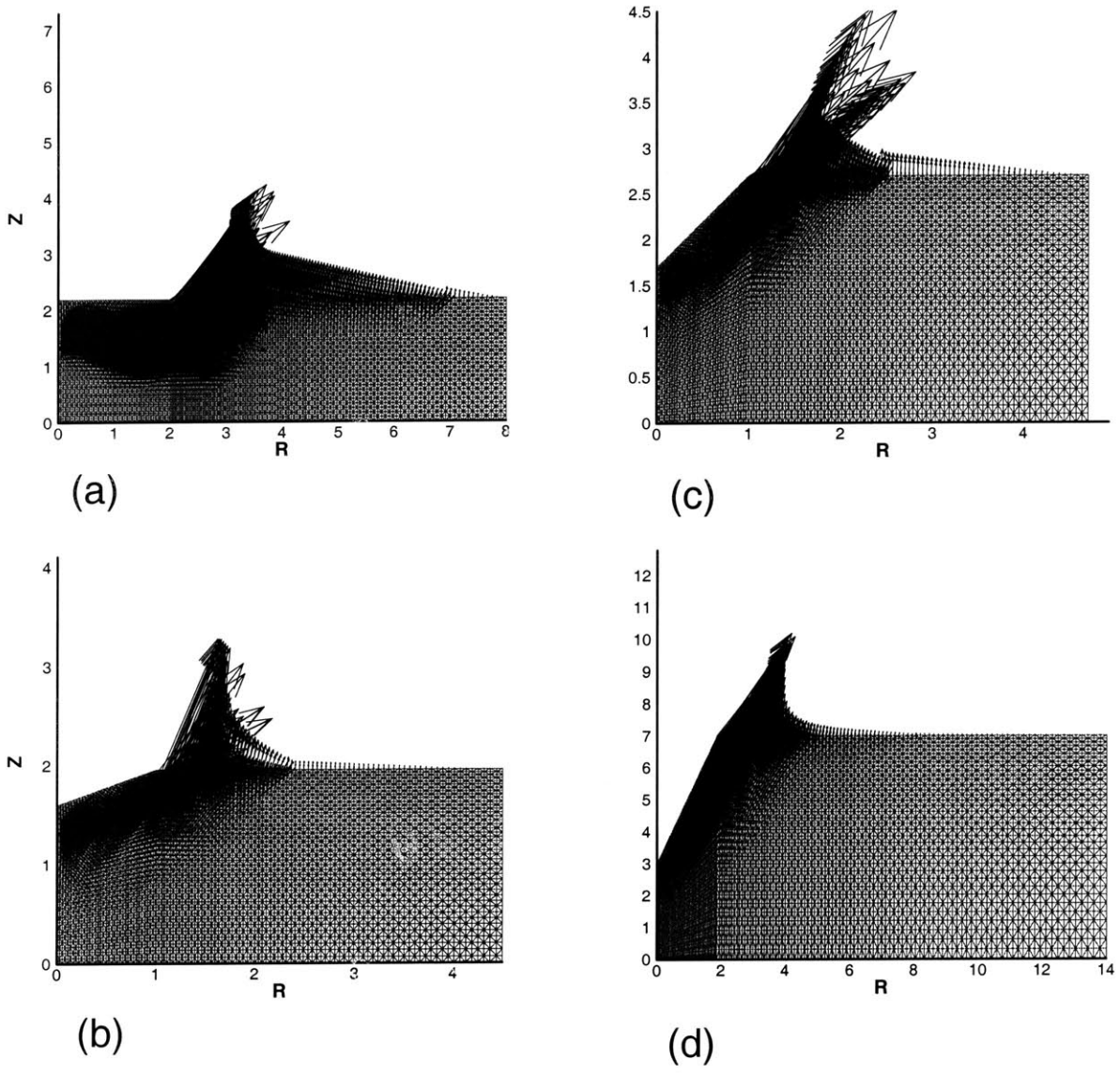

Figure 2-8: Velocity fields for upper bound conical indentation solutions: (a) $\theta = 0$, (b) $\theta = 70°$, (c) $\theta = 45°$, (d) $\theta = 25°$ (all results for $\varphi = 10°$), from Ref. [93].

2.3.5 Application to Berkovich and Cube Corner Indentation

By way of application, we consider two commercially available indenter geometries that are commonly employed in instrumented indentation tests, the 3-sided pyramidal Berkovich and cube corner indenter. As it is common practice in indentation analysis (see Section 2.2, also Ref. [86]), the 3-sided pyramids are approximated as cones so that the normalized projected contact area A_c/h^2 of the cone is the same as that of the real indenter, i.e., $A_c/h_c^2 = \pi \tan^2 \theta$ (see Tab. 2.1). In the light of the results displayed in Fig. 2-7, it is readily understood that the effective cone angle of $\theta_B = 70.32°$ for the Berkovich indenter and $\theta_{CC} = 42.28°$ for the cube corner indenter ensure the uniqueness of the reverse problem. Figure 2-9 displays the H^+/c - relations determined with the upper bound approach for those two semi-apex angles. Following the dimensionless expression in Eq. (2.29), we fit the obtained results in a power-series of the form:

$$\frac{H^+}{c} = \frac{\delta'(\varphi,\theta)}{\tan\varphi} = \frac{1}{\tan\varphi}\sum_{k=1}^{k=N}\left(a_k(\theta)\tan\varphi\right)^k \tag{2.38}$$

where coefficients $a_k(\theta)$ depend only on the semi-apex angle. In the interval $\varphi \in [3°, 30°]$, a $N = 6$ power expression (i.e., fifth-order in $\tan\varphi$) fits perfectly the results, and the coefficients $a_k(\theta_B)$ and $a_k(\theta_{CC})$ are given in Tab. 2.4. While this fitting function is strictly valid only in the interval for which it was fitted, it may serve for limited extrapolation to higher friction angle. Furthermore, it is interesting to remark that the asymptotic values for a frictionless material, i.e., $\lim_{\varphi\to 0}(H^+/c) = a_1(\theta)$, come very close to the value given in (2.18) obtained by extensive elastoplastic finite element simulations ($H/c = 2H/\sigma_y \simeq 5.6$; [50]). However, as the friction angle increases, we observe a strong deviation from this 'rule-of-thumb' value [206], generally admitted for metallic materials. In fact, internal friction kinematically impedes the 45° slip lines commonly observed for frictionless materials and as a consequence increases the plastic yield volume and thus the overall dissipation capacity of the system, which translates into a higher hardness value, and which is captured by the results displayed in Fig. 2-9. The stress state of the material beneath the indenter is a highly compressive triaxial stress state with a hydrostatic component that gives rise to an amplified shear strength behavior due to the internal friction.

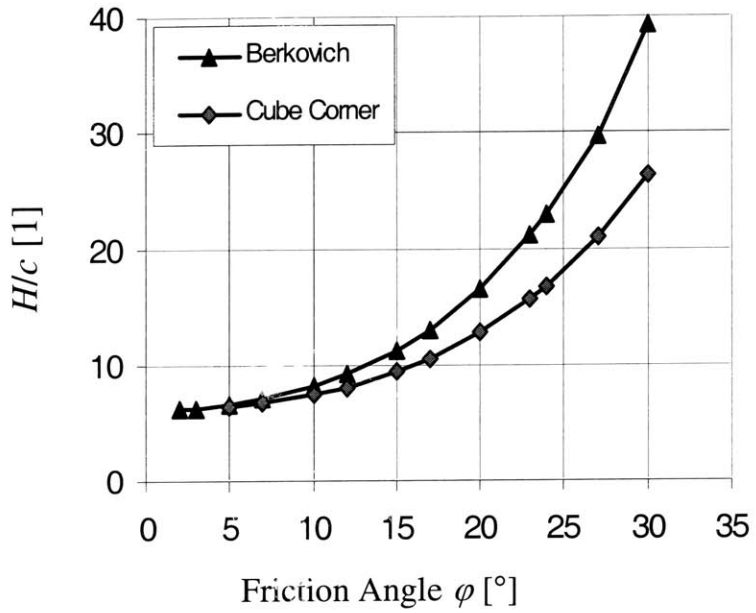

Figure 2-9: Upper bound solutions for the hardness-to-cohesion ratio for two (equivalent conical) indenter geometries: Berkovich indenter ($\theta_B = 70.32°$) and Cube Corner indenter ($\theta_{CC} = 42.28°$) (Data from Ref. [93]).

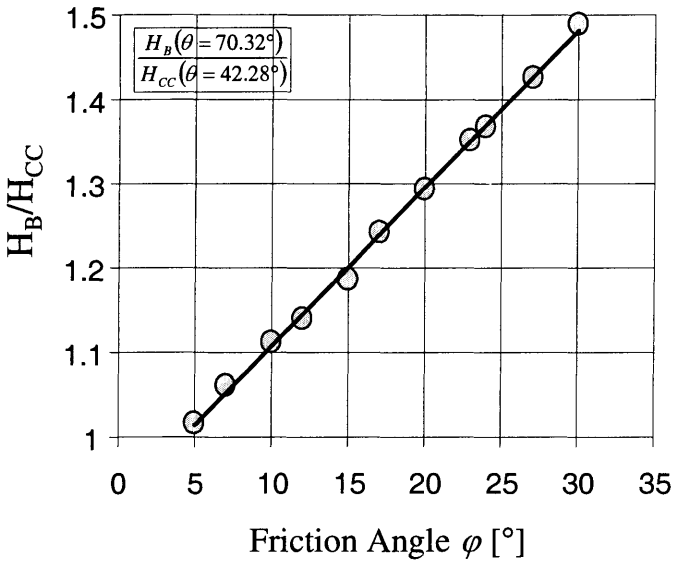

Figure 2-10: Hardness-ratio (Berkovich/cube corner) vs. friction angle (from Ref. [92]).

	a_1	a_2	a_3	a_4	a_5	a_6
$\theta_B = 70.32°$	5.7946	2.9455	−2.6309	4.2903	−3.4887	2.7336
$\theta_{CC} = 42.28°$	5.9455	2.4253	−2.7578	4.0152	−3.2938	2.5369

Table 2.4: Coefficients of power-series fit Eq. (2.38) for H/c relations of Berkovich indenter (θ_B) and Cube Corner indenter (θ_{CC}) assimilated to equivalent cones of same projected contact area.

On this basis, we propose a dual indentation technique from a combination of Berkovich and cube corner hardness values. Given the dimensionless expression (2.29), it is possible to determine the friction angle of the material from the ratio of two hardness measurements:

$$\frac{H_1}{H_2} = \frac{\mathcal{H}_c(\varphi, \theta_1)}{\mathcal{H}_c(\varphi, \theta_2)} = \frac{\delta'(\varphi, \theta_1)}{\delta'(\varphi, \theta_2)} \tag{2.39}$$

Figure 2-10 displays the hardness ratio for the Berkovich and cube corner indenters ($\theta_1 = \theta_B; \theta_2 = \theta_{CC}$) as a function of the friction angle in the interval $\varphi \in [5°, 30°]$. The figure confirms that there is a unique relation between the hardness ratio and the friction angle, which provides a means of assessing φ from the difference in hardness between a Berkovich indentation test and a cube corner indentation test. While small for very small friction angles, the hardness ratio becomes significant for greater friction angles; at these larger φ, the ratio appears to increase almost linearly with φ in the interval considered. Once the friction angle is determined, it is possible to determine the cohesion from the H/c curves displayed in Fig. 2-9. To our knowledge, this simple technique is the only one currently available for extracting strength properties of cohesive-frictional materials at small volumes. We will validate this novel method in Chapter 3 for a model cohesive-frictional material, prior to applying the technique to heterogeneous cohesive-frictional materials in the core of this thesis.

2.4 Indentation Modulus

The second quantity that is extracted from an indentation test is the indentation modulus defined by Eq. (2.2), which is an instantaneous measure of the elastic properties of the indented material. In fact, in contrast to the yield design assumption that the work provided to the materials system during loading is entirely dissipated, actual indentation experiments reveal

that a small proportion of this work is stored in form of elastic deformation, which is released upon unloading (see Fig. 2-1). It has been proposed that the initial unloading response is purely elastic [223, 216]; and can be employed to extract the elastic properties of the indented material. As in Section 2.3, we start with a dimensional analysis of the physical quantities at stake during unloading, and present the tools required to link the indentation modulus to the elastic properties of the material.

2.4.1 Dimensional Analysis

In contrast to the loading phase, the unloading portion of the $P-h$ response is characterized by an additional length parameter, the maximum depth $h_{\max}$, at which unloading starts. The force P during unloading is now a function of seven independent physical quantities: the elastic constants (Young's modulus E , Poisson's ratio ν), the strength parameters (cohesion c, friction angle φ), the indenter displacement h, the maximum depth $h_{\max}$, and the indenter half angle θ:

$$P = f_U\left(\nu, E, c, \varphi, h, h_{\max}, \theta\right) \tag{2.40}$$

Dimensional analysis yields:

$$\frac{P}{Eh^2} = \Pi_\gamma\left(\nu, \frac{c}{E}, \varphi, \frac{h}{h_{\max}}, \theta\right) \tag{2.41}$$

Hence, in contrast to the dimensionless loading response in Eq. (2.16a), the dimensionless force P/Eh^2 during unloading is *a priori* no longer simply proportional to the square of the indenter displacement h; but depends as well on $h/h_{\max}$ [50]. In an indentation test, the unloading slope $S = \frac{dP}{dh}$ is evaluated at $h/h_{\max} = 1$. Hence, if we derive the unloading response with respect to the indenter displacement and evaluate the result at $h/h_{\max} = 1$, we obtain:

$$\begin{aligned} \frac{S}{Eh_{\max}} &= \frac{1}{Eh_{\max}}\frac{dP}{dh}|_{h/h_{\max}=1} \\ &= 2\Pi_\gamma\left(\nu, \frac{c}{E}, \varphi, \frac{h}{h_{\max}} = 1, \theta\right) + \Pi'_\gamma\left(\nu, \frac{c}{E}, \varphi, \frac{h}{h_{\max}} = 1, \theta\right) \equiv \Pi_\delta\left(\nu, \frac{c}{E}, \varphi, \theta\right) \end{aligned} \tag{2.42}$$

where $\Pi'_\gamma = d\Pi_\gamma/dh = (1/h_{\max})\, d\Pi_\gamma/d\,(h/h_{\max})$. Equation (2.42) reveals that the contact stiffness S increases with the indentation depth in an indentation experiment, all other parameters

$(\nu, c/E, \varphi, \theta)$ held constant. On the other hand, since the contact stiffness is evaluated at the maximum indentation depth, the second unknown of the contact problem, the contact area A_c, is still given by the dimensionless expression in Eq. (2.16b), which we use in Eq. (2.42) to obtain a new invariant:

$$\frac{S}{E\sqrt{A_c}} = \frac{\Pi_\delta\left(\nu, \frac{c}{E}, \varphi, \theta\right)}{\sqrt{\Pi_\beta\left(\frac{E}{c}, \nu, \varphi, \theta\right)}} \tag{2.43}$$

Finally, a comparison of Eq. (2.43) with the BASh-relation Eq. (2.2) yields:

$$\frac{S}{E\sqrt{A_c}} = \frac{2}{\sqrt{\pi}}\frac{M}{E} = \mathcal{M}\left(\nu, \frac{c}{E}, \varphi, \theta\right) \tag{2.44}$$

Dimensional analysis therefore suggests that the indentation modulus M is a function of both elastic and plastic properties of the material for a given indenter geometry. Several observations however are in favor of applying elasticity solutions to the unloading portion of indentation response:

- Experimental observations [216] suggest that the unloading portion of the curve is fully elastic. Cyclic loading at the beginning of unloading tend to trace the same path suggesting that reverse plasticity phenomena are negligible and that the unloading portion of the $P-h$ response can be safely considered as purely elastic.

- Cheng and Cheng [48, 50] and Dao et al. [66] performed a large series of elastoplastic finite element simulations (with and without plastic hardening), and demonstrate that the indentation modulus is insensitive to plastic properties (yield strength σ_y, power exponent n). The results which are illustrated in Fig. 2-11 in form of a plot of $\left(1-\nu^2\right) S/Ea = 2\left(1-\nu^2\right) M/E$, do almost not depend on neither the strength-to-stiffness ratio ($\sigma_y/E = 2c/E$), nor on the power-law exponent n of the power-law strain hardening material ($\sigma = \sigma_y + k\varepsilon^n$).

While these results were established for cohesive materials, it is reasonable to assume that they also hold for cohesive frictional materials:

$$\frac{S}{E\sqrt{A_c}} = \mathcal{M}(\nu, \theta) \Leftrightarrow M = M(E, \nu) \tag{2.45}$$

The indentation unloading response is purely elastic and all plasticity effects that the material exhibits during the loading phase of indentation are incorporated in the evolution of the contact area, which evolves in such a way as to maintain a constant pressure beneath the conical indenter. This finding is remarkable, as it allows to employ elastic contact solutions to determine the link between the indentation modulus M and the elastic properties (E, ν). This is shown next.

2.4.2 Indentation Modulus vs. Elastic Properties: The Galin-Sneddon Solution

The earliest attempt to relate the unloading portion of the curve with the elastic characteristics of the materials can be found in the work of Tabor et al. [223, 216]. By means of cyclic loading-unloading on the material, they confirmed experimentally that the unloading branch of the curve was purely elastic, and that the deformation characteristics of the contact surface conformed with the Hertz contact solution for the elastic deformation of spherical surfaces [223]. One can generalize the concepts by considering the elastic indentation problem of an axisymmetric smooth rigid indenter on an elastic half-space.

The main focus of contact mechanics is the determination of size and exact shape of the contact area. Unlike classical mechanical problems, the contact zone is unknown so that areas where displacements (in the contact region), and those where forces (free surface) are prescribed, are not known *a priori*. This makes the analysis intrinsically non-linear, since the surface boundary conditions have to be written under conditions of a point $\underline{z}$ that is either situated in the contact zone or in the stress free surface. The contact problem between a rigid axisymmetric indenter and an infinite half-space is described by the following set of equations,

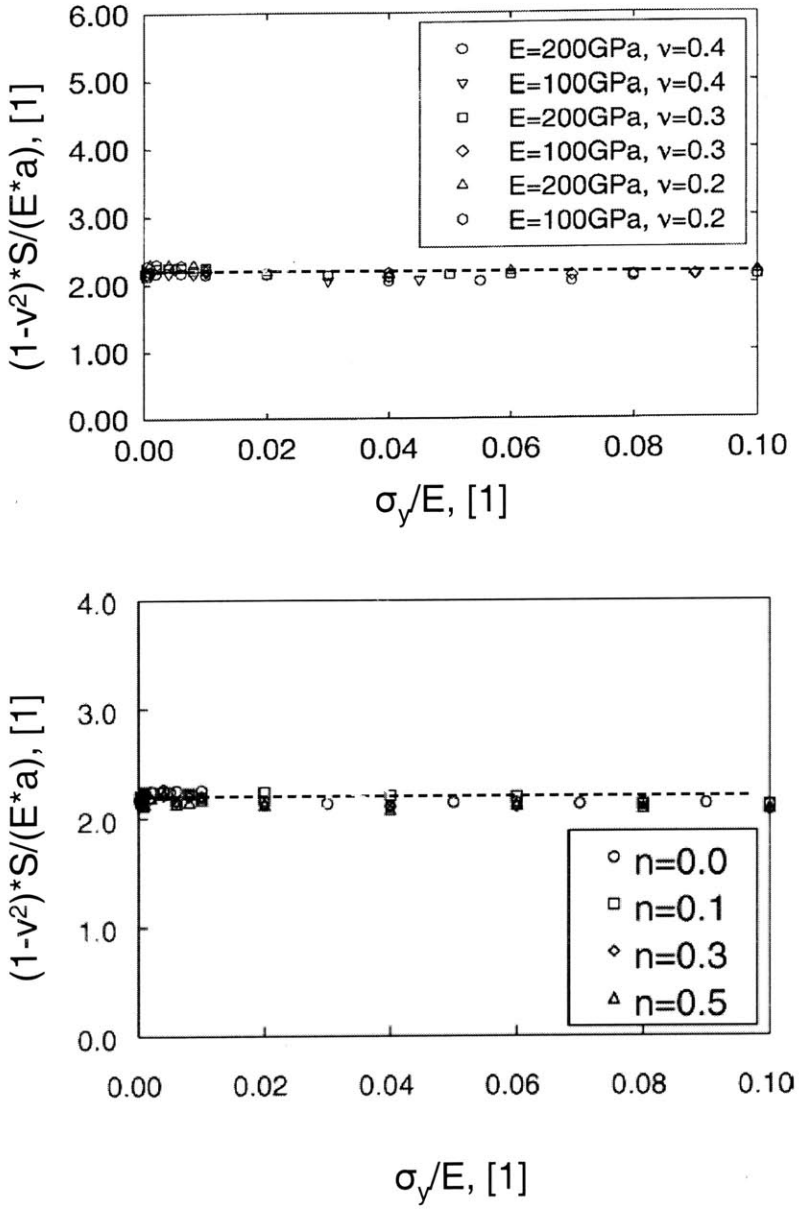

Figure 2-11: Finite Element simulations of Cheng et al. [50] of frictionless conical indentation ($\theta = 68°$) on an elasto-plastic cohesive half-space. The dimensionless parameter $\left(1-\nu^2\right) S/Ea = 2M/E$, where a represents the projected constant radius, appears to be independent of the strength-to-stiffness ratio σ_y/E, the Poisson's ratio ν, and the strain hardening power exponent n (from Refs. [48] and [50]).

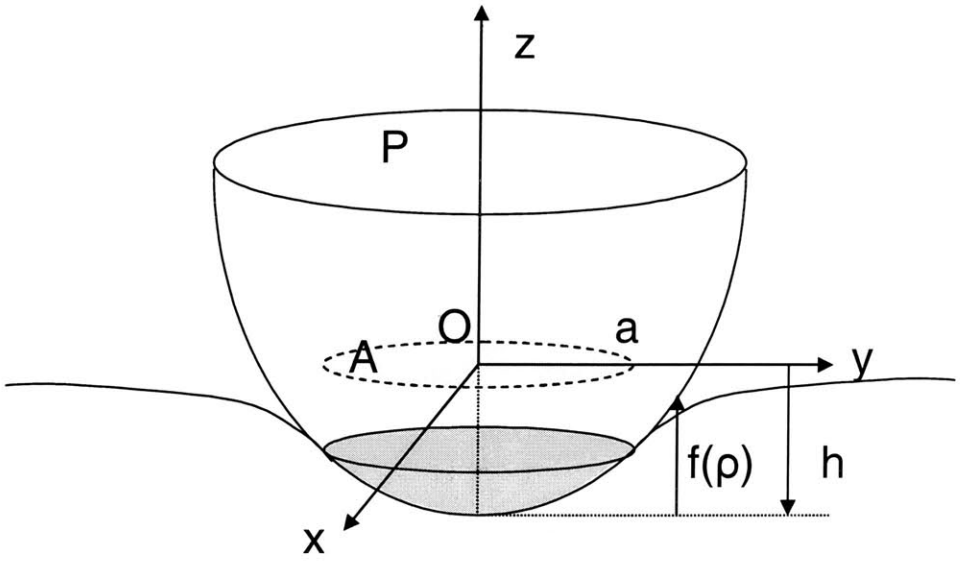

Figure 2-12: Contact between a rigid axi-symmetric indenter of shape $f(\rho)$ and an infinite half-space. The total applied load is P, the indentation depth is h and the projected area of contact is A.

written in polar coordinates (ρ, θ, z) [214]:

$$\begin{aligned}
\operatorname{div} \boldsymbol{\sigma} &= 0 && \text{(2.46a)}\\
\boldsymbol{\sigma} &= F(\boldsymbol{\varepsilon}) && \text{(2.46b)}\\
\boldsymbol{\varepsilon} &= \frac{1}{2}(\boldsymbol{\nabla}\underline{u} + \boldsymbol{\nabla}^t\underline{u}) && \text{(2.46c)}\\
P &= -\int_{\rho=0}^{a}\int_{\theta=0}^{2\pi} \sigma_{zz}(\rho,\theta,0)\rho d\rho d\theta && \text{(2.46d)}\\
u_z(\rho,\theta,0) &= -h + f(\rho);\ \rho < a && \text{(2.46e)}\\
\sigma_{\rho z}(\rho,\theta,0) &= 0;\ \ \rho > 0 && \text{(2.46f)}\\
\sigma_{zz}(\rho,\theta,0) &= 0;\ \rho > a && \text{(2.46g)}
\end{aligned}$$

where P is the total load applied, in direction z as shown on Fig. 2-12, $f(\rho)$ defines the axi-symmetric shape of the indenter, and a is the contact radius. Equation (2.46a) is the static equilibrium condition, Eq. (2.46b) gives the stress strain relation through a function F, Eq. (2.46c) derives strain from displacements, and the remaining relations are the boundary

conditions for the total load Eq. (2.46d), the vertical displacement in the contact region Eq. (2.46e), the zero shear stress on the surface Eq. (2.46f) which includes the frictionless contact condition, and the stress-free boundary condition outside the contact zone Eq. (2.46g).

There are several ways of solving the above set of equations, the more traditional one being the method developed by Lea and Raddock [146,147] and further formalized by Sneddon [213, 214][9], which consists in performing on all problem equations two dimensional Fourier transforms in the directions of the surface coordinates x and y. In the case of axi-symmetry, this integral transform is called a Hankel transform on the polar coordinates ρ and θ. The polar coordinates ρ and θ are transformed into a variable ξ of dimension L^{-1}. The area of contact is circular by symmetry and its projected radius a is kept as an unknown. It turns out that the equations written with a new set of non-physical coordinate can be solved analytically in the transformed space. Finally, the integral transforms are performed backwards to come back to the initial problem. Following this procedure, the expressions for h and P for an isotropic half-space read:

$$h = a\int_{\rho=0}^{a} \frac{f'(\rho)d\rho}{\sqrt{a^2-\rho^2}} \tag{2.47}$$

$$P = 2\frac{E}{1-\nu^2}\int_{\rho=0}^{a} \frac{\rho^2 f'(\rho)d\rho}{\sqrt{a^2-\rho^2}} \tag{2.48}$$

where f is any smooth convex function, and f' stands for its derivative with respect to ρ. This result implicitly relies on an assumption about the contact area, through a. By inverting Eqs. (2.47) or (2.48), the contact radius a can be expressed as a function of the prescribed depth h or load P. The displacements in the half-space are given by:

$$u_\rho(\rho,z) = -\frac{1}{2(1-\nu)}\int_0^\infty (1-2\nu-\xi z)A(\xi)e^{-\xi z}J_1(\rho\xi)d\xi \tag{2.49}$$

$$u_z(\rho,z) = \frac{1}{2(1-\nu)}\int_0^\infty (2-2\nu+\xi z)A(\xi)e^{-\xi z}J_0(\rho\xi)d\xi \tag{2.50}$$

where $A(\xi)$ depends on the shape of the indenter and J_0 and J_1 are Bessel functions of the first

[9] The solution for a frictionless axisymmetric indentation has apparently been found earlier by Galin [89] (See discussion in Ref. [30]).

kind.

It is interesting to write here the solutions of Eqs. (2.47) and (2.48) for an axisymmetric indentation with a cone of semi-apex angle θ, for which:

$$f(\rho) = \frac{\rho}{\tan\theta} \tag{2.51}$$

In this case,

$$A(\xi) = \frac{1}{\tan\theta}\frac{1-\cos(a\xi)}{\xi^2} \tag{2.52}$$

and

$$u_\rho(\rho < a, 0) = \frac{1-2\nu}{4(1-\nu)}\frac{\rho}{\tan\theta}\left[\ln\frac{\rho/a}{1+\sqrt{1-(\rho/a)^2}} - \frac{1-\sqrt{1-(\rho/a)^2}}{(\rho/a)^2}\right] \tag{2.53}$$

$$u_z(\rho > a, 0) = \frac{1}{\tan\theta}\left[a\sin^{-1}\left(\frac{a}{\rho}\right) + \sqrt{\rho^2-a^2} - \rho\right] \tag{2.54}$$

$$\sigma_{zz}(\rho < a, 0) = \frac{1}{2\tan\theta}\frac{E}{1-\nu^2}\cosh^{-1}\left(\frac{a}{\rho}\right) \tag{2.55}$$

Eq. (2.55) shows a stress singularity for $\rho = 0$ right below the tip of an infinitely sharp cone. This is not the case for smooth indenters, but it appears in the case of a flat punch for $\sigma_{\rho z}(\rho = a, 0)$. Equations (2.47) and (2.48) give the explicit values of the depth and load as a function of the contact radius:

$$h = \frac{\pi}{2}\frac{a}{\tan\theta} \tag{2.56}$$

$$P = \frac{\pi}{2}\frac{E}{1-\nu^2}\frac{a^2}{\tan\theta} \tag{2.57}$$

Eliminating a from (2.56) and (2.57) gives the load *vs.* depth relation:

$$P = \frac{2}{\pi}\frac{E\tan\theta}{1-\nu^2}h^2 \tag{2.58}$$

As expected from the dimensional analysis, P is scaled by h^2, which provides an interesting insight into the non linearity of the contact problem: for each increment of load, both the area of contact and the depth of indentation increase. Similarly, a and h are linearly related, and

one can define the contact depth as the distance measured on the $z-$axis between the indenter tip and the contact edge. From Eq. (2.56) we obtain the following relation:

$$h_c = \frac{a}{\tan\theta} = \frac{2}{\pi}h \tag{2.59}$$

Equation (2.59) suggests that elastic indentation always produces sink-in. In fact, provided that the material remains purely elastic, the contact depth to indentation depth ratio will always be a constant, $h_c/h = 2/\pi = 0.64$. Furthermore, if one rewrites P and h in Eqs. (2.56) and (2.57) as a function of the projected area of contact $A_c = \pi a^2$, then one obtains

$$h = \frac{\sqrt{\pi}}{2}\frac{\sqrt{A_c}}{\tan\theta} \tag{2.60}$$

$$P = \frac{1}{2}\frac{E}{1-\nu^2}\frac{A_c}{\tan\theta} \tag{2.61}$$

Finally, deriving Eq. (2.61) with respect to depth, the shape of the indenter defined by θ disappears, and we obtain the BASh formula Eq. (2.2) [39]:

$$S = \frac{dP}{dh} = \frac{2}{\sqrt{\pi}}M\sqrt{A_c} \tag{2.62}$$

together with the sought link between the indentation modulus and the elastic properties of the isotropic half-space:

$$M = \frac{E}{1-\nu^2} \tag{2.63}$$

While originally derived for indentation by a rigid cone, Bulychev et al. showed that Eq. (2.62) also applies to spherical and cylindrical indenters (see review in Ref. [31]). Subsequently, Pharr, Oliver and Brotzen in their classical paper [191] demonstrated that Eq. (2.62) applies to any indenter that can be described as a solid of revolution of a smooth function. Using Sneddon's solutions [213], they proceeded by algebraically manipulating Eq. (2.48) into:

$$P = 2\frac{E}{1-\nu^2}\left[\int_{\rho=0}^{a}\frac{f'(\rho)d\rho}{\sqrt{a^2-\rho^2}} - \int_{\rho=0}^{a} f'(\rho)\sqrt{a^2-\rho^2}d\rho\right] \tag{2.64}$$

Noting that the first term inside the bracket is simply the displacement h, Eq. (2.64) can be

differentiated with respect to a to give:

$$\frac{dP}{da} = 2\frac{E}{1-\nu^2}\frac{dh}{da} + \frac{P}{a} - 2\frac{E}{1-\nu^2}\frac{d}{da}\int_{\rho=0}^{a} f'(\rho)\sqrt{a^2-\rho^2}d\rho \tag{2.65}$$

The third term on the right hand side of Eq. (2.65) was shown to be equal to P/a, thus canceling out the second term and reducing Eq. (2.64) to:

$$\frac{dP}{da} = 2\frac{E}{1-\nu^2}\frac{dh}{da} \tag{2.66}$$

The initial unloading stiffness, $S = \frac{dP}{dh}$, is then reduced to:

$$S = \frac{dP}{dh} = \frac{dP/da}{dh/da} = \frac{2}{\sqrt{\pi}}\sqrt{A_c}M \tag{2.67}$$

which is the BASh formula Eq. (2.62) together with the indentation modulus M, assuming an infinitely rigid indenter, Eq. (2.63).

The effect of indenter compliance can be considered by substituting for the indentation modulus M the result of the Hertz contact solution of two elastically deformable bodies [114]:

$$\frac{1}{M} = \frac{1-\nu^2}{E} + \frac{1-\nu_{in}^2}{E_{in}} \tag{2.68}$$

where E, ν and E_{in}, ν_{in} are the elastic constants of the indented material and the indenter, respectively. It must be checked from case to case whether the compliance of the diamond indenter needs to be considered in the evaluation of the elastic properties of materials by way of indentation (see also Section D.3.1 and Fig. D-5). Strictly speaking, diamond crystals are transversely isotropic. Given the hexagonal symmetry of their crystal structure there are 5 independent constants required to fully describe the elasticity tensor. The mechanical properties of diamonds will therefore be a function of orientation of the crystallographic plane. This may explain the large range of experimental values reported in the literature: $E_{in} = 800 - 1200$ GPa, $\nu_{in} = 0.06 - 0.07$. Exact properties are usually provided by the manufacturer. The International Standards Organization has recently issued a draft international standard (ISO 14577-2002, [127]) in which the use of $E_{in} = 1,140$ GPa, $\nu_{in} = 0.07$ for diamond indenters is recommended. These values will be used throughout the rest of this thesis.

2.4.3 Limitations of and Extensions to the Galin-Sneddon Solution

The Galin-Sneddon solution can be seen as a first-order displacement solution, in the sense that it enforces through Eq. (2.46e) points on the undeformed surface in a distance ρ to the symmetry axis to be situated after deformation vertically along a straight line defined by the cone shape function. Strictly speaking, this contact condition is only valid if the points do not move radially as well, hence in the absence of any radial displacements. Effectively, however, points on the originally flat surface with coordinates $(\rho, z = 0)$ move to the final positions beneath the indenter given by:

$$r = \rho + u_\rho(\rho < a, 0) \tag{2.69a}$$

$$z = u_z(\rho < a, 0) = -h + \frac{\rho}{\tan\theta} \tag{2.69b}$$

where $u_\rho(\rho < a, 0)$ is the first-order radial displacement solution given by Eq. (2.53). Equation (2.69) completely describes the actual shape of the deformed surface in the contact zone. Not surprisingly, only in the case of $\nu = 1/2$, for which $u_\rho(\rho < a, 0) = 0$, is the shape of the indenter consistent with the geometry of the rigid indenter, while for all other Poisson's ratios, the material surface appears to penetrate into the rigid indenter, thus violating the non-penetration condition. This second-order effect due to the radial displacement was identified by Hay et al. [111] by means of elastic finite-element simulations in which the geometry of the surface in the region of contact was forced to match that of the rigid cone and compared with the Galin-Sneddon solution. The finding of the analysis was incorporated in the BASh formula through a correction factor:

$$S = \beta(\nu, \theta)\frac{2}{\sqrt{\pi}}\sqrt{A_c}M \tag{2.70}$$

where $A_c = \pi a^2$ needs to be determined using the actual contact radius from the rigid cone boundary condition. For frictionless contact (no shear stresses parallel to the interface), $\beta(\nu = 1/2, \theta) = 1$, while for all other Poisson's ratios, $\beta(\nu, \theta) > 1$; as displayed in Fig. 2-13. The figure shows that the deviation from the Galin-Sneddon solution, expressed by the correction factor $\beta(\nu, \theta)$, increases with decreasing Poisson's ratio and indenter semi-apex angle θ. Hay et al. also proposed semi-empirical models to estimate the correction factor for cube corner indentation

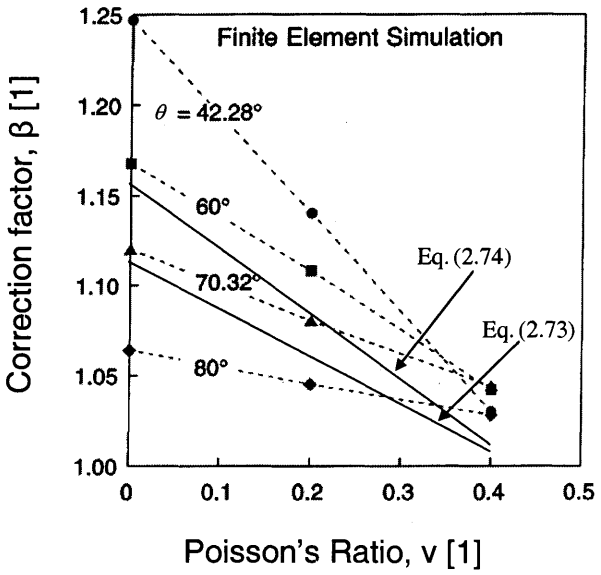

Figure 2-13: Results of finite element simulations [111] for the relation between correction factor β and Poisson's ratio ν (adapted from Ref. [111]).

($\theta_{CC} = 42.28°$) and Berkovich indentation ($\theta_B = 70.32°$) assimilated to cones of equivalent area-to-depth ratio:

$$\beta(\nu, \theta_{CC} = 42.28°) = 1 + \kappa(\nu) \cot \theta_{CC} \tag{2.71}$$

$$\beta(\nu, \theta_B = 70.32°) = \pi \frac{\pi/4 + 0.15483073\kappa(\nu) \cot \theta_B}{(\pi/2 - 0.83119312\kappa(\nu) \cot \theta_B)^2} \tag{2.72}$$

where $\kappa(\nu) = (1 - 2\nu) / (4(1 - \nu))$.

The case of adhesive (no-slip) contact between the half-space and the indenter can be seen as a limit case that eliminates the second-order effect due to the radial displacement. The adhesive contact problem has been addressed analytically by Mossakovskii 1954 [174], 1963 [175], Goodman 1962 [102], Spence 1968 [215], and is reviewed in detail by Borodich and Keer [31, 30]. Once the point of the surface contacts with the indenter, the radial displacement does not change further with the increase of load, thus naturally ensuring that the shape of the material surface coincides with the surface of the rigid indenter. Incorporating this boundary

condition in the analytical solution procedure, Borodich and Keer [31] derived analytical expressions for the correction factor for punches of monomial shapes. For a flat punch ($\theta = \pi/2$), the correction with respect to the frictionless contact problem is:

$$\beta(\nu, \theta = \pi/2) = \frac{(1-\nu)\ln(3-4\nu)}{(1-2\nu)} \tag{2.73}$$

and for a cone with large half-tip angles $\theta = \pi/2 - \alpha$, for which a linearization is possible, $\tan\alpha \approx \alpha$:

$$\beta(\nu, \theta = \pi/2 - \alpha) = \frac{2(1-\nu)}{\sqrt{3-4\nu}} \tag{2.74}$$

Remarkably, but not surprisingly, whatever the indenter geometry, $\beta = 1$ for $\nu = 1/2$, while $\beta > 1$ for any other value of the Poisson's ratio, with a maximum value of $\beta(\nu = 0, \theta = \pi/2) = \ln(3) = 1.0986$ for the flat indenter, and $\beta(\nu = 0, \theta = \pi/2 - \alpha) = 2/\sqrt{3} = 1.1547$. The corrections factors derived from the adhesive contact problem are also displayed in Fig. 2-13, showing that they constitute upper bounds for cones of large tip-angles and relatively small Poisson's ratios, $\nu \leq 0.3$. For all practical purposes, we retain that the Galin-Sneddon solution is a lower bound of the contact stiffness S, while any effect of friction and second-order effects due to radial displacement increase the contact stiffness:

$$\frac{2}{\sqrt{\pi}}\sqrt{A}M \leq S = \frac{dP}{dh} \leq \beta(\nu, \theta)\frac{2}{\sqrt{\pi}}\sqrt{A}M \tag{2.75}$$

In other words, use of the BASh formula (2.2) yields upper bound estimates of the indentation modulus and related elastic properties.

Equation (2.67) is based on the elastic solution for indenters that can be described by a smooth solid of revolution (spherical, conical, elliptical, etc.) [191]. Berkovich and Vickers indenters (four- and three-sided pyramidal cones, respectively), which are more commonly applied in instrumented indentation techniques, cannot be described as bodies of revolution. However, it has been found experimentally and by means of finite element simulations that the deviation from Eq. (2.67) of pyramidal and other geometrical shapes during unloading is negligible [137, 191, 66, 219]: The geometric constant $c^* = 1.142$ for the Vickers pyramid indenter (square cross section), and $c^* = 1.167$ for the Berkovich indenter (triangular cross section) differ little

from $c^* = 2/\sqrt{\pi} = 1.128\,4$ of the axisymmetric indenters.

It can be seen that the correction factor introduced in the case of frictional contact is a mere consequence of the Poisson's ratio, ν. As a result when the Poisson's effect becomes negligible, for example in the case of an incompressible medium $\nu \rightarrowtail 1/2$, then the proposed solution yields the frictionless result, $\frac{dP}{dh} \rightarrow \frac{2}{\sqrt{\pi}}\sqrt{A}M$ and the correction factor collapses to 1. It is extremely interesting to note that the correction factor ranges from C=ln(3) = 1.0986 for $\nu = 0$, to C$\rightarrow$1 at $\nu \rightarrow 0.5$, and as a result Eq. (2.2) is within 10% (for materials with positive Poisson's ratio). In other words, Eq. (2.2) can be used without large error, even when the indenter is not a true body of revolution or friction between the indenter and material is present; that is, Eq. (2.2) can be considered as a general characteristic of elastic indentation mechanics. In this case, E can be determined from the measured slope at the onset of unloading, provided that a reasonable estimate of the Poisson's ratio[10] and an independent measure of the contact area A_c upon unloading are available.

2.5 Area of Contact

The key to a successful determination of strength and elasticity properties from indentation tests relies on the determination of the correct projected contact area at the point of initial unloading, A_c. This is not an easy task.

2.5.1 Direct Measurements

Traditionally, the contact area has been determined by direct measurement of the size of the residual hardness impression after complete unloading, as shown in Fig. 2-14. As one may expect, the residual imprints may deviate from the initial contact area at maximum load if there is significant elastic recovery on unloading. Fortunately, it has been experimentally observed that the residual imprint left on the surface of an indented specimen is in very good agreement with the contact area at maximum load [216]. In other words, even in the case of an appreciable recovery in depth during unloading, there is practically no change in the diameter (or contact

[10] However, it is not necessary to know the value of the Poisson's ratio with great precision to obtain a good value of the elastic modulus, as $E \propto (1-\nu^2)$ and $\nu \leq 1/2$.

radius a) of indentation. Refined analysis using finite element simulations confirmed that elastic recovery effects are appreciable only for materials with extremely high values of H/M [191, 66]. It is therefore reasonable to use the final imprint for the determination of the hardness and the indentation modulus from Eqs. (2.1) and (2.2).

2.5.2 Oliver and Pharr Method

For practical reasons some means other than direct observation of the hardness impressions is needed to measure contact areas, since imaging very small indentations is both time-consuming and difficult. An original method for conical indentation that circumvents the necessity to measure the contact area, was suggested by Oliver and Pharr [184] in the classical paper of 1992, which is now extensively used (see also the 2004 review paper by the authors [185]). The method is based on the assumption that the elastic contact height-to-indentation depth relation (2.59), i.e. $h_c/h = 2/\pi$ equally applies to the elastic recovery in elastoplastic indentation characterized by a residual indentation depth h_f. This assumption is shown schematically in Fig. 2-15, and is expressed by:

$$h_c - h_f = \frac{2}{\pi}\left(h_{\max} - h_f\right) \tag{2.76}$$

Since $h_{\max}$ and h_f are measurable quantities, one can determine the contact depth h_c from Eq. (2.76), and subsequently the contact area $A_c = \pi\left(h_c \tan\theta\right)^2$. In practice, however, the residual indentation depth h_f is very sensitive to non ideal surface preparations. By considering that the elastic unloading is scaled, for conical indentation, by a power-two function,

$$P = c\left(h - h_f\right)^2;\ h - h_f = 2\frac{P}{S} \tag{2.77}$$

the final depth is no longer needed. Indeed, a combination of Eqs. (2.1) and (2.2) yields:

$$\frac{h_c}{h_{\max}} = 1 - \epsilon\frac{P_{\max}}{S h_{\max}} \tag{2.78}$$

where $\epsilon = 2\left(1 - 2/\pi\right) = 0.73$. Equation (2.78) is also valid for other indenter shapes: $\epsilon = 1$ for a flat punch, and $\epsilon = 0.75$ for a paraboloid.

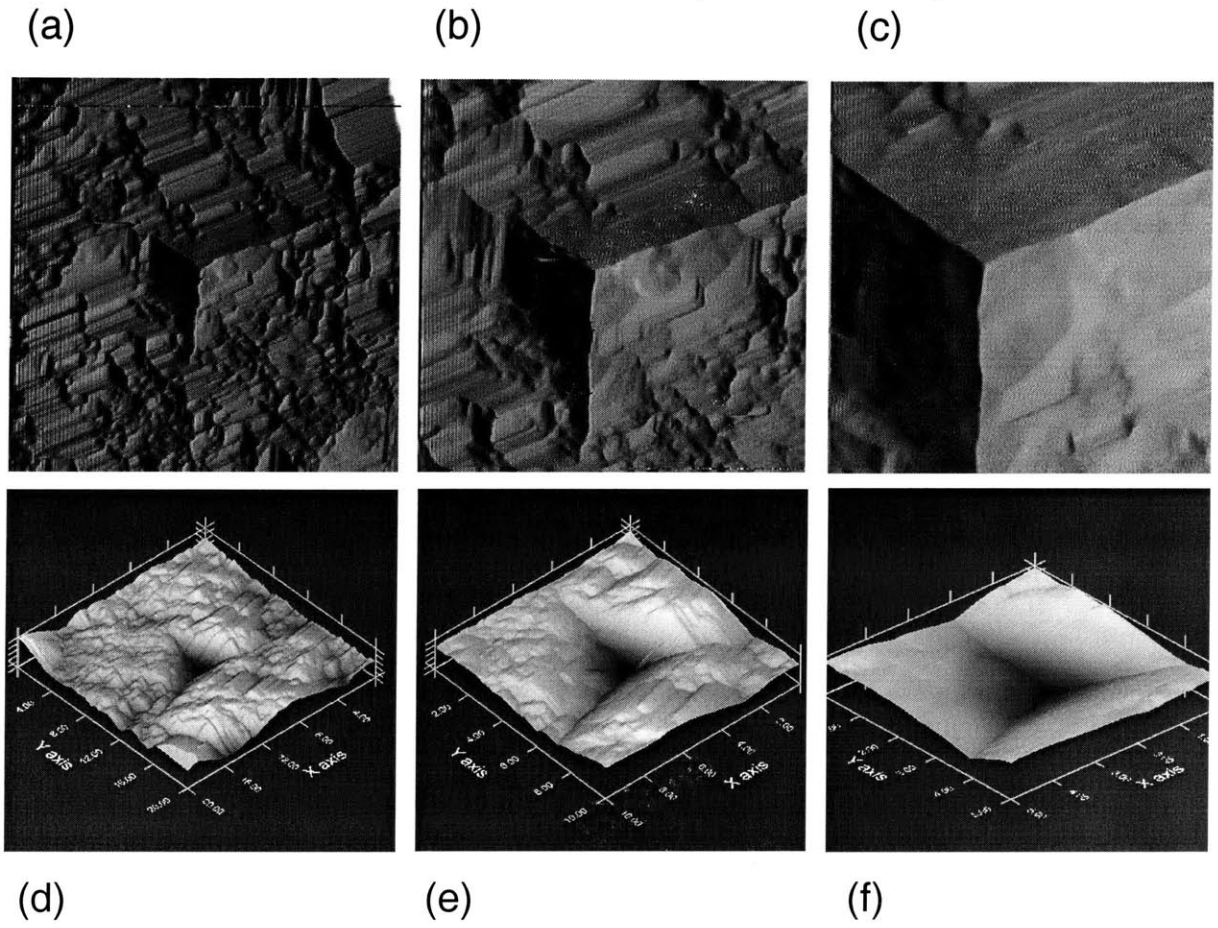

Figure 2-14: Gradient, (a)-(c), and 3-D topographic , (d)-(f), views of AFM images of residual impressions after microindentation in a shale material. Image Sizes: (a) and (d) $20 \times 20\mu m^2$, (b) and (e) $10 \times 10\mu m^2$, (c) and (f) $5 \times 5\mu m^2$

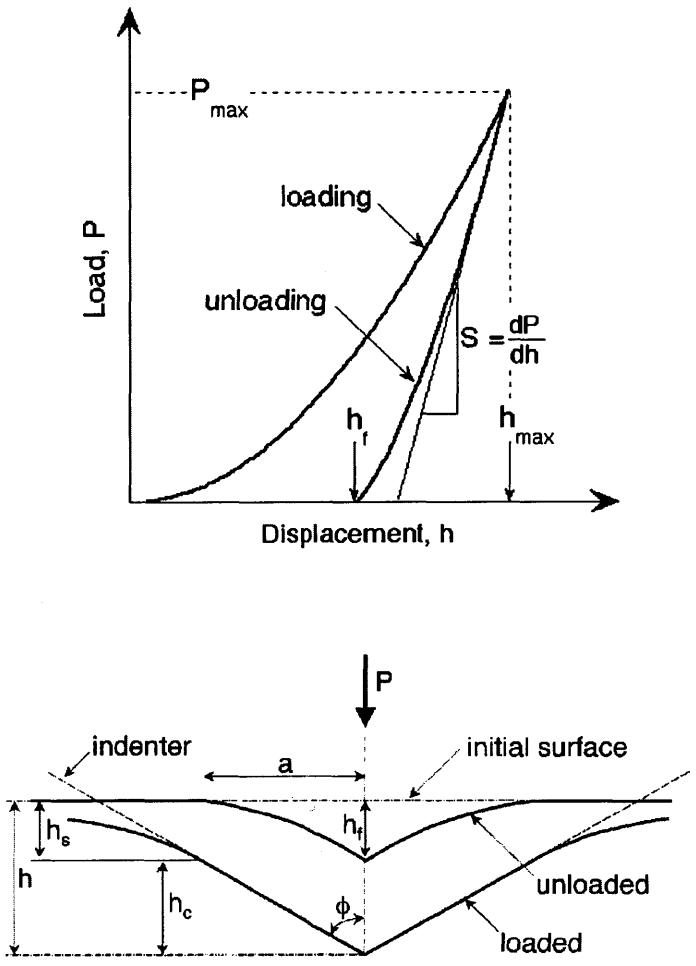

Figure 2-15: Determination of the area of contact with the Oliver and Pharr method [184], wher h_c is related to $h_{\max}$ and $P_{\max}/S_{\max}$ (from Ref. [184]).

The main assumption incorporated in this analysis is that the surface area beyond the contact points conforms with the elasticity solutions: it assumes that the material sinks-in. The main assumption of the Oliver and Pharr method is that the shape of the deformed solid outside the area of contact is elastic. This is not true when plastic deformations occur around the indenter to form material pile-up. Indeed, Eq. (2.78) cannot predict $h_c/h > 1$ which may be the source of important errors, particularly in plastic dilating materials (which are cohesive frictional materials). The second concern about this method is that most of the unloading curves in Berkovich indentation tests obey to a power relation of the form:

$$P = b(h - h_f)^m \tag{2.79}$$

with values for the power-law exponent in the range $1.2 \leq m \leq 1.6$ for a large range of tested materials [185]. By comparing this experimental scaling relation with the closed form elastic solutions for the flat punch ($P \propto h$), conical indenter ($P \propto h^2$) and paraboloid of revolutions ($P \propto h^{3/2}$) [213], it appeared that the unloading curves are best approximated by an indenter that behaves like a paraboloid of revolution, ($m = 1.5$); and the value $\epsilon = 0.75$ was recommended for Berkovich indentation. The conclusions are somewhat surprising because the axi-symmetric equivalent of the Berkovich indenter is a cone, for which $m = 2$. This discrepancy has since been explained by the concept of an "effective indenter shape" [185]: During loading the localized area around the indent gets heavily distorted and as a consequence, upon unloading, permanent deformations remain on the surface of the material. Reloading that region involves a conical surface that pushes against a concave surface. According to Oliver and Pharr, such a phenomenon can be well approximated by a paraboloid indenter pressed against a flat surface.

2.5.3 Cheng and Cheng Method

A more recent attempt to develop a method that can circumvent, by design, the need for measuring the contact area is the one proposed by Cheng and Cheng [47], who used finite element indentation simulations for a wide variety of elasto-plastic materials with different work hardening characteristics to examine pile-up during conical indentation (see also the work of Giannakopoulos and coworkers in Refs. [97,98]). The proposed method relies on the work of

indentation which can be directly measured from the $P-h$ response. The remarkable result the authors obtain is that the ratio of the irreversible work to the work of indentation is a unique function of the hardness-to-indentation modulus ratio, H/M, irrespective of the work hardening characteristics of the material:

$$\frac{W_{tot}-W_{el}}{W_{tot}} \approx 1-5\frac{H}{M} \tag{2.80}$$

where W_{tot} (the area under the loading curve) is the total work of indentation, and W_{el} (the area under the unloading curve) is the work recovered during unloading. Furthermore, using Eqs. (2.1) and (2.2) to eliminate the contact area, we obtain:

$$\frac{4}{\pi}\frac{P_{\max}}{S^2} = \frac{H}{M^2} \tag{2.81}$$

Recalling that W_{tot}, W_{el}, $P_{\max}$, S are all measurable from the load-displacement data, Eqs. (2.80) and (2.81) form a closed system that can be used for the evaluation of hardness and indentation modulus without the need for measuring the area of contact. Once the hardness and indentation modulus are obtained then the area of contact can be calculated from Eqs. (2.1) and (2.2). Presumably this area should account for any pile-up or sink-in phenomena. To our knowledge, this method has not been validated in actual indentation tests. Furthermore, some limitations of the method may arise from the way Eq. (2.80) was determined:

- The finite element simulations were performed with an equivalent cone angle of 68°; and it is not clear whether Eq. (2.80) would still hold for other semi-apex angles and indenter geometries.
- Equation (2.80) was fitted from finite element simulations of von Mises materials; and it is not clear whether it would still be valid for cohesive-frictional materials.

The accuracy of these methods in calculating the area of contact at maximum load will be further explored in Chapter 3. Generally speaking, experimental evidence and finite element simulations suggest that the Oliver and Pharr method for calculating the contact area is in reasonable agreement with the true contact area, provided the material response around the indenter contact perimeter is not experiencing pile-up deformations [185,49,50].

2.5.4 Application of Dual Indentation Technique

One problem which we will face in this work concerns the determination of the contact areas in the dual indentation technique (see Section 2.3.4). The principle of the technique is to carry out two indentation tests with different indenter geometries, e.g., a Berkovich and a cube corner indenter. The only quantities that are directly measured are the loads $\left(P^{\exp(1)}, P^{\exp(2)}\right)$, the maximum indentation depths $\left(h^{\exp(1)}, h^{\exp(2)}\right)$ and the unloading slopes $\left(S^{\exp(1)}, S^{\exp(2)}\right)$. Assuming the validity of the BASh formula (2.2), the contact area in the indentation test is given by:

$$A_c^{(i)} = \frac{\pi}{4}\left(\frac{S^{\exp(i)}}{M}\right)^2 \tag{2.82}$$

where superscript ($i = 1, 2$) stands for indentation test (for instance, Berkovich = 1; cube corner = 2); M is the indentation modulus that is linked to the elastic properties of the material and the indenter by Eq. (2.68). If we had an independent means to determine M, Eq. (2.82) would allow us to determine the contact area. In return, given that the indentation modulus is the same in both tests, we can determine the ratio of the contact area directly from the measured unloading slopes:

$$\frac{A_c^{(1)}}{A_c^{(2)}} = \left(\frac{S^{\exp(1)}}{S^{\exp(2)}}\right)^2 \tag{2.83}$$

Hence, it suffices to determine A_c in one indentation geometry accurately to determine A_c from the unloading slopes for the other indentation geometry. Furthermore, Eq. (2.83) is readily employed to determine the hardness ratio (which serves as an input for the determination of the friction angle via Fig. 6-3 from Eq. (2.1):

$$\frac{H^{(1)}}{H^{(2)}} = \frac{P^{\exp(1)}}{P^{\exp(2)}} \times \left(\frac{S^{\exp(2)}}{S^{\exp(1)}}\right)^2 \tag{2.84}$$

For the determination of the individual hardness values, an iterative procedure is suggested. Instead of measuring the contact area, we estimate the projected contact area by any approximate method, say the Oliver and Pharr method, giving us $A_c^{est(1)}$, $A_c^{est(2)}$; from which we determine a first estimate of the hardness and the indentation stiffness from Eqs. (2.1) and

(2.2):

$$H^{est(i)} = \frac{P^{\exp(i)}}{A_c^{est(i)}};\ M^{est(i)} = \frac{2}{\sqrt{\pi}} S^{\exp(i)} \left(A_c^{est(i)}\right)^{-1/2} \tag{2.85}$$

If $M^{est(1)} = M^{est(2)}$, the estimate is correct, and hence:

$$M^{est(1)} = M^{est(2)} = M^{\exp(1)} \tag{2.86}$$

If $M^{est(1)} \neq M^{est(2)}$, the estimates may not be correct, and we need to proceed in an iterative fashion. We first need to verify that one of the two contact area estimates is exact. Let us assume that this was the Berkovich indentation stiffness ($i = 1$):

$$M^{est(1)} = M^{\exp(1)};\ A_c^{est(1)} = A_c^{\exp(1)} \tag{2.87}$$

We can then readily check whether the contact area estimation is valid for the cube corner ($i = 2$), from:

$$A_c^{(2)} = \left(\frac{M^{est(2)}}{M^{\exp(1)}}\right)^2 A_c^{est(2)} \tag{2.88}$$

Hence, if the corner cube indentation stiffness estimate $M^{est(2)}$ coincides with the Berkovich indentation stiffness $M^{\exp(1)}$, the contact area has been correctly determined. In the contrary case, we need to correct the estimated contact area $A_c^{est(2)}$ using (2.88). Finally, we obtain the cube corner hardness from:

$$H^{(2)} = H^{est(2)} \left(\frac{M^{\exp(1)}}{M^{est(2)}}\right)^2 \tag{2.89}$$

where $H^{est(2)} = P^{\exp(2)}/A_c^{est(2)}$ is the estimated Corner cube hardness. Of course, the obtained value of the hardness is more accurate as the value of $M^{\exp(1)}$ is more accurate. Note that $M^{\exp(1)}$ and $M^{est(2)}$ are the indentation stiffness values, which include the material stiffness and the indenter compliance as defined by Eq. (2.68).

We recall that the derivation of the above procedure relies on the validity of BASh relation. As was discussed in Section 2.4.3, however, second order effect may impose an error in the formulation that needs to be corrected. It is interesting to note that the aforementioned procedure, which relies on the ratio of data collected from two indenter geometries, tends to reduce

such error (the new error will now be $\beta' = \frac{\beta^1}{\beta^2}$, where $\beta' < \beta^1, \beta^2$ since $\beta^1, \beta^2 > 1$) or even eliminate such error (in cases where the $\beta-$factor is not a function of θ, $\beta' = \frac{\beta^1}{\beta^2}$ collapses to 1). For the time being, an estimate of the $\beta-$factor for cohesive-frictional material does not exist. In the light of such a correction factor, Eqs. (2.82) – (2.89) should be modified accordingly.

2.6 Chapter Summary

An indentation test is a surface test which provides access to bulk properties of the indented material. This first chapter on indentation analysis focussed on the underlying mechanical principles that allow one to translate indentation data into meaningful mechanical properties: self-similarity of the indentation test, advanced limit analysis, and elastic contact mechanics. This background provides a strong argument that instrumented indentation can give reliable estimates of the hardness and indentation modulus of materials provided that the P *vs* h response is properly measured and that the area of contact is obtained correctly. While the indentation analysis of homogeneous cohesive materials like metals is well advanced, we have discussed in this chapter the possibilities of extending the analytical tools to cohesive-frictional materials. The link between indentation modulus and the elastic properties remains unaffected, provided that the correct contact area is determined. In contrast, the link between hardness and cohesion is a strong function of the internal friction. From the limit analysis solutions (see also Ref. [92]), we propose a novel dual indentation technique. This dual indentation method is highly reductionist in nature: it is based on the geometrical self-similarity of the conical indentation test and on yield design assumptions, reducing the number of parameters governing the hardness-to-cohesion ratio to two, the friction angle φ and the semi-apex angle θ. In this reduced $(H/c, \varphi, \theta)$ invariant space, it is possible to ensure the uniqueness of the inverse analysis and extract the strength properties of cohesive-frictional materials. This method has several advantages, but also restrictions, compared to other inverse analysis methods:

1. The main advantage of the method is the ease of utilization: Compared to advanced finite element elastoplastic inverse analysis of indentation data, the method requires as input only two hardness values corresponding to two indenter geometries (semi-apex angle θ). By means of fundamental dimensionless relations for the hardness-to-cohesion ratio, we

find that the hardness-to-hardness ratio is a unique function of the friction angle, which ensures the uniqueness of the reverse problem. We demonstrated this method for two indenters commonly employed in instrumented indentation, Berkovich and cube corner indenters approximated as cones of different semi-apex angles. Of course, the same method could be employed with any other semi-apex angle, and the method is the more efficient the higher the H/c–contrast between two semi-apex angles for a given friction angle. We should also note that such a contrast is not achieved by spherical indentation of different sphere radius-to-indentation depth ratios, R/h, which replaces the apex semi-angle in the dimensionless relation of Eq. (2.17), i.e., $H/c = \mathcal{H}_s(\varphi, R/h)$, making the conical indentation test the most efficient way to extract cohesion and friction angle from hardness measurements. We come to this conclusion from lower and upper bound H/c–solutions for spherical indentation which have been obtained with the novel computational solution of the limit analysis problem [93]. Not surprisingly, we also found that it is not possible to extract the friction angle from the hardness ratio of two indenter geometries that do not belong to the same family of self-similar indenter shapes; for instance from a combination of conical and spherical indentation; entailing the non-uniqueness of the reverse problem (for details, see Ref. [93]). This emphasizes that the geometrical self-similarity is a necessary condition for the uniqueness of the proposed inverse procedure.

2. The main analytical tools we employ in this method are fundamental $H/c = \mathcal{H}_c(\varphi, \theta)$ relations which have been developed in Ref. [93] from a novel computational implementation of the limit theorems in axisymmetric conditions. One restriction of the approach relates to the assumption of the normality rule (or principle of maximum plastic work), which is at the very basis of the existence of the limit theorems of yield design, and which cannot capture non-associated flow behavior of the plastically deforming material. From the perspective of dimensional analysis, the consideration of a non-associated flow rule adds one additional independent quantity, the dilatation angle, to the set of parameters in Eq. (2.15), but cannot be handled by the proposed yield design solution procedure in which the dilatation angle equals the friction angle. For such materials, advanced finite element simulations are required. In this case, the proposed method can be used to determine initial values of the cohesion and friction angle for the iterative inverse analysis. A

similar remark can be made for contact friction (which has been investigated for cohesive materials, [51]) and strain hardening effects, which we ignore in our yield design solutions.

3. It could also be (and has been) argued that yield design approaches cannot capture piling-up or sinking-in phenomena, as yield design evaluates the dissipation capacity of a materials system for a fixed geometry. Indeed, in our upper-bound simulations, we assumed the surface surrounding the indenter to be flat, which is far from what is observed on topographic images (see Fig 2-14) in indentation tests particularly for very sharp indenters like the cube corner. However, compared to the material bulk volume that contributes to the overall dissipation capacity (see Fig. 2-8), the additional contribution of the pile-up material volume can be expected to be of second-order in the evaluation of Eq. (2.22) of the maximum dissipation the material system can afford. Of course, the piling-up or sinking-in phenomena cannot be neglected in the evaluation of the hardness values from the definition of Eq. (2.1), which is an input in our method. Hence, like all indentation procedures, the successful determination of the strength properties from the two indentation tests relies on the determination of the correct projected contact area.

This novel dual indentation technique will be validated in Chapter 3 for a model cohesive-frictional material, bulk metallic glass; together with the other tools presented in this chapter, the BASh formula, the Oliver and Pharr method for contact area determination, and so on.

Chapter 3

Indentation Analysis of a Cohesive-Frictional 'Model' Material: Bulk Metallic Glass

This chapter illustrates the application of instrumented indentation for a cohesive-frictional 'model' material: amorphous metal or bulk metallic glass (BMG). The rational of validating the tools of indentation analysis presented in Chapter 2 for this 'model' material is twofold: (1) Bulk metallic glass is a fine-tuned man-made cohesive-frictional material, which is much more homogeneous than highly heterogeneous 'natural' composites with which we will be concerned in subsequent chapters of the thesis; and (2) the cohesive-frictional nature of BMG was recently identified through a number of investigations ranging from the atomistic scale [159] to the macroscopic scale [72, 158], including indentation testing and comprehensive 3-D elastoplastic finite-element reverse analysis of Berkovich indentation tests [236, 206]. Given this background, BMG appears to us an ideal model material to validate the concepts introduced in Chapter 2: determination of the contact area, indentation modulus, hardness; and the translation of these indentation data into mechanical properties. A special focus will be on the validation of the dual indentation technique for the extraction of the cohesion and the friction angle of this cohesive-frictional model material. Furthermore, this chapter will also allow us to provide a 'hands-on' introduction to indentation testing, including indentation set-up and calibration

procedure, which are critical for obtaining reliable indentation data.

3.1 Indentation Set-up and Calibration Procedure

The loading and unloading branches of the load-displacement or $P-h$ curve, which give access to the micromechanical properties of the indented material, depend on the experimental set-up, i.e., machine compliance, friction between the indenter and indented material, specimen clamping, sharpness of the indenter tip, and so on. The high precision equipment combined with a careful execution of the experiments allow one to minimize errors in the experimental data. The indentation equipment is calibrated before each test to ensure the accurate recording of the $P-h$ material response. The important features of data collection, machine calibration and potential sources of error are briefly described in this section.

3.1.1 Indentation Equipment

Nanoindentation experiments in this study are carried out using two instruments located in the Nanomechanical Technology Laboratory —the so-called 'Nanolab'— in the Department of Materials Science and Engineering at M.I.T. These are the NanoTest 600 of Micro Materials Ltd., and the Triboindenter of Hysitron Inc. Table 3.1 summarizes specifications of both indenter systems, which are critical in performing indentation tests.

The indenter system of Micro Materials Ltd. has a NanoTest option and a MicroTest option. The first allows monitoring the P–h relationship in a load range of 0 to 500 mN, and in a displacement range of 0 to 20 μm, with resolutions of 3 nN and 0.06 nm, respectively [170]. The MicroTest allows indentations at higher loads and displacements: 20 N and 20 μm respectively. The increase in maximum allowable force and displacement comes with a reduction in the resolution: Loads and displacements are now recorded with a resolution of 15-20 nN and 0.2-0.23 nm respectively. In the Micromaterials set-up, a pendulum pivoting around frictionless leaf springs applies the load to the specimen (Fig. 3-1a). A current passes through a coil mounted at the top of the pendulum and attracts the coil to a fixed permanent magnet. This sets the indenter into motion to the specimen surface which is firmly clamped to the loading stage. The displacement of the indenter (depth h of penetration into the specimen) is

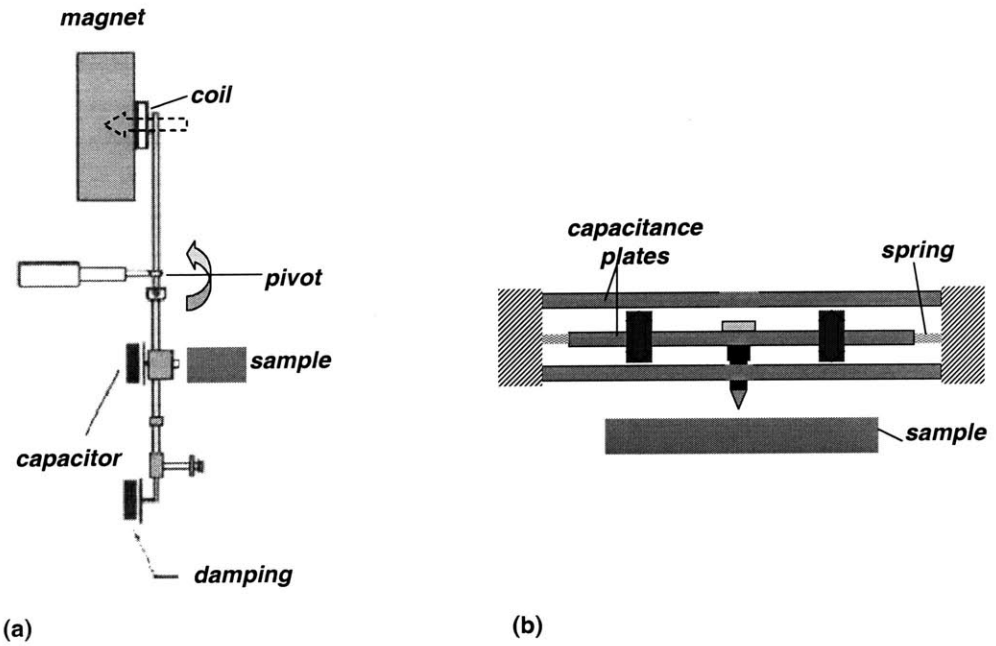

Figure 3-1: Cross-section schematic of a) Micromaterials and b)Triboindenter transducer set-up (from [170] and [124]).

continuously monitored and recorded by the change in the voltage of a parallel plate capacitor. In this way, the complete $P - h$ response is obtained [170]. $P(V)$ and $h(V)$ are calibrated by the user, as is frame compliance C_f. A vibration isolation platform and an acoustic enclosure ensure no interference of noise and thermal drifts on the experiments.

The heart of the Hysitron's testing instruments is the patented three-plate capacitive transducer that is both the actuator and sensor of the instrument [124]. The force is applied electrostatically while the displacement is simultaneously measured by the change in capacitance (Fig. 3-1b). To apply a force, a large DC bias (up to 600 V) is applied to the bottom plate of the capacitor. This creates an electrostatic attraction between the center plate and the bottom plate, pulling the center plate down. The force is calculated from the magnitude of the voltage applied[1]. The maximum load force available from the transducer is approximately 12 mN. This arrangement gives resolutions of 1 nN in load and 0.04 nm in displacement. The electrostatic force constant of the transducer is calibrated prior to each testing to maintain a linearized

[1]This is not actually calibrated by the user, just the maufacturer.

Manufacturer	Hysitron Inc.	Micro Materials Ltd.	
	Triboindenter	MicroTest	NanoTest
Maximum Force [mN]	12	20,000	500
Load Resolution [nN]	1	15-20	2-3
Load Noise Floor [nN]	100	100	100
Maximum Depth [μm]	20	20	15
Displacement Resolution [nm]	0.04	0.2-0.23	0.05-0.06
Displacement Noise Floor [nm]	0.2	-	-
Thermal Drift [nm/sec]	<0.05	<0.1	<0.1
Machine Compliance [nm/mN]	14	0.3-0.4	0.3-0.4
Specimen Clamping [nm/mN]	~0.01	~0.01	~0.01

Table 3.1: Specification of nanoindenters. Values provided by the manufacturers some of which rely on accurate calibrations prior to testing.

relationship between bias voltage and force. This instrument includes a piezoelectric actuator to establish tip-sample contact in the loading train.

3.1.2 Calibration Issues

A list of factors that affect the accuracy of the recording of the $P-h$ response are listed in Tab. 3.2. In general, load detection is less susceptible to errors compared to the depth measurements. Several factors that can be recorded in the depth data might not be attributed to the material response, and should be excluded before analyzing the $P-h$ response:

1. Specimen Clamping: Specimens are attached directly to a stub holder[2] by means of a suitable adhesive. The main criterion for choosing an adhesive is that the layer formed is thin and stiff once set and does not significantly contribute to the system compliance. The highly localized deformation response of the system excludes any boundary effects to the indentation response. In our study, we employ cyanoacrylate "Superglue".

2. System Compliance: Depth measurements during an indentation test incorporate the effect of instrument deformation resulting from the reaction forces during loading. To account for this additional deformation, one needs an estimate of the frame compliance, through calibrations that are performed on the machine. Considering that the specimen-indenter and the load frame are springs in series the total compliance, C_T, can be written

[2]The stub holder is firmly clamped, either mechanically (Microtest) or magnetically (Hysitron) to the stage.

	P	h
Specimen Clamping	×	✓
System Compliance	×	✓
Noise/Thermal Drift	×	✓
Vibrations	✓	✓
Spring Constants	✓	×

Table 3.2: Factors influencing the recorded $P - h$ response.

as:

$$C_T = C_s + C_f \tag{3.1}$$

where $C_s = 1/S$ is the specimen compliance (S being the contact stiffness; see Section 2.4), and C_f is the frame compliance. Assuming a linear elastic response on unloading, the material compliance can be linked to the indentation modulus M of the material using the BASh formula Eq. (2.2):

$$C_T = \frac{\sqrt{\pi}}{2M}\frac{1}{\sqrt{A_c}} + C_f \tag{3.2}$$

The machine compliance C_f is then determined by several large load indents using a Berkovich indenter with large indentation depths ($h_c > 1/3$ tip radius) in a reference material sample of known elastic properties, typically fused quartz. A graph of the measured compliance C_T vs. $A_c^{-1/2}$ for a series of indents yields a straight line with the machine compliance as the y-axis intercept. In this calibration procedure, the area of contact A_c is calculated using the different techniques presented in Section 2.5. It is readily understood that this calibration procedure depends on the accuracy of the contact area determination and the relevance of the elasticity assumption, and may therefore incorporate significant inaccuracy in the machine compliance estimation [238]. To eliminate this source of inaccuracy, Van Vliet et al. [238] suggested to make a direct compression test on the system in the absence of any sample to determine C_f. Typical values of the compliance of our machines are approximately 1 nm/mN (see Tab. 3.1), which translates into an error of 12 nm displacement contribution for the maximum forces (for Hysitron indentations). Hence, the error induced by a wrong machine compliance is the more significant the smaller the indentation depth i.e., in nanoindentation tests, and needs to be taken into account carefully. On the other hand, in the case of microindentation tests, operated

to indentation depths in the micrometer range, the machine compliance plays a minor role. Furthermore, while the machine compliance introduces little inaccuracy in the $P-h$ response of soft materials, the effect of the compliance of the system becomes significant when indenting on very hard materials. As we will see, this is the case for indentation testing of Bulk Metallic Glass (BMG) presented in this chapter. Figure 3-2 shows the effect of machine compliance on the $P-h$ response obtained from Berkovich indentation on Vitreloy 1^{TM}, the BMG investigated in our study. In particular, the unloading contact stiffness appears to be very sensitive to the machine compliance, which therefore strongly affects the determination of the indentation modulus M. A careful system compliance calibration is therefore essential in order to avoid any errors in the $P-h$ response, and in the indentation modulus/hardness evaluation. Using the direct stiffness approach [238], we found a machine compliance of $C_f = 0.3854$ nm/mN for the Micro Materials indenter. The fact that the indentation modulus M we determine for BMG by way of indentation as shown here below, is very close to the actual $M-$modulus of the material (determined from known elasticity properties using (2.68)), is strong evidence of the accuracy of the frame compliance determination.

3. Noise/Thermal Drift: A change in depth under constant load can be observed due to dimensional instabilities of the apparatus to thermal changes. This change in depth imposes a 'thermal drift' error onto the actual depth values. The indentation instruments are equipped with an acoustic enclosure that has been designed to minimize the amount of temperature changes during testing. The enclosure also blocks air currents and acts as an acoustic buffer to help eliminate additional errors. There is a large door in the front that is used to access the sample stage for loading and unloading of samples. This set-up ensures that noise and thermal drift are restricted to very low levels (Angstroms/second, see Tab. 3.1). Given the indentation depths achieved in most nanoscale indentations ($h < 200$nm), the thermal drift effect on the indentation data can be significant. It should be noted that thermal and noise drift corrections are taken into account in our data since the software offers automated corrections. To account for thermal drift errors both instruments allow for hold periods at either the beginning (0% of maximum load-Hysitron) or the end (90% of unloading-Micromaterials) of a test were data points are accumulated and a thermal

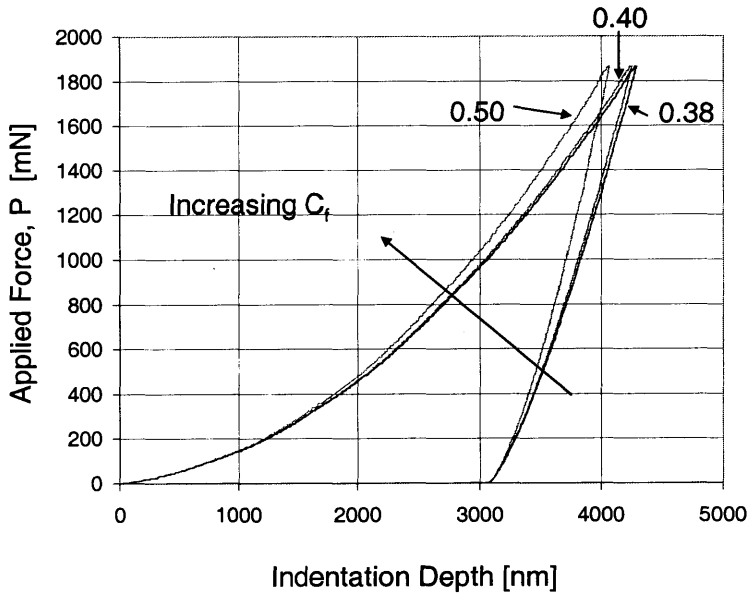

Figure 3-2: Effect of frame comliance on the $P-h$ response. Load vs. displacement curves are for Berkovich indentations on BMG.

drift rate is calculated that is later applied to the whole data.

4. Vibration: Both instruments provide anti-vibration platforms that damp noise in high and low frequency ranges. The errors induced by potential vibrations during testing are minimized to 100 nN for load and 0.2 nm for depth. This ensures a high quality of the recorded data.

3.2 The 'Model' Material: Bulk Metallic Glass

3.2.1 Background

Most metals crystallize as they cool, arranging their atoms into a highly regular spatial pattern called a Bravais lattice or crystalline. If crystallization does not occur, and the atoms settle into a nearly random arrangement akin to a liquid, the final form of the solid is a metallic glass. The difficulty in making a metallic glass is to cool the metallic liquid (which has a disordered structure as well) rapidly enough so that there is not enough time for the ordered, crystalline structure to develop. This was recognized in the 1960s, when it was found that thin ribbons, wires, or sheets of metals can be produced in an amorphous state with exceptional mechanical properties after being cooled down at high rates (over 10^5 K/s) [112],[206]. More recently, new alloys have been developed that form glasses at much lower cooling rates, around 1 to 100 K/s. While still fairly rapid, this rate is slow enough that bulk ingots of these metallic alloys can be cast, and they will solidify to form glasses. Metallic glasses are mostly prepared by casting methods[3] or by consolidation of glassy powders in the supercooled liquid region, through a process of warm-extrusion [135].

Bulk metallic glasses have been of great technological and scientific interest since their discovery in 1960, and are considered today as emerging structural materials due to their high strength and large elastic deformation capacity prior to the onset of plastic deformation (see Fig. 3-3). Typical metallic glass has a Young's modulus on the order of 100 GPa, and uniaxial tensile strength of roughly 2 GPa for Zr-based glasses (between 1.3 and 1.5 GPa for

[3] An alloy ingot is prepared by arc melting pure metals in a purified argon atmosphere. Bulk amorphous alloys are then prepared in Pd or Zr based system by repeated melting of their molten alloys fluxed with B_2O_3 (from [176]).

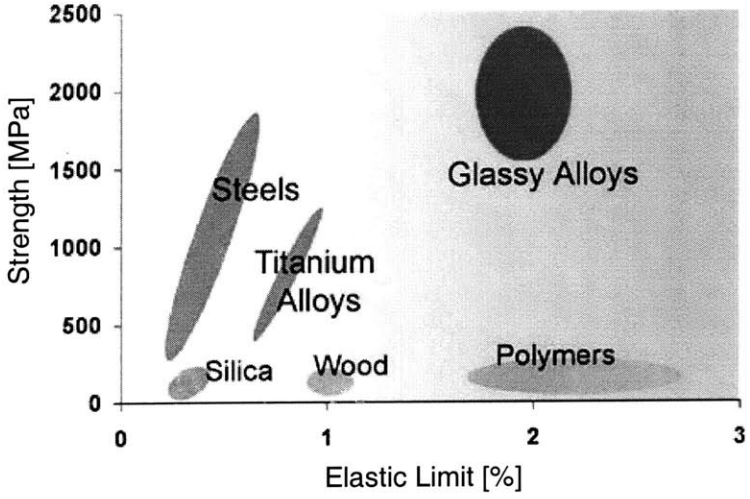

Figure 3-3: Typical strengths and elastic limits for various materials. Metallic glasses (Glassy Alloys) are unique (Image Source: http://www.its.caltech.edu/~vitreloy/development.htm).

Pd-based metallic glasses), thus allowing for a pure elastic deformation, in uniaxial tension of about 1/50 for Zr-based glasses (compared to 1/400 for steel). In addition, metallic glasses posses an excellent strength to weight ratio, usually around 300 kPa/kg/m^3 (compared to 63 kPa/kg/m^3 for steel), and relatively high fracture toughness values: Fatigue fracture toughness values of approximately 20 MPa m$^{1/2}$, and notched toughness in excess of 100 MPa m$^{1/2}$. These exceptional mechanical properties make metallic glasses an extremely appealing material and have prompted intensive research.

The exceptional material properties of metallic glasses with many possibilities for structural applications were overshadowed by the tendency of early material developments to fail in localized shear bands entailing minor ductile catastrophic failures [236]. The potential applications of these materials with the restrictions at stake called for detailed mechanical investigations, but the limitation to small specimen volumes (the fast cooling rates restricted the size of the products to mm-size ribbons or sheets) made conventional macroscopic mechanical tests difficult. With the development of depth sensing indentation techniques (for a recent survey, see Ref. [206]) and concurrent manufacture of metallic glasses in bulk form (BMG) a renewed interest arose. Of these alloys, Zr-based bulk metallic glasses are now commercially available

	Average	Scatter	References
Elastic Modulus [GPa]	92.23	83–100.4	[112],[158],[55],[217]
Poisson's Ratio [1]	0.37	0.351–0.38	[112],[158],[55],[217]
Compressive strength, Σ_c [GPa]	1.88	1.83–1.9	[249],[158],[35],[254],[154]
Tensile strength, Σ_t [GPa]	1.47	1.2–1.9	[35],[55],[254],[154]
Vickers Hardness [GPa]	5.29	5.03–5.40	[249],[112],[100],[55]

Table 3.3: Summary of mechanical properties for Zr-based Bulk Metallic Glass as found in the literature

as engineering materials, the best known example of which is the Zr-based metallic glass of composition $Zr_{41.2}Ti_{13.8}Cu_{12.5}Ni_{10}Be_{22.5}$ (nominal composition in at.%), which goes by the commercial name Vitreloy 1^{TM}. We concentrate our discussions here on this class of BMG. Our interest in the material stems from the recent evidence that BMGs exhibit a pressure sensitive shear strength behavior which is evidence of the cohesive-frictional nature of these materials.

3.2.2 Mechanical Properties at Multiple Scales

A summary of different studies of mechanical properties of Vitreloy 1^{TM} is given in Tab. 3.3. While the data show some scatter, the average values show a great deal of consistency. The elastic properties of Vitreloy 1^{TM} are well known by now from both ultrasonic measurements [55], [158] and FE inverse analysis of microindentation data [236]: Young's modulus $E \simeq 96$ GPa, Poisson's ratio $\nu \simeq 0.36$. Furthermore, there is a growing body of both experimental and theoretical evidence that metallic glasses are cohesive-frictional materials that obey to a Mohr-Coulomb criterion, and not purely cohesive materials of the Von Mises kind, as it was originally suggested.

Donovan [72] derived the cohesive-frictional nature of Pd-based metallic glass ($Pd_{40}Ni_{40}P_{20}$) at the macroscale, from uniaxial compression, plane-strain compression, plane-strain tension and shear tests. The macroscopic results proved that the $Pd_{40}Ni_{40}P_{20}$ metallic glass obeys a Mohr-Coulomb criterion,

$$f(\boldsymbol{\sigma}) = \tau + \alpha\sigma_n - c = 0 \tag{3.3}$$

with the following strength properties:

$$c = 795 \pm 25 \text{ MPa} \quad \text{and} \quad \tan\varphi = 0.113 \pm 0.03 \tag{3.4}$$

where $\tau = (\sigma_I - \sigma_{III})/2$ is the shear stress, $\sigma_n = (\sigma_I + \sigma_{III})/2$ is the normal stress, and α is the friction coefficient. These macroscopic findings were confirmed by Lu and Ravichandran [158] by means of an extensive experimental investigation of the triaxial strength behavior of Zr-based metallic glass. By fitting the Mohr-Coulomb criterion (3-2) to four principal failure stresses reported in the paper [(434; 434; 2480), (602; 602; 2740), (1000; 1000; 3320); (1508; 1508; 4050)], we find:

$$c = 755 \text{ MPa} \quad \text{and} \quad \alpha = \tan\varphi = 0.18 \tag{3.5}$$

These values are consistent with the friction coefficient of $\tan\varphi = 0.16$ reported in the paper obtained by fitting 23 representative triaxial stress states to the Mohr-Coulomb criterion of Eq. (3-2); to capture the orientation of the shear bands observed in the experiment, the authors employ a modified Mohr-Coulomb criterion, in which the mean stress $\sigma_m = (\sigma_I + \sigma_{II} + \sigma_{III})/3$ replaces the normal stress $\sigma_n = (\sigma_I + \sigma_{III})/2$ (see Fig. 3-4a):[4]

$$g(\boldsymbol{\sigma}) = \tau + \beta\sigma_m - c = 0 \tag{3.6}$$

with the following strength values:

$$c = 804 \text{ MPa}; \quad \beta = 0.17 \tag{3.7}$$

At the microscale, a further evidence of the cohesive-frictional nature of Zr-based metallic glass was provided by Vaidyanathan et al. [236], by means of a comprehensive 3-D finite element elastoplastic inverse analysis of microindentation tests operated to a maximum indentation depth of 9×10^{-6} m. By fixing the tensile yield strength in the simulations to a value of $f_t = 1.9$ GPa, the authors showed that the load-depth prediction using a Mohr-Coulomb criterion with

[4]Function (3.6) can be interpreted as a non-associated flow rule of BMG, but was not introduced as such by Lu and Ravichandran [158]. In fact, the strength behavior of BMG in the triaxial tests of Lu and Ravichandran is well captured by a Mohr-Coulomb criterion of the form (2.25a), which does only depend on the two extreme principal stresses, σ_I and σ_{III}, while the flow behavior appears to be goverend as well by the intermediate principal stress σ_{II}. This motivated the authors to propose considering the modified Mohr-Coulomb criterion (3.6). In return, this modification has little influence on the cohesion and friction coefficient; so that the fitted values (3.5) can without big error be assimilated with the cohesion and friction coefficient in the sense of a Mohr-Coulomb material.

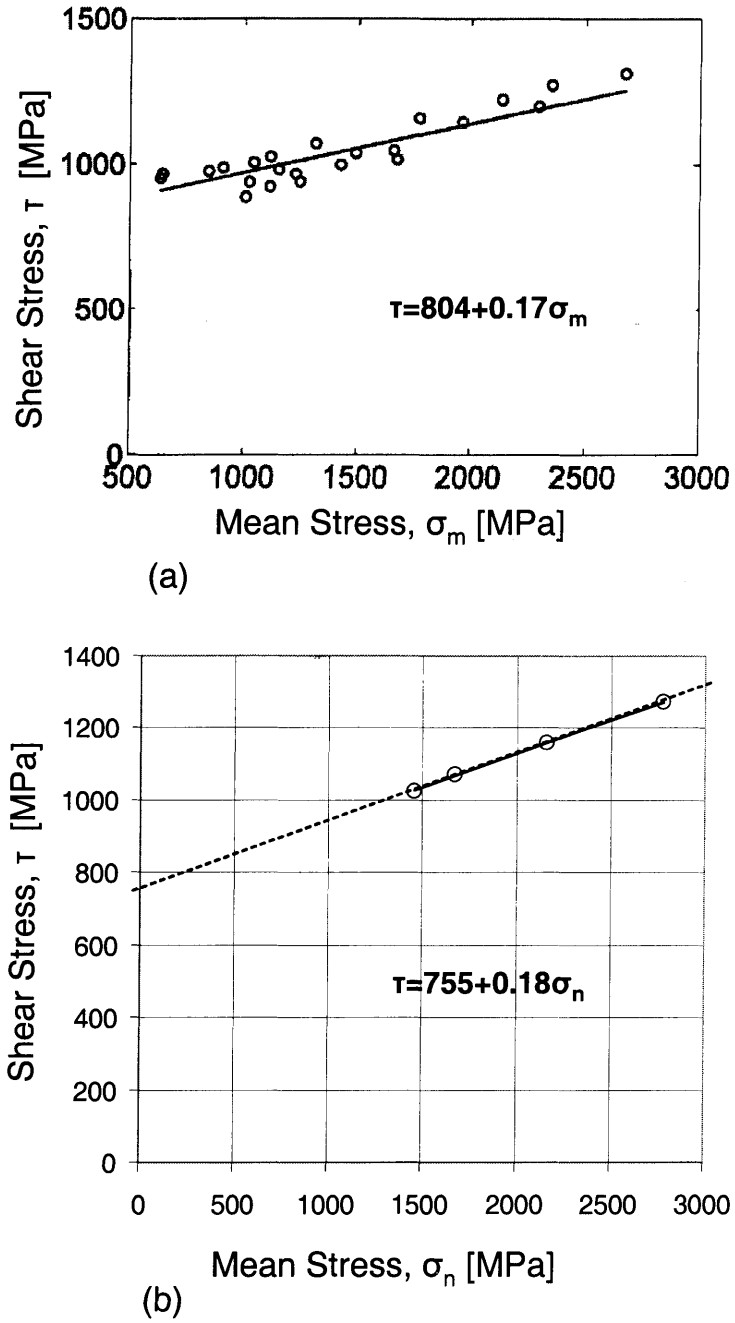

Figure 3-4: Triaxial strength domain for Zr-based metallic glass (Vitreloy 1^{TM}), from [158]. a) A modified Mohr-Coulomb criterion where the shear stress, $\tau = \frac{(\sigma_I - \sigma_{III})}{3}$, depends on the mean stress, $\sigma_m = \frac{(\sigma_I + \sigma_{II} + \sigma_{III})}{3}$. b) Mohr-Coulomb envelope of shear stress, $\tau = \frac{(\sigma_I - \sigma_{III})}{3}$, *vs* the normal stress, $\sigma_n = \frac{(\sigma_I + \sigma_{III})}{2}$.

a friction coefficient of,

$$\tan\varphi = 0.13 \tag{3.8}$$

follows the results more closely than a von Mises material behavior. Finally, Lund and Schuh [159] provide theoretical atomistic arguments in favor of the cohesive-frictional behavior of metallic glass through an intriguing analogy between the relative motion of randomly packed atoms in a metallic glass and the cohesive-frictional response of randomly packed particles in a granular solid [151]. This suggestion was confirmed by molecular statics simulations of Zr- and Cu-based metallic glasses, from which the authors derive the following friction coefficient:

$$\tan\varphi = 0.123 \pm 0.004 \tag{3.9}$$

It is remarkable to note from Eqs. (3.4) to (3.9) that the friction angle of metallic glasses is almost the same over eight orders of length magnitude: from the scale of its atoms to the macroscale of laboratory test specimens. This scale independence is most likely related to the high homogeneity of the materials, a consequence of their amorphous structure created during the rapid cooling which prevents an ordered, crystalline structure to develop. It is for this reason that we have chosen metallic glass as a 'model' material for validating the tools of indentation analysis for cohesive-frictional materials presented in Chapter 2, and in particular the yield design solutions and the dual indenter technique of Section 2.3.4. Furthermore, bulk metallic glass shows an almost elastic-perfectly plastic behavior in uniaxial compression/tension, with almost no strain hardening. This makes the application of a yield design approach even more appealing for this model material.

3.2.3 Choice of Material and Methods

The model material we investigate is Vitreloy 1^{TM}, an as-cast fully amorphous $Zr_{41.2}Ti_{13.8}Cu_{12.5}Ni_{10}Be_{22.5}$ bulk metallic glass, manufactured by Howmet Corporation, Greenwich, CT. It is the same Zr-based material composition investigated by Lu and Ravichandran [158] and Vaidyanathan et al. [236]. An indentation campaign with a Berkovich indenter and a cube corner indenter was performed with the MicroTest 600^{TM} nano/micro-indenter from Micro Materials Ltd. (see Tab. 3.1). A series of 100 Berkovich and 50 cube corner indentations were

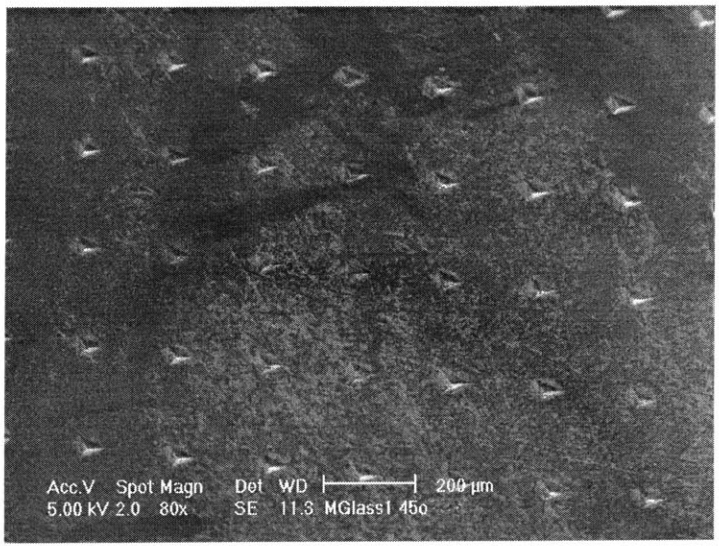

Figure 3-5: A grid of Berkovich indentations on a Bulk Metallic Glass. Grid size (spacing between indents) is 200 μm.

performed on a specimen of dimension $20 \times 20 \times 3$ mm. These indentation series were preformed on a grid with adjacent indents separated by 200 μm, a spacing that is large enough to avoid any possible interaction between consecutive tests (see Fig. 3-5). The indentations tests were load-controlled at a constant rate of 300 mN/s for the Berkovich indentations and 30 mN/s for the cube corner indentations. At maximum load, a dwell period of 15 s was imposed before unloading, and a hold period of 20 s at 90% of unloading facilitated the correction for any thermal drift effects in the system. The indentation data was analyzed in a statistical fashion to ensure the good repeatability of the results and their low standard deviation. Residual imprints of indents were examined under an Environmental Scanning Electron Microscope (FEI/Philips XL30 FEG ESEM) and an Optical Microscope, both located in the Center of Materials Science and Engineering at M.I.T.

3.3 Indentation Results

Table 3.4 gives a summary of the directly measured indentation data (see Section 2.1.2), namely the maximum force $P_{\max}$, the maximum indentation depth $h_{\max}$, the unloading slope (or contact

		Berkovich	Cube Corner
	#	100	50
$P_{\max}$	[mN]	$11,472 \pm 172$	$1,083 \pm 32$
$h_{\max}$	[nm]	$10,870 \pm 64$	$7,692 \pm 38$
S	[mN/nm]	4.83 ± 0.06	1.55 ± 0.02
W_e	[nJ]*	$15,575 \pm 0.375$	0.355 ± 0.028
W_p	[nJ]*	$28,531 \pm 0.531$	2.684 ± 0.117
A_c	[μm^2]	$2,116 \pm 11$	211 ± 9

Table 3.4: Summary of measured quantities from Berkovich and Cube Corner indentations: Mean $\pm$ St.Dev. The contact area A_c was determined from visual inspection of five residual impressions (* 1 nJ $= 10^{-9}$ N.m).

stiffness) S, the elastic and plastic work W_e and W_p, and the projected contact area A_c measured by visual inspection after unloading. The very low standard deviation of all the data is an indication of the high repeatability of the test procedure (including sample preparation), and of the homogeneity (in a statistical sense) of the indented BMG material. In a first step, we analyze the results in the light of the dimensional analysis presented in Chapter 2, to identify limits of the concept of self-similarity which is at the very basis of indentation analysis.

3.3.1 $P - h$ Responses

Figure 3-6a which displays the ensemble of $P - h$ curves for the two indenter geometries (Berkovich and cube corner), shows the high repeatability of the indentation test procedure. It is readily seen from the figure that the force required to drive the blunt Berkovich indenter to roughly the same indentation depth as the cube corner is much higher: $P_{\max} = 11,472\,\mu$N for $h_{\max} = 10,870\,$nm in the case of Berkovich indentations *vs.* $P_{\max} = 1,083\,\mu$N for $h_{\max} = 7,692\,$nm in the case of cube corner indentations (see also Tab. 3.4). This is consistent with the yield design results of Figs. 2-7 and 2-8 (see Section 2.3.4) comforting the simple idea that a sharp pyramid (cube corner) is easier to drive into a cohesive-frictional material half-space than a blunt one (Berkovich).

The $P-h$ curves in Fig. 3-6a are displayed in a log-log scale which facilitates the analysis of the $P \propto h^m$ scaling relation. Following the dimensional analysis presented in Sections 2.2 and 2.3.1, the indentation force P should scale, for pyramidal indenters (i.e., $d = 1$ in Eq. (2.10)), with h^2, so that P/h^2 does not depend on the indentation depth. Indeed, recalling relation

(2.16a), we should have:

$$\frac{P}{h^2} = c \times \Pi_\alpha \left(\frac{E}{c}, \nu, \varphi, \theta \right) \tag{3.10}$$

Figure 3-6a shows that the experimental $P-h$ curves for the loading part approach the power-two scaling relation (displayed as dashed lines) only in an asymptotic fashion for indentation depths $h \geq 200\,\text{nm}$, and this for both Berkovich and cube corner indentation. For very small indentation depths, roughly $P \propto h$, which is indicative of a flat punch (the more for Berkovich indentation than for cube corner). The way by which the scaling changes in the course of the indentation tests is displayed in Fig. 3-6b in a plot of P/h^2 *vs.* the indentation depth. The fact that P/h^2 depends on the indentation depth implies the existence of a length scale, say ℓ, which affects the indentation response at small indentation depths and which becomes negligible at larger indentation depth, so that the P/h^2 curves converge towards a constant, as shown in Fig. 3-6b; hence instead of relation (3.10):

$$\frac{P}{h^2} = c \times \Pi_\alpha \left(\frac{E}{c}, \nu, \varphi, \theta, \frac{\ell}{h} \right) \tag{3.11}$$

Possible candidates for this additional length scale are either of intrinsic nature related to the existence of a material length scale (such as the one considered in strain gradient plasticity models used to explain indentation size effects [181], [123], [242]), or of experimental nature related to imperfect indenter geometry, surface roughness of surface layers by oxidation or hardening from preparation procedures [86]. We keep the existence of potential indentation size effects in mind, but note as well that for our BMG investigation these are almost negligible at the chosen scale of maximum indentation depth.

3.3.2 Contact Stiffness S

A certain portion of the unloading $P-h$ response was fitted to a function of the form (Eq. (2.79)):

$$P = b(h - h_f)^m \tag{3.12}$$

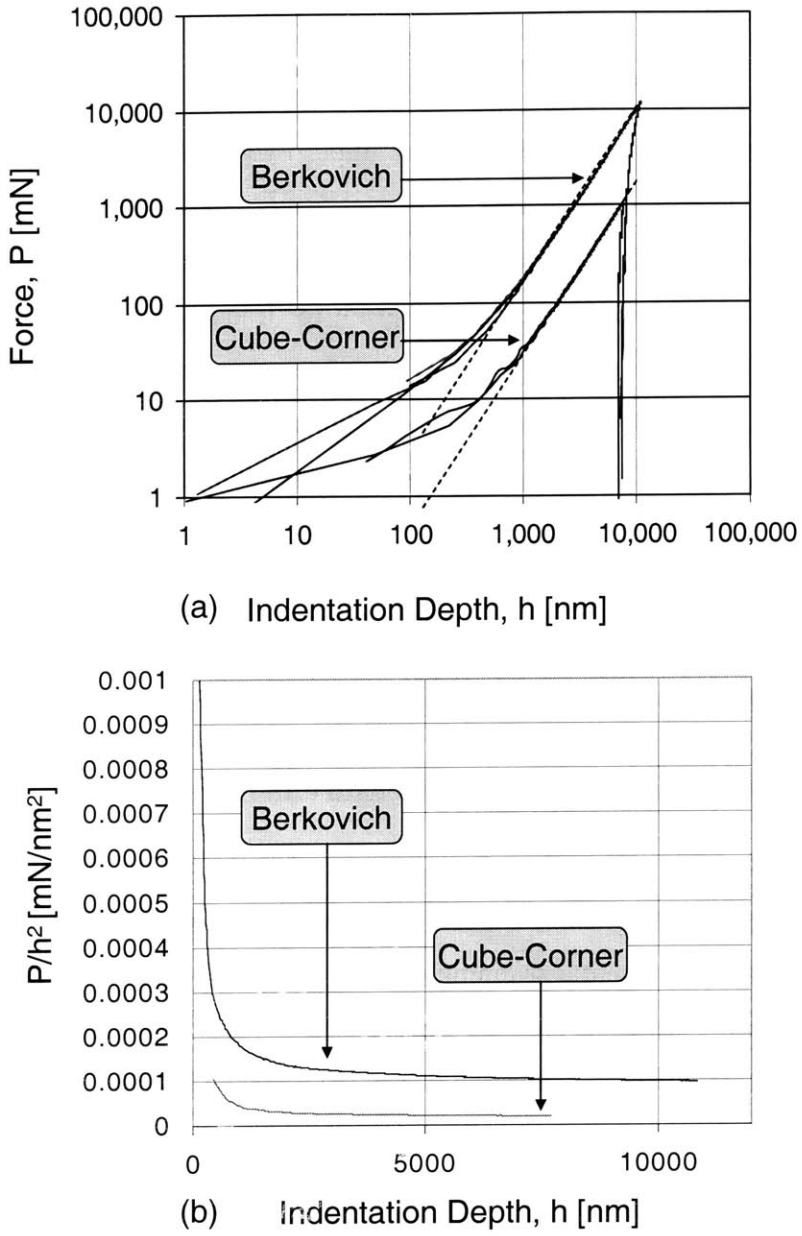

Figure 3-6: a) $P - h$ curves for Berkovich and cube corner indentation in metallic glass. Note the log-log scale showing the repeatability of the test procedure and the $P \propto h^m$ scaling, which for $h \geq 200\,\text{nm}$ is close to $m = 2$ (dashed lines) consistent with dimensionless Eq. (2.16a). b) The dimensionless parameter P/h^2 is plotted versus the indentation depth, h. Consistent with Eq. (3.10) P/h^2 becomes independent of h for large indentation depths, roughly greater than 2 μm.

and the contact stiffness, S, was estimated by differentiating Eq. (3.12) with respect to h and evaluating it at $h = h_{\max}$:

$$S = mb\,(h_{\max} - h_f)^{m-1}$$

Oliver and Pharr [184] recommended that the upper two-thirds (66%) of the curve should be used for the fitting process. Varying this percentage from 40−80% affected the $S-$determination by less than 2%. For the rest of our analysis the two-thirds recommendation of Oliver and Pharr will be employed. Figure 3-7 displays a histogram (or frequency plot) of the contact stiffness $S = \frac{dP}{dh}\big|_{h_{\max}}$ showing a remarkable repeatability of the test data for both Berkovich and cube corner indentation with very small standard deviations, on the order of 1.2% of the respective mean values (Tab. 3.4). This is the more remarkable as the indentation stiffness is obtained from a derivation of the $P-h$ unloading relation with respect to h. Figure 3-8 shows that $S/h_{\max}$ is invariant with respect to $h_{\max}$, thus confirming the theory (from dimensional analysis) that $S/h_{\max}$ for a given cohesive-frictional material and given indenter geometry does not depend on the indentation depth according to Eq. (2.42).

3.3.3 Area of Contact A_c: Direct Measurements

One key input to indentation analysis is the projected contact area, which we measured using microscopy images. After indentation the specimens were examined both under an optical microscope and an environmental scanning electron microscope (ESEM), as shown in Fig. 3-9. The projected contact areas as seen through the microscope on a plan-view were measured using straight line measurements, and the values are reported in Tab. 3.4. The accuracy of the length measurements was on the order of 0.1 μm, which translates into an accuracy of $\pm 10\,\mu\text{m}^2$ in the area calculations.

Furthermore, an interesting observation is that the impression left by Berkovich indentation on the surface has a slight concave cushion-like profile (see Fig. 3-10), while cube corner indentations leave a very strong convex barrell-shape impression visible in the optical microscope images on Figs. 3-9d and 3-11a. Since cushion-like images are indicative of sink-in and barrel-shape profiles of pile-up phenomena (see e.g., [98]), the profiles provide evidence that the Berkovich indentation in BMG leads to some (minimal) sinking-in, while cube corner indentation entails significant piling-up, which can be clearly seen in the scanning images in Fig.

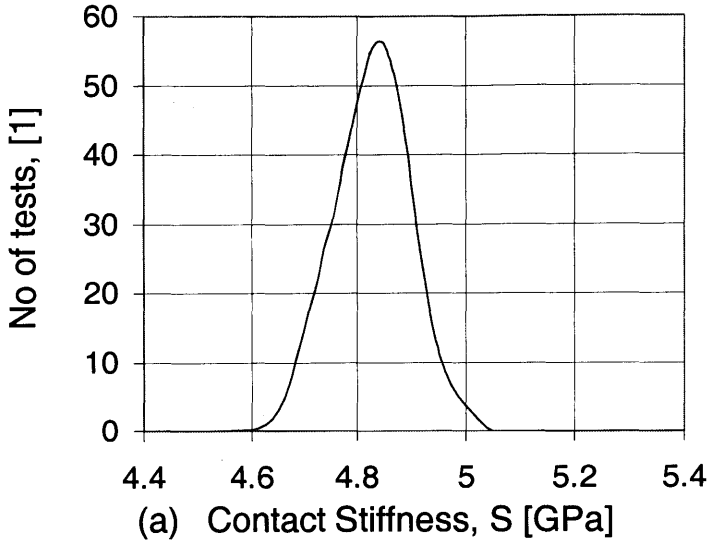

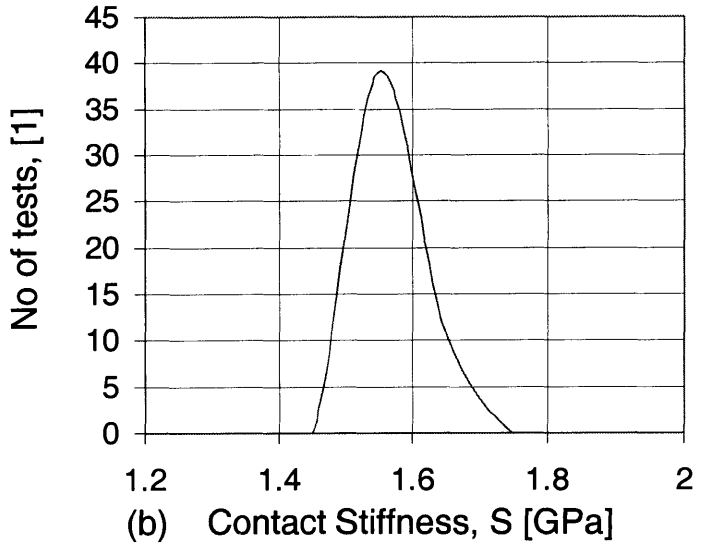

Figure 3-7: Frequency diagrams of the indentation stiffnesses of Berkovich (a) and Cube Corner (b) indentations on Vitreloy 1^{TM}.

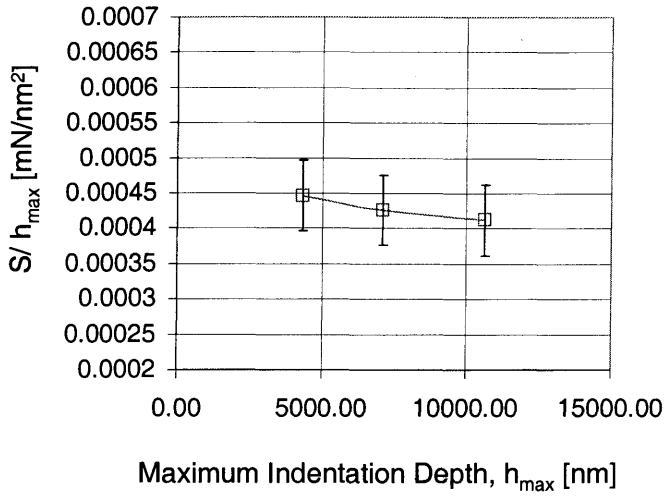

Figure 3-8: The almost constant relation between the normalized contact stiffness, $S/h_{\max}$, and the indentation depth, $h_{\max}$ proves the invariance of the S/h coefficient.

3-12. A quantification of these sinking-in/piling-up phenomena is possible by using the area functions in Eq. (2.12) and the equivalent cone angles of Berkovich and cube corner indenters (see Tab. 2.1):

$$\frac{h_c}{h_{\max}} = \sqrt{\frac{1}{\pi}\frac{A_c}{h^2}}\cot\theta \tag{3.13}$$

Using $\theta_B = 70.32°$ for the Berkovich indenter and $\theta_{CC} = 42.28°$ for the cube corner indenter together with the values for A_c and $h_{\max}$ reported in Tab. 3.4, we obtain:

$$\text{Berkovich:} \qquad \frac{h_c}{h_{\max}} = 0.85 \tag{3.14a}$$

$$\text{Cube Corner} \quad : \quad \frac{h_c}{h_{\max}} = 1.17 \tag{3.14b}$$

The fact that $h_c/h_{\max} < 1$ for the Berkovich indentation and $h_c/h_{\max} > 1$ for the cube corner confirms the visual observations that Berkovich indentation in BMG entails a sink-in, while cube corner indentation leads to pile-up. This difference between Berkovich and cube corner indentation seems to be related to the intensity of the plastic failure mechanism that occur in the indentation tests. Indeed, a careful examination of the failed surfaces reveals that the

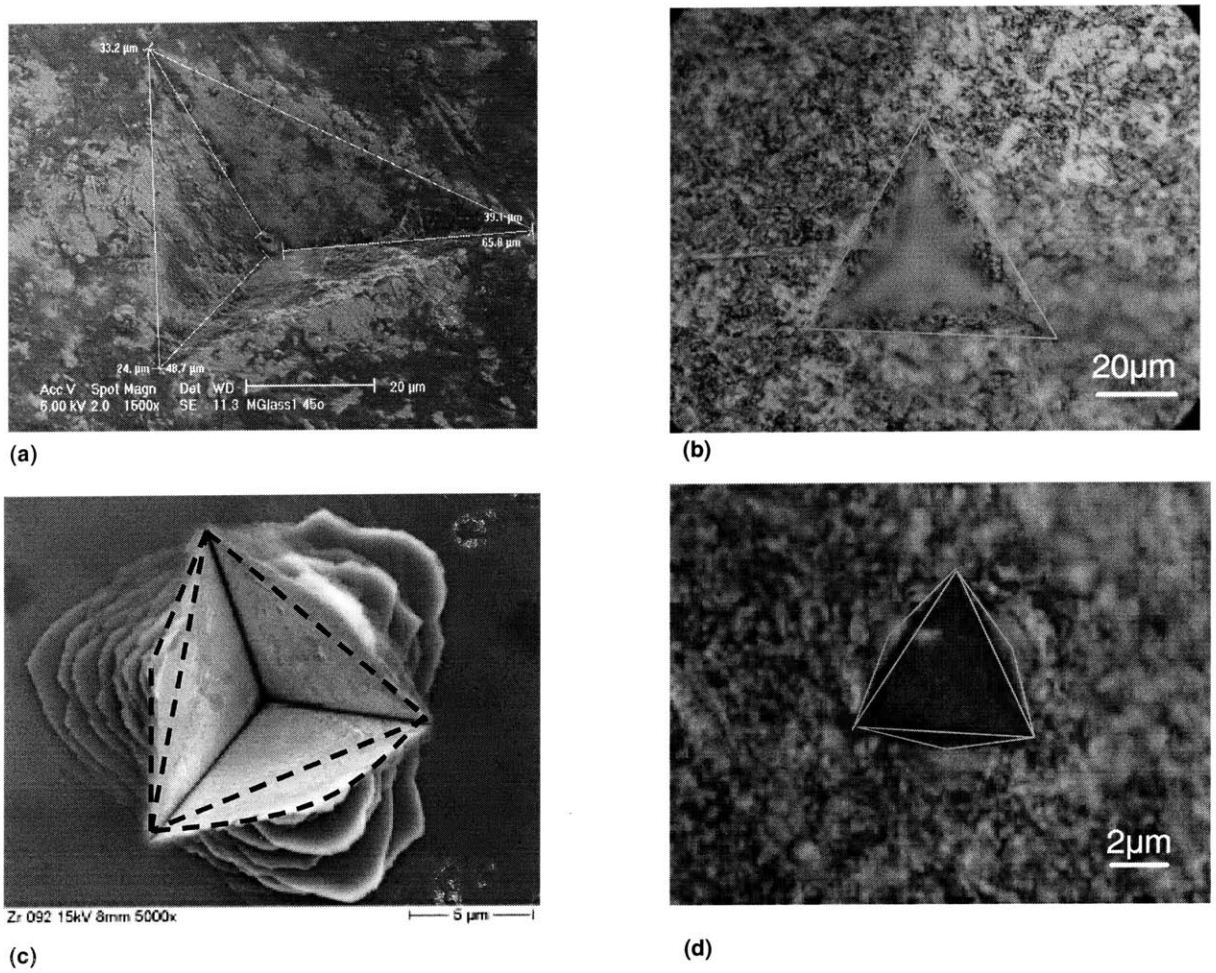

Figure 3-9: Microscopy images of residual impressions left on the surface of BMG after indentation. Images (a) and (b) are for Berkovich indentations whereas images (c) and (d) are for cube corner indentations. Image (c) is from Moser [173] from unpublished work.

(a)

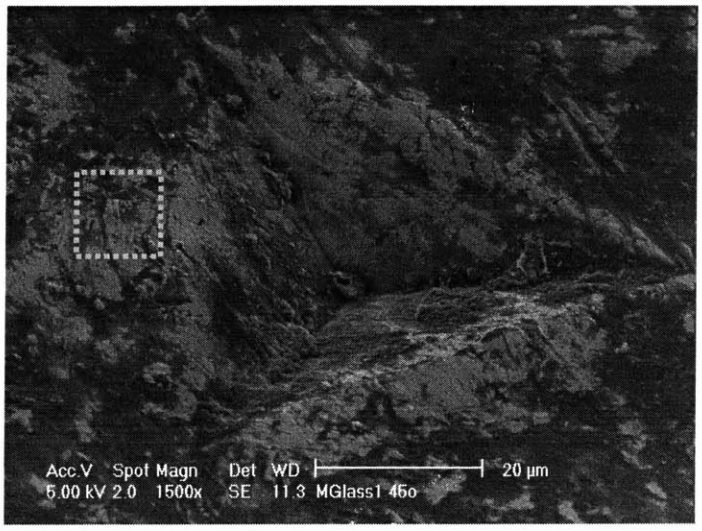

(b)

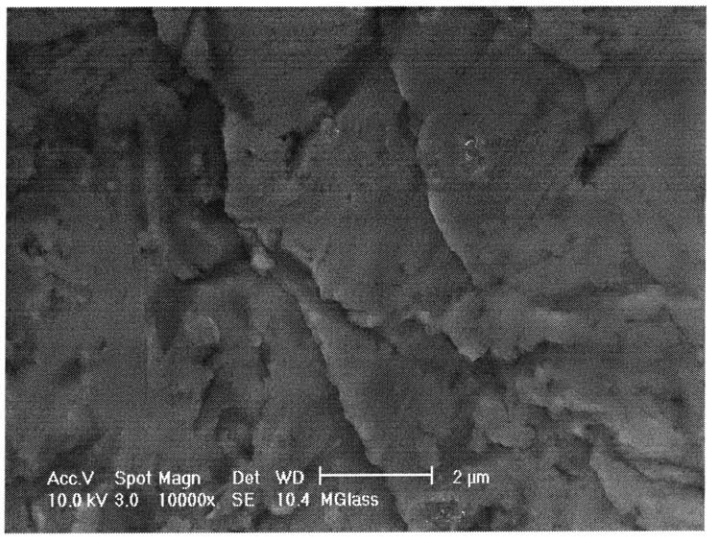

Figure 3-10: a) ESEM image of the residual imprint of a Berkovich indentation. A magnification of the right hand side of the image (b) clearly demonstrates the shear band formation.

material below the indenter concentrates in localized shear bands as primary mechanism of inelastic deformation (see e.g., [236],[206]), and this in both Berkovich indentation (Fig. 3-10) and cube corner indentation (Fig. 3-11). On the other hand, while the spacing of the shear bands in the Berkovich indentation is on the order of $2\,\mu$m (Fig. 3-10b), atomic force microscopy images of the periphery of the cube corner impression (Fig. 3-11b) reveal a denser formation of such shear bands with a regular spacing equal or smaller than $1\,\mu$m. This provides evidence that the pile-up found in cube corner indentation can be attributed to the higher density of shear bands that form during loading. While the more localized form of plastic deformation in cube corner *vis-a-vis* the Berkovich indentation is consistent with the plastic failure mechanism obtained analytically with the implementation of the upper bound yield design approach (see Fig. 2-8), the finite size of the shear bands appears to us a prime cause of the indentation size effects which we observe in the P/h^2 curves for small indentation depths (see Fig. 3-6b and Eq. (3.11)). These effects are observed at h of similar order as the shear band spacing, $\ell = O(h)$. On the other hand, for the maximum indentation depths of roughly $10\,\mu$m, the shear band spacing is almost an order of magnitude smaller than $h_{\max}$, so that the tools of continuum indentation analysis can be applied with some confidence.

A final question we want to address is the dimensionless nature of the contact area-to-indentation depth relation (2.16b), according to which A_c/h^2 should not depend on the indentation depth:

$$\frac{A_c}{h^2} = \Pi_\beta\left(\frac{E}{c}, \nu, \varphi, \theta\right) \tag{3.15}$$

To verify this relation, we performed Berkovich indentation tests to three maximum indentation depths of $4\,\mu$m, $7\,\mu$m and $11\,\mu$m. Figure 3-13a displays the $P-h$ curves. After indentation, the areas of contact were measured from optical images (see Fig. 3-14), and the results were analyzed in light of the dimensionless relation of Eq. (3.15). Figure 3-13b displays the results in a plot of A_c/h^2 *vs.* h showing some scale effects, but with some tendency towards an asymptote for larger indentation depth, very similar to the P/h^2 results shown in Fig. 3-6b. Hence, for the chosen maximum indentation depth, we can conclude that A_c/h^2 tends towards a constant value, which is in good agreement with the theory of indentation analysis based on self-similarity.

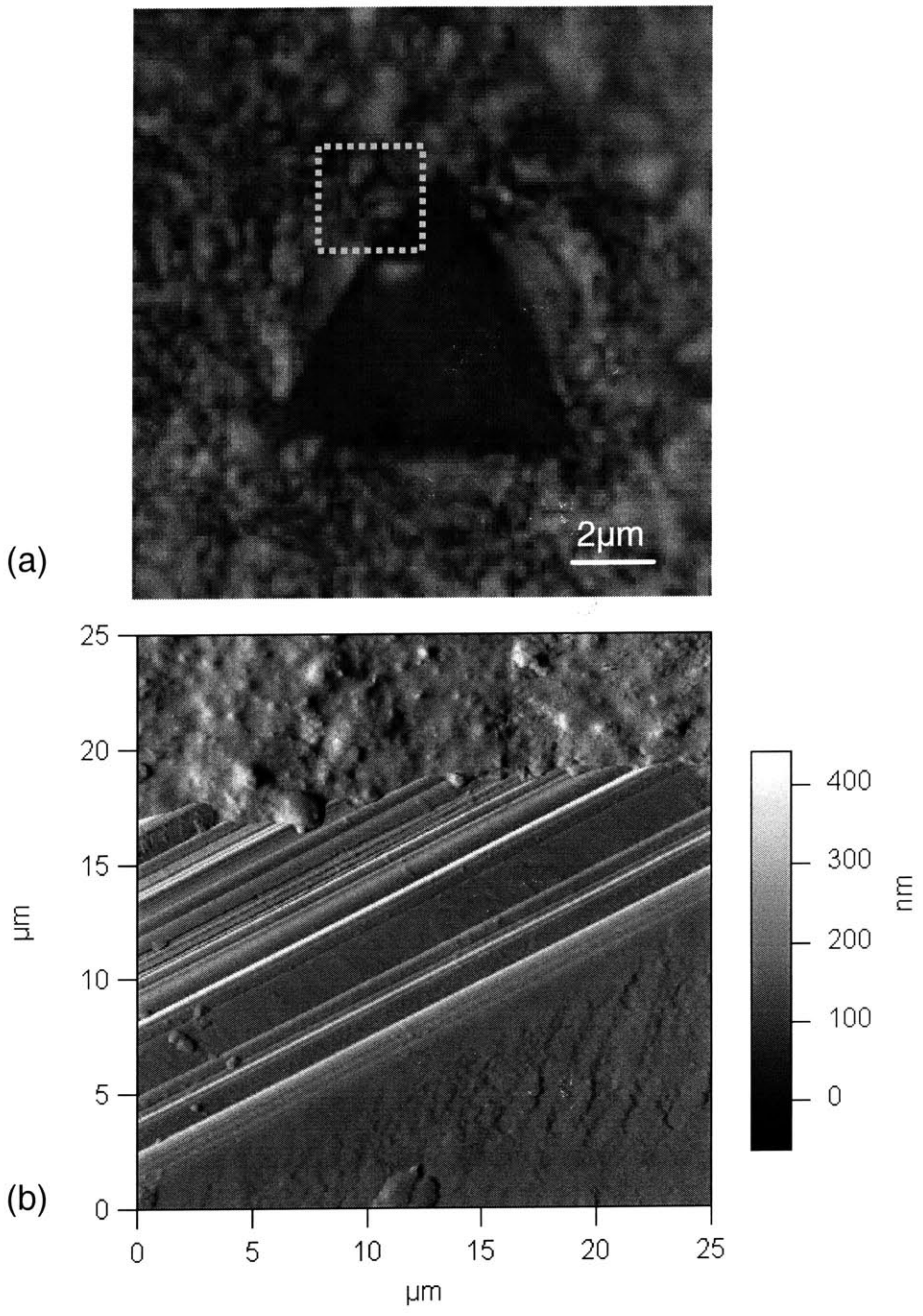

Figure 3-11: Optical microscope image of a cube corner indent (a). An atomic force microscopy image of the shear band formation is shown in (b) (courtesy of K.J. Van Vliet).

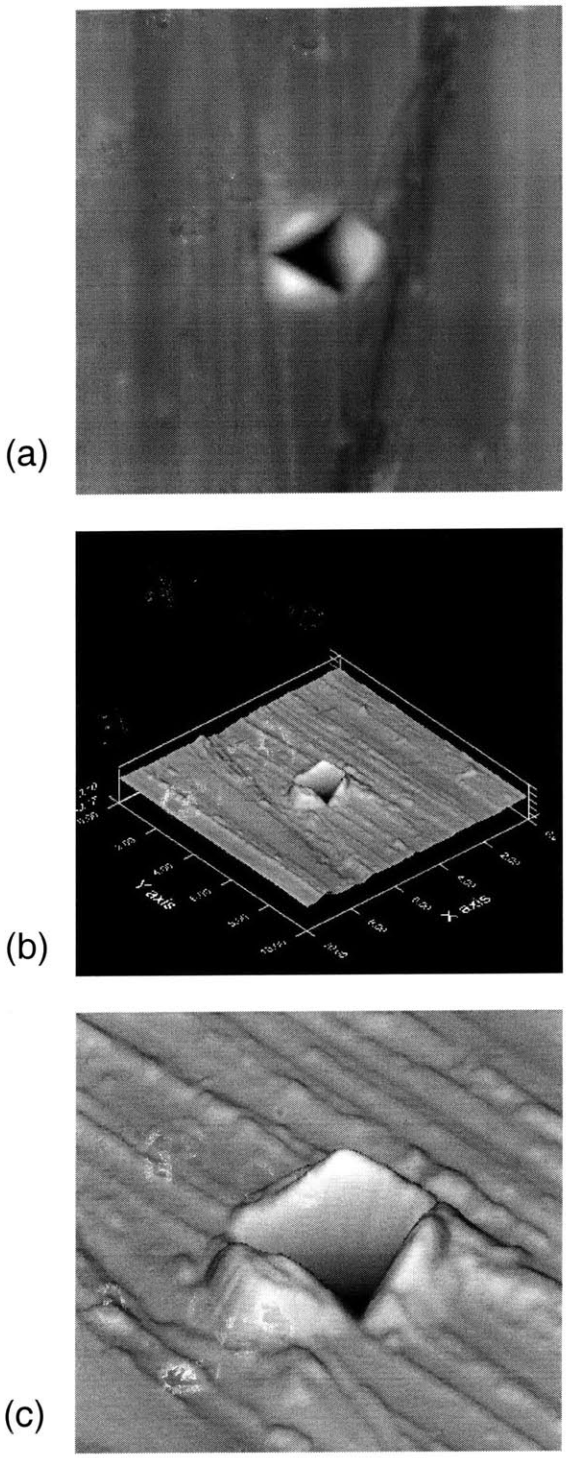

Figure 3-12: Topographic, atomic force microscopy images of the residual imprint of a cube corner Indentation on Vitreloy 1: (a) Plan view image, Image size $10 \times 10\mu m^2$; (b) 3-D view of the scan, $10 \times 10\mu m^2$; (c) Magnified view of the indented region.

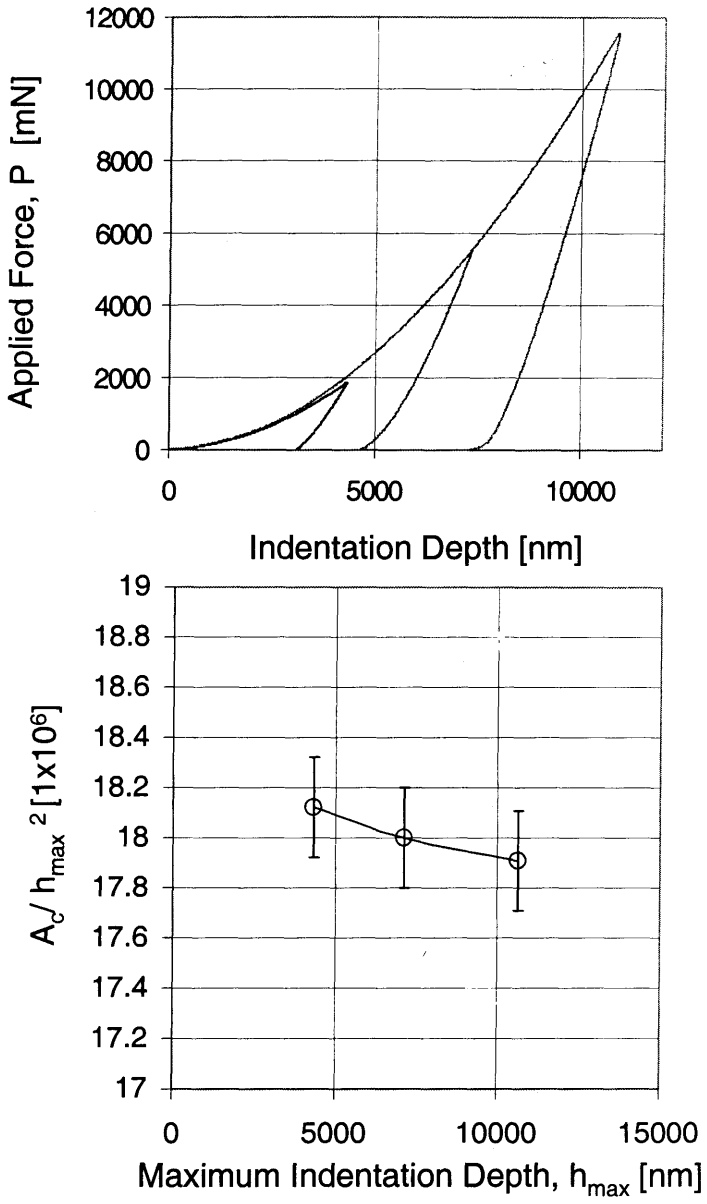

Figure 3-13: a) $P - h$ curves for Berkovich indentations at three different depths: $h \approx 4, 7, 11$. b) Scaling of A_c/h^2 with the maximum indentation depth.

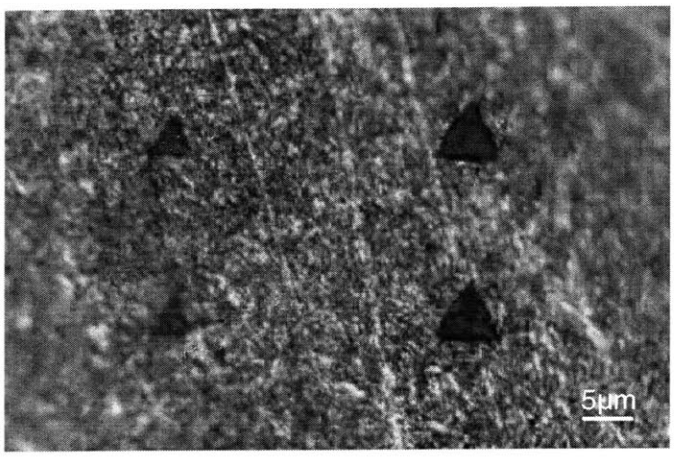

Figure 3-14: Optical images of Cube Corner indentations at different depths ($h = 4, 7, 11\,\mu$m).

3.4 Validation of the Tools of Indentation Analysis

The aim of indentation analysis is to link indentation data to meaningful mechanical properties i.e., relating hardness to strength properties (see Section 2.3) and relating indentation modulus to elastic properties (see Section 2.4). The focus of this section is to validate the tools of indentation analysis, namely the novel dual indentation technique and the BASh formula. The input for this validation are the directly measured indentation data presented in Section 3.3: the maximum force $P_{\max}$, the unloading slope S, and the measured projected contact area A_c. Because the elastic properties of Vitreloy 1$^{\text{TM}}$ are well known, we start with validating the BASh formula (2.2), before turning to the validation of the hardness-strength relations using the Dual Indentation Technique. An investigation of the relevance of indirect methods to determine the contact area (see Section 2.5) is presented separately in Section 3.5.

3.4.1 Indentation Modulus

The use of the BASh formula (2.2) requires as input the unloading slope S, and the projected contact area A_c. Using the mean indentation data from Tab. 3.4, we determine the indentation

modulus for the Berkovich and cube corner test:

$$M^B = \frac{\sqrt{\pi}}{2}\frac{4.83 \pm 0.06}{\sqrt{2,116}}\frac{\text{mN}}{\text{nm} \times \mu\text{m}} = 93.05 \pm 1.2\,\text{GPa} \tag{3.16a}$$

$$M^{CC} = \frac{\sqrt{\pi}}{2}\frac{1.55 \pm 0.02}{\sqrt{211}}\frac{\text{mN}}{\text{nm} \times \mu\text{m}} = 94.57 \pm 1.2\,\text{GPa} \tag{3.16b}$$

An interesting observation is that the indentation moduli determined with the BASh formula from both the Berkovich and cube corner data are of the same order; and that the difference in between them is just slightly greater than the standard deviation. In order to relate the indentation modulus to the elastic properties, we recall Eq. (2.68):

$$\frac{1}{M} = \frac{1}{M_{mat}} + \frac{1}{M_{in}} = \frac{1-\nu^2}{E} + \frac{1-\nu_{in}^2}{E_{in}} \tag{3.17}$$

where M_{mat} is the plane stress modulus of the indented material, BMG, and M_{in} the plane stress modulus of the diamond indenter. Using the known elastic properties of the diamond indenter ($E_{in} = 1,140$ GPa, $\upsilon_{in} = 0.07$), the plane stress moduli of BMG which we obtain from the Berkovich and cube corner indentation moduli (Eq. (3.16)) are:

$$M_{mat}^B = 101.27 \pm 1.37\,\text{GPa} \tag{3.18a}$$

$$M_{mat}^{CC} = 103.07 \pm 1.45\,\text{GPa} \tag{3.18b}$$

For validation purposes, we compare these results with the plane stress modulus deduced from ultrasonic measurements [158] (small stress amplitude measurements):

$$M_{mat}^{UV} = \frac{96}{1-0.36^2} = 110.29\,\text{GPa} \tag{3.19}$$

Hence, what we find is that the plane stress moduli (3.18) we determine with the BASh formula from our indentation tests underestimate the actual plane stress modulus of BMG by roughly $7-8\%$. There may be several reasons for this underestimations, but one that can be excluded is the second-order effect due to radial displacements (see Section 2.4.3), since neglecting this effect entails an overestimation of the determined elasticity properties [111]. One possible reason of this underestimation is the energy dissipation induced by shear band formation during loading

(see Figs. 3-10 and 3-11), which is likely to be sensed upon unloading in the activation of the elasticity of the bulk material. In such a case, however, the cube corner results should yield smaller elasticity values than the Berkovich results; this is not observed. The most likely reason, therefore, appears to be the impurity of the tested Vitreloy 1^{TM} sample, leading to consistent lower elasticity values than the one obtained by ultrasonic measurements. In favor of this interpretation is the fact that the elasticity properties we determine from microindentation tests are in very good agreement with the range of elasticity values reported for Vitreloy 1^{TM} in the literature (see Tab. 3.3). We can therefore conclude that the BASh formula for estimating the indentation modulus of the material, which relies on the elastic unloading of the $P-h$ response, can give accurate estimates of the indentation modulus of cohesive-frictional materials provided the area of contact is measured properly.

3.4.2 Berkovich and Cube Corner Hardness

The second condensed quantity of an indentation test is the hardness of Eq. (2.1). Using the mean indentation data from Tab. 3.4, we determine the hardness for the Berkovich indentation results and the cube corner indentation results for the maximum indentation depth:

$$H^B = \frac{11,472 \pm 172\,\text{mN}}{2,116\,\mu\text{m}^2} = 5.42 \pm 0.08\,\text{GPa} \tag{3.20a}$$

$$H^{CC} = \frac{1,083 \pm 32\,\text{mN}}{211\,\mu\text{m}^2} = 5.13 \pm 0.15\,\text{GPa} \tag{3.20b}$$

Consistent with the cohesive-frictional nature of BMG (see Fig. 2-9), the Berkovich hardness H_B is found to be greater than the cube corner hardness H_{CC}, which forms the background of the dual indentation technique (see Section 2.3.4). Furthermore, an interesting observation is that the Berkovich hardness is on the same order of Vickers hardness values reported in the literature (see Tab. 3.3). To quantify this link, it is useful to recall that the Vickers hardness test has the same equivalent cone angle as the Berkovich indenter (see Tab. 2.1). The Vickers hardness method consists of indenting the material by a load of 1 to 100 kg (approximately 10 to 1000 N) with a diamond indenter, in the form of a right pyramid with a square base and an angle of 136° between opposite faces. The full load is normally applied for 10 to 15 seconds. The two diagonals (d_1 and d_2) of the indentation left on the surface of the material

after removal of the load are measured using a microscope and the average, d, is calculated. The Vickers hardness is the quotient obtained by dividing the load in [kg] by the area of indentation in [mm^2]:

$$HV = \frac{2P\sin\left(\frac{136}{2}\right)}{d^2} = 1.854\frac{P}{d^2} \tag{3.21}$$

Noting that the projected contact area of the Vickers indenter is $A_c = 2d^2$, a comparison of Eq. (3.21) with Eq. (2.1) leads to a relation between Vickers Hardness and Indentation Hardness of the form:

$$H^V = 1.0785 \times HV \tag{3.22}$$

where the conversion factor 1.0785 is a geometric constant. In other words the Vickers hardness is roughly 8% lower than hardness defined as the average pressure beneath the indenter. Applying this correction factor to the range of Vicker hardness values reported in Tab. 3.3, the Vickers indentation hardness is $H^V = 5.42 - 5.82\,\text{GPa}$. The lower value is in perfect agreement with our Berkovich hardness value (3.20a), which given the difference in indenter geometry and test method, provides evidence of the consistency of our indentation data.

Finally, it is interesting to check the relevance of the dimensionless relation (2.17), according to which the hardness should not depend on the indentation depth:

$$H = c \times \mathcal{H}\left(\frac{E}{c}, \nu, \varphi, \theta\right) \tag{3.23}$$

Using the maximum force and the projected contact area determined for a maximum indentation depth of $4\,\mu$m, $7\,\mu$m and $11\,\mu$m, we find that the Berkovich hardness is almost constant: $H^B = 5.47 - 5.46 - 5.42$ GPa. While a small indentation size effect can be noted, it is found to be smaller than the standard deviation in the considered indentation depth range. This confirms our previous analysis of the P/h^2-scaling relation (Fig. 6-5b) and the A_c/h^2-scaling relation (Fig. 3-13), that possible indentation size effects vanish for indentation depths larger than the characteristic size of small scale heterogeneities, such as the shear band spacing. Hence, the hardness values in Eq. (3.20) can be used with some confidence for the validation of the dual indentation technique.

3.4.3 Validation of Dual Indentation Technique

The premise of the dual indentation technique presented in Section 2.3.4 is that it is possible to extract the cohesion and the friction angle of a cohesive-frictional material from two hardness measurements obtained from two indentation tests with two indenter geometries, i.e., Berkovich and cube corner indenters both approximated as cones of equivalent semi-apex angles. The input for the method are the hardness values as in Eq. (3.20). The dual indentation technique consists of the following two steps:

1. Using the Berkovich-to-cube corner hardness ratio in Fig. 6-3, we extract the friction angle; i.e., with the values in Eq. (3.20):

$$\frac{H^B}{H^{CC}} = 1.057 \Rightarrow \varphi = 7.3^\circ \tag{3.24}$$

2. Use of the friction angle in Fig. 2-9 (Eq. (2.38)) yields the H^B/c and H_{CC}/c ratio. Since the hardness values are known (i.e., Eq. (3.20)), we solve for the cohesion c:

$$\tan\varphi = 0.13 \Rightarrow \left\{ \begin{array}{c} H^B = 7.15\,c \\ H^{CC} = 6.78\,c \end{array} \right\} \Rightarrow c = 760 \pm 20\,\text{MPa} \tag{3.25}$$

To validate the method, we compare the determined cohesion and friction angle with cohesion and friction angle values of BMG reported in the literature (see Section 3.2.2): The friction coefficient $\tan\varphi = 0.13$ agrees remarkably well with the values in Eqs. (3.8) and (3.9) obtained respectively from extensive 3-D finite element back calculation of Berkovich indentation $P - h$ curves [236] and from molecular simulations [159]. The friction coefficient also agrees reasonably well with (3.5) obtained by Lu and Ravichandran [158] from a large series of macroscopic multiaxial compression tests. Furthermore, the cohesion $c = 760 \pm 20\,\text{MPa}$ is on the same order of the cohesion values reported from macroscopic tests by Donovan [72] for $Pd_{40}Ni_{40}P_{20}$ metallic glass and by Lu and Ravichandran [158] for Vitreloy 1^{TM}, the same material we tested here. Our value slightly underestimates the reported cohesion values by 5%, which could be attributed to the fact that our results are based on an upper bound solution, which overestimates the $H/c-$ratio, thus underestimating the cohesion for a given friction an-

gle. For purpose of completeness, we should also note that our cohesion value (as well as the one reported from macroscopic testing [72, 158]) is smaller than the cohesion that has been applied in the 3-D finite element back calculations of Vaidyanathan et al. [236], in which the uniaxial tension has been fixed to a relatively high value of $f_t = 1.9$ GPa, corresponding to a cohesion of $c = f_t(1+\sin\varphi)/2\cos\varphi = 1,080$ MPa. The order of magnitude of the employed tensile strength appears to us to be rather on the order of the macroscopic compressive strength (see Tab. 3.3), in which case the cohesion would turn out to be $c = f_c(1-\sin\varphi)/2\cos\varphi = 840$ MPa, on the same order as the value we determined.

In a last step, we need to verify the yield design assumption $c/E \to 0$, which is at the basis of the Dual Indentation Technique, and which reduces here to $0.76/96 = 8 \times 10^{-3}$. The fact that $c/E \ll 1$ seems to be sufficient to justify *a posteriori* the use of the yield design solution for the extraction of the cohesion and friction angle.

3.5 Validation of Indirect Methods of Contact Area Determination

The validation of the tools of indentation analysis in Section 3.4 was based on the direct measurements of the projected contact area A_c. Such direct measurements may be appropriate for validation purposes of the BASh formula, the Dual Indentation Technique, and so on; but fail to meet the needs of day-to-day indentation practice, requiring a method that circumvents the need of direct measurements. Two of these methods were described in Section 2.5, namely the Oliver and Pharr method and the Cheng and Cheng method. The focus of this section is to validate these methods for BMG, and discuss the limitations of these methods with respect to the extraction of the indentation modulus and the hardness.

3.5.1 The Oliver and Pharr Contact Area Estimator

The Oliver and Pharr method of Eq. (2.78),

$$\frac{h_c}{h_{\max}} = 1 - \epsilon\frac{P_{\max}}{Sh_{\max}} \tag{3.26}$$

provides a means to estimate the contact height h_c from the sole knowledge of the maximum force $P_{\max}$, the unloading slope S, and the maximum indentation depth $h_{\max}$; hence using the mean values from Tab. 3.4 in (3.26) (letting $\epsilon = 0.75$ as recommended by Oliver and Pharr [184, 185]):

$$\text{Berkovich:} \quad \frac{h_c^{est}}{h_{\max}} = 1 - 0.75 \times \frac{11,472}{4.83 \times 10,870} = 0.84 \tag{3.27a}$$

$$\text{Cube Corner} \quad : \quad \frac{h_c^{est}}{h_{\max}} = 1 - 0.75 \times \frac{1,083}{1.55 \times 7,692} = 0.93 \tag{3.27b}$$

These values need to be compared with Eq. (3.14) determined from direct measurements of the contact area. It is remarkable to note that the Oliver and Pharr method estimates with high accuracy (the error is smaller than 2%) the contact height in Berkovich indentation. On the other hand, since this method –by design– can only capture sink-in phenomena, it obviously fails to predict the pile-up observed in cube corner indentation. This error affects quadratically the contact area estimation, as one can see when using the equivalent cone area function:

$$\frac{A_c^{est}}{h_{\max}^2} = \pi \left(\frac{h_c^{est}}{h_{\max}} \right)^2 \tan^2 \theta \tag{3.28}$$

Hence, for BMG, the Oliver and Pharr method is expected to predict close to 3% the exact contact area in Berkovich indentation, while an error of more than 35% is to be expected in cube corner indentation:

$$\frac{A_c^{est}}{A_c} = \left(\frac{h_c^{est}}{h_c} \right)^2 = \left\{ \begin{array}{l} 0.97 \text{ Berkovich} \\ 0.63 \text{ Cube Corner} \end{array} \right\} \tag{3.29}$$

The error in the contact area estimation strongly affects the estimation of both indentation modulus:

$$\frac{M^{est}}{M} = \sqrt{\frac{A_c}{A_c^{est}}} = \frac{h_c}{h_c^{est}} = \left\{ \begin{array}{l} 1.02 \text{ Berkovich} \\ 1.26 \text{ Cube Corner} \end{array} \right\} \tag{3.30}$$

and hardness:

$$\frac{H^{est}}{H} = \frac{A_c}{A_c^{est}} = \left(\frac{h_c}{h_c^{est}} \right)^2 = \left\{ \begin{array}{l} 1.03 \text{ Berkovich} \\ 1.58 \text{ Cube Corner} \end{array} \right\} \tag{3.31}$$

Finally, our analysis here is based on the ideal equivalent cone geometry and area function (3.28). The results, however, still hold in the case of an imperfect indenter geometry described by a fitted area function of the form (2.13). Figure 3-15 displays frequency plots of the indentation modulus and hardness of our 100 Berkovich and 50 cube corner indentation tests in which the contact height was estimated with the Oliver and Pharr method. The figure confirms our analysis that application of the Oliver and Pharr method to Berkovich indentation entails reasonable estimates of the indentation modulus and the hardness, while the application to cube corner indentation largely overestimates both M and H. Moreover, an interesting observation is that the results are well represented by a normal distribution with the following mean (μ) and remarkable low standard deviations (s) in both Berkovich indentation (100 tests):

$$\begin{aligned} \mu^{B}_{M^{est}} &= 95.14 \text{ GPa} \quad s_{M^{est}} = 1.82 \text{ GPa} \quad \tfrac{s}{\mu} = 1.9\% \\ \mu^{B}_{H^{est}} &= 5.67 \text{ GPa} \quad s_{H^{est}} = 0.17 \text{ GPa} \quad \tfrac{s}{\mu} = 3.1\% \end{aligned} \tag{3.32}$$

and cube corner indentation (50 tests):

$$\begin{aligned} \mu^{CC}_{M^{est}} &= 124.25 \text{ GPa} \quad s_{M^{est}} = 2.06 \text{ GPa} \quad \tfrac{s}{\mu} = 1.7\% \\ \mu^{CC}_{H^{est}} &= 8.06 \text{ GPa} \quad s_{H^{est}} = 0.26 \text{ GPa} \quad \tfrac{s}{\mu} = 3.3\% \end{aligned} \tag{3.33}$$

3.5.2 The Cheng and Cheng Contact Area Estimator

The Cheng and Cheng method (see Eq. (2.80)) circumvents by design the estimation of the contact area by evoking the elastic and total energy. On the other hand, using Eqs. (2.1) and (2.2) in Eq. (2.80) and solving the result for the projected contact area, the method provides the following contact height estimation:

$$\frac{h_c^{est}}{h_{\max}} = \frac{2}{\pi} \times \frac{P_{\max}}{S h_{\max}} \times 5 \frac{W_t}{W_e} \times \cot\theta \tag{3.34}$$

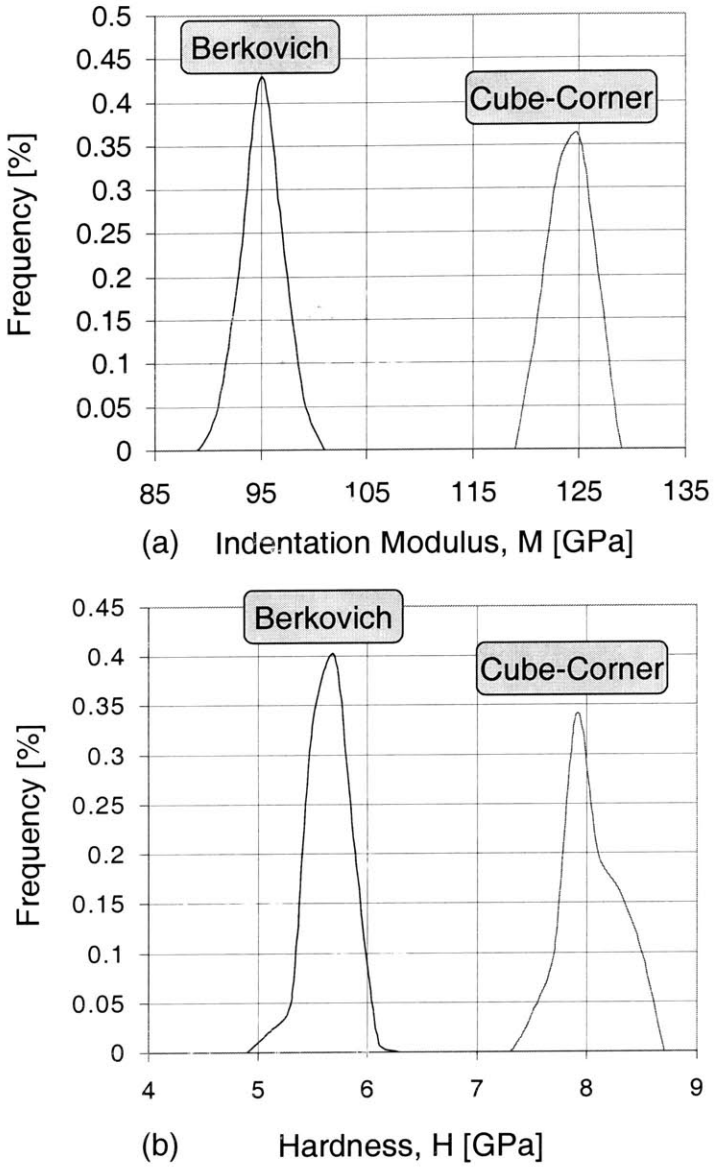

Figure 3-15: Frequency plots of (a) indentation modulus and (b) hardness of BMG obtained with Berkovich and Cube corner indenters. The area of contact was estimated using the Oliver and Pharr method.

Using the mean values from Tab. 3.4 in Eq. (3.34) we obtain:

$$\text{Berkovich} \quad : \quad \frac{h_c^{est}}{h_{\max}} = 0.70 \Rightarrow \frac{M^{est}}{M^B} = 1.21; \; \frac{H^{est}}{H^B} = 1.46 \tag{3.35a}$$

$$\text{Cube Corner} \quad : \quad \frac{h_c^{est}}{h_{\max}} = 2.72 \Rightarrow \frac{M^{est}}{M^{CC}} = 0.43; \; \frac{H^{est}}{H^{CC}} = 0.18 \tag{3.35b}$$

The results show that the Cheng and Cheng method, in contrast to the Oliver and Pharr method, is qualitatively able to accommodate pile-up phenomena, $h_c^{est}/h_{\max} > 1$. However, quantitatively the method performs rather poorly by overestimating both the sink-in phenomena in Berkovich indentation, to a greater extend the pile-up phenomena in cube corner indentation. As a consequence, the indentation modulus and hardness estimated with this method are of little quantitative interest.

3.5.3 Return to Dimensional Analysis

To fully understand strength and limits of the contact area estimators, it is appropriate to return to first principles, i.e., dimensional analysis, by recalling the dimensionless relations of Eq. (2.16) that characterize hardness, and Eq. (2.42) which characterizes the elastic unloading slope:

$$\frac{P_{\max}}{ch_{\max}^2} = \Pi_\alpha\left(\frac{E}{c}, \nu, \varphi, \theta\right) \tag{3.36a}$$

$$\frac{A_c}{h_{\max}^2} = \Pi_\beta\left(\frac{E}{c}, \nu, \varphi, \theta\right) \tag{3.36b}$$

$$\frac{S}{Eh_{\max}} = \Pi_\delta\left(\frac{c}{E}, \nu, \varphi, \theta\right) \tag{3.36c}$$

Recombining Eq. (3.36a) and Eq. (3.36c) allows us to identify a new dimensionless number which figures in both the Oliver and Pharr method Eq. (2.78) and the Cheng and Cheng method Eq. (3.34):

$$\frac{P_{\max}}{Sh_{\max}} = \frac{c}{E} \times \frac{\Pi_\alpha\left(\frac{E}{c}, \nu, \varphi, \theta\right)}{\Pi_\delta\left(\frac{c}{E}, \nu, \varphi, \theta\right)} = \Pi_\epsilon\left(\frac{c}{E}, \nu, \varphi, \theta\right) \tag{3.37}$$

This dimensionless number is independent of the indentation depth, as is the indentation modulus–to–hardness ratio, as one can show by substituting Eqs. (3.36b) and (3.37) in the

BASh formula Eq. (2.2):

$$\frac{M}{H} = \frac{\sqrt{\pi}}{2}\frac{\sqrt{\Pi_\beta}}{\Pi_\epsilon} = \Pi_\phi\left(\frac{c}{E}, \nu, \varphi, \theta\right) \tag{3.38}$$

Finally, Eq. (3.38) allows us to rewrite the contact area Eq. (3.36b) in the dimensionless form:

$$\frac{A_c}{h_{\max}^2} = \frac{4}{\pi}\left(\frac{P_{\max}}{Sh_{\max}}\right)^2\left(\frac{M}{H}\right)^2 \tag{3.39}$$

respectively, with the help of Eq. (3.28), the contact height–to–indentation depth ratio:

$$\frac{h_c}{h_{\max}} = \frac{2}{\pi} \times \frac{P_{\max}}{Sh_{\max}} \times \frac{M}{H} \times \cot\theta \tag{3.40}$$

Equation (3.40) is to be compared to the Oliver and Pharr method of Eq. (3.26) and the Cheng and Cheng method of Eq. (3.34):

1. The key assumption of the Oliver and Pharr method is that elastic indentation solutions remain valid during unloading in elastoplastic indentation, as is implicit in the ϵ - factor. A comparison of Eqs. (3.26) and (3.40) yields an expression for ϵ as a function of the two invariants (see Eqs. (3.37) and (3.38)):

$$\epsilon = \frac{Sh_{\max}}{P_{\max}} - \frac{2}{\pi} \times \frac{M}{H} \times \cot\theta \tag{3.41}$$

   Without difficulty we verify that the elastic (conical) indentation solution yields the ϵ - factor suggested by Oliver and Pharr:

$$\text{Elastic: } \frac{Sh_{\max}}{P_{\max}} = 2;\ \frac{M}{H} = 2\tan\theta \Rightarrow \epsilon = 2\left(1 - 2/\pi\right) \simeq 0.73 \tag{3.42}$$

   While strictly valid only for the elastic solution, Oliver and Pharr suggest that this values also applies to elastoplastic indentation, and this independent of the cone angle. It is interesting to determine ϵ for the Berkovich and cube corner indentation by using the mean values of Tab. 3.4 and the actually measured M/H - values from Eqs. (3.16) and

(3.20) in Eq. (3.41). This yields:

$$\text{Berkovich} \quad : \quad \frac{Sh_{\max}}{P_{\max}} = 4.58; \; \frac{M^B}{H^B} = 17.17 \Rightarrow \epsilon = 0.67 \tag{3.43a}$$

$$\text{Cube Corner} \quad : \quad \frac{Sh_{\max}}{P_{\max}} = 11.01; \; \frac{M^{CC}}{H^{CC}} = 18.43 \Rightarrow \epsilon = -1.90 \tag{3.43b}$$

In contrast to the elastic solution Eq. (3.42), we find that the dimensionless number $Sh_{\max}/P_{\max}$ defined by Eq. (3.37) strongly depends on the cone angle θ in elastoplastic indentation, and that it is much greater than the elastic value $Sh_{\max}/P_{\max} = 2$. Similarly, the indention modulus-to-hardness ratio of Eq. (3.38) is much greater than the elastic values ($M^B_{el}/H^B_{el} = 1.82$ and $M^{CC}_{el}/H^{CC}_{el} = 5.59$), but less sensitive to the cone angle. Given these significant differences, it is almost surprising that ϵ in elastoplastic Berkovich indentation of Eq. (3.43a) comes very close to the elastic value of Eq. (3.42), which explains the excellent estimates via Eqs. (3.27a) to (3.31) obtained with the Oliver and Pharr method for Berkovich indentation. On the other hand, the poor performance of this method for cube corner indentation appears to be related to the fact that elastoplastic cube corner indentation deviates significantly from the elastic sink-in solution.

2. The key assumption of the Cheng and Cheng method is the link of Eq. (2.80) between the indention modulus-to-hardness ratio of Eq. (3.38) and the unloading-loading energy ratio:

$$\frac{M}{H} = \kappa \frac{W_t}{W_e} \tag{3.44}$$

where $\kappa = 5$ was found to fit well elastoplastic finite element results for a given indenter conical indenter geometry ($\theta = 68°$) [50]. Use of $\kappa = 5$ in Eqs. (3.44) and (3.40) yields Eq. (3.34), which we have seen provides a poor quantitative prediction of the contact height in both Berkovich and cube corner indentation. It is interesting, therefore, to determine the κ factor for our BMG indentation data, by using the mean values of Tab. 3.4 and the actually measured M/H - values from Eqs. (3.16) and (3.20) in Eq. (3.44). This yields:

$$\kappa = \frac{M}{H}\frac{W_e}{W_t} = \left\{ \begin{array}{l} 6.1 \text{ Berkovich} \\ 2.2 \text{ Cube Corner} \end{array} \right\} \tag{3.45}$$

The κ - factor of the Cheng and Cheng method appears to be highly sensitive to the cone angle, and ostensibly to the friction angle, i.e. $\kappa = \kappa = (\theta, \varphi, ...)$. Given the deviation from Cheng and Cheng's value $\kappa = 5$, the poor performance of the method is not surprising.

In summary, the existing indirect methods for estimating the projected contact area all suffer from the same problem: these involve semi-empirical constants (ϵ in the Oliver and Pharr method, κ factor in the Cheng and Cheng method) that depend on the material properties of the indented material and the indenter geometry. It can only be speculated that the good performance of the Oliver and Pharr method in BMG Berkovich indentation is related to the flat indenter geometry, which limits pile-up deformation during loading, so that the unloading response is actually dominated by the elastic sink-in of the surrounding material, which is the key assumption of the method. On the other hand, the Cheng and Cheng method which has the ability to capture pile-up phenomena is, at this stage of its development, rather qualitative than quantitative.

Lastly, a comment on statistical analysis of indentation data is in order. According to the dimensionless relation of Eq. (3.38) the M/H for a homogeneous material should be a constant for a given cone angle. This relation should be understood in an average sense, as one can never exclude, in real indentation experiments, random errors in the determination of M and H related to surface roughness, material imperfections, etc. that give rise to a scatter in individual values of M and H (Fig. 3-15). If this random error is related to surface properties, the error should translate into a $M - H$ scaling relation. Figure 5-22 displays the $M - H$ scaling relations for Berkovich indentation and cube corner indentation, in which the contact area was estimated by means of the Oliver and Pharr method (mean values and standard deviations are given by Eqs. (3.32) and (3.33)). It is remarkable to note that the Berkovich indentation modulus scales with $M_B^{est} \propto \left(H_B^{est}\right)^{0.54}$ which is very close to the theoretical scaling relation $M \propto \sqrt{H}$ one would expect from random errors in contact area estimation. This good agreement confirms the good performance of the Oliver and Pharr method for Berkovich indentation, and the small difference in the scaling relation can be attributed to the improper area estimation with the Oliver and Pharr method. However, the (non-random) error in the area estimation one commits with the Oliver and Pharr method in cube corner indentation translates in a strong deviation from the $M \propto \sqrt{H}$ relation, as the estimated cube corner indentation modulus scales with

$M_{CC}^{est} \propto \left(H_{CC}^{est}\right)^{0.26}$! This underscores the importance of a correct contact area estimation.

3.5.4 Elasticity Corrector Method for Dual Indentation Analysis

The absence of a method that accurately predicts the contact area for different indenter geometries (semi-apex angle θ) is a problem for the application of the Dual Indentation Technique developed in Section 2.3.4 and validated in Section 3.4.3 using hardness values that were determined from direct contact area measurements. In Section 2.5.4, we proposed a new method for the determination of the contact areas particularly for the application in dual indentation analysis. Validating this method for BMG is the focus of this section.

The method is based on the validity of the BASh formula Eq. (2.2) and the assumption that the indentation modulus, Eq. (2.68), is the same for both indenter geometries. This yields Eq. (2.83), linking the contact area ratio to the contact stiffness ratio. Use of the mean values of Tab. 3.4 yields the following result for BMG:

$$\left(\frac{A_c^B}{A_c^{CC}}\right)^{est} = \left(\frac{S^B}{S^{CC}}\right)^2 = \left(\frac{4.83}{1.55}\right)^2 = 9.71 \tag{3.46}$$

This ratio compares rather well with ratio of the measured contact areas A_c^B and A_c^{CC} from Tab. 3.4; $A_c^B/A_c^{CC} = 10.03$. The difference is actually smaller than the error induced by the accuracy of the surface measurement technique of $10\,\mu\text{m}^2$ (see Section 3.3.3). On this basis, a good estimate of the hardness ratio is provided by Eq. (2.84), which with values from Tab. 3.4 yields for BMG:

$$\left(\frac{H^B}{H^{CC}}\right)^{est} = \frac{P_{\max}^B}{P_{\max}^{CC}} \times \left(\frac{S^{CC}}{S^B}\right)^2 = \frac{11,472}{1,083} \times \frac{1}{9.71} = 1.09 \tag{3.47}$$

The hardness ratio compares reasonably well with the experimentally determined ratio (3.24) of $H^B/H^{CC} = 1.06$. Use of the estimated hardness ratio of Eq. (3.47) in Fig. 6-3 yields a friction angle of $\varphi^{est} = 9.1°$, and substitution of this friction angle in Eq. (2.38) allows us to determine the hardness-to-cohesion ratios:

$$\tan\varphi^{est} = 0.16 \Rightarrow \left\{ \begin{array}{c} \left(H^B/c\right)^{est} = 7.81 \\ \left(H^{CC}/c\right)^{est} = 7.19 \end{array} \right\} \Rightarrow c = ? \tag{3.48}$$

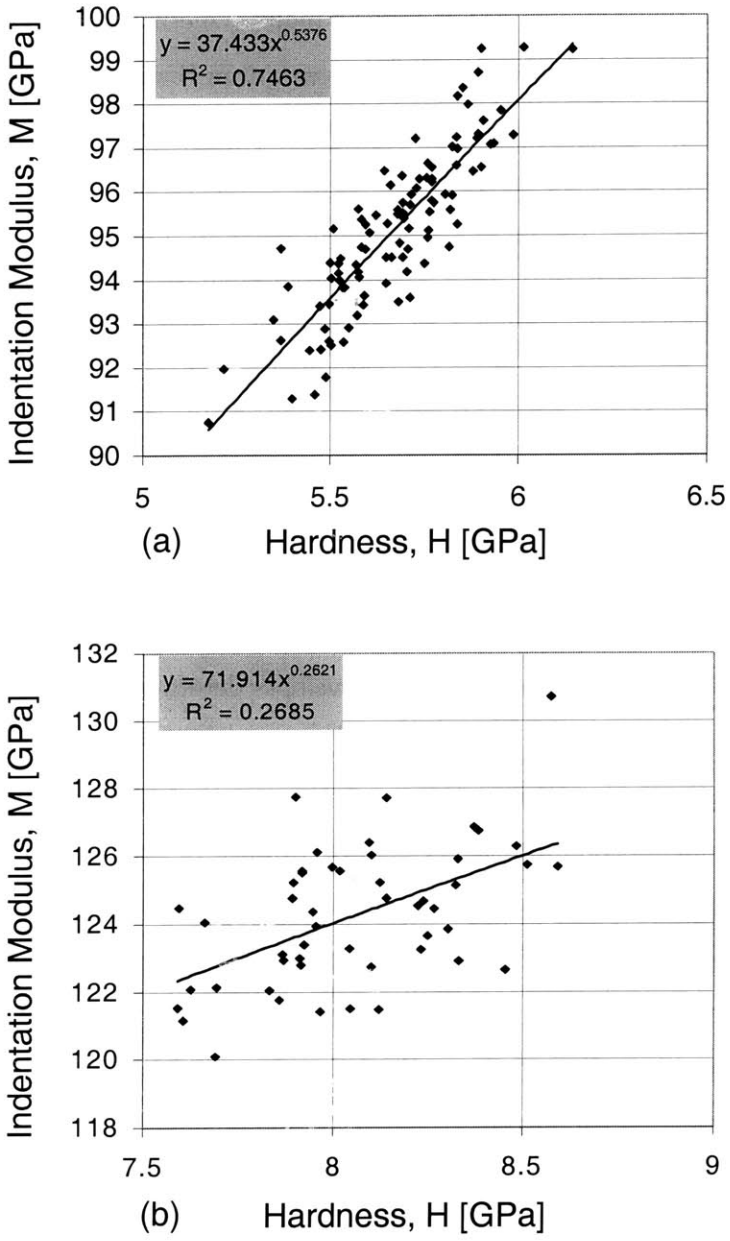

Figure 3-16: $M - H$ scaling relations for Berkovich and Cube Corner indentations.

In order to determine the cohesion, we need at least one hardness value, either the Berkovich hardness or the cube corner hardness, and need to assume that at least one of the two indentation test series was determined with a correct contact area. This is not an easy choice theoretically, given the shortcomings of existing indirect methods. However, given the excellent results we obtained with the Oliver and Pharr method in Berkovich indentation, we suggest to employ the Berkovich indentation hardness derived with the Oliver and Pharr method as the 'correct' indentation result; i.e., from Eq. (3.32):

$$\begin{aligned} H^B &\stackrel{def}{=} \mu^B_{Hest} = 5.67\,\text{GPa} \\ &\Downarrow \\ c^{est} &= \tfrac{5.67}{7.81} = 730\,\text{MPa} \end{aligned} \tag{3.49}$$

Both, friction coefficient $\tan\varphi^{est} = 0.16$ and cohesion $c^{est} = 730\,\text{MPa}$, compare very well with the values determined from direct contact area measurements given by Eq. (3.25), and are in very good agreement with experimental values reported for bulk metallic glass. This is exemplified in Fig. 3-17, which compares the experimental strength envelope of Lu and Ravichandran [158] with the Mohr-Coulomb envelopes determined from Eqs. (3.25) and (3.48)–(3.49).

Finally, the indirect method we propose here employs only measured quantities, the contact stiffness and the indentation force, to provide an estimate of the contact areas in Berkovich and cube corner indentation, and the only assumption is that the Berkovich hardness is correctly evaluated with the Oliver and Pharr method. Following the developments in Section 2.5.4, one could employ directly the mean values of the Berkovich and cube corner indentation modulus estimated with the Oliver and Pharr method (i.e., Eqs. (3.32) and (3.33)) to correct the cube corner contact area from Eq. (2.88):

$$\frac{A_c^{(2)}}{A_c^{est(2)}} = \left(\frac{M^{est(2)}}{M^{\exp(1)}}\right)^2 = \left(\frac{\mu^{CC}_{Mest}}{\mu^{B}_{Mest}}\right)^2 = \left(\frac{124.25}{95.14}\right)^2 = 1.71 \tag{3.50}$$

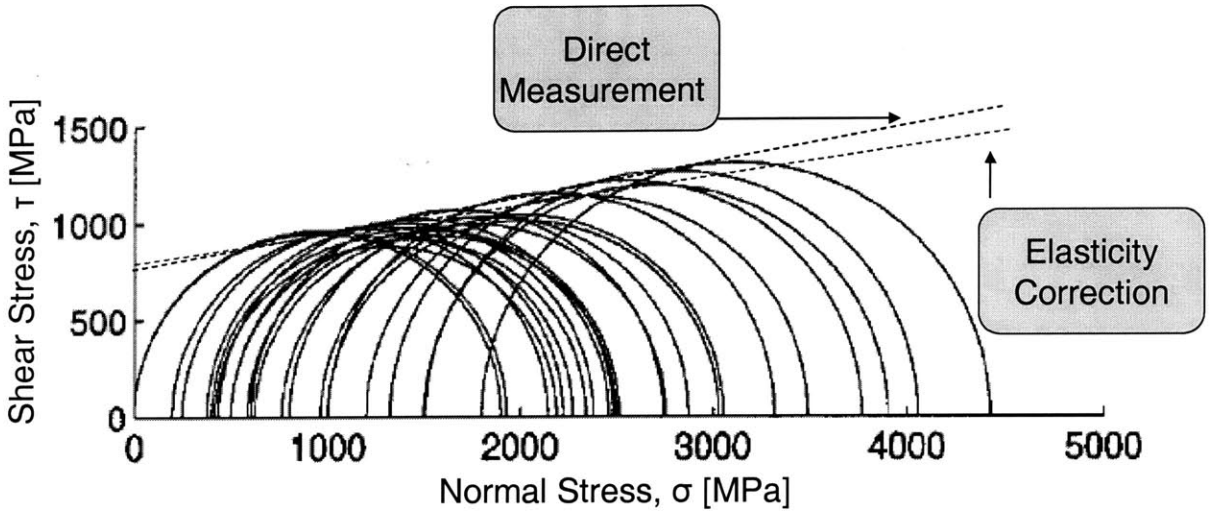

Figure 3-17: Comparison of predicted yield envelope with experimental data from [158].

and to correct the cube corner hardness accordingly:

$$H^{(2)} = H^{est(2)} \left(\frac{M^{\exp(1)}}{M^{est(2)}} \right)^2 = \mu_{H^{est}}^{CC} \left(\frac{\mu_{M^{est}}^{B}}{\mu_{M^{est}}^{CC}} \right)^2 = \frac{8.06}{1.71} = 4.73\,\text{GPa} \tag{3.51}$$

Since this modified elastic corrector method is based on the assumption that the Berkovich indentation modulus and hardness $M^B = \mu_{M^{est}}^{B}$ and $H^B = \mu_{H^{est}}^{B}$ determined with the Oliver and Pharr method are the correct values, we can employ the dual indentation technique using the corrected value of the cube corner hardness (3.51):

$$\left(\frac{H^B}{H^{CC}} \right)^{est} = \frac{\mu_{H^{est}}^{B}}{\mu_{H^{est}}^{CC}} \left(\frac{\mu_{M^{est}}^{CC}}{\mu_{M^{est}}^{B}} \right)^2 = \frac{5.67}{4.73} = 1.20 \tag{3.52}$$

Application of Eq. (3.52) in the dual indentation technique yields a friction angle of $\varphi^{est} = 14.9°$, and a cohesion of:

$$\tan\varphi^{est} = 0.27 \Rightarrow \left\{ \begin{array}{c} \left(H^B/c\right)^{est} = 11.179 \\ \left(H^{CC}/c\right)^{est} = 9.3449 \end{array} \right\} \Rightarrow c^{est} = 510\,\text{MPa} \tag{3.53}$$

	BASh, M_{mat} [GPa]		Dual Indentation Technique	
Contact Area, A_c	Berkovich	Cube Corner	c [MPa]	$\tan\varphi$ [1]
Direct Measurement	101.3	103.1	760 ± 20	0.13
Oliver & Pharr	**103.8**	139.4	–	–
Cheng & Cheng	124.9	42.2	–	–
Elasticity Corrector (S)	–	–	**730**	**0.16**
Mod. Elasticity Corrector (M)	103.8	103.8	510	0.27
Literature	110.3		$755 - 840$	$0.12 - 0.18$

Table 3.5: Summary of validation of tools of indentation analysis for Bulk Metallic Glass. M_{mat} stands for the plane stress modulus of BMG. Boldface type indicates the techniques we recommend for indentation analysis of cohesive-frictional materials.

Hence, compared to the contact area estimation (3.46), the modified elastic corrector method shown in Eq. (3.50) does not perform that well, most likely because this approach propagates the error in the indentation stiffness determination into the hardness ratio. In fact, our derivation is based on the rules of self-similarity of the conical indentation test, which appear to be perturbed by the error in the contact area estimation. For practical purposes, we therefore recommend to use the contact area estimation of Eq. (3.46) based on only measured quantities: the contact stiffness S.

3.6 Chapter Summary

The results presented in this first part of the thesis provide strong evidence that a combination of high accuracy indentation testing and advanced indentation analysis allows one to translate indentation data into meaningful mechanical properties of cohesive-frictional materials. Table 3.5 summarizes the results of our indentation analysis of Berkovich and cube corner indentation tests on a model cohesive-frictional material, Bulk Metallic Glass:

1. The fundamental equation to translate indentation data into elastic properties is the BASh formula (2.2), which appears to give highly accurate results for both Berkovich indentation and cube corner indentation data provided the area of contact is measured or estimated properly. For our model material, BMG, we did not find that the BASh formula overestimates the indentation modulus due to second-order effects in radial displacements (see Section 2.4.3). This could be due to the fact that plastic dilating deformation which

take place in cohesive-frictional materials, counterbalance the elastic contraction behavior. Hence, the BASh formula appears to us as a reliable tool to translate indentation data into elasticity properties of the indented material.

2. The novel dual indentation method we here propose allows one to translate hardness values into strength properties of cohesive-frictional materials. The cohesion and friction angle values we obtain with this method for BMG are in excellent agreement with values reported in the literature, which confirms that bulk metallic glasses are cohesive-frictional materials of the Mohr-Coulomb type.

3. The accuracy of any indentation method depends on the quality of the determination of the projected contact area. This is not an easy task: in the validation of the BASh formula and the dual indentation technique for bulk metallic glass, we measured the contact area by direct measurement of the residual hardness impression after a complete unloading. For practical reasons, however, some means other than direct observation of the hardness impressions is needed. We have tested several methods proposed in the open literature (and implemented in many indentation software programs), and found that the Oliver and Pharr method provides reasonable estimates of the contact area for Berkovich indentation, in which the plastic deformation behavior below the indenter is constrained. In the case where excessive pile-up is present, like in cube corner indentation, the estimates provided by the method are largely in error. To circumvent the introduction of errors in our dual indentation technique we propose a new method based on (1) a correction of the contact area using directly measured quantities (contact stiffness S), and (2) the accuracy of the Oliver and Pharr method in Berkovich indentation. The results obtained with this elasticity corrector method in dual indentation analysis of BMG are in excellent agreement with results based on direct measurements of the contact area. The ease of utilization makes this method even more appealing for day-to-day application in indentation testing.

The experimental results presented for Vitreloy 1^{TM} (see Tab. 3.5) validate the indentation technique, and provide the basis for indentation analysis of more complex, highly heterogeneous cohesive-frictional materials: natural composites.

Part III

EXPERIMENTAL MICROPOROMECHANICAL INVESTIGATION

Chapter 4

Multi-Scale Think Model for CBM

Concrete, based mainly on Portland cement, water and aggregates, is the most widely used material on Earth. Current estimates of world cement manufacture are of the order of 1.7×10^9 tons/year, enough to produce well over 6 km^3 of concrete per year or at least 1 m^3 per person [95]. However, the omnipresence of concrete in construction belies its complexity. The complex chemical reactions that occur when a gray powder (cement) is transformed, by the simple addition of water, at room temperature, to a rigid solid, creates one of the most heterogeneous class of materials in existence. The most prominent feature of this heterogeneous microstructure is the large amount of porosity which manifests itself from the length scale of a few atomic diameters to millimetric dimensions. There have been very few attempts so far to link the mechanical behavior of this heterogenous material to composition and structure, and identify a fundamental unit of material invariant properties. This is what we attempt in this thesis through a multiscale investigation of the mechanical properties of cement-based materials at multiple scales and the use of advanced homogenization theories to translate micromechanical properties into macroscopic properties. This chapter reviews the multi-scale structure of cement-based materials. Chapter 5 demonstrates how the concepts of indentation testing and analysis can be adapted for multi-phase and multi-scale composites like cement-based materials (CBM) to identify properties of different phases present in the microstructure. As an application, Chapter 6 illustrates how this novel approach, based on nanoindentation analysis, allows the identification of microstructural changes induced by heat curing and heat treatment of CBM. These indentation results will form the backbone for later development of a multiscale

micromechanics based model that predicts mechanical properties of cement-based materials on the basis of composition and structure.

4.1 Chemical Reactions and Material Formation

The solid we call cement paste and which forms the binding matrix for all cementitious systems, is the resulting product of the chemical reaction between cement and water, a reaction commonly referred to as hydration. It is therefore natural to start our multiscale investigation of the mechanical behavior of CBM by familiarizing ourselves with the mineralogical composition and physical properties of cement, as well as the resulting hydration products.

4.1.1 Portland Cement

Manufacturing

Cement is a generic term for a material which in the presence of water develops cohesive properties that make it possible to bind a particulate matter together. The first use of cementing agents can be traced back to the ancient Egyptians, Greeks and Romans who used calcined limestones, sand and crashed stone to produce an ancient form of concrete. Today's cements do not differ fundamentally from this natural historic occurrence. Cement is made from a mixture of clay and calcareous materials. The essential ingredients are lime and silica, which are abundantly found in suitable forms of chalk (or limestone) and clay, respectively. The manufacturing process is simple: first, the raw materials are proportioned to supply the desired amounts of lime, silica, aluminum oxide and iron oxide; and then heated in rotary kilns. The heat treatment during the mixing process involve temperatures on the order of 1500°C, at which the material undergoes sintering, partial fusion reactions and chemical composition changes [226]. The resulting particles, called clinker, of almost spherical shape (a few centimeter in size), are cooled and ground to a fine powder, Portland cement, of mean particle diameter $\sim 20\,\mu$m [4].

Mineralogical Phase	Shorthand Notation	mass %
$3CaO.SiO_2$	C_3S	50-70
$2CaO.SiO_2$	C_2S	15-30
$3CaO.Al_2O_3$	C_3A	5-10
$4CaO.Al_2O_3.Fe_2O_3$	C_4AF	5-15

Table 4.1: Typical mineralogical composition of a Portland cement.

Chemical Composition

The silica and calcium rich materials are mixed at high temperature and interact with one another to form a series of more complex products until a state of chemical equilibrium is attained. Due to the relatively fast cooling rates the crystallization process is not complete and a certain degree of amorphous material is present in the clinker phase [226]. Nevertheless, cement can be considered as being in a state of frozen or quasi-equilibrium where different compounds coexist. In an ordinary Portland cement, four compounds are regarded as the major constituents, these being: tricalcium silicates, C_3S, dicalcium silicates, C_2S, tricalcium aluminates, C_3A, and tetracalcium aluminum ferrites, C_4AF[1]:

$$\left.\begin{array}{r} \text{Limestone} \rightarrow CaO+CO_2 \\ \\ \\ \text{Clay} \rightarrow SiO_2+Al_2O_3+Fe_2O_3+H_2O \end{array}\right\} \overset{1500°C}{\rightarrow} \left\{\begin{array}{c} 3CaO.SiO_2 \equiv C_3S \\ 2CaO.SiO_2 \equiv C_2S \\ 3CaO.Al_2O_3 \equiv C_3A \\ 4CaO.Al_2O_3Fe_2O_3 \equiv C_4AF \end{array}\right. \tag{4.1}$$

A typical mineralogical composition of Portland cement is given in Tab. 4.1.

4.1.2 Hydration of Portland Cement

Once cement and water is mixed the material is in a state of suspension. The mixture can withstand limited shear and flows like a (non-Newtonian) fluid (Fig. 4-1a). As time goes on, the cement reacts with water forming hydration products that percolate to form a rigid solid which can withstand shear stresses (Fig. 4.1b). In fact, all four clinker phases of Portland cement (see Tab. 4.1) react with the water in a process that is called hydration. In the following

[1] Cement chemists' notation is used throughout; C=CaO; S=SiO_2; A=Al_2O_3; F=FeO_3; $\bar{S}$=SO_3. Thus, C_3S=$3CaOSiO_2$. Dashes in the formula C-S-H emphasizes its variable composition.

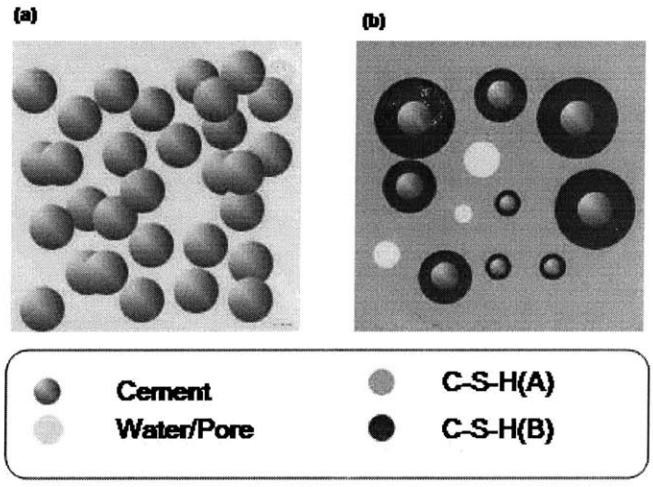

Figure 4-1: Schematic of cement hydration: (a) Cement paste at the plastic-fluid state once cement and water is mixed, (b) Cement paste in the hardened state after cement and water reacted (a few days) to form a connected network of solids that precipitate under water.

presentation, we separately describe the hydration of aluminates and silicates. They form the most important part of the microstructure of a cement paste.

Aluminate Hydration

The hydration of the tricalcium aluminates, C_3A, is a rapid process that leads to calcium aluminates which are called AFm phases. A set[2] of hydration reactions is [226]:

$$\begin{aligned} 2C_3A + 27H &\longrightarrow C_4AH_{19} + C_2AH_8 \\ 2C_3A + 21H &\longrightarrow C_4AH_{13} + C_2AH_8 \\ C_3A + CH + 12H &\longrightarrow C_4AH_{13} \end{aligned} \tag{4.2}$$

[2]The expression "set" indicates that the reactions are consistent among themselves. Depending on the source slightly different writings can be found.

In addition to this phase, Ettringite (AFt in the notation of Taylor [226]) forms in the presence of sulfates (SO_4^{2-}) and water:

$$C_3A + 3C\bar{S}H_2 + 26H \longrightarrow C_6A\bar{S}_3H_{32} \tag{4.3}$$

Once the sulfate ions are consumed, the Ettringite becomes an AFm phase according to the following reaction:

$$2C_3A + C_6A\bar{S}_3H_{32} + 4H \longrightarrow 3C_4A\bar{S}_3H_{12} \tag{4.4}$$

The hydration of tetracalcium aluminum ferrites, C_4AF, is very similar to the hydration of C_3A except for the slower kinetics. The reactions (4.2) can be written analogously with the aluminum being replaced by iron. The characteristic length of the end products of the aluminate hydration is in the 10^{-6} m range.

Silicate Hydration

The hydration of silicates, C_3S and C_2S, leads to the main products of cement hydration. The hydration of the two silicate phases is very similar, differing only in their rate of formation, and can be divided in three stages [226]:

1. Dissolution of the clinker grains (C_3S and C_2S);
2. Diffusion of the ions in the interstitial solution;
3. Precipitation as the saturation point for the different hydrates is attained.

As the precipitation takes place, the ion concentration in the solution is lowered and more clinker is dissolved. Making the approximate assumption that the final reaction product of C_3S and C_2S is $C_{3.4}S_2H_8$ [227] the reactions of hydration can be written as:

$$\begin{aligned} 2C_3S + 10.6H &\longrightarrow C_{3.4}S_2H_8 + 2.6CH \\ 2C_2S + 8.6H &\longrightarrow C_{3.4}S_2H_8 + 0.6CH \end{aligned} \tag{4.5}$$

Equation (4.5) suggests that the hydration of tricalcium silicates and dicalcium silicates yield the same hydration products, namely Calcium Hydroxide (CH) and Calcium-Silicate-Hydrates

Mineralogical Phase	vol %	Crystallinity	Morphology	Dimensions
C-S-H	50-70	Very Poor	Unresolved	$10 - 100\,\text{nm}$
CH	15-20	Very Good	Solid Hexagonal	$10 - 100\,\mu\text{m}$
$C_4A\bar{S}_3H_{12}$	1-5	Good	Solid slender needles	$10 \times 0.5\,\mu\text{m}$
$C_6A\bar{S}_3H_{32}$	1-5	Fair-Good	Solid Thin hexagonal plates	$1 \times 1 \times 0.1\,\mu\text{m}$

Table 4.2: Typical mineralogical composition and physical characteristics of a cement paste (from Ref. [169]).

(C-S-H). In addition, both silicates require approximately the same amount of water for their hydration, but C_3S produces more than twice as much (on a mass basis) CH as is formed by the hydration of C_2S. The calcium hydroxide (CH) usually constitutes approximately 10 to 20 vol% of the hydration product.

4.2 Phases in Hardened Cement Paste (hcp)

From the chemical reactions that occur during hydration, it is readily understood that the resulting solid, the hardened cement paste (hcp), is a multiphase composite material. It consists of the hydration products of the different cement phases and residues of unhydrated cement particles, in addition to water filling the pores. Table 4.2 shows a typical mineralogical composition together with their relative volumetric proportions found in Portland cements. Although there are five distinct chemical phases in the cement paste, which are detailed below, there are two phases that dominate in volumetric proportions: C-S-H and CH, which constitute more than 85% of the total volume. Therefore, the macroscopic mechanical behavior of cementitious materials is expected to be governed by the mechanical properties of these phases. Special emphasis is placed on their description and characterization.

4.2.1 Calcium Silicate Hydrates: C-S-H

Calcium silicate hydrates (C-S-H) build up the main binding phase in all Portland cement-based systems. They account for $50 - 70\%$ of the volume, and are considered to be the most important contributors to the mechanical properties of cementitious systems. Their high relative proportion makes C-S-H the only percolated phase in hcp, and as a consequence the macroscopic

mechanical behavior heavily depends on it. The fact that the term C-S-H is hyphenated signifies that it is not a well defined compound, but that it exists in several different forms [226]. The chemical formula $C_{3.4}S_2H_8$ used in the hydration reaction (Eq. 4.5) is only an approximate one because the actual composition of this hydrate experiences significant local variabilities. For an Ordinary Portland Cement (OPC), the Calcium-to-Silica (Ca/Si)-ratio varies between 1.2 and 2.3 with a mean of 1.75, and the structural water content, that is the water chemically bound in the crystal structure, varies even more [198]. The morphology of C-S-H also varies from poorly crystalline fibers to a reticular or crumbled sheet-like network. Of primary importance is their colloidal nature[3], with an extremely high surface area of 100 to 700 m^2/g (about a thousand times greater than the surface area of cement particles). Due to their colloidal dimensions and a tendency to cluster, C-S-H crystals could only be visualized with the advent of electron optical microscopy. The most striking feature of the C-S-H matrix is the porous nature. A large volume fraction of nanometer size pores is present in all cement-based materials independent of their processing and mix proportions. This striking feature suggest a gel like morphology that is responsible for the peculiar macroscopic mechanical behavior: pressure sensitive strength capacity, poromechanical response, volumetric instability in Relative Humidity changes, and so on.

The structure and composition of calcium silicate hydrates has been the subject of many experimental and theoretical attempts over the last 100 years. The foundations were laid by Le Chatelier with his groundbreaking work in 1887 (cited from [180]), who noted the gel like morphology of C-S-H phase and identified crystalline phases of the hydration products. Le Chatelier's investigation relied on the available equipment at the time which were limited to low magnification optical microscopes. As new experimental methods and data become available new models were designed to re-interpret the very nature of C-S-H phase. A brief review of different models concerning the C-S-H structure categorized by their length–scales is given below.

[3] A system of finely divided particles, which are approximately 10 to 10,000 angstroms in size. 1 angstrom = 10^{-10}m.

Authors	Primary Exp. Basis	Type	Refs
Taylor [1984/1993]	XRD, Chemical Analysis	Disordered	[226]
Richardson and Groves [1992/2004]	TEM, SEM	Disordered/Crystalline	[197, 199]
Cong and Kirpkpatrick [1996]	^{29}Si MAS NMR ^{1}H-^{29}Si CPMAS NMR	Disordered	[57]
Nonat and Lecoq [1996]	NMR studies	Crystalline	[182]
Chen et al [2004]	NMR, Chemical Analysis	Disordered	[41]

Table 4.3: Summary of models for the atomic-stochiometric structure of C-S-H.

Atomic Structure and Stoichiometry of C-S-H

The smallest scale models are atomistic-molecular models describing the structure and stoichiometry of the C-S-H. First indications of the main features of the C-S-H nanostructure were obtained from comparisons of C-S-H with known (about 30) crystalline calcium silicate hydrates [226]. It was suggested that C-S-H resembles the natural mineral of Tobermorite [106] or the mineral of Jennite [29]. A great deal of information has been gained on the nanostructure of C-S-H in recent years principally from the use of trimethilsilylation (TMS) and solid state nuclear magnetic resonance (NMR) spectroscopy. The model of Taylor [226] together with more recent contributions from Richardson [198], Jennings [130], Faucon [83] and other researchers suggest that C-S-H can be visualized as a Tobermorite with many imperfections and irregularities; such that it becomes nearly amorphous, possibly intermixed at a very fine scale with a similar version of Jennite. In addition, it has been found that C-S-H consists of dimeric and higher polymeric species, mainly linear pentamers and octamers, suggesting a 2,5,8...(3n-1) sequence of linear silicate chain lengths. It is also generally accepted that dimers dominate in high C/S-ratio systems, and that the chain length by polymerization increases as the C/S-ratio decreases [198].

Most contributions to the atomistic structure can be traced back to the groundbreaking work of Taylor [226] in the early 1960s. From an in-depth investigation of the crystal chemistry of the phases of the lime-silica-water system at different temperatures, Taylor postulated the resemblance of two types of C-S-H, C-S-H (I) and C-S-H (II), with naturally occurring minerals of Tobermorite and Jennite, respectively. These minerals have a layered structure based on calcium sheet flanked on each side by linear silicate 'dreierketten' chains as demonstrated by

Si MAS NMR[4] measurements (see [57] and references therein). In Tobermorite, two oxygen atoms from non-bridging tetrahedra coordinate to calcium ions; while in Jennite only one oxygen of the non-bridging tetrahedra coordinate to the calcium ions of the sheet, and the other oxygen is provided by hydroxide ions. Their crystal structure has only been recently decoded and their limiting formulas can be described by $Ca_5H_2Si_6O_{18}.8H_2O$ (Ca/Si=0.83) for 1.4-nm Tobermorite, and $Ca_9H_2Si_6O_{18}(OH)_8.6H_2O$ (Ca/Si=1.5) for Jennite [29]; see Fig. 4-2. Later models suggested modifications of these crystals structures in an effort to capture experimentally observed trends; in particular:

- Scanning Electron Microscope (SEM) and Transmission Electron Microscope (TEM) studies reveal small scale variabilities in the composition of the C-S-H phase, while the Ca/Si ratio in different regions of neat hydrated C_3S and C_2S exhibits large variabilities of values ranging between 1.2 and 2.1 with a mean value around 1.75 [197, 198]. The length scale of these investigation was around 100 nm.

- C-S-H tends to become compositionally more uniform with age. A bimodal distribution was observed at early ages that seems to unify as the paste matures [197, 199]. The mean Ca/Si-ratio during that process was noted to remain almost unaffected. The primary inconsistency between experimental data of cement pastes and the minerals of Jennite and Tobermorite is the higher mean Ca/Si-ratios experimentally observed. Several models were proposed over the years in an attempt to increase the Ca/Si-ratio and meet the experimental observations. The absence of a unique stoichiometry gave rise to many different models all of which are crystal-chemical possible. We acknowledge the ones of Richardson and Groves [197, 199], Cong and Kirkpatrick [57], Nonat and Lecoq [182, 183], Chen et al. [41], and a modified version of Taylor's' original proposition [226]. Richardson and Groves model incorporates a lot of variables which make it very flexible and which converges to most of the other models under specific assumptions [197, 199]. The modified Taylor model suggests that the bimodal distribution experimentally observed at early ages is a reflection of a defect-Tobermorite model and a defect-Jennite model that give peaks of Ca/Si at 1.2 and 2.3 respectively. Taylor then suggested that as the material

[4] Magic angle spinning nuclear magnetic resonance.

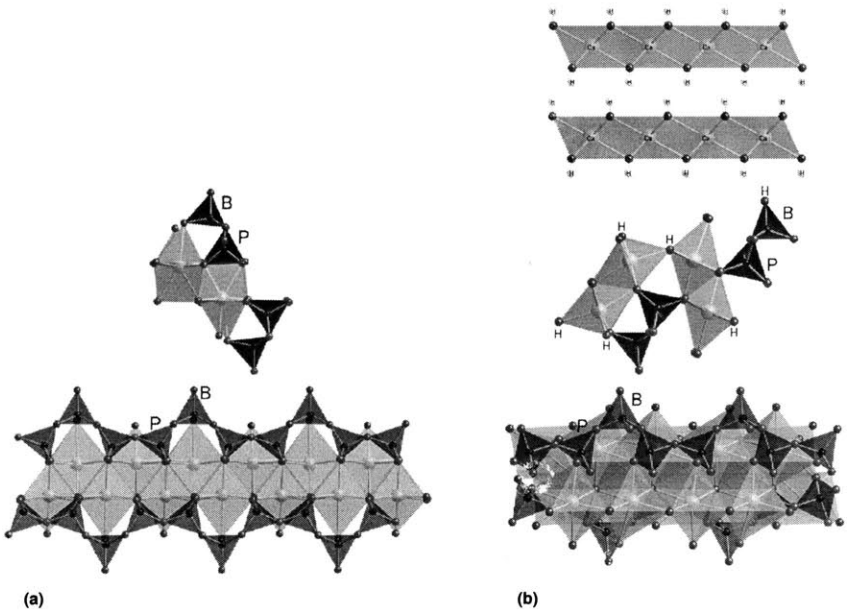

Figure 4-2: a) Schematic diagrams showing dreirkette chains present in 1.4nm-Tobermorite projected along [010] (top) and [210] (bottom). The chains have a kinked pattern where some silicate tetrahedra share O-O edges with the central Ca-O layer (P=Paired tetrahedra) and others that do not (B=Bridging tetrahedra). b) Schematic diagrams showing dreirkette chains present in Jennite projected along [010] (top) and [100] (bottom). (from Ref. [199])

ages the two precipitates interact with each other to form a unimodal distribution of an amorphous mixture of Jennite-Tobermorite contributions. Based on experimental data on synthetic C-S-H, Cong and Kirkpatrick [57] argued that the existence of Tobermorite structures dominates in their system, and as a consequence they suggested a Tobermorite defect model. Chen et al. [41] reconciled solubility curves for specimens with a broad range of compositions and attempted to interpret the data as representing a spectrum of metastable phases whose internal structure ranges from purely Tobermorite-like to largely Jennite-like. Intermediate stages suggest a defective Jennite-Tobermorite mixture. Based on recent evidence from atomic force microscopy (AFM) image analysis of grown C-S-H crystals [183], Nonat and Lecoq suggested that the C-S-H phase is not necessarily amorphous, and that the Ca/Si ratio can be altered by incorporating OH^- and Ca^{2+} ions in the interlayer space of a Tobermorite crystal.

There is still a fundamental question regarding the nature of C-S-H particles: What is the stoichiometry of C-S-H particles occurring in cementitious materials? Or on a more fundamental level: Are C-S-H phases crystalline or amorphous? In the absence of a definite answer to these nagging questions, there is an increasing body of experimental evidence that suggests that independent of their atomic nature, C-S-H precipitates to form particles of nanometer dimension that eventually agglomerate to form a gel network. The extremely high specific surface area of these materials, their nanometer size porosities, and their continuous interaction with water all hint towards the gel like properties of the material. Figure 4-3 shows recent atomic force microscopy and transmission electron microscopy (TEM) images testifying towards the colloidal nature of C-S-H systems. All three images, taken from different researchers on different cement based samples, suggest particles on the order of tens of nanometers. This is discussed below.

Colloidal Structure of C-S-H

The tendency of C-S-H to agglomerate and form clusters yields a characteristic microstructure in the range of a few nm to hundreds of nm. Several models were proposed over the years in an attempt to deduce specific characteristics of this microstructure. Since the microstructure cannot be directly observed, research focused on finding *the* hidden underlying structure that is consistent with a variety of experimental observations (Tab. 4.4). Most models originate from

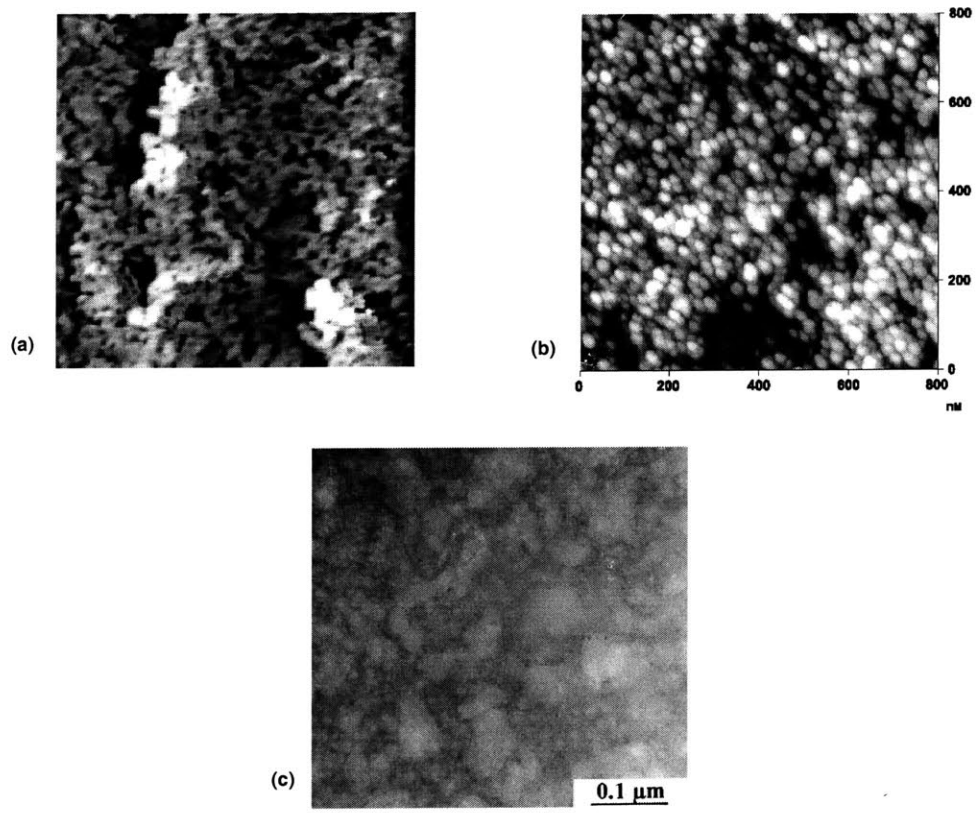

Figure 4-3: Microscopy images demonstrating the nanoparticulate nature of C-S-H, a) Topographic, atomic force microscpy image of C-S-H nanoparticles ($60 \times 30 \times 5$ nm) precipitated after a single crystal of calcite was immersed in a sodium silicate solution [192], Image Size: 5×5 μm^2, b) AFM image of the surface of a cement paste cast against a calcite single crystal, revealing particles with a mean size of $30 - 50$ nm [183], Image Size: 0.8×0.8 μm^2, c)TEM image of high performance concrete showing particles ranging in size from $20 - 60$ nm [91].

Authors	Primary Experimental Basis	Type	Selected Characteristic
Powers [1958]	Water Sorption Volume of pores	Colloid	Gel products 28% pore volume
Kantro et al [1970]	Hysteresis of water sorption	Layer Tobermorite	High surface area gel
Feldman and Sereda [1970]	Nitrogen sorption Length/Modulus/Weight vs. RH	Layers	Clay like structure with important role of interlayer water
Wittmann [1979]	Modulus vs. RH	Colloid	Important role of water in spaces between particles
Jennings [1994/2000]	Density Composition Surface Area Fractal	Colloid	Consistent with as much experimental data as possible

Table 4.4: Summary of models for the 1–100nm structure of C-S-H , from [225].

the groundbreaking works of Powers et al. [194], who deduced a gel-type colloidal microstructure of C-S-H from water sorption and pore volume data. Power's model was debated and advanced by Feldman and Sereda [85] who suggested that C-S-H, similarly to clay particles, form a three dimensional assemblage of C-S-H sheets which tend to form a subparallel, few layer thick group, and which enclose pores of dimension of the interlayer spaces and upwards. This model is consistent with surface area measurements and sorption isotherm data. It also gives a great deal of information about the state of water and porosity at this scales. Wittman's 'Munich model' [246] combines elements of the previous models, and focuses much on the state of the structural water in spaces between particles, which was substantiated by relative humidity measurements. But in all these early models, C-S-H is treated as a single phase (with some variability), and no distinction between different types of C-S-H is made. Furthermore, none of these models is conclusive on the link between microstructure and mechanical behavior of the material.

Two Types of C-S-H

Recent evidence suggest that calcium-silicate-hydrates, C-S-H, in cement based materials exist in, at least, two different forms. First observations can be traced back to Taplin [224], who attributed the two families to the inner and outer hydration products. Early indicative studies employed light microscopy of thin sections [65], which were later confirmed by means of

Classification	Reference
Outer Product – Inner Product	Taplin [224] , Richardson [198], Groves [105]
Middle Product – Late Product	Scrivener [207], Taylor [226]
Phenograins – Groundmass	Diamond and Bonen [68]
Low Density – High Density	Jennings and Tennis [130, 227]

Table 4.5: Classification of the two morphological entities of C-S-H found in the open literature.

high resolution TEM of ground and redispersed material [105, 65, 196, 198], X-Ray mapping of flat polished sections [225, 198], Neutron Scattering [229] and other techniques. These studies provide clear evidence of the existence of two morphological entities of C-S-H. More recently, based on a comprehensive analysis of disparate measurements of specific surface area of hcp reported in the open literature, Jennings and Tennis [130, 227] proposed a colloidal model for the two types of C-S-H, with identical chemical composition but distinct pore volume fractions and geometry. The two types of C-S-H have been referred to in the literature as the C-S-H portions of phenograins – groundmass [68], outer product – inner product [224], low density – high density [130, 227], or middle product – late product [207, 226]. Table 4.5 summarizes the different classifications of the two types of C-S-H.

Recent TEM images of Richardson [199] displayed in Fig. 4-4a-c show a distinct difference in morphology of the two types of C-S-H. At lower magnification (Fig. 4-4d [82]) the two types of C-S-H can be distinguished by differences in the gray scale exhibiting sharp propagation fronts probably related to diffusion processes in the material that occur during hydration. From these images it becomes apparent that:

- A clear, distinct border exists between the two types of C-S-H, which hints towards a threshold in the physicochemical formation process.
- A distinct difference in morphology and packing density is evident (see magnifications of the two types in Figures 4-4b and 4-4c).
- The regions the two types of C-S-H occupy extend over several micrometers in width.

While the existence of two types of C-S-H appears today as a well-established fact in cement chemistry (see Tab. 4.5), little is known about their mechanical properties and their contribution to the overall macroscopic mechanical performance of cement-based materials. This will

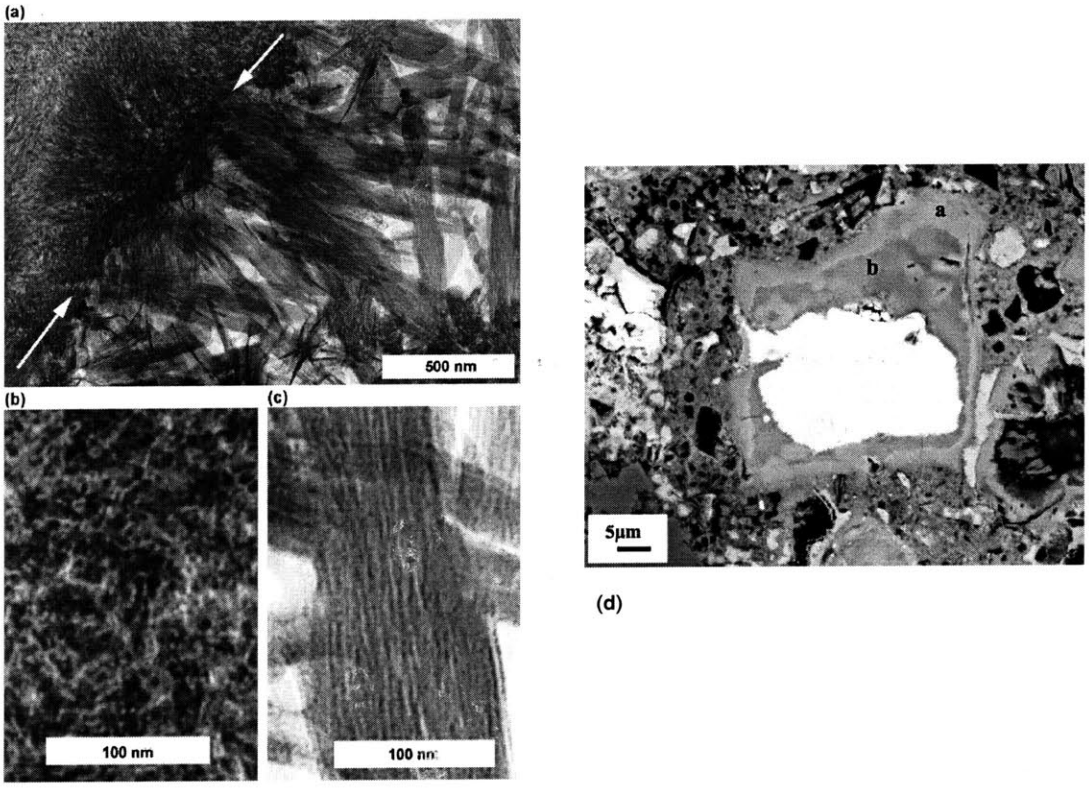

Figure 4-4: TEM (left) [199] and SEM (right) [82] images of Portland cement pastes. Image b and c are magnification of the dense and loose parts of image a. The two significantly different morphologies can be distinguished in all images of different magnifications.

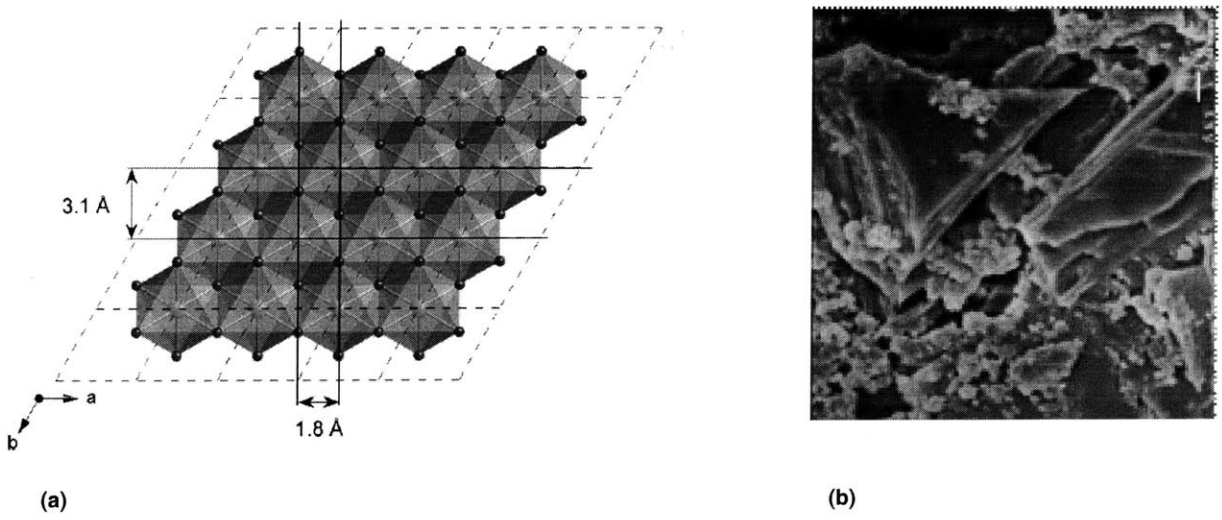

Figure 4-5: a) CH Stochiometry: A single layer of CH crystal structure ($a = b = 3.593$ Å; $c = 4.909$ Å) illustrating the 3.1 ($= b \times \sin(60)$) and 1.8 ($= a/2$) Å repeat distances (from Ref. [199]). b) SEM image of CH crystal found in a Portland cement paste of $w/c = 0.5$.

be one of the focus of Chapters 5, 6, and 10.

4.2.2 Calcium Hydroxide Crystals (CH)

Calcium hydroxide (CH) is often described by its mineral name Portlandite. It occupies 10−20% of the solid volume in hcp, and appears to grow in regions initially occupied by water. In contrast to C-S-H, CH is a compound with a definite stoichiometry (Fig. 4-5a). Under ideal conditions of crystallization, it tends to form crystals with a distinctive hexagonal prism morphology [226] (Fig. 4-5b). But as hydration proceeds, the main deposits of CH become massive and of indeterminate shape, though the good cleavage persists. Actual crystal sizes vary from a few micrometer to several hundreds micrometer, and depend on temperature, hydration time, available space, and impurities present in the system [167]. TEM studies reveal that a small proportion of CH in cement pastes, especially in the case of low w/c−ratio, is cryptocrystalline and intimately mixed with the C-S-H [105]. Inclusions of CH at that scale were also identified by decomposition and diffraction patterns [226].

E [GPa]	Poisson's Ratio ν	Hardness [GPa]	Method	Reference
35.24			E	[20]
48			E	[247]
$39.77 < E < 44.22$	$0.305 < \nu < 0.325$		B	[171]
36 ± 3		1.35 ± 0.5	I	[2]
38 ± 5		1.20 ± 0.4	I	[58,59,60]

Table 4.6: Elastic properties of Portlandite crystals found in the literature, E= Extrapolation, B= Brillouin Spectrum, I= Indentation, .

Several experimental studies on the elastic behavior of CH are reported in the literature (Tab. 4.6):

- Beaudoin [20] and Wittmann [247] measured the elastic modulus of CH compacts pressurized to different levels to obtain specimens with different porosities. The elastic modulus E of these compacts was obtained from three-point bending tests. The intrinsic modulus of CH was found by extrapolating to zero porosity, log E versus porosity curves. The logarithmic relation between E and porosity shows a good fit in the range of porosities considered, however no theoretical argument support that the assumed relationship should hold for low porosity values.

- Monteiro [171] used the elastic stiffness coefficients of CH, determined by the use of Brillouin Light Spectrum[5] in the Voight-Reuss (V-R) and Hashin-Strikman (H-S) stiffness bounds, to obtain the following range of elastic modulus and Poisson's ratio:

$$E_{CH} = 39.77 - 44.89 \text{ GPa}; \ \nu_{CH} = 0.305 - 0.343 \text{ (V-R)} \tag{4.6}$$

$$E_{CH} = 39.77 - 44.22 \text{ GPa}; \ \nu_{CH} = 0.305 - 0.325 \text{ (H-S)} \tag{4.7}$$

  where E_{CH}, ν_{CH} are the intrinsic elastic modulus and Poisson's ratio of CH crystals. By intrinsic, we mean the elastic properties of the material at zero porosity.

- Acker [2] and Constantinides and Ulm [58,59,60] measured the elastic properties of CH by performing indentations on large crystals found in the microstructure of cement pastes.

[5] Measurements of the ultrasonic and hypersonic longitudinal velocities, on grown crystals and at different directions, provide the stiffness coefficients.

The elasticity data summarized in Tab. 4.6 show a fair amount of consistency, so that the elastic properties of CH can be regarded as known. In contrast, very little is known about the strength behavior of CH. The only information about strength comes from hardness measurements performed by nanoindentation. The data of Acker [2] and Constantinides and Ulm [58,59] agree at a hardness value of approximately $1.2 - 1.35$ GPa, which translates for a pure cohesive material into a uniaxial strength of (see Section 2.3.1, Eq. (2.18)):

$$\sigma_y \simeq \frac{H_{CH}}{2.8} = 430 - 480 \text{ MPa} \tag{4.8}$$

The relatively high strength of CH compared with typical strength values of hcp suggests that CH crystals in hcp contribute to the overall strength behavior. However, large crystals with distinct cleavage and small surface area are often sources of significant stress concentrations that make CH a limiting contributor to the strength of hcp [180]. Finally, due to the high solubility of CH, the presence of CH makes cement-based materials more vulnerable to chemical attack (see e.g. Refs. [116,58]).

4.2.3 Minor compounds: Calcium Sulfates, Aluminates and Ferrites

Calcium sulfates, aluminates, and ferrites occupy approximately 15% of the solid volume in the cement paste (Tab. 4.2). Their contribution to the macroscopic mechanical performance is generally assumed to be limited. The influence of Ettringite becomes more significant for mortars, because of the tendency of Ettringite to accumulate in the aggregate-cement paste interface [164]. In fact, Ettringite, together with CH crystals, dominate the interface properties. It should also be noted that in ordinary Portland cement paste, Ettringite eventually transforms into monosulfate hydrate, C_4ASH_{18}, which forms hexagonal, plate crystals. The characteristic length scale of these compounds is in the range of 10^{-8} m to 10^{-6} m [226]. Information in the literature concerning the mechanical behavior of these compounds is scarce. The only information we found were estimates of the elastic moduli (Bulk Modulus, K and Shear Modulus, G) of Ettringite by extrapolating elastic measurements of compact specimens of different porosities to a zero porosity value [256]:

$$K = 47.9 \text{ GPa}; \qquad G = 19.9 \text{ GPa} \tag{4.9}$$

which correspond to an elastic modulus of $E = 52.4$ GPa and a Poisson's ratio of $\nu = 0.32$. To our knowledge, there is no information about the strength behavior of Ettringite.

4.2.4 Unhydrated Cement Grains: Clinker Phases

The proportional presence of unhydrated cement grains in hcp highly depends on the cement particle size and duration of hydration. Some clinker grains can be found in hardened cementitious systems even long after hydration. The amount of unhydrated cement is often expressed by the degree of hydration defined as the percentage of current cement content, $c(t)$, to the initial cement content, c_0; $\xi = c(t)/c_0$. The particle size of cement grains is anywhere between 1 to 50 μm, where 50 μm is usually the maximum cement particle size in modern cements [4]. As the hydration proceeds, the smallest particles dissolve first, and the large ones gradually start decreasing in size. Due to the limited space available, the hydration products tend to crystallize in close proximity and often appear as a coating on the clinker grain. In addition, since the hydration products occupy more space than the cement and water from which they form, complete hydration cannot occur if the water-to-cement ratio (w/c) is below a certain value. Powers and Brownyard demonstrated experimentally that a w/c–ratio of 0.42[6] is sufficient to completely hydrate the cement in a mix [180]. For $w/c < 0.42$ there will always be some cement left unhydrated in the system.

The mechanical properties of the clinker phases have only recently been measured [239,2]. Indentation tests on all clinker phases yield results about the elastic modulus and hardness (Tab. 4.7). The measured elastic and hardness values are one to two orders of magnitude higher than all other cement paste constituents. The clinker phases can therefore be considered as a natural reinforcement to cement based materials. In fact, by reducing the w/c-ratio a significant proportion of clinker phases (together with the enhancement of the mechanical properties) remain in the system at no additional cost. The effect of clinker phases on the mechanical properties of CBM will be further explored in following chapters.

[6] At a $w/c < 0.42$ free access to water will tend to increase tha maximum possible degree of hydration. Therefore, in cases of small cement paste samples, hydrated under saturated conditions (water curing) the limiting w/c-ratio which impedes complete hydration might get to values as low as 0.38.

Clinker Phases	E [GPa]	H [GPa]	σ_y [GPa]
C_3S	135 ± 7	8.7 ± 1	3.1
C_2S	130 ± 20	8.0 ± 2	2.9
C_3A	145 ± 10	10.8 ± 1.5	3.9
C_4AF	125 ± 25	9.5 ± 3	3.4

Table 4.7: Mechanical properties of clinker phases reported in [239], [2]. The uniaxial strength σ_y for a cohesive (frictionless) material is determined from Eq. (2.18).

4.3 Pore and Water Phases in HCP

The porosity in cement based systems is probably the most important component in the microstructure. But rather than a single pore space and morphology, the pore structure of hcp comes in a large variety manifesting itself over several orders of length scales. Indeed, a typical pore size distribution shows an impressive range of porosities ranging from atomic diameters to millimetric dimensions. It is worth recalling that the only porous material phase in the system is the C-S-H gel. Therefore, the total porosity trapped in the system due to the initial mix design (packing arrangement of particles and water) is either allocated in between or within the C-S-H phase. The various types of pores are categorized in terms of their length scales (see Fig. 4-6).

Interlayer Space and Gel Porosity in C-S-H

The porosity of C-S-H that results from the chemical formation of the C-S-H structure is often referred to as gel-porosity (for colloidal interpretations) or interlayer space (for clay type/layered interpretations). Traditionally, the porosity ϕ_0 has been determined from measuring the density of saturated and oven dried C-S-H:

$$\rho^* = \phi_0 + \rho_s (1 - \phi_0) \tag{4.10}$$

where ρ^* is the specific mass density of saturated C-S-H, $\rho_s (1 - \phi_0)$ is the specific mass density of the oven-dried C-S-H, while ρ_s is the specific mass density of the C-S-H solid phase occupying the volume fraction $1 - \phi_0$ in the C-S-H. Depending on the C-S-H model (see Section 4.2.1) different values for the gel porosity can be found in the literature. The interlayer space in Powers model is 1.8 nm [194] and amounts to $\phi_0 = 28\%$ of gel porosity in C-S-H. Feldman and

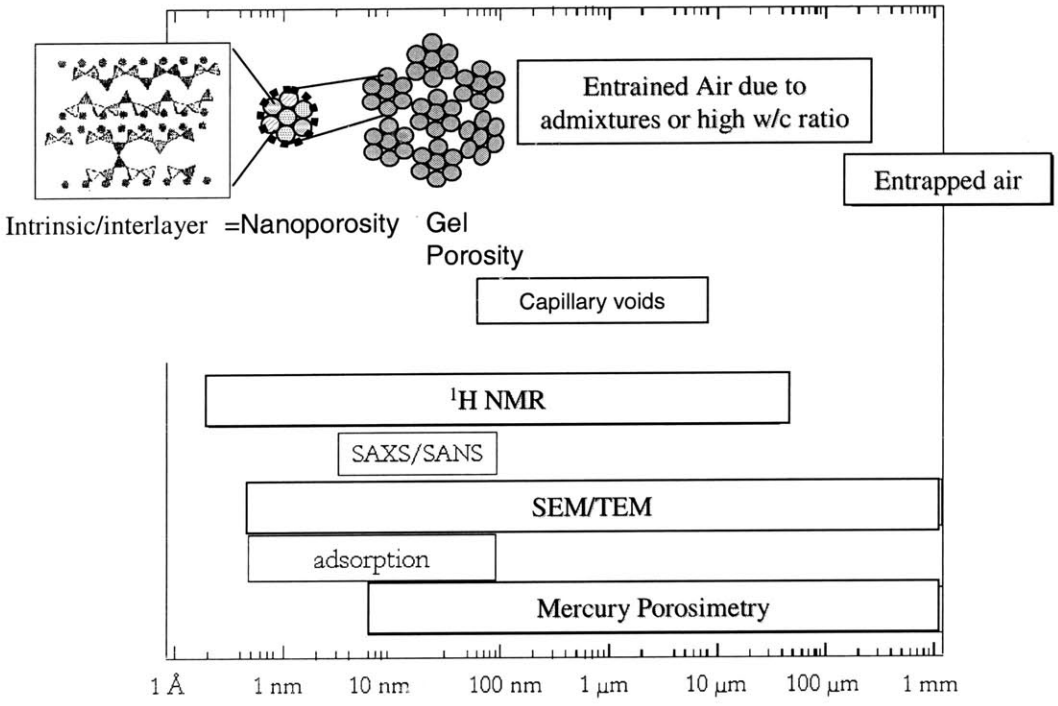

Figure 4-6: Classification of the different pores that might be present to concrete according to their size. The range of C-S-H particles and clusters is also indicated (adapted from Ref. [193]).

Sereda [85] suggest that the interlayer space varies from 0.5 to 2.5 nm, but they do not provide values for the porosity. Jennings and Tennis colloidal model of the two types of C-S-H [130, 227] differentiates between the interlayer space and the gel porosity:

$$\rho_J^* = \phi_J + \varphi_0 (1 - \phi_J) + \rho_s (1 - \varphi_0)(1 - \phi_J) \; ; \; J = LD, HD \tag{4.11}$$

where $\rho_s = 2.8$ is the specific density of the basic building block, i.e., the true C-S-H solid phase, which mixes with a interlayer space porosity of $\varphi_0 = 18\%$ to form a globule-type building block. This globule-type building block forms two different types of C-S-H, a low density C-S-H characterized by a gel porosity of $\phi_{LD} = 37.3\%$; and a high density C-S-H phase characterized by a gel porosity of $\phi_{HD} = 23.7\%$. There is general agreement that the amount of interlayer porosity (and the saturating structural water) forms an integral part of the C-S-H solid and that the void size is too small to have an adverse effect on the macroscopic mechanical behavior of hcp. On the other hand, water in these small voids can be held by hydrogen bonding, and its removal under certain conditions may contribute to drying shrinkage and creep [167].

Capillary Pores

Capillary voids represent the unfilled residues of the space between the cement grains. The total volume of a cement-water mixture remains essentially unchanged during the hydration process [180]. By contrast, the average bulk density of the hydration products is considerably lower than the density of anhydrous Portland cement. Thus, cement hydration may be considered as a process during which the space originally occupied by cement and water is replaced more and more by the space filled with hydration products. The space not occupied by the cement or the hydration products forms the capillary pore space. In contrast to the gel pores, this kind of pore is large enough to be detected by SEM investigations. In well-hydrated, low $w/c-$ratio pastes, the capillary void diameters may range from 10 to 100 nm. In high $w/c-$ratio pastes at early ages of hydration, the capillary voids may be as large as 3 to 5 μm. In general, the volume and size of the capillary voids is determined by the initial distance between the anhydrous cement particles in the freshly mixed cement paste (i.e., $w/c-$ratio) and the degree of cement hydration. From a mechanics point of view, it has been suggested that the pore size distribution,

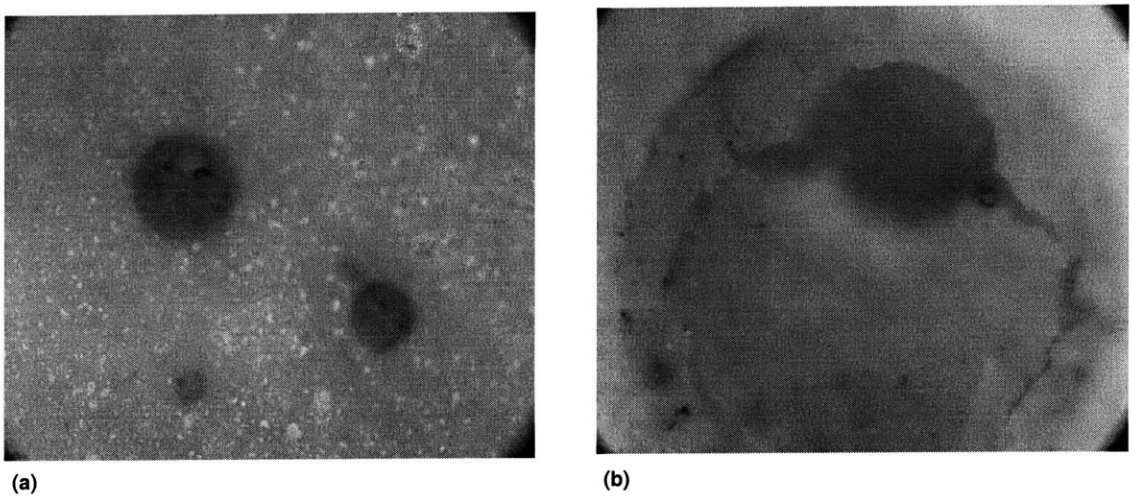

Figure 4-7: (a) Air voids trapped during the mixing of a cement paste. (b) A magnification of the larger pore. Cracks originating from the void circumference are evident.

not the total capillary porosity, is a better criterion for evaluating the characteristics of hcp [167]. Due to the nature of their formation, capillary voids are generally irregular in shape. This is in contrast with air voids (discussed below) which usually exhibit nearly perfect spherical morphology (see Figs. 4-7a-b).

Air Voids

Air voids are usually attributed to improper vibration, i.e., entrapped air during mixing (as large as 3 mm) or entrained air voids introduced with the aid of admixtures (10 to 200 μm). Both air voids types are much larger than the capillary space and may adversely affect the mechanical properties of concrete, particularly the strength that shows a scale dependency with the size of inhomogeneity [27]. Large voids are usually the sites of stress concentrations and are inhibitors of fracture processes, limiting strength due to the localized phenomena taking place on the circumference (Fig. 4-7b). This type of pore can be excluded by proper mix-design and vibration during the cement paste preparation.

Diamond [69] noted that some of the pores present in cement paste are derived from the

hollow shell (Hadley grain) hydration mechanism. Such pores represent a space that is rather within than in between the original cement grains. This type of pore is associated with diffusion processes, and is present in cement pastes of low w/c-ratios. From a mechanical point of view, their influence is as detrimental as the other capillary pores and no distinction is made provided that their volumetric proportions are included in the analysis.

4.4 Length Scales of Observation and Morphological Characterization

In the preceding sections, we identified the different phases present in concrete and their structure. To complete the characterization, it is instructive to separate the different microstructural features according to their length scales, and identify the morphological characteristics of the constituents at the different scales [58,60]. This categorization has its origin in the separation of scale principle of continuum micromechanics (see e.g., [218, 253]), to which we will come back in later chapters of this thesis.

4.4.1 Level 0 ($L = 10^{-10} - 10^{-8}$m): Single Colloidal Particle

At the nanometer scale, the elementary components of the different constituents are the primary building blocks of the different crystal or amorphous structures of the phases. Chemical structures and morphological characteristics were described in Section 4.2.1. Much is known about the atomic structures of the minor compounds CH, Ettringite and clinker phases, but there is still an incomplete knowledge regarding the C-S-H phases. This is the level at which the C/S-ratio gives indications about the crystal structure and the length of the silica chains of the C-S-H sheets. Jennings [130] suggests that several sheets (of eventual layered structure) form a colloidal particle of spherical dimension to which he refers as globules. The packing density of the structural arrangement of C-S-H lamellae is very high, on the order of $1 - \varphi_0 = 0.821$ in Jennings model, determined from the specific densities (see Tab. 4.8). The remaining interlayer space forms an 18% nanoporosity, and the water filling this space is not a bulk water phase, but probably structural water, as suggested in Wittmann's 'Munich' model [246]. Very little, however, is known about the mechanical properties of the colloidal particles.

LEVEL	Density $[kg/m^3]$		Porosity [%]	Mass Content [%]	
0: C-S-H solid	ρ_{sat}	ρ_{dry}	φ_0, ϕ_0	$\frac{\Delta m}{\rho_0^{fl}}$	
Basic Building Block	2,800		–	–	[131](a)
Globules	2,480	2,300	18(b)	18	[131](a)
I: C-S-H matrix					
C-S-H_{LD}	1,930	1,440	37.3 ± 0.1(c)	49(d)	[131](a)
C-S-H_{HD}	2,130	1,750	23.7 ± 0.1(c)	38(d)	[131](a)
II: Cement paste					
C_3S-Clinker	3,150		–	–	
C_2S-Clinker	3,280		–	–	
C_3A-Clinker	3,030		–	–	
C_4AF-Clinker	3,730		–	–	
CH	2,240		–	–	
III: Mortar					
Sand	2,650		–	–	[116]

Table 4.8: Intrinsic properties of cement paste and mortar constituents I:
[a] Density values of C-S-H as predicted from the quantitative colloidal model of C-S-H by Jennings [28,29].
[b] Nanoporosity (intra-globular porosity) filled by structural water;
[c] Gelporosity (inter-globular porosity) of low density and high density C-S-H (excludes nanoporosity);
[d] Δ m = change in mass content due to drying at 105° C; includes structural water in nanoporosity and bulk water in gelporosity.

4.4.2 Level I ($L = 10^{-8} - 10^{-7}$m): C-S-H Gel Matrix

At a scale of tens to hundreds nanometer, colloidal particles ('globule') agglomerate around two characteristic patterns with distinct packing arrangements. Their existence has been postulated by many researchers; their pore volume has been quantified by Jennings and Tennis [130]; and their mechanical behavior has been measured by Acker [2] and Constantinides and Ulm [58]. Jennings et al. [130, 131] postulate that the two types of C-S-H have the same solid building block ('globule') and differ only in the packing modes of these fundamental building block. Figure 4-8 displays the colloid model proposed by Jennings [130, 131], which provides elementary dimensions of the C-S-H solid phase: a solid phase of a characteristic size of 5.6×10^{-9} m, which includes the 18% intra-solid nanoporosity representative of the interlayer space within the C-S-H. This solid phase together with gel porosity yields two characteristic forms of the C-S-H, a low density form (LD C-S-H) and a high-density form (HD C-S-H). The difference between the two C-S-H phases is the gel porosity, respectively the packing density: the LD C-S-H is

characterized by a gelporosity of roughly $\phi_{LD} = 37\%$, and the HD C-S-H is characterized by a gelporosity of roughly $\phi_{HD} = 24\%$. It is intriguing to note here that the corresponding packing densities, $1 - \phi_{LD} = 0.63$ and $1 - \phi_{HD} = 0.76$, come very close to two maximum packing densities of mono-sized spherical packing [128,209,71]: The packing density of LD C-S-H is of striking similarity of the so-called random close packing (RCP)[7] of ~ 0.64, and the packing density of HD C-S-H is of striking similarity of the highest possible density of ordered spheres, known as the face-centered cubic lattice, of $\pi/\sqrt{18} = 0.74$ (see Appendix E). In all cases, the order of magnitude of the packing densities seems to confirm Jenning's postulate that the two types of C-S-H are composed of mono-sized building blocks of probably spherical dimension. It will be one focus of our multiscale investigation to decode the mechanical significance of these packing densities.

Furthermore, the dual packing arrangement of C-S-H appears to be consistent with the formation process. Figure 4-9 shows the Powers and Brownyard model [194] in a slightly modified form. Following the original model, immediately after mixing, the unhydrated cement particles in a fresh paste are dispersed in an aqueous solution (Fig. 4-9(a)). During the first few minutes, the reaction rate is very rapid, and C-S-H form a coating around the cement grains. As hydration proceeds, hydration products including calcium hydroxide, precipitate from the saturated solution in the capillary pores or spaces.

The C-S-H formed during this period appears to precipitate in a characteristic pattern with uniform porosity (about $10 - 100\,\text{nm}$ in size). They correspond to the outer product or LD C-S-H. Any microcrystalline CH and minor compounds formed during this period is included into the LD C-S-H structure. Since 1 cm^3 of cement produces 2.2 cm^3 of cement gel, about half of the gel forms inside the original boundary of the cement grain, and half is deposited in the surrounding water filled space. Eventually, bridging occurs between cement particles and the paste stiffens into its final shape (Figs. 4-9(b) to 4-9(c)). Further hydration which involves some complex diffusion processes, results in further deposition of cement gel at the expense of unhydrated cement and capillary pore water. During this period, HD C-S-H is formed which

[7] Donev et al. [71] remark that the random close packing (RCP) concept is ill-defined, because it may depend on the packing protocol. They suggest instead to refer to the RCP packing density as the maximally random jammed (MRJ) state, corresponding to the least ordered among all jammed packings. For a variety of order metrics, it appears that the MRJ state has a density of 0.637 and is consistent with what has traditionally been thought of as RCP

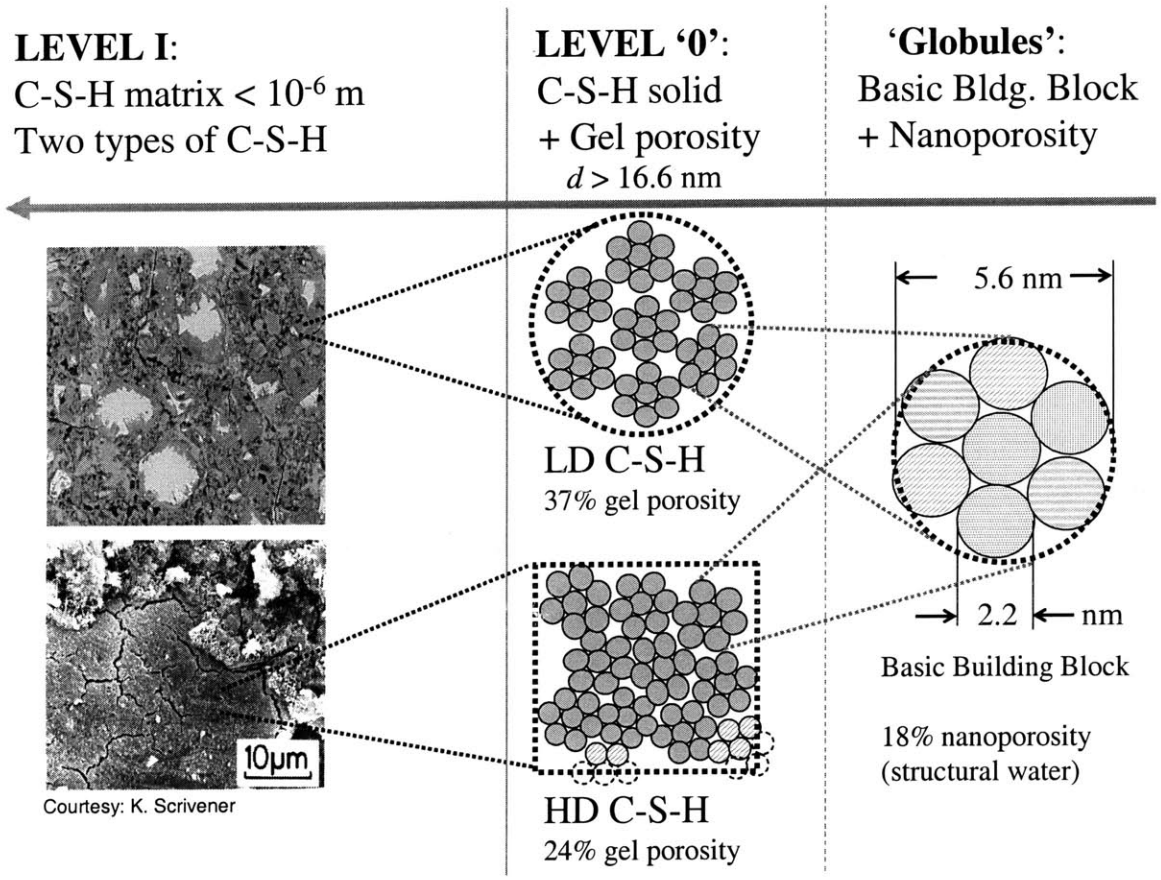

Figure 4-8: Jenning's colloid model of the two types of C-S-H [130, 131].

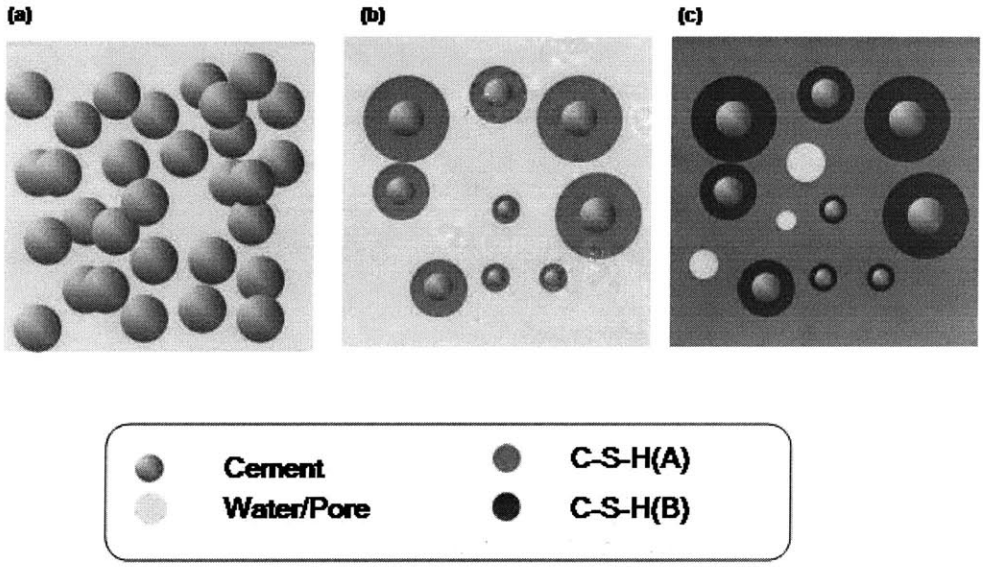

Figure 4-9: Evolution of cement paste microstructure with time: a) cement intially mixed with water, b) LD CSH forms first as a rim around cement particles, until it percolates and stiffens the matrix. c) Mature cement paste where LD CSH forms a matrix with cement inclusions and HD CSH rims. Pore space that might not be filled by the hydration products remains in the system (common for high $w/c-$ratios).

appears to have a lower porosity and pore diameter (about $5 - 50\,\text{nm}$). It is apparent from the current description that the characteristic patterns, and as a consequence the mechanical performance of each C-S-H phase does not change either with the degree of hydration or with the $w/c-$ratio. The only thing that changes is the volumetric proportions of the two types of C-S-H, which appear to depend on the $w/c-$ratio and probably also on the cement particle size. Recalling that a $w/c-$ratio of 0.42 is enough to cause complete hydration, we suggest:

- For $w/c < 0.42$, it is expected that both types of C-S-H coexist. In addition to unhydrated cement particles, they form the cement paste at this scale.
- For $0.42 < w/c < 0.6$, cement particles are completely consumed by hydration, the two types of C-S-H are still present, and their relative proportions vary as a function of the $w/c-$ratio.
- For $w/c > 0.6$, all C-S-H formed is LD C-S-H due to the large space available for the hydration products to precipitate. In addition, a new group of pores appears, which grows in volumetric proportions and probably in size with increasing $w/c-$ratio.

The proposed modified Powers and Brownyard [58] model is consistent with measurements of pore size distribution [167] that suggest the presence of a pore group of 100 nm size irrespective of the $w/c-$ratio: LD C-S-H gel porosity. On the other hand, measured degree of hydration and surface area developments in time [130] show that the surface area curve tends to flatten out during the last stages of hydration (Fig. 4-10), which suggests that this period is intimately related to the formation of a low surface area compound: HD C-S-H. Finally, omitting large pores (> 132 nm), a single pore-size distribution was found to characterize $w/c > 0.6$ cement-based materials (Fig. 4-11, [167]). This provides strong evidence of a uniform microstructure for all materials: LD C-S-H. In addition, it shows that the increase in total porosity in hcp resulting from increasing $w/c-$ratios manifests itself in the form of larger pores only (see Fig. 4-11). For $w/c-$ratios less than 0.6, the pore size distribution shifts to lower volumes, which is a consequence of the varying volumetric proportions of the two types of C-S-H (see Fig. 4-11).

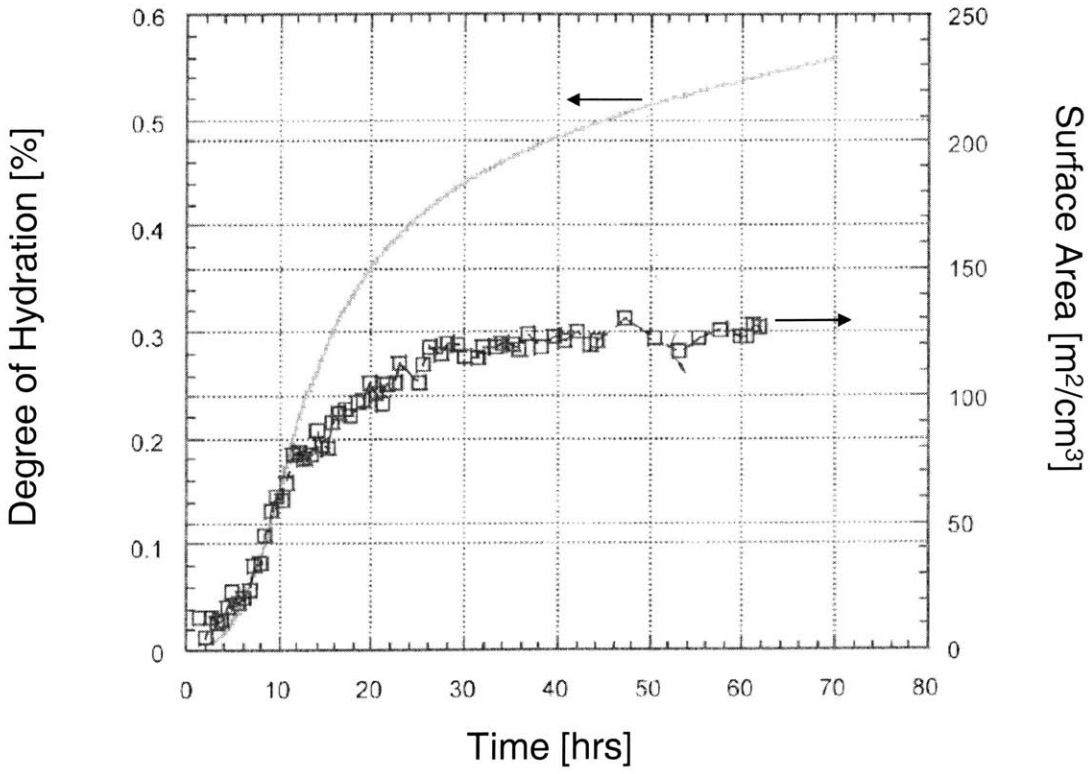

Figure 4-10: Degree of reaction and rate of reaction for a typical cement paste with $w/c-$ratio of 0.4 (after [229]). It is obvious that after 12 to 14 hours the surface area cease to increase at the same rate as the amount of reaction product suggests that the product form during that period contributes little to the overall surface area.

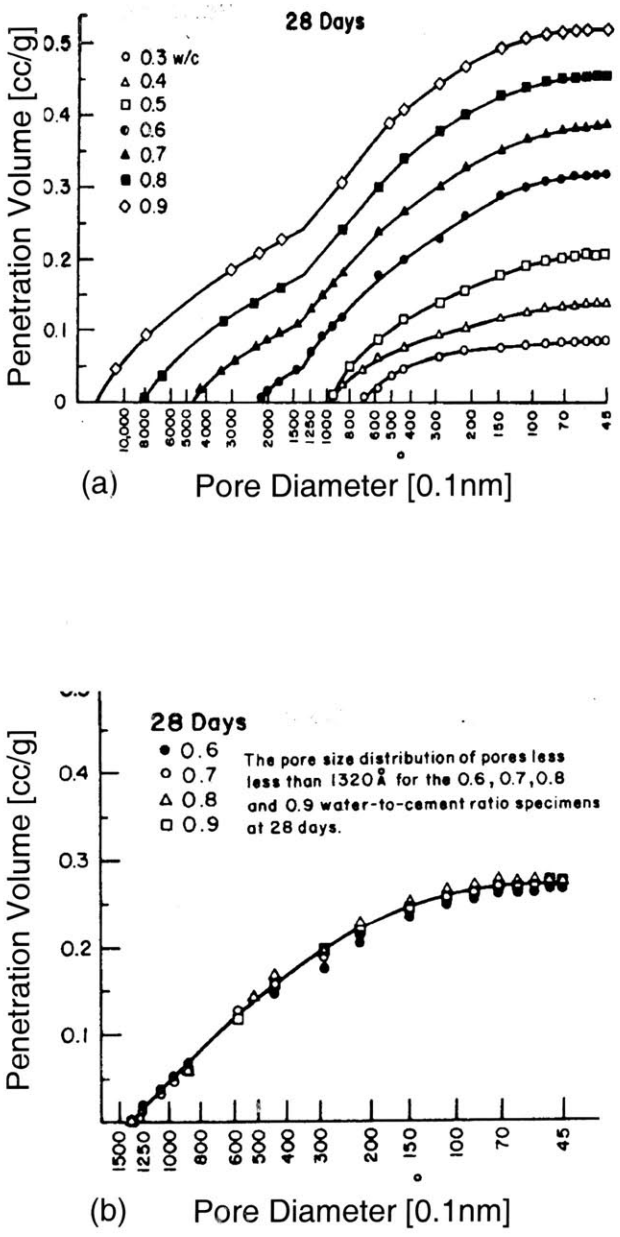

Figure 4-11: (a) Pore size distribution obtained by mercury porosimetry in hardened cement pastes of different $w/c-$ratios [167]. (b) Pore size distribution of small pores in cement pastes of varying water/cement ratios. Figure (a) replotted after ommiting the larger pores ($>$ 132 nm) [167].

4.4.3 Level II ($L = 10^{-6} - 10^{-4}$m): Cement Paste

The structure and properties of cement paste at Level II and above are generally well accepted and understood. Due to the relatively large characteristic length scale of the different inhomogeneities present at that scale, direct visual observation is possible by SEM and other microscopy imaging techniques. Consequently, there is a high degree of consistency among the different models proposed in the literature. It is generally agreed that the two types of C-S-H from Level I form a homogeneous matrix that accommodates large Portlandite crystals, as well as the residues of unhydrated cement clinker. Other phases potentially present at this scale, include entrained air incorporated by the use of admixtures (i.e., for freeze-thawing protection), capillary porosity ($> 1\mu$m) present for high $w/c-$ratio material systems, and so on. Level II can be considered as representative of the macroscopic mechanical performance of cement pastes.

4.4.4 Level III ($L = 10^{-3} - 10^{-2}$m): Mortar--Concrete

At Level III, sand particles contribute to the heterogeneous nature of mortar and concrete, which is composed of three phases: a cement paste matrix (formed by the phases of Level II), sand and aggregate inclusions, and surrounding interfacial transition zone (ITZ). Several models have been proposed in the literature, which consider mortar as a two-phase material, or three phase material ([152, 109, 90, 118], etc.). The porosity at this scale is assumed to be incorporated into the different phases below (Level 0, I and II).

4.5 Volumetric Proportions

To complete this presentation of the microstructure of cement-based materials, a quantification of the different hydration products is in order. We note in particular the models of Powers and Brownyard [194] and the model of Jennings and Tennis [227], which we will use in later developments of this thesis.

4.5.1 Powers-Brownyard Model

Based on 12 years of extensive research, Powers and Brownyard presented an empirical model for the phase distribution in hardened cement paste. This model is a benchmark in cement re-

search as it allowed the first quantitative calculations of the volumetric proportions in cement-based materials. In the following years, Powers slightly modified his model to account for self-dessication and water entrainment phenomena. In their 1948 paper, Powers and Brownyard ([194], see also presentation in Hansen [108]) provided the following empirical relations to calculate the relative volumetric proportions of chemical shrinkage (V_{cs}), capillary pores (V_{cp}), porous gel phase (V_{gel}), and unhydrated cement (V_{cl}):

$$\begin{aligned} V_{cs} &= 0.20\,(1-p)\,\xi && \text{Chemical Shrinkage} \\ V_{cp} &= p - 1.32\,(1-p)\,\xi && \text{Capillary Pores} \\ V_{gel} &= 2.12\,(1-p)\,\xi && \text{Gel Pores} \\ V_{cl} &= (1-p)\,(1-\xi) && \text{Unhydrated Cement} \end{aligned} \tag{4.12}$$

where ξ is the degree of hydration, and p is the initial porosity, that is, the space initially occupied by water:

$$p = \frac{w/c}{w/c + \rho_w/\rho_c} \tag{4.13}$$

where $\rho_c = 3,150\,\mathrm{kg/\,m^3}$, $\rho_w = 1,000\,\mathrm{kg/\,m^3}$ is the cement and water mass density, respectively. Equations (4.12) provide the volumetric proportions of all constituents per volume of cement paste, V. There is, however, a small percentage of chemical shrinkage that the material undergoes during development and Eqs. (4.12) will therefore have to be normalized with respect to the new volume, $V - V_{cs}$. It is readily understood from Eqs. (4.12) that the two variables controlling cement paste microstructure are the initial w/c–ratio and degree of hydration, ξ. Figure 4-12 shows the evolution of the volumetric proportions of the different constituents as a function of the degree of hydration, ξ, for a cement paste of $w/c = 0.5$. It is readily observed that as the hydration progresses the volume of the residual clinker phases is consumed and the amount of capillary pores is reduced (filled with hydration gel products). The degree of hydration, however, is of primary importance for the early age development of the material but it is generally accepted that after 28 days this hydration degree reaches an asymptotic value. For most practical purposes (materials > 1 month old), it is therefore the initial w/c–ratio that controls materials microstructure and eventually macroscopic mechanical performance. Finally,

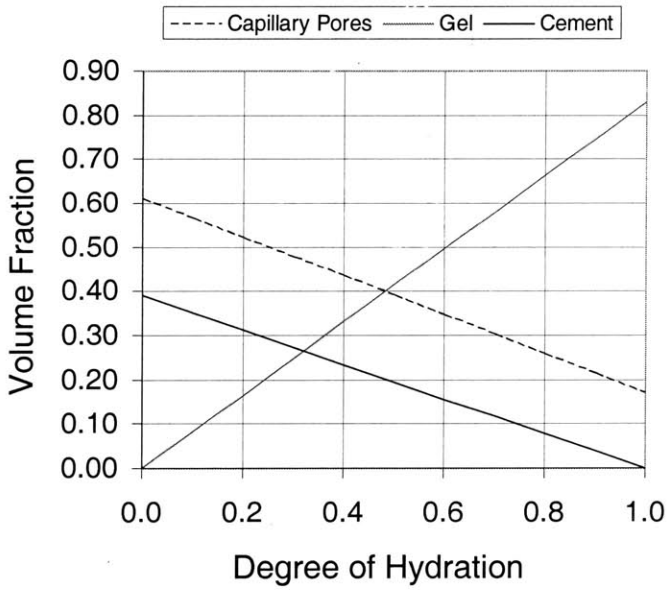

Figure 4-12: Volume fractions of cement paste constituents as a function of the degree of hydration as predicted by the Powers-Brownyard model ($w/c = 0.5$).

we note that in Powers-Brownyard model the gel phase is composed of 28% pores, (V_{gp}), and 82% solids, (V_{gs}):

$$\begin{aligned} V_{gp} &= 0.60\,(1-p)\,\xi \quad \text{Gel Pores} \\ V_{gs} &= 1.52\,(1-p)\,\xi \quad \text{Gel Solid} \end{aligned} \tag{4.14}$$

A final comment concerns the conditions under which Eqs. (4.12) were obtained: The specimens from which the data was obtained were kept in sealed conditions, i.e., water was not allowed to enter or leave the system. Under such conditions a phenomenon commonly referred to as self-dessication takes place: water from the capillary pores is consumed, and as a consequence the relative humidity inside the specimen drops and hydration is retarded. In cases in which specimens are exposed to a permanent water supply (immersed in water), self-dessication is minimal and Eqs. (4.12) should be modified accordingly.

In summary, the PB model is of great interest as it provides a simple quantification of the volume fractions of the microstructure. However, it concentrates on the gel phase and does not incorporate all the hydration products. In particular, cement composition is not specifically considered and the model fails to distinguish between the two types of C-S-H phases.

4.5.2 Jennings-Tennis Model

The Jennings and Tennis model [227] aims to fill the gap left by the Powers-Brownyard model: find volumetric proportions of all constituents. The basis of the model is that C-S-H forms as one of two types, High- or Low-density C-S-H. Based on this concept, a microstructure for C-S-H was proposed that is consistent with a series of experimental data (surface area measurements, nitrogen sorption etc.) and provide a means of quantifying, through physical chemistry, the volumetric proportions of each cement paste constituent (hydration products), including the two types of C-S-H. The model assumes simple stoichiometric reactions for the hydration of the four dominant compounds in Portland cement, C_3S, C_2S, C_3A, and C_4AF (see Eq. (4.2) and (4.5)). Given the composition of the cement and the water/cement ratio (w/c-ratio), the governing chemical and kinetic equations provide a means of computing the quantity of the various phases present in the microstructure at any given time:

$$
\begin{aligned}
&\mathrm{V}_{uc} = c\,(1-\xi_{total})\left(\tfrac{1}{\rho_c}\right) && \text{Unhydrated Cement}\\
&\mathrm{V}_{CH} = c\,(0.189\xi_1 p_1 + 0.058\xi_2 p_2) && \text{Portlandite}\\
&\mathrm{V}_{AFm} = c\,(0.849\xi_3 p_3 + 0.472\xi_4 p_4) && \text{AFm}\\
&\mathrm{V}_{cp} = (1-c) - c\sum_{i=1}^{4}(\xi_i p_i \Delta_i) && \text{Capillary Pores}\\
&\mathrm{V}_{CSH\ \text{solid}} = c\,(0.347\xi_1 p_1 + 0.461\xi_2 p_2) && \text{C-S-H solid}\\
&\mathrm{V}_{CSH\ \text{pores}} = 0.62\mathrm{V}_{CSH\ \text{solid}} && \text{Gel Pores}\\
&\mathrm{V}_{total\ \text{pores}} = \mathrm{V}_{CSH\ \text{pores}} + \mathrm{V}_{cp} && \text{Total Porosity}
\end{aligned}
\tag{4.15a}
$$

where V_x is the volume of the x (e.g., CH) in 1 g of paste; c is the initial weight of cement (in grams) in 1 g of paste, $c = \frac{1}{1+\frac{w}{c}}$; ξ_i is the degree of hydration of reactant i and p_i is the percent of i in cement, where $i = 1$ represents values for C_3S, $i = 2$ for C_2S, $i = 3$ for C_3A, $i = 4$ for C_4AF, ρ_c is the cement mass density computed from a weighted average of the densities of the compounds in the cement, and Δ_i is the volume change based upon the difference in solid volume between the products and the reactants (using the stoichiometry of Eqs. (4.2) and (4.5) and data in Tab. (4.9). The values calculated for these are $\Delta_1 = 0.437\text{cm}^3/\text{g}$, $\Delta_2 = 0.503\text{cm}^3/\text{g}$, $\Delta_3 = 0.397\text{cm}^3/\text{g}$, $\Delta_4 = 0.136\text{cm}^3/\text{g}$. The volumes of Eqs. (4.15a) have dimensions of volume per mass of paste. Using the assumption of constant total volume, a conversion of values to values with dimensions of volume per volume of paste can be made by dividing by the ratio of V/D where V is the initial volume of the paste, $V = \left(\frac{c}{\rho_c}\right) + (1-c)$, and D is the D-dried weight of the paste, $D = c + (0.24\xi c)$.

In this model, the distribution of C-S-H into each type is determined by assuming that the LD C-S-H is the only component of the microstructure that contributes appreciably to the surface area as measured by nitrogen. Each type of C-S-H contains a specific amount of total gel porosity: none of the pores in HD C-S-H are accessible to nitrogen, while only some of the pores in LD C-S-H are accessible to nitrogen. Nitrogen adsorption data on D-dried samples is used to calibrate the model and provide estimates of the formation of the two types of C-S-H. This is achieved by introducing the ratio of the mass of LD C-S-H to the total mass of C-S-H:

$$
\mathcal{M}_r = \frac{\mathrm{S}_{N_2}\mathrm{M}_D}{\mathrm{S}_{LD}\mathrm{M}_t} \tag{4.16}
$$

Compound	Formula	Density [kg/m^3]	Molecular Weight [kg/mol]	Molar Volume [$\times 10^{-5}$ m^3/mol]
Alite	C_3S	3150	0.228	7.24
Belite	C_2S	3280	0.172	5.24
Aluminate	C_3A	3030	0.270	8.92
Ferrite	C_4AF	3730	0.486	13.03
Water	H_2O	1000	0.018	1.80
Gypsum	$\bar{S}CH_2$	2320	0.172	7.41
Calcium Hydroxide	CH	2242	0.074	3.31
AFm, saturated	$C_4A\bar{S}H_{12}$	1990	0.658	34.6
AFm, D-dried	$C_4A\bar{S}H_8$	2400	0.550	22.9
C-S-H, saturated	$C_{3.4}S_2H_8$	1770	0.455	25.9
C-S-H, D-dried	$C_{3.4}S_2H_3$	2300	0.365	12.8

Table 4.9: Values used in the J-T model for the calculations of the volumetric proportions of each constituents, from Ref. [227].

where S_{N_2} is the specific surface area of the dried paste (determined from nitrogen sorption isotherms), M_D is the mass of dried paste, S_{LD} is the surface area per gram of D-dried LD C-S-H (which is not independently measurable), and M_t is the total mass of C-S-H. Using multiple linear regression, an equation for M_r is obtained [227] that is applied to other data:

$$\mathcal{M}_r = 3.017\frac{w}{c}\xi - 1.347\xi + 0.538 \tag{4.17}$$

where w/c is the water/cement ratio and ξ is the degree of hydration. Once the mass ratio is calculated, via Eq. (4.17), the volume of HD C-S-H is given by:

$$V_{HD} = \frac{M_t\,(1 - \mathcal{M}_r)}{\rho_{HD}} \tag{4.18}$$

and the volume of LD C-S-H by:

$$V_{LD} = \mathcal{M}_r\frac{M_t}{\rho_{LD}} \tag{4.19}$$

where ρ_x is the density of $x = LD, HD$, and M_t is the total mass of C-S-H. The additional volume V_P of pores in LD C-S-H is given by:

$$V_P = V_{LD} - \frac{M_r M_t}{\rho_{HD}} \tag{4.20}$$

The variables remaining to be determined are ρ_{HD}, ρ_{LD} and S_{LD}. Values obtained after optimizing the model are proposed in Ref. [227]: For saturated specimens, $\rho_{HD}^{sat} = 2130$ kg/m^3, $\rho_{LD}^{sat} = 1930$ kg/m^3, and for dry specimens $\rho_{HD}^{dry} = 1750$ kg/m^3, $\rho_{LD}^{dry} = 1440$ kg/m^3, $S_{LD} = 247$ m^2/g. Given these values and relations (4.16)-(4.20) one can quantify the relative proportions of LD to HD C-S-H present in a given cement paste system as a function of the degree of hydration, ξ, and the initial $w/c-$ratio.

4.6 Chapter Summary: Four-Level Microstructural Think Model of Cement-Based Materials

Is it possible to link the mechanical behavior of cement-based materials to composition and structure, and identify fundamental units of material invariant properties (the mechanical 'blueprint')? – This is the overarching theme of this part of the thesis devoted to cement-based materials. As a starting point, we have divided the heterogeneous microstructure of cement-based materials into different levels of material observation representing characteristic microstructural features of this multi-scale and multi-phase natural composite material (see also Refs. [58,60,235]). We owe this approach to the theory of continuum micromechanics (see e.g., [218, 253]). A phase, in the sense of continuum micromechanics, is not necessarily a chemical phase as in physical chemistry, but rather a material domain characterized by a distinct morphology and (on-average) constant mechanical properties. Such phases in heterogeneous materials are referred to as micro-homogeneous phases. We apply and adopt this approach for the multi-phase and multi-scale heterogeneities present in cement-based materials. The result of this endeavor is the four-level microstructural think model of cement-based materials displayed in Fig. 4-13, which summarizes the elements developed in Sections 4.1−4.4. Each level in this representation is separated from the next one by at least one order of length scale, reflecting the separation of length scale assumption required to define a representative elementary volume (R.E.V.). Hence, moving from one level to the another is expected to change the observable material behavior.

The lowest level we consider is Level 0 representing a single particle of C-S-H of a characteristic length-scale on the order of 10^{-8} m, which we associate with a micro-homogeneous

C-S-H solid phase, – the globule in terms of Jennings colloidal model [130]. At a level still below constituting the atomic scale (see Section 4.2.1), this solid phase is composed of highly packed minerals with imperfections and irregularities and interlayer space amounting to a nanoporosity of $\varphi = 18\%$. There is still a lack of knowledge about the organizational pattern of the minerals, and in particular how the stoichiometry of C-S-H, imperfections thereto and the physical state of water in the interlayer space translate into a characteristic sheet packing density of $1 - \varphi = 0.82$. At this stage of knowledge available, it can only be speculated that the relatively high density value at Level 0, which is well above the highest possible density of ordered spheres ($\pi/\sqrt{18} = 0.74$, [209]), and recently found random packing limits of ellipsoids of the same order [71], hints towards an important role of the structural water in the organization of the single C-S-H particle. Some very recent studies using molecular dynamics simulations [101] and AFM investigations [150, 133] provide first indications about the very nature of the solid phase at this scale and will be further discussed in Chapter 8. Research into the mechanical behavior of the material at nanometer scale is still in its infancy, and requires no-doubt detailed knowledge of the stoichiometric nature of C-S-H and the state of the water filling the interlayer space. Advances in experimentation coupled with model-based simulations based on molecular dynamics and quantum mechanics are expected, in the close future, to shed light on the physics at stake at this scale. Given the current state of knowledge, we restrict ourselves to the single C-S-H globule, considering that the minerals and structural water form a micro-homogeneous phase in the sense of continuum micromechanics.

Level I is the scale of agglomeration of C-S-H globules in two distinct packing morphologies, LD C-S-H and HD C-S-H. We will discuss in Chapter 5 why and how the mechanical properties of the material at this scale can be assessed by nanoindentation. From Jennings model, we retain the striking similarity of the packing densities of LD C-S-H and HD C-S-H with maximum packing densities of mono-sized spherical systems (see Section 4.4.2). The packing modes may not necessarily be of a spherical nature, but it appears as the simplest think model that can capture an amorphous structure of the two types of C-S-H at the considered scale while being consistent with porosity and surface measurements and pore size distributions. The two packing densities should, however, not be seen as deterministic packing morphologies, in the sense that C-S-H globules agglomerate only in one or the other form; but rather that C-S-H globules

organize in a large variety of packing densities varying from random to ordered. Hence, the two packing morphologies have a statistical meaning and are representative, in the sense of micro-homogeneous phases, of a characteristic distribution of C-S-H phases in a low-density and a high-density form. While the chemo-physical origin of these packing densities is still not known, it can be (and has been) speculated that they are of chemical origin, or more precisely of kinetic origin reflecting the precipitation of the hydration products in an unconfined *vs.* a confined space. If this holds true, the relative occurrence of one or the other packing should be affected by hydration conditions, particularly the $w/c-$ ratio and environmental conditions.

The two types of C-S-H, CH crystals, capillary porosity and residual clinker phases in low $w/c-$ materials form the cement paste at Level II, which is recognized as a highly heterogeneous material system, and which varies in functions of the properties and proportions of its components, and in particular of the C-S-H. This composite forms the binding matrix for all cementitious systems, mortar and concrete which manifest themselves on Level III.

It is on the basis of this four-level think model of the microstructure of cement-based materials that we can now turn to the experimental investigation of the mechanical behavior of the materials at multiple scales, aiming at identifying fundamental units of material invariant stiffness and strength properties.

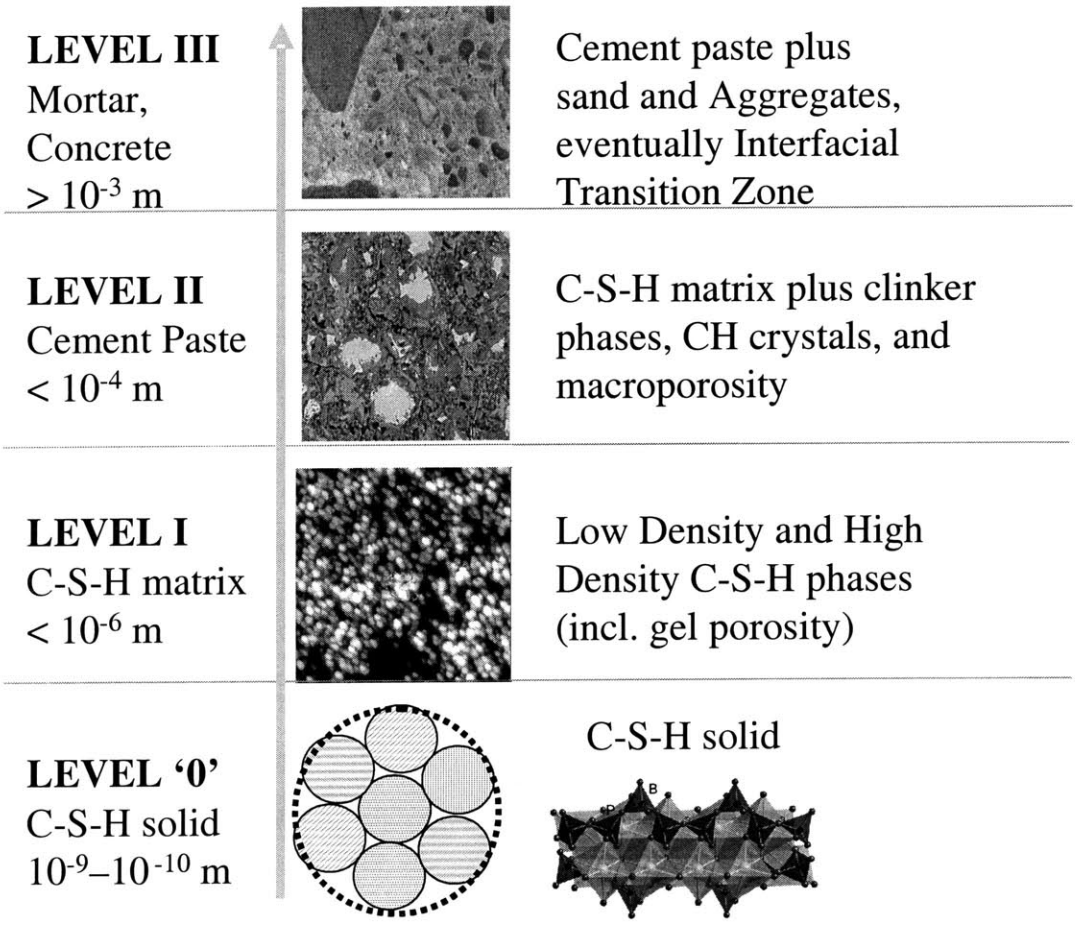

Figure 4-13: Four-level microstructural schematic of cement-based materials: Level 0 = Single particle, Level I = Agglomeration, Level II = Cement Paste, Level III = Mortar/Concrete. Image Credits: Level 0 = from Ref. [130], Level I = from Ref. [183], Level II = courtesy of K.Scrivener, Level III = from NIST website [http://www.bfrl.nist.gov/].

Chapter 5

Indentation on Multi-phase Composites: Grid Indentation Technique

Is it possible to apply continuum indentation analysis to heterogeneous materials and, if so, how? The indentation analysis presented in Chapter 2 is restricted to homogeneous material systems. In contrast, as we have seen in Chapter 4, cement-based materials like most other natural solids are multi-phase and multi-scale composites with heterogeneities that manifest themselves from the scale of the C-S-H phases to the macroscopic scale of the mortar-concrete composite. This particular feature of natural composites makes the application of continuum indentation analysis questionable. In this chapter we propose an original way of extending the indentation analysis techniques to multi-scale composites. In particular we present a grid indentation technique that under certain restrictions can provide both quantitative and qualitative information about microstructure and properties of the indented composite material. The large amount of data is treated in a statistical sense: (1) a statistical analysis of the results gives access to the mechanical properties and volumetric proportions of all involved phases, whereas (2) a spatial representation of the mechanical properties measurements provides information about the morphological arrangement of different phases. This is illustrated here for Berkovich indentation in a model multiphase material: hardened cement paste.

5.1 Choosing a Length Scale: Thin-Film Analogy

Instrumented indentation is becoming a standardized test for the evaluation of mechanical properties of materials (see Chapter 2), yet its potential for and application to composite material systems has been largely neglected. A search in the literature on indentation on composite materials yielded only two very recent publications [77, 139], signifying the absence of knowledge in this field. This is not surprising, given the complexity of the mechanical response of a material system when microstructure interferes with indentation testing (see Fig. 5-1), which makes it difficult to translate – by means of the tools of continuum indentation analysis – indentation data into meaningful mechanical properties. In what follows, we propose a way that reduces by design this complexity by a careful choice of indentation length scales which allows one to apply the tools of continuum indentation analysis.

5.1.1 Indentation Length Scales

Continuum indentation analysis is generally based on the assumption of homogeneity of material properties and that the stress-strain relation remains the same for any depth of indentation [30]. Like all continuum analyses, continuum indentation analysis is based on the concept of a representative elementary volume (R.E.V.) of characteristic size $\mathcal{L}$ that needs to obey to the scale separability condition:

$$d \ll \mathcal{L} \ll (h, a, D) \tag{5.1}$$

where (h, a) is the indentation depth and the indentation radius that define the order of magnitude of the variation of the position vector $\underline{x}$; D is a characteristic length scale of the microstructure and d is the characteristic size of the (largest) heterogeneity contained in the R.E.V. Provided that Eq. (5.1) is satisfied, an indentation test operated to an indentation depth h gives access to the material properties that are characteristic of a material system at a length scale of $\mathcal{L}$ (see Fig. 5-1). On the other hand, since most indentation solutions are based on the similarity approach, and derived from the infinite half-space model (which by definition has no length scale), and from the assumption of uniform material properties (see Section 2.2), the properties extracted – by means of an inverse analysis – from indentation tests are averaged quantities characteristic of a material length scale defined by the indentation depth or the in-

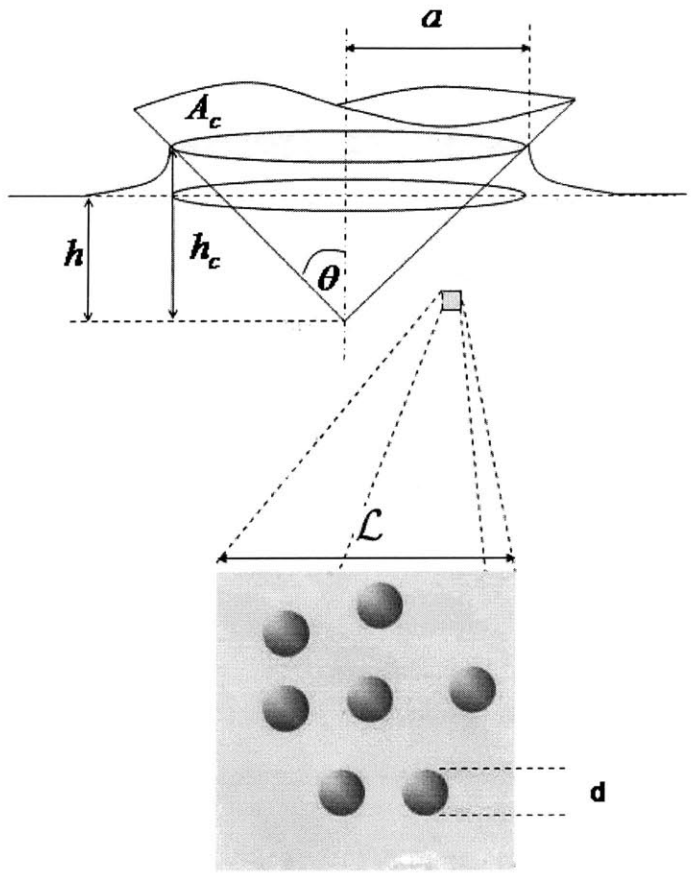

Figure 5-1: Geometrical and material length scales involved in indentation on composites.

dentation radius. A good estimate is that the characteristic size of the material domain sensed by an indentation is on the order of $\max(h, a)$; roughly $3h$ for Berkovich indentation and h for the corner cube. Given the self-similarity of the indentation test, choosing the indentation depth, therefore, comes to choose the length scale of material investigation. One question that arises is what happens when the length scale of the microstructure D is on the order of the indentation depth h, i.e., when microstructure interferes with indentation testing, for which the classical tools of continuum indentation analysis fail to apply.

5.1.2 Phase Properties: $h \ll D$

What we aim to derive is a critical indentation depth below which the effect of microstructure does not interfere significantly with the indentation results, so that an indentation test performed to such a depth gives access to the intrinsic properties of the material composing the microstructure rather than to the microstructure itself. The simplest geometrical representation of a heterogeneous particulate system is a layered system, which turns out to be also the most severe one among other possible configurations [77]. Such layered systems have been investigated in some detail in the context of indentation on thin films, one of the most popular current applications of nanoindentation. In the case of this thin-film analogy, we equate film thickness, t, with the characteristic length scale of the microstructure D in (5.1), and explore thin film indentation models to identify a critical indentation depth below which one actually measures the properties of the homogeneous phase, i.e., the film stiffness E_f and the film hardness H_f.

The majority of models for thin film indentation rely on phenomenological arguments or finite element simulations and tend to relate the composite modulus, E_{eff}, to the elastic moduli of the film, E_f, and the substrate materials, E_s:

$$E_{eff} = E_f + (E_f - E_s)\mathcal{I}_M \tag{5.2}$$

where $\mathcal{I}_M$ is a weight function that depends on the indentation depth-to-film thickness ratio, h/t. In fact, as $\mathcal{I}_M \to 0$ the effect of the substrate is eliminated and $E_{eff} \to E_f$. Several models have been proposed in the literature to estimate $\mathcal{I}_M$ and quantify the effect of the substrate on the composite response. By using the Hankel's transform method, Li and Chou [155] calculated the Green's function for a coated substrate and evaluated the displacement, stress field and load-indentation depth relation of the thin-film/substrate system under an axisymmetrically distributed loading on the plane surface of the film. King [137] studied the effect of the substrate on the global response using finite element simulations, whereas Gao et al. [94] devised a first order rigorous moduli-perturbation method to derive a closed-form solution for the contact compliance of an uncracked film/substrate medium:

$$\mathcal{I}_M^G = \frac{2}{\pi}\tan^{-1}\left(\frac{t}{a}\right) + \left[(1-2\nu)\left(\frac{t}{a}\right)\ln\left(\frac{1+\left(\frac{t}{a}\right)^2}{\left(\frac{t}{a}\right)^2}\right) - \frac{\frac{t}{a}}{1+\left(\frac{t}{a}\right)^2}\right][2\pi(1-\nu)]^{-1} \tag{5.3}$$

In this approach which is based on a perturbation calculation of the elastic energy of a coated substrate indented with a flat punch of radius a, the assumption is made that the mechanical properties of both materials do not differ widely. The model was validated by Chen and Vlassak [43] by means of finite element analysis, showing that the model is correct for moduli mismatch ratio in the range $0.5 - 2$. On the other hand, the weight function suggested by Gao et al. [94] was found to overestimate the substrate effect when the film is stiffer than the substrate and that the substrate influence is underestimated if the film is more compliant. Yu et al. [252] have considered the elastic solution of an axi-symmetric mixed boundary value problem. An elastic layer is assumed to be either in frictionless contact or perfectly bonded to a semi-infinite elastic half-space. In this work spherical, conical and flat-ended cylindrical indenters were considered. The results are obtained by solving a Fredholm integral equation of the second kind with a continuous symmetrical kernel which depends on the bonding conditions. With the aid of finite element calculations, Chen and Vlassak [43] compared the theoretical results of Yu et al. [252] with numerical results and showed very good agreement. Perriot and Barthel [190] proposed a method relying on the work by Li and Chou [155], in which they calculated the Green's function for a coated substrate. Since Li and Chou's stress/strain relation could not be inverted, it is of little use for contact problems. Using the auxiliary fields introduced by Sneddon, however, Perriot and Barthel have reformulated Li and Chou's expression to allow the problem to be inverted at low numerical cost. They have found that, whatever the indenter shape, all curves almost have the same shape, regardless of the moduli mismatch between the layer and the substrate. This shape is very much like that provided by Gao et al. [94], and is in very good agreement for the moduli mismatch ratio in the range $0.5 - 2$. Perriot and Barthel have empirically extended Gao's function of Eq. (5.3) to a wider range of moduli mismatch ratio ($E_f/E_s = 0.01 - 100$):

$$\mathcal{I}_M^{PB} = \left[1 + \left(\frac{t}{a}k\right)^n\right]^{-1} \tag{5.4a}$$

where a is the contact radius, n is an empirical constant ($n = 1.27$) and k is defined by:

$$\log(k) = -0.093 + 0.792\log\left(\frac{E_s}{E_f}\right) + 0.05\left(\log\left(\frac{E_s}{E_f}\right)\right)^2 \tag{5.5}$$

Equations (5.2) to (5.5) show a fair degree of consistency and suggest that substrate effects are

negligible for stiffness mismatch ratio $E_f/E_s \in [0.01, 10]$ as long as the indentation depth h is smaller or equal to 10% of the film thickness t. This is also illustrated in Fig. 5-2 in which the critical h/t-ratio for which the error in the modulus estimation does not exceed 10% is plotted against the moduli mismatch ratio E_f/E_s.

Similar concepts have been extended to hardness. Buckle [38] proposed that the hardness of a composite system, H_{eff}, could be expressed as:

$$H_{eff} = H_s + (H_f - H_s)\,\mathcal{I}_H \tag{5.6}$$

where $\mathcal{I}_H$ is an empirical parameter. Estimates for this parameter have been provided by several researchers: Bhattacharaya and Nix [25] proposed estimates on the basis of finite element simulations which discriminate between hard-on-soft, and soft-on-hard systems:

$$\text{Soft-on-Hard:} \qquad \mathcal{I}_H = \exp\left(-\frac{Y_f}{Y_s}\frac{E_f}{E_s}\left(\frac{h}{t}\right)^2\right) \tag{5.7a}$$

$$\text{Hard-on-Soft:} \qquad \mathcal{I}_H = \exp\left(-\frac{H_f}{H_s}\frac{Y_f}{Y_s}\sqrt{\frac{E_f}{E_s}}\frac{h}{t}\right) \tag{5.7b}$$

where Y_f and Y_s stand for the uniaxial strength of the material. It is readily understood that substrate effects become negligible as $\mathcal{I}_H \to 1$ (or $\frac{h}{t} \to 0$). To obtain an order of magnitude of this effect, we calculated the critical $h/t-$ratio for which the H_{eff} is within 10% of the film hardness, H_f. In calculating $(h/t)_{10\%}$ we assumed that there is no moduli mismatch between the two phases, $E_f = E_s$, and that the hardness ratio equals the ratio of the yield strengths[1]. Figure 5-2 shows the critical values of h/t calculated from relations 5.6 and 5.7a as a function of H_f/H_s. Several things become apparent:

- As the contrast between the substrate-film properties becomes significant, the restrictions on the indentation depth required to get good estimates of the film properties become more stringent. This is especially true for hard-on-soft systems for which the h/t relation seems to evolve much faster with the hardness ratio H_f/H_s. A similar trend is found for the stiffness.

[1] For cohesive materials where the hardness is directly proportional to the yield strength this assumption holds in fact true. For cohesive-frictional materials however some deviation may exist.

	Aspect Ratio	$a_c/r_p, h/t_p$	
Case	(height/diameter)	Hard/Soft	Soft/Hard
Particle	1.0	0.8	0.7
Needle	5.0	1.3	0.65
Thin Film	0.05	0.25	1.1

Table 5.1: Normalized contact radius or depth up to which an effect in hardness of less than 10% is measured for different particle geometries. Finite element results from [77].

- In calculating the results in Fig. 5-2, we assumed that the elastic modulus of the two phases is the same. A look on Eq. (5.7a) suggests that any mismatch in the elastic moduli will tend to alleviate the restriction on the allowable indentation depth.

The above models have been developed for a very specific geometric arrangement, the thin film, but they are generally considered to be a very good first order approximation for more general substrate systems. The only available information for particulate systems in the literature is a finite element study by Durst et al. [77] who performed numerical investigations for overlaying-substrate systems having a yield strength ratio of $0.5 - 2$. The different geometries considered in their analysis are shown in Fig. 5-3 and the finite element simulations results are displayed in Fig. 5-4. Table 5.1 summarizes the ratios of the length scales for which continuum indentation analysis can be applied without any significant deviation. It appears that the thin film geometry yields the most strict restrictions on the depth of indentation and, therefore, use of the thin-film analogy to define a critical indentation depth with respect to the size of the heterogeneity seems to be a conservative choice.

In summary, in order to apply continuum indentation analysis to heterogeneous systems, the indentation depth should be at most 1/10 of the characteristic size of the microstructure D in order to access phase properties. This rule of thumb, also known as 1/10−rule of Buckle [38], is a rough first estimate and in cases where the contrast between the mechanical properties of the two phases becomes significant ($\left(\frac{E}{E_s}, \frac{H}{H_s}\right) \notin [0.01, 10]$), the method tends to be either too strict (like soft films on hard substrates) or too relaxed (hard films on soft substrates). In all cases, at higher indentation depths, the indentation response interferes with microstructure, and special care should be taken in the interpretation of the indentation results.

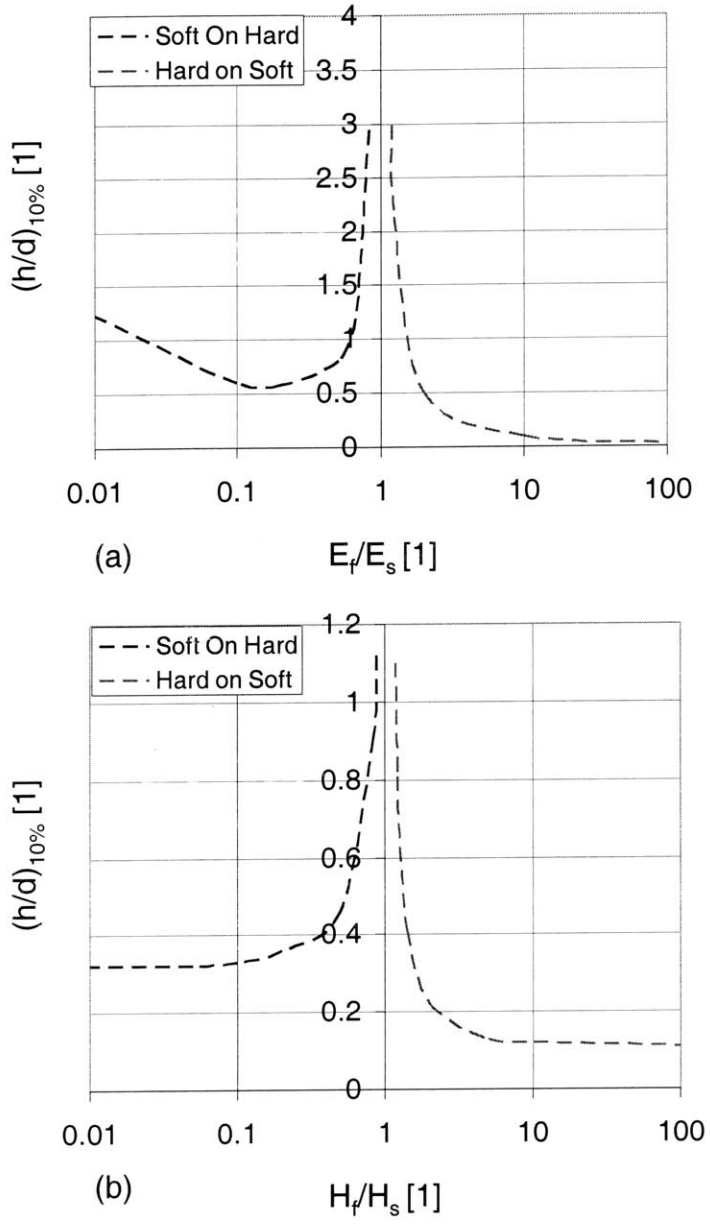

Figure 5-2: (a) Critical $h/D-$ratio vs. E_f/E_s as predicted by Perriot and Barthel [190] for which the composite modulus, E_{eff}, is within 10% of the film modulus, E_f. (b) Critical $h/D-$ratio vs. H_f/H_s as predicted by Bhattacharaya and Nix [25] for which the composite hardness, H_{eff}, is within 10% of the film hardness, H_f.

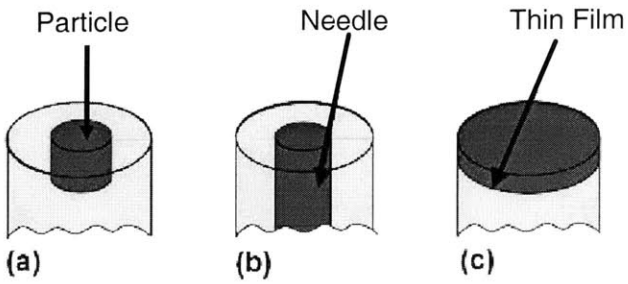

Figure 5-3: Geometries considered in the simulations of Durst *et al.*, adapted from Ref. [77].

5.1.3 Composite Properties: $h \gg D$

To complete the thin film analogy, it is useful to provide an estimate for the indentation depth that gives access to composite properties. The finite element simulations of Durst et al. [77] (see Fig. 5-4) suggest that the response reaches an asymptotic values for $a/t > 2$. Equating t with D, it is possible to estimate that an indentation depth operated to $h > 2D\cot\theta$ (with θ the equivalent semi-apex angle; see Tab. 2.1) should give access to composite material properties. Hence, it is in between the two limit cases, $0.01 < h/D < 2\cot\theta$ that microstructure is expected to strongly affect the indentation response on heterogeneous materials.

5.2 Grid Indentation Technique

5.2.1 Gedanken Experiment

Consider a material to be composed of two phases of different mechanical properties and characterized by a length scale D. If the indentation depth is much smaller than the characteristic size of the phases, $h \ll D$ (Section 5.1.2) then a single indentation test gives access to the material properties of either phase 1 or phase 2. If, in addition, a large number of tests ($N \gg 1$) is carried out on a grid (Fig. 5-5) defined by a grid spacing ℓ that is larger than the characteristic size of the indentation impression, so to avoid interference in between individual indentation tests, and much larger than the characteristic size of the two phases $\left(\ell\sqrt{N} \gg D\right)$, so that the

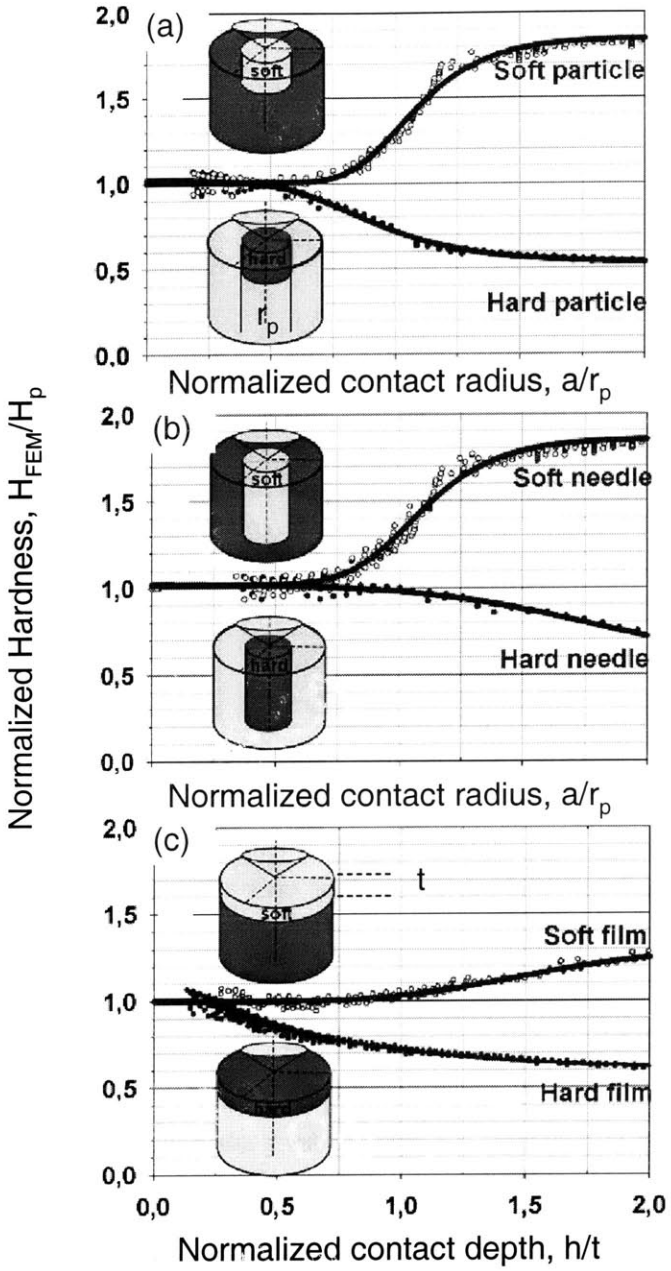

Figure 5-4: Finite element simulation results of Durst *et al.* [77] for the indentation behaviour of soft and hard particles for three different geometrical arrangements. a) Cylindrical Particle: Normallized hardness H_{FEM}/H_p for soft and hard particles (ratio of yield strength is 2 (0.5)) as a function of normalized contact radius. b) Needle Shape: Normallized hardness H_{FEM}/H_p for soft and hard particles (aspect ratio 1.0) as a function of normalized contact radius. c) Thin film: Normallized hardness H_{FEM}/H_p for soft and hard particles (aspect ratio 0.05) as a function of normalized contact radius.

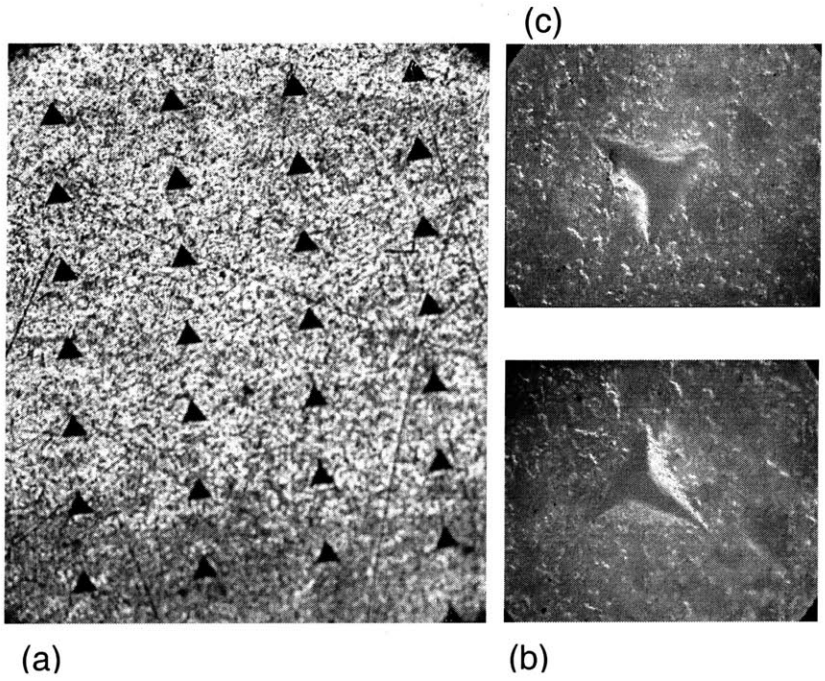

Figure 5-5: Optical microscope images of a 10×10 indentation grid: (a) example of microindentation grid ; (b) and (c) residual impressions on a cement paste (magnification x100).

locus of indentation has no statistical bias with respect to the spatial distribution of the two phases, the probability of encountering one or the other phase is equal to the surface fraction occupied by the two phases near the indentation surface. Provided that a similar distribution is found equally on other surfaces, the local or near-surface volume fraction can be assimilated with the volume fraction of the two phases present in the (isotropic) material. Consider next an indentation test performed to a maximum indentation depth that is much larger than the characteristic size of the individual phases, $h \gg D$ (Section 5.1.3). It is readily understood, by letting $D = d$ in the scale separability condition of Eq. (5.1), that the properties extracted from such an indentation test are representative in a statistical sense of the average properties of the composite material.

The simple gedanken experiment has all the ingredients of statistical indentation analysis that need to be performed when it comes to natural composite materials. The key results of

such analysis are distributions and their derivatives (i.e., histograms or frequency diagrams) of mechanical properties determined by a large number of indentation tests at a specific scale of material observation defined by the indentation depth. Generally speaking, small indentation depths ($h < 0.1\,D$) give access to mechanical phase properties, and potentially to volume fractions:

$$f_J = \frac{N_J}{N};\ \sum_{J=1}^{n} N_J = N \tag{5.8}$$

where N_J is the number of indentations on material phase J, that can be identified by the difference in material properties; that is f_J is the volume fraction of a 'mechanically' identifiable material phase. In turn, greater indentation depths ($h > 2D\cot\theta$) give access to homogenized material properties of the composite. The principle is displayed in Fig. 5-6. Finally, a mapping of mechanical properties allows one to identify characteristic morphologies within the resolution defined by the grid size.

5.2.2 Deconvolution Technique

The simple gedanken experiment is based on the premise that the two phases have two properties of sufficient contrast which makes it possible to easily separate one phase from the other in small scale indentation tests. Natural composite materials are generally more complex, requiring the use of some elementary statistical relations to analyze the indentation data. Let us assume that the distribution of the mechanical property $x = H, M$ of each phase J is best approximated by the normal or Gaussian distribution:

$$p_J(x) = \frac{1}{\sqrt{2\pi s_J^2}} \exp\left(-\frac{(x-\mu_J)^2}{2s_J^2}\right) \tag{5.9}$$

where the mean μ_J is the arithmetic mean of all N_J values of each phase, while the standard deviation, s_J, or the root mean square deviation, is a measure of the dispersion of these values:

$$\mu_J = \frac{1}{N_J}\sum_{k=1}^{N_J} x_k;\ s_J^2 = \frac{1}{N_J - 1}\sum_{k=1}^{N_J}(x_k - \mu_J)^2 \tag{5.10}$$

The case of a single phase, $n = 1$, corresponds to the case of a homogenous material, for which mean value and standard deviation describe the properties of the material in a statistical sense.

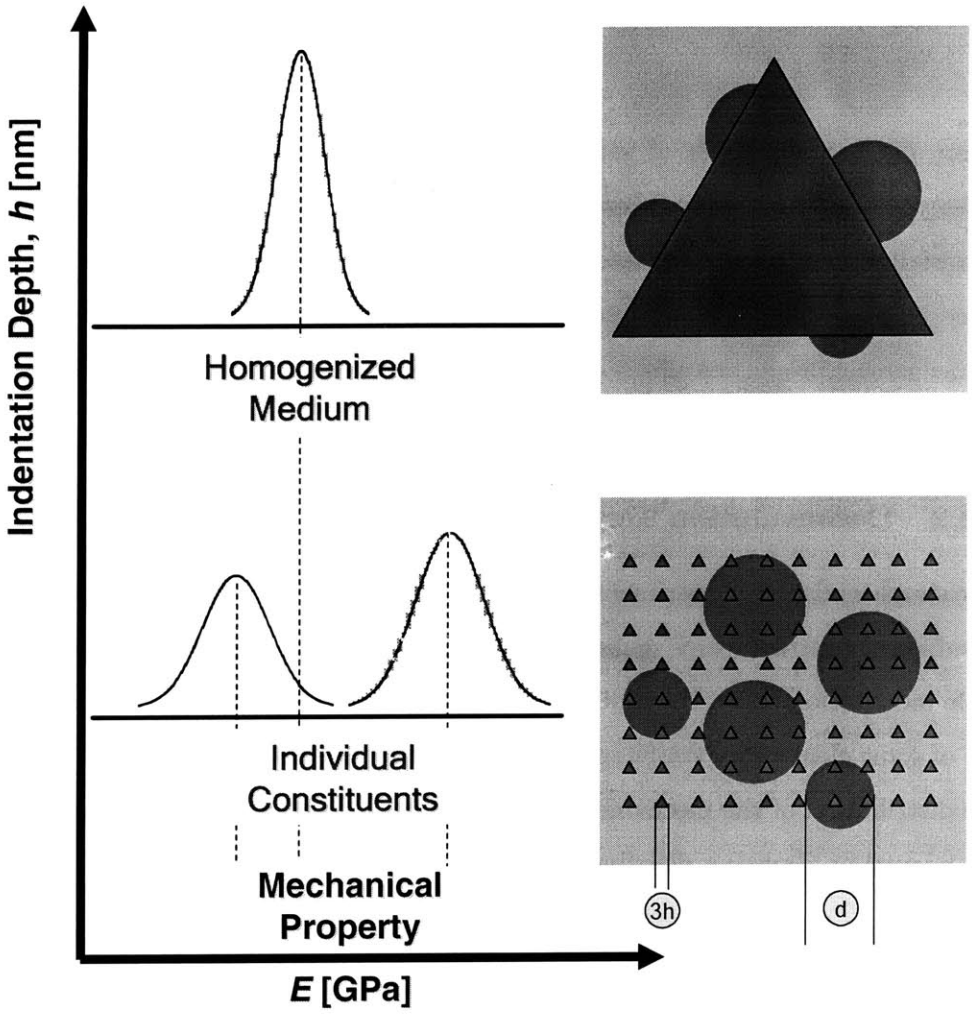

Figure 5-6: Schematic of the principle of the proposed grid-indentation technique for heterogeneous materials. Bottom: At low indentation depths ($h << d$) the individual constituents can be identified giving rise to multimode ditributions. Top: At high indentation depths ($h >> d$) the properties of a homogenized medium is obtained.

In the case of several phases ($J = 1, n$), that all follow a normal distribution, and which do not (mechanically) interact with each other, the overall frequency distribution of the mechanical property $x = H, M$ obeys to the following theoretical probability density function:

$$P(x) = \sum_{J=1}^{n} f_J \, p_J(x) \tag{5.11}$$

where f_J is the volume fraction of phase J subjected to the constraint:

$$\sum_{J=1}^{n} f_J = 1 \tag{5.12}$$

Hence, there is a total of $3n - 1$ unknowns in the problem (5.11); (f_J, μ_J, s_J) for each phase reduced by the compatibility condition state in Eq. (5.12). If empirical frequency densities are obtained by nanoindentation in form of discrete values P^i, one can determine the unknowns by minimizing the standard error:

$$\min \sum_{i=1}^{m} \frac{\left(P^i - P(x_i)\right)^2}{m} \tag{5.13}$$

where P^i is the observed value of the experimental frequency density, $P(x_i) = \sum_{J=1}^{n} f_J \, p_J(x_i)$ is the value of the theoretical probability density function (5.11) at point x_i, and m is the number of intervals (bins) chosen to construct the histogram (see Tab. 5.2). The number of observed values P^i should exceed the number of unknowns, and will obviously be smaller than the total number of tests; hence:

$$3n - 1 \leq m < N \tag{5.14}$$

5.2.3 Discussion

In the application of the deconvolution technique to natural composites, the number of phases n is generally known in advance. Indeed, in small scale indentation ($h \ll D$), n is determined by the number of distinct chemical phases (identified e.g. by XRD analyses) and/or morphological units (identified, e.g., by microscopy) that compose the microstructure. In turn, large scale indentation ($h \gg D$) for which $n = 1$ represents the composite phase.

It is useful to have a closer look on the two key assumptions of the proposed deconvolution

Histogram and Frequency Distribution
The histogram is a graphic interpretation of the variability of experimental information. For a specific set of experimental data the histogram is constructed as follows: From the observed experimental data we choose a range on the abscissa (for a 2-d graph) sufficient to include the largest and smallest observed values (range of data), and divide this range into convenient number (m) of intervals (bins). Then count the number of observations within each interval and draw vertical bars with heights representing the number of observations in the respective intervals. Alternatively the heights of the bars may be expressed in terms of the fraction of the total number of observations in each interval. The experimental discrete frequency distribution $\left(P^i\right)$ is then obtained by dividing the ordinates of the histogram by its total area. A question arises about chosen number of intervals and the corresponding bin size. Truth is that the choice of interval number will change the shape of the frequency plot. Generally speaking the number of intervals should be larger than the number of unknowns, $3n-1$, restricted of course by the total number of tests (N); hence $3n-1<m<N$. A small number of intervals will lead to a significant loss of information, whereas a large number to intervals (compared to the number of tests) will lead to artifacts with misleading information.

Table 5.2: Histogram and discrete frequency distribution.

technique:

1. *The mechanical phase properties of each phase are normal distributed.* For $n=1$ (homogeneous system), this assumption can be checked easily using the Chi-square test (see e.g. [7]). Considering a sample of N measurements for a given random variable, the χ^2-test compares the observed frequencies $P^1, P^2, P^3, ..., P^m$ in m intervals with the corresponding frequencies $P\left(x_1\right), P\left(x_2\right), P\left(x_3\right), ...P\left(x_m\right)$ from an assumed theoretical distribution:

$$\sum_{i=1}^{m} \frac{\left(P^i - P\left(x_i\right)\right)^2}{P\left(x_i\right)} \tag{5.15}$$

which approaches the χ^2-distribution with $f=m-1$ degrees of freedom as $N \rightarrow \infty$. On this basis if an assumed distribution yields for a given set of data:

$$\sum_{i=1}^{m} \frac{\left(P^i - P\left(x_i\right)\right)^2}{P\left(x_i\right)} < c_{1-a,f} \tag{5.16}$$

where $c_{1-a,f}$ is the value of the appropriate χ_f^2-distribution at the cumulative probability

$1-a$, the assumed probability distribution is an acceptable model at the significance level a. By way of illustration, Fig. 5-7 displays the χ^2-test for a Gaussian distribution of the Berkovich indentation results of bulk metallic glass (see Chapter 3) at a significance level of 5%, using a commercial statistical software, Crystal Ball^{TM}. Strictly speaking, other distributions (like the log-normal) showed a better fit to our data but the choice of the normal distribution was driven by mathematical tractability and convenience. The normal distribution will therefore serve in the rest of this thesis as the preferred probability density function describing the random variability of our experimental data. For a multiphase system, $n > 1$, the assumption of Gaussian distribution is simply the most convenient distribution for deconvolution purposes of the indentation data. In this case, a χ^2-test, because of the minimization (5.13), provides a means to quantify the quality of the fit of the unknowns of the problem, $(f_J, \mu_J, s_J)\,; J = 1, n$; but it would probably fail to validate the assumed normal distribution of phase properties. For all practical purposes, it is convenient to fit the observed frequencies P^i $(i = 1, m)$ successively from "left to right", starting with the phase with the smallest mean, and introducing successively the phases with higher means to minimize the standard error (5.13). While we are not aware of a mathematical proof for the uniqueness of this left-to-right fitting, the procedure turns out to work very well, converging to a specific set of fitted values, $(f_J, \mu_J, s_J)\,; J = 1, n$, which we consider as phase properties.

2. *The interaction between different phases that are sensed in indentation testing is negligible.* We have seen in Section 5.1.2, from the thin-film analogy, that the effect of mechanical interactions between different phases can be reduced by a careful choice of the indentation depth, $h/D \leq 1/10$. Of course, in highly heterogeneous materials, it is difficult to completely avoid mechanical interaction between different phases in indentation on multiphase systems. For instance, the indentation response in a matrix phase adjacent to an inclusion will be affected by boundary effects, and even more so indentation on a stiff inclusion on a softer matrix (the 'hard-on-soft' scenario in Figs. 5-2 and 5-4) will always be more compliant then the inclusion. On the other hand, provided that a large number of tests is carried out, which respect on-average the $1/10-$rule-of-thumb, the probability of identifying in-situ phase properties is very high. A similar remark can be made regarding

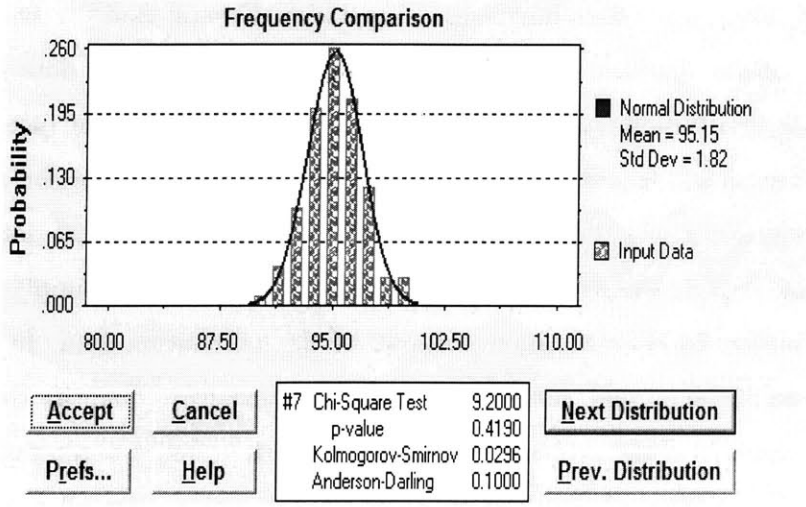

(a)

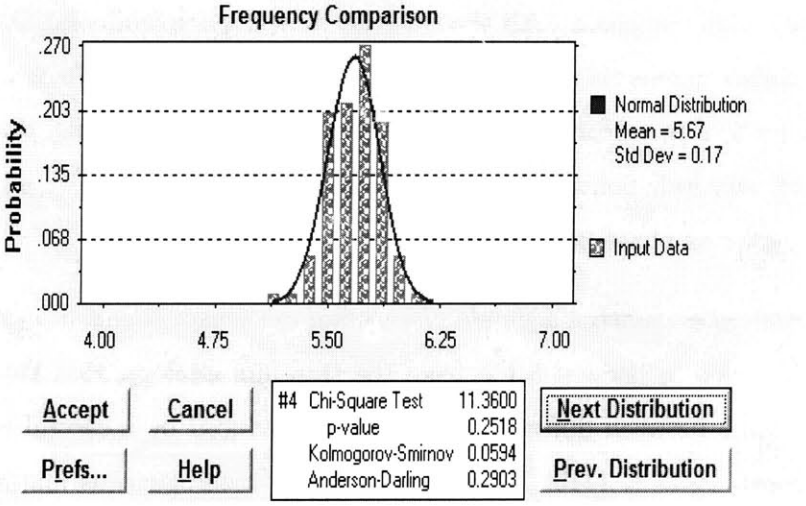

(b)

Figure 5-7: Frequency diagrams and the corresponding normal distributions for the indentation modulus (a) and hardnes (b) measurements of Berkovich indentations on BMG. The goodness-of-fit tests of chi-square test (χ^2) and Kolmogorov-Smirnov (K-S) was performed using a statistical software, Crystal Ball.

large-scale indentation tests $h/D \gg 1$, in which the effects of microstructure cannot be avoided over the entire $P-h$ indentation response. Indeed, since h increases continuously from 0 to $h_{\max}$, one cannot exclude indentation depths that violate the $h/D \gg 1$ scale separability condition. On the other hand, provided that $h_{\max}/D \gg 1$ (or more precisely $h_{\max}/D > 2\cot\theta$), it is reasonable to assume that the final properties $P_{\max}$ and $h_{\max}$ do not depend much on the nature of the first indented heterogeneities, the bluntness of the indenter, surface roughness, etc. The derived indentation data at maximum indentation depth $h_{\max}$, namely $P_{\max}$ and $S_{\max}$, can therefore be used with confidence in continuum indentation analysis of the composite behavior.

A validation of the proposed grid indentation technique on a model material (Ti-TiB) is outlined in Appendix D.

5.3 Application of Grid Indentation to Natural Composites: Cement Paste

The grid indentation technique presented in Section 5.2 is very general and can be applied to any composite material whether man-made, geological or biological, satisfying the two key assumptions: (1) normal distribution of individual phases and (2) negligible mechanical interaction between different phases in indentation testing. The purpose of this section is to demonstrate the use, strength and limitations of this approach through an application to a challenging multiphase and multiscale composite: hardened cement paste. The highly heterogeneous structure of cement paste, which is the main binding matrix of all cementitious composites, was discussed in Chapter 4. It is the premise of the proposed grid indentation technique to complete the characterization by means of a mechanical investigation of properties at multiple scales. In particular, we focus the investigation of the properties at two different scales of the four-level microstructure of cement-based materials (Fig. 4-13): the C-S-H matrix (Level I, see Section 4.4.2) and the cement paste composite (Level II).

Mineral	wt%	Mineral	wt%
C_3S	72	C_4AF	1
C_2S	17	Na_2O+K_2O	0.7
C_3A	5	Free Lime	1.6

Table 5.3: Composition of Cement (US Gypsum Co., Chicago, Il)

5.3.1 Materials and Methods

Specimen Preparation

The material investigated in this and Chapter 6 is a white cement paste. It is the same material tested by Thomas and Jennings for weight-loss experiments [230]: White portland cement with a low aluminates content (US Gypsum Co., Chicago, IL, cement composition given in Tab. 5.3) was cast into plastic molds at a water/cement ratio of $w/c = 0.5$, to form bars measuring $0.25\,\mathrm{m} \times 0.025\,\mathrm{m} \times 0.025\,\mathrm{m}$. The specimens were hydrated under limewater at room temperature and kept in such conditions until testing.

For the indentation testing, the square plate specimens were cut into slices of approximate thickness $5 - 10\,\mathrm{mm}$. The surfaces were ground and polished with silicon carbide papers and diamond particles to obtain a very flat and smooth surface finish. This was achieved in six stages of decreasing fineness with the last one being in the range of 250 nm final surface roughness. Special attention was paid to keep the specimens flat and parallel on both sides, since this could influence the angle of indentation and thus the result of the measurements. After polishing, the samples were placed in an ultrasonic bath to remove the dust and diamond particles left on the surface or in the pore structure. The age of the material at testing was 5 months.

Indentation Parameters

The two scales investigated, namely Levels I and II of cementitious materials (Fig. 4-13), are show-cases of heterogeneous composite materials: The submicron scale, Level I, is the scale of individual components and phases present in cementitious materials; while the submillimeter scale, Level II, is the length scale of a homogeneous composite behavior. According to the results of Section 5.1, the mechanical properties of the individual phases (Level I) should be accessible by indention testing with maximum indentation depths $h_{\max}/D \leq 1/10$, while

composite properties should be accessible by indentation depths $h_{\max}/D \gg 1$, where D stands for the characteristic size of individual phases and microstructure. We refer to the former as *nano*indentation and to the latter as *micro*indentation:

- In *nano*indentation the maximum indentation depth must be such to respect the scale separability condition (5.1) and the 1/10−rule-of-thumb:

$$d_0 << h_{\max} \leq D_I/10 \tag{5.17}$$

Hence, in order to obtain the properties of LD and HD C-S-H, d_0 and D_I represent the characteristic sizes of respectively the heterogeneity within LD and HD C-S-H, and the microstructure of C-S-H. Possible candidates for d_0 are the single colloidal particle in C-S-H (see Section 4.4.1) or the gel porosity of similar size, i.e., $d_0 \sim 5.6\,\text{nm}$ as suggested by Jennings et al. ([130], see also Fig. 4-8) On the other hand, the characteristic size of the microstructure D_I is more difficult to estimate, as the microstructure itself depends on mix proportions, hydration degree, etc., and may differ for LD C-S-H and HD C-S-H. SEM, ESEM and TEM images of $w/c = 0.5$ cement pastes in the literature ([199], [82], see also Fig. 4-4) suggest that a length scale of $D_I \sim 1 - 3\,\mu\text{m}$ is characteristic of the porous C-S-H gel matrix, which we adopt in this study. Hence, an appropriate indentation depth that allows one to access the properties of the C-S-H phases by nanoindentation is:

$$\text{Level I} : h_{\max} \in [100, 300]\ \text{nm} \tag{5.18}$$

For smaller depths the indentation response will be affected by the discrete nature of the colloidal particles, and for larger depths substrate effect related to the presence of other phases will prohibit access to intrinsic properties of the C-S-H. The order of magnitude of $h_{\max}$ in Eq. (5.18) also allows access to the *in-situ* properties of CH and eventually residual clinker phases if present. In deed, the elementary size of the Portlandite crystal structure is on the order of $5\,\text{Å} = 0.5\,\text{nm}$ (Fig. 4-5) and the size of the crystals present in cementitious materials is on-average of micrometer dimension, which falls in the range of values that were used in (5.17) to estimate (5.18). We should emphasize, however, that (5.17) is only satisfied in an average sense, and that the presence of 'violators' of these

conditions is inevitable. For instance, nanoindentation responses dominated by adjacent capillary voids of a characteristic size of $10 - 100\,\text{nm}$ (see Section 4.3). The error induced by indentation on such phases that do not satisfy (5.17) should be of random nature, and should be captured by the statistical analysis method (see Section 5.2.2).

- In *micro*indentation aiming at properties of the homogenized medium, the indentation depth is lower-bounded by the size of the microstructure, i.e., $D_I \sim 1 - 3\,\mu\text{m}$. While there is theoretically no restriction to the maximum indentation depth, a natural limit derives from the capacity of the equipment (see Section 3.1, Tab. 3.1). A reasonable choice for hcp is a maximum indentation depth of:

$$\text{Level II} : h_{\max} \sim 10\,\mu\text{m} \tag{5.19}$$

Finally, we need to situate the target indentation depths in the context of the grid indentation technique performed on a highly heterogeneous material (see Fig. 5-5). A convenient way to achieve on-average indentation depths as specified in Eqs. (5.18) and (5.19) is to employ a series of load-controlled indentation depths. This requires some experimental iterations. We found that a maximum load of $P_{\max} = 500\,\mu\text{N}$ ($475 \pm 8\,\mu\text{N}$ after correcting for the spring constant, see Section 3.1.2) yields an average maximum indentation depth of $h_{\max} = 167 \pm 53\,\text{nm}$ in nanoindentation, and that $P_{\max} = 1,000\,\text{mN}$ ($996 \pm 6\,\text{mN}$ after correction) yields $h_{\max} = 9,873 \pm 678\,\text{nm}$ suitable for microindentation. In all indentation tests, a trapezoidal load history was prescribed, defined by a loading time $\tau_L = 10\text{s}$, a holding time $\tau_H = 5\text{s}$, and an unloading time $\tau_U = 10\text{s}$ (Fig. 5-8). In addition, a hold period of 20 seconds at 90% of unloading facilitated the correction for any thermal drift effects in the system.

For the purpose of a repeatability study, three grid indentation experiments of 100 (10×10) indents on different areas of the same surface were performed with a Berkovich indenter. Residual imprints of *micro*indents were examined under an Optical Microscope located in the Center of Materials Science and Engineering at M.I.T. Individual tests were analyzed based on the method presented in Chapter 2. Table 5.4 summarizes details of the experimental program for both nanoindentation and microindentation.

	Series	N*-1	N*-2	N*-3	M**-1
	#	100	100	100	10
$P_{\max}^{***}$	[μN]	476 ± 7	471 ± 10	477 ± 7	$996,180 \pm 6,200$
$h_{\max}$	[nm]	155 ± 41	189 ± 65	161 ± 47	$9,873 \pm 678$
S	[μN/ nm]	25.97 ± 5.08	23.77 ± 5.78	24.31 ± 7.50	966 ± 32
τ_L	[s]	10	10	10	10
τ_H	[s]	5	5	5	50
Machine****	–	HYS	HYS	HYS	MM

Table 5.4: Experimental program and mean $\pm$ standard deviation of indentation results: (*) Nanoindentation tests, (**) Microindentation tests. (***) The deviation of the maximum force from the expected value is due to the spring force correction (see Section 3.1.2). (****) Machines: MM = MicroMaterials, HYS = Hysitron.

Indentation Analysis

Indentation results were analyzed both individually and globally: An individual test gives access to mechanical information of the indented region and a series of tests describes the composite material behavior. Typical $P - h$ curves for the two indentation depths are illustrated in Fig. 5-8. Some of the curves tend to deviate from the theoretical parabolic $P - h$ relationship, either due to improper contact detection or severe damage during loading. Such curves where detected manually (visual inspection) and excluded from the analysis. The largest percentage of discarded curves was related to surface preparation procedures, and the number of tests excluded for this reason was generally smaller than 5% of the total number. Figure 5-9 shows examples of curves that were excluded from (or corrected for) our analysis. Such curves are easily detectable from their large (compared to the average value) recorded maximum penetration depth in the force-driven indentation tests. Individual tests were analyzed based on the methodology presented in Chapter 4: A function of the form $P = b(h - h_f)^m$ was fitted to the unloading portion of the $P - h$ curve and the indentation stiffness S was evaluated at maximum load $P_{\max}$. The indentation modulus M and indentation hardness H were then calculated from Eqs. (2.1) and (2.2), where the area of contact at maximum load A_c was estimated with the Oliver and Pharr method (see Section 2.5 and Eq. (2.78)). Optical images of residual indents of microindentations (Fig. 5-5) demonstrated that there were no visible pile-ups in the Berkovich tests, suggesting that the Oliver and Pharr method would yield accurate results (see discussion in Section 2.5). The large amount of analyzed indentation data was then treated in a statistical

fashion:

1. **Frequency Diagrams and Distributions:** Similar to the procedure presented in Section 3.3 for homogeneous materials, frequency plots are used to analyze indentation data on a composite material. For small indentation depths, $h << D$, such plots give rise to multimode distributions, each peak corresponding to the mechanical manifestation of a phase[2]. In order to extract mechanical properties of the involved phases the deconvolution technique presented in Section 5.2.2 is employed. For indentation depths much greater than the largest characteristic length-scale of heterogeneities, $h >> D$, the different mechanical phases tend to merge into a single peak, which is the mechanical manifestation of the composite material (here, hardened cement paste).

2. **Mechanical Maps:** The analysis of each indentation curve provides information about the mechanical properties at a point of the grid. The discrete data system can then be transformed in a continuous distribution of mechanical properties by linearly interpolating the nodal values over the whole indented surface (grid region). For the *micro*indentation results a square grid of 100 μm spacing was formed (see Fig. 5-5), whereas for the nanoindentation results a 10 μm grid size was used. As shown below, such a mapping of nano-mechanical properties provides information about the morphological arrangement of the different phases in a composite material.

5.3.2 *Nano*indentation Results (Level I): Frequency Plots

Figure 5-10 shows the frequency diagrams of the indentation modulus and hardness for the N-1 specimen (see Tab. 5.4) obtained from 100 nanoindentation tests with an on-average indentation depth of 155 ± 41 nm. At the considered scale the material is highly heterogenous, as testified by the multiple peaks of indentation properties. To analyze the data, we choose to consider four phases ($n = 4$): residues of pore spaces (MP), two types of C-S-H (LD C-S-H and HD C-S-H), Portlandite crystals (CH). There may also be some residues of cement particles (CL) present, but as we have seen in Chapter 4 (Tab. 4.7), the stiffness and hardness

[2] In the case of Nanoindentation on cement paste the mechanical phase coincides with a chemical phase. Such a scenario provides a direct link between physical chemistry and mechanics.

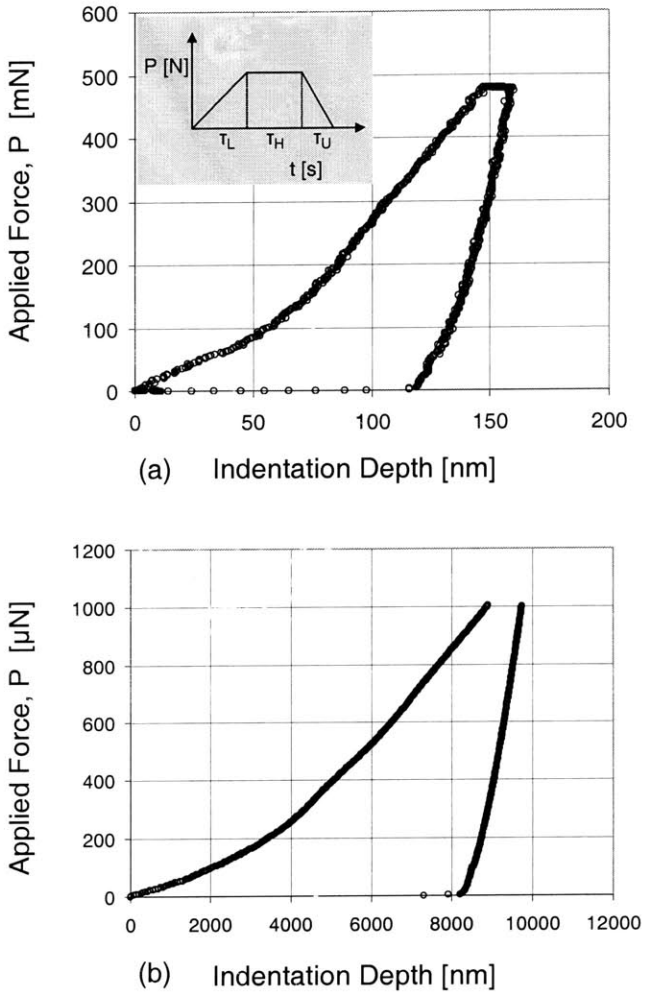

Figure 5-8: Typical nanoindentation (a) and microindentation (b) $P - h$ curves on cement paste.

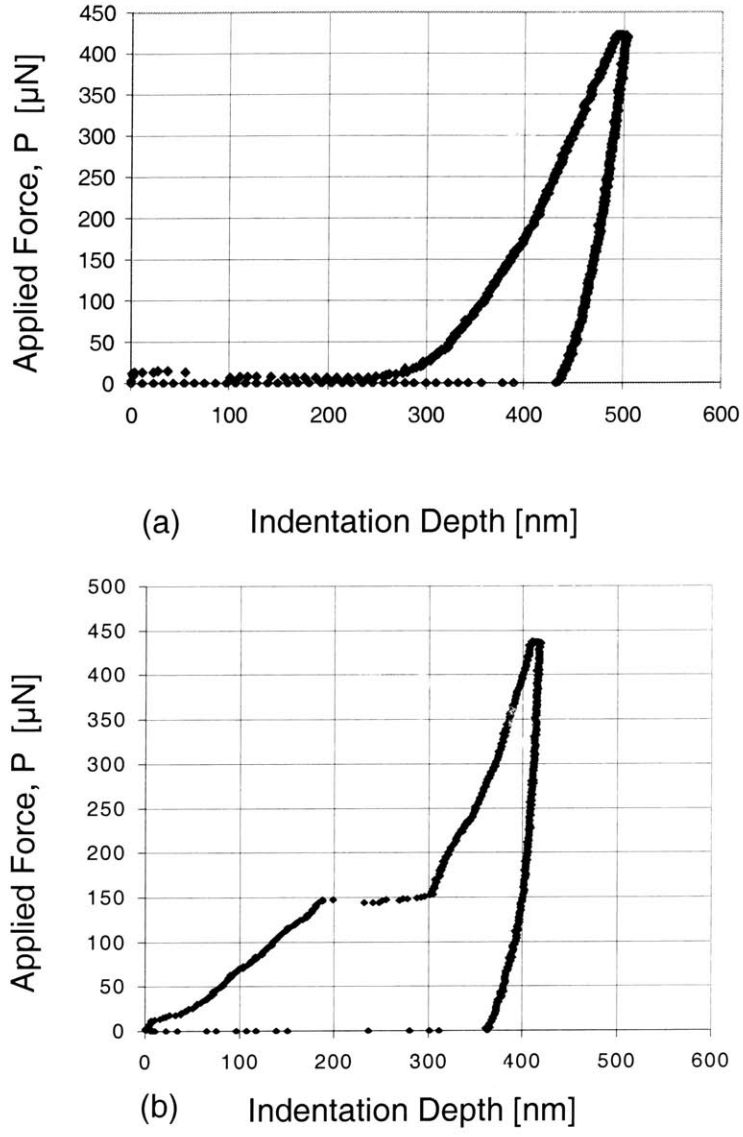

Figure 5-9: Examples of $P - h$ curves that have been either corrected or eliminated from our analysis. (a) A case where the surface area has been incorectly detected. Such curves can be corrected by shifting the origin on the horizontal axis accordingly and proceeding with analyzing the data in the usual way. (b) A case of discontinuity jump, on the indentation depth, during loading.

properties of the clinker phases are at least an order of magnitude higher than the one we find in nanoindentation. This is consistent with the fact that $w/c = 0.5$ cement-based materials are close to complete hydration. We therefore concentrate our analysis on the indentation stiffness and hardness values situated within $M \in [0;50]$ GPa, $H \in [0,1.5]$ GPa, which covers the aforementioned four phases. Following the deconvolution technique of Section 5.2.2, we assume that the mechanical properties (M and H) of each phase are normally distributed, characterized by Eqs. (5.9) and (5.10). The statistical analysis is preformed in a truncated fashion in an attempt to emphasize the region where the C-S-H phases exist. The problem then consists in finding the $3 \times 4 = 12$ unknowns (μ_J, s_J, f_J) of the 4 phases involved, J =MP, LD C-S-H, HD C-S-H, CH, that characterize the theoretical density function $P(x) = \sum_{J=1}^{4} f_J p_J(x)$ which minimizes the standard error (i.e., Eq. (5.13)), for the given set of experimentally obtained discrete values P^i, subject to the constraint:

$$\sum_{J=1}^{4} f_J = 1 - f_r; \qquad f_r = \frac{N_r}{N} \tag{5.20}$$

where f_r is the volumetric proportion of the high stiffness/hardness phases, N_r is the number of data points having stiffness (or hardness) greater than 50 GPa (or 1.5 GPa) and N is the total number of tests (here, 100). The number of bin sizes used at this level, Level I, was, $m_{\mathrm{I}} = 12$, satisfying Eq. (5.14); $m_{\mathrm{I}} = 12 > 3 \times 4 - 1 = 11$. The optimization was performed using the SOLVER function in EXCEL. The resulting best fits of Gaussian distributions of indentation modulus and hardness, which give access to the means, standard deviations, and volume fractions of all 4 phases are shown in Figs. 5-11 to 5-14. The results are listed in Tab. 5.5, and deserve some comments.

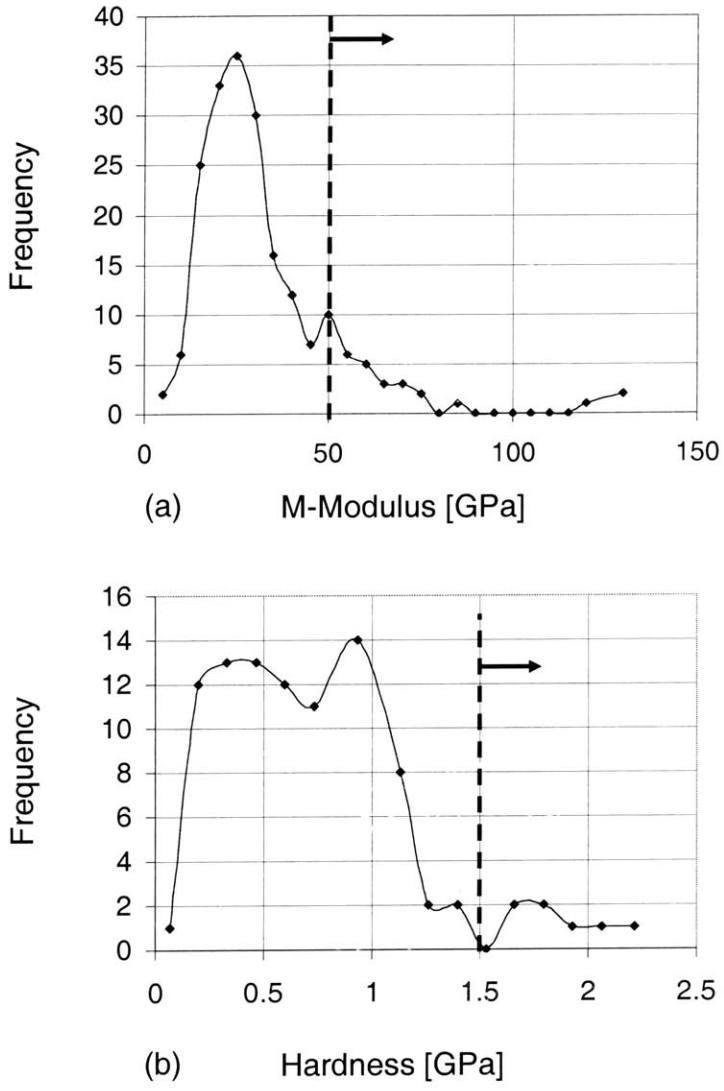

Figure 5-10: Frequency plots of indentation modulus (a) and hardness (b) for N-1. Values greater than $M > 50, H > 1.5$ (probably related to clinker or secondary phases) were excluded from our analysis in order to concentrate our attention in the low mechanical regime: $0 < M < 50; 0 < H < 1.5$.

	J	[−]	MP	LD C-S-H	HD C-S-H	CH
N-1	M	[GPa]	9.2 ± 1.6	19.6 ± 2.8	29.5 ± 3.8	38.6 ± 2.5
	$\left(\frac{s}{\mu}\right)$	[%]	17	14	13	6
	f	[%]	7	46	27	12
	H	[GPa]	0.24 ± 0.07	0.49 ± 0.2	0.95 ± 0.17	1.40 ± 0.03
	$\left(\frac{s}{\mu}\right)$	[%]	29	41	18	2
	f	[%]	14	45	45	1
N-2	M	[GPa]	8.3 ± 2.4	18.1 ± 3.6	29.0 ± 4.2	40.9 ± 3.5
	$\left(\frac{s}{\mu}\right)$	[%]	29	20	15	9
	f	[%]	10	52	26	9
	H	[GPa]	0.13 ± 0.05	0.42 ± 0.18	0.92 ± 0.03	1.30 ± 0.07
	$\left(\frac{s}{\mu}\right)$	[%]	38	43	3	5
	f	[%]	7	68	12	5
N-3	M	[GPa]	5.7 ± 0.8	18.8 ± 5.7	31.6 ± 3.1	44.2 ± 1.4
	$\left(\frac{s}{\mu}\right)$	[%]	14	30	10	3
	f	[%]	1	66	20	12
	H	[GPa]	0.14 ± 0.03	0.46 ± 0.10	0.85 ± 0.19	1.30 ± 0.25
	$\left(\frac{s}{\mu}\right)$	[%]	21	22	22	19
	f	[%]	15	42	41	15
ALL	M	[GPa]	8.7 ± 1.9	18.8 ± 3.9	30.1 ± 4.7	41.2 ± 5.6
	$\left(\frac{s}{\mu}\right)$	[%]	22	21	16	14
	f	[%]	9	49	27	12
	H	[GPa]	0.18 ± 0.07	0.47 ± 0.15	0.85 ± 0.08	1.31 ± 0.20
	$\left(\frac{s}{\mu}\right)$	[%]	39	32	9	15
	f	[%]	10	53	20	12

Table 5.5: Summary of grid indentation results for three different trials of 100 indentations obtained after statistical analysis of the frequency diagrams: Indentation Modulus, Hardness, Volume fractions, and Coefficients of Variations for all constituent phases.

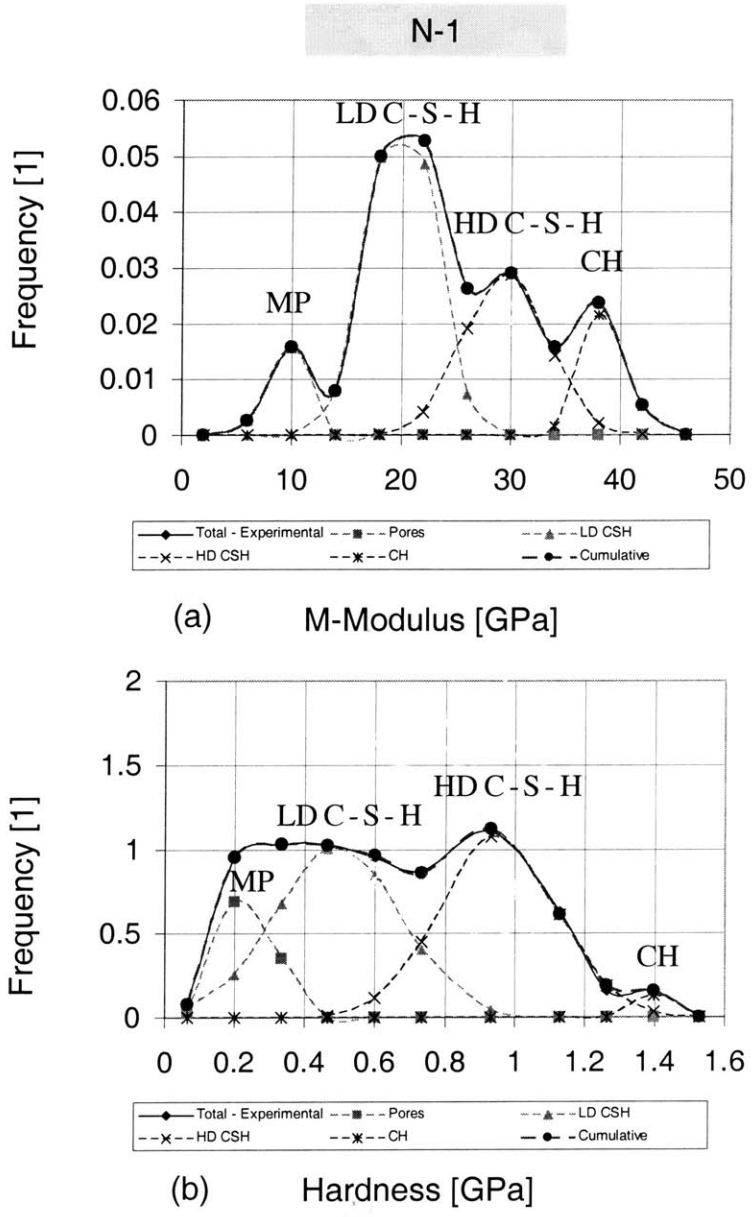

Figure 5-11: Best fitted Gaussian distributions for the different phases found in cement pastes microstructure - Control 1: Macropores, LD C-S-H, HD C-S-H, CH. The summation of the fitted Gaussian distribution is in very good agreement with the experimentally observed one.

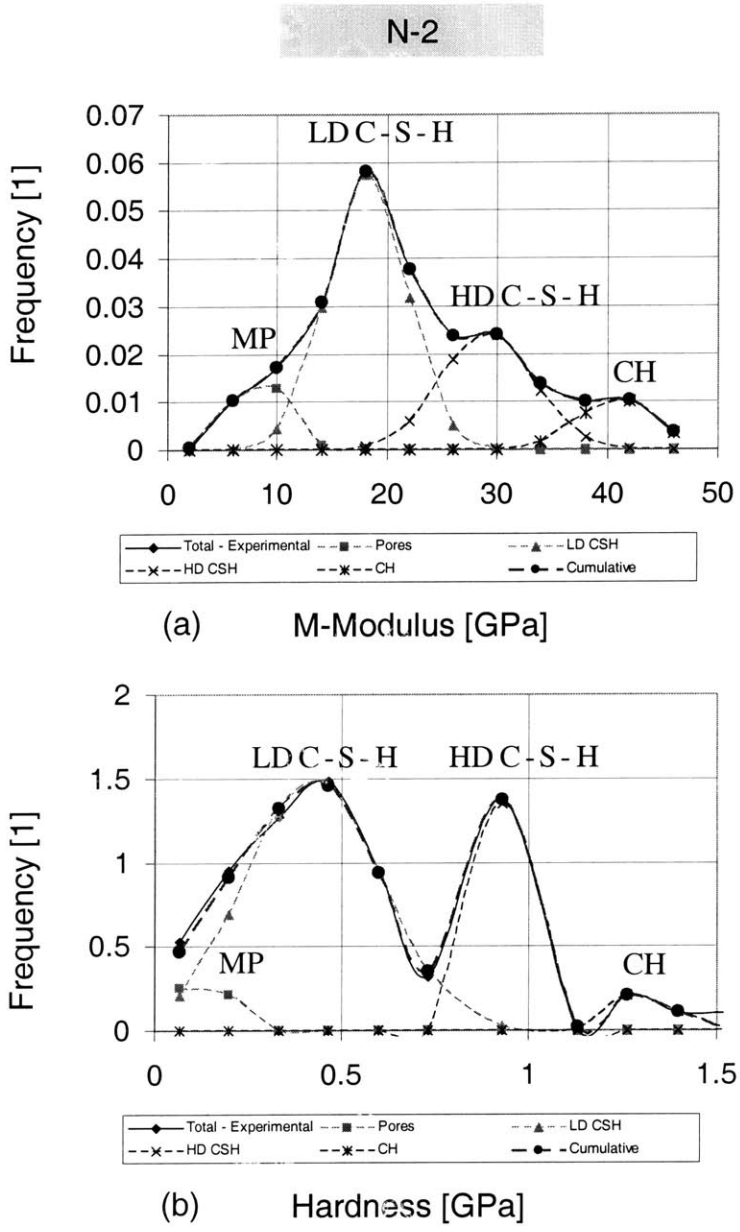

Figure 5-12: Best fitted Gaussian distributions for the different phases found in cement pastes microstructure - Control 2: Macropores, LD C-S-H, HD C-S-H, CH. The summation of the fitted Gaussian distribution is in very good agreement with the experimentally observed one.

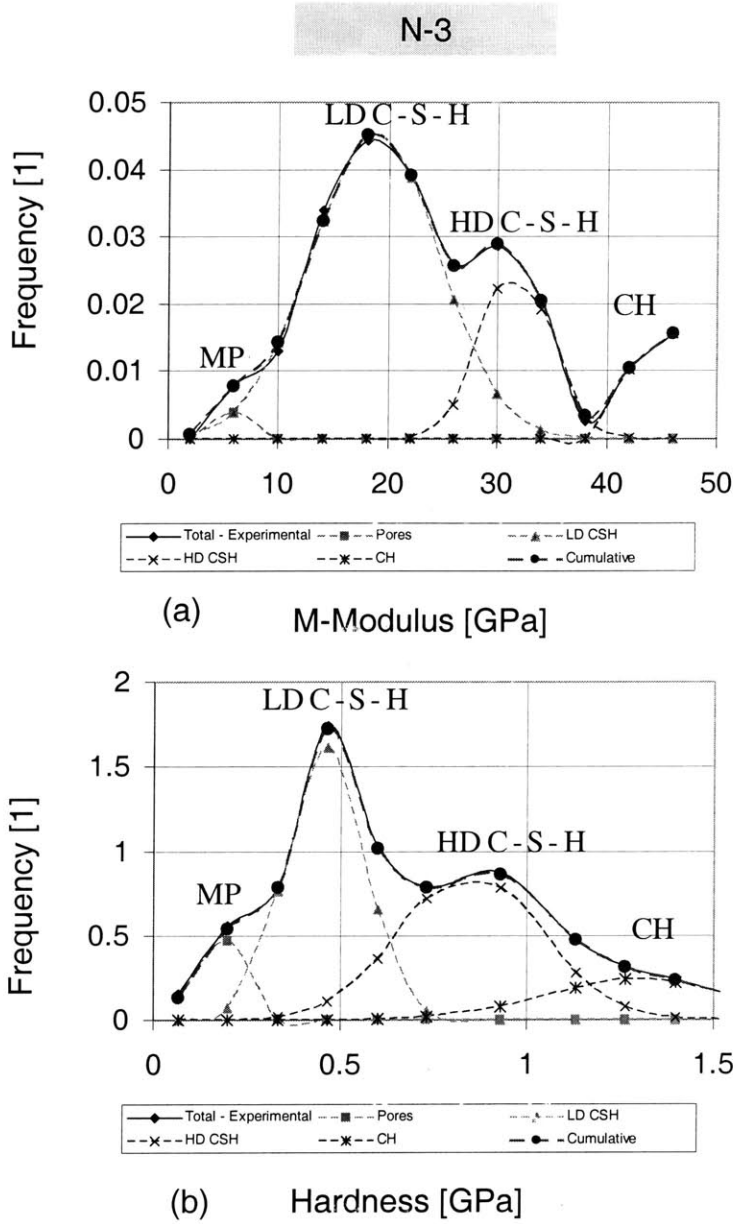

Figure 5-13: Best fitted Gaussian distributions for the different phases found in cement pastes microstructure - Control 3: Macropores, LD C-S-H, HD C-S-H, CH. The summation of the fitted Gaussian distribution is in very good agreement with the experimentally observed one.

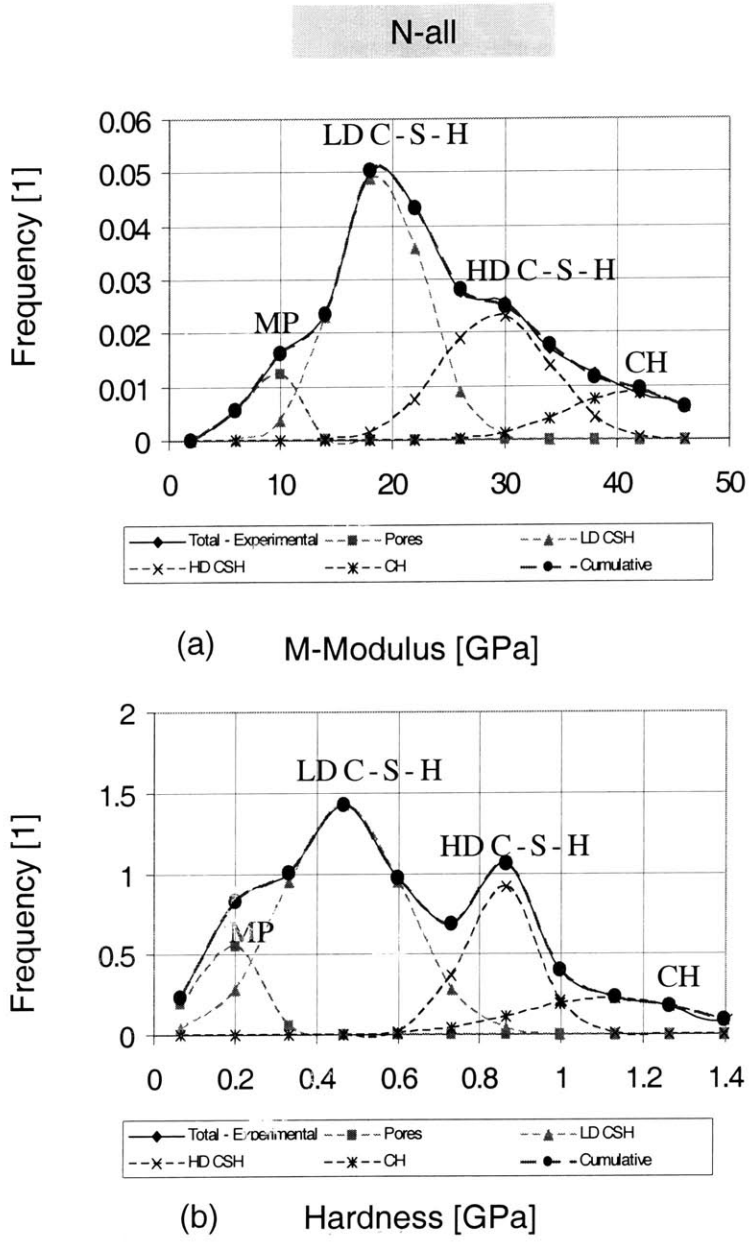

Figure 5-14: Best fitted Gaussian distributions for the different phases found in cement pastes microstructure - Control 1-3: Macropores, LD C-S-H, HD C-S-H, CH. The summation of the fitted Gaussian distribution is in very good agreement with the experimentally observed one.

Mean Values of all Four Phases are Reproducible

The fitted mean values of indentation modulus and hardness of the 4 phases considered do not significantly vary from one test series to another:

$$M = \left\{ \begin{array}{lllll} \text{N-1} & \text{N-2} & \text{N-3} & \text{N}-\text{all} & \\ \text{[GPa]} & \text{[GPa]} & \text{[GPa]} & \text{[GPa]} & \\ 9.2 & 8.3 & 5.7 & 8.7 & \text{Macropores} \\ 19.6 & 18.1 & 18.8 & 18.8 & \text{LD C-S-H} \\ 29.5 & 29.0 & 31.6 & 30.1 & \text{HD C-S-H} \\ 38.6 & 40.9 & 44.2 & 41.2 & \text{CH} \end{array} \right. \tag{5.21}$$

$$H = \left\{ \begin{array}{lllll} \text{N-1} & \text{N-2} & \text{N-3} & \text{N}-\text{all} & \\ \text{[GPa]} & \text{[GPa]} & \text{[GPa]} & \text{[GPa]} & \\ 0.24 & 0.13 & 0.14 & 0.18 & \text{Macropores} \\ 0.49 & 0.42 & 0.46 & 0.47 & \text{LD C-S-H} \\ 0.95 & 0.92 & 0.85 & 0.85 & \text{HD C-S-H} \\ 1.40 & 1.30 & 1.30 & 1.31 & \text{CH} \end{array} \right. \tag{5.22}$$

In particular, the difference in mean values of the C-S-H phases and the CH-phase is on the order or smaller than the respective standard deviations, and hence statistically insignificant. It is interesting to observe that the mean values obtained by deconvoluting the total number of tests (N−all) is not a simple average of all the mean values obtained in each test. Are those repeatable values representative of the intrinsic properties of each phase? This question will be further explored in Section 5.4 of this chapter.

Indentation Hardness Exhibits More Scatter Than Indentation Modulus

The deviation of the mechanical properties of each phase from their mean values shows some significant variation between different test series. Looking at the nature of this scatter provides insight in the significance. The spread of the data for each phase, here quantified in terms of the standard deviation and coefficient of variation (Tab. 5.5), is a result of a combination of (at least) three phenomena:

- The natural variability of each phase (i.e., variable density or packing modes in the case of the C-S-H phases). For instance, it is well known that local variabilities like porosity or other heterogeneities tend to affect strength properties (and/or hardness) in a more pronounced way than elasticity properties.

- The mechanical interaction between phases, which affects the hardness more than the indentation modulus (see Section 5.1.2 and Fig. 5-2).

- Error introduced in the calculations of M and H, which is due to estimating the area of contact (see Section 2.5). Since $M \propto A_c^{-1/2}$ and $H \propto A_c^{-1}$, an error in the contact area estimation is expected to affect hardness more significantly than the indentation modulus.

It therefore becomes apparent that the indentation modulus results obtained by indentation contain less uncertainty than the indentation hardness values, and should therefore be the preferred quantity for comparison purposes and for understanding the microstructure. Indeed, the data in Tab. 5.5 show that the coefficient of variation for hardness of all phases is consistently higher than the coefficient of variation of the indentation modulus.

Finally, a comment is due on the scatter of the data obtained for the two types of C-S-H. It is interesting to note that the coefficient of variation of the LD C-S-H is significantly higher than the one of HD C-S-H, hinting towards a more ordered and homogeneous structure of the latter. Of great interest is also the coefficient of variation of Portlandite crystals (15%). Given their crystalline nature, one would expect a scatter much less than the rest of the phases. It is therefore reasonable to assume that the primary source of variability for this hard phase is the substrate effect that cannot be avoided in full (see Section 5.1.2).

Volumetric Proportions are Better Estimated Through M-modulus Analysis

The volumetric proportions of each phase calculated from the deconvolution of hardness and modulus somewhat vary from one series to another (see Tab. 5.5). It is useful to emphasize that the deconvolution procedure works best when there are clear peaks in the experimentally obtained distribution. In cases where the peaks merge the fitting process suffers from pronounced non-uniqueness. In fact, the error minimization process converges to several minima for different combination of volumetric proportions and standard deviations. While the mean values

of the involved phases are little affected, the estimated standard deviations and volumetric proportions could be largely in error.

Indentation modulus plots tend to show clear peaks and as a consequence the extracted volume fractions f show a high degree of repeatability:

$$f = \left\{ \begin{array}{cccc} \text{N-1} & \text{N-2} & \text{N-3} & \text{N}-\text{all} \\ [\%] & [\%] & [\%] & [\%] \\ 7 & 10 & 1 & 9 \quad \text{Macropores} \\ 46 & 52 & 66 & 50 \quad \text{LD C-S-H} \\ 27 & 26 & 20 & 27 \quad \text{HD C-S-H} \\ 11 & 9 & 12 & 12 \quad \text{CH} \end{array} \right. \tag{5.23}$$

The small deviations observed between tested specimens can be attributed to local variabilities of the materials microstructure. By contrast, the volume fractions extracted from fitting the hardness distribution show a large variability, which should be attributed to fitting errors (not clear peaks). Generally speaking, the discrepancy between the volume fractions calculated from the indentation modulus and hardness tends to become less significant as the number of tests increases. The volume fraction results for all three samples (N−all) given in Tab. 5.5 converge for both M and H:

$$(f)_{N-all} = \left\{ \begin{array}{cc} M & H \\ [\%] & [\%] \\ 9 & 10 \quad \text{Macropores} \\ 50 & 53 \quad \text{LD C-S-H} \\ 27 & 20 \quad \text{HD C-S-H} \\ 12 & 12 \quad \text{CH} \end{array} \right. \tag{5.24}$$

It is suggested that the indentation modulus deconvolution which usually shows a clear separation of phases, should be used for estimating volume fractions.

Volume Proportions Vary with Location but Converge for Large N

The volume fractions estimated for the three test series show some variability associated probably to the spatial distribution of mechanical phases, which is a reminder that the hydration

reaction and as a consequence the resulting volumetric proportions of the formed phases are complicated functions of the particle size, local w/c-ratio, etc. (see Section 4.2). It is therefore reasonable to expect some unavoidable local variability. On the other hand, as the size of the sample area and thus the number of tests increases, the effect of local variability should fade out and the volume fractions should converge towards some statistically representative values. The results of a convergence study of the volume fractions of the LD and HD C-S-H phases, which are shown in Fig. 5-15, support this suggestion. Within the context of a square grid-indentation technique proposed here, a linear length estimate of the required sampling size is provided by $l\sqrt{N}$, where l is the grid spacing between indents and N is the number of indentations. Figure 5-15 which shows the indentation results for a grid spacing of $l = 10$ μm and for $N = 5, 10, 30, 50, 100, 200$, and 300 suggests that a sampling region on the order of $10\sqrt{30} \simeq 55\,\mu$m is enough to provide converging values of the relative volumetric proportions of the two C-S-H phases. This is in line with the separation of scales principle (Eq. 5.1) which suggests that the characteristic size of an R.E.V. should be an order of magnitude higher than the characteristic length scale of any heterogeneity (here, $d \simeq 1 - 3\,\mu\text{m} \ll 55\,\mu\text{m}$).

Negligible Effect of Bin Size on Deconvolution Results

One could argue that the results obtained with the deconvolution technique heavily depend on the bin-size chosen to represent the experimental probability density P^i. To further investigate this issue we have increased the number of bins by 50% ($m_I = 18$) and evaluated the best fitted curves for each resulting histogram by minimizing the quadratic error in Eq. (5.13). Furthermore, we also fitted the results for two bin sizes, $m_I = 12$ and $m_I = 18$, by simultaneously minimizing the total quadratic error for the two bin-sizes:

$$\min \left[\left(\sum_{i=1}^{m} \left(P^i - P\left(x_i\right) \right)^2 \right)_{m_I=12} + \left(\sum_{i=1}^{m} \left(P^i - P\left(x_i\right) \right)^2 \right)_{m_I=18} \right] \tag{5.25}$$

Figures 5-16 and 5-17 display the fitting results, which are summarized in Tab. 5.6. While the choice of the bin-size may have some effect on the obtained results, the mean values of each phase is relatively little affected, and the difference between the different bin size fitting results is in all cases much smaller than the standard deviation. This shows that the deconvolution

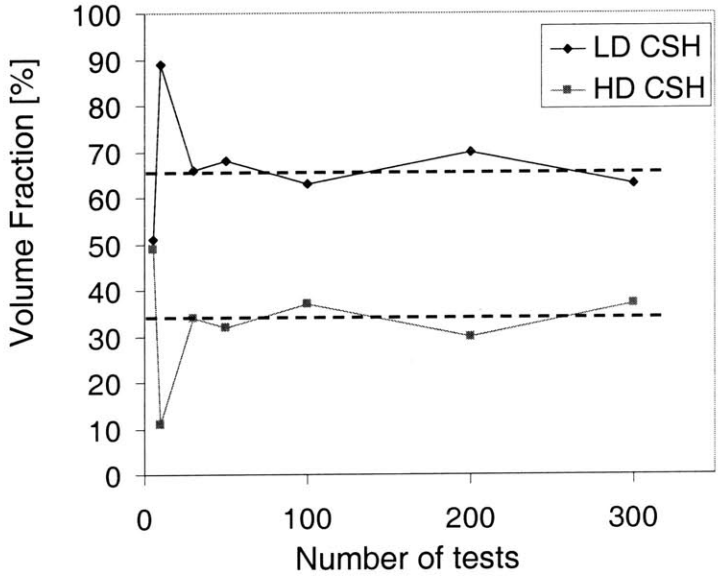

Figure 5-15: Convergence of the relative volumetric proportions of LD and HD C-S-H with increasing number of indentations (or sampling area).

N−all			MP	LD C-S-H	HD C-S-H	CH
m=12	M	[GPa]	8.7 ± 1.9	18.8 ± 3.9	30.1 ± 4.7	41.2 ± 5.6
	$\left(\frac{s}{\mu}\right)$	[%]	22	21	16	14
	f	[%]	9	50	27	12
	H	[GPa]	0.18 ± 0.07	0.47 ± 0.15	0.85 ± 0.08	1.31 ± 0.20
	$\left(\frac{s}{\mu}\right)$	[%]	39	32	9	15
m=18	M	[GPa]	9.1 ± 2.3	19.0 ± 4.0	32.0 ± 5.0	44.0 ± 3.1
	$\left(\frac{s}{\mu}\right)$	[%]	25	21	16	7
	f	[%]	8	49	24	14
	H	[GPa]	0.16 ± 0.06	0.47 ± 0.17	0.87 ± 0.08	1.08 ± 0.21
	$\left(\frac{s}{\mu}\right)$	[%]	38	36	9	19
m=12+18	M	[GPa]	9.1 ± 2.3	18.8 ± 4.0	31.0 ± 4.0	41.0 ± 3.9
	$\left(\frac{s}{\mu}\right)$	[%]	25	21	13	10
	f	[%]	8	51	25	13
	H	[GPa]	0.16 ± 0.07	0.47 ± 0.17	0.87 ± 0.08	1.19 ± 0.16
	$\left(\frac{s}{\mu}\right)$	[%]	43	36	9	14

Table 5.6: Summary of grid indentation results for three different trials of 100 indentations obtained after statistical analysis of the frequency diagrams: Indentation Modulus, Hardness, Volume fractions, and Coefficients of Variations for all constituent phases.

technique is quite robust for extracting the phase properties of highly heterogeneous materials, provided a large experimental data base (here, all series) and provided that condition (5.14) is satisfied.

*Nano*indentation Results (Level I): Mechanical Maps

Indentation testing allows monitoring the spatial distribution of indents. In our *Nano*indentation campaign a square grid of 10 μm spacing (between indents) was used. The analysis of each indentation curve provides information about the mechanical properties (M, H) at each grid point. These properties are, strictly speaking, representative of a material domain of characteristic length scale $\max(h, a)$. Hence, provided that the grid spacing is larger than the characteristic length scale of the materials sensed in each test, mapping of the properties over the grid region provides information about the morphological arrangement of the phases within the microstructure. This is a second result of the proposed grid-indentation technique. A convenient and simple way to generate these maps is by transforming the discrete data system into a

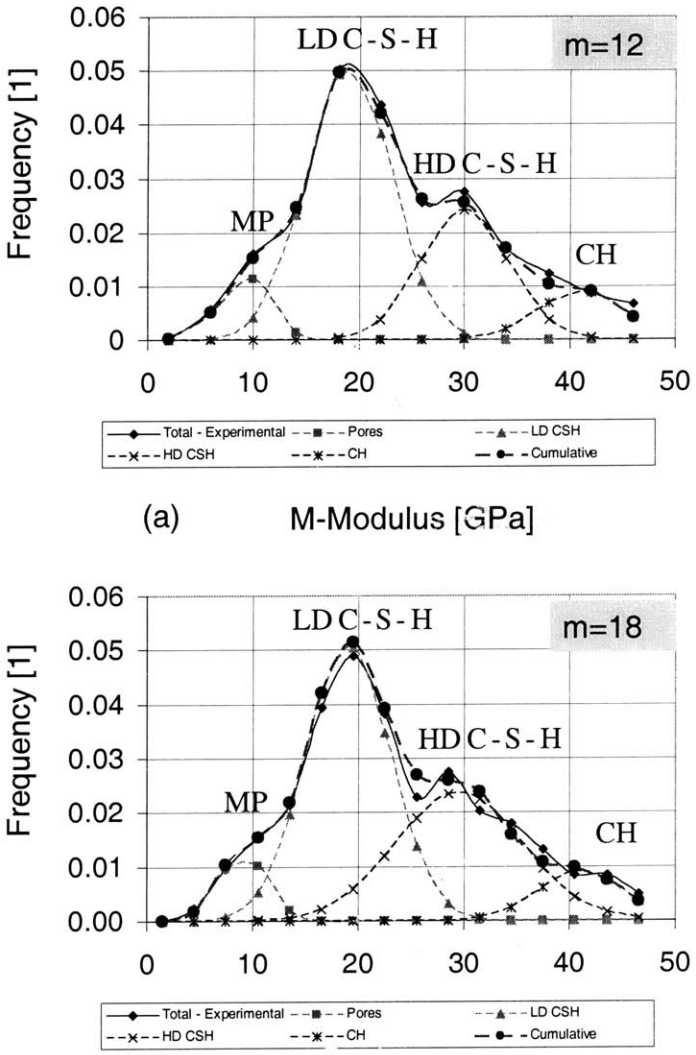

Figure 5-16: Frequency distributions for the indentation modulus of white cement paste, $w/c = 0.5$ for two different bin sizes: $m = 12$ and 18. The best fitted normal distributions were obtained after minimizing the average error of the two distributions.

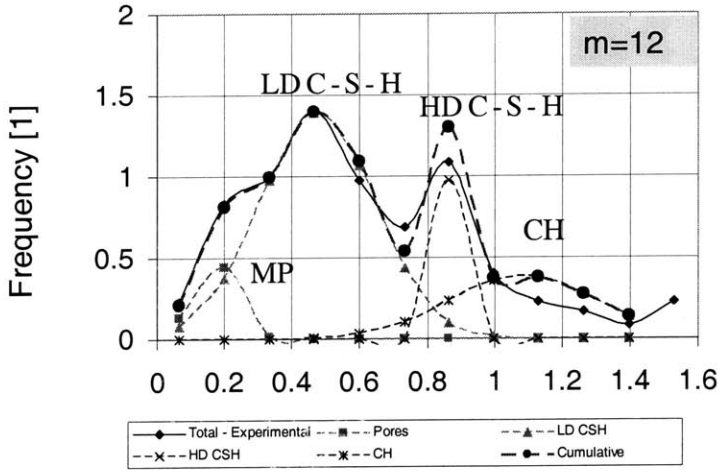

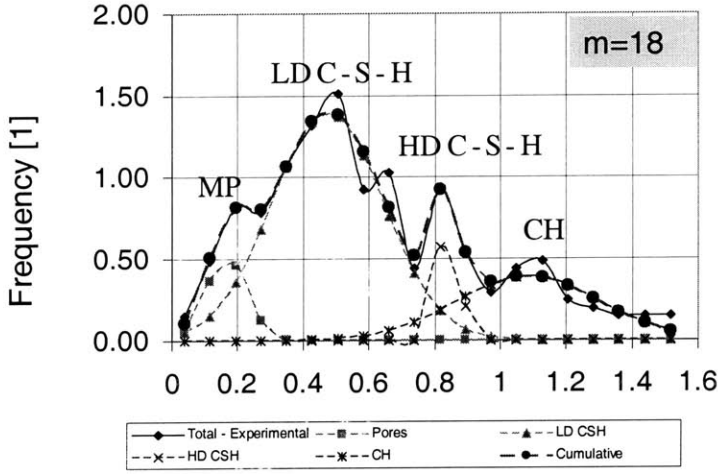

Figure 5-17: Frequency distributions for the indentation hardness of white cement paste, $w/c = 0.5$ for two different bin sizes: $m = 12$ and 18. The best fitted normal distributions were obtained after minimizing the average error of the two distributions.

continuous distribution of mechanical properties by linearly interpolating the grid point values over the grid region. The result of this mapping can be displayed as contour plots in either 3-D images or plan views (see Fig. 5-18). Such a contour depiction of mechanical properties requires the selection of min-max limits between different phases. As the frequency plots 5-11 to 5-14 show, there is some significant overlap in the distribution between different phases, which makes it difficult to define clear boundaries between phases. As a first order approach we chose equal size domains centered around the mean values of each phase:

1. Macroporosity domain $0 - 13$ GPa: Values situated in this range are associated with regions for which the mechanical response is dominated by high porosity. For purpose of comparison, these areas are indicative of the macroporosity.

2. Low-Density C-S-H domain $13-26$ GPa: Values situated in this range are contained within the second peak in the frequency plots 5-11 to 5-14, and are associated with regions in which the mechanical response is dominated by the LD C-S-H.

3. High-Density C-S-H domain $26 - 39$ GPa: Values situated in this range correspond to the third peak in the frequency plots 5-11 to 5-14, and are attributed to the dominant mechanical effect of the HD C-S-H.

4. CH domain and unhydrated clinker ≥ 39 GPa: The higher stiffness values are indicative of Portlandite and unhydrated clinker phases. While the first tends to grow in regions of high $w/c-$ratios adjacent to macropores and in between LD C-S-H, the residual clinker phases are generally rimmed by HD C-S-H.

Figure 5-19 shows plan views of contour plots of the indentation modulus for the three series N-1, N-2 and N-3. An SEM image of a cement paste of $w/c = 0.5$ at 28 days is also shown in the figure, and demonstrates the qualitative resemblance of the mechanical maps with optical images. Hence, the mechanical maps provide a means to characterize the morphology of the microstructure at the scale defined by the chosen (nano)indentation depth, and allows visualizing microstructural features. In particular, for hardened cement paste, the contour plots provide a snapshot of the formation process of the cement paste: unhydrated clinker particles are rimmed by HD C-S-H which can be associated with so-called 'inner products' (see Tab. 4.5 and

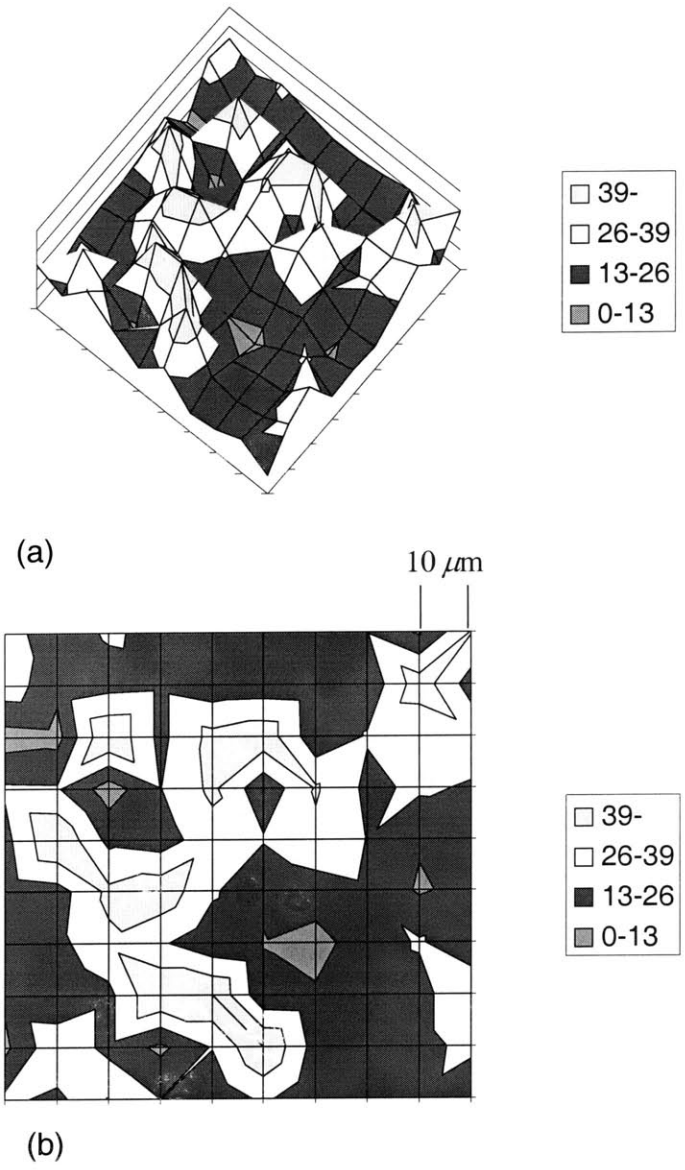

Figure 5-18: Three-dimensional (3-d) view (a) and plan view (b) of a mechanical contour plot of indentation modulus on cement paste. Grid (inter-indentation) spacing = 10 μm

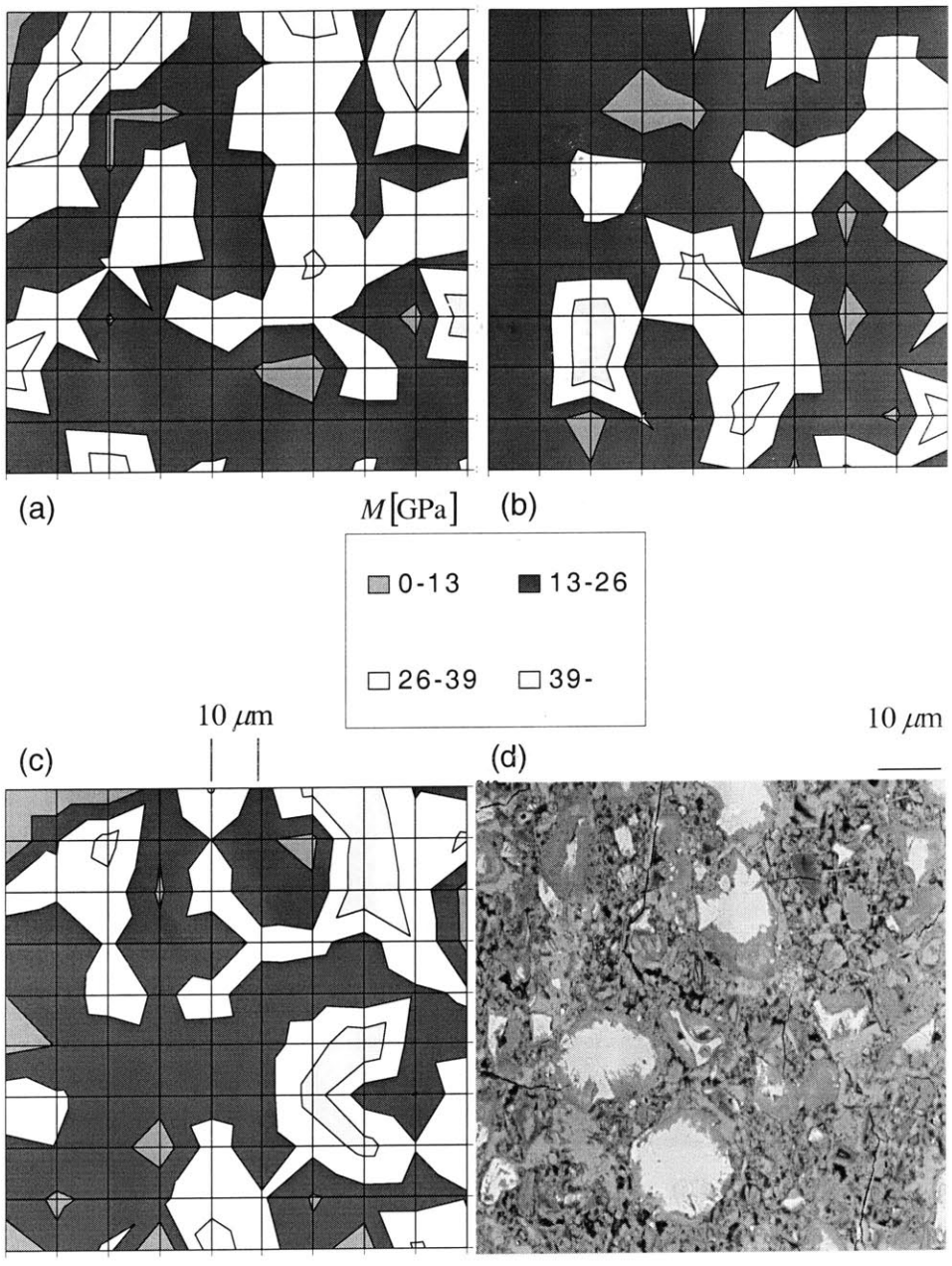

Figure 5-19: Plan views of mechanical maps of indentation modulus (N-1 (a), N-2 (b), N-3 (c)). A similar magnification of an SEM image (d) (courtesy of K. Scrivener) is also shown for comparison. Image size: 150×150 μm^2, Grid spacing = 10 μm.

Fig. 4-4). Further away from high stiffness phases is the LD C-S-H phase (or 'outer products'), which seems to be the percolated matrix phase in the materials system. The unfilled residues of water, that is the space not filled by hydration products, can also be visualized in both SEM and mechanical maps. Of great importance is also the repeatability of the microstructural features obtained by mapping the mechanical properties. The three images obtained from three test series are very similar suggesting that a grid surface of 100 μm $\times$ 100 μm is able to avoid any statistical bias in the detection of microstructural features. This is consistent with the convergence of volume fraction predictions with increasing size of sampling region, presented in Fig. 5-15. The morphological characterization of the microstructure provided by the mechanical mapping technique completes the characterization of the Level I properties and morphological arrangement of hcp. As will be discussed later, this will form the backbone of the development of micromechanical models for stiffness and strength upscaling.

5.3.3 *Micro*indentation Results (Level II)

Figure 5-20 shows the frequency diagrams of the *micro*indentation modulus and hardness obtained from a series of 10 microindentation tests operated to a maximum indentation depth of roughly 10 μm (see Tab. 5.4). Consistent with the ideas put forward in Fig. 5-6, the material response 'homogenizes' as the depth of indentation increases and the multi-mode distribution collapses into a mono-modal distribution (Fig. 5-20), representative of the homogenized medium, hardened cement paste. Assuming that the mechanical properties of cement paste are normally distributed, one can calculate the mean values and standard deviation from Eq. (5.10):

$$\text{Cement Paste} \quad \left\{ \begin{array}{lll} & M & H \\ \mu \text{ [GPa]} & 21.6 & 0.515 \\ s \text{ [GPa]} & 3.2 & 0.07 \\ \frac{s}{\mu} \text{ [\%]} & 15 & 14 \end{array} \right. \tag{5.26}$$

Alternatively, one can use the deconvolution technique presented in section 5.2.2 with identical results. This is also shown in Fig. 5-20, and the chosen number of bins was $m_{II} = 7$, satisfying Eq. (5.14) (for $n = 1$). An interesting observation is that the homogenized response reflected in Eq. (5.26) is not equal to the simple statistical average of the phase properties weighted by

their volume fraction (which would correspond to the so-called Voigt bound, yielding[3] $\langle M \rangle = 25.5 \pm 11.9$ GPa, $\langle H \rangle = 0.70 \pm 0.48$ GPa). Instead, the mean values in Eq. (5.26) come very close to the ones of the low density C-S-H phase, which seems to dominate over all other phases. Furthermore, it is interesting to note that the homogenization process is associated with a significant reduction of the degree of variability. The large range of values for M and H found in nanoindentation (Figs. 5-11 to 5-14) is significantly reduced at the microscopic scale, and the standard deviation and coefficient of variation in microindentation is considerably smaller than in nanoindentation. The mean values obtained from mechanical testing at the microscopic scale (Level II) represent a mechanical averaging process that yields homogeneous macroscopic properties.

5.4 Material Invariant Properties of C-S-H

The indentation moduli and hardness for the two types of C-S-H which are the outcome of the grid indentation technique proposed in Section 5.2, are insensitive to bin sizes, spatial location in cement paste, number of tests, time, etc. They can therefore be considered as intrinsic material properties. To further investigate the intrinsic nature of these properties, we compare our results with values existing in the literature. Since the C-S-H phases cannot be reproduced in large scales, data on their mechanical performance are scarce. In fact the only information comes from indentation testing or by extrapolating macroscopic testing of different porosities to zero porosity. This is now discussed.

[3] We use here standard notations of continuum micromechanics; that is, for the volume average

$$\langle Y \rangle = \frac{1}{V} \int y(\underline{x})\, dV$$

Appendix B provides a summary of notations used in this thesis.

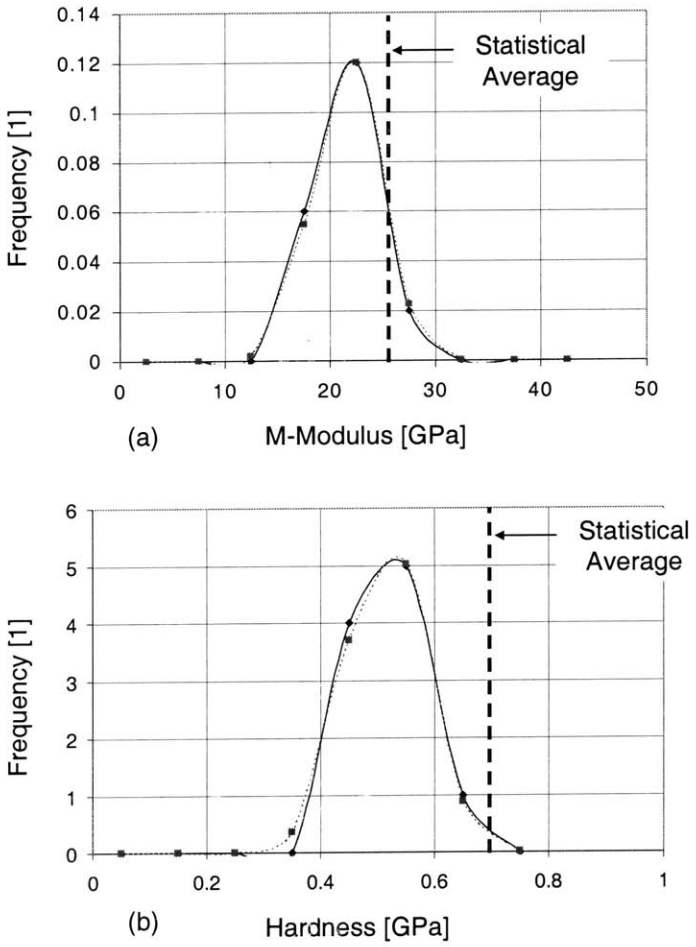

Figure 5-20: Frequency diagrams of the *micro*indentation modulus (a) and hardness (b). The dotted lines represent the statistical averages calculated from the *nano*indentation data.

5.4.1 Comparison with Existing Data

Indentation Modulus

The mean values of LD and HD C-S-H almost perfectly agree with results presented by Acker [2] obtained by nanoindentation on an ultra high performance cementitious material of $w/c = 0.2$:

$$(M)_i = \begin{cases} M & \left(\frac{s}{\mu}\right)_H & \\ [\text{GPa}] & [\%] & \\ - & - & \text{Macropores} \\ 20 \pm 2 & 10 & \text{C/S<1 C-S-H} \\ 31 \pm 4 & 13 & \text{C/S>1 C-S-H} \\ 36 \pm 3 & 8 & \text{CH} \end{cases} \tag{5.27}$$

The values obtained here for white cement paste are also consistent with our previous nanoindentation results of a normal cement paste of Type I, $w/c = 0.5$ ($M_{LD} = 23.0 \pm 2.2$ GPa, $M_{HD} = 31.2 \pm 2.4$ GPa) [58,59,60]. Furthermore, the value of the indentation modulus for Portlandite crystals, $M_{CH}^{Ind} = 41.0 \pm 3.9$ GPa is in very good agreement with values reported in the literature, $M_{CH}^{\text{exp}} = 38 - 48$ GPa (see Tab. 4.6 in Section 4.2.2). Beside indentation testing, the only experimental based estimate of the intrinsic C-S-H gel elasticity comes from the 1966 work of Helmuth and Turk [113], who prepared different cement paste specimens of different capillary porosities and measured their macroscopic elastic properties using a resonance frequency method[4]. The elastic properties of the C-S-H gel were obtained by fitting an empirical function to the experimental data of the form:

$$E = E_g \left(1 - V_{cw}\right)^3 \tag{5.28}$$

[4]Resonance frequency methods involve the determination of the natural frequency of vibrations of a specimen, which based on knowledge of the density of the material, can be transformed into an estimate of its modulus of elasticity.

where V_{cw} is the capillary porosity[5] and E_g is the elastic modulus of the paste for zero capillary porosity, which is an approximation for the C-S-H gel. An estimate of E_g was obtained by measuring the slope of the best fitted straight line on a plot E *vs.* $(1-p_c)^3$; from which $E_g = 31$ GPa, which would translate into an indentation modulus of $M_g = E_g/\left(1-\nu^2\right) \approx 33$ GPa (assuming a Poisson's ratio of $\nu = 1/4$). In the absence of any capillary porosity the material is left with the hydration products. The $w/c-$ratio used in Helmuth and Turks experiments ranged between $0.4 - 0.7$ which suggests that the gel is a mixture of LD C-S-H, HD C-S-H, Portlandite crystals and any unhydrated cement (for $0.40 < w/c < 0.42$). The porosity was varied by reducing the $w/c-$ratio, and as a result the material tends to consist of more HD C-S-H and less LD C-S-H. The extrapolated value which appears to be very close the one of HD C-S-H ($M_{HD} = 31 \pm 4$ GPa), is probably the homogenized value of the extrapolated mixture found from experiments.

Indentation Hardness

Reported values for hardness of cement paste constituents are scarce. The only information comes from the work of Acker [2] who reported indentation hardness values for the Portlandite crystals and the two types of C-S-H:

$$(H)_i = \left\{ \begin{array}{ccl} H & \left(\frac{s}{\mu}\right)_H & \\ \text{[GPa]} & \text{[\%]} & \\ - & - & \text{Macropores} \\ 0.80 \pm 0.2 & 25 & \text{C/S<1 C-S-H} \\ 0.90 \pm 0.3 & 33 & \text{C/S>1 C-S-H} \\ 1.35 \pm 0.5 & 36 & \text{CH} \end{array} \right. \tag{5.29}$$

Acker's values seem to agree reasonably well with our experimental data with the exception of the LD C-S-H. To be more precise, Acker [2], reports a value of 0.8 GPa for a C-S-H phase having C/S< 1. While the indentation modulus of this phase correlates very well with

[5]The capillary porosity used in Helmulth and Turk was the one defined in Powers and Brownyard model (see section 4.5.1) and was found by correcting the evaporable water (representative of total porosity) for the constant water, as assumed in the Powers and Brownyard model, held within the gel pores.

our indentation modulus of LD C-S-H phase (see (5.27)), the hardness appears to deviate. Furthermore we associate the low modulus/hardness values of C-S-H with a low density phase which according to Jennings [130] does not appear to deviate in chemical composition (the only difference being porosity). Our results which show a fair degree of consistency between the three different specimens tested, are also consistent with previously obtained data, and will be further investigated in the following chapter, prior to drawing any conclusions. Finally, the cement paste hardness we obtain at Level II (see (5.26)) compares very well with microhardness results reported by Igarashi et al. [125] on a cement paste of $w/c = 0.5$; $H = 560$ MPa.

Volumetric Proportions

Measured data of the volumetric proportions of the different phases present in hcp are scarce, and most of the data available are based on semi-empirical chemical reaction models, as the ones presented in Section 4.5. In particular, to our knowledge only two models exist for the two-types of C-S-H: the Tennis and Jennings (J-T) model [227] and the one proposed by Bernard et al. [23]. Figure 5-21 displays the volumetric proportions of these two models for a $w/c = 0.5$ cement paste as a functions of the hydration degree. In order to compare our experimental volumetric proportions with the chemical reaction modeling results, we first need an estimate of the hydration degree of our hcp, which we obtain from the number of indentation results that display a higher indentation modulus than 50 GPa, and which are attributed to residual clinker phases. This provides a measure of the clinker volume fraction f_{cl} which with the help of the Powers model ($f_{cl} = (1 - \xi)\left(\frac{\rho_w/\rho_c}{w/c+\rho_w/\rho_c}\right)$) yields an estimate of the degree of hydration:

$$\xi \simeq \Xi\,(1 - f_r) = \begin{cases} 82\% & \text{N-1} \\ 94\% & \text{N-2} \\ 98\% & \text{N-3} \\ 94\% & \text{N-All} \end{cases} \tag{5.30}$$

Similar to the individual volume fraction, the hydration degree displays some variations from one surface to another, and we base our analysis on all three series, i.e. $\xi \simeq 94\%$. Use of this value in Figure 5-21, yields the following ratio of volume fractions of LD C-S-H vs. HD C-S-H for the two models:

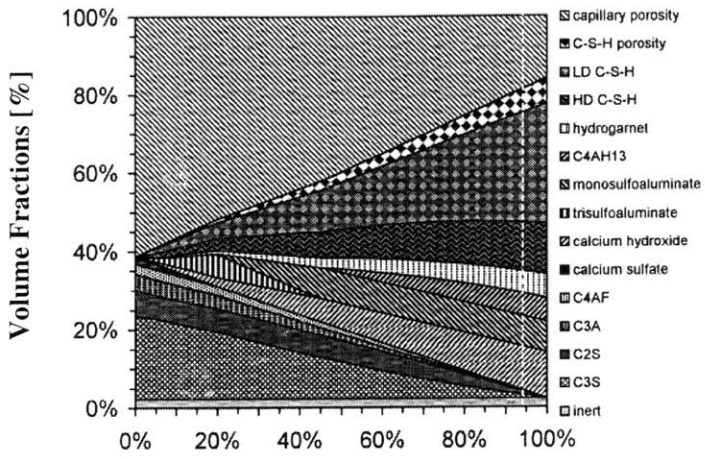

(a) **Hydration Degree [%]**

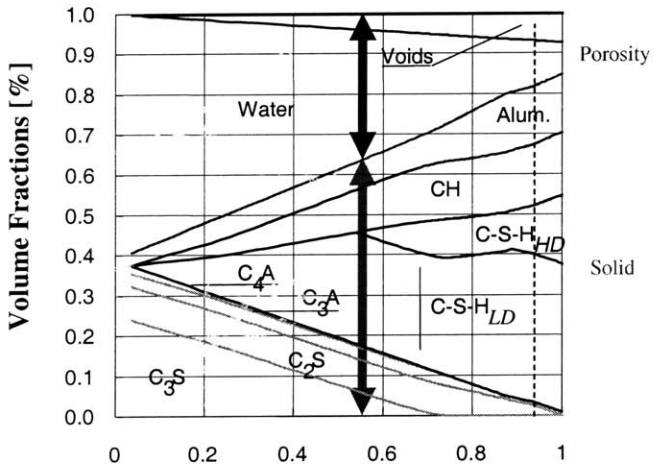

(b) **Hydration Degree [%]**

Figure 5-21: Volumetric proportions of cement paste constituents as predicted by the Jennings [130] (a) and Bernard *et al.* [23] (b) models.

$$\text{Models: } (\xi \simeq 0.94) = \left\{ \begin{array}{cccc} f_{LD}/f_{HD} & f_{LD} & f_{HD} & \text{Ref.} \\ & [\%] & [\%] & \\ 2.2 & 31 & 69 & [227] \\ 2.9 & 26 & 74 & [23] \end{array} \right. \tag{5.31}$$

These values compare reasonable well with the value we obtain with the grid-indentation technique:

$$\text{NI-tests: } = \left\{ \begin{array}{cccc} f_{LD}/f_{HD} & f_{LD} & f_{HD} & \\ & [\%] & [\%] & \\ 1.7 & 37 & 63 & \text{N-1} \\ 2.0 & 33 & 67 & \text{N-2} \\ 3.3 & 23 & 77 & \text{N-3} \\ 2.1 & 32 & 68 & \text{N-All} \end{array} \right. \tag{5.32}$$

One can go a step further and compare the volumetric proportions of the CH crystals present in the investigated microstructure with the one predicted in Fig. 5-21. The prediction of the chemistry models, however, include all hydration phases including the AFm and AFt phases produced in the hydration of the C_3A and C_4AF (see section 4.1), which makes a direct comparison difficult, as our deconvolution technique considers only 4 phases. In order to do so, we compare the relative CH volume normalised by the volume of C-S-H, $\frac{f_{CH}}{f_{CSH}}$. The experimentally found $\left(\frac{f_{CH}}{f_{CSH}}\right)^{\text{exp}} = 0.17 = 15/85$, and compares well with the model predictions: $\left(\frac{f_{CH}}{f_{CSH}}\right)^{J-T} = 0.21 = 17/83$ [227], $\left(\frac{f_{CH}}{f_{CSH}}\right)^{B} = 0.32 = 24/76$ [23]. Given the variability of these systems and the assumptions introduced in the chemistry models and the senstivity of the deconvolution technique one should not expect accuracies higher than 10-15%. Given the reasonable agreement between experiments and model estimates one can use the experimental data as first order approximations to the true volumetric proportions.

5.4.2 A Posteriori Check of Invariants

Before we conclude this chapter, we return to dimensional analysis. In particular we would like to address the question how far the dimensionless relations of continuum indentation analysis (see Sections 2.3.1 and 2.4.1) hold for heterogenous materials, i.e., the self-similarity relations

(3.36):

$$\frac{P}{Mh^2} = \Pi_\alpha\left(\frac{c}{M},\nu,\varphi,\theta\right) \tag{5.33a}$$

$$\frac{A_c}{h^2} = \Pi_\beta\left(\frac{c}{M},\nu,\varphi,\theta\right) \tag{5.33b}$$

The previous relations hold for each indentation test performed on a homogeneous material. If we indent on a heterogeneous material, each of the previous invariants should actually be a discrete random variable. Hence, for an indentation on a given phase the relations should be independent of the indentation depth (at least theoretically). Vice versa, if the invariants do show some scaling with the indentation depth, it is most likely that the separation of scale condition (5.1) is not satisfied, so that the indented material cannot be considered as homogeneous in an average sense. Therefore, an investigation of any possible scaling of the invariants should provide a means to verify or falsify the separation of scale condition, on which our continuum indentation analysis is based. In checking the scaling relationships, however, one needs to separate the different phases. There is *a priori* no theoretical argument that the invariants for each phase ($\Pi^i_\alpha, \Pi^i_\beta, \Pi^i_\gamma; i$ =MP, LD C-S-H, HD C-S-H, CH,CL) should have the same value. In fact, as relations (5.33) show, the actual value of Π_α and Π_β is a function of the mechanical properties of each phase ($\frac{c}{M},\nu,\varphi$) and of geometry effects (θ).

To analyze the indentation data, we will assume relevance of the Oliver and Pharr method to determine estimates of the indentation modulus and the hardness $(M,H)^{est}$. Using these estimates in (5.33), we determine estimates of Π_α and Π_β from:

$$\Pi^{est}_\alpha = \frac{P_{\max}}{M^{est}h^2_{\max}} \tag{5.34a}$$

$$\Pi^{est}_\beta = \frac{P_{\max}}{H^{est}h^2_{\max}} \tag{5.34b}$$

Figure 5-22 displays the invariants vs. indentation depth, $h_{\max}$, and identifies data for individual phases. It is useful to recall (see Eqs. (2.57) and (2.59)) that in the case of Berkovich indentation into a linear isotropic elastic half-space, the invariants are $\Pi^{el}_\alpha = 2/\pi\tan\theta = 1.78$ and $\Pi^{el}_\beta = 4/\pi\tan^2\theta = 9.95$. The Π^{est}_α values we obtain from our experiments are all somewhat smaller than the elastic values, except for the clinker phase (CL) which has Π^{est}_α values on the same

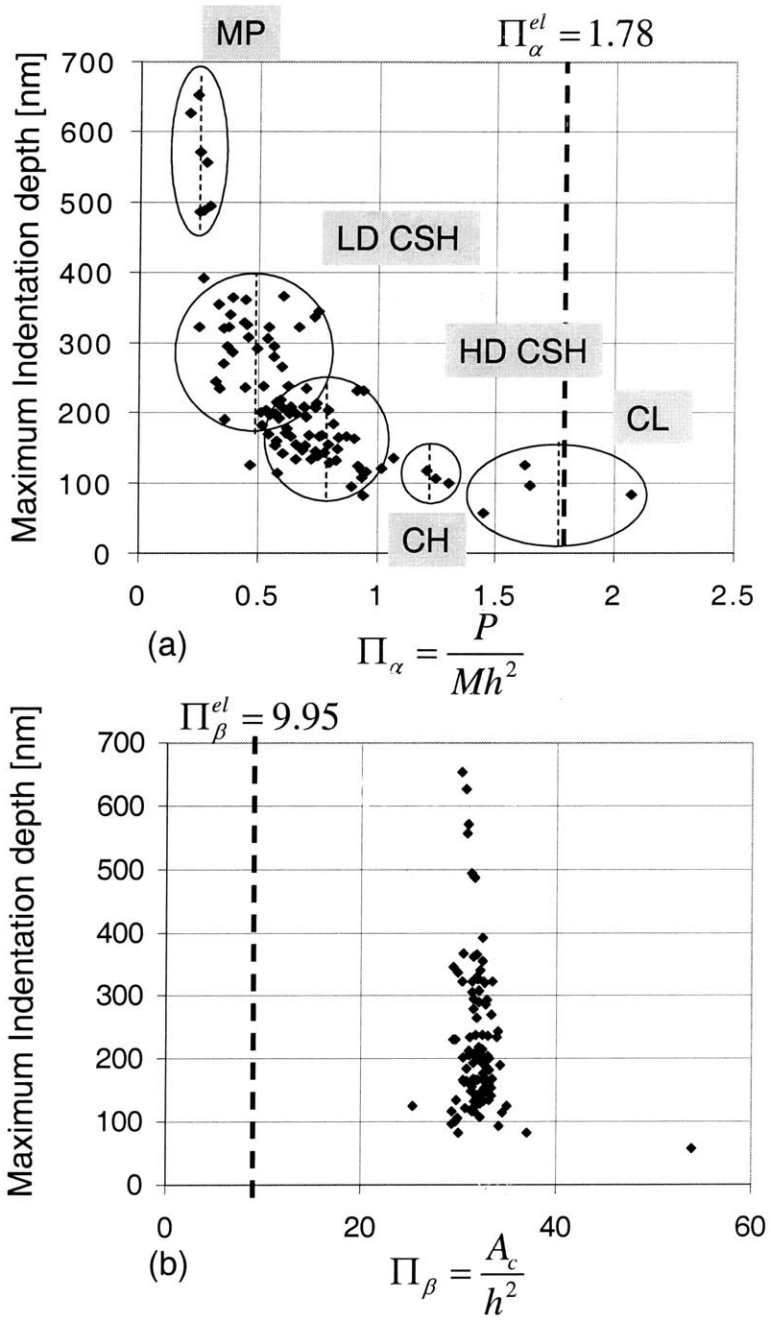

Figure 5-22: Scaling relations for indentation tests (N-1) on white cement paste. The inavariants $\Pi_\alpha^{est} = \frac{P_{\max}}{M^{est} h_{\max}^2}$ (a) and $\Pi_\beta^{est} = A_c/h_{\max}^2$ (b) are shown as a function of the maximum indentation depth.

order. Similarly, our Π_β^{est} values are significantly higher than than the elastic value. The most interesting observation is that Π_β^{est} has an extremely low standard deviation, and that the value Π_β takes for different phases and different indentation depths does not vary in large proportions, with an overall mean of 32.06 ± 2.64 (8.2%). This and the fact that $\Pi_\beta^{est} > \Pi_\beta^{el}$ suggest that the contact area is evolving in such a way to accommodate the plastic behavior underneath the indenter. Furthermore, recalling that $A_c/h_c^2 = 24.6$ for the ideal Berkovich indenter, the higher value of $\Pi_\beta^{est} = A_c/h_{\max}^2$ can be attributed to an imperfect indenter geometry which is captured in the experimental procedure through the calibrated area function (see Section 2.2.3). On the other hand, the values of Π_α vary quite significantly, ranging from $\Pi_\alpha^{est} \approx 0.25$ for the MP-phase to $\Pi_\alpha^{est} \approx 1.75$ for the CL-phase. In the light of Eq. (5.33a), it is most likely that this variation is a consequence of the dependence of Π_α on the cohesion-to-stiffness ratio, c/M. A means of quantifying this dependence of the heterogeneous indentation response is the indentation modulus-to-hardness ratio, estimated from $(M/H)^{est} = \Pi_\beta/\Pi_\alpha$ for the different phases, i:

$$(M/H)_i^{est} = \begin{cases} 56.9 & \text{MP} \\ 40.0 & \text{LD C-S-H} \\ 35.6 & \text{HD C-S-H} \\ 34.5 & \text{CH} \\ 14.5 & \text{CL} \end{cases} \tag{5.35}$$

Since Π_β is almost the same for all phases, M/H is a mere reflection of the variation of $1/\Pi_\alpha$. The values of $(M/H)^{est}$ for all phases are all greater than the elastic value, $(M/H)^{el} = 2\tan\theta = 5.59$. An interesting observation is that the mean M/H values of LD C-S-H, HD C-S-H and CH are very close to each other, while MP and CL tend to deviate significantly. Our value for CL, which was calculated based on the maximum values of hardness and indentation moduli found in our specimens (N−all)[6], $(M/H)^{est} = 14.5$, is very close to the one of pure clinker phases [239,2] (see Tab. 4.7 with $(M/H)_{C_3S} = 15.5$, $(M/H)_{C_2S} = 16.3$, $(M/H)_{C_3A} = 13.4$ and $(M/H)_{C_4AF} = 13.2$), which is a further validation of our indentation results. This provides *a posteriori* evidence that the proposed grid-indentation technique for heterogeneous materials

[6]The presence of the substrate can only reduce the indentation hardness and moduli evaluation. We therefore assume that the maximum value of hardness and moduli contains the least error among all $M \notin [0;50]$ GPa, $H \notin [0,1.5]$ GPa.

applied with a deliberately chosen indentation depth satisfies the separation of scale condition in Eq. (5.1), which is a pre-requisite for the application of continuum indentation analysis.

5.5 Chapter Summary

We have raised the question of how to adapt and employ indentation techniques for highly heterogeneous materials. The novel grid indentation technique we here propose has the premise to extend the domain of application of classical indentation techniques to multi-phase composite systems. The experimental basis of the method is a large series of indentation tests carried out on a surface. Each indentation test is a single statistical event, and the properties extracted from continuum indentation analysis, namely M and H, are considered as random variables. This requires a careful choice of the maximum indentation depth, which must be such not to interfere with microstructure[7]. In this chapter, we propose (1) to employ a thin-film analogy to determine the maximum indentation depth which ensures that effects of the heterogeneous microstructure are minimal; and (2) to check *a posteriori* relevance by means of a dimensional analysis of invariants. Based on this self-consistent method, it is possible to perform data modeling by means of some elementary statistical analysis, which allows one to determine mechanical phase properties, volume fractions and morphological arrangements. A further validation on another composite material is given in Appendix D.

The proposed grid-indentation technique is general and can be applied to any composite material system. The method offers new opportunities for materials research into the intrinsic behavior of heterogeneous materials. It is of particular interest for materials that cannot be produced in bulk quantities and when the in-situ mechanical properties of a phase is of interest. The ability of the technique to extract first order estimates of the volumetric proportions of each phases becomes of value when phases present in the composite have similar (or identical) chemical structure and cannot be decomposed by other techniques (e.g., X-ray or chemical analysis). Such a situation arises in many multiphase particulate materials systems in which

[7]Instrumented indentation equipment usually operate at load control environments and as a consequence the resulting maximum depth is a function of the imposed maximum load and the indented material's mechanical properties. Strictly speaking one needs to impose a restriction on the maximum allowable depth of indentation in order to avoid bias in our grid indentation technique. Such a function however is available only in some of the commercially available indenters.

		M	H	f	M/H
		[GPa]	[GPa]	[%]	[1]
LEVEL I	Macroporosity	9.1 ± 2.3	0.16 ± 0.07	8	56.9
	LD C-S-H	18.8 ± 4.0	0.47 ± 0.17	51	40.0
	HD C-S-H	31.0 ± 4.0	0.87 ± 0.08	25	35.6
	CH	41.0 ± 3.9	1.19 ± 0.16	13	34.5
	*CL	148 ± 7	8.7 ± 1	3	14.5
LEVEL II	Cement Paste	21.6 ± 3.2	0.515 ± 0.07	100	41.9

Table 5.7: Summary of grid indentation results for two different levels (I and II) obtained after statistical analysis of the frequency diagrams: Indentation Modulus, Hardness, Volume fractions, and Modulus to Hardness ratios for all constituent phases.*Values for C_3S, from Ref. [239].

the difference between phases (in a mechanical sense) is primarily driven by density (packing density, porosity, etc.) rather than by chemical composition.

The main component of all cementitious system, the C-S-H phase, is an example of such a material. This C-S-H manifests itself in (at least) two different forms of similar (or even identical) chemical composition, but different density. Since it is still difficult to control the density during manufacturing, the proposed indentation method is currently the only available technique to rigorously investigate the mechanical properties of the different C-S-H phases. The application of the grid indentation technique to a white cement paste illustrates the robustness of the technique, which provides access to material properties, that do not change from one cement-based material to another as a function of mix proportions. Instead, they are intrinsic material (invariant) properties. These values are summarized in Tab. 5.7.

Chapter 6

Multi-scale Mechanical Performance of CBM: Effect of Moderate Heat Application (60°C) on C-S-H

The focus of this chapter is the investigation of the effect of moderate heat application (60°C) on the mechanical behavior of cement-based materials. The multi-scale structure presented in Chapter 4, and the grid indentation technique developed in Chapter 5 provide a convenient framework for such an investigation. Moderate temperature applications applied at an early stage of hydration (heat curing)[1] can significantly accelerate the mechanical properties development and reduce the deformation capacity of the system. It has been found however that this early age benefits are counterbalanced by a long term loss in strength and an increase in permeability. Later experiments have shown that this problem can be suppressed by applying heat at a later stage of the hydration (heat treatment). While both techniques—heat curing and heat treatment—are commonly employed in practice, little is known about the actual mechanisms that control this macroscopically observed behavior. We therefore aim in this chapter to utilize the nanomechanical exploration equipment (nanoindentation) together with advanced analysis techniques (grid indentation) in order to monitor the multi-scale evolution processes associated

[1] By heat curing we define the curing of specimens at elevated temperature (here 60 °C); in contrast to a heat treatment, which refers to the exposure of specimens to short temperature cycles at a hardened state.

with moderate heat application to cement-based materials. In particular we focus our discussion on two levels: 1) At Level II, we measure the macroscopic effect by doing microindentations; 2) At Level I, we attempt to identify the sources of such a macroscopic response by measuring the mechanical behavior of the material invariant properties identified in Chapter 5 and the microstructural evolution that the heat application induces. Special emphasis is placed on the two types of C-S-H (Level I) where most changes are expected to take place and where little is known regarding structure and mechanical properties.

Temperature applications coupled with a reduced $w/c-$ratio can provide a material with enhanced mechanical properties, $E \simeq 50\text{GPa}$ and $\Sigma_c \simeq 190\text{MPa}$, and reduced deformation potential [257]. There are some fundamental questions remaining however: What is the impact of these variables on the microstructure of cement paste and in particular on the C-S-H phases? Is the fundamental chemical formation changing? and are there ways to improve the behavior even more? Results presented in this chapter aim at providing answers to these questions and hopefully contribute to the better understanding of this complicate mechanical system.

6.1 Heat Curing and Heat Treatment

Cement chemistry research has established that heat curing of cementitious materials at early ages coarsens the capillary pore system, decreases the volume of mesopores, and increases the degree of polymerization of the silicates. Evidence for a coarser pore structure has been provided by Bentur using mercury porosimetry and H_2O and N_2 adsorption [21]. These results were confirmed and refined since by various techniques, ranging from backscattered electrons in scanning electron microscopy [138, 79], impedance spectroscopy measuring electrical conductivity [76], and systematic studies of the pore-size distribution using methanol exchange technique and weight-loss measurement on drying [230]. The increase of the degree of polymerization with time and temperature has been shown by Silicon-29 Nuclear Magnetic Resonance Spectroscopy [251, 126].

The general interest in the behavior of heat cured cementitious materials stems from the use of high-temperature curing in concrete technology for obtaining both a high early-strength (see Fig. 6-1) and a significant decrease of time dependent deformation (creep and shrinkage),

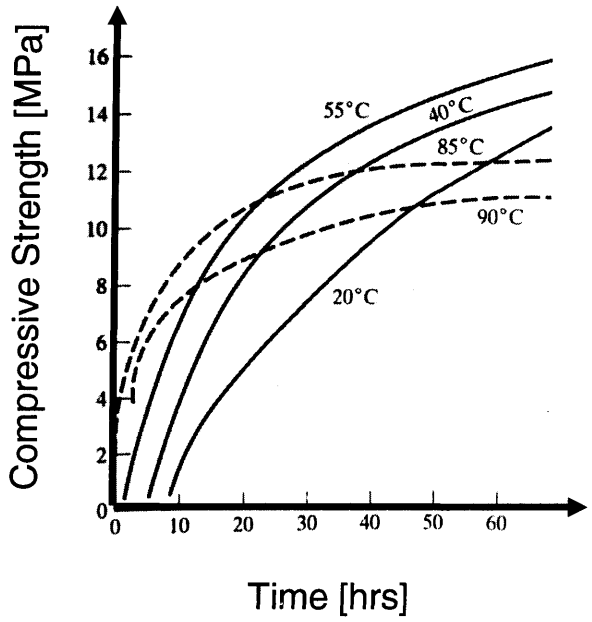

Figure 6-1: Strength developement of normal cement paste with time for different curing temperatures (adapted from [169]).

particularly in the precast concrete industry. However, it was quickly recognized that long-term properties are often negatively influenced by elevated curing temperature, as strength and other mechanical properties are often reduced and permeability increased [21, 79]. This paradoxical behavior has not been explained satisfactorily. In fact, it is still not clear at which scale and to which extent an increase of the degree of polymerization affects the mechanical performance, and to which extent this densification of the C-S-H is cancelled out by the coarsening of the capillary porosity, and how both phenomena contribute to the overall macroscopic mechanical behavior: loss in long-term strength behavior and decreased creep and shrinkage behavior.

The experimental data presented above indicate that the temperature application favors the densification of the C-S-H matrix and produces material with improved time dependent deformation. Heat curing, however, suffers from the drawback of macroporosity generation that impacts on the macroscopic strength (see Fig. 6-1). To overcome this problem, it is common

practice in industry to apply heat at later stages of hydration (heat treatment) such that the improved creep performance is obtained without the generation of macroporosity (since most of the reaction has taken place prior to heat application). It has been experimentally found that heat treatment significantly improves creep and shrinkage behavior while the degree of polymerization increases. Interestingly, those benefits were not associated with a reduction in strength and increase in permeability as observed for the heat cured specimens [187]. Delayed heating is of interest for several reasons:

- Heat treatment is commonly applied in ultra high performance concrete (UHPC) as means of improving shrinkage and creep performance bypassing at the same time the consequences associated with heat curing.
- There are several specialized structures (nuclear reactors, batching plants, chimneys etc.) in practice that are occasionally exposed to moderate temperatures after construction, and it is important to know the effect of heat cycles on their mechanical behavior.
- Fundamentally, it is of scientific interest to find out whether the main hydration product, C-S-H, can be converted after formation to yield a material with a reduced deformation potential.

The mechanical behavior of heat cured and heat treated specimens is not yet clear. While both techniques are commonly employed in the industry, there is still a fundamental understanding lacking about the physical mechanisms associated with these processes. It is readily understood that our current lack of knowledge stems from the fact that the different phenomena observed experimentally manifest themselves at different scales: the degree of polymerization relates to the C-S-H which manifests itself at a characteristic length-scale of some tens of nanometer (Level 0); while the mesoporosity of gel-porosity relates to the morphology of the C-S-H at a characteristic length scale of 100 nm (Level I); and the macroporosity at a scale of micrometers (Level II). Therefore, explaining this paradoxical behavior of thermally cured/treated cement-based materials calls for a multiscale investigation of the mechanical nano-, micro- and macro-properties. This will be achieved here by means of the multi-scale model proposed in Chapter 4 and grid indentation technique developed in Chapter 5.

6.1.1 Materials and Methods

The cement paste investigated in this study is the same as that tested in Chapter 5 for the validation of the grid indentation technique (also the same as that tested by Thomas and Jennings for weight-loss experiments) [230]: White portland cement with a low aluminates content (US Gypsum Co., Chicago, IL, cement composition given in Tab. 5.3) was cast into plastic molds at a water/cement ratio of $w/c = 0.4$ and 0.5, to form bars measuring $0.25\,\mathrm{m} \times 0.025\,\mathrm{m} \times 0.025\,\mathrm{m}$. The paste was hydrated under limewater at room temperature (Control specimen, labeled 'C'), and at a temperature of 60 °C for different times: 1 day (Heat-cured specimen, labeled 'HC-1'), and continuously for 28 days (Heat-cured specimen, labeled 'HC-28'). A certain batch of the control specimens were also subjected to a 60 °C temperature for 24 hours at the age of 28 days (Heat Treated-'HT') and then continued hydration at room temperature. The heat curing and heat treatment were performed using the procedure described in [230]: specimens were placed into a programmable water bath of limewater, and the temperature was controlled using a thermometer placed next to the specimens. The maximum temperature of 60 °C was chosen to avoid secondary high- temperature reactions, such as the decomposition of Ettringite into monosulfate, which would hamper interpretation of the results. After the heat curing/treatment, the specimens were cooled to room temperature under sealed conditions, and kept in limewater until testing. The tested specimens, w/c–ratio, age at testing, and indentation details are reported in Tab. 6.1.

6.2 Indentation Results

The four-level microstructure of cement-based materials displayed in Fig. 4-13 forms much of the backbone of our investigation of heat-cured and normal cement-based materials. Levels I and II, which is the length scale of the C-S-H matrix and of the cement paste, respectively, are the focus of the experimental investigation of the mechanical properties by means of nano- and microindentation. Level 0, which is the scale of the C-S-H solid phase, will be included in the discussion. Level III which is the scale of mortar and concrete, will not be considered in this investigation.

Indentation tests were load-controlled: a trapezoidal load was applied, 10-5-10 s (see Section

Specimen	Control ('C')	'HC-1'	'HC-28'	'HT'
w/c [1]	0.5	0.4	0.5	0.5
Duration [d]	0	1	28	1
Age [mth]	5	17	5	4
Nano-Tests #	3×100	2×100	2×100	2×100
$P_{\max}$ [μN]	468.11 ± 23.22	470.43 ± 15.18	469.86 ± 20.42	471.01 ± 14.14
$h_{\max}$ [μN]	217.71 ± 143.40	194.82 ± 92.97	204.85 ± 125.03	190.78 ± 91.27
S [$\frac{\mu N}{nm}$]	25.06 ± 7.25	25.14 ± 7.13	27.36 ± 8.19	24.32 ± 6.75
Micro-Tests #	10	10	30	10
$P_{\max}$ [μN]	$996,180 \pm 6,200$	$998,116 \pm 1,699$	$997,955 \pm 1,637$	$997,153 \pm 2,134$
$h_{\max}$ [nm]	$9,873.41 \pm 678.23$	$8220,135 \pm 694.81$	$8,793.89 \pm 610.99$	$9,863.38 \pm 698.12$
S [$\frac{\mu N}{nm}$]	965.91 ± 32.40	854.19 ± 16.49	$1,118.20 \pm 58.83$	961.11 ± 42.19

Table 6.1: Specimen description and experimental program. Control specimen was cured at 20°C. Heat curing temperature was 60°C. After heat-curing specimens were kept at 20°C. Micro-Tests refer to microindentation tests operated with a maximum indentation depth of 10×10^{-6} m, Nano-Tests refer to nanoindentation tests operated with a maximum indentation depth of 200 nm. Machines: (*) MM = MicroMaterials, (**) HYS = Hysitron.

5.3.1 and Table 5.4). The hardness and indentation moduli were extracted from the material response based on the analysis tools presented in Chapter 5.

6.2.1 Level I: C-S-H properties and microstructural evolution

We recall that Level I is the scale of the C-S-H matrix of a characteristic size on the order of 10^{-6} m. Results presented in Chapter 4 and 5 suggest that the C-S-H manifests itself in (at least) two different forms: in what follows we adopt Jennings [130] interpretation of a low-density phase (LD) and a high-density phase (HD). According to Jennings [130], that what distinguishes these two phases is the gel porosity of 24% for HD C-S-H, and 37% for LD C-S-H. The gel porosity has a characteristic dimension $\leq 10^{-8}$ m, so that an indentation test that captures the composite behavior of the two types of C-S-H must be on the order of $h \geq 10^{-7}$ m. Following our discussion in Section 5.3.1 and results obtained in Refs. [2, 58, 60], a maximum penetration depth of 200 nm was chosen in the present nanoindentation campaign. 200 to 300 nanoindentation tests (see Tab. 6.1) were programmed for each specimen with a grid-size of 10^{-5} m so to avoid interference in between single indents (see Fig. 5-5). The results are analyzed in terms of frequency diagrams of the mechanical properties and in terms of mechanical maps as discussed in Section 5.3.

			MP	LD C-S-H	HD C-S-H	CH	CL
Control ('C')	M	[GPa]	9.1 ± 2.3	18.8 ± 4.0	31.0 ± 4.0	41.0 ± 3.9	–
	$\left(\frac{s}{\mu}\right)$	[%]	25	21	13	10	–
	f	[%]	8	51	25	13	3
'HC-1'	M	[GPa]	4.0 ± 5.4	17.8 ± 4.3	29.8 ± 2.3	41.1 ± 2.7	–
	$\left(\frac{s}{\mu}\right)$	[%]	134	24	8	6	–
	f	[%]	2	50	29	10	9
'HC-28'	M	[GPa]	5.2 ± 5.0	18.0 ± 3.1	28.5 ± 2.62	36.0 ± 3.5	–
	$\left(\frac{s}{\mu}\right)$	[%]	96	17	9	10	–
	f	[%]	16	28	31	20	5
'HT'	M	[GPa]	9.9 ± 2.5	18.3 ± 3.8	29.1 ± 5.3	44.9 ± 5.9	–
	$\left(\frac{s}{\mu}\right)$	[%]	25	21	18	13	–
	f	[%]	6	48	30	12	3

Table 6.2: Nanoindentation results: Indentation stiffness and volume fractions obtained from a statistical analysis of the frequency plots and cumulative distribution. The maximum indentation depth was 200 nm.

Frequency Plots of Nanoindentation Stiffness

In addition to the frequency plot for the control specimen ('C') in Fig. 5-16, Figs. 6-2 to 6-4 display frequency plots of the nanoindentation stiffness for the 1 day heat cured specimen ('HC-1', Fig. 6-2), the 28 day heat cured specimen ('HC-28', Fig. 6-3), and the 1-day heat treated specimen ('HT', Fig. 6-4). The frequency diagrams were prepared based on the methodology described in Section 5.2.2, and the fitting procedure followed the technique developed in Section 5.3.2. Consistent with trends observed in Chapter 5, the figures display a clear multi-modal distribution of the mechanical properties, and each peak corresponds to the mechanical manifestation of a chemical-morphological unit present in the microstructure. The intensity of each mechanical manifestation is representative of the intrinsic property of the phase: These are the macro-porosity, the LD C-S-H, the HD C-S-H, and Portlandite (CH) and residual clinker phases (CL). The global experimental curves in Figs. 6-2 to 6-4 were treated in similar fashion as in Section 5.3.2 which makes it easy to determine graphically (from a combination of the frequency plot and the best fitted Gaussian distributions) the intrinsic properties of the different phases, their standard deviations, and their volume fractions. These values are summarized in Tab. 6.2:

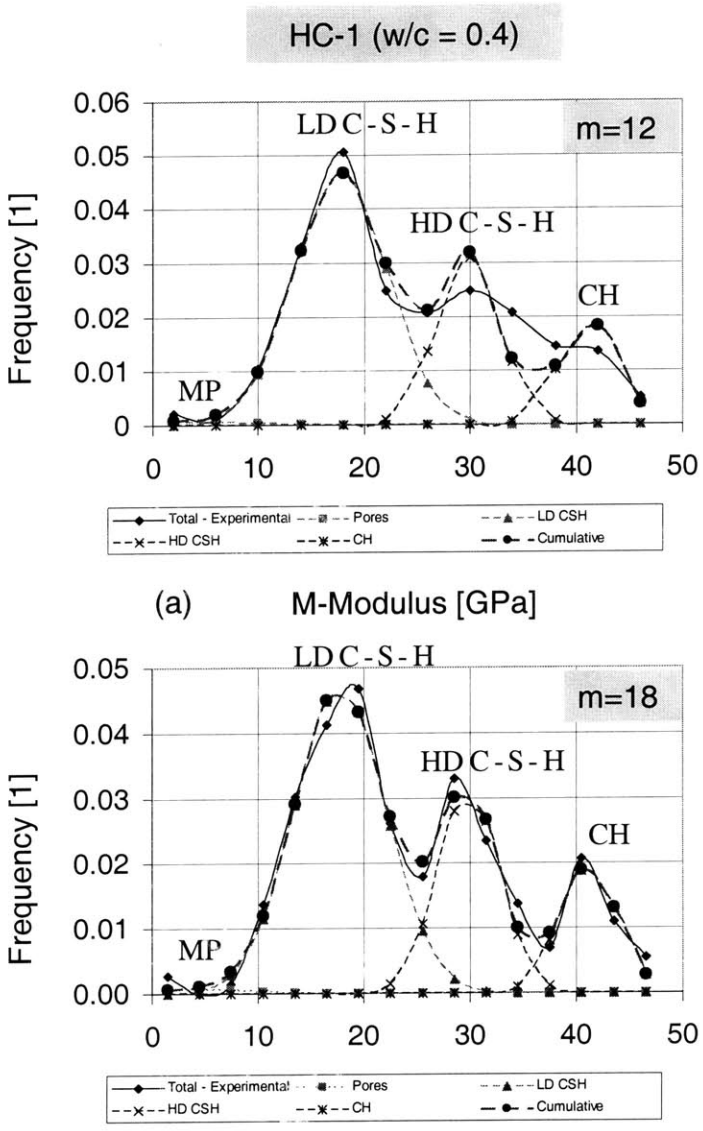

Figure 6-2: One-day heat cured specimen 'HC-1' ($w/c = 0.4$): Frequency plot of indentation modulus determined by grid nanoindentation (No. of tests = 200).

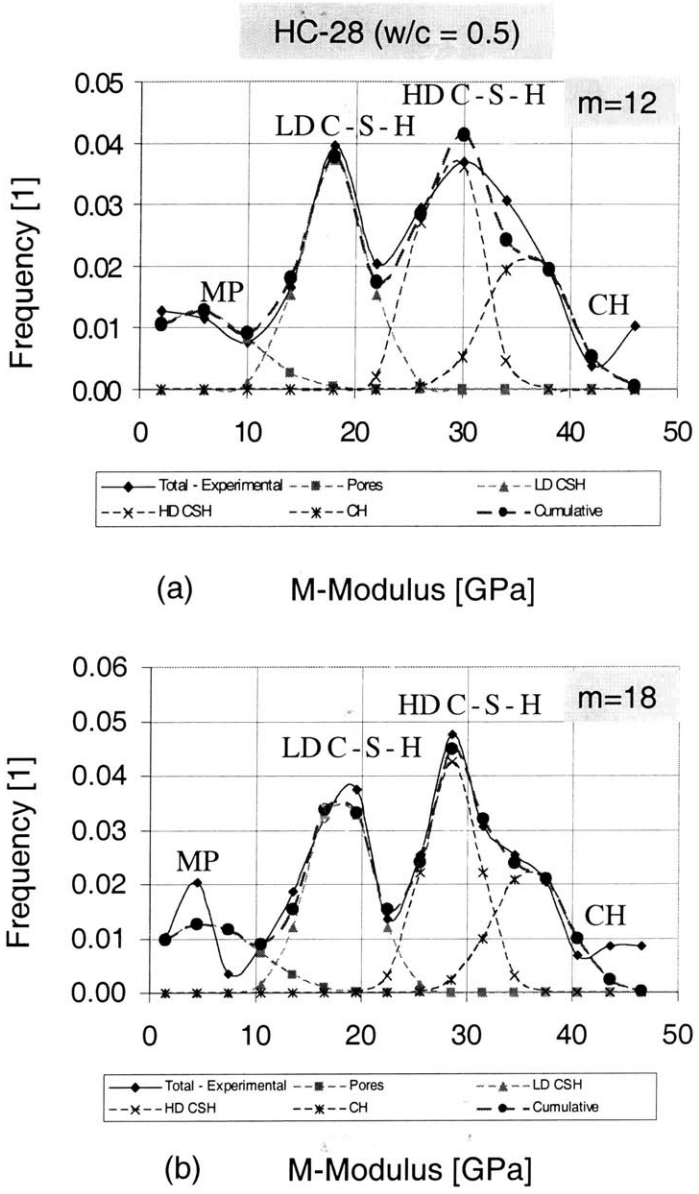

Figure 6-3: 28-day heat cured specimen 'HC-28' ($w/c = 0.5$): Frequency plot of indentation modulus determined by grid nanoindentation (No. of tests = 200).

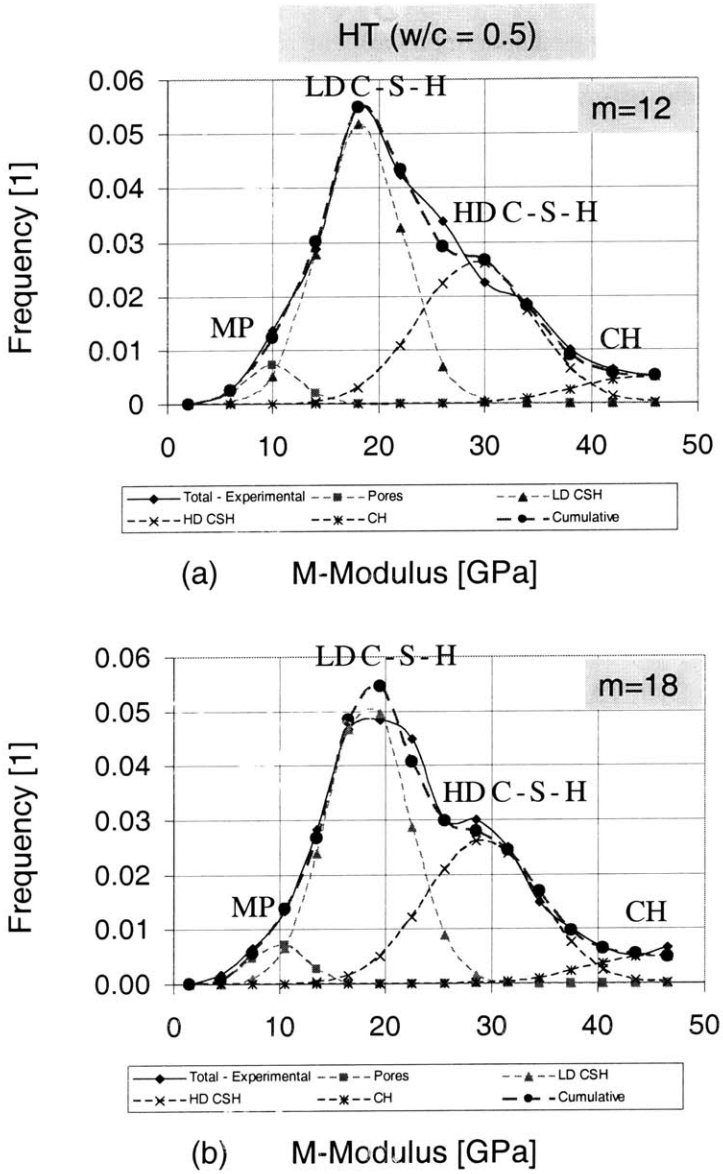

Figure 6-4: One-day heat treated specimen 'HT' ($w/c = 0.5$): Frequency plot of indentation modulus determined by grid nanoindentation (No. of tests = 200).

Mean Values and Intrinsic Properties The indentation modulus of the LD C-S-H and HD C-S-H remains almost unaffected by the thermal curing and treatment: the LD C-S-H reduces only slightly for the heat cured specimens (HC-1 and HC-28) compared with the control specimen, while the heat treated specimens appear to remain virtually unchanged. The relative changes in mechanical properties are much smaller than the standard deviations and should not be considered statistically representative. Same trends are observed for the HD C-S-H: Heat curing application shifts slightly the indentation modulus ($M_{HD} = 31.0$ GPa for the control specimen to $M_{HD} = 29.8$ GPa, $M_{HD} = 28.5$ GPa for the 1-day and 28-day thermally cured specimens. Similarly, the heat treatment process has no statistically significant effect on the elasticity, $M_{HD} = 29.1$ GPa compared to $M_{HD} = 31.0$ GPa for the control (no heat treatment). It therefore appears that the application of moderate heat has little if any effect on the elastic moduli of the individual chemical phases. Furthermore, these values are in excellent agreement with previous reported results obtained on other cementitious materials; see discussion in Section 5.4. The excellent agreement seems to confirm that the determined stiffness values of the two C-S-H phases are independent not only of the mix proportions ('HC-1' [$w/c = 0.4$] and DUCTAL^{TM} [$w/c = 0.2$]), but most likely as well of the thermal curing ('HC-1' and 'HC-28') in the considered temperature range and of thermal treatment ('HT' and DUCTAL^{TM}). Instead, these properties are intrinsic to the formation process of the C-S-H phases. Finally the elastic properties of the Portlandite phases appear to remain unaffected by the application of these moderate heat conditions (Tab. 6.2).

Relative Volumetric Proportions In fact, thermal curing induces changes in the volumetric proportions of the different phases:

$$f = \left\{ \begin{array}{cccc|l} \text{C} & \text{HC-1} & \text{HC-28} & \text{HT} & \\ \text{[\%]} & \text{[\%]} & \text{[\%]} & \text{[\%]} & \\ 8 & 2 & 16 & 6 & \text{Macropores} \\ 51 & 50 & 28 & 48 & \text{LD C-S-H} \\ 25 & 29 & 31 & 30 & \text{HD C-S-H} \\ 13 & 10 & 20 & 13 & \text{CH} \\ 3 & 9 & 5 & 3 & \text{CL} \end{array} \right. \tag{6.1}$$

1. The heat curing appears to favor the formation of HD C-S-H. The relative proportion of LD-to-HD C-S-H shifts from $51/25 = 2.0$ in the control specimen to $50/29 = 1.7$ in the 1-day heat cured specimen ('HC-1') and $28/31 = 0.9$ in the 28-day heat cured specimen ('HC-28'). Heat curing, therefore, appears to be associated with a densification of the C-S-H matrix at Level I. This densification is a function of the heat curing duration, with prolonged 60°C hydrations to favor higher densifications. In return, this densification of the matrix appears to occur at the expense of an increase in porosity at the considered scale. If we attribute an indentation stiffness ($0 - 13$ MPa) to a nanoindentation into a bulk phase dominated by this macroporosity, the volume fraction obtained from the fitting of the Gaussian distribution in Figs. 6-2 to 6-4 increases from 8% for the control specimen, 'C',to 16% for the 28 heat cured specimen, 'HC-28'. Any possible increase of macroporosity for the HC-1 specimen might have been obscured by the reduced initial $w/c-$ratio which tends to reduce the total porosity (see Section 4.5). Given the $w/c-$ratio of the 1-day heat cured specimen, $w/c = 0.4 < 0.42$, one should expect little to no capillary porosity in this material. The fact that a small proportion of macroporosity exists (2%) in the 1-day heat cured specimen suggests that there is a certain degree of macroporosity generated in response to C-S-H densification.

2. On the other hand, the volumetric proportions of the C-S-Hs remain almost unaffected when heat is applied at a hardened state (heat treatment). The ratio of the LD to HD C-S-H for the heat treated specimen, $48/30 = 1.6$ is only slightly reduced (control, $51/25 = 2.0$). This comes to suggest that the formation of HD C-S-H under moderate temperature conditions is favoured at the early stages of hydration where the physicochemical environment together with the 60°C temperature application promote the formation of a HD C-S-H form. It is a HD C-S-H formation that takes place in heat cured specimens, rather than a LD to HD conversion.

3. A further result that is evident from the frequency plots is a change in volume fraction of a high stiffness phase $M \geq 50$ GPa. This phase corresponds to residual clinker phases (X = C_3S, C_2S, C_3A, C_4AF), which have been reported to have nanoindentation stiffness values of $M_X > 125$ GPa [2, 239]; see Tab. 4.7. As it was discussed in Chapter 5, due

to the high contrast between the moduli of clinker phases and the substrate (C-S-H) the scaling conditions (5.33a) are almost never satisfied, resulting in indentation moduli in the range anywhere from $50 - 140$GPa. Provided that there is enough contrast for those phases to be separated in the frequency plots, this phenomenon poses no restriction on the grid indentation analysis. The values obtained however represent the clinker-substrate composite response and should be treated with caution. The volume fraction of the clinker phases seems to remain relatively unaffected by the heat curing process. We recall however that the activation energy of the hydration reaction is around 400 J/g thus moderate temperatures during curing can significantly accelerate hydration. If one could consider the mechanical properties of the residual clinker phases at the early stages of hydration, a more significant deviation would have been expected: The heat cured specimens are expected to have a significantly lower volume of clinker phases, as the accelerated degree of hydration would have consumed their largest volumetric percentage. It should be emphasized, however, that the accelerated rate of reaction is particularly evident at the early stages, where the rate determining step is a chemical reaction and therefore up to 1-2 days the reactions have normal temperature dependency. At later timepoints, the rate-determining step is diffusion which is less sensitive to temperature, and as a result the deviation in degree of hydration tends to decrease. The large values of residual clinkers observed in the case of the HC-1 specimen ($f_{cl} = 0.09$) can be attributed to the reduced $w/c-$ratio used for that specimen and probably the younger age (see Tab. 6.1). Finally a comment is due on the volumetric proportions of Portlandite crystals: In general the CH content scales with the degree of hydration for a given CBM system (see Eq. (4.5) in Section 4.1). While such a relationship is evident from the experimental data obtained from our indentation analysis, the high percentage of CH for the HC-28 specimen is more significant than the others. This suggests that heat curing promotes a higher volumetric proportion of CH phases present at Level II, in the form of large crystals.

Mapping of Nanoindentation Stiffness

As it was proposed in Chapter 5, a second way of analyzing the grid indentation results consists in mapping the mechanical properties obtained during nanoindentation. Each indentation result

is assigned to a point on the grid that corresponds to the center of the indent. The discrete data points are linearly interpolated in between grid points to obtain continuous fields of mechanical properties, with a resolution defined by the grid spacing of 10^{-5} m. The results are displayed on the $x - y$ plane in form of contour plots that capture ranges of mechanical properties. We briefly recall the scheme used in the mapping procedure (see Section 5.3.2):

1. Macroporosity domain $0 - 13$ GPa
2. Low-Density C-S-H domain $13 - 26$ GPa
3. High-Density C-S-H domain $26 - 39$ GPa
4. Unhydrated clinker and CH domain ≥ 40

Figures 6-5 to 6-8 display each the results of two maps of 100 nanoindentation results for the control specimen ('C' – Figs. 6-5), the 1-day heat cured specimen ('HC-1' – Figs. 6-6), the 28-day heat cured specimen ('HC-28' – Figs. 6-7), and the 1-day heat treated specimen ('HT' - Figs. 6-8). The contour plots substantiate the analysis of the frequency plots: they highlight the creation of a new pore class as a consequence of the heat curing (Figs. 6-6 and 6-7), and provide evidence of a substantial change of percolation of the C-S-H phases (Figs. 6-6 and 6-7):

- *Heat curing creates macroporosity:* While almost absent in the control specimen 'C' (a single point in Fig. 6-5 represents rather a statistical event than a morphological pattern), the macroporosity domain becomes an identifiable morphological pattern in the maps of the 1-day and 28-days heat cured specimens (Figs. 6-6 and 6-7), in which the macropores occupy regions several times the grid spacing of 10^{-5} m.
- *Heat curing changes the morphology:* In the control specimen (Figs. 6-5), the continuous (percolated) solid phase appears to be the LD C-S-H, which forms a matrix that accommodates residual clinker phase encapsulated into a rim of HD C-S-H. By contrast, in the heat cured specimens (Figs. 6-6 and 6-7), there is a larger proportion of HD C-S-H present which tends to percolate throughout the microstructure, while the LD C-S-H appears to be disconnected and situated around the large macropores. It almost appears as if the HD C-S-H forms a continuous matrix that accommodates the macroporosity encapsulated into a rim of LD C-S-H.

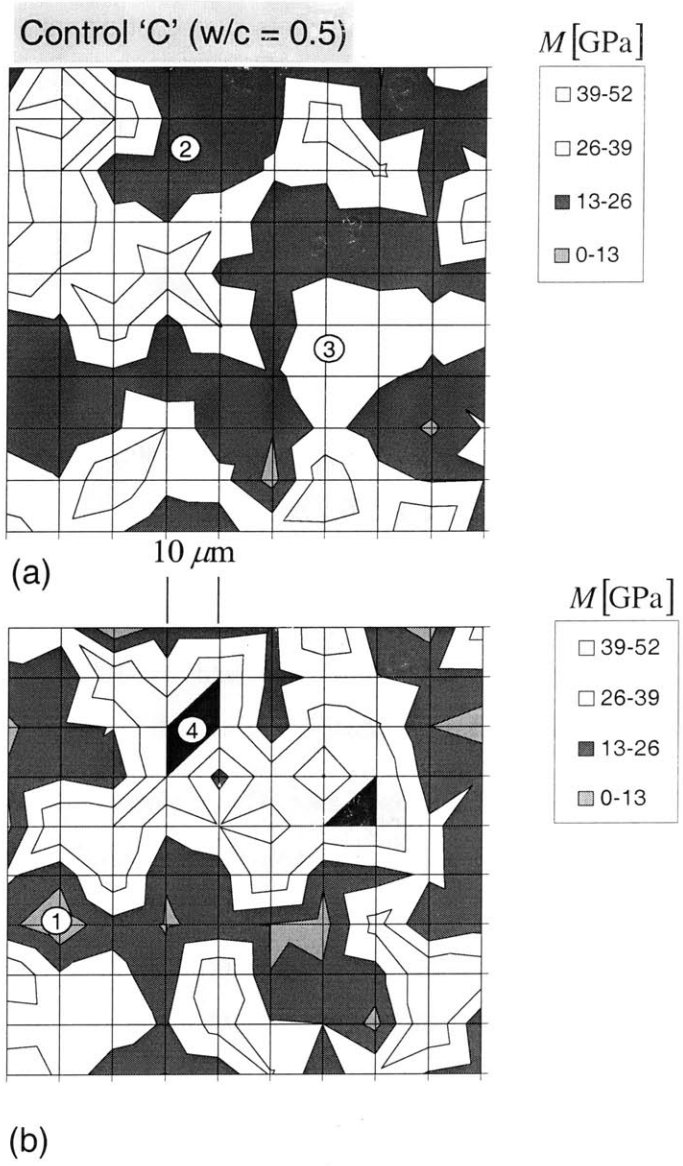

Figure 6-5: Control specimen 'C' ($w/c = 0.5$): Contour plots of the spatial distribution of stiffness (in GPa) in the microstructure obtained by grid nanoindentation (grid spacing = 10^{-5} m). Each grid point corresponds to a single nanoindentation test (unloading from a maximum indentation depth of 3×10^{-7} m). The two figures display the spatial variability that one may expect using this novel technique of 'mechanical mapping'. The numbers in the figure are attributed to 1 = porosity, 2 = LD C-S-H, 3 = HD C-S-H, 4 = CH and clinker phases.

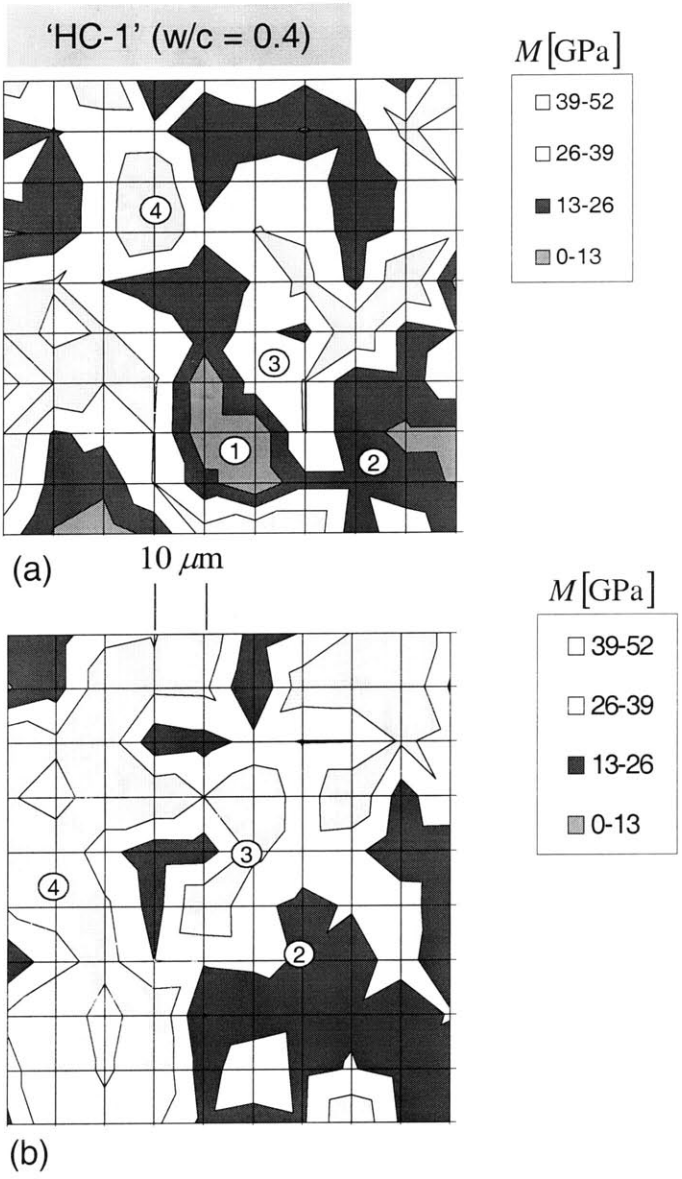

Figure 6-6: One-day heat cured specimen 'HC-1' ($w/c = 0.4$): Contour plots of the spatial distribution of stiffness (in GPa) in the microstructure obtained by grid nanoindentation (grid spacing = 10^{-5} m). Each grid point corresponds to a single nanoindentation test (unloading from a maximum indentation depth of 3×10^{-7} m). The numbers in the figure are attributed to 1 = porosity, 2 = LD C-S-H, 3 = HD C-S-H, 4 = CH and clinker phases.

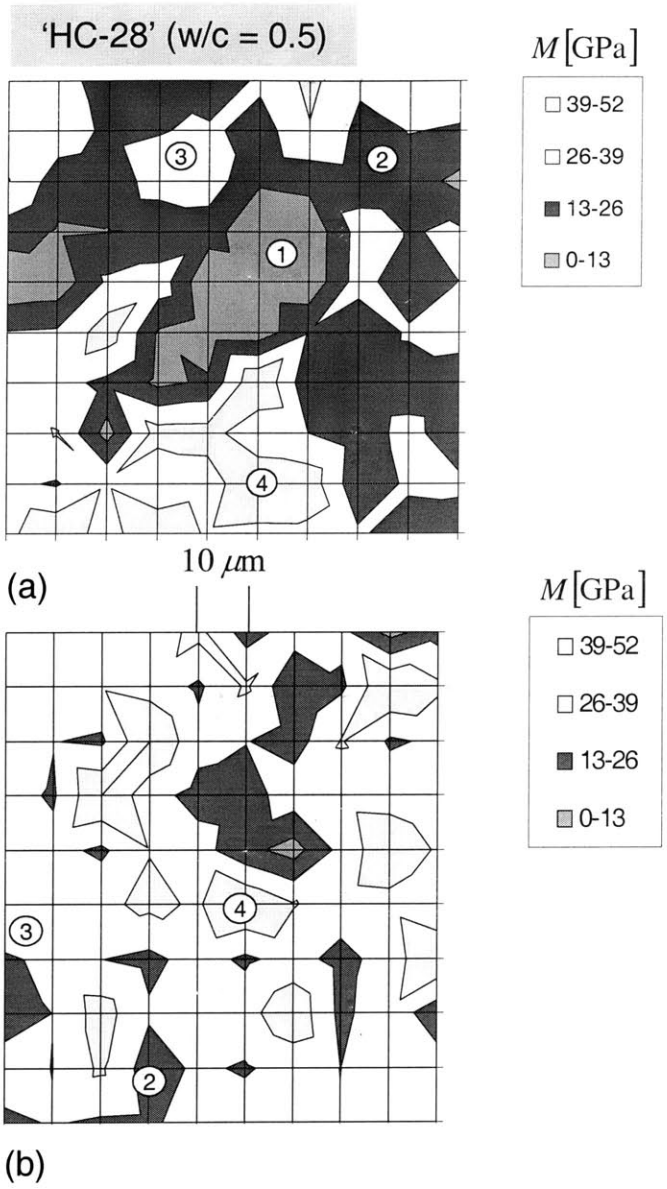

Figure 6-7: 28-day heat cured specimen 'HC-28' ($w/c = 0.5$): Contour plots of the spatial distribution of stiffness (in GPa) in the microstructure obtained by grid nanoindentation (grid spacing $= 10^{-5}$ m). Each grid point corresponds to a single nanoindentation test (unloading from a maximum indentation depth of 3×10^{-7} m). The two figures show the creation of a large concentrated macroporosity (a) and the percolation of the HD-C-S-H phase (b) in the microstructure. The numbers in the figures are attributed to 1 = porosity, 2 = LD C-S-H, 3 = HD C-S-H, 4 = CH and clinker phases.

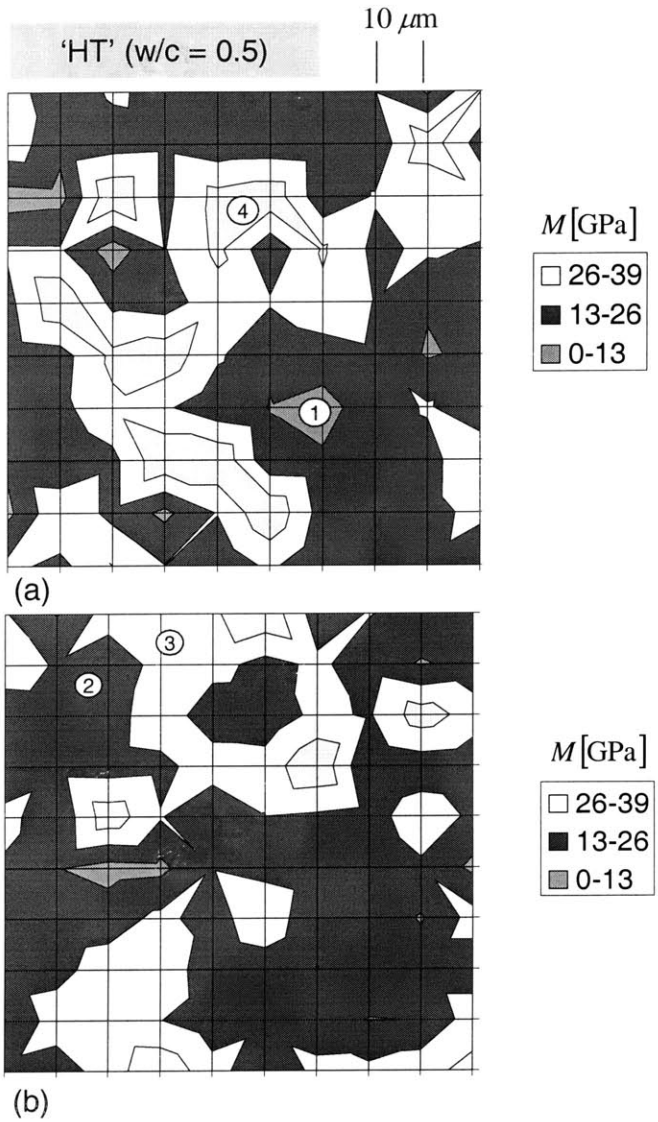

Figure 6-8: One-day heat treated specimen 'HT' ($w/c = 0.5$): Contour plots of the spatial distribution of stiffness (in GPa) in the microstructure obtained by grid nanoindentation (grid spacing = 10^{-5} m). Each grid point corresponds to a single nanoindentation test (unloading from a maximum indentation depth of 3×10^{-7} m). The numbers in the figure are attributed to 1 = porosity, 2 = LD-C-S-H, 3 = HD-C-S-H, 4 = CH and clinker phases.

			MP	LD C – S – H	HD C – S – H	CH
Control'C'	H	$[GPa]$	0.16 ± 0.07	0.47 ± 0.17	0.87 ± 0.08	1.19 ± 0.16
	$\left(\frac{s}{\mu}\right)$	[%]	43	36	9	14
'HC – 1'	H	$[GPa]$	0.14 ± 0.07	0.47 ± 0.15	0.85 ± 0.07	1.20 ± 0.22
	$\left(\frac{s}{\mu}\right)$	[%]	50	32	8	18
'HC – 28'	H	$[GPa]$	0.20 ± 0.10	0.45 ± 0.15	0.89 ± 0.11	1.37 ± 0.07
	$\left(\frac{s}{\mu}\right)$	[%]	50	33	12	5
'HT'	H	$[GPa]$	0.20 ± 0.16	0.43 ± 0.12	0.80 ± 0.15	1.29 ± 0.12
	$\left(\frac{s}{\mu}\right)$	[%]	80	28	19	9

Table 6.3: Nanoindentation results: Indentation hardness, coeeficient of variations, and volume fractions obtained from a statistical analysis of the frequency plots. The maximum indentation depth was 200 nm.

- *No significant morphological change is induced by heat treatment:* Heat treatment at 60°C has little impact in the morphological arrangement of the microstructure. A small increase in the volume fractions of the HD C-S-H as reported by the frequency analysis is also evident in the mechanical maps, Fig. 6-8. The LD C-S-H, however, continues to be the percolated phase in the systems. This mapping methodology further demonstrates the insensitive nature (at least at Level I) of the microstructure to the heat application in the hardened state of the material.

Nanohardness Results

Frequency plots of the nanohardness values obtained by grid indentation are displayed in Figs. 5-17 and 6-9 to 6-11. Similar to the nanostiffness values, it is possible to attribute from the frequency plots specific hardness values to the different phases. Consistent with the above analysis (see Section 6.2.1) the hardness values of LD and HD C-S-H remain unaffected by the heat application whether this is applied at the early stages of hydration (heat curing) or at later hardened state (heat treatment). The hardness values of the 1-day heat cured specimen ('HC-1' – Figs. 6-9), the 28-day heat cured specimen ('HC-28' – Figs. 6-10), and the 1-day heat treated specimen ('HT' – Figs 6-11) differ little from the control specimen hardness, ('C' – Figs. 5-14). The actual values obtained from the frequency analysis are summarized in Tab. 6.3: The value of the MP, LD C-S-H, HD C-S-H remain almost constant at a value of $H_{MP} \simeq 0.16$,

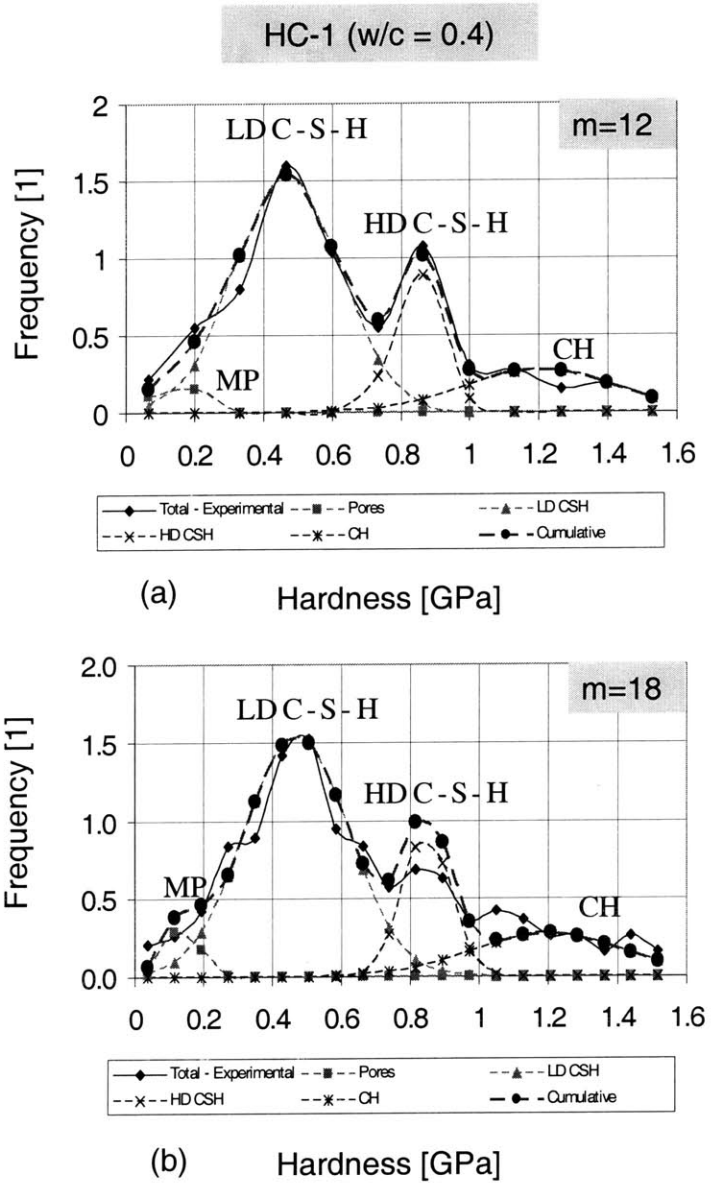

Figure 6-9: One-day heat cured specimen 'HC-1' ($w/c = 0.4$): Frequency plot of indentation hardness determined by grid nanoindentation (No. of tests = 200).

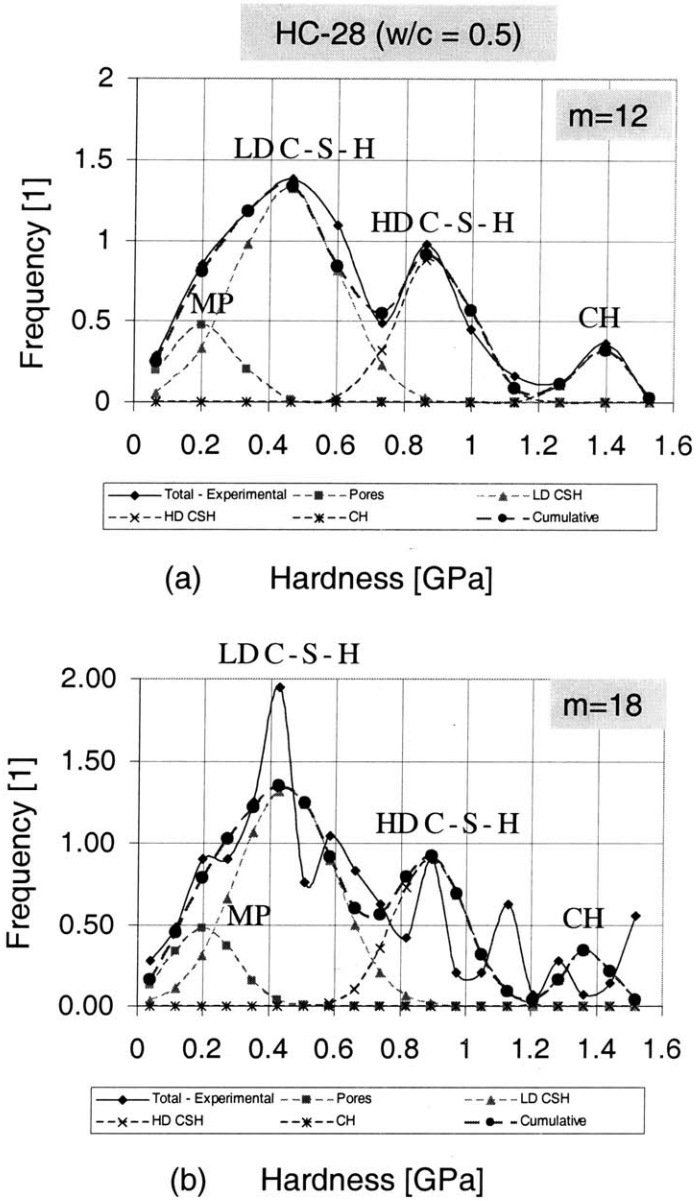

Figure 6-10: 28-day heat cured specimen 'HC-28' ($w/c = 0.5$): Frequency plot of indentation hardness determined by grid nanoindentation (No. of tests = 200).

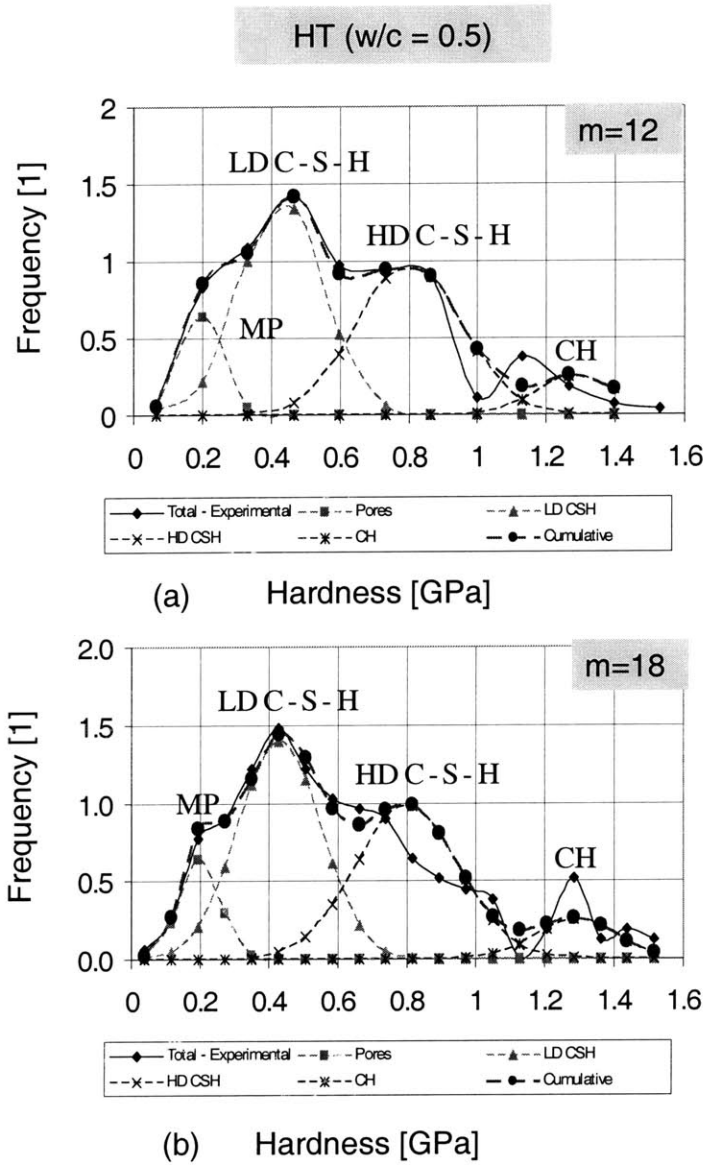

Figure 6-11: One-day heat treated specimen 'HT' ($w/c = 0.5$): Frequency plot of indentation hardness determined by grid nanoindentation (No. of tests = 200).

$H_{LD} \simeq 0.45$, $H_{HD} \simeq 0.84$, $H_{HD} \simeq 1.30$ respectively. A small increase in the hardness values of the CH phase with temperature application maybe attributed to a densification process that the material undergoes until a complete disintegration at $(400-600°C)$. The increase, however, is within the limits of the standard deviation and cannot be considered statistically significant.

Nanocreep Results

The indentation loading phase is followed by a dwelling phase, during which the maximum load is kept constant over a specific period of time. During this phase, the displacement is recorded as a function of time. A plot of the indentation depth vs. time allows one to assess the creep behavior of the material under investigation. The extraction of creep properties from indentation requires the use of an analytical model of indentation on a viscoelastic material. The extraction process is a matter of current, intense research and a detailed exposition goes beyond the scope of this presentation [50,237]. However, a first order estimate of the creep process of the material can be obtained by modeling the data in a simplified way. Two possibilities are explored to characterize this creep behavior. The first one is motivated by creep theory of cementitious composites [18, 3], according to which the creep rate in the absence of any length-time scale evolves with t^{-1}. This phenomenon is explored by using a logarithmic function to fit the experimental data:

$$h(t) - h(0) = A \ln(Bt + 1) \tag{6.2}$$

where $h(0)$ is the penetration depth at the beginning of the dwelling period; and A, B are fitting parameters that characterize the dimensionless indentation creep rate:

$$\frac{d\bar{h}}{d\bar{t}} = \exp(-\bar{h}) \; ; \; \bar{h} = \frac{h(t) - h(0)}{A} ; \bar{t} = Bt \tag{6.3}$$

The fitting parameter A (of dimension $[A] = L$) can be seen as a characteristic length scale, and B (of dimension $[B] = T^{-1}$) as a characteristic rate constant, that allow characterizing the time dependent deformation.

A second way of exploring the creep rate in an indentation test was suggested by Mayo et al. [166], who found that the steady-state strain rate, at each point under the indenter, scales

with the penetration rate divided by the current contact depth:

$$\dot{\epsilon}_{int} = \frac{1}{h_c}\frac{dh}{dt} \tag{6.4}$$

While Eqs. (6.2) and (6.4) are rather qualitative than quantitative, they provide a first-order means for comparing the creep behavior of heat-cured and normal cement-based materials. The steady state calculations were performed only at the microindentation results were the holding period was enough (150 s) to resolve this regime. The 5 s holding period employed for the nanoindentation tests did not allow access to the steady state creep domain.

Figure 6-12 display frequency plots of the two creep parameters A and B that were obtained by fitting Eq. (6.2) to the indentation depth vs. time curve during the dwelling period of roughly 5 s. We note:

1. The creep parameter A of length dimension has two characteristic peaks for the control specimen, which reduces to only one peak in the heat cured and heat treated specimens. The first peak situated around $A = 3 - 5$ nm characterizes all four materials at the nanoscale, and can be identified as the characteristic value of A of the HD C-S-H phase. The second peak situated around $A = 8 - 10$ nm is characteristic of the LD C-S-H phase. This peak almost disappears as a result of heat curing. Although for heat cured specimens this is consistent with the preferred formation of LD C-S-H into HD C-S-H (see Tab. 6.2), the data seems inconsistent for the heat treated specimens which showed no significant shift in volumetric proportions. It appears that there is a second mechanism were temperature application operates: Apart from densifying the matrix through enhanced HD formation it seems to operate at the interlayer level where structural water is situated (Level 0). To get a better understanding of this confusing result we plotted the A parameter versus the indentation modulus and hardness. Figure 6-13 shows the intuitive result that harder and stiffer material exhibit less creep. What is of primary importance, however, is to see the effect of heat curing and heat treatment on the scaling behavior of A vs. H, M: The best fitted lines demonstrate a shift on the vertical axis. Recalling that the indentation moduli and hardness of both phases remain unaffected, such a shift suggests that the intrinsic creep capacity of the LD and HD C-S-H phases

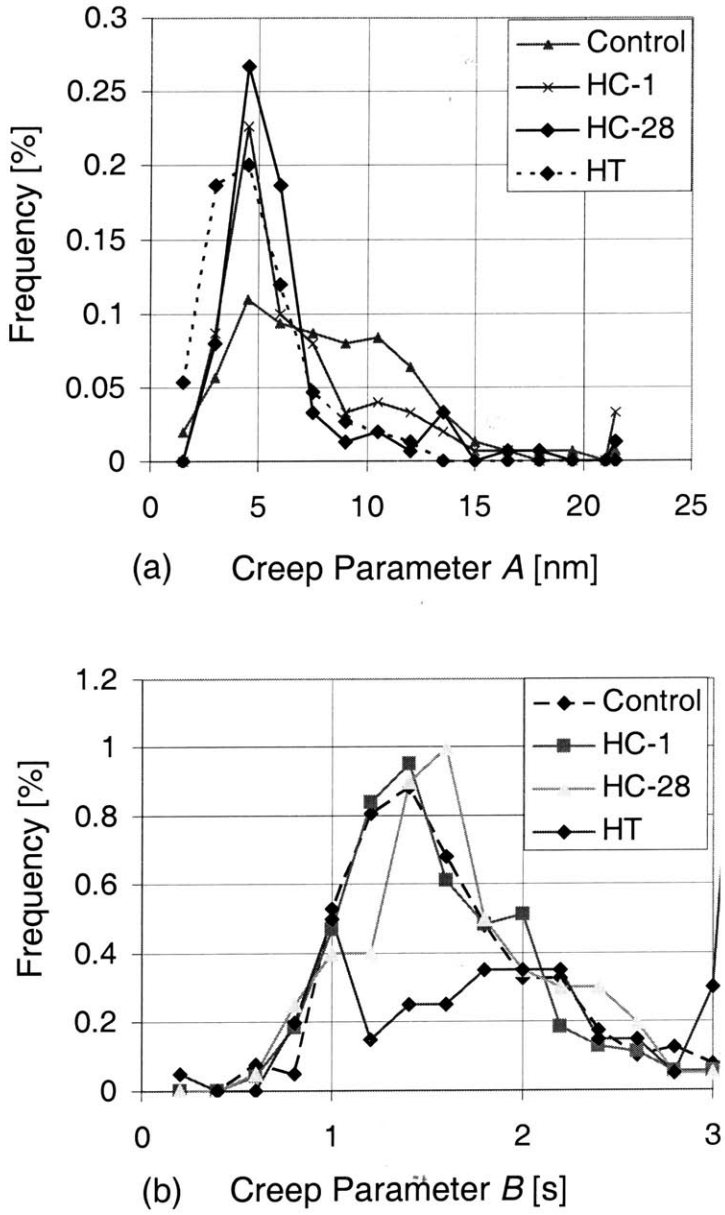

Figure 6-12: Frequency plot of the creep length scale (a) and time scale (b) parameters, determined from grid nanoindentation.

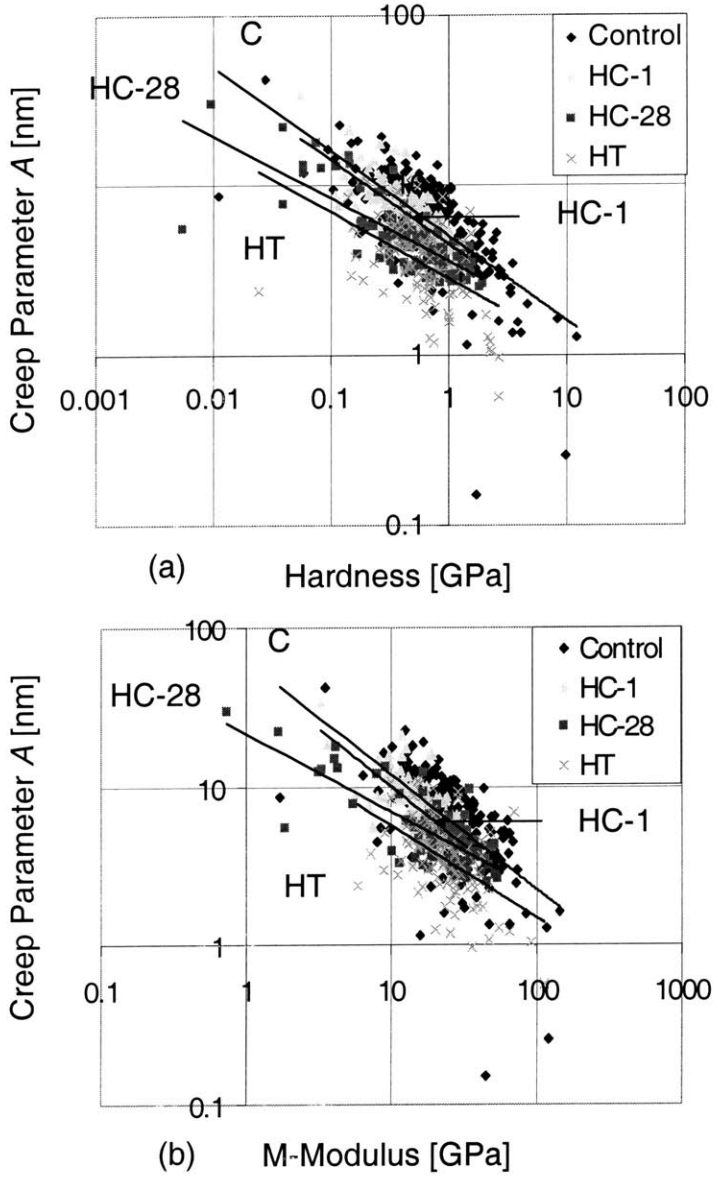

Figure 6-13: Scaling relations of the creep length parameter A with the indentation modulus M (a) and hardness H (b) for the control ('C') heat cured ('HC-1, 'HC-28') and heat treated ('HT') specimens.

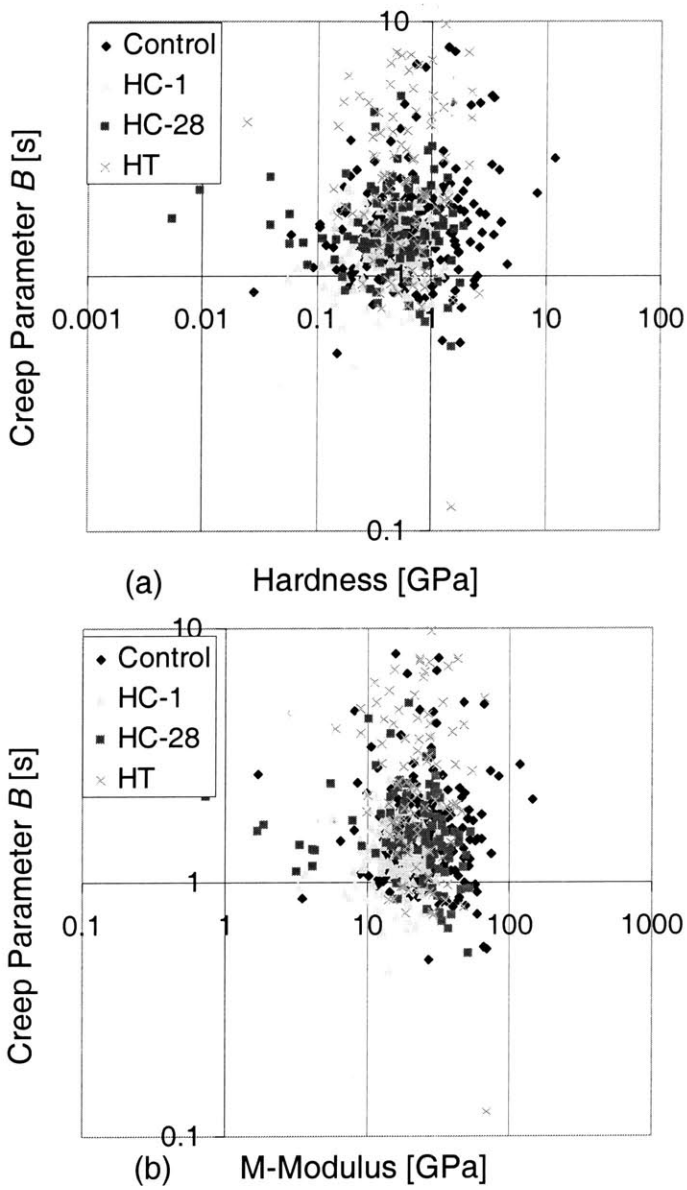

Figure 6-14: Scaling relations of the creep time parameter B with the indentation modulus M (a) and hardness H (b) for the control ('C'), heat cured ('HC-1, 'HC-28'), and heat treated ('HT') specimens.

reduces by the application of heat, more for the heat treated specimens than for the heat cured specimens. Using the indentation moduli values from table 6.2 into the best fitted lines of Fig. 6-13 yields estimates of the creep coefficients A:

$$(A) = \begin{cases} \text{LD C-S-H} & \text{HD C-S-H} & \\ 8.0\text{nm} & 4.4\text{nm} & (\text{'C'}) \\ 6.3\text{nm} & 4.4\text{nm} & (\text{'HC-1'}) \\ 5.1\text{nm} & 4.0\text{nm} & (\text{'HC-28'}) \\ 4.0\text{nm} & 3.0\text{nm} & (\text{'HT'}) \end{cases} \tag{6.5}$$

Results in (6.5) suggest that the effect of temperature on the A parameter is both a function of duration and time of application. It primarily shows that heat effect initially operates on the LD C-S-H ('HC-1') and eventually affects both LD and HD C-S-H creep capacity ('HC-28'). It is also impressive to note that the application of heat brings the creep capacity of the two phases very close to each other ('HC-28' and 'HT'). In particular, heat treatment has a more drastic effect that results in a creep ratio of $A_{LD}/A_{HD} = 4/3 = 1.33$. This clarifies the fact that A_{LD} and A_{HD} cannot be resolved from the frequency plots of Fig. 6-12, as they merge together into a single peak. While the actual mechanism that leads to the reduction in A is not identifiable from the indentation techniques, this finding suggests that temperature application improves creep behavior by affecting C-S-H phases at the interlayer nanometer level (Level 0). Finally, a comment is due on the magnitude of this length parameter A characterizing the creep response: A value for A of $3 - 8$ nm compares well with the globule size suggested by Jennings (~5nm) and a characteristic length of creep deformation suggested by Wittmann (~5nm). All three values are in favour of the interpretation that most of the deformation is on the characteristic size of the individual C-S-H solids which suggests that the individual globules are highly involved in the creep process.

2. The rate constant B is almost constant for all four materials. Fitted for a 5 s dwelling duration, it is on the order of $B = 1.3 - 1.5\ \text{s}^{-1}$. There is a slight difference of the peak value between HC-1 and HC-28, but this difference is smaller than the standard

deviation. Hence, in sharp contrast to the length parameter A, the rate of the time dependent deformation is not affected by the thermal treatment. It is impressive also to note that the scaling of B vs. H, M shows no apparent trend signifying the independence of the time scale of deformation (see Fig. 6-14). Heat treatment seems to be associated with a certain degree of disorder as the spread in the values gets more significant. The mean value however remains the same.

3. The results on heat treated specimens suggest that the application of heat operates at two levels: There is a conversion of LD to HD C-S-H (limited for heat treatment and more pronounced in the case of heat curing) that tends to densify and stiffen the matrix (Level I), and there is a second independent mechanism at Level 0 that enhances the globule and makes it less susceptible to time dependent deformation. Associating the creep behavior to the movement of lamellae along water occupied interfaces, indentation results would suggest that temperature application reinforces these sites probably by means of removing interlayer water or hydroxyl groups from that region and bringing the lamellae closer together (for example transforming from a 1.4 nm Tobermorite to 1.1 nm Tobermorite - the difference being 1 layer of water molecules). This is consistent with the reported increase in polymerization of the heat cured and heat treated specimens, their reduction in weight [230], and the reduction in the basal spacing [56].

6.2.2 Level II: Microindentation Results and Cement Paste Properties

An indentation depth on the order of roughly 10^{-5} m was used to access Level II. A depth of this magnitude tends to homogenize the composite response of all phases found at Level I. In fact this is reflected by the low standard deviation observed for our results as compared to nanovalues. Table 6.4 summarizes the *micro*indentation results on the control specimen ('C'), the heat cured specimens ('HC-1', HC-28'), and the heat treated specimens ('HT'). The results are average values and standard deviation of respectively 10 indentation tests for the control specimen 'C', the 1-day heat cured specimen ('HC-1'), and the heat treated specimens ('HT') and 30 indentation tests for the 28-days heat cured specimen 'HC-28' (see Tab. 6.1). The higher number of indentation tests for the HC-28 sample was necessary because of a higher standard deviation of the elasticity, which is due to the large macropores that interfere at the micro-

indentation scale of 10^{-5} m. While the mean values obtained for the control specimen allow an interpretation as characteristic properties of the homogenized material, i.e., cement paste, given the size of the macropores generated in heat-cured specimen, a continuous interpretation should be handled with care. Nevertheless, some interesting trends become apparent which are discussed below.

Indentation Modulus

The elastic indentation stiffness remains practically unaffected by heat curing; the slight increase in mean value from 19.1 GPa for the control specimen 'C' to 19.5 GPa for 'HC-28' is smaller than the standard deviation. It appears that the two competing mechanisms that characterize the mechanical effect of heat curing at a scale below, that is the densification of the C-S-H matrix and the generation of a macroporosity, cancel each other out. In return, the higher standard deviation for heat cured specimens is indicative of a higher degree of disorder, induced at a scale below by the creation of the macroporosity. The slightly higher elasticity of the 1-day heat cured specimen HC-1, is due to the lower w/c ratio of 0.4 which leaves a higher proportion of high stiffness residual clinker phases in the material than in the $w/c = 0.5$ materials, and which affects the elasticity of the cement paste. Consistent with the nanoindentation results the indentation modulus of heat treated specimens (HT) is virtually unaffected by the thermally applied conditions. The almost unchanged modulus reflects the insignificant modification of the microstructure happening at a scale below (Level I).

Hardness

The hardness which is a measure of the strength properties (see Eq. (2.15)), decreases for the $w/c = 0.5$ materials ('C' and 'HC-28') by roughly 20% as a consequence of the heat curing. This is consistent with strength data on heat cured specimens found in the literature [79]. In other words, in contrast to the stiffness properties, the densification of the C-S-H matrix does not compensate for the increase in macroporosity in terms of strength properties. An interesting result is that the 1-day heat cured specimen ('HC-1') has a greater microhardness than both the control specimen ('C') and the 28-day heat cured specimen ('C'), which is an opposite trend to what has been observed at the scale of the individual components (Level I). The higher

		Control ('C') ($w/c = 0.5$)	HC-1 ($w/c = 0.4$)	HC-28 ($w/c = 0.5$)	HT ($w/c = 0.5$)
M	[GPa]	19.1 ± 1.7	21.0 ± 2.0	19.5 ± 4.9	20.2 ± 2.1
H	[MPa]	498 ± 8	780 ± 17	406 ± 18	495 ± 10
A	[nm]	205 ± 25	172 ± 14	161.7 ± 0.5	150.2 ± 12
		$(150 \pm 17)^*$	$(142 \pm 13)^*$	$(123 \pm 19)^*$	$(115 \pm 19)^*$
B	[s^{-1}]	0.39 ± 0.12	0.44 ± 0.10	0.47 ± 0.17	0.48 ± 0.15
		(0.89 ± 0.14)	(0.74 ± 0.10)	(1.07 ± 0.31)	(1.10 ± 0.10)
$\dot{\epsilon}_{int}$	[$s^{-1} \times 10^{-4}$]	2.8	2.7	2.5	2.4
p	[%]	42	36	43	43

Table 6.4: Microindentation results: Indentation stiffness, hardness and creep characteristics determined from indentation curves. The maximum indentation depth was approximately 10μm. * = creep parameters fitted for a 10 s dwelling period.

hardness for HC-1 can be attributed to the lower $w/c-$ratio which is known to reduce not only the volume of the macroporosity but also its characteristic size. In addition the amount of residual clinker left in the microstructure is known to contribute to the amplification of the internal friction which in turn highly affects the hardness behavior of materials (see Fig. 2-9 in Chapter 2).

Consistent with our indentation investigation at Level I the hardness of the heat treated specimen remains relatively unchanged. This is in line with the unaffected nature of the intrinsic hardness of the two types of C-S-H and also the insignificant shift in relative volumetric proportions of all phases. Parrott [187] reported uniaxial compression data on a cement paste of $w/c-$ratio of $w/c = 0.5$ that has been normally cured and heat treated at a later stage for 24 hours. Parrott's results showed that the strength of the material was insensitive to the heat treatment process, which is consistent with our hardness results.

Creep

The heat cured and heat treated specimens clearly exhibit a smaller time dependent deformation. This is readily depicted from Fig. 6-15 which displays the indentation creep as a function of time during the dwelling period. To quantify this behavior, the logarithmic function of Eq. (6.2) is fitted through the curve for the dwelling period of 150 s. A second fit was performed for a dwelling period of 10 s, in order to check the sensitivity of the fitting parameters with respect to the time scale of observation. The values of the two constants A and B are reported in Tab.

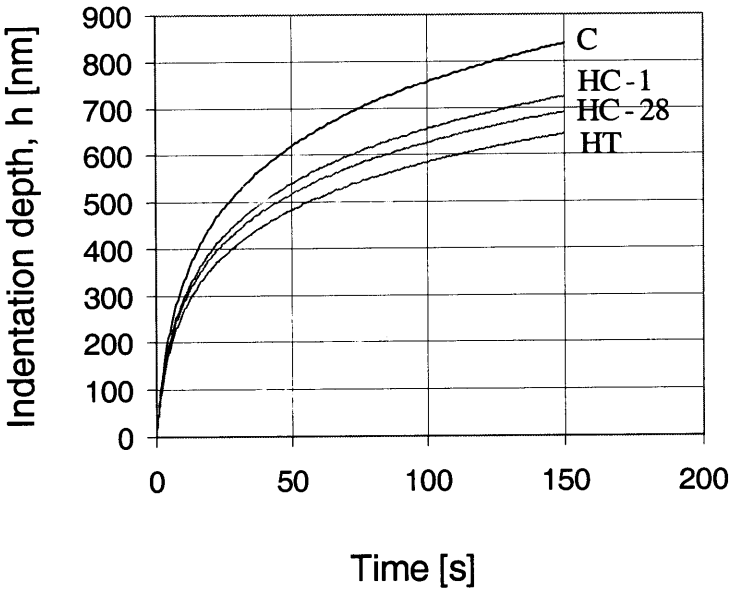

Figure 6-15: Microindentation creep.

6.4, together with the steady-state creep rate $\dot{\epsilon}_{int}$ fitted according to Eq. (6.4). It is interesting to note that the difference in the rate constant B in between the samples is smaller than the standard deviation, so that this rate constant seems to be not the most affected by heat curing. Similarly, neither the initial indentation creep rate $dh/dt\,(t=0) = A \times B$ ($A \times B = 80\,\mathrm{nm/s}$ for the control specimen 'C', $A \times B = 76\,\mathrm{nm/s}$ for both heat cured specimen 'HC-1' and 'HC-28', and $A \times B = 81\,\mathrm{nm/s}$ for the heat treated specimen) nor the steady-state creep rate $\dot{\epsilon}_{int}$ appear to be the quantities the most affected by heat curing. Instead, it is the characteristic length A that decrease from $A = 205\,\mathrm{nm}$ for the control specimen 'C' to $A = 162\,\mathrm{nm}$ and $A = 150\,\mathrm{nm}$ for the heat cured 'HC-28' and heat treated 'HT' specimens respectively, entailing a smaller time dependent deformation of the thermally conditioned specimens. This change of the characteristic length scale A as a consequence of thermal treatment is indicative of two phenomena taking place at two different scales: a) a change of the microstructure manifested by a shift in the relative volumetric proportions between LD and HD C-S-H (Level I), b) reduction in the creep capacity of the individual globules probably due to polymerization and condensation reaction activated by thermal energy (Level 0). The significant reduction of the heat treated specimens which show no change in the relative volumetric proportions, are in favor of this interpretation. This is also consistent with the shift in the A parameter for the LD and HD C-S-H observed in Fig. 6-13. We also fitted the logarithmic function to a shorter dwelling period of 10 s. The obtained values (denoted by $(x)^*$) show some sensitivity with respect to the time scale of observation, but the trend remains the same: the characteristic length scale A decreases as a consequence of heat curing while the values for the rate constant are on the same order, and come very close to the nanoindentation rate constants derived from Fig. 6-13. This result is an indication that, provided the same time scale of observation (dwelling period duration), the creep rate constant is independent of the length scale.

6.3 Discussion

The results obtained are discussed here in the light of the multi-scale structure of cementitious materials displayed in Fig. 4-13. It is composed of four scales that are separated by at least one order of length magnitude, as discussed in details below.

6.3.1 Level 0: C-S-H Solid - Globule

The lowest level we consider in our analysis is the scale of the C-S-H solid phase, which forms at early ages by the hydration of C_3S and C_2S. We refer to this scale as Level 0, the level at which stoichiometric arrangements and physical chemistry are linked with the mechanical performance of the CBM systems. The colloid model proposed by Jennings (Fig. 4-8) [130, 131] provides elementary dimensions of the C-S-H solid phase: a solid phase of a characteristic size of 5.6×10^{-9} m, which includes a 18% intra-solid nanoporosity representative of the interlayer space within the C-S-H. The mechanical response at this scale is dominated by the surface properties of the C-S-H gel, and the water present at this scale is structural water. Indentation results presented above come to suggest that heat curing causes removal of some of the interlayer water with significant improvements on the time dependent deformation of the material. Seeing C-S-H matrix from a gel point of view, this polymerization process can be associated with the condensation reaction, a key reaction in the aging of silica where hydrolyzed molecules are linked together releasing water molecules in turn. A simplified version of the condensation reaction is given by:

$$\text{-Si-OH+HO-Si} \leftrightarrow \text{-Si-O-Si-+}H_2O \tag{6.6}$$

A slight increase in the total water released on drying (see Tab. 6.4) and a reduction in the total weight [230] are in favour of this interpretation. While the condensation reaction may affect the creep behavior of the material it has little effect on the overall elastic and strength behavior (see below). It is highly possible that the mechanical response of the individual solid particle is much higher than the agglomerate response rendering its actual value to the composite response of secondary importance.

6.3.2 Level I: C-S-H Matrix

The solid phase (globule) together with gel porosity yields two characteristic forms of the C-S-H, a low density form and a high-density form, which manifests itself at a scale above. The difference in between the two C-S-H phases is the gel porosity, respectively the packing density: the LD C-S-H is characterized by a gel porosity of roughly $\phi_{LD} = 37\%$, and the HD C-S-H is characterized by a gel porosity of roughly $\phi_{HD} = 24\%$.

Invariant C-S-H Elasticity Properties and Packing Density

The difference in gel porosity, respectively in packing density ($1 - \phi_{LD} = 63\%$ vs. $1 - \phi_{HD} = 76\%$) entails different composite stiffness values of the two types of C-S-H that are accessible by nanoindentation [58]. Since the nano indentation stiffness results (see values in Tab. 6.2) change insignificantly as a consequence of thermal curing and treatment, it is unlikely that the gel porosity (or the C-S-H packing), and the nature of the interparticle bonds at this level are significantly affected by heat curing or heat treatment. It is intriguing to remark that the LD C-S-H packing density is on the order of the random packing density of spheres of 64%, which corresponds to the maximum packing density in the random close-packed limit (known as RCP)[2]. In return, the HD C-S-H packing density slightly exceeds the densest possible packing in three dimensions (a problem known as the Kepler problem), which is the close-packed hexagonal or cubic structure, and which has a packing density of 74% (see Refs. [128 – 71]). This is significant as it would confirm the conjecture of Jennings's colloid model: that the two-types of C-S-H are manifestations of the same solid, the only difference being an unstructured (random) order of the LD C-S-H vs. a highly structured order of the HD C-S-H. While the chemo-physical origin of these structures is still not known, the universal packing density of the two types of C-S-H is a good candidate to explain the material invariant nature of the nanoelasticity properties, that are (almost) insensitive to heat curing and heat treatment. There is important independent evidence that the degree of silicate polymerization in the C-S-H phase increases with temperature application and duration (heat curing or heat treatment) as shown by Silicon-29 Nuclear Magnetic Resonance Spectroscopy [251, 126]. This observation combined with our experimental finding, that the indentation modulus and hardness do not change with heat application, suggest that the mechanical properties of the material are independent of the degree of polymerization. Also this comes to suggest that the packing density (or relative proportion of LD/HD) are also independent of the degree of polymerization. It can be speculated that the degree of silicate polymerization is associated with the orientation of the chemical elements in the C-S-H solid phase and is restricted within the globule at Level 0, where the interlayer

[2]More recent concepts refer to the RCP as the maximally random jammed state (MRJ), corresponding to the least ordered among all jammed packings, which has been shown to have a density of 63.7%, which is very close the traditional definition of the random close-packed limit; see [71], and references cited herein.

structure is simulated. This polymerization however has little influence on the mechanical properties (hardness and elasticity) of the two-types of C-S-H (although creep is affected). The overall picture that emerges is that, given the unique characteristic packing modes of these two phases, the nanoindentation stiffness properties are true (invariant) material properties.

Nanohardness Properties of C-S-H

Similar to the indentation moduli values, the nanohardness appear to be independent of the $w/c-$ratio and any moderate heat (60°C) applied to the material at an early or a hardened state (see Tab. 6.3): We find two characteristic hardness values for the two types of C-S-H, that have a relatively high scatter and which appear to be independent of heat curing. Some interesting observations also emerge:

1. The nanohardness ratio of the HD C-S-H to LD C-S-H is almost constant in all three specimens,

$$\frac{H_{HD}}{H_{LD}} = \begin{cases} 1.85 & (\text{'C'}) \\ 1.81 & (\text{'HC-1'}) \\ 1.97 & (\text{'HC-28'}) \\ 1.86 & (\text{'HT'}) \end{cases} \tag{6.7}$$

   The nanohardness ratio may be attributed to the characteristic packing density of the two types of C-S-H, and more precisely to the number of contacts required to mechanically stabilize the packing. Indeed, it has been recently shown that the random packing of spheres is characterized by on-average six points of contacts [71], while a high-density packing of spheres has a maximum of twelve points of contacts [209] (that is twice as much as the one in the random close-packed limit (RCP), which almost perfectly correlates with the measured nanohardness ratio in Eq. (6.7)). Rather than a coincidence, we see here a second piece of evidence (in addition to the packing density) supporting the hypothesis of the characteristic packing patterns of the LD C-S-H and the HD C-S-H. It suggests that the hardness (and thus the strength properties) of the two types of C-S-H is a mere consequence of the packing density, and more precisely of the number of contacts stabilizing each solid sphere in the system. The higher the packing and thus the number of contact points, the greater the number of degrees of freedom along which the system

can dissipate energy at the limit stage associated with strength, and which translates into the measured nanohardness values.

2. The invariance of the two nanohardness values further enforces the idea that there is little change in the morphological arrangements of the two phases (at Level I), and that packing density and nature of bonding remains the same. The experimental observation that the degree of polymerization is not related to the volumetric proportions of the two phases comes to suggest that the formation of the two microstructures, or two characteristic packing modes, is a consequence of kinetic or other chemophysical reasons [230]. Furthermore, this demonstrates that the LD and HD C-S-H hardness and, as a consequence the macroscopic strength behavior, is driven by the porosity contained in them and that changes that may be happening within the globule structure are of little significance macroscopically.

Nanocreep Properties of C-S-H

The creep properties expressed by the constants A and B (see Figs. 6-12 and 6-13) are fitted parameters that are qualitative in nature, rather than being physical quantities that can be used to quantify the creep behavior of the nanocomponents of cementitious materials. Nevertheless, the main observations obtained by nanoindentation provide a clear hint towards the scale of the origin and the effect of microstructure on the time dependent deformation of cementitious materials. In particular:

1. The fact that the characteristic rate constant B is the same irrespective of the density of the C-S-H implies that the rate determining mechanism of creep is situated at a scale below the one where the density becomes apparent in form of two types of C-S-H. It provides some evidence that the time dependent deformation originates from the C-S-H solid phase, i.e., from the basic building block of C-S-H at a length scale of some nanometer (see Fig. 4-8). Further results on nano and microindentation on heat cured and heat treated specimens are in favour of this interpretation. This conclusion, is consistent with what has been speculated for a long time by several researchers [194, 17, 3], that the origin of creep is situated somewhere in the 18% nanoporosity, involving most likely the

structural water.

2. By contrast, application of heat curing or heat treatment to cementitious materials affects the creep magnitude expressed by the characteristic length scale A. Application of heat tends to reduce the A parameter for the two phases, with heat applied at a hardened state to have more drastic results. In terms of Jennings colloidal model, creep deformation can be visualized in two ways: 1) globules moving relative to each other with the number of bonds remaining the same; or 2) time dependent deformation is taking place within each globule either through a crystallization, condensation or any other aging process, as response to stress or strain localizations. Indentation results presented in this chapter come to suggest that probably both phenomena are at stake, although a conclusive remark cannot be verified. Further investigation is required to elucidate these issues.

6.3.3 Level II: Cement Paste

The two-types of C-S-H plus CH and residual clinker and the macroporosity are the components of the cement paste. Its macroscopic mechanical behavior is therefore intimately related with the mechanical response of all these phases as well as their interactions. At this scale, it appears that two competing mechanism are at work as a result of heat curing: (1) the densification of the C-S-H matrix, and (2) the creation of the macroporosity. These phenomena, however, are not mutually independent. To illustrate our purpose, we compare the total porosity of the control specimen with the total porosity of the 28-d heat cured specimen. The total porosity is the sum of the $\varphi_0 = 18\%$ nanoporosity included in the C-S-H solid phase, the $\phi_{LD} = 37\%$ and $\phi_{HD} = 24\%$ gel-porosity of the LD C-S-H and HD C-S-H, and the macroporosity ϕ_0, hence (see e.g. [235]):

$$p = [\varphi_0 (1 - \phi_{LD}) + \phi_{LD}] f_{LD} + [\varphi_0 (1 - \phi_{HD}) + \phi_{HD}] f_{HD} + \phi_0 \tag{6.8}$$

where f_{LD} and f_{HD} represent the volume fractions of the LD C-S-H phase and the HD C-S-H phase present in the cement paste. Using the values from Tab. 6.2, we obtain for the control specimen $p_C = 0.41$ and for the 28-day heat cured specimen $p_{HC-28} = 0.42$. The almost prefect agreement of the total porosity of control specimen and heat-cured specimen confirms that the

creation of the macroporosity due to heat curing is a consequence of the conversion of LD C-S-H into HD C-S-H. In contrast, heat treatment is associated with little morphological changes. The relative proportions of LD , HD and CH are little affected. Using the volumetric proportions of the individual chemical constituents in (6.8) yields an estimate for the total porosity, $p_{HT} = 0.42$. These estimated values of total porosity are to be compared with porosity measurements performed on the specimens by drying them at 105°C for 24 hours (see Tab. 6.4). Several things become apparent: a) The measured porosities are slightly overestimated suggesting that a certain degree of chemically bound water might have been released on heating at 105°C; b) The HC-28 and HT specimens released slightly higher proportion of water (1%) which is in favor of the condensation reaction that tends to release water in return; c) It is impressive to see that the total porosity remains little affected by heat curing (densification process) and heat treatment process. The total porosity appears to be highly dependent on the initial mix proportions (see $p_{HC-1} = 0.35$ for 'HC-1' in Tab. 6.4) and not on the curing conditions. This suggests that the densification process is associated with local contraction phenomena and not with global shrinkage deformations. This conversion observed in the case of heat cured specimens reduces the gelporosity, but is compensated by the creation of macroporosity, so that the total porosity remains almost constant. It is this internal transformation of mesoporosity into macroporosity that affects the mechanical properties of heat cured cement pastes. Regarding the elasticity, the densification of the C-S-H phase appears to compensate for the increase in macroporosity. On the other hand, the decrease in strength is a clear consequence of the macroporosity generation, and is not compensated by the densification of the C-S-H matrix. This coarsening of the macroporosity, as it is often referred to in the literature [21], leads to stress concentrations in the C-S-H matrix, leading to a lower overall material strength, particular in high w/c ratio cement-based materials. It is noteworthy that the scatter of the hardness values of the cement

paste is quite small, when compared to the scatter of the hardness values at all scales below:

$$\left(\frac{s}{\mu}\right)_H = \begin{cases} \text{Cement Paste} & \\ \quad 1.6\% & (\text{'C'}) \\ \quad 2.2\% & (\text{'HC-1'}) \\ \quad 4.4\% & (\text{'HC-28'}) \\ \quad 2.0\% & (\text{'HT'}) \end{cases} \tag{6.9}$$

The small scatter, as expressed by (6.9), is not only a clear indication of the homogenized nature of the properties obtained by indentation at the scale of the cement paste, but also a clear indication that one detrimental phenomenon is at work governing the strength properties of the cement paste: the coarsening of the macroporosity. This phenomenon seems to dominate over other possible effects such as a reduced hydration degree of the allite and ferrite phase in high temperature hydration [78], that have been correlated in the past with the observation of a reduced strength capacity. Rather chemical in origin, the strength loss due to thermal curing appears to us a consequence of the change of microstructure at the scale of the cement paste. It is interesting to note that the microhardness values for the three $w/c = 0.5$ materials ('C', 'HC-28', and 'HT') are very close to the nano-hardness values of the LD C-S-H (see Tab. 6.3). This may not be a coincidence. In fact, regarding the control specimen, with almost non-detectable macroporosity, the closeness of nano- and micro-hardness values would hint towards relevance of the weakest link theory, according to which the strength behavior is governed by the weakest phase in the material system, which is the LD C-S-H phase and which appears to dominate the strength behavior of the cement paste. A similar argument can be made for the 28-day heat-cured material ('HC-28'): the generation of the macroporosity leads to higher stress concentrations in the C-S-H matrix; and in particular in the LD C-S-H surrounding the macropores (see Fig. 6-7), which therefore becomes dominant in the strength behavior of the cement paste. Regarding the $w/c = 0.4$ material ('HC-1'), despite the creation of the macroporosity and the lowest C-S-H matrix hardness (Level I), the microhardness is greater than the hardness of the C-S-H matrix. It is unlikely, however, that this increase in microhardness is a consequence of the heat treatment, but should be attributed to the reinforcing effects of (almost) rigid clinker phases present in this low w/c material. This frictional enhancement, which is

sensed at the microindentation scale, translates into a higher microhardness value. Here, a possible source of macroscopic strength enhancement by means of mix proportions becomes apparent. Finally, heat treatment which neither exhibits a change in the microstructure nor a change in the intrinsic hardness has little deviation from the control specimen at macroscopic scales.

Application of heat appears to affect the macroscopic time dependent deformation in two ways: a) by reducing the intrinsic creep capacity of the only creeping phases LD and HD C-S-H; and b) changing the relative volumetric proportions and morphological characteristics (for early age heating only). The smaller time dependent deformation of heat-cured specimen is a clear consequence of the densification of the C-S-H phase. In contrast to the strength performance, the creep behavior seems not to be affected by the macroporosity generation. It is a result of a denser C-S-H structure dominated by a low creeping HD C-S-H phase, that confines the time dependent deformation of LD C-S-H. Provided the same time scale of observation, the creep rate is the same at all scales. In the case of heat treated specimens it is the reduction of the intrinsic creep capacity of the globule that leads to a reduction in the A_{LD} and A_{HD} which eventually translates into an overall macroscopic creep reduction. The reduced creep capacity can be attributed to the condensation reaction that removes hydroxyl groups and water from the interlayer space (within globule) and polymerizes the material. It is impressive to see that the C-S-H phase can be converted at a hardened state to a phase with reduced creep capacity by simply exposing it to 60°C for a few days. This comes at no expenses of strength or elasticity reduction. Here, a possible source of improved creep performance by means of heat treatment becomes apparent.

6.4 Chapter Summary

Experimental data presented in this chapter provides clear evidences of the C-S-H contributions at the macroscopic mechanical performance. Much of the results obtained by the newly developed technique of massive grid nanoindentation hint towards two characteristic packing patterns of the C-S-H, that can explain much of the macroscopically observed stiffness, strength and creep behavior of cementitious composites. The two level experimental investigation of the

effect of heat curing and heat treatment on white cement paste comes to suggest that the mechanical properties of the two types of C-S-H are intrinsic material properties that do not depend on mix-proportions, thermal conditions, age of cement, etc., but are rather intrinsic to the chemical phases that are formed during the hydration of the C_3S and C_2S. The results presented above demonstrate clearly that the macroscopically observed mechanical evolution is a reflection of the changes in the relative volumetric proportions of the different phases present in the microstructure as well as their morphological arrangement in space. In other words the very nature of the formation products is unique, and remains unaffected by moderate heat application, and it is only the kinetics of the chemical reaction that change. We have to note however that heat application appears to be associated with an increase in polymerization and a decrease in water content which is reflected as a reduced deformation potential. These changes however, appear to be linked with Level 0 of our multi-scale structure at length scales of 10^{-9}m situated within the individual particles and, as a consequence, they have little influence on the intrinsic C-S-H (and the macroscopic) stiffness and strength behavior. They do, however, influence the creep potential of the material, which suggests that most of the deformation behavior takes place at the C-S-H lamellar level where water molecules and hydroxyl groups become important. While the analysis of creep data obtained by indentation is still in its infancy, the technique holds great promise for shedding some light on the industrially relevant deformation processes.

Part IV

MICROPOROELASTIC MODELING

Chapter 7

Multi-scale Microporoelastic Model for CBM Systems

This chapter is devoted to the development of a microporomechanics model for cement-based materials. It is an extension of a previously developed model [58,60] to account for pressure build-up inside the saturated pore space. The multi-scale structure presented in Chapter 4 and the indentation results of Chapter 5 make it possible now to upscale poroelastic properties from very fine scales of CBM materials, where cementitious materials do no more change – in a statistical sense – from one mix proportion to another. This scale is the scale of the C-S-H phases, where the morphology and the mechanical properties are intrinsic, being determined by the chemical formation process, which is deterministic by nature. With this scale in mind, it becomes possible to employ advanced homogenization techniques of microporomechanics that became recently available [40, 73, 74], and adapt them to meet the requirements of the multi-scale microstructure of cementitious materials, starting at the scale where physical chemistry meets mechanics. The results of this challenging endeavor are estimates of the poromechanics properties of cementitious materials at multiple scales. This is, in short, the focus of this chapter. With such a tool in hand, one can quantify the relative contribution of each constituent on the macroscopic poroelastic performance and in knowledge of the volumetric proportions of the different constituents present in the microstructure can translate chemical composition into mechanical performance.

7.1 Elements of Continuum Micromechanics Applied to CBM Systems

There has been significant improvement in the field of micromechanics over the last fifty years. The development of new materials with complex microstructures requires modeling techniques to predict macroscopic properties. As the tools for microstructural manipulations at the nanometer scale become available, the demands towards the predictive and illustrative mechanical techniques increase. Continuum micromechanics represents the systematic approach to obtain mechanical properties at a larger length scale based on the properties of the material below this length scale. Most of the developments in this field focused until recently only on the linear elastic properties in small deformations [253]. More recent contributions extend the approach to the micromechanical analysis of porous media and strength properties. The first idea in studying heterogeneous material systems—that is materials that are composed of different phases—is to address them in a continuous fashion. This is often referred to as the continuum micromechanics approach [218]. The origins of continuum micromechanics can be traced back to the pioneering work of Eshelby [80], who solved the linear elastic problem of an elliptical inclusion in an infinite medium (see Appendix C). That approach laid out the foundations for a class of upscaling methods, based on volume averaging and stress-strain localization (see Section 7.1.2).

7.1.1 Representative Element Volume (R.E.V.) and Equivalent Homogeneous Medium (E.H.M.)

Central to continuum micromechanics techniques is the concept of the Representative Element Volume (R.E.V.). The R.E.V. refers to a sample material volume of the composite, which contains a sufficient number of phase volumes or subvolumes V_r so that it is indeed statistically representative of the composite. Homogenization techniques aim at replacing this inhomogeneous complex volume by its equivalent homogeneous material body (E.H.M.) such that, from a mechanics point of view, it behaves in the same manner. Consider now a structural element (Fig. 7-1) characterized by a length scale Λ, composed of a composite material from which an R.E.V. with a characteristic length scale L can be extracted. Provided an R.E.V. can be

legitimately defined then the structural analysis can be followed using an E.H.M. with uniform mechanical properties. The two following conditions must be met to guarantee the R.E.V. and E.H.M. existence:

1. $L \ll \Lambda, \lambda$, where Λ is the length scale of the macroscopic structure in which the considered material exists, and λ is the fluctuation length of the prescribed mechanical loading. This condition ensures that the continuum mechanics techniques can be applied and the differential tools of structural analysis for continuous stress and deformation fields can be determined.

2. $L \gg l$, where l is the length scale of the heterogeneities considered in the micromechanical analysis. This condition is necessary to assign homogeneous properties to the macroscopic scale.

These two conditions are also called the separation of scales principle, which in summary reads:

$$l \ll L \ll \Lambda; \qquad L \ll \lambda \tag{7.1}$$

The concept of R.E.V. and the separation of scales principle is of extreme importance as it seems to provide a dividing boundary between continuum theories and micromechanics. For length scales greater than L we can safely use continuum mechanics and reproduce properties of the material as a whole. Once the scale becomes comparable with L, microstructural features should be included in the analysis. Equation (7.1) needs to be confirmed for any application of the upscaling schemes. The multi-scale structure of CBM presented in Fig. 4-13 was designed to comply with this principle.

7.1.2 The Three Steps in Continuum Micromechanics

The continuum micromechanics procedure can be summarized in three steps which are detailed below [253]:

Representation

The representation deals with the description of the considered system. Usually some simplifications in the geometrical description are necessary to deal with complex microstructures.

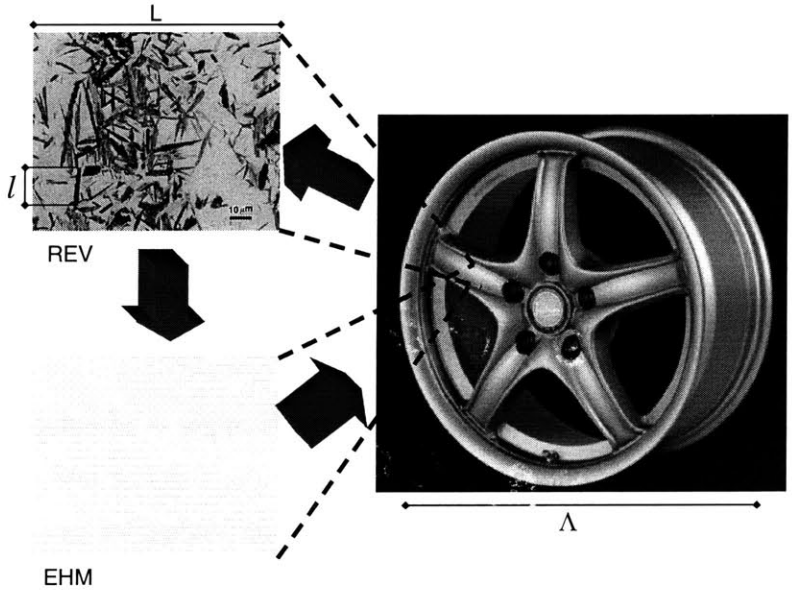

Figure 7-1: A structural element which is made out of a composite materials characterized by its representative element volume (R.E.V.). Homogenization techniques aim in replacing the complex R.E.V. element with an equivalent homogeneous medium (E.H.M.) to assist further analysis using the tools of continuum mechanics.

Different phases need to be identified with their mechanical properties and their geometrical nature. A phase, in continuum micromechanics, as will become clearer in following developments, is not necessarily a distinct material but rather a subdomain of the overall matter characterized by an on-average constant stress or strain state. The classical poromechanics theory is based on a two-phase representation of a porous medium as a solid-fluid composite. As we will see, such a representation falls short in representing a multi-scale porous material such as concrete. Finally, the volume fractions and the mechanical properties of the considered phases are important parameters. An alternative to the use of volume fractions can be the statistical representation of different equivalent R.E.V.s. Then the probability to find a certain mechanical property at a point in space becomes the descriptive variable of the representation. An underlying hypothesis that is made during the analysis is the ergodicity [141], that is the equivalence between spacial and ensemble averages[1]. Averages are therefore all denoted like the following average of for example the elasticity moduli (see also Section 5.3.3):

$$\langle \mathbb{C} \rangle = \frac{1}{|V|} \int_V \mathbb{C}\,(\underline{\mathbf{z}})\, dV \tag{7.2}$$

with $\mathbb{C}$ being the fourth order elasticity tensor.

Localization

Localization establishes the link between a macroscopic strain (or stress), prescribed at the boundary ∂V of the R.E.V., and the microscopic strain (or stress) in the individual (homogeneous) phases composing the R.E.V. With the representation of the R.E.V. at hand, the next step is the mechanical analysis of this representation. Two types of boundary conditions are generally considered, called Hashin conditions:

- *Homogeneous stresses applied on the boundary.* In this case, the tractions $\mathbf{T}^d = \boldsymbol{\Sigma}.\mathbf{n}$ are applied where $\boldsymbol{\Sigma}$ is the macroscopically applied stress tensor and $\mathbf{n}$ is the outward normal vector on the considered R.E.V. V with boundary ∂V. With these boundary conditions,

[1]The ergodicity hypothesis is further explored in Chapter 5, where we aim in comparing experimentally obtained spatial averages and ensemble averages. The probability of touching a phase with an indenter appears to be very well correlated with its volumetric proportions.

the stress average is then:

$$\langle \boldsymbol{\sigma} \rangle = \frac{1}{|V|} \int_V \boldsymbol{\sigma}(\underline{\mathbf{z}})\, dV = \boldsymbol{\Sigma} \tag{7.3}$$

where $\boldsymbol{\sigma}$ is the microscopic stress tensor. The average macroscopic deformations are then defined as:

$$\mathbf{E} = \langle \boldsymbol{\varepsilon} \rangle = \frac{1}{|V|} \int_V \boldsymbol{\varepsilon}(\underline{\mathbf{z}})\, dV \tag{7.4}$$

where $\boldsymbol{\varepsilon}$ is the microscopic deformation tensor.

- *Homogeneous deformations applied on the boundary.* The displacement $\boldsymbol{\xi}^d = \mathbf{E}.\underline{z}$ is applied on ∂V with $\mathbf{E}$ being the homogeneous macroscopic strain and $\underline{z}$ the local coordinate vector. The average of the microscopic strains then follows:

$$\langle \boldsymbol{\varepsilon} \rangle = \frac{1}{|V|} \int_V \boldsymbol{\varepsilon}(\underline{\mathbf{z}})\, dV = \mathbf{E} \tag{7.5}$$

and in which case one defines the macroscopic stress as:

$$\boldsymbol{\Sigma} = \langle \boldsymbol{\sigma} \rangle = \frac{1}{|V|} \int_V \boldsymbol{\sigma}(\underline{\mathbf{z}})\, dV \tag{7.6}$$

Equations (7.3) and (7.5), which are commonly referred to as the average stress and average strain theorems respectively [1], can be rigorously proven provided the homogeneous boundary conditions are applied at the boundary. The assumption of homogenous boundary conditions which itself produces homogeneous field in the body is valid far enough from the boundary, i.e. almost everywhere in the R.E.V. provided the scale separation conditions presented in Eq. (7.1) is respected. The localization then consists in determining the microscopic stresses and strains as functions of the macroscopically applied boundary conditions. In the simplest case, that is for linear elastic problems, the microscopic and macroscopic stresses and strains are linked through the localization relations of the type:

$$\boldsymbol{\varepsilon}(\underline{z}) = \mathbb{A} : \mathbf{E} \tag{7.7}$$

$$\boldsymbol{\sigma}(\underline{z}) = \mathbb{B} : \boldsymbol{\Sigma} \tag{7.8}$$

where $\mathbb{A}$ and $\mathbb{B}$ represent the fourth order stress and strain localization tensors, or concentration tensors, respectively. They provide a direct link between micro ($\boldsymbol{\varepsilon}(\underline{z})$, $\boldsymbol{\sigma}(\underline{z})$) and macro ($\mathbf{E}$, $\boldsymbol{\Sigma}$) properties. In some special cases these tensors can be evaluated through the solution of elastic boundary value problems (B.V.P.). In other cases they can be bound through average relations.

Eshelby's Solution An analytical expression of the strain concentration tensor $\mathbb{A}$ can be obtained in the particular simple case of a composite consisting of one ellispsoidal inclusion perfectly bonded to an infinite isotropic matrix, subjected to uniform strains $\mathbf{E}^0$ at infinity. In this case, Eshelby (1957) [80] showed that the strains in the inclusion are uniform and read:

$$\boldsymbol{\varepsilon}_p = \left[\mathbb{I} + \mathbb{P}_p^0 : (\mathbb{C}_p - \mathbb{C}^0)\right]^{-1} : \mathbf{E}^0 \tag{7.9}$$

where $\mathbb{C}_p$ is the stiffness of the inclusion, and $\mathbb{C}^0$ the one of the matrix. The tensor $\mathbb{P}_p^0$ depends on the shape of the inclusion, and on the stiffness properties of the matrix. Analytical forms of these tensors are provided for specific shapes of the inclusion. The spherical inclusion case which is of particular interest to this thesis is detailed in Appendix C.

The case of an inclusion in an infinite matrix can be extended in several manners to real composites, first by playing with the shape of the ellipsoid. For instance, cylindrical or penny-shaped inclusions can be used to model cylinders or cracks; second, by assigning an arbitrary stiffness $\mathbb{C}^0$ to the heterogeneous environment of an inclusion, different homogenization schemes are obtained. Finally, the strain $\mathbf{E}^0$ experienced locally by the inclusion may be different from the overall boundary condition $\mathbf{E}$.

Dilute Scheme For a composite containing very few non-interacting inclusions denoted by $r > 1$ in a matrix of stiffness $\mathbb{C}^1$, the strains inside the inclusions are directly given by Eq. (7.9), where $\mathbf{E}^0$ coincides with the uniform strain $\mathbf{E}$ applied at the boundary of the R.E.V. This dilute estimate of the strain concentration tensor $\mathbb{A}_r^{dil}$ in the inclusions is obtained in the form:

$$\mathbb{A}_r^{dil} = \left[\mathbb{I} + \mathbb{P}_r^1 : (\mathbb{C}_r - \mathbb{C}^1)\right]^{-1} \tag{7.10}$$

In the matrix, $\mathbb{A}_1^{dil}$ is obtained from the compatibility relation $\langle \mathbb{A} \rangle = \mathbb{I}$ in the form:

$$\mathbb{A}_1^{dil} = \mathbb{I} - \sum_{r>1} f_r \left[\mathbb{I} + \mathbb{P}_r^1 : (\mathbb{C}_r - \mathbb{C}^1) \right]^{-1} \tag{7.11}$$

Interactions Between Phases The analytical dilute case can be extended to a real multiphase composite by considering the interaction between inclusion phases: the strain in each phase r is assumed to be the one in an inclusion of stiffness $\mathbb{C}_r$ embedded in a fictitious matrix of stiffness $\mathbb{C}^0$, subjected to a uniform strain $\mathbf{E}^0$:

$$\boldsymbol{\varepsilon}_r = \left[\mathbb{I} + \mathbb{P}_r^0 : (\mathbb{C}_r - \mathbb{C}^0) \right]^{-1} : \mathbf{E}^0 \tag{7.12}$$

The strain average combined with Eq. (7.12) yields the following expression of $\mathbf{E}^0$

$$\mathbf{E}^0 = \left\{ \sum_r f_r \left[\mathbb{I} + \mathbb{P}_r^0 : (\mathbb{C}_r - \mathbb{C}^0) \right]^{-1} \right\}^{-1} : \mathbf{E} \tag{7.13}$$

where $\mathbf{E}$ is the strain applied to the R.E.V. From Eqs. (7.7), (7.9) and (7.13), the estimated expression of the strain concentration tensor becomes:

$$\mathbb{A}_r^{est} = \left[\mathbb{I} + \mathbb{P}_r^0 : (\mathbb{C}_r - \mathbb{C}^0) \right]^{-1} : \left\{ \sum_s f_s \left[\mathbb{I} + \mathbb{P}_s^0 : (\mathbb{C}_s - \mathbb{C}^0) \right]^{-1} \right\}^{-1} \tag{7.14}$$

Mori-Tanaka Scheme In a matrix/inclusion morphology let index 1 correspond to the matrix, and $r > 1$ to the inclusion phases. If we replace the reference stiffness $\mathbb{C}^0$ by the stiffness of the matrix $\mathbb{C}_1$, we obtain an explicit expression of the localization tensor which takes into account particle interaction, called the Mori-Tanaka estimate [172]:

$$\mathbb{A}_r^{MT} = \left[\mathbb{I} + \mathbb{P}_r^0 : (\mathbb{C}_r - \mathbb{C}_1) \right]^{-1} : \left\{ \sum_{s>1} f_s \left[\mathbb{I} + \mathbb{P}_s^0 : (\mathbb{C}_s - \mathbb{C}_1) \right]^{-1} \right\}^{-1} \tag{7.15}$$

Self-Consistent Scheme For polycrystals where all phases play similar roles in the microstructure, the self-consistent estimate uses as a reference stiffness $\mathbb{C}^0$, the unknown homogenized stiffness $\mathbb{C}^{SC}$. In such a scheme the localization tensor is now obtained in an implicit

fashion:

$$\mathbb{A}_r^{SC} = \left[\mathbb{I} + \mathbb{P}_r^{SC} : (\mathbb{C}_r - \mathbb{C}^{SC})\right]^{-1} : \left\{ \sum_{s>1} f_s \left[\mathbb{I} + \mathbb{P}_s^{SC} : (\mathbb{C}_s - \mathbb{C}^{SC})\right]^{-1} \right\}^{-1} \tag{7.16}$$

The validity of this scheme was confirmed for polycrystals for which the phase volume fractions do not differ much from each other [253].

Homogenization

The final step is homogenization, which is based on volume averaging over the R.E.V. of the constitutive relations defined at the scale of the phases. Homogenization delivers the macroscopic poroelastic properties of the E.H.M. as a function of the microscopic phase properties, their volume fractions, and their specific morphologies. This means expressing the macroscopic strains and stresses as functions of the microscopic stresses and strains. An important relation that is used in this procedure is the Hill-Mandel lemma (see Ref. [253]) which guarantees the equivalence of the macroscopic work and the spatial average of the microscopic work. While in general the average of the product is different from the product of the averages it is impressive to see that homogeneous boundary conditions (see Section 7.1.2) yield:

$$\langle \boldsymbol{\sigma} : \boldsymbol{\varepsilon} \rangle = \langle \boldsymbol{\sigma} \rangle : \langle \boldsymbol{\varepsilon} \rangle = \boldsymbol{\Sigma} : \mathbf{E} \tag{7.17}$$

where $\boldsymbol{\sigma}$ has to fulfill the equilibrium conditions and $\boldsymbol{\varepsilon}$ has to be compatible, but both do not have to be associated. In addition, either $\boldsymbol{\sigma}$ has to fulfill the homogeneous stress condition on ∂V or $\boldsymbol{\varepsilon}$ the homogeneous deformation condition, both mentioned above.

7.2 Micromechanical Representation of CBM

The detailed homogenization process as applied to cementitious materials requires a multi-scale homogenization process for each level of the microstructure defined in Fig. 4-13, and detailed below.

7.2.1 Level 0: Nanoparticle-Solid Phase

We start our micromechanical modeling of the complex microstructure of cement-based materials at a length scale at which the material properties do not change from one cement-based material to another. This is the scale where physical chemistry meets mechanics; that is, the mechanical properties are solely defined by the physical chemistry of the formation process of the material. In what follows, we will adopt Jennings interpretation of the C-S-H microstructure as discussed in Section 4.5.2: an amorphous colloidal structure of the C-S-H, organized in 'globules' (see Fig. 6-6), composed of basic building blocks and an intra-globules porosity. The way by which the porosity can be assessed, at this scale, is from mass density measurements. This porosity which manifests itself at a scale smaller than the characteristic solid dimension of 2.2×10^{-9} m, is $\varphi_0 = 18\%$ irrespective of the type of C-S-H. Instead, it is intrinsic to the C-S-H solid phase, and can be associated with the nanoporosity filled by structural water (and not bulk water). Above this scale, there is a second type of porosity, the gel porosity, but which was found to differ from one type of C-S-H to another, as detailed below. Hence, from a poromechanics point of view, it is appropriate to consider this solid phase ('globules' in Jennings terminology) which includes a 18% intra-solid porosity filled by structural water, as the elementary solid phase of a poromechanics representation of cement-based materials. Current experimental methods are unable of providing mechanical properties at this small scale, and as a consequence little is known about the mechanical behavior of this solid phase. A layered representation assumed in some of the models found in the literature suggests an anisotropic mechanical behavior for the solid phase. Nevertheless, the random orientation of the particles in space suggests that an equivalent isotropic solid phase can be legitimately employed.

7.2.2 Level I: C-S-H phases – Gel Porosity – C-S-H matrix

Volume Fractions

The solid phase of Level 0 together with gel-porosity forms different types of C-S-H phases. These phases manifest themselves in units larger than 16.6×10^{-9} m [131], as sketched in Fig. 6-6. We refer to this level as Level I, as it represents the smallest material length scale that is presently accessible by mechanical testing, i.e., nanoindentation (see Chapter 5 and Refs.

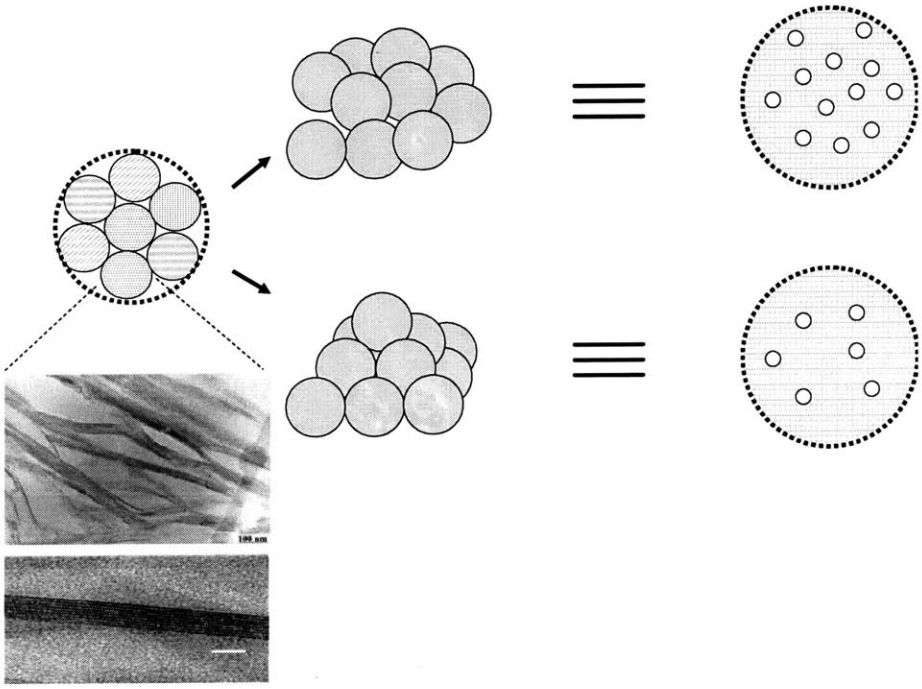

Figure 7-2: Micromechanical representation of C-S-H phases. The particluate nature of C-S-H phases is replaced by an equivalent system of solid phase intermixed with various volume fractions of porosities.

[59, 60]). At Level I, the C-S-H exists in at least two different forms, a low density (LD) and a high density (HD) form (Fig. 6-6). The difference between the two types of C-S-H relates to the gel porosity of roughly 24% for HD C-S-H, and 37% for LD C-S-H [130], due to the different packing density of the C-S-H solid of the two types of C-S-H; in addition to the 18% nanoporosity within the C-S-H solid phase at Level 0 (Fig. 6-6). In contrast to the nanoporosity, the gel porosity has a characteristic dimension of the solid phase, i.e., on the order of 5.6×10^{-9} m, in which the water present can be considered as a bulk water phase – in the sense of poromechanics theory. The gel porosity can be defined in a standard manner:

$$\phi_0^{LD} = \frac{V_{f,LD}}{V_{LD}} = 0.37; \;\; \phi_0^{HD} = \frac{V_{f,HD}}{V_{HD}} = 0.24 \tag{7.18}$$

where $V_{f,J}$ is the pore volume, and V_J the reference volume ($J = HD, LD$). The gel porosity values are also intrinsic to all cement-based materials: they are a consequence of the formation process of C-S-H in the course of hydration. That what changes from one cement paste material to the other is the volumetric proportion of HD C-S-H and LD C-S-H, within the C-S-H matrix. From a poromechanics point of view, an averaging quantity characterizing the pore space that is occupied by bulk water is:

$$\phi_0^I = \phi_{LD} f_{LD} + \phi_{HD} f_{HD} \tag{7.19}$$

where f_{LD} and f_{HD} are the volumetric proportions of the LD and HD C-S-H defined as:

$$f_{LD} = \frac{V_{LD}}{V_I}; \;\; f_{HD} = \frac{V_{HD}}{V_I}; \;\; f_{LD} + f_{HD} = 1 \tag{7.20}$$

Morphological Arrangement

Most of the experimental data on C-S-H suggests that the load bearing phase of CBM systems is essentially a colloidal system of C-S-H particles (i.e., globules), in which repulsive forces are in equilibrium with cohesive bonds. While the very nature of the bonding continuity in between particles is not currently known, it is most likely that the deformation behavior in the agglomerate system originates from the deformation in the pore space. In such a scenario, it is not the globule elasticity that is of primary importance but rather the contact regions in between particles, i.e., the interparticle porosity, that governs deformation. In fact deformation in the

crystalline structure vis-à-vis deformation at the interface between C-S-H particles involves much higher forces, energies and stiffness. The simplest continuous representation of such a discrete system comes to replace an assembly of grains by a continuous solid phase intermixed with some porosity (Fig. 7-2). The exact morphological arrangement is still hard to resolve and, as a result, several micromechanical schemes will be considered in parallel. The assumption of continuity provides a convenient way to localize the total elastic deformation in a conceptual continuous C-S-H solid phase, which physically occurs both in very stiff, solid particles and in contact regions between them.

7.2.3 Level II: Cement Paste – Capillary Porosity – n Solid phases

Level II refers to the cement paste, which manifests itself at a characteristic length scale of $10^{-6} - 10^{-4}$ m (Fig. 6-5). At this scale, the porous C-S-H matrix (composed of two types) together with the unhydrated cement products (clinker phases denoted here as CL), large Portlandite crystals (CH = $Ca(OH)_2$), aluminates (AFm, AFt) and the macro-porosity ϕ_0 (which is often referred to as capillary porosity, and which is generally present only in high $w/c-$ratio materials) form the cement paste. For purposes of poromechanical modeling, we will concentrate our efforts on the C-S-H phase that dominates in volumetric proportions, neglecting any secondary solid phases (CH, AFm, AFt see section 4.1) that seem to play only minor role in macro-poro-elasticity due to their low volume fractions and insignificant contrast in mechanical elastic properties with the C-S-H matrix. The volume fractions of the considered phases at this level can be defined in the usual manner:

$$f_r = \frac{V_r}{V_{II}} \text{ for } r = CSH, MP, CL \tag{7.21}$$

In contrast to previous levels, Level II is a clear case of a matrix-inclusion morphology. The total porosity p^{II} of a cement paste is the sum of the nanoporosity, the gel-porosity and the capillary porosity [235]:

$$p^{II} = \left[\left(\varphi_0\left(1-\phi_{LD}\right)+\phi_{LD}\right) f_{LD} + \left(\varphi_0\left(1-\phi_{HD}\right)+\phi_{HD}\right) f_{HD}\right] f_{CSH} + \phi_0 \tag{7.22}$$

where f_{LD} and f_{HD} represent the volume fractions of the LD C-S-H phase and the HD C-S-H phase present in the cement paste. The total porosity is the relative change of mass that is measured by means of weighting experiments on a fully saturated and a dried cement paste oven dried at 105°C. By contrast, other techniques such as poromercury intrusion (PMI), do not allow to assess the total porosity, as the technique typically fails for pore throat radii smaller than 7×10^{-9} m. From a poromechanics point of view, the porosity which is filled by a bulk water phase is the total porosity minus the nanoporosity (filled by structural water):

$$\phi_0^{II} = \phi_{LD} f_{LD} + \phi_{HD} f_{HD} + \phi_0 \tag{7.23}$$

The dominating phase, at this scale, is the porous C-S-H matrix, which can occupy up to 90% of the volume of a cement paste.

7.2.4 Level III: Mortar and Concrete

Level III of a characteristic length scale greater than 10^{-3} m refers to mortar and concrete; that is a composite material composed of a porous cement paste matrix (CP), and sand particle inclusions (i) in the case of mortar, and additional aggregate inclusions in the case of concrete. Some authors consider in addition the Interfacial Transition Zone (ITZ) between inclusions and matrix, which has been focus of many micromechanical modeling attempts (e.g., Refs. [90, 117]). From a poromechanics point of view, the cement paste matrix is a porous matrix, while – except for special applications – any porosity contained in the aggregates is rather of occluded nature. The total porosity at Level III, that can be assessed by weighting experiments, is:

$$p^{III} = (1 - f_i)\, p^{II} + \left(\phi_{ITZ} - p^{II}\right) f_{ITZ} \tag{7.24}$$

where f_i and f_{ITZ} represent the volume fractions of the inclusions and of the ITZ, while ϕ_{ITZ} is the porosity of the ITZ, which has been argued to differ (in some cases) from the porosity of the cement paste. A lower bound of the inclusion volume fraction is obtained by letting $\phi_{ITZ} = p^{II}$.

Figure 7-3 summarizes the model structure of CBM systems that will serve as the basis for the forthcoming upscaling relations. This suggested microporomechanics representation

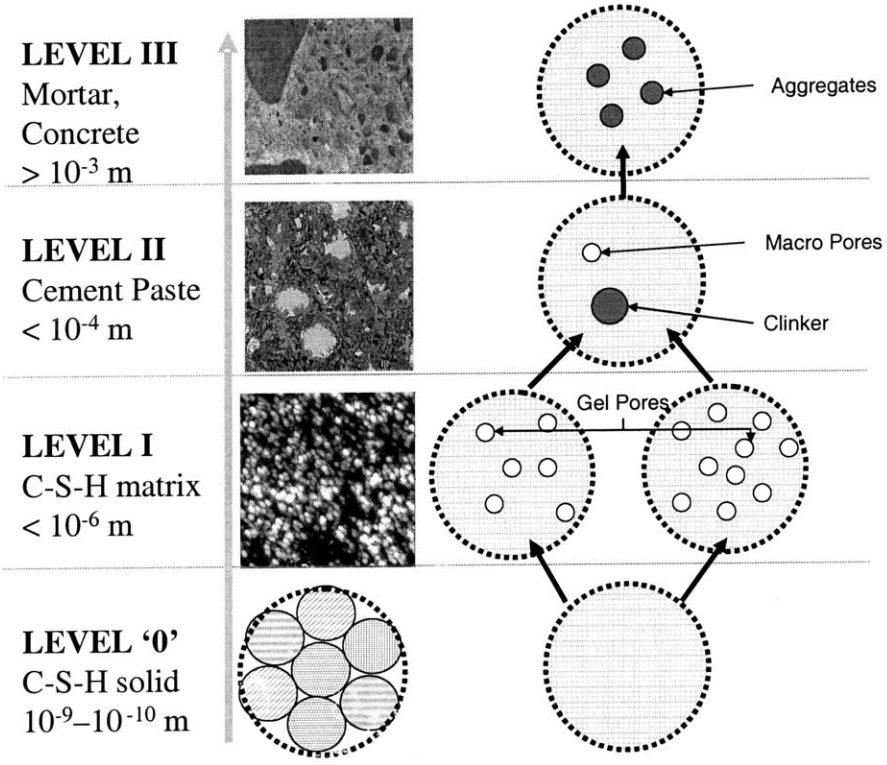

Figure 7-3: Summary of the proposed micromechanical representation for CBM systems.

of CBM systems is certainly reductionist, reducing the complexity of such materials to an isotropic solid phase. It allows however to reduce the macroscopically observed variability to a few invariant material properties that have been accessed by nanoindentation (see Chapter 5) and volumetric proportions that are readily available either from nanoindentation (see Chapter 5) or from chemical reaction models (see Chapter 4 and further developments in Chapter 8).

7.3 Localization and Homogenization

7.3.1 Level 0: Invariant Properties of C-S-H

The two phases of C-S-H are composed of a solid phase and a saturated pore space. This solid-fluid interaction is captured by microporomechanics theory. The theory of micromechanics applied to porous systems, called microporomechanics, is now well established (Dormieux et al.

[40, 73, 74]). It assumes that a porous medium (R.E.V.), here the C-S-H$_J$ phase ($J = LD, HD$), is composed of a biconnected solid and pore space. From a macroscopic point of view, the classical relations of poroelasticity applied to isotropic media read [26, 62]:

$$\boldsymbol{\Sigma}_J = K_J^0 E_v \mathbf{1} + 2G_J^0 \mathbf{E}_d - b_J^0 p_J \mathbf{1} \tag{7.25a}$$

$$\left(\phi - \phi_J^0\right)_J = b_J^0 E_v + \frac{p_J}{N_J^0} \tag{7.25b}$$

where superscript 0 indicates that the quantity is defined at Level 0, and subscript $J = LD, HD$ indicates that the quantity is defined in R.E.V. $J = LD, HD$. K is the bulk modulus, G is the shear modulus, b the Biot coefficient and N the solid Biot modulus. $\left(\phi - \phi_J^0\right)_J$ is the change of porosity where ϕ_J^0 is the C-S-H$_J$ ($J = LD, HD$) porosity given in Eq. (7.18), and p_J the fluid pressure. In addition, $\boldsymbol{\Sigma}$, is the macroscopic stress tensor and $\mathbf{E}$, is the macroscopic strain tensor which may be decomposed in its deviatoric, $\mathbf{E}_d$, and volumetric parts, $\mathbf{E}_v$:

$$\mathbf{E} = \mathbf{E}_d + \frac{1}{3} E_v \mathbf{1} \tag{7.26}$$

In the macroscopic poroelasticity theory, solids and fluids coexist at the same location. From a microscopic point of view, solid and fluid phases are dissociated. For a zero applied strain $\mathbf{E}$, b_J^0 relates the fraction of pore pressure rise to a stress increase $\boldsymbol{\Delta\Sigma} = -b_J^0 \boldsymbol{\Delta} p \mathbf{1}$, while N_J^0 translates it into a porosity change: $\left(\phi - \phi_J^0\right)_J = p_J / N_J^0$. In this case, p_J and $\mathbf{E}$ are independent loading conditions to which the R.E.V. is subjected:

$$\underline{\boldsymbol{\xi}} = \mathbf{E} \cdot \underline{z} \quad (\partial V) \tag{7.27}$$

$$\boldsymbol{\sigma} \cdot \underline{n} = -p\, \underline{n} \quad (\mathcal{I}^{sf}) \tag{7.28}$$

where ∂V is the external surface of the R.E.V., and $\mathcal{I}^{sf}$ the interface between solid and fluid phases.

Within the framework of microporomechanics theory, it is convenient to apply a continuous description of the microscopic stresses:

$$(\forall \underline{z} \in V) \quad \text{in } V_0 : \boldsymbol{\sigma}(\underline{z}) = \left(k(\underline{z}) - \frac{2}{3} g(\underline{z})\right) \epsilon(\underline{z})\, \mathbf{1} + 2g(\underline{z})\, e_{ij}(\underline{z}) + \boldsymbol{\sigma}^p(\underline{z}) \tag{7.29}$$

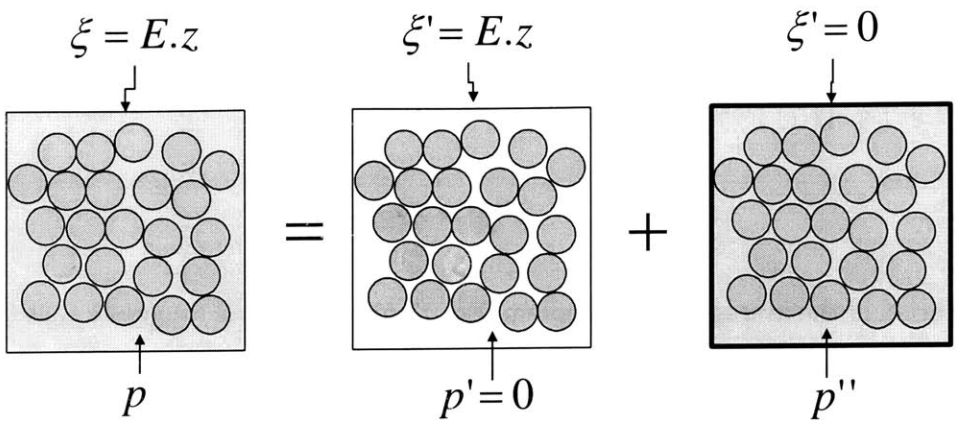

Figure 7-4: Linear decomposition of the poromechanical problem in two sub-problems.

where $\boldsymbol{\sigma}(\underline{z})$ and $\boldsymbol{\varepsilon}(\underline{z})$ stand for the local stress and strain tensors, $\epsilon = \varepsilon_{ii}$ is the microscopic volume strain; and $e_{ij} = \varepsilon_{ij} - \frac{1}{3}\epsilon\delta_{ij}$ is the microscopic deviator strain. $(k(\underline{z}), g(\underline{z}))$ and $\boldsymbol{\sigma}^p(\underline{z})$ are respectively the isotropic stiffness properties and an eigenstress whose spatial distribution within the R.E.V. is given by:

$$(k(\underline{z}), g(\underline{z})) = \begin{cases} 0 & (V_p) \\ (k_s, g_s) & (V_s) \end{cases} \quad \boldsymbol{\sigma}^p(\underline{z}) = \begin{cases} -p\mathbf{1} & (V_p) \\ 0 & (V_s) \end{cases} \tag{7.30}$$

where V_p and V_s stand for the domains occupied by pores and solids respectively, and (k_s, g_s) are the stiffness properties of the assumed isotropic C-S-H solid phase.

We now attempt to link macroscopic quantities $\left(K_J^0, G_J^0\right), b_J^0$ and N_J^0 with microscopic quantities such as (k_s, g_s), ϕ_J^0. Given the linearity of the mechanical problem with respect to stress $\boldsymbol{\sigma}$ and strain $\mathbf{E}$ we decompose the problem in two particular load cases (see Fig. 7-4): In the first one (denoted by $'$) the fluid pressure is zero ($p = 0$), and the R.E.V. is loaded as a skeleton with empty pores. In the second load case (denoted by $''$) the fluid is pressurized under the strain boundary condition $\mathbf{E} = \mathbf{0}$.

First Sub-Problem: Drained Conditions $(p = 0)$

The first load case corresponds to a classical micromechanics problem in which a composite material composed of a solid and empty inclusions is subjected to a uniform boundary condition

Eq. (7.27). In this case, following classical micromechanics (see Ref. [253]), the local strain $\boldsymbol{\varepsilon}'(\underline{z})$ is related to the macroscopic strain $\mathbf{E}$ by means of a forth order localization tensor $\mathbb{A}$, defined in Eq. (7.7) (see Section 7.1.2):

$$\boldsymbol{\varepsilon}'(\underline{z}) = \mathbb{A}(\underline{z}) : \mathbf{E} \tag{7.31}$$

Application of the average strain theorem, Eq. (7.5) to Eq. (7.31) suggests that the localization tensor should satisfy the compatibility condition:

$$\langle \mathbb{A}(\underline{z}) \rangle = \mathbb{I} \tag{7.32}$$

Using Eq. (7.31) in Eq. (7.29) together with Eq. (7.30), the stress volume average $\boldsymbol{\Sigma}'$ in this load case is:

$$\boldsymbol{\Sigma}' = \langle \boldsymbol{\sigma}'(\underline{z}) \rangle = \langle \mathbb{C}(\underline{z}) : \mathbb{A}(\underline{z}) \rangle : \mathbf{E} \tag{7.33}$$

and the change of porosity:

$$\left(\phi - \phi_J^0\right)' = \phi_J^0 \mathbf{1} : \langle \boldsymbol{\varepsilon}'(\underline{z}) \rangle_{V_p} = \phi_J^0 \mathbf{1} : \langle \mathbb{A}(\underline{z}) \rangle_{V_p} : \mathbf{E} \tag{7.34}$$

Finally, a comparison of Eqs. (7.33) and (7.34) with Eqs. (7.25a) and (7.25b) allows to identify the homogenized stiffness tensor and the Biot coefficients:

$$\mathbb{C}_J^0 = \langle \mathbb{C}(\underline{z}) : \mathbb{A}(\underline{z}) \rangle \tag{7.35}$$

$$\mathbf{b}_J^0 = \phi_J^0 \, \mathbf{1} : \langle \mathbb{A} \rangle_{V_p} \tag{7.36}$$

Note that the isotropic forms of Eqs. (7.35) and (7.36) yield the classical estimates of poromechanics, that involve the homogenized bulk modulus, k_J, and the solid phase stiffness properties, (k^s, g^s) :

$$k_J = \left(1 - \phi_J^0\right) A_s^v k_s; \quad g_J = \left(1 - \phi_J^0\right) A_s^d g_s \tag{7.37}$$

$$\mathbf{b}_J^0 = b_J \, \mathbf{1} \text{ with } b_J = 1 - \frac{k_J}{k^s} \tag{7.38}$$

Second Sub-Problem: Undrained Conditions ($\mathbf{E}''= 0$)

In the second load case, the macroscopic state Eqs. (7.25a) and (7.25b) read:

$$\boldsymbol{\Sigma}'' = \boldsymbol{\Sigma}^p = -\mathbf{b}_J^I \, p_J \tag{7.39}$$

$$\left(\phi - \phi_J^0\right)'' = \frac{p_J}{N_J^0} \tag{7.40}$$

From a micromechanics point of view, the second subproblem corresponds to a micro-to-macro eigenstress problem. This problem is conveniently solved using Levin's theorem (Ref. [253]):

$$\boldsymbol{\Sigma}^p = \langle \boldsymbol{\sigma}^p(\underline{z}) : \mathbb{A}(\underline{z}) \rangle \tag{7.41}$$

Levin's theorem can be readily derived by applying Hill-Mandel Lemma (see Eq. (7.17)) to the strain field, $\boldsymbol{\varepsilon}'$, and to the stress field, $\boldsymbol{\sigma}''$:

$$\left\langle \boldsymbol{\sigma}'' \colon \boldsymbol{\varepsilon}' \right\rangle = \boldsymbol{\Sigma}'' : \mathbf{E} \tag{7.42}$$

where the left hand side of Eq. (7.42) reads:

$$\left\langle \boldsymbol{\sigma}'' \colon \boldsymbol{\varepsilon}' \right\rangle = \left\langle \boldsymbol{\varepsilon}'' \colon \mathbb{C}(\underline{\mathbf{z}}) : \boldsymbol{\varepsilon}' \right\rangle + \left\langle \boldsymbol{\sigma}^p : \boldsymbol{\varepsilon}' \right\rangle \tag{7.43}$$

By a second application of Eq. (7.17) to the strain field , $\boldsymbol{\varepsilon}''$, and stress field , $\boldsymbol{\sigma}'$, and observing that for the specific load case $\langle \boldsymbol{\varepsilon}'' \rangle = 0$, yields $\left\langle \boldsymbol{\varepsilon}'' \colon \mathbb{C}(\underline{\mathbf{z}}) : \boldsymbol{\varepsilon}' \right\rangle = 0$. A comparison of Eq. (7.42) with Eq. (7.43) yields Levin's theorem as defined in Eq. (7.41). Using Eq. (7.30) in Eq. (7.41), and combining this result with Eq. (7.39), we obtain:

$$\boldsymbol{\Sigma}'' = \boldsymbol{\Sigma}^p = -\mathbf{b}_J^0 \, p_J \equiv -\phi_J^0 \, \mathbf{1} : \langle \mathbb{A} \rangle_{V_p} \, p_J \tag{7.44}$$

A straightforward comparison of Eqs. (7.44) and (7.36) shows that the Levin theorem provides a second means to determine the Biot coefficient tensor. Furthermore, the porosity change in this subproblem needs to be counterbalanced by an opposite change in the solid matrix in order

for the zero strain boundary condition to be satisfied:

$$\left(\phi - \phi_J^0\right)'' = \phi_0 \mathbf{1} : \ \left\langle \boldsymbol{\varepsilon}''(\underline{z}) \right\rangle_{V_p} = (1 - \phi_0)\mathbf{1} : \left(- \left\langle \boldsymbol{\varepsilon}''(\underline{z}) \right\rangle_{V_s} \right) \tag{7.45}$$

If we use in Eq. (7.45) the compatibility condition and Hooke's law, we obtain:

$$\begin{aligned} \left(\phi - \phi_J^0\right)'' &= -(1 - \phi_J^0)\mathbf{1} : \mathbb{C}_s^{-1} : \left\langle \boldsymbol{\sigma}''(\underline{z}) \right\rangle_{V_s} && (7.46) \\ &= -\frac{(1 - \phi_J^0)}{3k_s} \left\langle \boldsymbol{\sigma}''(\underline{z}) \right\rangle_{V_s} && (7.47) \end{aligned}$$

Furthermore one needs to get an estimate of the strain in the pore phase, which can be achieved by employing the stress average theorem of Eq. (7.3) in Eq. (7.29):

$$\boldsymbol{\Sigma}'' = \left\langle \boldsymbol{\sigma}''(\underline{z}) \right\rangle = (1 - \phi_J^0) \left\langle \boldsymbol{\sigma}''(\underline{z}) \right\rangle_{V_s} - \phi_J^0 p_J \mathbf{1} \tag{7.48}$$

Finally, using Eq. (7.44) in Eq. (7.48), and substituting this result in Eq. (7.46), the porosity change in the subproblem reads:

$$\left(\phi - \phi_J^0\right)'' = \frac{\phi_J^0}{k_s} (\langle A^v \rangle_{V_p} - 1) p_J \tag{7.49}$$

Last, from a comparison of Eq. (7.49) with Eq. (7.40), the solid Biot modulus is obtained by:

$$\frac{1}{N_J^0} = \frac{\phi_J^0}{k_s} (\langle A^v \rangle_{V_p} - 1) \tag{7.50}$$

Note that the isotropic form of Eq. (7.50) yields the classical estimate of poromechanics:

$$\frac{1}{N_J^0} = \frac{b_J^0 - \phi_J^0}{k_s} \tag{7.51}$$

Equations (7.35), (7.36) and (7.50) give the expression of the homogenized material poroelastic properties as a function of stiffness of the solid, (k_s, g_s), and the components of the strain concentration tensor (A^v, A^d), $\mathbb{A}(\underline{z})$:

$$\mathbb{A}(\underline{z}) = A^v(\underline{z})\mathbb{J} + A^d(\underline{z})\mathbb{K} \tag{7.52}$$

where J_{ijkl}=1/3 $(\delta_{ij}\delta_{kl})$ and $\mathbb{K} = \mathbb{I} - \mathbb{J}$ are the spherical and deviatoric projections of the forth order identity tensor $I_{ijkl} = \frac{1}{2}(\delta_{ik}\delta_{jl} + \delta_{il}\delta_{jk})$, and δ_{ij} is the Kronecker delta. While the localization tensor can be estimated using developments shown in Section 7.1.2, the solid stiffness properties (k_s, g_s) are still not experimentally determined. The mechanical response will therefore need to be resolved in an alternative way.

7.3.2 Level I: Poroelastic Properties of C-S-H Matrix - Double Porosity Model

The C-S-H matrix is composed of two porous materials, the LD C-S-H phase and the HD C-S-H phase, each of which is described by poroelastic constitutive equations of the form of Eq. (7.25). To derive the poroelastic constitutive equations of the C-S-H matrix, we adopt a continuous description of the stress field in the heterogeneous R.E.V.:

$$\text{in } V_I : \boldsymbol{\sigma}(\underline{z}) = \left(k(\underline{z}) - \frac{2}{3}g(\underline{z})\right)\epsilon(\underline{z})\,\mathbf{1} + 2g(\underline{z})\,e_{ij}(\underline{z}) + \boldsymbol{\sigma}^p(\underline{z}) \tag{7.53}$$

together with the distributions of the elastic properties $(k(\underline{z}), g(\underline{z}))$ and the eigenstress $\sigma^p(\underline{z})$:

$$(k(\underline{z}), g(\underline{z})) = \begin{cases} (k_{LD}, g_{LD}) \text{ in } V_{LD} \\ (k_{HD}, g_{HD}) \text{ in } V_{HD} \end{cases} \quad \sigma^p(\underline{z}) = \begin{cases} -b^0_{LD}\, p_1 \text{ in } V_{LD} \\ -b^0_{HD}\, p_2 \text{ in } V_{HD} \end{cases} \tag{7.54}$$

where $\epsilon = \varepsilon_{ii}$ is the microscopic volume strain; and $e_{ij} = \varepsilon_{ij} - \frac{1}{3}\epsilon\delta_{ij}$ is the microscopic deviator strain. $(k_j, g_j), (j = LD, HD)$ are the elastic properties of the LD– and HD C-S-H phases that occupy domains V_{LD} and V_{HD} in the R.E.V. For purpose of argument, we will assume that the fluids present within the two types of C-S-H are not at the same pressure.

Following the linear microporomechanics already applied in Section 7.3.1 [74],we decompose the problem in two sub-problems:

First Sub-Problem: Drained Conditions $(p = 0)$

The first sub-problem corresponds to overall drained conditions, for which $p_1 = p_2 = 0$. We assume that the R.E.V. is subjected to a uniform displacement boundary condition, so that the

solid boundary conditions to which the solid phase is subjected read:

$$\text{on}\,\partial V \;:\; \underline{\xi}'(\underline{z}) = \mathbf{E}\cdot\underline{z} \tag{7.55a}$$

$$\text{on}\,\mathcal{I}_{sf} \;:\; \boldsymbol{\sigma}\cdot\underline{n} = 0 \tag{7.55b}$$

Here, ∂V stands for the boundary of the R.E.V., and $\mathcal{I}_{sf}$ represents the solid-fluid interfaces. $\underline{\xi}'(\underline{z})$ stands for the microscopic displacement field, and $\mathbf{E}$ is the macroscopic strain tensor, which is related to the microscopic strain by an isotropic strain localization condition:

$$\boldsymbol{\varepsilon}'(\underline{z}) = \mathbf{e}'(\underline{z}) + \frac{1}{3}\epsilon'(\underline{z})\boldsymbol{\delta} = a^d(\underline{z})\,\mathbf{E}_d + \frac{1}{3}a^v(\underline{z})\,E_v\boldsymbol{\delta} \tag{7.56}$$

where $a^d(\underline{z})$ and $a^v(\underline{z})$ are the deviator strain and the volumetric strain localization factors. Equation (7.53) together with the elastic distribution Eq. (7.54) yields after volume averaging the macroscopic stress:

$$\Sigma'_m = \langle\sigma'_m\rangle = K^I E_v;\quad K^I = f_{LD}k_{LD}A^v_{LD} + f_{HD}k_{HD}A^v_{HD} \tag{7.57a}$$

$$\mathbf{S}' = \langle\mathbf{s}'\rangle = 2G^I\mathbf{E}_d;\quad G^I = f_{LD}g_M A^d_M + f_{HD}g_{HD}A^d_{HD} \tag{7.57b}$$

where $A^v_J = \langle a^v(\underline{z})\rangle_{V_J}$ and $A^d_J = \langle a^d(\underline{z})\rangle_{V_J}$ stand for volume averages of the localization factors over the C-S-H subdomains, and $f_J = V_J/V$ represent the volume fractions satisfying $f_{LD} + f_{HD} = 1$. On the other hand, the change of the gel-porosity in the subproblem reads $(J = LD, HD)$:

$$\left[(\phi-\phi_0)^I_J\right]' = f_J\left[(\phi-\phi_0)^0_J\right]' = b^I_J E_v \tag{7.58a}$$

$$b^I_J = f_J b^0_J A^v_J \tag{7.58b}$$

where superscript $0, I$ indicates the scale ('Level') at which the quantity is defined. For instance, b^0_J stands for the Biot coefficients given by Eq. (7.36).

Second Sub-Problem: Undrained Conditions ($\mathbf{E}''= 0$)

The second sub-problem we consider is the zero-displacement boundary problem, while the gel-porosity is pressurized. From linear microporoelasticity, it is known that the problem is conveniently solved using Levin's theorem, delivering a relation between the macroscopic and the microscopic eigenstresses [40, 74]:

$$\boldsymbol{\Sigma}'' = \langle \boldsymbol{\sigma}^p (\underline{z}) : \mathbb{A} (\underline{z}) \rangle \tag{7.59}$$

where $\mathbb{A}(\underline{z})$ is the forth-order strain localization tensor. Application of the eigenstress distribution Eq. (7.54) in Eq. (7.59) yields the macroscopic mean stress in this subproblem:

$$\Sigma''_m = -b^I_{LD} p_1 - b^I_{HD} p_2 \tag{7.60}$$

where we verify that $b^I_{LD} = f_{LD} b^0_{LD} A^v_{LD}$ and $b^I_{HD} = f_{HD} b^0_{HD} A^v_{HD}$ obtained in the first sub-problem Eq. (7.58) are the Biot coefficients associated with the pressures in gel-porosity of the two type of C-S-H. Because the constitutive equation for the change of the porosity in each subdomain is given by Eq. (7.25b), the change of porosity reads:

$$\left[(\phi - \phi_0)^I_J \right]'' = f_J \left(b^0_J \langle \epsilon'' \rangle_{V_J} + \frac{p_J}{N^0_J} \right) \tag{7.61}$$

We need to eliminate $\langle \epsilon'' \rangle_{V_J}$ in Eq. (7.61). To this end, we determine the stress average in this sub-problem on account of Eqs. (7.53) and (7.54):

$$\begin{aligned} \Sigma''_m &= f_{LD} \langle \sigma''_m \rangle_{V_{LD}} + f_{HD} \langle \sigma''_m \rangle_{V_{HD}} \\ &= f_{LD} k_{LD} \langle \epsilon'' \rangle_{V_{LD}} + f_{HD} k_{HD} \langle \epsilon'' \rangle_{V_{HD}} - f_{LD} b^0_{LD} p_1 - f_{HD} b^0_{HD} p_2 \end{aligned} \tag{7.62}$$

Then, we use Eq. (7.60) in Eq. (7.62) to express the average strain in the porous matrix $\langle \epsilon'' \rangle_{V_J}$ as a function of p_J:

$$\left(f_{LD} b^0_{LD} - b^I_{LD} \right) p_1 + \left(f_{HD} b^0_{HD} - b^I_{HD} \right) p_2 = f_{LD} k_{LD} \langle \epsilon'' \rangle_{V_{LD}} + f_{HD} k_{HD} \langle \epsilon'' \rangle_{V_{HD}} \tag{7.63}$$

which suggests, using Eq. (7.58) or (7.60):

$$\langle \epsilon'' \rangle_{V_J} = \frac{b_J^0}{k_J} (1 - A_J^v) \, p_J \tag{7.64}$$

with no summation on repeated subscripts. Finally, use of Eqs. (7.64) and (7.61) yields:

$$\left[(\phi - \phi_0)_J^I \right]'' = \frac{p_J}{N_J^I}; \; \frac{1}{N_J^I} = \frac{f_J}{N_J^0} + f_J \frac{\left(b_J^0\right)^2}{k_J} (1 - A_J^v) \tag{7.65}$$

Lastly, a superposition of the two subproblems yields the macroscopic state equations of the C-S-H matrix:

$$\Sigma_m = \Sigma_m' + \Sigma_m'' = K^I E_v - b_{LD}^I p_1 - b_{HD}^I p_2 \tag{7.66a}$$

$$(\phi - \phi_0)_J^I = b_J^I E_v + \frac{p_J}{N_J^I}; \; J = LD, HD \tag{7.66b}$$

The resulting state equations are recognized as the state equations of a double-porosity material without interaction of the fluid pressures on the deformation of the solid part of the porous subdomains (i.e., Eq. (7.64)). Given the similar size of the porosity in the LD– and HD C-S-H, as defined by the packing densities, it is reasonable to anticipate little difference in pressure between the two types of C-S-H. In this case, the poroelastic state equations of the C-S-H matrix reduce to:

$$\Sigma_m = K^I E_v - b^I p \tag{7.67a}$$

$$(\phi - \phi_0)^I = b^I E_v + \frac{p}{N^I} \tag{7.67b}$$

and the poroelastic constants are given by:

$$K^I = f_{LD} k_{LD} A_{LD}^v + f_{HD} k_{HD} A_{HD}^v \tag{7.68a}$$

$$G^I = f_{LD} g_M A_M^d + f_{HD} g_{HD} A_{HD}^d \tag{7.68b}$$

$$b^I = b_{LD}^I + b_{HD}^I = f_{LD} b_{LD}^0 A_{LD}^v + f_{HD} b_{HD}^0 A_{HD}^v \tag{7.68c}$$

$$\frac{1}{N^I} = \frac{1}{N_{LD}^I} + \frac{1}{N_{HD}^I} \tag{7.68d}$$

7.3.3 Level II: Poroelastic Properties of Cement Paste

Let us turn now to cement paste: a composite of a porous C-S-H matrix (C-S-H) and macroporosity (MP), in addition to some inclusion phases (residual clinker (CL)). For purpose of clarity we derive the poroelastic state equations of cement paste for two particular cases:

a) Macroporosity embedded in a C-S-H matrix, which is the case of cement pastes with $w/c > 0.42$ and

b) A C-S-H matrix reinforced by clinker inclusions, which is the microstructure prevailing in low $w/c-$ratios $w/c < 0.42$ (see Section 4.5.1).

Two-scale Double Porosity Model ($w/c > 0.42$)

In contrast to the C-S-H matrix (Level I), the main feature here at Level II is that the porosity manifests itself at two different scales: a microporosity situated within the porous matrix, and macroporosity. The constitutive equations of the porous matrix are assumed to be defined by Eq. (7.67). Given the difference in size of the porosities involved, we assume a different pressure in the micro- and macroporosity. Proceeding as before, we adopt a continuous description of the stress field in the heterogeneous R.E.V., of Eq. (7.53), together with the following distributions of the elastic properties $(k(\underline{z}), g(\underline{z}))$ and the eigenstress $\sigma^p(\underline{z})$:

$$(k(\underline{z}), g(\underline{z})) = \begin{cases} (K^I, G^I) \text{ in } V_M \\ (0,0) \text{ in } V_{\phi 2} \end{cases} \quad \sigma^p(\underline{z}) = \begin{cases} -b^I p_1 \text{ in } V_M \\ -p_2 \text{ in } V_{\phi 2} \end{cases} \tag{7.69}$$

where V_M stands for the volume occupied by the porous matrix in the R.E.V., and $V_{\phi 2}$ for the macroscopic pore space. We decompose the problem into two sub-problems:

First Sub-Problem: Drained Conditions ($p_1 = p_2 = 0$)

The first sub-problem corresponds to overall drained conditions, for which $p_1 = p_2 = 0$. The boundary conditions are still defined by Eq. (7.55), and an isotropic strain localization condition of the form of Eq. (7.56) is applied. This yields after volume averaging the macroscopic stress

in the form:

$$\Sigma'_m = K^{II} E_v; \quad K^{II} = (1-\phi_{02})\, K^I A^v_M \tag{7.70a}$$

$$\mathbf{S} = 2G^{II}\mathbf{E}_d; \quad G^{II} = (1-\phi_{02})\, G^I A^d_M \tag{7.70b}$$

where $A^v_M = \langle a^v(\underline{z})\rangle_{V_M}$ and $A^d_M = \langle a^d(\underline{z})\rangle_{V_M}$; $1-\phi_{02} = V_M/V$ is the volume fraction of the porous matrix in the R.E.V. K^{II} and G^{II} are recognized as the macroscopic drained elastic stiffness properties of the cement paste. On the other hand, there are two associated changes of porosity; the microporosity and the macroporosity. The microporosity is defined per unit of (undeformed) matrix volume V_M so that the change of porosity at the macroscale in the considered subproblem is:

$$\left[(\phi_1-\phi_{01})^{II}\right]' = (1-\phi_{02})\left[(\phi_1-\phi_{01})^I\right]' = b_1^{II} E_v \tag{7.71a}$$

$$b_1^{II} = (1-\phi_{02})\, b^I A^v_M. \tag{7.71b}$$

In return, the change in macroporosity reads:

$$\left[(\phi_2-\phi_{02})^{II}\right]' = b_2^{II} E_v \tag{7.72a}$$

$$b_2^{II} = \phi_{02} A^v_{\phi 2} \tag{7.72b}$$

where $A^v_{\phi 2} = \langle a^v(\underline{z})\rangle_{V_{\phi 2}}$. Herein, b_1^{II} and b_2^{II} are the Biot coefficients associated with the micro- and the macroporosity, respectively.

Second Sub-Problem: Undrained Conditions ($\mathbf{E}''=\mathbf{0}$)

The second sub-problem we consider is the zero-displacement boundary problem, for which Levin's theorem of Eq. (7.59) applies. Application of the eigenstress distribution Eq. (7.69) in Eq. (7.59) yields the macroscopic stress in this subproblem:

$$\Sigma''_m = -(1-\phi_{02})\, b^I A^v_M\, p_1 - \phi_{02} A^v_{\phi 2} p_2 = -b_1^{II} p_1 - b_2^{II} p_2 \tag{7.73}$$

There are two changes of porosity to be considered: the change in microporosity,

$$\left[(\phi_1 - \phi_{01})^{II}\right]'' = (1 - \phi_{02}) \left(b_M \langle \epsilon'' \rangle_{V_M} + \frac{p_1}{N^I}\right) \tag{7.74}$$

and the change in macroporosity:

$$\left[(\phi_2 - \phi_{02})^{II}\right]'' = \phi_{02} \langle \epsilon'' \rangle_{V_{\phi 2}} = -(1 - \phi_{02}) \langle \epsilon'' \rangle_{V_M} \tag{7.75}$$

We need to eliminate $\langle \epsilon'' \rangle_{V_M}$ in Eqs. (7.74) and (7.75). To this end, we determine the stress average in this sub-problem on account of Eq. (7.69):

$$\begin{aligned} \Sigma''_m &= (1 - \phi_{02}) \langle \sigma''_m \rangle_{V_M} + \phi_{02} \langle \sigma''_m \rangle_{V_{p2}} \\ &= (1 - \phi_{02}) K^I \langle \epsilon'' \rangle_{V_M} - (1 - \phi_{02}) b^I p_1 - \phi_{02} p_2 \end{aligned} \tag{7.76}$$

Then, we use Eq. (7.73) in Eq. (7.76) to express the average strain in the porous matrix $\langle \epsilon'' \rangle_{V_M}$ as a function of p_1 and p_2:

$$\begin{aligned} (1 - \phi_{02}) \langle \epsilon'' \rangle_{V_M} &= \frac{1}{K^I} \left[\Sigma''_m + (1 - \phi_{02}) b^I p_1 + \phi_{02} p_2\right] \\ &= \frac{1}{K^I} \left[\left((1 - \phi_{02}) b^I - b_1^{II}\right) p_1 + \left(\phi_{02} - b_2^{II}\right) p_2\right] \end{aligned} \tag{7.77}$$

Finally, substitution of Eq. (7.77) in Eqs. (7.74) and (7.75) yields the change of the microporosity:

$$(\phi_1 - \phi_{01})'' = \frac{p_1}{N_{11}} + \frac{p_2}{N_{12}} \tag{7.78a}$$

$$\frac{1}{N_{11}} = (1 - \phi_{02}) \left(\frac{b^I}{K^I} \left(b^I - b_1^{II}\right) + \frac{1}{N^I}\right) \tag{7.78b}$$

$$\frac{1}{N_{12}} = \frac{b^I}{K^I} \left(\phi_{02} - b_1^{II}\right) \tag{7.78c}$$

and the change of the macroporosity:

$$(\phi_2 - \phi_{02})'' = \frac{p_1}{N_{21}} + \frac{p_2}{N_{22}} \tag{7.79a}$$

$$\frac{1}{N_{21}} = \frac{1}{K^I}\left(b_1^{II} - (1-\phi_{02})\, b^I\right) \tag{7.79b}$$

$$\frac{1}{N_{22}} = \frac{1}{K^I}\left(b_2^{II} - \phi_{02}\right) \tag{7.79c}$$

The symmetry of the skeleton Biot moduli $N_{12} = N_{21}$ is readily shown, by substituting Eq. (7.72b) into Eq. (7.78c) and Eq. (7.71b) into Eq. (7.78b):

$$\frac{1}{N_{12}} = \phi_{02}\frac{b^I}{K^I}\left(1 - A^v_{\phi 2}\right) \tag{7.80a}$$

$$\frac{1}{N_{21}} = (1-\phi_{02})\frac{b^I}{K^I}\left(A^v_M - 1\right) \tag{7.80b}$$

Then use of the strain localization compatibility condition in one of the two relations yields the solution of the other moduli. For instance, replacing $\phi_{02}A^v_{\phi 2} = 1 - (1-\phi_{02})\, A^v_M$ in (7.80a) gives:

$$\frac{1}{N_{12}} = (1-\phi_{02})\frac{b^I}{K^I}\left(A^v_M - 1\right) = \frac{1}{N_{21}} \tag{7.81}$$

Last, a superposition of the two subproblems yields the macroscopic state equations of the isotropic double-porosity system:

$$\Sigma_m = \Sigma_m' + \Sigma_m'' = K^{II}E_v - b_1^{II}p_1 - b_2^{II}p_2 \tag{7.82a}$$

$$\phi_1 - \phi_{01} = b_1^{II}E_v + \frac{p_1}{N_{11}} + \frac{p_2}{N_{12}} \tag{7.82b}$$

$$\phi_2 - \phi_{02} = b_2^{II}E_v + \frac{p_1}{N_{21}} + \frac{p_2}{N_{22}} \tag{7.82c}$$

where all seven poroelastic constants are known here as functions of the poroelastic properties of the porous matrix, and of two strain localization factors, $A^v_{\phi 2}$ (or A^v_M) and A^d_M. An estimate of these factors provided, for example, by a Mori-Tanaka [172] scheme reads:

$$A^v_{\phi 2} = \frac{4G^I + 3K^I}{3\phi_{02}K^I + 4G^I};\ A^v_M = \frac{1-\phi_{02}A^v_{\phi 2}}{1-\phi_{02}} \tag{7.83a}$$

$$A^d_M = \frac{1-\phi_{02}A^d_{\phi 2}}{1-\phi_{02}} = \frac{8G^I + 9K^I}{6\phi_0\left(2G^I + K^I\right) + 8G^I + 9K^I} \tag{7.83b}$$

For purpose of comparison of the poroelastic properties, it is useful to evaluate the poroelastic constants for the same pressure in both meso- and macroporosity, $p_1 = p_2 = p$, for which the state equations are given by:

$$\Sigma_m = K^{II} E_v - b^{II} p \tag{7.84a}$$

$$(\phi - \phi_0)^{II} = b^{II} E_v + \frac{p}{N^{II}} \tag{7.84b}$$

with the poroelastic constants:

$$K^{II} = (1 - \phi_{02})\, K^I A_M^v \tag{7.85a}$$

$$G^{II} = (1 - \phi_{02})\, G^I A_M^d \tag{7.85b}$$

$$b^{II} = b_1^{II} + b_2^{II} \tag{7.85c}$$

$$b^{II} = b^I + (1 - b^I)\, \phi_{02} A_{\phi 2}^v \tag{7.85d}$$

$$\frac{1}{N^{II}} = \frac{1}{N_{11}} + \frac{2}{N_{12}} + \frac{1}{N_{22}} \tag{7.85e}$$

$$\frac{1}{N_{11}} = (1 - \phi_{02}) \left(\frac{b^I}{K^I} \left(b^I - b_1^{II} \right) + \frac{1}{N^I} \right) \tag{7.85f}$$

$$\frac{1}{N_{12}} = (1 - \phi_{02}) \frac{b^I}{K^I} \left(A_M^v - 1 \right) \tag{7.85g}$$

$$\frac{1}{N_{22}} = \frac{1}{K^I} \left(b_2^{II} - \phi_{02} \right) \tag{7.85h}$$

Inclusions in a Porous Matrix ($w/c < 0.42$)

We now consider the case of CBM systems of low w/c–ratios, which eliminate the capillary porosity and favours the presence of residual clinker phases. Following previous developments we consider an heterogeneous stress distribution in the porous C-S-H matrix V_M and the clinker inclusion, V_c :

$$\text{in } V_{II} : \boldsymbol{\sigma}(\underline{z}) = \left(k(\underline{z}) - \frac{2}{3} g(\underline{z}) \right) \epsilon(\underline{z})\, \mathbf{1} + 2g(\underline{z})\, e_{ij}(\underline{z}) + \boldsymbol{\sigma}^p(\underline{z}) \tag{7.86}$$

together with the following distributions of $(k(\underline{z}), g(\underline{z}))$ and the eigenstress $\sigma^p(\underline{z})$:

$$(k(\underline{z}), g(\underline{z})) = \begin{cases} (K^I, G^I) & \text{in } V_M \\ (k_c, g_c) & \text{in } V_c \end{cases} \quad \sigma^p(\underline{z}) = \begin{cases} -b^I p^I & \text{in } V_M \\ 0 & \text{in } V_c \end{cases} \tag{7.87}$$

where V_M stands for the volume occupied by the porous matrix in the R.E.V., and V_c for the residual clinker phase. Again we decompose the problem in two sub-problems:

First Sub-Problem: Drained Conditions $(p = 0)$

The first sub-problem corresponds to overall drained conditions, for which $p = 0$. The boundary conditions are still defined by Eq. (7.55), and an isotropic strain localization condition of the form of Eq. (7.56) is applied. This yields after volume averaging the macroscopic stress in the form:

$$\Sigma'_m = K^{II} E_v; \quad K^{II} = (1 - f_c) K^I A^v_M \tag{7.88a}$$

$$\mathbf{S} = 2G^{II} \mathbf{E}_d; \quad G^{II} = (1 - f_c) G^I A^d_M \tag{7.88b}$$

Furthermore, the change of porosity in this subproblem is:

$$\left[(\phi_1 - \phi_{01})^{II}\right]' = (1 - f_c)\left[(\phi_1 - \phi_{01})^I\right]' = b^{II} E_v \tag{7.89}$$

$$b^{II} = (1 - f_c) b^I A^v_M \tag{7.90}$$

Second Sub-Problem: Undrained Conditions $(\mathbf{E}'' = \mathbf{0})$

The second sub-problem considers, as usual, that the space is pressurized, while the R.E.V. is subjected to a zero macroscopic displacement on the boundary which preserves the original volume of the R.E.V. Levin's theorem applied to this sub-problem yields

$$\Sigma''_m = -(1 - f_c) b^I A^v_M p_1 = -b^{II} p_1 \tag{7.91}$$

The change in porosity in the porous matrix also reads:

$$\left[\left(\phi_1 - \phi_{01}\right)^{II}\right]'' = \left(1 - f_c\right)\left(b^I \left\langle \epsilon''\left(\underline{z}\right)\right\rangle + \frac{p^I}{N^{II}}\right) \tag{7.92}$$

This must be complemented by the compatibility condition which ensures zero displacement on the boundary:

$$\left(1 - f_c\right)\left\langle \epsilon''\left(\underline{z}\right)\right\rangle_{V_M} = -f_c \left\langle \epsilon''\left(\underline{z}\right)\right\rangle_{V_c} = -f_c \left\langle \sigma''_m \right\rangle_{V_c} / k_c \tag{7.93}$$

The average stress theorem provides additional information to the problem:

$$\begin{aligned} \Sigma''_m &= f_c \left\langle \sigma''_m \right\rangle_{V_c} + \left(1 - f_c\right)\left\langle \sigma''_m \right\rangle_{V_M} && (7.94) \\ &= f_c \left\langle \sigma''_m \right\rangle_{V_c} + \left(1 - f_c\right) K^I \left\langle \epsilon'' \right\rangle_{V_M} - \left(1 - f_c\right) b^I p && (7.95) \end{aligned}$$

Finally, a combination of Eqs. (7.91), (7.93) and (7.94) yields an estimate for $\left\langle \epsilon'' \right\rangle_{V_M}$:

$$\left\langle \epsilon'' \right\rangle_{V_M} = \frac{b^I \left(1 - A^v_M\right)}{\left(k_c + K^I\right)} p \tag{7.96}$$

which with the help of Eq. (7.92) provides an estimate of the Biot skeleton modulus:

$$\frac{1}{N^{II}} = \frac{\left(1 - f_c\right)}{N^I} + \left(1 - f_c\right) \frac{\left(b^I\right)^2 \left(1 - A^v_M\right)}{\left(k_c + K^I\right)} \tag{7.97}$$

These completes the estimates of the poroelastic properties at this level which are summarized below:

$$\begin{aligned} K^{II} &= \left(1 - f_c\right) K^I A^v_M \\ G^{II} &= \left(1 - f_c\right) G^I A^d_M \\ b^{II} &= \left(1 - f_c\right) b^I A^v_M \\ N^{II} &= \left[\frac{\left(1-f_c\right)}{N^I} + \left(1 - f_c\right) \frac{\left(b^I\right)^2 \left(1-A^v_M\right)}{\left(k_c+K^I\right)}\right]^{-1} \end{aligned} \tag{7.98}$$

7.3.4 Level III: Poroelastic Properties of Mortar/Concrete - Inclusions in a Porous Matrix

At Level III, the material is composed of a porous matrix (the cement paste) and non-porous inclusions of approximately spherical shape that are assumed to be randomly distributed. From

a morphological point of view, the porosity belongs to the phases at a level below (cement paste). Given the separability of scale condition, the porosity does not enter the Level III, but is already included in the poroelastic properties of the cement paste that serve as input. We adopt a continuous description of the stress field in the heterogeneous R.E.V.:

$$\text{in } V_{III} : \boldsymbol{\sigma}(\underline{z}) = \left(k(\underline{z}) - \frac{2}{3}g(\underline{z})\right)\epsilon(\underline{z})\,\mathbf{1} + 2g(\underline{z})\,e_{ij}(\underline{z}) + \boldsymbol{\sigma}^p(\underline{z}) \tag{7.99}$$

together with the following distributions of the elastic properties $(k(\underline{z}), g(\underline{z}))$ and the eigenstress $\boldsymbol{\sigma}^p(\underline{z})$:

$$(k(\underline{z}), g(\underline{z})) = \begin{cases} (K^{II}, G^{II}) & \text{in } V_M \\ (k_i, g_i) & \text{in } V_i \end{cases} \qquad \boldsymbol{\sigma}^p(\underline{z}) = \begin{cases} -b^{II} p^{II} & \text{in } V_M \\ 0 & \text{in } V_i \end{cases} \tag{7.100}$$

where (K^{II}, G^{II}) are the elastic properties of the porous cement paste Eq. (7.98), (k_i, g_i) are the stiffness properties of the (assumed isotropic) aggregate inclusion phase; and $b_M = b^{II}$ is the Biot coefficient of the porous cement paste of Eq. (7.98). Following the linear microporomechanics approach, we decompose the problem in two sub-problems:

First Sub-Problem: Drained Conditions $(p = 0)$

The first sub-problem corresponds to drained conditions, for which $p = 0$. We assume that the R.E.V. is subjected to a uniform displacement boundary condition, so that the solid boundary conditions to which the solid phase is subjected read:

$$\text{on } \partial V_{III} \quad : \quad \underline{\xi}'(\underline{z}) = \mathbf{E} \cdot \underline{z} \tag{7.101a}$$

$$\text{on } \mathcal{I}_{sf} \quad : \quad \boldsymbol{\sigma} \cdot \underline{n} = 0 \tag{7.101b}$$

The macroscopic strain tensor $\mathbf{E}$ is related to the microscopic strain by the strain localization condition:

$$\boldsymbol{\varepsilon}'(\underline{z}) = \mathbb{A}(\underline{z}) : \mathbf{E} \tag{7.102}$$

$\mathbb{A}(\underline{z})$ satisfies the compatibility condition:

$$\mathbf{E} = \boldsymbol{\varepsilon}'(\underline{z}) \Leftrightarrow \mathbb{I} = (1 - f_i) \langle \mathbb{A} \rangle_{V_M} + f_i \langle \mathbb{A} \rangle_{V_i} \tag{7.103}$$

where $f_i = |V_i| / |V_{III}| = 1 - f_M$ is the inclusion volume fraction. Use of Eq. (7.102) in Eq. (7.99) together with the elastic distribution Eq. (7.100) yields after volume averaging, the macroscopic stress, and the homogenized stiffness of the composite:

$$\begin{aligned} \Sigma'_m &= K^{III} E_v; \;\; K^{III} = (1 - f_i) K^{II} A_M^v \\ \mathbf{S} &= 2G^{III} \mathbf{E}_d; \;\; G^{III} = (1 - f_i) G^{II} A_M^d \end{aligned} \tag{7.104a}$$

The change of the porosity in the subproblem reads:

$$\left[(\phi - \phi_0)^{III} \right]' = (1 - f_i) \left[(\phi_1 - \phi_{01})^{II} \right]' = b^{III} E_v \tag{7.105}$$

$$b^{III} = (1 - f_i) b^{II} A_M^v \tag{7.106}$$

where b^{III} is the homogenized Biot coefficient.

Second Sub-Problem: Undrained Conditions ($\mathbf{E}''= 0$)

The second sub-problem we consider is the zero-displacement boundary problem, where the porosity is pressurized. For the eigenstress distribution of Eq. (7.100), we obtain the macroscopic stress and the homogenized Biot coefficients from Levin's theorem in Eq. (7.41):

$$\boldsymbol{\Sigma}'' = \langle \boldsymbol{\sigma}^p(\underline{z}) : \mathbb{A}(\underline{z}) \rangle = -\mathbf{b}^{III} p^{III}; \;\; \mathbf{b}^{III} = b^{III} \mathbf{1} \tag{7.107}$$

$$b^{III} = -(1 - f_i) b^{II} A_M^v \tag{7.108}$$

The change of the porosity in the subproblem is:

$$\left[(\phi - \phi_0)^{III} \right]'' = (1 - f_i) \left(b^{II} \langle \epsilon''(\underline{z}) \rangle_{V_M} + \frac{p}{N_M} \right) \tag{7.109}$$

where $N_M = N^{II}$. We eliminate $\langle \epsilon''(\underline{z}) \rangle_{V_M}$ in Eq. (7.109) to the benefit of pressure p, by considering the stress average in this sub-problem, in which $\mathbf{E}'' = \langle \boldsymbol{\varepsilon}''(\underline{z}) \rangle = f_i \langle \boldsymbol{\varepsilon}''(\underline{z}) \rangle_{V_i} +$

$(1-f_i)\langle\varepsilon''(\underline{z})\rangle_{V_M}=0$:

$$\begin{aligned}\boldsymbol{\Sigma}'' &= (1-f_i)\langle\boldsymbol{\sigma}''\rangle_{V_M}+f_i\langle\boldsymbol{\sigma}''\rangle_{V_i} &(7.110a)\\ &= f_i\langle\sigma_m''\rangle_{V_i}+(1-f_i)K^I\langle\epsilon''\rangle_{V_M}-(1-f_i)b^{II}p &(7.110b)\end{aligned}$$

Thus, from the equality of Eqs. (7.107) and (7.110):

$$\langle\epsilon''\rangle_{V_M}=\frac{b^{II}(1-A_M^v)}{(k_i+K^{II})}p \tag{7.111}$$

Finally, use of Eq. (7.111) in Eq. (7.109) yields:

$$\begin{aligned}\left[(\phi-\phi_0)^{III}\right]''&=\frac{p}{N^{III}};\\ \frac{1}{N^{III}}&=\frac{(1-f_i)}{N^{II}}+(1-f_i)\frac{\left(b^{II}\right)^2(1-A_M^v)}{(k_i+K^{II})}\end{aligned} \tag{7.112}$$

In summary, a superposition of the two subproblems yields the macroscopic state equations of the mortar/concrete material:

$$\begin{aligned}\Sigma_m &= K^{III}E_v-b^{III}p &(7.113a)\\ (\phi-\phi_0)^{III} &= b^{III}E_v+\frac{p}{N^{III}} &(7.113b)\end{aligned}$$

together with the poroelastic constants:

$$\begin{aligned}K^{III} &= (1-f_i)K^{II}A_M^v &(7.114a)\\ G^{III} &= (1-f_i)G^{II}A_M^d\ . &(7.114b)\\ b^{III} &= (1-f_i)b^{II}A_M^v &(7.114c)\\ N^{III} &= \left[\frac{(1-f_i)}{N^{II}}+(1-f_i)\left(b^{II}\right)^2\frac{(1-A_M^v)}{(k_i+K^{II})}\right]^{-1} &(7.114d)\end{aligned}$$

The input to this homogenization step are the poroelastic properties of porous cement paste, $\left(K^{II},G^{II}\right)$, b^{II}, $N_M=N^{II}$, the inclusion volume fraction f_i, and an estimate of the volume average of the matrix strain concentration tensor $\langle\mathbb{A}\rangle_{V_M}$. Given the matrix–inclusion morphology, such an estimate is suitably provided by the Mori-Tanaka scheme stated in Eq. (7.15).

Undrained Poroelastic Properties

In order to assess the undrained properties, at Level III, one needs to find the relation between macroscopic stress and strain when the fluid mass $m = \rho_{fl}\phi$ stays constant in the R.E.V. Here, ρ_{fl} stands for the fluid density and varies with the pore pressure. In the linear case:

$$\rho_{fl} = \rho_{fl}^0 \left(1 + \frac{p}{K_{fl}}\right) \tag{7.115}$$

where K_{fl} is the fluid bulk modulus and ρ_{fl}^0 is the reference fluid density (for water $K_{fl} = 2.3$ GPa). Then the change of fluid mass contained in the R.E.V. is such that:

$$\frac{m - m_0}{\rho_{fl}^0} = \phi - \phi_0 + \phi_0 \frac{p}{K_{fl}} \tag{7.116}$$

With Eq. (7.116), the two poro-elastic states Eqs. (7.113a) and (7.113b) are written in the form:

$$\boldsymbol{\Sigma} = \mathbb{C}_{u,\text{hom}}^{III} : \left(\mathbf{E} - \mathbf{B}^{III} \frac{m - m_0}{\rho_{fl}^0}\right) \tag{7.117}$$

$$\frac{m - m_0}{\rho_{fl}^0} = \mathbf{b}^{III} \colon \mathbf{E} + \frac{p}{M^{III}} \tag{7.118}$$

where:

- M^{III} is the Biot modulus for the porous solid and is defined by:

$$\frac{1}{M^{III}} = \frac{1}{N^{III}} + \frac{\phi_0}{K_{fl}} \tag{7.119}$$

- $\mathbb{C}_{u,\text{hom}}^{III}$ is the macroscopic undrained stiffness tensor

$$\mathbb{C}_{u,\text{hom}}^{III} = \mathbb{C}_{\text{hom}}^{III} + M^{III}\, \mathbf{b}^{III} \otimes \mathbf{b}^{III} \tag{7.120}$$

- $\mathbf{B}^{III}$ is the second order tensor of Skempton coefficients

$$\mathbf{B}^{III} = M^{III} (\mathbb{C}_{u,\text{hom}}^{III})^{-1} : \mathbf{b}^{III} \tag{7.121}$$

In the isotropic case, $\mathbb{C}^u_{\text{hom}} = 3K^u_{\text{hom}}\mathbb{J} + 2G_{\text{hom}}\mathbb{K}$ and $\mathbf{B} = B\mathbf{1}$, with

$$K^u_{\text{hom}} = K_{\text{hom}} + Mb^2; B = \frac{Mb}{K^u_{\text{hom}}} \tag{7.122}$$

7.4 Chapter Summary

We have presented a microporomechanics model that can provide poroelastic properties predictions at multiple scales, provided the knowledge of the intrinsic properties of the individual components and their volumetric proportions. While the intrinsic drained properties of the LD and HD C-S-H have been obtained through indentation testing (see Chapter 5) their poroelastic counterparts have to be resolved in a reverse analysis formulation. This calibration procedure will be detailed in Chapter 8. With those material invariant properties in hand one can calculate the poroelastic response of any material system independent of mix proportions and conditions of testing:

1. Given the elastic properties of the solid phase and the packing modes of the two types of C-S-H, one can calculate with the use of Eqs. (7.37) and (7.51) the poroelastic constants of the two types of C-S-H.

2. The predicted poroelastic estimates of Level 0 along with the volume fractions of the two types of C-S-H are incorporated in Eq. (7.68) that determine the poroelastic constants of the C-S-H matrix.

3. The homogenized values of the C-S-H matrix are incorporated in Level II (Eq. (7.85) or Eq. (7.98)) which yields, with knowledge of volumetric proportions of the clinker and capillary porosity the poroelastic constants of Level II (cement paste).

4. In the case where aggregates are present in the microstructure, then the cement paste estimates serve as input in Eq. (7.114) that, along with the elastic properties of the sand particles, yields the poroelastic estimates of the mortar composite (Level III).

5. Finally, the predicted values with the pore fluid bulk modulus are used in Eqs. (7.119)-(7.122) to predict the undrained poroelastic estimates of CBM systems.

Figure 7-5 summarizes the multi-step microporomechanics model now in place. The proposed model reduces the complexity of cement-based materials to 14 parameters: they are the elastic properties of the C-S-H solid phase (k_s, g_s); the elastic properties of the clinker phase (k_{cl}, g_{cl}); the elastic properties of the aggregates (k_g, g_g); the bulk modulus of the fluid phase, k_{fl}; the volume fractions of the two types of C-S-H, (f_{LD}, f_{HD}); the volume fractions of the C-S-H matrix, (f_{CSH}); the volume fractions of the clinker phase, (f_{cl}); and the pore space at each level, $\phi^0_{LD}, \phi^0_{HD}, f_{cp}$. The elastic properties of the C-S-H solid phase, the clinker phase, the aggregates, and the pore fluid, together with the porosities of the two types of C-S-H, are assumed to be constant (9 parameters). Thus for each cement-based material of given mix proportions, only the four parameters describing the volumetric proportions at each level are required: f_{LD}, f_{CSH}, f_{cl}, f_g. The remaining volume fractions of the HD C-S-H and the capillary pore space, and cement paste matrix are obtained by employing the compatibility condition, $\sum f_i = 1$, at each level: $f_{HD} = 1 - f_{LD}$, and $f_{cp} = 1 - f_{CSH} - f_{cl}$, $f_m = 1 - f_g$.

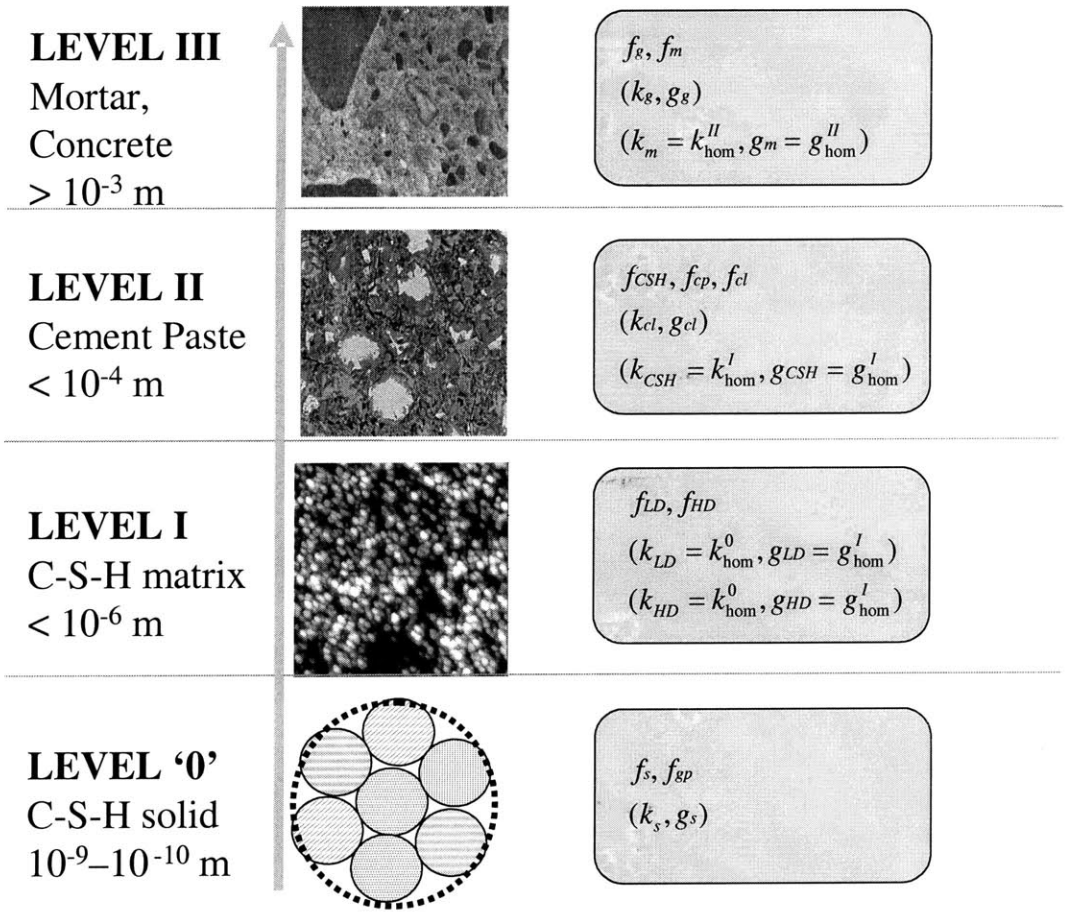

Figure 7-5: Details of the parameters involved in the multi-scale poroelastic model proposed in this chapter.

Chapter 8

Microporoelastic Model Calibration and Validation

This chapter is devoted to the calibration and validation of the microporoelastic model presented in Chapter 7. In a first step, we calculate the C-S-H solid stiffness using the indentation results of the two types of C-S-H and an inverse micromechanical approach. With an estimate of the C-S-H solid stiffness in hand, one can calculate the poroelastic properties of any CBM specimen using the microporoelastic model of Chapter 7 and the methodology summarized in Section 7.4. The predictive capabilities of the model will firstly be compared with a set of experimental data on cement paste and mortar for validation purposes. It will be shown that the drained and undrained micromechanical predictions are within close agreement with experimental data. Furthermore, as a second validation step, we apply the model to experimental data presented on thermally (Chapter 6) and chemically [58, 60] treated specimens. It is shown, that provided the volumetric proportions of the specimens are reliably predicted, then the macroscopic poroelastic estimates can be well-predicted independently of the mix design of the specimens, environmental conditions or testing conditions.

8.1 C-S-H Solid Stiffness: Model Calibration

8.1.1 Current state of knowledge

The information that is available about the two types of C-S-H are the porosities determined by mass density measurements (see Tab. 4.8), and composite stiffness values determined independently by nanoindentation (see Tab. 5.7). The overall picture that emerges from a combination of these independent measurements is that the difference in mechanical performance of the two types of C-S-H is a consequence of their packing density, while the solid phase is the same, having the same mass density and as a consequence same mechanical properties. These nanomechanical properties are currently still out of reach of direct mechanical measurements; what is measured experimentally are the homogenized properties of the two types of C-S-H. The determination of the nanomechanical properties (k_s, g_s), therefore, can only be achieved by an inverse application of the homogenization relations. As input we have values for the indentation modulus, M_{HD} and M_{LD}, and for the porosity, ϕ_0^{LD} and ϕ_0^{HD}. The unknowns are the stiffness properties of the C-S-H solid phase, k_s and g_s, and one homogenized property per type of C-S-H, e.g., the Poisson's ratio, ν_{HD} and ν_{LD}.

8.1.2 Matrix-Inclusion *vs.* Polycrystal Morphology

We found in Chapter 5 that the indentation modulus of HD vs. LD C-S-H is:

$$\frac{M_{HD}}{M_{LD}} = \frac{31.0}{18.8} = 1.65 \tag{8.1}$$

We have heretofore explained such a difference using the Mori-Tanaka localization scheme (see Eq. (7.15)). However, such a high ratio may well be at the limit of what this classical localization scheme can predict. To show this, let us recall:

$$M = \frac{E}{1-\nu^2} = 4G\frac{3K+G}{3K+4G} \tag{8.2}$$

where (K, G) stand for bulk and shear modulus. In the case of a porous material, (K, G) are related to the properties of the matrix (g_s, k_s) and the volume fraction of the porosity ϕ_0 by

(application of the MT-scheme, Eq. (7.15) in Eq. (7.35)):

$$K = \frac{4k_s g_s (1-\phi_0)}{3\phi_0 k_s + 4g_s} \tag{8.3a}$$

$$G = g_s \frac{(1-\phi_0)(8g_s+9k_s)}{6\phi_0(2g_s+k_s)+8g_s+9k_s} \tag{8.3b}$$

Use of Eq. (8.3) in Eq. (8.2) yields:

$$\frac{M}{m_s} = \frac{1}{2}\frac{(7-5\nu_s)\left(-13\phi_0+2\phi_0\nu_s+15\phi_0\nu_s^2-14+10\nu_s\right)(1-\phi_0)}{(7-5\nu_s+5\phi_0+5\phi_0\nu_s)(-8\phi_0+10\phi_0\nu_s-7+5\nu_s)} \tag{8.4}$$

where $m_s = E_s/\left(1-\nu_s^2\right)$ is the plane stress modulus of the solid phase, and ν_s is the solid Poisson's ratio. It should be noted that the effect of the Poisson's ratio does not strongly affect the M/m_s relation, as Fig. 8-1 shows. It may therefore be most appropriate to consider the two limit cases when analyzing indentation results of a porous material:

$$\frac{3}{4}\frac{(1-\phi_0)(11\phi_0+12)}{(3+5\phi_0)(2\phi_0+3)} = \lim_{\nu=0.5}\frac{M}{m_s} \leq \frac{M}{m_s} \leq \lim_{\nu=0}\frac{M}{m_s} = \frac{7}{2}\frac{(13\phi_0+14)(1-\phi_0)}{(7+5\phi_0)(8\phi_0+7)} \tag{8.5}$$

For the porosity of the two types of C-S-H ($\phi_{LD} = 37.3\%; \phi_{HD} = 23.7\%$), assuming the same m_s value, the Mori-Tanaka scheme of Eq. (8.5) allows capturing the following limits:

$$1.34 = \lim_{\nu=0}\frac{M_{HD}}{M_{LD}} \leq \frac{M_{HD}}{M_{LD}} \leq \lim_{\nu=0.5}\frac{M_{HD}}{M_{LD}} = 1.38 \tag{8.6}$$

These values are somewhat below (or at the limit of) the indentation modulus ratio of Eq. (8.1). Another approach which captures different morphologies may be more appropriate to explain the indentation results. The limitation of the Mori-Tanaka model could be related to the underlying matrix-inclusion morphology captured by the scheme. It is interesting to explore another morphology; here, the polycrystal morphology embedded in the self-consistent scheme. In the case of a self-consistent scheme (SCS), (K, G) for a porous continuum are given in the implicit form:

$$K = k_s\left(1-\frac{\phi_0}{1-\alpha}\right);\ \alpha=\frac{3K}{3K+4G} \tag{8.7a}$$

$$G = g_s\left(1-\frac{\phi_0}{1-\beta}\right);\ \beta=\frac{6\,(K+2G)}{5\,(3K+4G)} \tag{8.7b}$$

which yields the explicit form:

$$\frac{K}{k_s}=\frac{4G\,(1-\phi_0)}{4G+3k_s\phi_0} \tag{8.8}$$

$$\begin{aligned}\frac{G}{g_s} &= \frac{1}{2}-\frac{5}{4}\phi_0-\frac{3}{16}r_s\,(3-\phi_0) \\ &+\frac{1}{16}\sqrt{\left(64-320\phi_0+400\phi_0^2+r_s\left(144-168\phi_0-120\phi_0^2\right)+r_s^2\left(81-54\phi_0+9\phi_0^2\right)\right)}\end{aligned} \tag{8.9}$$

where $r_s = k_s/g_s = 2\,(1+\nu_s)\,/3\,(1-2\nu_s)$. The previous relations yield:

$$\frac{M}{m_s}=\frac{G}{4g_s}\frac{(3r_s+4)\,(12r_s+4G/g_s-9r_s\phi_0)}{(3r_s+1)\,(3r_s+4G/g_s)} \tag{8.10}$$

Note that $M/m_s > 0$ requires $\phi_0 < 1/2$, as the SCS has a percolation threshold. Furthermore, M/m_s is undefined for an incompressible solid ($\nu_s = 1/2$) but, similar to what we have observed experimentally, the Poisson's ratio plays a minor role on the M/m_s ratio (see Fig. 8-1). For evaluation purposes, we evaluate Eq. (8.10) for $\nu_s = 0$ ($r_s = 2/3$):

$$\lim_{\nu_s=0}\frac{M}{m_s}=\frac{3}{8}\frac{45\phi_0^2-48\phi_0+11+(3-5\phi_0)\sqrt{\left(49-114\phi_0+81\phi_0^2\right)}}{5-9\phi_0+\sqrt{\left(49-114\phi_0+81\phi_0^2\right)}} \tag{8.11}$$

For the porosity of the two types of C-S-H ($\phi_{LD} = 37.3\%; \phi_{HD} = 23.7\%$), assuming the same m_s value, we then obtain:

$$2.03=\lim_{\nu=0}\frac{M_{HD}}{M_{LD}}\leq\frac{M_{HD}}{M_{LD}} \tag{8.12}$$

The self-consistent scheme (or polycrystal) allows one to capture higher M_{HD}/M_{LD} values than the Mori-Tanaka scheme. Recall that the self-consistent scheme represents a polycrystal in which each phase could play the role of the solid phase, while the Mori-Tanaka scheme represents a matrix-inclusion morphology where the inclusion is the porosity. Hence, our $M_{HD}/M_{LD}-$ratio

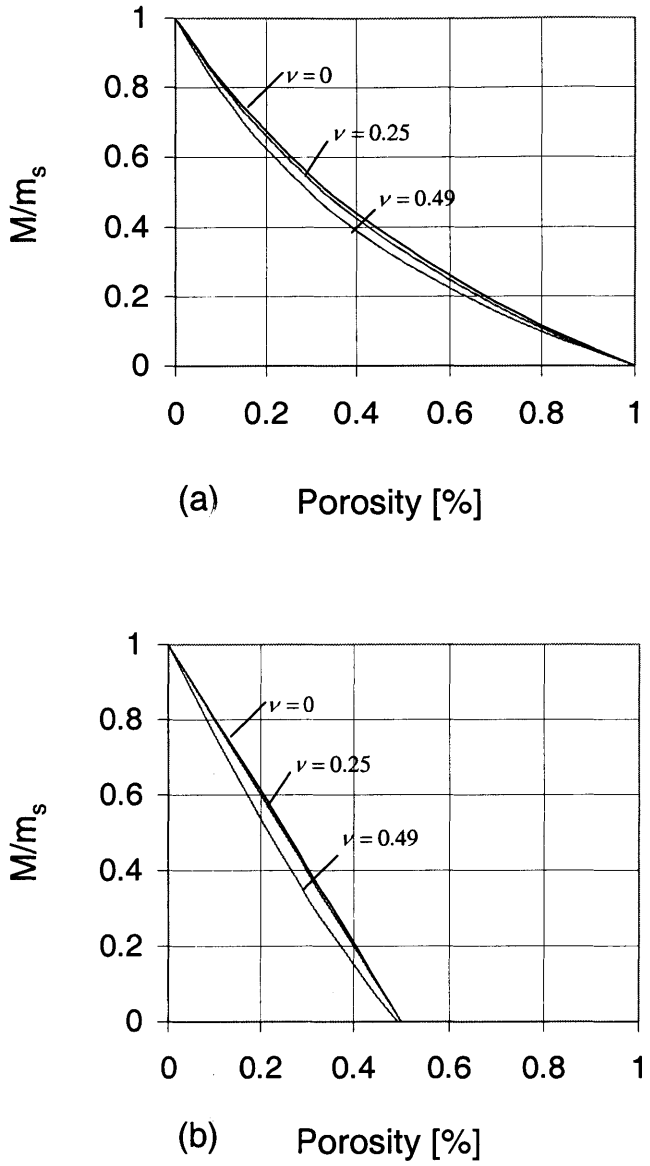

Figure 8-1: Evolution of the M/m_s ratio for various Poisson's ratios as a function of porosity as predicted by the Mori-Tanaka (a) and the Self-Consistent-Scheme (b).

suggests that the two types of C-S-H are more representative of a polycrystal structure than of a matrix-inclusion porosity. Furthermore, it is also useful to evaluate the M_{HD}/M_{LD} −ratio by assuming that the LD C-S-H represent a random close packing (RCP) $1-n=0.637$, and the HD C-S-H a face-centered cubic lattice (FCCL) $1-n=\pi/\sqrt{18}=0.74$. By letting $\phi_0=n$ in Eq. (8.11), we obtain the following M_{HD}/M_{LD} ratio associated with these limit packing schemes:

$$1.73=\lim_{\nu_s=0}\frac{M_{HD}}{M_{LD}}\leq\frac{M_{HD}\left(n=0.260\right)}{M_{LD}\left(n=0.363\right)} \tag{8.13}$$

Remarkably, the lower bound value of 1.73 is within 5% of the experimental ratio of 1.65 (Eq. (8.1)). Note that for $\nu_s=1/5$, we obtain, with the self-consistent scheme, $M_{HD}/M_{LD}=1.76$, and for $\nu_s=1/4$ we obtain $M_{HD}/M_{LD}=1.77$. By contrast, the Mori-Tanaka estimate of Eq. (8.4) yields for the packing limit cases $1.25\leq M_{HD}/M_{LD}\leq 1.28$. This confirms our previous suggestion that the structure of C-S-H comes much closer to a polycrystal structure than to a matrix-pore space morphology. It is on this basis that it is possible to evaluate an order of magnitude of the solid stiffness m_s:

$$\frac{M_{LD}}{m_s}\left(1-n=0.637\right)\leq\lim_{\nu_s=0}\frac{M_{LD}}{m_s}=0.28539\Rightarrow m_s\left(LD\right)\geq 65.9\text{ GPa} \tag{8.14a}$$

$$\frac{M_{HD}}{m_s}\left(1-n=\pi/\sqrt{18}\right)\leq\lim_{\nu_s=0}\frac{M_{HD}}{m_s}=0.49323\Rightarrow m_s\left(HD\right)\geq 62.9\text{ GPa} \tag{8.14b}$$

The values obtained with $M_{LD}=18.8$ GPa and $M_{HD}=31.0$ GPa are surprisingly close, suggesting that $m_s\left(LD\right)=m_s\left(HD\right)$. While (8.14) define a lower bound corresponding to $\nu_s=0$, we should note that the Poisson's ratio does not strongly affect the value of m_s and weakly affects $E_s=m_s\left(1-\nu_s^2\right)$ in the range $0\leq\nu_s\leq 1/4$. For instance, for $\nu_s=1/4$ we obtain $m_s\left(LD\right)=66.1$ GPa and $m_s\left(HD\right)=63.6$ GPa, which correspond to a Young's modulus of $E_s\left(LD\right)=62.0$ GPa and $E_s\left(HD\right)=59.6$ GPa. The effect of the Poisson's ratio on E_s becomes strong close to incompressibility of the solid phase (which is a case not defined by SCS), as shown in Fig. 8-2, displaying $E_s\left(LD\right)$ and $E_s\left(HD\right)$ in function of the Poisson's ratio ν_s. Given the way how M_{LD} and M_{HD} are determined from statistical analysis, the closeness of LD- and HD-stiffness is remarkable. Finally, the previous analysis also applies to the indentation stiffness values of previously published values, in which we found $M_{LD}=19.7$ GPa and $M_{HD}=32.5$ GPa, hence a ratio of $M_{HD}/M_{LD}=1.65$. The ratio is just 5% smaller than the one predicted

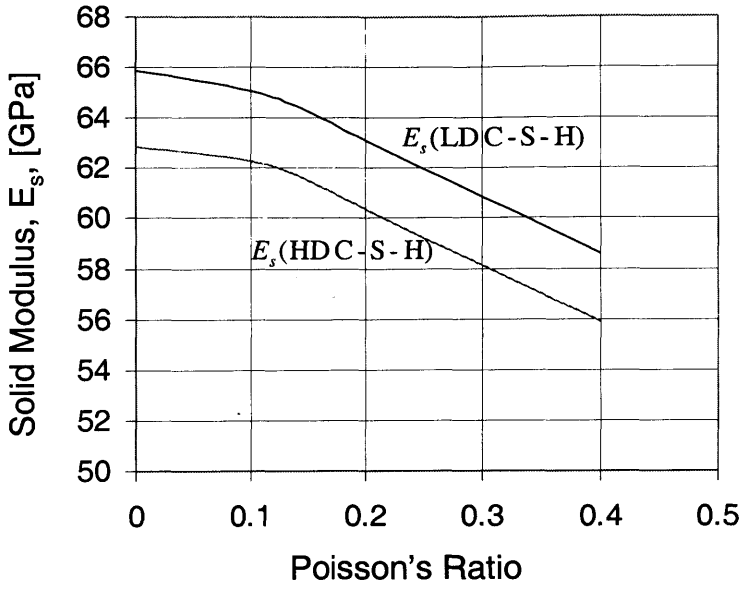

Figure 8-2: Effect of the Poisson's ratio ν on the invesre calculation of the solid Young's modulus E_s.

by Eq. (8.13), and yields $m_s\,(LD) \geq 69.1$ GPa and $m_s\,(HD) \geq 65.9$ GPa, which is 10% higher than the values given by Eq. (8.14). Hence, the trend is clearly towards a polycrystalline structure of C-S-H. This is not in contradiction with the fact that C-S-H is organized around two limiting packing densities, which characterizes granular materials. In fact, the SCS predicts a zero stiffness at a packing density of $1 - \phi_0 = 0.5$ (see Fig. 8-2) which is not so far of the random loose-packed limit (RLP)[1] of $1 - n = 0.56$. This underlines the consistency between the polycrystalline model and the mechanical behavior of granular materials. Indeed, the self-consistent model of Hershey (1954) and Kröner (1958) is based on averaging the stress and strain in a spherical grain over all orientations (cited from Ref. [141]). A more rigorous test of the specific LD and HD structures specified by the colloid model of C-S-H can be obtained by making a forward application of the micromechanical prediction of the indentation modulus of an aggregated system of particles (here approximated by the self-consistent scheme) with

[1]The random loose-packed limit (RLP) corresponds to to the loosest random packing that is still mechanically stable under a given applied load.

an intrinsic solid stiffness of $m_s = 65$ GPa (average value of the two estimates). Figure 8-3 shows the predicted indentation modulus of such a system as a function of the packing density. The value of the solid spheres is recovered for a packing density of 1, whereas a complete loss of mechanical performance is predicted at a packing density of 0.5. The value of the C-S-H solid is to be compared with atomic level simulations reported in [189]. The Young's modulus of Hamid's structure (Ca/Si= 1) calculated from the matrix of elastic constants, was found to be $E_s^{AS} = 57.1$GPa at 0 K very close to the values calculated from our inverse analysis ($E_s\,(LD) = 62.0$ GPa and $E_s\,(HD) = 59.6$ GPa). It is impressive to note that atomistic simulations which neglect the presence of any defect in the system suggest stiffness values which are in close proximity to estimates calculated from nanoindentation input data. This further enforces the solid phase assumption and that the polycrystal morphology is a suitable representation for this class of material systems at this level. Finally, the experimental modulus values for the two types of C-S-H are also plotted in Fig. 8-3, using the random jam-packed density (64%) for the LD C-S-H and the close-packed density (76%) for the HD C-S-H. These are in very good agreement with the predicted values, providing more explicit and detailed support for the colloid model of C-S-H suggested by Jennings [130].

Intrinsic Poro-elastic Constants of the Two Types of C-S-H

With the solid phase stiffness in hand and the classical estimates of poroelasticity, (7.37) and (7.51), one can calculate the poroelastic constants of the two types of C-S-H:

$$\begin{aligned} b_{HD}^0 &= 0.54 \quad N_{HD}^0 = 133.43 \text{ GPa} \\ b_{LD}^0 &= 0.72 \quad N_{LD}^0 = 114.37 \text{ GPa} \end{aligned} \tag{8.15}$$

As it was expected the low density C-S-H with a higher fraction of porosity has a higher Biot coefficient. Given the intrinsic nature of the two C-S-H phases, these poroelastic constants can be considered to be universal constants for all cementitious materials. Table 8.1 summarizes the poroelastic constants of the C-S-H solid and two packing modes.

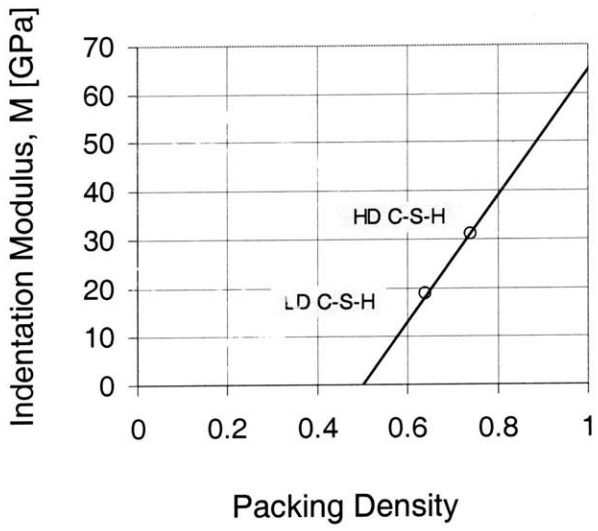

Figure 8-3: Micromechanical predictions and experimental values of the indentation modulus vs. the packing denisty of colloidal C-S-H particles.

			Globule	LD C-S-H	HD C-S-H
Elastic Constants	E	[GPa]	60.8*	17.7	28.9
	ν	[−]	0.25	0.24	0.24
	g	[GPa]	24.3	7.1	11.7
	k	[GPa]	40.5	11.3	18.5
Poroelastic Constants	E^u	[GPa]	−	18.4	29.4
	k^u	[GPa]	−	14.3	20.3
	ν^u	[−]	−	0.29	0.26
	b	[−]	−	0.71	0.54
	N	[GPa]	−	114.4	133.4
	M	[GPa]	−	5.9	6.0
	B	[−]	−	0.29	0.16

*Average value between $E_s(LD)$ and $E_s(HD)$

Table 8.1: Elastic and poroelastic constants obtained by indentation and inverse analysis, respectively.

RESONANT FREQUENCY AND PULSE VELOCITY METHODS
The elastic properties of a material can be measured by 1) determining the resonant frequency of a specimen (Resonant frequency technique - RF) or 2) determining the velocity at which short pulses of vibration travel through the specimen (Ultrasonic Pulse Velocity method - UPV). These two methods require as input parameter the density of the material which needs to be independently measured. The UPV method requires in addition an estimate of the Poisson's ratio. The mechanical load applied to the specimens during these dynamic testing is limited and the mechanical degradation is therefore minimal, which makes the techniques of non-destructive nature.

Table 8.2: Dynamic methods for measuring elasticity properties.

8.2 Model Validation

We aim in this section to quantify the predictive capabilities of the model in terms of drained and undrained poroelastic properties. In doing so, we compare micromechanical predictions with a set of macroscopic mechanical data obtained on Level II (cement paste) and III (mortar) simulating drained (RF testing) and undrained (UPV testing) conditions, (see Tab. 8.2).

8.2.1 Materials

Mix Proportions

The materials we consider here are a cement paste and mortar prepared at a water:cement ratio of $w/c = 0.5$, using an ordinary Type I Portland cement. The mortar composition is characterized by a water-cement-sand mass ratio of $w/c/s = 1/2/4$, using a fine Nevada sand of density $\rho^I = 2,650$ kg/m^3, $d_{60} = 0.23$ mm and $d_{30} = 0.17$ mm. These materials have been under investigation at M.I.T. for several years, and are well characterized by mechanical testing at multiple scales, from nanoindentation [60, 58, 59], ultrasonic measurements of the elastic properties [60, 58], to triaxial strength and deformation properties [115, 233, 116, 117], and creep properties [22].

Volumetric Proportions

The volumetric proportions of the hydration products can be calculated based on the Powers model described in Section 4.5.1: Given the initial w/c–ratio, $w/c = 0.5$, and assuming com-

plete hydration $\xi = 1$ (commonly employed for mature cement pastes of $w/c > 0.42$, see Section 4.4.2) one can calculate the volumetric proportion of the hydration products, C-S-H matrix and capillary porosity, from (see Section 4.5.1):

$$\phi^0 = \left(\frac{w/c}{w/c + \rho_w/\rho_c}\right) - 1.32\left(1 - \left(\frac{w/c}{w/c + \rho_w/\rho_c}\right)\right) = 0.10 \tag{8.16}$$

$$f_{CSH} = 2.12\left(1 - \frac{w/c}{w/c + \rho_w/\rho_c}\right) = 1 - \phi^0 = 0.90 \tag{8.17}$$

From mass density measurements of the hardened cement paste and mortar (see Tab. 6.1), it is possible to determine the sand inclusion volume fraction (Level III):

$$\rho^* = \langle\rho\rangle_V \Leftrightarrow f_I = \frac{\rho^* - \rho^M}{\rho^I - \rho^M} = 0.36 \pm 0.03 \tag{8.18}$$

where ρ^M stands for the density of the porous matrix (cement paste, Level II), and ρ^* for the density of the inclusion-matrix composite (mortar, Level III). The obtained values are consistent with mass measurements of saturated and dried specimens which yield (see Tab. 8.3):

$$f_I = 1 - \left(\frac{\Delta m^*}{\Delta m^M}\right) = 0.31 \pm 0.03 \tag{8.19}$$

where Δm^* and Δm^M represent the change in mass content due to drying of the composite (mortar) and porous matrix (cement paste), respectively:

$$\frac{\Delta m^*}{\rho_0^{fl}} = \frac{M^*_{sat} - M^*_{dry}}{\rho_0^{fl} V}; \frac{\Delta m^M}{\rho_0^{fl}} = \frac{M^M_{sat} - M^M_{dry}}{\rho_0^{fl} V} \tag{8.20}$$

where V stands for the specimen volume, $M^*_{sat} = \rho^*_{sat} V^*, M^M_{sat} = \rho^M_{sat} V^M$ and M^*_{dry}, M^M_{dry} for the actual measured masses of the saturated and dried materials, and $\rho_0^{fl} = 1{,}000$ kg/m^3 is the water mass density.

8.2.2 Level I: LD + HD C-S-H → C-S-H matrix

The C-S-H matrix (Level I) is composed of two porous materials, the HD C-S-H phase and the LD C-S-H phase. The poroelastic properties of the C-S-H matrix are determined from Eqs.

(7.68a), (7.68b), (7.68c) and (7.68d):

$$\text{in } V_I : \left\{ \begin{array}{c} K^I_{\text{hom}} = \langle kA^v \rangle_{V_{CSH}} = k_{HD} + (k_{LD} - k_{HD})\, f_{LD} A^v_{LD} \\ G^I_{\text{hom}} = \langle gA^d \rangle_{V_{CSH}} = g_{HD} + (g_{LD} - g_{HD})\, f_{LD} A^d_{LD} \\ b^I_{\text{hom}} = \langle bA^v \rangle_{V_{CSH}} = b_{HD} + (b_{LD} - b_{HD})\, f_{LD} A^v_{LD} \\ 1/N^I_{\text{hom}} = 1/N^I_{LD} + 1/N^I_{HD} \end{array} \right\} \tag{8.21}$$

where we employed the consistency condition $f_{LD}A^v_{LD} + f_{HD}A^v_{HD} = 1$ and $f_{LD} + f_{HD} = 1$. Given this compatibility condition, it is readily understood that the poroelastic properties of the C-S-H matrix are all situated in between the values of the low-density and the high density C-S-H phase, i.e.,

$$\text{in } V_I : \left\{ \begin{array}{c} E^{LD} \leq E^I_{\text{hom}} < E^{HD} \\ b^{LD} \leq b^I_{\text{hom}} < b^{HD} \\ 1/N^I_{LD} \leq 1/N^I_{\text{hom}} < 1/N^I_{HD} \end{array} \right\} \tag{8.22}$$

where $E^{LD} = 21.7$ GPa and $E^{HD} = 29.4$ GPa are the drained stiffness properties of the low-density and the high-density C-S-H phases, which are determined directly from nanoindentation [58]. Between these bounds, the poroelastic properties depend on the w/c–ratio, which affects the volume fractions f_{HD} and f_{LD} of the two types of C-S-H (see Fig. 9-5). These volume fractions are also directly measurable, either by nanoindentation (see Chapter 5), or by hydration models (see Section 4.5). In this case, the determination of the poroelastic properties requires estimates for the concentration factors A^v_{LD} and A^d_{LD} in (8.21). Using the estimate given by the Mori-Tanaka scheme (see Eq. (7.15) and Appendix (C)), in which we choose the low density phase as matrix, gives:

$$A^v_{LD} \equiv A^{v,MT}_{LD} = \frac{1 + \alpha_{LD}\,(\kappa - 1)}{f_{LD}\,[1 + \alpha_{LD}\,(\kappa - 1)] + f_{HD}} \tag{8.23}$$

$$A^d_{LD} \equiv A^{d,MT}_{LD} = \frac{1 + \beta_{LD}\,(\eta - 1)}{f_{LD}\,[1 + \beta_{LD}\,(\eta - 1)] + f_{HD}} \tag{8.24}$$

where $\kappa = k_{HD}/k_{LD}$, $\eta = g_{HD}/g_{LD}$, and where α_{LD} and β_{LD} are given by (C.13).

The outcome of this homogenization step are the stiffness parameters of the C-S-H matrix, k^{CSH}_{hom} and g^{CSH}_{hom}, and the poroelastic constants. For a $w/c = 0.5$ cementitious material, for which $f_{LD} = 0.7$ and $f_{HD} = 0.3$, we obtain $k^{CSH}_{\text{hom}} = 15.2$ GPa and $g^{CSH}_{\text{hom}} = 9.6$ GPa, thus an

elastic stiffness of $E = 23.8$ GPa, and the poroelastic constants:

$$w/c = 0.5: \quad b^I_{\text{hom}} = 0.67 \quad N^I_{\text{hom}} = 131.1 \text{ GPa} \quad M^I = 6.6 \text{ GPa} \quad B^I = 0.24 \tag{8.25}$$

The outcome of this homogenization step is summarized in Tab. 8.3.

8.2.3 Level II: C-S-H matrix + MP → Cement Paste

At Level II, the composite material is composed of a porous C-S-H matrix, and an additional capillary porosity. This case is covered by relations (7.85), developed for the double porosity model. The homogenized value from Level I ($K^I_{\text{hom}}, G^I_{\text{hom}}, b^I_{\text{hom}}, N^I_{\text{hom}}$) will serve as input data for this homogenization step. The volume fractions of the phases are also known from Power's model as detailed before. For a $w/c = 0.5$ cement paste, for which all clinker phases are consumed in the hydration reactions, the problem reduces to a composite material composed of a porous matrix (C-S-H matrix of volume fraction $f_{CSH} = V_{CSH}/V_{II} = 0.90$, stiffness $k_{CSH} = K^I_{\text{hom}}; g_{CSH} = G^I_{\text{hom}}$), and a pore space $\phi_0 = 1 - f_{CSH} = 0.10$, for which:

- The drained bulk modulus and shear modulus are given by Eqs. (7.85a) and (7.85b) respectively:

$$\text{in } V_{II}: \left\{ \begin{array}{l} K^{II}_{\text{hom}} = f_{CSH} k_{CSH} A^v_{CSH} \\ G^{II}_{\text{hom}} = f_{CSH} g_{CSH} A^d_{CSH} \end{array} \right\} \tag{8.26}$$

  By estimating the concentration factors with a Mori-Tanaka scheme, the drained stiffness properties of the $w/c = 0.5$ cement paste are $k^{II}_{\text{hom}} = 13.0$ GPa, $g^{II}_{\text{hom}} = 7.9$ GPa, thus a drained Young's modulus of $E^{II}_{\text{hom}} = 19.6$ GPa. We also note that the undrained bulk modulus is $K^{u,II}_{\text{hom}} = 15.9$ GPa, and the associated Young's modulus $E^{u,II}_{\text{hom}} = 20.2$ GPa.

- The Biot coefficient is derived from Eq. (7.85c), by adding to the Biot coefficient associated with the capillary porosity the contribution of the porous matrix:

$$\text{in } V_{II}: b^{II}_{\text{hom}} = b^{II}_1 + b^{II}_2 = \phi_0 A^v_f + f_{CSH} b^I_{\text{hom}} A^v_{CSH} \tag{8.27}$$

  For the $w/c = 0.5$ cement paste, for which the capillary porosity is relatively small ($\phi_0 = 10\%$), the Biot coefficient associated with this capillary porosity is small as well,

$b_1^{II} = \phi_0 A_{\phi_0}^v = 0.17$, and the overall Biot coefficient is dominated by the contribution of the porous C-S-H matrix, $b_2^{II} = f_{CSH} b_{\text{hom}}^I A_{CSH}^v = 0.55$; which yields a total of $b_{\text{hom}}^{II} = 0.72$.

- The skeleton Biot modulus is derived from Eq. (7.85e), where the contributions of the porous matrix and the one of macroporosity are incorporated:

$$\text{in } V_{II}: N_{\text{hom}}^{II} = \left[(1-\phi_0) \left(\frac{b^I}{K^I} \left(b^I - b_1^{II} \right) + \frac{1}{N^I} \right) + 2\,(1-\phi_0) \frac{b^I}{K^I} \left(A_M^v - 1 \right) + \frac{1}{K^I} \left(b_2^{II} - \phi_0 \right) \right]^{-1} \tag{8.28}$$

For the $w/c = 0.5$ cement paste, we obtain $N_{\text{hom}}^{II} = 102.1$ GPa. The overall Biot modulus is then determined from Eq. (7.119), by considering as effective porosity the sum of the capillary and the weighted gel porosity, i.e. $\phi_0^{II} = \phi_0 + f_{CSH} \times \phi_0^{CSH}$; thus in summary for the $w/c = 0.5$ cement paste, for which $\phi_0^{II} = 0.34$:

$$w/c = 0.5: \quad b_{\text{hom}}^{II} = 0.72 \quad N_{\text{hom}}^{II} = 102.1 \text{ GPa} \quad M^{II} = 5.4 \text{ GPa} \quad B^{II} = 0.24 \tag{8.29}$$

8.2.4 Level III: Cement Paste + Inclusions → Mortar/Concrete

At Level III, the material is composed of a porous matrix (the cement paste) and non-porous inclusions. From a morphological point of view, the porosity belongs to the phases at a level below (cement paste). Given the separability of scale condition, the porosity does not enter the Level III, but is already included in the poroelastic properties of the cement paste that serve as input. Consequently, the drained elastic properties are obtained from the application of Eq. (8.21) to the two-phase system (porous matrix and inclusions), neglecting any interface zone around the aggregates; i.e.:

$$\text{in } V_{III}: \left\{ \begin{array}{l} K_{\text{hom}}^{III} = k_M + (k_I - k_M)\, f_I A_I^v \\ G_{\text{hom}}^{III} = g_M + (g_I - g_M)\, f_I A_I^d \end{array} \right\} \tag{8.30}$$

where $k_M = K_{\text{hom}}^{II}$ and $g_M = G_{\text{hom}}^{II}$ are the elastic properties of the cement paste matrix, k_I and g_I the elastic properties of the aggregate inclusions of volume fraction $f_i = V_i/V_{III}$ given by mass density measurements (see Eqs. (8.18) and (8.19)), while A_i^v and A_i^d are strain localization

factors. For this case, the Biot parameters, b and N, are given by Eqs. (7.114c) and (7.114d):

$$\text{in } V_{III}: \left\{ \begin{array}{l} b_{\text{hom}}^{III} = (1-f_i)\, A_M^v b_{\text{hom}}^{II} = (1-f_i A_i^v)\, b_{\text{hom}}^{II} \\ N_{\text{hom}}^{III} = \left[\frac{(1-f_i)}{N^{II}} + (1-f_i)\left(b^{II}\right)^2 \frac{\left(1-A_M^v\right)}{(k_i+K^{II})} \right]^{-1} \end{array} \right\} \tag{8.31}$$

For the $w/c = 0.5$ mortar with a sand volume fraction of roughly $f_i = 1/3$ and known elasticity properties ($E_i = 62.5; \nu_i = 0.21$), we obtain $K_{\text{hom}}^{III} = 17.3$ GPa, $G_{\text{hom}}^{III} = 11.0$ GPa, thus a drained Young's modulus of $E_{\text{hom}}^{III} = 27.2$ GPa, an undrained Young's modulus $E_{\text{hom}}^{u,II} = 27.9$ GPa, along with the following poroelastic properties:

$$w/c = 0.5: \quad b_{\text{hom}}^{III} = 0.59 \quad N_{\text{hom}}^{III} = 293.6 \text{ GPa} \quad M^{III} = 7.3 \text{ GPa} \quad B^{III} = 0.22 \tag{8.32}$$

where we employed $\phi_0^{III} = (1-f_i)\,\phi_0^{II} = 0.23$ for the determination of the overall Biot modulus.

8.2.5 Discussion

The developed upscaling scheme delivers estimates of the poroelastic properties of cementitious materials at multiple scales, that are difficult to assess experimentally. Particularly, static tests in which simultaneously the mean stress and the pore pressure are monitored are difficult to perform in the purely elastic range, and involve very early on plastic deformation. The static stiffness that is reported from such tests is often much smaller than the dynamic stiffness measured on the same material. By way of example, Tab. 8.3 reports the dynamic Young's modulus determined by Ultrasound Pulse Velocity (UPV) and Resonance Frequency (RF) of the cement paste and mortar we consider in this study, together with the static stiffness obtained from the unloading branch of a uniaxial compression test. From this table, it is readily seen that the static modulus is some $10-20\%$ smaller than the dynamic stiffness. Hence, a consistent comparison with the estimated stiffness values obtained by upscaling should be made with the dynamic stiffness values. More precisely,

- In UPV-tests, the stiffness is determined from the velocity with which a wave travels through the saturated sample (for details see e.g., Ref. [58]). Given the high frequency (in the 500 kHz – 1,000 kHz), it is unlikely that liquid mass can escape the sample; and the

		Level I	Level II	Level III
Measured		C-S-H Matrix	Cement Paste	Mortar
ρ_{sat}	[kg/m^3]	–	$1,898 \pm 9$	$2,171 \pm 15$
$\frac{\Delta m}{\rho_0^{fl}}$	[%]	–	39.7 ± 1.1	27.5 ± 0.4
E_{Static}	[GPa]	–	18.6 ± 0.6	21.6 ± 0.4
E_{RF}	[GPa]	–	21.7 ± 0.1	25.2 ± 0.1
E_{UPV}	[GPa]	–	22.8 ± 0.5	26.5 ± 1.8
Predicted				
E_{hom}	[GPa]	23.8	19.6	27.2
ν_{hom}	[1]	0.24	0.25	0.27
E^u_{hom}	[GPa]	24.4	20.2	27.9
ν^u_{hom}	[1]	0.28	0.29	0.28
b_{hom}	[1]	0.67	0.72	0.59
N_{hom}	[GPa]	131.1	102.1	293.6
M_{hom}	[GPa]	6.6	5.4	7.3
B	[1]	0.24	0.24	0.22

Table 8.3: Measured versus predicted properties of a $w/c = 0.5$ cement paste and mortar:
ρ_{sat} = mass density of saturated sample;
Δ m = change in mass content due to drying at 105° C;
E_{UPV} = Young's modulus determined by Ultrasonic Pulse Velocity;
E_{RF} = Young's modulus determined by Resonance Frequency;
E_{Static} = Young's modulus determined from uniaxial unloading tests.
Predicted (MT = Mori Tanaka; SCS = Selfconsistent Scheme):
E_{hom} = drained Young's modulus;
ν_{hom} = drained Poisson's ratio;
E^u_{hom} = undrained Young's modulus;
ν^u_{hom} = undrained Poisson's ratio;
b_{hom} = Biot coefficient;
N_{hom} = Skeleton Biot modulus;
M_{hom} = overall Biot modulus;
B = Skempton coefficient.

conditions can be assumed to be approximately undrained. Hence, UPV-measurements are suitably compared with the undrained stiffness values.

- In RF-tests, a sample is brought into vibration, and the stiffness is determined from the frequency response (for details see e.g., Ref. [58]). Given the time it takes to reach a constant frequency, it is likely that the conditions are not completely undrained, and in a first approximation the values obtained can be associated with drained stiffness values, which explains that RF-stiffness are generally $1 - 1.5$ GPa smaller than UPV-measurements.

Table 8.3 also summarizes the stiffness values (and poroelastic constants) obtained by upscaling. It is interesting to note that the undrained stiffness values of the cement paste is within 10% of the UPV-stiffness ($E_{\text{hom}}^{u,II} = 20.2$ GPa versus $E_{UPV}^{II} = 22.8 \pm 0.5$); and also the drained stiffness values is within 11% of the RF-measurements ($E_{\text{hom}}^{II} = 19.6$ GPa versus $E_{RF}^{II} = 21.7 \pm 0.1$). This good agreement is a clear indication of the predictive capabilities of the homogenization scheme for the cement paste, that is the capability of the model to capture the strain localization in the solid phases. Since the strain localization is intimately related to the Biot coefficient and Biot moduli, we may infer that the stiffness validation includes the validation of b_{hom}^{II} and N_{hom}^{II} (calculated values reported in (8.29)). The small discrepancy observed between measured and predicted values may be attributed to the presence of Portlandite crystals which have been neglected in the Level II homogenization, and which might be responsible for an additional 10-11% stiffness contribution.

By contrast, the stiffness values obtained by homogenization of the mortar are slightly greater than the experimental values for both the undrained, +5%, ($E_{\text{hom}}^{u,III} = 27.9$ GPa versus $E_{UPV}^{III} = 26.5 \pm 1.8$) and the drained case, +7% ($E_{\text{hom}}^{III} = 27.2$ GPa versus $E_{RF}^{II} = 25.2 \pm 0.1$). This is an indication of an additional micromechanical feature which adds a compliance to the composite material of non negligible magnitude (difference on the order of 10%), and which has not been taken into account in our upscaling scheme. Several contributions in the literature suggest the existence of an Interfacial Transition Zone (ITZ) between the inclusions and the cement paste matrix, which may well explain this difference. This zone is known to be – on average – a zone of a higher porosity than the cement paste matrix. The Biot coefficient determined by neglecting the ITZ, therefore, appears as a lower bound of the actual Biot coefficient of the mortar.

8.3 Thermally and Chemically Treated Systems

The micromechanical model presented in Chapter 7 is general and can be equally applied to any cement based material provided the knowledge of the volumetric proportions of all constituents and their elastic properties. In the validation section of this chapter (Section 8.2) we have estimated the volume fractions through the Powers model. When it comes to chemically affected

systems, the predictive capabilities of the model breaks down and one needs to proceed in an alternative way.

8.3.1 Heat Curing and Heat Treatment

This section investigates the use of our microporomechanics model to thermally affected systems: heat cured and heat treated specimens investigated in Chapter 6. The input requirements for all levels are summarized in Tab. 8.4. The volumetric proportions of all constituents were evaluated from the deconvolution technique developed in Chapter 5. For purposes of microporomechanical analysis the effect of Portlandite crystals is lumped into the volumetric proportions of the C-S-H constituent treating it all as one single phase (similar to Powers model). Furthermore one needs estimates of the elastic moduli of the involved constituents. The elastic moduli of the two types of C-S-H were obtained using the indentation analysis tools presented in Chapter 2 and 5. As it was shown in Chapter 6 the elastic properties of the two types of C-S-H remain almost unaffected by the thermal process and it is only the volumetric proportions that are significantly affected. The input data, which is summarized in Tab. 8.4, is incorporated in relation (7.35) that provide predictions of cement pastes elasticity ($K^{II}_{\text{hom}}, G^{II}_{\text{hom}}$). The Young's modulus can then be readily obtained using standard relations of elasticity, $E^{pre} = \frac{\left(9K^{II}_{\text{hom}} G^{II}_{\text{hom}}\right)}{\left(3K^{II}_{\text{hom}} + G^{II}_{\text{hom}}\right)}$. The predicted values are compared with experimental macroscopic data (E^{exp}) obtained by microindentation (see Section 6.2.2). It is impressive to see that the micromechanical predictions are in close agreement with experimental values ($\pm 10\%$). Slight discrepancies observed between experiments and predictions should be attributed to inaccurate determination of the volumetric proportions of the individual chemical constituents.

8.3.2 Calcium Leaching

An interesting case study of our micromechanical model is the scenario where cementitious materials are subjected to the dissolution of calcium from their solid skeleton. Such a scenario arises when the calcium concentration in the saturated pore solution falls below the chemical equilibrium of the solid phases bound in the solid skeleton leading to the progressive decal-

		'C'	'HC-1'	'HC-28'	'HT'	'CL'
Young's Modulus	LD C-S-H	18.8	17.8	18.0	18.3	3.0
	HD C-S-H	31.0	29.8	28.5	29.1	12.0
Volume Fractions	f_{LD}	67	63	47	62	70
	f_{HD}	33	37	53	38	30
	f_{CSH}	89	89	79	92	86
	f_{cp}	8	2	16	5	14
	f_{CL}	3	9	5	3	0
Predictions	E^{pre}	18.7	21.6	17.2	19.5	3.5
vs.	$E^{\exp}$	18.0	19.7	18.3	19.0	3.6
Measurements	$1-\frac{E^{pre}}{E^{\exp}}$	−4	−10	+6	−3	+3

Table 8.4: Input and Output properties of several thermally and chemically affected systems. Measured versus predicted Young's moduli. 'C'=Control, 'HC-1'=1-day heat cured, 'HC-28'=28-days heat-cured, 'HT'=Heat-treated, 'CL'=Calcium leached.

cification of the different minerals. The resulting material is one of increased macroporosity[2] and reduced mechanical performance of the two C-S-H types. In contrast to thermally treated systems the elastic modulus of the two types of C-S-H ($E_{LD}^{CL} = 3$ GPa, $E_{HD}^{CL} = 12$ GPa) reduces significantly due to the decalcification process (see Tab. 8.4). It is interesting to note that while the intrinsic properties of the two types are significantly reduced the volumetric proportions remain unchanged from the degradation process ($f_{LD} = 0.70, f_{HD} = 0.30$). Substituting the input data into Eq. (7.35) yields macroscopic estimates of the calcium leached material. It is impressive to note that the predictions of the micromechanical model ($E^{pre} = 3.5$ GPa) are within 3% of the experimentally obtained (UPV) values ($E^{mea} = 3.6$ GPa).

The applicability of the model to thermally and chemically affected CBM systems verifies the robust predictive nature of the model, which provides reliable macroscopic estimates in light of knowledge of three crucial parameters: a) Morphological arrangement at all considered levels; b) Elastic properties of all involved constituents; and c) Volumetric proportions of all phases.

[2] Portlandite crystals dissolve into Calcium ions and water leaving in return empty spaces which manifest themselves as macroporosity present at Level II, equivalent of capillary porosity.

8.4 Chapter Summary

Continuum micromechanics and advanced microstructural modeling of cement chemistry together with advanced micromechanical testing (such as nanoindentation) provide a rational means to estimate the elastic/poroelastic properties of highly heterogeneous materials such as cement-based materials, and to confirm that cement-based materials are poromechanics materials that are sensitive to the pore pressure that manifests itself at multiple scales.

If we admit that the gel porosity is the smallest pore space in cement-based materials in which water occurs as a bulk water phase, the poromechanical effect of this porosity dominates over fluid pressure effects. The gel porosity of 24% and 37% in high-density and low-density C-S-H, which is the same for all cement-based materials, confines the Biot coefficient within $0.54 < b^0 \leq 0.72$ (see Fig. 8-4). Except for the case of an excessive capillary porosity, this base Biot coefficient decreases gradually at larger scales, because of the addition of non-porous solid phases (Portlandite,aggregates, etc.), but is generally expected to be larger than twice the (bulk water) porosity. This relatively high value of the Biot coefficient indicates that the deformation of cementitious materials is not only governed by the deformation of the solid phases, but also by a change of the porosity, particularly of the gel porosity in the C-S-H, which is on the same order as the macroscopic deformation. In a similar way, a pressure build-up or a pressure decrease (e.g., capillary pressure) also entails a non-negligible change of this gel porosity, resulting in swelling or shrinkage of these materials.

The Skempton coefficient B, which is a measure for the sensitivity of porous material to drained and undrained conditions, is almost constant over several orders of magnitude, starting from the scale of the LD- and HD C-S-H (Level 0), to the scale of the cement paste (Level II), and mortar or concrete composite (Level III) (see Fig. 8-4). It is on the order of $B = 0.20 - 0.25$, which is a rather small value for a porous material with such a high porosity. In turn, this rather small value explains the little difference between drained and undrained elastic properties, and may well explain the little consolidation effect that cement-based materials generally experience.

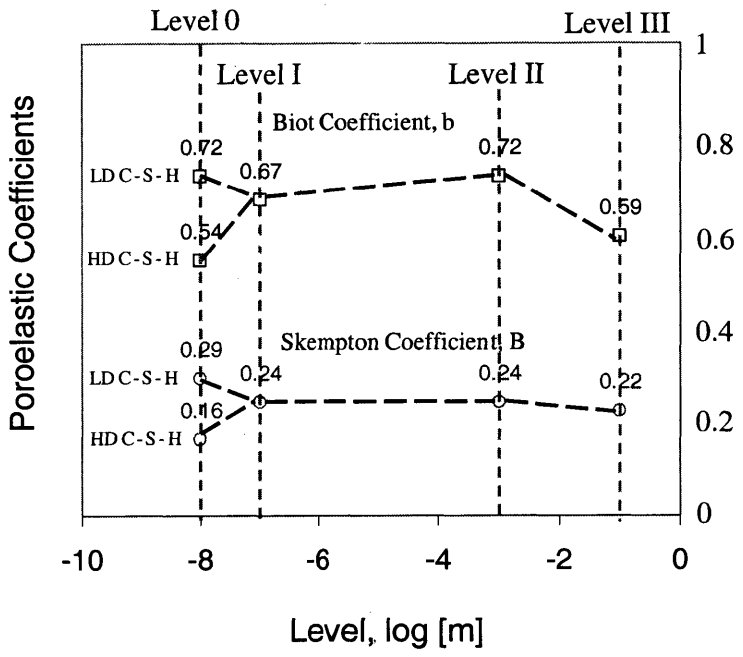

Figure 8-4: Evolution of biot coefficient b and Skempton coefficient B over the different levels of characterization. These results are for a cement paste and mortar of w/c-ratio of 0.5 (see details in Section 8.2 and Tab. 8.3)

Chapter 9

Development of an Engineering Poroelastic Prediction Tool

This chapter is devoted to the development of an engineering model that can predict the poroelastic properties of any CBM system at multiple scales. To this end, we couple the microporoelastic model presented in Chapter 7 with a chemical reaction model that can predict the volumetric proportions of CBM constituents for a given mix design. The resulting product is an engineering tool that can deliver the macroscopic poroelastic behavior of all cement-based materials irrespective of initial $w/c-$ratio, degree of hydration, type of testing (drained or undrained), etc. The engineering tool is then used to demonstrate the effect of $w/c-$ratio on the multi-scale mechanical performance of cementitious materials. It is shown that the micromechanical estimates are in excellent agreement with available experimental data, further validating not only the used localization schemes but also the obtained intrinsic properties values, chemical reaction models, and assumed morphological arrangements.

9.1 Development of an Engineering Model

We attempt in this section to devise an engineering model that can provide predictions of the elastic properties of cementitious materials for a given set of commonly known information (mix design parameters). The central theme of this model will be a balance between ease of utilization and accuracy of predictions. The developed four-level upscaling scheme requires, at

	Input			Output	
	Volume Fractions	Properties	Mor.	Properties	Scheme
LEVEL '0'	f_s^{LD} f_{gp}^{LD} f_s^{HD} f_{gp}^{HD}	k_s g_s k_{gp} g_{gp}	PC	k_{LD}^{est} g_{LD}^{est} k_{HD}^{est} g_{HD}^{est}	SC
LEVEL 'I'	f_{LD} f_{HD}	k_{LD} g_{LD} k_{HD} g_{HD}	MI	k_{CSH}^{est} g_{CSH}^{est}	MT
LEVEL 'II'	f_{CSH} f_{CH} f_{CL} f_{CP}	k_{CSH} g_{CSH} k_{CH} g_{CH} k_{CL} g_{CL} k_{MP} g_{MP}	MI	k_{Paste}^{est} g_{Paste}^{est}	MT
LEVEL 'III'	f_P f_i	k_P g_P k_i g_i	MI	k_{Mortar}^{est} g_{Mortar}^{est}	MT

Table 9.1: Input-Ouput parameters involved in the three level upscaling scheme for CBM materials. * PC=Polycrystal, MI=Matrix-Inclusion **SC=Self-Consistent, MT=Mori-Tanaka

each level, input of two of the elastic constants (i.e., bulk and shear moduli k_i, g_i), and of the volume fractions, f_i, of the involved phases, i. Finally one needs to assume a morphological arrangement of the involved quantities which will define the choice of the localization scheme. Table 9.1 summarizes the input-output structure of the proposed model. The following section proposes a way such that the input requirements of the micromechanical model can be directly determined from the mix design proportions.

9.1.1 Volumetric Proportions

Quantification of the relative volume of the different constituents present in cement-based materials microstructure can be achieved either experimentally (nanoindentation, see Chapter 5, or Mass-density measurements, see Section 8.2) or theoretically, by modeling the chemical reactions of cement particles (Section 4.5.1). In what follows, we will use the chemistry models presented in Section 4.5.1 that can provide the volumetric proportions of CBM constituents for a given mix proportion. A simple set of equations was proposed by Powers - see Eq. (4.12) - which can be applied to all Portland cements (Type I to V) and which avoids the more rigorous and complex calculations of the stoichiometric relations. The separation of the C-S-H into its two types, however, needs to be done with the help of J-T model that proposes a simple relation fitted on experimental results of surface area and nitrogen-accessible porosity (see Section 4.5.2).

The critical mix parameter that provides some control over the microstructure is the initial $w/c-$ratio. Depending on the initial $w/c-$ratio the resulting microstructure will have different volumetric proportions of the hydration products that are allocated in different levels of our 4-level structure. The compatibility condition, $\sum f_i^J = 1$ must be satisfied at all levels, $J = 0, I, II, III$.

Level III: Mortar/Concrete

Typical mix parameters provided by the manufacturer are the mass percentages of water, cement and sand denoted here by w, c, s respectively. Given this initial mix design $(w/c/s)$ one can calculate the volume fractions at Level III:

$$f_i = \frac{s/\rho_s}{w/\rho_w + c/\rho_c + s/\rho_s} \tag{9.1}$$

$$f_P = 1 - f_i \tag{9.2}$$

where ρ_w, ρ_c, ρ_s are the densities of the raw materials; water, cement and sand. While the density of water and cement are generally constant ($\rho_w = 1000$ kg/m^3, $\rho_c = 3150$ kg/m^3) the density of sand particles will vary depending on the type of sand particles used. It should be noted that Eq. (9.1) assumes that the volume of the mixture remains constant during hydration, an assumption which is generally supported by experimental results [180].

Level II: Cement Paste

Power's model provides a simple set of equations (Eq. (4.12)): for a given degree of hydration, the relative volumetric proportions of the clinker, macropores and gel phases as a function of $w/c-$ratio. The gel phase is representative of the C-S-H, CH and any other minor compounds (see Section 4.2.3) formed during hydration. It can be estimated from the chemical reactions (see Section 4.5.2) that the majority of the volumetric proportions of the gel (close to 90%) is composed of C-S-H independently of the degree of hydration and initial $w/c-$ratio. For the purpose of simplicity we will therefore assume that the gel phase described in Powers model corresponds solely to the C-S-H component.

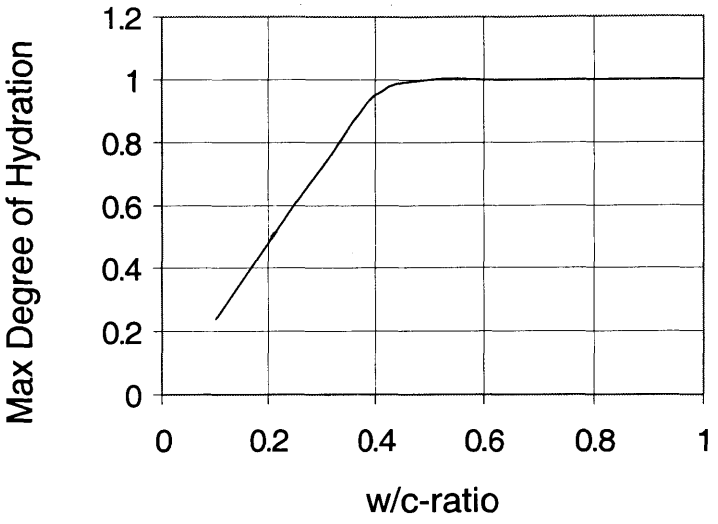

Figure 9-1: Maximum possible degree of hydration ξ, vs. w/c–ratio as predicted by Powers model.

Maximum degree of hydration, ξ_{max} It has been experimentally found by Powers [194] that complete hydration cannot occur if the w/c–ratio is below a certain value (see Chapter 4). Even though the exact value of this critical w/c–ratio is a function of the cement composition and cement particle distribution an average value for all cements can be calculated using Powers model: For a given w/c–ratio the degree of hydration progresses provided there is space available for the hydration products to precipitate ($V_{cp} > 0$). In cases where the space is filled ($V_{cp} \rightarrow 0$) then the hydration should stop ($\xi \rightarrow \xi_{max}$). An estimate of the maximum degree of hydration, ξ_{max}, can be calculated from Eq. (4.12), by letting the capillary porosity go to zero, $V_{cp} \rightarrow 0$. The resulting ξ_{max} vs. w/c relation is shown in Fig. 9-1. The calculated relationship may well be approximated by:

$$\begin{aligned} \xi_{max} &= 2.38\left(\tfrac{w}{c}\right) \quad \text{for } 0 \leq \tfrac{w}{c} \leq 0.42 \\ \xi_{max} &= 1 \qquad\qquad \text{for } \tfrac{w}{c} > 0.42 \end{aligned} \tag{9.3}$$

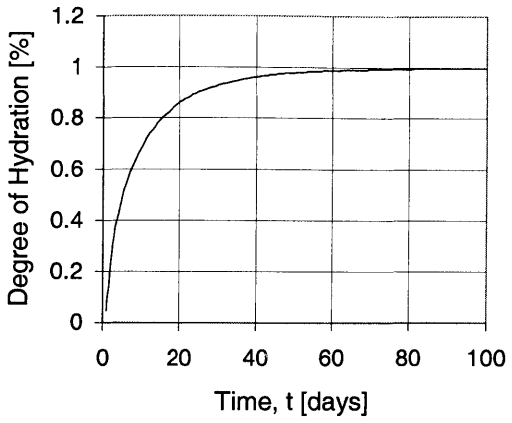

Figure 9-2: An Avrami type evolution characterizing the kinetics of degree of hydration of C_3S vs. time.

Clinker Phases	a	b	c
C_3S	0.25	0.90	0.70
C_2S	0.46	0.00	0.12
C_3A	0.28	0.90	0.77
C_4AF	0.26	0.90	0.55

Table 9.2: Experimentally obtained constants used in Avrami equations, from Ref. [226].

Generally speaking, the degree of hydration can be linked to the age of the sample, t - in days, by assuming that the kinetics of the chemical reaction follow the Avrami equation:

$$\xi = 1 - \exp\left(-a\left(t-b\right)^c\right) \tag{9.4}$$

where a, b, and c are empirical constants that need to be fitted by experiments. Taylor [226] provided experimental values for these constants that are given in Tab. 9.2.

Given that Power's model does not separate the different cement compounds but rather considers cement as one phase, we will assign a global degree of hydration following the kinetics of C_3S which is the dominant cement compound in most commercial cements (i.e., see Tab. 4.1). Figure 9.2 shows the degree of hydration of the C_3S as a function of time t in days. It is

readily understood that most of the reaction occurs after a few weeks with 92% of the cement being consumed by 28 days and 99% by two months. In what follows, we will be concerned with mature pastes (> 4 months) where the effects of age (i.e., degree of hydration) becomes negligible. In such a case the degree of hydration can be approximated by $\xi_{\max}$ which becomes a function of only the $w/c-$ratio and can be calculated by (9.3)[1]. Given the existence of this relation, $\xi = \Xi(w/c)$, the volumetric proportions of all constituents present in cement paste microstructure become unique functions of the initial $w/c-$ratio (see Eq. (4.12)).

Water (CP), Cement (CL) and Reaction Products (C-S-H) The gross space available for the products of hydration consists of the absolute volume of the dry cement together with the volume of the added water. This volumetric space is occupied by the different constituents depending on the $w/c-$ratio. The $w/c-$ratio defines the total volume of porosity left in the system after hydration as well as the maximum degree of hydration that can be achieved. Figure 9-3 shows the Powers model predictions (4.12) for the volumetric proportions of all phases where the maximum possible degree of hydration (see Fig. 9-1) has been used for a given $w/c-$ratio. The required volume fractions for Level II of the micromechanics model ($f_{CSH}, f_{cl}, f_{cp} \equiv \phi^0$) can be readily obtained either from Eq. (4.12) or from Fig. 9-3. For $w/c > 0.42$, complete hydration is always possible. In contrast, $w/c < 0.42$ provides insufficient water to completely hydrate all cement present in the microstructure, with subsequent residual clinker phases left in the system. In what follows, we will concentrate on mature pastes (age > 1 month) where hydration effects become negligible. As we have seen in the experimental part of this thesis, the C-S-H phase is composed of two types. Powers model does not provide a separation of the two C-S-H phases and this need to be done in an alternative way.

Level I: Separating the 2-types of C-S-H

Estimates for the relative presence of the two types of C-S-H has been provided by Jennings and Tennis [130, 227] who fitted experimental data of surface area and porosity measurements in an attempt to quantify the relative presence of the two. Their model, which has been presented in

[1]Strictly speaking, the degree of hydration of a given cement paste is a complicated function of the $w/c-$ratio, time after mixing, cement composition, cement particle distribution etc. Nevertheless the dominating factor that prevails over all other parameters is the initial $w/c-$ratio.

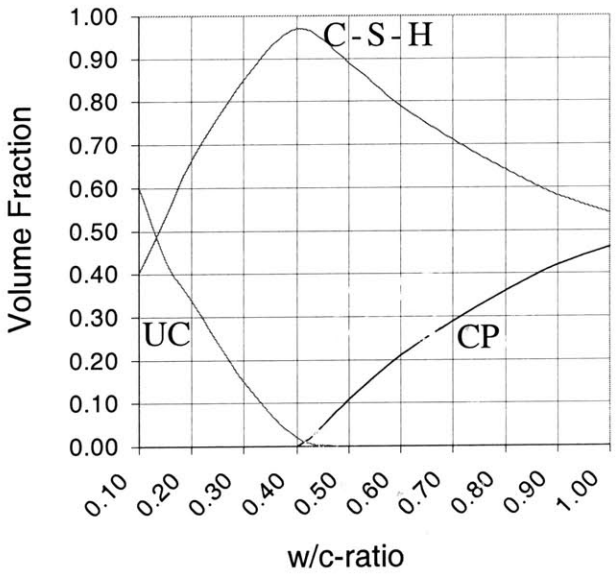

Figure 9-3: Volumetric proportions predictions for different $w/c-$ratios.

Section 4.5.2, provides a quantification of the two types of C-S-H. Combining Eqs. (4.18) and (4.19) yields an estimate for the LD volume fraction:

$$f_{LD} = \frac{\mathcal{M}_r \frac{M_t}{\rho_{LD}}}{\mathcal{M}_r \frac{M_t}{\rho_{LD}} + \frac{M_t(1-\mathcal{M}_r)}{\rho_{HD}}} = \frac{\mathcal{M}_r}{\mathcal{M}_r + (1-\mathcal{M}_r)\frac{\rho_{LD}}{\rho_{HD}}} \tag{9.5}$$

where we recall that $\mathcal{M}_r$ is the mass of LD C-S-H over the total C-S-H mass. Fitting the experimental data shown in Fig. 9-4, Tennis and Jennings [227] provided an analytical expression of $\mathcal{M}_r$ as a function of the degree of hydration and the initial $w/c-$ratio, see Eq. (4.17):

$$\mathcal{M}_r = 3.017\frac{w}{c}\xi - 1.347\xi + 0.538 \tag{9.6}$$

Combining Eqs. (9.6) and (9.5) one can get the relative proportions of LD C-S-H and HD C-S-H for any $w/c-$ratio and degree of hydration. Figure 9-5 shows f_{LD} as a function of the $w/c-$ratio for the maximum degree of hydration (see Eq. (9.3)) that can be achieved in each case. The experimental data obtained by nanoindentation in Chapter 6 is also shown for comparison. The very good agreement between experiments and Eq. (9.6) validates the function provided by J-T, Eq. (9.5). It should be noted, however, that the range of applicability of Eq. (9.5) is within $0.25 \leq w/c \leq 0.5$, the range for which the experimental data was fitted. The tendency of the function to show a minimum at around $w/c = 0.22$ and to even extend at values higher $f_{LD} > 1$ for $w/c > 0.6$, should be considered as artifact of the fitting process. In order to get a function that can provide estimates for $w/c-$ratio $0.25 \geq w/c \geq 0.5$ we extracted from Fig. 9-4 the experimental $\mathcal{M}_r$ corresponding to the maximum degree of hydration for the different $w/c-$ratios for which the function was initially fitted ($w/c = 0.25, 0.33, 0.44, 0.5$) and replotted the calculated f_{LD} (from Eq. (9.5)) on a separate graph (Fig. 9-5a). The experimental points obtained by nanoindentation are also included. It can be seen that a linear function, which minimizes the least square error, provides an excellent fit to the data:

$$\begin{aligned} f_{LD} &= 2.12\left(\tfrac{w}{c}\right) - 0.36 \quad 0.17 \leq w/c \leq 0.64 \\ f_{LD} &= 0 \qquad\qquad\quad w/c \leq 0.17 \\ f_{LD} &= 1 \qquad\qquad\quad w/c \geq 0.64 \end{aligned} \tag{9.7}$$

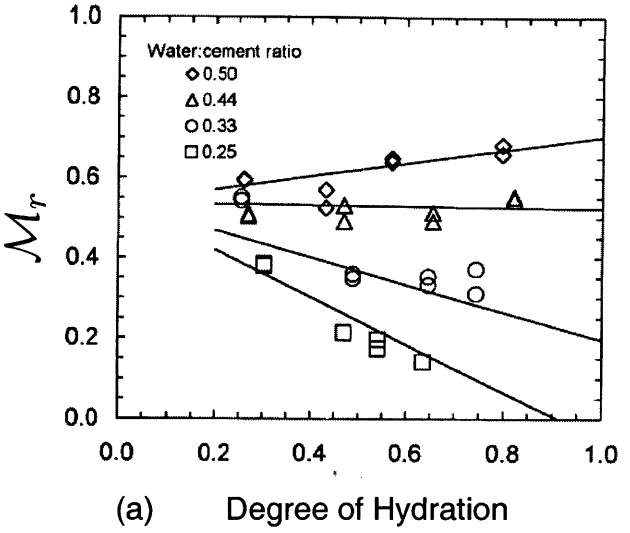

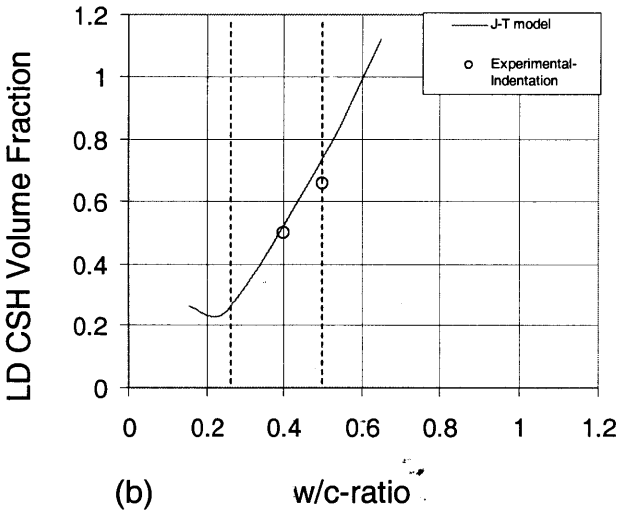

Figure 9-4: (a) J-T predictions and experimental data of the molar ratio of LD C-S-H to total C-S-H, vs. the degree of hydration for different $w/c-$ratios. (b) Comparison between the preditions of the J-T model and experimental data obtained by indentation of the volumetric proportions of the LD C-S-H phase vs. $w/c-$ratio.

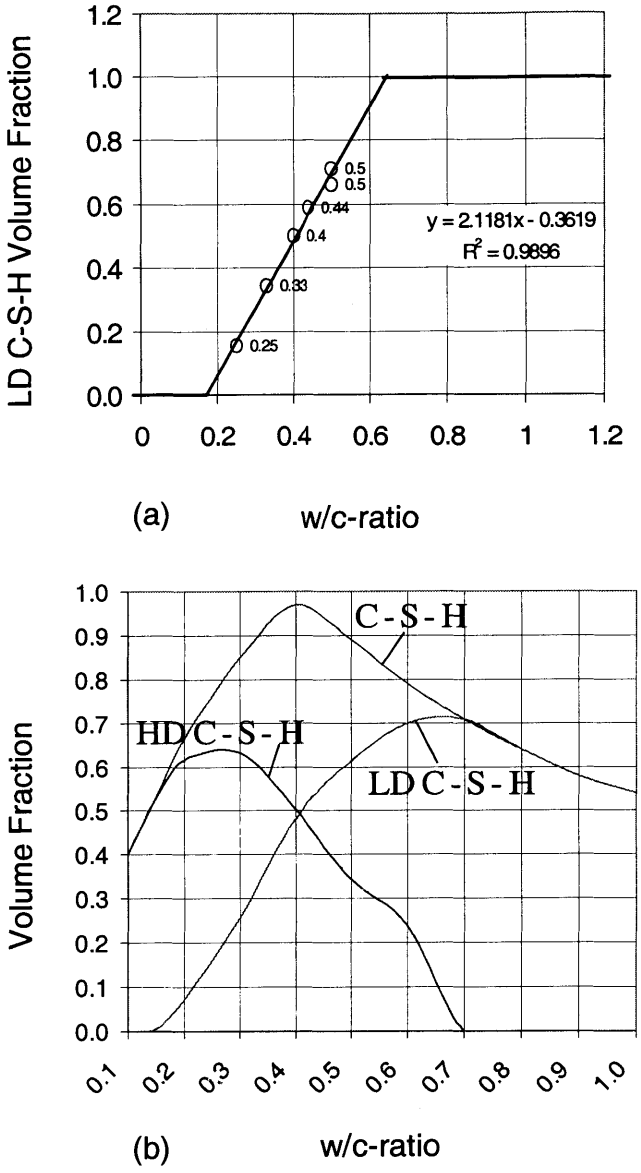

Figure 9-5: (a) Best fitted linear line for the discrete experimental data [w/c = 0.25 (J-T), 0.33 (I), 0.4 (J-T), 0.5 (J-T and I)]. J-T=Jennings and Tennins model, I=Indentation. (b) Separation of the two types of C-S-H based on the proposed best fitted line.

Using the compatibility condition $\sum f_i = 1$, one can estimate the volumetric proportion of HD C-S-H from $f_{HD} = 1 - f_{LD}$. Figure 9-5 and Eq. (9.7) suggest that the higher the $w/c-$ratio the higher the percentage of LD C-S-H. The two limiting cases ($f_{LD} = [0, 1]$) are obtained when the water-cement ratio reaches the values ($w/c \in [0.17, 0.64]$):

- The best fitted line suggests that for $w/c > 0.64$ all C-S-H formed is LD C-S-H. This result is consistent with mercury porosimetry results presented in Section 4.4.2 that suggest a uniform microstructure for $w/c > 0.6$ (see Fig. 4-11).
- At the other extreme, the LD C-S-H is eliminated from the microstructure provided the $w/c-$ratio is less than 0.17. It is interesting to note that this value is close to the one used for most Ultra High Performance Cementitious (UHPC) materials ($w/c = 0.15 - 0.20$), which are generally known to have a uniform microstructure and superior mechanical performance [2].

Figure 9-5 shows the relative proportions of the C-S-H phases present in CBM as a function of $w/c-$ratio. The two C-S-H phases have been separated based on the scheme presented in Eq. (9.7).

Level 0: LD and HD C-S-H

The required volumetric proportions at Level 0 are the porosities, $f_{gp}^J = \phi^J$, and packing densities, f_s^J, of the two types of C-S-H, $J = LD, HD$:

$$f_{gp}^{LD} = 0.37, \; f_{gp}^{HD} = 0.24 \tag{9.8a}$$

$$f_s^{LD} = 0.63, \; f_s^{HD} = 0.76 \tag{9.8b}$$

where the consistency condition $f_s^J = 1 - f_{gp}^J$ was used. We recall that the relative volumetric proportions at this scale are a consequence of two different packing modes of the C-S-H particle. We will therefore assume for the rest of this chapter that the values proposed in Eq. (9.8) are independent of the cement composition, degree of hydration, and $w/c-$ratio. With this relation we complete the volumetric proportion requirements for the micromechanical model.

9.1.2 Morphological Arrangement

The morphological arrangement is assumed to be independent of degree of hydration and $w/c-$ratio. The morphology of the phases is indirectly incorporated in our model through the choice of the used localization scheme. Level 0 which appears to have a colloidal gel nature is here approximated by the Self consistent scheme initially developed for polycrystalline materials. Levels I, II and III are simulated as matrix-inclusion geometries which is reasonably modeled with a Mori-Tanaka scheme. The assumed morphologies and corresponding localization schemes used for each level are summarized in Tab. 9.1.

9.1.3 Intrinsic Elastic Properties

The final informations required for microporomechanical upscaling are elastic properties of all constituent phases. We recall that a phase in micromechanics is not necessarily a chemical phase but rather a region with an on average uniform stress/strain. The upscaling model was designed to originate at the lowest level where chemical phases can be identified so that mechanical phases correspond to chemical phases. Such an approach provides a coupling between physical chemistry and mechanics, arising from multi-scale modeling and micromechanical theory. Strictly speaking, the LD/HD C-S-H phases are not distinct chemical phases, they appear however to have a distinct chemical-morphological arrangement which gives them properties that are independent of the degree of hydration and initial $w/c-$ratio. Table 9.3 summarizes the intrinsic properties of all constituents used in our modeling procedure:

- The values of LD and HD C-S-H were found to be a weak function of cement composition. In fact, white cement exhibited elasticity values which were on average 5-10% lower than other Type I cements. We have to note that, in practice white cement is the exception rather than the rule and as a consequence the majority of the data found in the literature is based on Type I-IV cements. A value of $E_{LD} = 21$ GPa and $E_{HD} = 31$ GPa was therefore chosen for the development of this engineering model.

- Power's model does not separate between the different cement phases but rather considers it as one phase. Generally speaking, the C_3S phase dominates in volumetric proportions and the elastic properties of this phase will be used as the elastic properties of cement.

LEVEL	E [GPa]	ν [1]
0: C-S-H solid		
Basic Building Block	N.A.	N.A.
Globules	60.8 [I.A.][a]	0.25 [I.A.][a]
I: C-S-H matrix		
C-S-H$_{LD}$	21 [58]	0.24 [145][b]
C-S-H$_{HD}$	31 [58]	0.24 [145][b]
II: Cement paste		
C_3S-Clinker	135 [239]	0.3
CH	38 [58]	0.305 [171][c]
III: Mortar		
Nevada Sand	62.5 [116]	0.21 [116]

Table 9.3: Intrinsic mean properties of cement paste and mortar constituents II: Elastic properties determined by Nanoindentation;
[a] [I.A.] = determined by Inverse Analysis, includes nanoporosity (intra-globular porosity) filled by structural water;
[b] Poisson's ratio estimated from Ref. [145];
[c] Poisson's ratio determined by extrapolation to zero porosity, from Ref. [171].

9.2 Micromechanical Predictions

In what follows, we couple the micromechanics model with cement chemistry models (Powers and J-T models, see Section 4.5) that can predict the volumetric proportions for a given $w/c-$ratio and degree of hydration ξ. To demonstrate its general use, we will confront the model with experimental data on cement paste (Level II) and mortar/concrete (Level III) found in the literature. The upscaling approach can be summarized as follows:

$$w/c/s \rightarrow \xi_{\max} \rightarrow \begin{array}{lll} \text{Level I} & f_{LD}, f_{HD} & \\ \text{Level II} & f_{CSH}, f_{CL}, f_{MP} & \rightarrow \\ \text{Level III} & f_{CP}, f_i & \end{array} \begin{array}{ll} \text{Level I} & K^I, G^I, b^I, N^I \\ \text{Level II} & K^{II}, G^{II}, b^{II}, N^{II} \\ \text{Level III} & K^{III}, G^{III}, b^{III}, N^{III} \end{array} \tag{9.9}$$

For a given mix design, $w/c/s$, the maximum degree of hydration can be calculated, see Eq. (9.3). Given the $w/c/s$ proportions and an estimated value of ξ one can calculate the volumetric proportions of all involved constituents using Eqs. (9.1), (4.12) and (9.7) (see also Figs. 9-3 and 9-5). These input data is then incorporated in Eqs. (7.68), (7.85) – for $w/c > 0.42-$, Eq. (7.98) – for $w/c < 0.42-$, and Eq. (7.114) that can deliver the homogenized properties

of C-S-H (Level I), Cement Paste (Level II), and Mortar (Level III) respectively. Given the intrinsic nature of the two types of C-S-H the homogenization step at Level 0 can be omitted: it is the same for all CBMs.

9.2.1 Level I and II: Effect of $w/c-$ratio

In this section we take advantage of the coupled chemoporomechanical model to investigate the effect of $w/c-$ratio on the poromechanical behavior of CBM systems. It is generally agreed that the $w/c-$ratio is the most important parameter controlling the macroscopic mechanical behavior. Controlling the $w/c-$ratio is a means of manipulating the microstructure. Increasing the $w/c-$ratio tends to increase the total porosity of the system: we recall that the hydration reaction takes place at (almost) constant volume and as a consequence the amount of initial water is directly proportional to the total pore space left in the system. As a consequence, the lower the $w/c-$ratio the less the total porosity. We recall that there are two types of pores in the system: gel porosity and capillary porosity. Reducing the $w/c-$ratio tends to eliminate the capillary pores. In fact a $w/c-$ratio of $w/c \leq 0.42$ produces enough C-S-H, CH, etc. to fill all the space available, the area initially occupied by water. In turn, as the space becomes restricted the hydration cannot be completed in full. Figure 9-1 shows the maximum possible degree of hydration as a function of the $w/c-$ratio. As the hydration reduces below $w/c = 0.42$ there is a significant amount of clinker left in the system. In the range of $w/c = 0.1 - 0.2$ where most high performance concretes operate there might be a $74\% - 62\%$ of clinker (compared to the initial value) left inside the material. The large volumetric proportions of the the residual clinker coupled with their excellent mechanical performance ($E_{C_3S} = 135$ GPa) can significantly contribute to the macroscopic composite mechanical response.

Drained Response

Figure 9-6 shows the drained elastic properties of C-S-H (Level I) and cement paste (Level II) as a function of the $w/c-$ratio. At low $w/c-$ratio the C-S-H homogenized value approaches the one of the HD C-S-H; in turn, for high $w/c-$ratio the C-S-H response approaches that of the LD C-S-H:

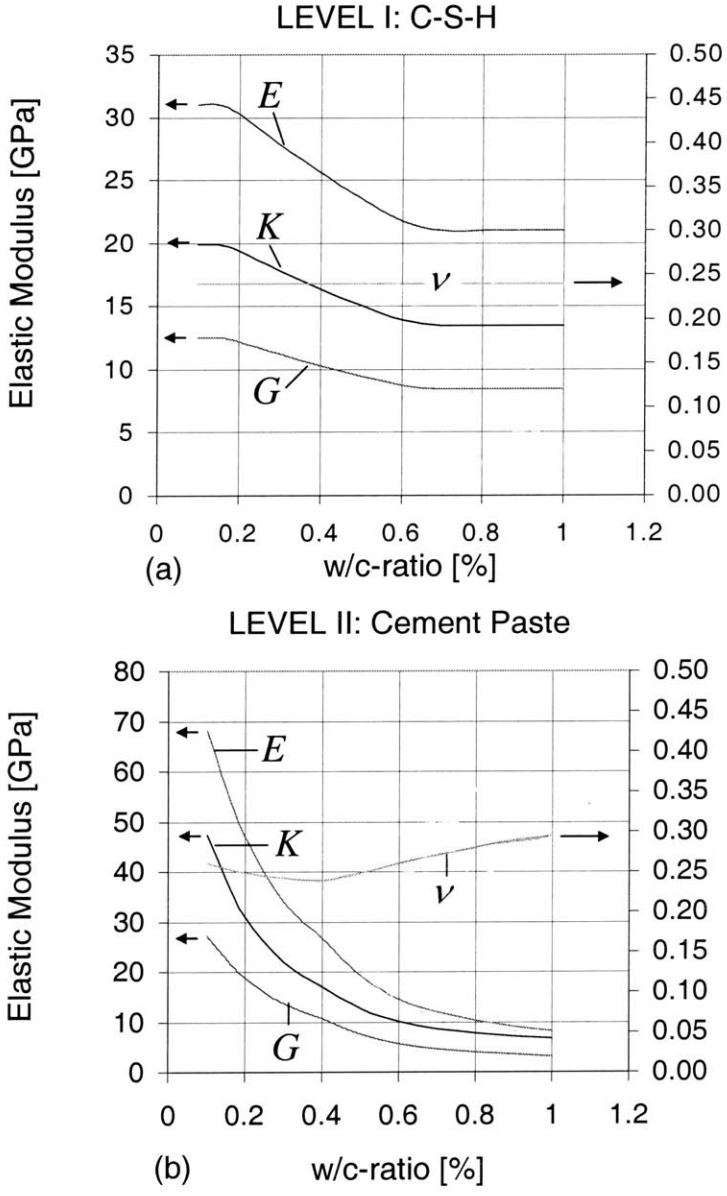

Figure 9-6: Micromechanical predictions of the elastic constants for different $w/c-$ratios at two different levels (Level I (a) and Level II (b)). The Poisson's ratio scale is shown on the secondary axis (right).

$$E^{HD} = 31 \quad K^{HD} = 19.87 \text{ GPa} \quad G^{HD} = 12.50 \text{ GPa} \quad \nu^{HD} = 0.24 \tag{9.10}$$

$$E^{LD} = 21 \quad K^{LD} = 13.46 \text{ GPa} \quad G^{LD} = 8.47 \text{ GPa} \quad \nu^{LD} = 0.24 \tag{9.11}$$

This can be attributed to the shift of the relative proportions between LD- and HD C-S-H as a function of $w/c-$ratio: the lower the $w/c-$ratio the higher the relative proportion of HD C-S-H to LD C-S-H and vice versa (see Fig. 9-5 and Eq. 9.7). A different picture arises at the macroscopic Level (Level II), where cement paste exists. The macroscopic stiffness monotonically decreases as the $w/c-$ratio increases. For values of $w/c > 0.42$, the drop in elasticity can be attributed to the increase of capillary porosity, which appears to be detrimental. For $w/c < 0.42$, the drop in elasticity is due to the consumption of clinker phases and the increase of the LD C-S-H. Of great interest is the evolution of the Poisson's ratio at these two levels. While it remains constant over the whole investigated range of $w/c-$ratios at Level I, in Level II it shows a minimum at around $w/c = 0.42$. It appears that the presence of inclusions, whether pores or clinker phases, tends to increase the Poisson's ratio of cement paste.

Undrained Response

Similar trends are observed for the undrained constants with the values of the undrained bulk modulus, K^{un}, elastic modulus, E^{un}, and Poisson's ratio, ν^{un}, to be shifted on the positive y-axis. This is due to the pressure build-up inside the saturated pore space that generates a higher composite elasticity in return. Figures 9-7 and 9-8 show the predicted poroelastic constants for the two levels (Level I and Level II) as a function of the $w/c-$ratio:

- *Biot Coefficient:* As was suggested by the compatibility condition, $f_{LD} + f_{HD} = 1$, the predicted Biot coefficient of Level I gradually shifts from the HD C-S-H values (for $0 \leq w/c < 0.17$) to the LD C-S-H as the $w/c-$ratio increases ($w/c > 0.64$). At a higher level (Level II) the Biot coefficient monotonically increases: for $0 \leq w/c \leq 0.42$ the increase is due to the consumption of the clinker phases and the presence of additional LD C-S-H phase as compared to the HD C-S-H phase, while for values greater than 0.42 the increase is primarily due to the capillary porosity which makes its appearance at $w/c = 0.42$ and increases in volume with increasing $w/c-$ratio. For values of $w/c = 1$ the Biot coefficient gets values on the order of $b^{II} = 0.9$ signifying that the majority of the

deformation is localized within the pore phases present in all levels below (0, I, and II) rather than the solid phases.

- *Undrained Bulk and Young's moduli:* The sensitivity of the material to the fluid phases present in the pore spaces of Level I and II is shown in the calculated properties of the undrained Bulk K^{un} and Young's E^{un} moduli. The evolution shown in Fig. 9-7 while similar to the drained behavior of Fig. 9-6 is shifted on the vertical axis. To further demonstrate the effect of pore pressure we calculated the percentage increase of the undrained elastic moduli versus their drained counterparts, defined as $\left(A^{un} - A^{dr}\right)/A^{dr}$, where $A = E, K$. This is shown in Fig. 9-8. As expected, the percentage increase in poroelastic response is a function of the pore space which scales with the $w/c-$ratio. At Level I the percent-difference reaches a plateau for a $w/c = 0.64$, corresponding to the point where all C-S-H formed is LD C-S-H. At Level II the percent-difference monotonically increases with a change in slope observed at $w/c = 0.42$ due to additional contributions coming from the capillary porosity. These results demonstrate the sensitivity of the material to undrained saturated conditions. It is impressive to note that, while the bulk modulus is significantly affected, reaching undrained values which are 40% higher at $w/c = 1$, the Young's modulus remains relatively unchanged. This is due to the fact that the Young's modulus is a strong function of the shear modulus which remains unaffected by the poroelastic state.

9.2.2 Level III: Effect of Volume of Inclusions

The additional contribution of elastic behavior at Level III comes from the aggregates which are assumed to be spherical and randomly dispersed within the cement paste matrix. The only parameter that one can control at this Level is the initial mass of sand inclusions which will eventually define their volumetric proportions, f_i, in the composite, mortar. The effect of volume fractions of inclusions on the mortar elastic response is shown in Fig. 9-9. In order to demonstrate the effect of inclusions on the poroelastic response of CBM materials we consider cement pastes of two different water cement ratios ($w/c = 0.2$ and 0.6) with varying volumetric proportions of Nevada sand ($E = 62.5$ GPa, $\nu = 0.21$). The results which are shown in Fig. 9-9 suggest that:

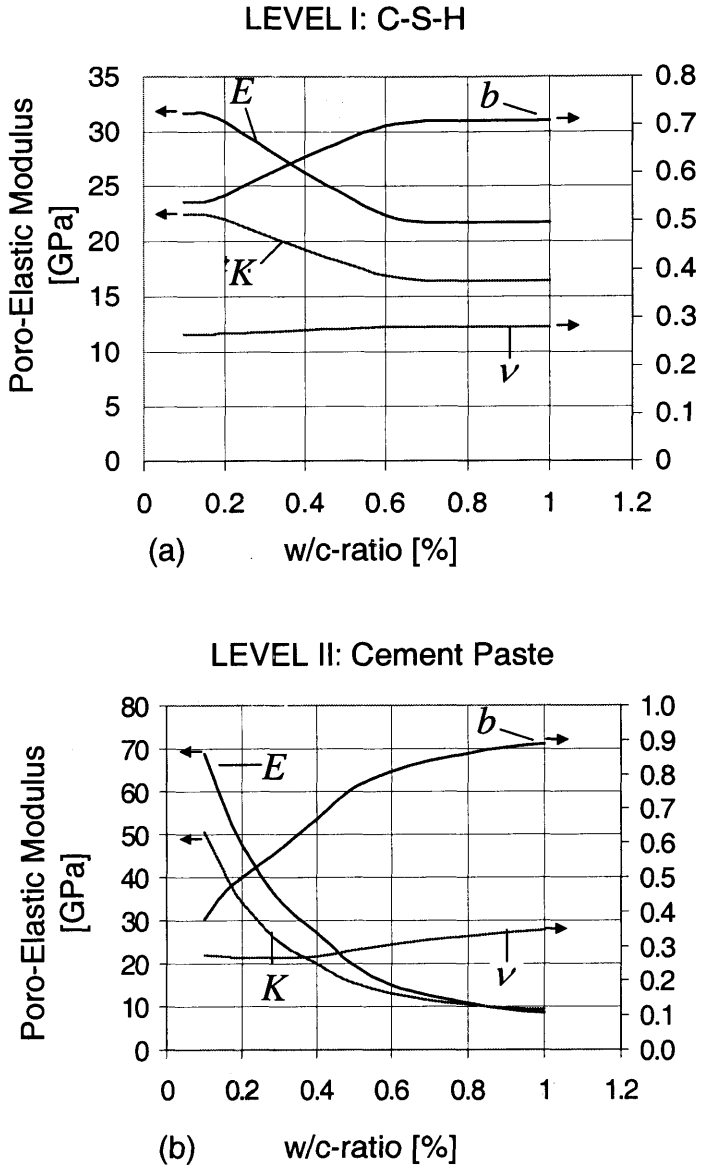

Figure 9-7: Micromechanical predictions of the undrained elastic constants for different $w/c-$ratios at two different levels (Level I (a) and Level II (b)). The Poisson's ratio and Biot coefficient scales are shown on the secondary axis (right).

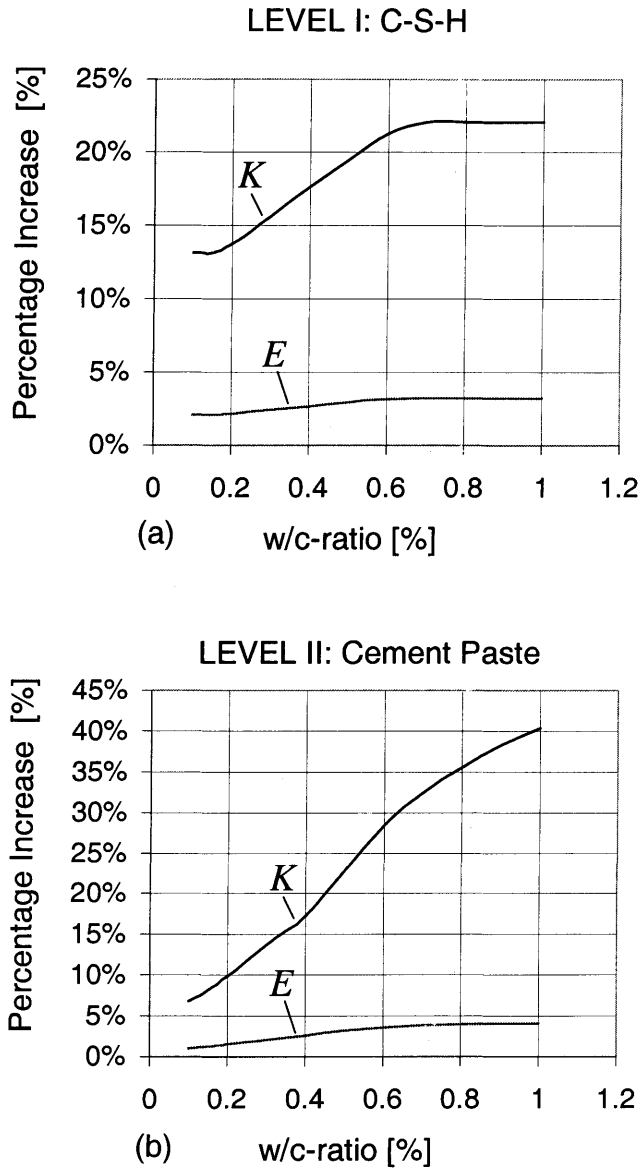

Figure 9-8: Percentage increase of undrained elastic properties as compared to the drained counterparts *vs.* the $w/c-$ratio. The percentage increase is defined as $\left(A^{un} - A^{dr}\right)/A^{dr}$ where $A = E, K$ and the superscript un and dr denote undrained and drained properties respectively.

- The percentage contribution of the inclusions on the homogenized bulk and shear moduli is very similar, i.e., bulk and shear moduli benefit in similar fashion indicated by the parallel evolution of the homogenized properties with volume of inclusions. This observation is also consistent for both cases of $w/c-$ratios considered.

- Figure 9-9 demonstrates the intuitive result that the elastic contribution of the sand particles becomes less important the lower the $w/c-$ratio. For $w/c < 0.42$, the residual clinker phases serve as natural reinforcement at a level below (Level II) which makes the contribution of sand particles almost zero. It is in fact suggested that for very low $w/c-$ratios, the sand particles can even reduce the composite elastic response.

- The addition of sand particles in cementitious materials tends to alleviate the poromechanical response. In fact, a plot of Biot coefficients for the two $w/c-$ratios demonstrates that there is a significant reduction in these coefficients occurring with increasing volume of sand particles.

The presentation of poroelastic properties of mortar completes our discussion on the coupling between chemistry, saturated porosity and elasticity. In the following section we will compare these predictions with experimental data found in the literature.

9.3 Comparison with Experimental Data

The results of our micromechanical model are compared with drained measurements[2] on cement paste and mortar specimens of varying mix compositions:

1. The results of Level II are confronted with elastic modulus measurements performed on cement paste specimens of varying $w/c-$ratios. We refer to the results of Helmulth and Turk reported in Ref. [113]. The elastic moduli of mature pastes (age>1 month) and of varying water cement ratios have been measured using a resonant frequency method. The fundamental resonance frequencies in flexure and torsion were used for calculating the Young's modulus, E^{mea}, and shear modulus, G^{mea}, respectively. Details of the experimental data and the corresponding micromechanical predictions are given in Tabs. 9.4

[2]Drained tests constitute the bulk of experimental values in the literature.

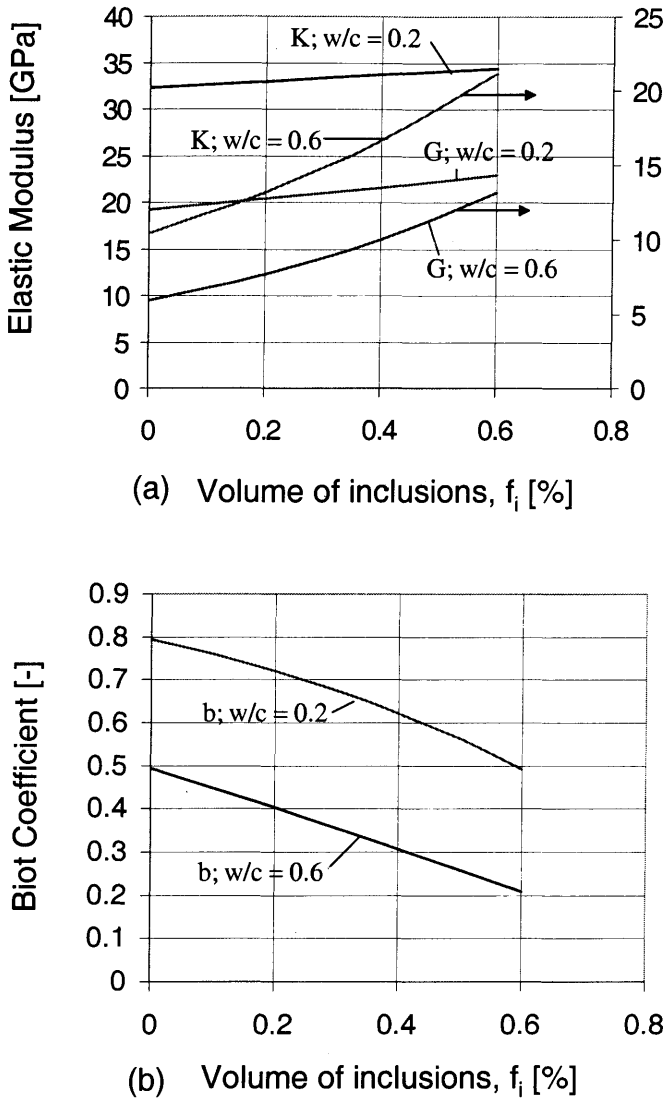

Figure 9-9: Efect of volume of inclusions on the homogenized elasticity of mortars of two $w/c-$ratios ($w/c = 0.2$ and 0.6). (a) Bulk and shear moduli vs. volume of inclusions. (b) Biot coefficient vs. volume of inclusions.

and 9.5. Figure 9-10a shows a comparison between the micromechanical predictions (Fig. 9-6) and the experimental data of Helmuth and Turk. It is impressive to note the excellent agreement between the measured quantities (E^{mea}, G^{mea}) and the predicted ones (E^{pre}, G^{pre}). Using standard relations of elasticity one can calculate the bulk modulus, $K = \frac{GE}{3(3G-E)}$, and Poisson's ratio, $\nu = \frac{E}{2G} - 1$, of the material. These are shown in Fig. 9-10b. The agreement continues to be very good but not as high as the measured quantities. It appears that the calculated quantities (especially the Poisson's ratio) are very sensitive to the exact values of E and G. In any case, the predicted values are in very close agreement suggesting the validity of the proposed model.

2. To further demonstrate the predictive capabilities of the model at the lower end of $w/c-$ratio, we compare our predictions with a results on an ultra high performance material, Ductal. The degree of hydration of Ductal was found experimentally to be $\xi = 45\%$ [2]. Use of this value in Eq. (9.3) suggests a $w/c-$ratio of $w/c \simeq 0.18$ which is on the order of the reported values used for these materials, $0.17 < w/c < 0.24$ [2]. Use of these values in Power's model yields estimates of the volume fractions of unhydrated cement particles and C-S-H matrix: $f_{cl} = 0.37, f_{CSH} = 0.63$. Use of the volumetric proportions in Eq. (4.12) yields an estimate of Ductal's elastic properties: $E_{pre}^{Ductal} = 50.0$ GPa and assuming a Poisson's ratio of $\nu_{pre}^{Ductal} = 0.25$ gives a Bulk modulus of $K_{pre}^{Ductal} = 33.3$ GPa and a shear modulus of $G_{pre}^{Ductal} = 20.0$ GPa. Young's modulus values reported in Ref. [257] of $E_{\text{exp}}^{Ductal} \simeq 50.0$ GPa are in excellent agreement with our predictions. In some cases, the material is combined with steel fibers and higher values up to $58-60$ GPa have also been reported [2].

3. The predictions of Level III were compared with experimental measurements reported by Hashin and Monteiro [109]. The specimens were mortars composed of cement paste with varying volume of sand inclusions (see Tab. 9.6) with mean diameters of 850μm. The elastic properties of the cement paste and the aggregates were reported in Ref. [109]:

$$\begin{aligned} k_{cp} &= 22.5 \text{ GPa} \quad g_{cp} = 11.8 \text{ GPa} \\ k_I &= 44.0 \text{ GPa} \quad g_I = 37.0 \text{ GPa} \end{aligned} \tag{9.12}$$

		Measured		Predicted	
Age	w/c	E^{mea}	G^{mea}	E^{pre}	G^{pre}
[mths]	[-]	[GPa]	[GPa]	[GPa]	[GPa]
8	0.641	14.34	5.62	13.73	5.65
8	0.622	15.09	5.96	14.31	5.92
8	0.579	17.15	6.79	15.91	6.56
8	0.554	18.25	7.20	17.03	6.96
8	0.389	28.60	11.24	27.14	10.43
8	0.368	30.04	12.07	28.73	11.03
14	0.300	36.56	13.92	34.52	13.40
14	0.298	36.08	13.78	34.71	13.48
14	0.295	36.97	14.54	35.00	13.60
14	0.858	6.92	3.15	10.83	3.66
14	0.853	6.92	2.74	10.94	3.68
14	0.668	11.04	4.52	13.07	5.29
14	0.664	11.38	4.32	13.15	5.34
14	0.479	20.57	8.02	21.10	8.32
14	0.478	20.16	8.16	21.16	8.34
14	0.376	28.12	10.76	28.12	10.79
14	0.361	28.74	10.76	29.28	11.24
6	0.67	11.38	4.59	13.02	5.26
6	0.645	12.0	4.66	13.62	5.59
6	0.623	13.30	5.14	14.27	5.90
6	0.566	15.43	6.03	16.48	6.77
6	0.565	16.05	6.24	16.52	6.78
6	0.56	16.59	6.51	16.75	6.86
6	0.556	16.53	6.37	16.93	6.93
6	0.556	16.05	6.31	16.93	6.93
6	0.482	21.05	8.64	20.92	8.26
6	0.467	21.53	8.29	21.84	8.57

Table 9.4: Experimental data of Helmuth and Turk versus micromechanical predictions for various $w/c-$ratios.

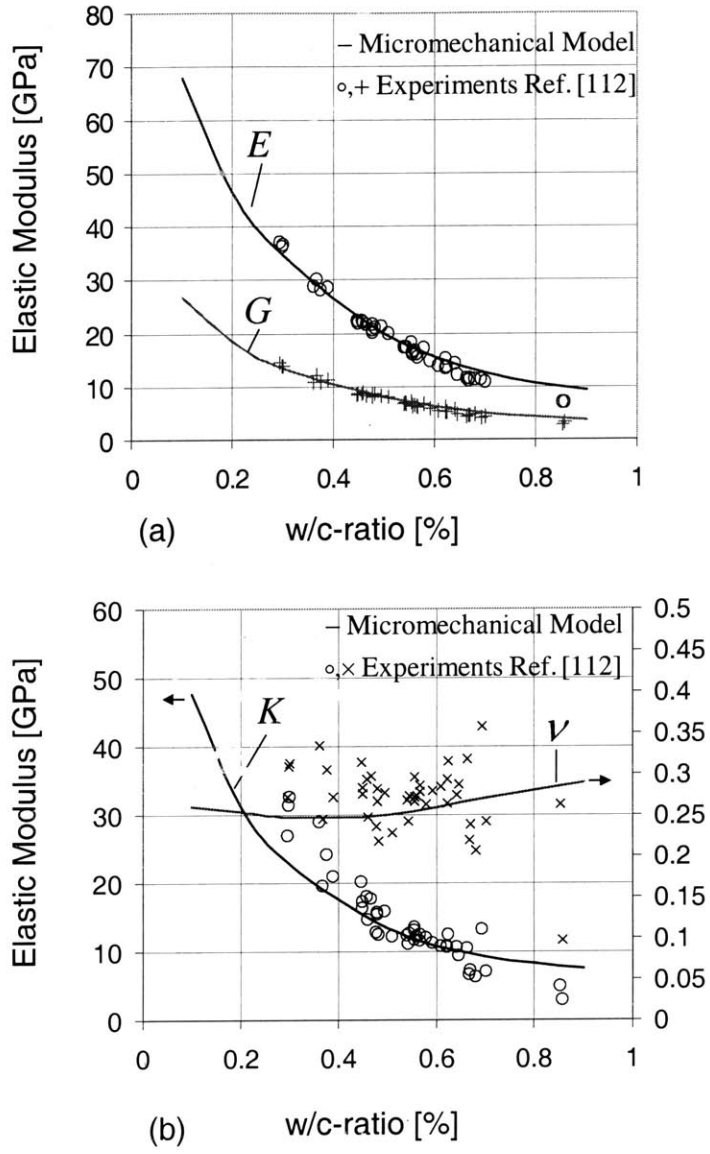

Figure 9-10: Elastic constants measurements (after Helmuth and Turk) vs. micromechanical predictions for (a) Young's modulus and shear modulus (E, G), (b) bulk modulus and Poisson's ratio (K, ν).

		Measured		Predicted	
Age	w/c	E^{mea}	G^{mea}	E^{pre}	G^{pre}
[mths]	[-]	[GPa]	[GPa]	[GPa]	[GPa]
6	0.46	22.08	8.84	22.28	8.72
6	0.45	21.88	8.57	22.92	8.93
7	0.624	13.71	5.21	14.24	5.89
7	0.608	13.92	5.41	14.78	6.12
7	0.591	14.74	5.76	15.42	6.37
7	0.544	17.28	6.79	17.51	7.13
7	0.543	17.21	6.92	17.56	7.15
7	0.541	17.21	6.79	17.66	7.18
7	0.457	22.36	8.64	22.47	8.78
7	0.449	22.36	8.71	22.99	8.96
7	0.448	22.36	8.50	23.05	8.98
24	0.702	10.90	4.39	12.46	4.87
24	0.693	11.18	4.11	12.59	4.98
24	0.68	11.24	4.66	12.82	5.14
24	0.509	19.89	8.09	19.36	7.75
24	0.494	21.19	8.29	20.21	8.03
24	0.479	21.53	8.50	21.10	8.32

Table 9.5: Experimental data of Helmuth and Turk versus micromechanical predictions for various $w/c-$ratios.

Figure 9-11 shows experiments versus modeling values. For small volume fractions of inclusions the micromechanical predictions are within 2% starting to deviate (not significantly, though, with a maximum of 15%) at higher proportions. This can be attributed to the presence of the interfacial transition zone that is known to provide additional compliance to the system.

9.4 Chapter Summary

The coupled chemoporoelastic model presented in this chapter provides a direct link between physical chemistry and mechanics and can predict the poroelastic properties of any CBM material independent of initial $w/c-$ratio, curing temperature, testing conditions (drained vs. undrained, etc.) and over several orders of magnitude in length scales. Since the model incorporates all chemical constituents, it provides a direct quantification tool for the contribution of each individual phase to the macroscopic mechanical response. It might as well serve as

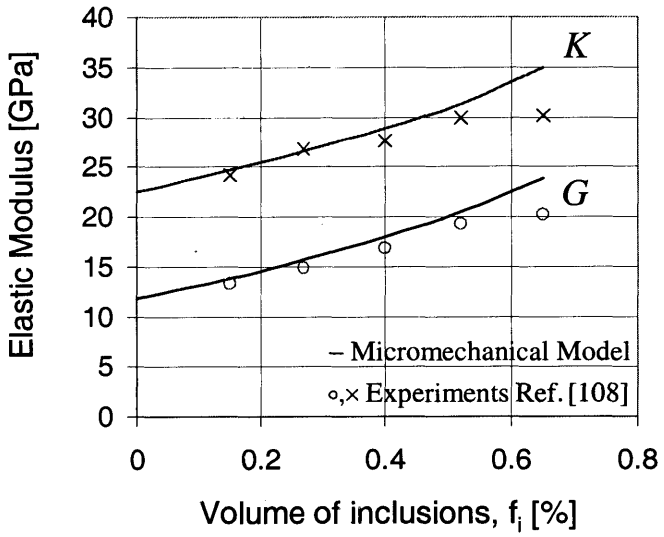

Figure 9-11: Experimental vs. predicted elastic moduli (K, G) as a function of the volume fraction of inclusions.

	Measured		Predicted	
f_i	K^{mea}	G^{mea}	K^{pre}	G^{pre}
[%]	[GPa]	[GPa]	[GPa]	[GPa]
15	24.14	13.35	24.69	13.82
27	26.81	14.87	26.62	15.68
40	27.69	16.91	28.94	18.00
52	29.96	19.26	31.31	20.57
65	30.12	20.23	34.98	23.84

Table 9.6: Measured versus predicted properties of a mortar with varying volumetric proportions of sand.

an optimization tool for tailoring the microstructure to deliver specific macroscopic properties. Figure 9-12 summarizes the predictive capabilities of the model as compared with experimental measurements for all the cases considered in this chapter. The excellent agreement between experimental data and micromechanical predictions validates several hypotheses:

- The volumetric proportions as suggested by the Powers model and the separation of the C-S-H phases proposed in Fig. 9-5 are accurately predicted.
- The intrinsic properties of all constituent phases suggested in Chapter 5 are reliable.
- The used micromechanical schemes (self-consistent scheme and Mori-Tanaka) provide reliable estimates of the mean stress/strain localization within each phase.

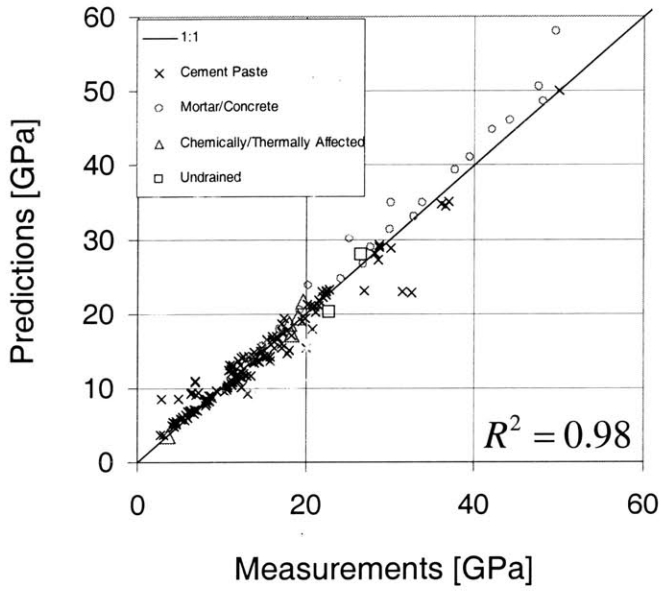

Figure 9-12: Summary of experimental results vs. predicted values for all cement based materials discussed in this chapter. The correlation coefficient between micromechanical predictions and experiments is also shown.

Part V

STRENGTH ASSESSMENT AND UPSCALING

Chapter 10

Indentation Estimates of C-S-H Strength

This last part of the thesis deals with the strength properties, their assessment by means of nanoindentation and their upscaling from the nano level to the macro scale. In previous chapters of this thesis, we have concentrated our efforts on the elastic properties of CBM. We have shown that a few invariant material properties, proposed in Chapter 5, are sufficient to upscale the poro-elastic macroscopic behavior of a range of CBM and capture their diversity which is generally attributed to volumetric mismatches. The focus of this part of the thesis is to summarize the salient features learned from this newly developed approach and lay the foundations for the upscaling of strength properties. Similarly to the upscaling of elasticity one has to first obtain the intrinsic mechanical properties of all constituents. This is the focus of this chapter. To this end, we use the dual indentation technique which has been proposed in Section 2.3.4, and validated in Section 3.4.3. Utilizing the hardness dependency on the indenter angle we will use two indenter geometries in back calculating the two parameters required to represent the strength envelope of C-S-H, which is a cohesive-frictional material. With these invariant mechanical properties in hand, we will develop in Chapter 11 a multi-scale mechanical model for the strength behavior of CBM systems. Finally, the proposed model will be calibrated and validated in Chapter 12 on a wide range of CBM materials found in the literature.

10.1 C-S-H Strength Properties

It is generally understood that the cohesion of cement based materials arises from the complicated interactions between the colloidal sized C-S-H particles. However the exact mechanisms that develop this cohesive properties are yet to be decoded. Quoting Pellenq and Van Damme [189]: "*Unlike other porous materials such as sandstone, brick, or porous glass, the interatomic bonding continuity of cement-based materials like concrete is far from obvious. When scrutinized at the micro- or nanoscopic level, the continuity of the ionic–covalent bonding in the solid phase is interrupted almost everywhere by water molecules or liquid water films. The same situation is found in set plaster. Yet, plaster and cementitious materials are able to withstand stresses of the same order of magnitude as rocks.*" There is an increasing body of experimental evidence that suggests that the short and medium range surface forces mediated by ionic correlation forces, with some minor additional contributions from Van der Waals and capillary forces are the essential components of C-S-H strength. While there is still some way to go regarding complete understanding of the nature of C-S-H bonding, there are no experimental data to aid this aim. We attempt in this section to provide a first order estimate of the C-S-H cohesion. Macroscopic experiments suggest that cement paste material can be reasonably represented, in compression, by a pressure dependent criterion of the Mohr-Coulomb or Drucker-Prager type [116]. It is therefore a fair assumption that the main component of cement paste, the C-S-H phase which dominates in volumetric proportions, follows such a criterion. Given the intrinsic nature of the two types of C-S-H we expect that mechanical properties extracted from the experimental tests will be intrinsic to all CBM systems.

This section is devoted to the extraction of strength estimates of the two types of C-S-H. We have presented in Chapter 2 a way of converting hardness data of a cohesive-frictional material to strength properties. The method, which has been validated in Section 3.4.3 on the model cohesive-frictional material of Bulk Metallic Glass, requires the input of hardness from two significantly different indenter geometries. In what follows, a Cube Corner and a Berkovich indenter is used. The dual indentation technique will now be used in order to get estimates of the strength properties of the two types of C-S-H.

	Series	Berkovich	Cube Corner
	#	300	300
$P^*_{\max}$	[μN]	476 ± 8	451 ± 18
$h_{\max}$	[nm]	155 ± 41	319 ± 115
S	[μN/ nm]	25.97 ± 5.08	26.89 ± 5.66
τ_L	[s]	10	10
τ_H	[s]	5	5
Machine**	-	HYS	HYS

Table 10.1: Experimental program and mean $\pm$ standard deviation of indentation results: (*) The deviation of the maximum force from the applied number is due to the spring force correction (see Section 3.1.2). (**) Machine: HYS = Hysitron.

10.1.1 Materials and Methods

The material investigated in this chapter is a white cement paste made from a White Portland cement (composition given in Tab. 5.3) and a water/cement ratio of $w/c = 0.5$. It is the same material tested by Thomas and Jennings in [230] and the one used in Chapter 5 as a model material for developing the deconvolution technique. The specimens were hydrated under limewater at room temperature and kept in such conditions until testing. The preparation procedure prior to testing and the calibration details prior to indentation testing were presented in Sections 5.3.1 and 3.1, respectively. A series of 300 Berkovich and 300 Cube Corner indentations were performed. The tests were load control with a maximum prescribed load of 500 μN. A small variation from the prescribed values is due to the spring constant compensation, which hold the capacitance plates in place (see Section 3.1). Both test series were performed with the Hysitron indenter located in the Nanomechanical Technology Laboratory of at M.I.T. Experimental details are shown in Table 10.1 and the specifications of the Hysitron machine can be found in Tab. 3.1.

10.1.2 Indentation Estimates of C-S-H Strength

In order to get an estimate of the strength behavior of the two types of C-S-H, we employ the dual indentation approach presented in Section 2.3.4. We recall that the dual indentation technique requires the input of indentation results of two indenter geometries (here Berkovich and Cube Corner) in order to provide an estimate of the strength parameters characterizing the indented material. We make the assumption *a priori* that both C-S-H phases are described

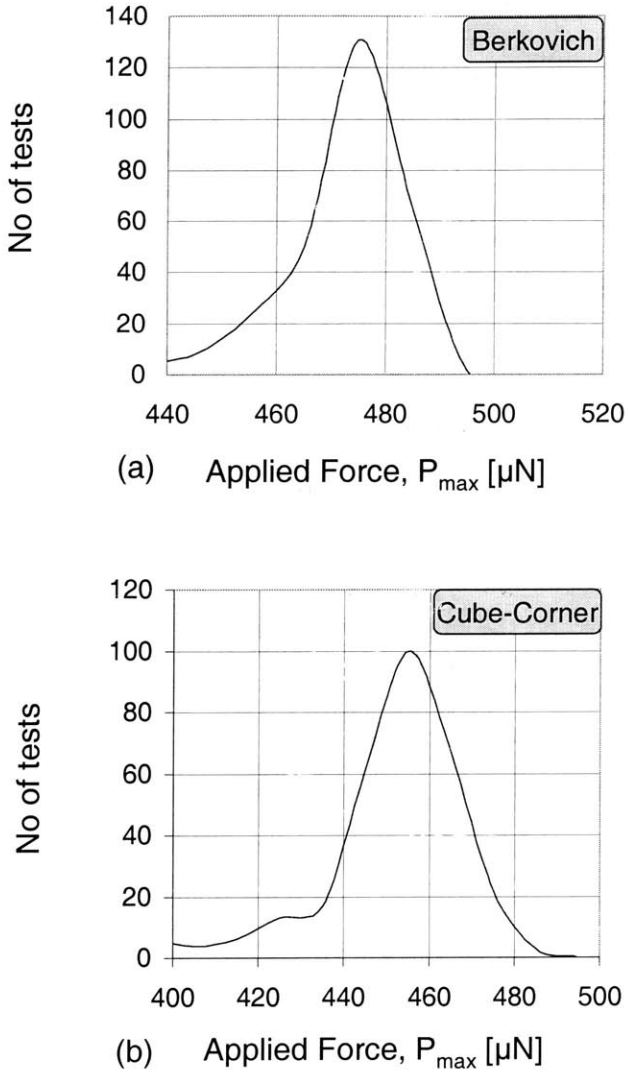

Figure 10-1: Histograms of maximum indentation force for Berkovich (a) and cube corner (b) indentations.

		Berkovich		Cube Corner	
		LD C-S-H	**HD C-S-H**	**LD C-S-H**	**HD C-S-H**
P	[μN]	476 ± 8	476 ± 8	451 ± 18	451 ± 18
M	[GPa]	18.8 ± 4.0	31.0 ± 4.0	26.7 ± 4.1	38.3 ± 4.0
H	[GPa]	0.47 ± 0.17	0.87 ± 0.08	0.825 ± 0.27	1.169 ± 0.02

Table 10.2: Indentation modulus and hardness of the two types of C-S-H for the Berkovich and cube corner indentation

by a pressure sensitive failure criterion of the Mohr-Coulomb type:

$$F_J = \sigma_I(1 + \sin(\varphi_J)) - \sigma_{III}(1 - \sin(\varphi_J)) - 2c_J \cos(\varphi_J) \leqslant 0 \tag{10.1}$$

where $\sigma_I \geq \sigma_{II} \geq \sigma_{III}$ are the principal stresses, c_J is the cohesion and φ_J the friction angle of the low density and high density C-S-H, $J = LD, HD$.

Figures 10-2 and 10-3 show the frequency plots of the Cube Corner results for the indentation modulus and hardness respectively. The corresponding Berkovich indentation results have been presented in Section 5.3, namely in Figs. 5-16 and 5-17. Similar to Section 5.3 properties for each phase were extracted using the deconvolution technique: minimizing the error between the experimentally obtained frequency distribution and the corresponding global distribution for two different bin sizes, $m = 12$ and 18. A summary of the indentation moduli and hardness for the two types of C-S-H is provided in Tab. 10.2.

Consistent with the BMG behavior, the material exhibited higher elastic modulus and hardness values than the ones observed in the Berkovich indentation (see Tab. 10.2), which is indicative of the pile-up around the Cube Corner indenter. The Cube Corner values will therefore need to be corrected prior to applying the dual indentation technique. To this end, we use the elasticity corrector method proposed in Section 3.5.4. The method which is based on the validity of BASh formula, Eq. (2.2),provides an easy means of correcting the Cube Corner results. Following the developments in Section 3.5.4, one could employ directly the mean values of the Berkovich and Cube Corner indentation modulus estimated with the Oliver and Pharr method (i.e., Eqs. (3.32) and (3.33)) to correct the Cube Corner contact area from Eq. (2.88):

$$\left[\frac{A_c}{A_c^{est}}\right]^J = \left[\left(\frac{M^{est(2)}}{M^{\exp(1)}}\right)^2\right]^J = \left[\left(\frac{\mu_{M^{est}}^{CC}}{\mu_{M^{est}}^{B}}\right)^2\right]^J = \left\{\begin{array}{ll} \text{LD C-S-H} & 2.02 \\ \text{HD C-S-H} & 1.53 \end{array}\right\} \tag{10.2}$$

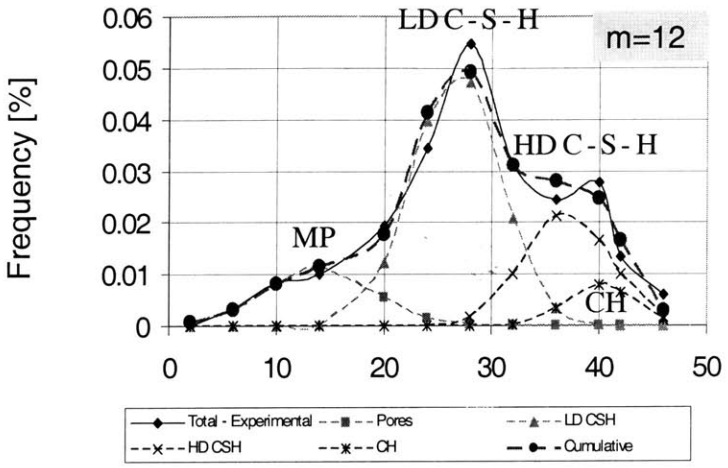

(a) Indentation Modulus, [GPa]

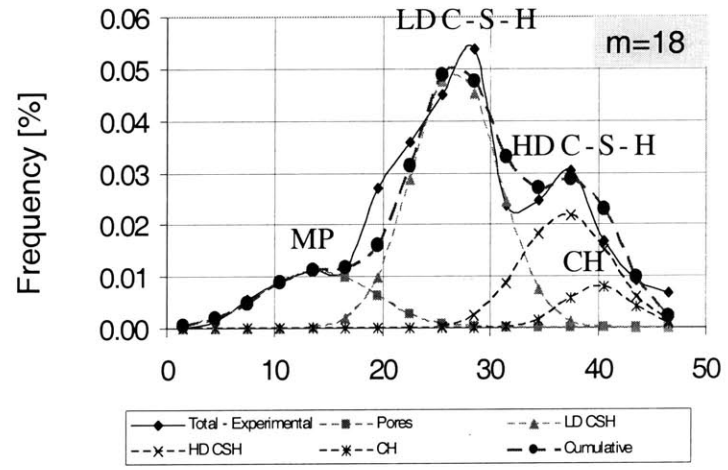

(b) Indentation Modulus, [GPa]

Figure 10-2: Frequency distributions for the cube corner indentation modulus of white cement paste, $w/c = 0.5$ for two different bin sizes: $m = 12$ (a) and 18 (b). The best fitted normal distributions were obtained after minimizing the average fitting error of the two distributions.

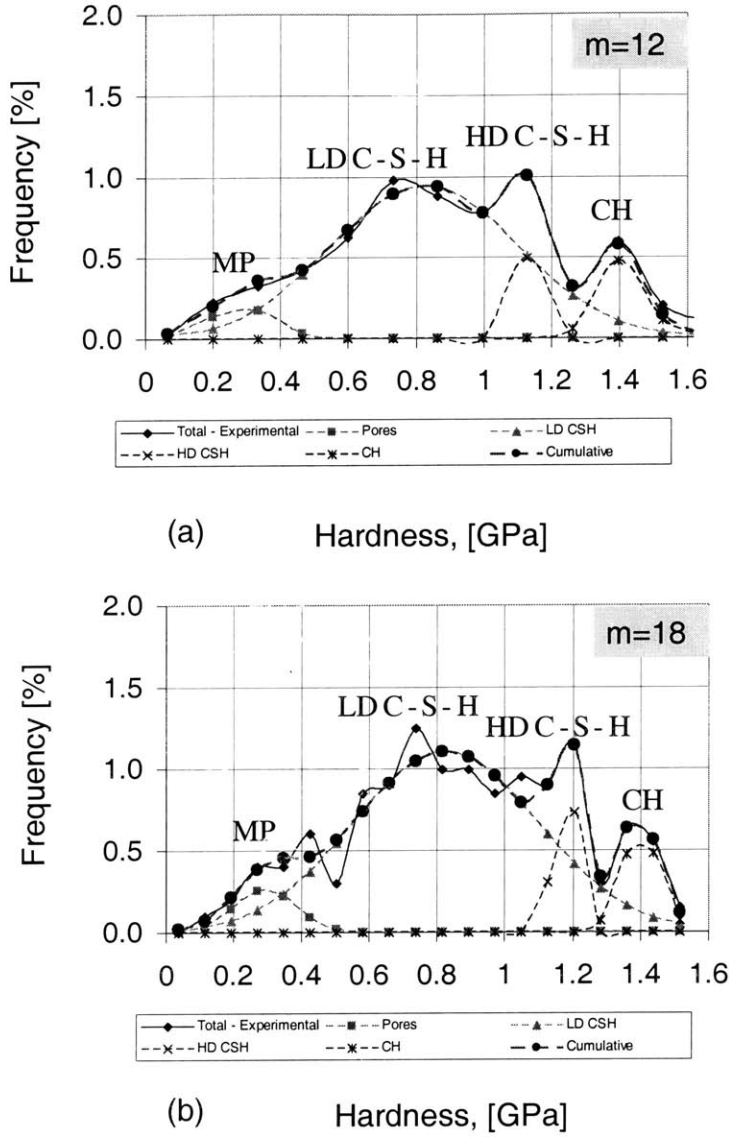

Figure 10-3: Frequency distributions for the cube corner indentation hardness of white cement paste, $w/c = 0.5$ for two different bin sizes: $m = 12$ (a) and 18 (b). The best fitted normal distributions were obtained after minimizing the average fitting error of the two distributions.

and to correct the Cube Corner hardness accordingly:

$$H_c^J = \left[H^{est} \left(\frac{M_B^{\exp}}{M_c^{est}} \right)^2 \right]^J = \left[\mu_{H^{est}}^{CC} \left(\frac{\mu_{M^{est}}^B}{\mu_{M^{est}}^{CC}} \right)^2 \right]^J = \left\{ \begin{array}{ll} \text{LD C-S-H} & 409 \text{ MPa} \\ \text{HD C-S-H} & 764 \text{ MPa} \end{array} \right\} \tag{10.3}$$

Since this elastic corrector method is based on the assumption that the Berkovich indentation modulus and hardness $M^B = \mu_{M^{est}}^B$ and $H^B = \mu_{H^{est}}^B$ determined with the Oliver and Pharr method are accurate values, we can employ the dual indentation technique using the corrected value of the Cube Corner hardness shown in Eq. (10 3):

$$\left(\frac{H^B}{H^{CC}} \right)^{est} = \frac{\mu_{H^{est}}^B}{\mu_{H^{est}}^{CC}} \left(\frac{\mu_{M^{est}}^{CC}}{\mu_{M^{est}}^B} \right)^2 = \left\{ \begin{array}{ll} \text{LD C-S-H} & 1.15 \\ \text{HD C-S-H} & 1.14 \end{array} \right\} \tag{10.4}$$

Use of the estimated hardness ratios (10.4) in Fig. 2-10 yields friction angles for the two types of C-S-H:

$$\varphi_{LD}^{est} = 12.2^\circ \tag{10.5}$$

$$\varphi_{HD}^{est} = 11.6^\circ \tag{10.6}$$

It is interesting to note that the angle of friction of the two phases is approximately the same, $\varphi^{est} = \varphi_{LD}^{est} \simeq \varphi_{HD}^{est} \simeq 12^\circ$. Substitution of these angles of friction in Eq. (2.38) allows us to determine the hardness-to-cohesion ratios:

$$\begin{array}{ll} \text{LD C-S-H} & \tan\varphi^{est} = 0.22 \Rightarrow \left\{ \begin{array}{l} \left(H^B/c\right)^{est} = 9.32 \\ \left(H^{CC}/c\right)^{est} = 8.15 \end{array} \right\} \Rightarrow c = ? \\ \text{HD C-S-H} & \tan\varphi^{est} = 0.21 \Rightarrow \left\{ \begin{array}{l} \left(H^B/c\right)^{est} = 8.96 \\ \left(H^{CC}/c\right)^{est} = 7.92 \end{array} \right\} \Rightarrow c = ? \end{array} \tag{10.7}$$

In order to calculate the cohesion, we will assume that the Berkovich indentation hardness

derived with the Oliver and Pharr method is the correct indentation result; i.e., from (3.32):

$$\left| \begin{array}{c} H^B \overset{def}{=} \mu^B_{H^{est}} = 870\,\text{MPa} \\ \Downarrow \\ c^{est}_{HD} = \frac{870}{9.22} = 97\,\text{MPa} \end{array} \right\| \left\| \begin{array}{c} H^B \overset{def}{=} \mu^B_{H^{est}} = 470\,\text{MPa} \\ \Downarrow \\ c^{est}_{HD} = \frac{470}{8.96} = 50\,\text{MPa} \end{array} \right| \tag{10.8}$$

The extracted cohesions and angles of friction for the two C-S-H phases are summarized below:

$$c_{LD} = 50\ \text{MPa} \quad \varphi_{LD} = 12° \tag{10.9a}$$

$$c_{HD} = 97\ \text{MPa} \quad \varphi_{HD} = 12° \tag{10.9b}$$

Within the assumption that the two phases follow a Mohr-Coulomb criterion, the two extracted properties (angle of friction, φ_J, and cohesion, c_J) are sufficient to define the whole failure envelope in the three-dimensional stress domain. These failure envelopes are graphically represented in Fig. 10-4. Owing to the same friction angle the failure envelopes of the LD C-S-H can be viewed as a shift on the vertical axis, yielding in the process a reduced cohesion strength. The values reported in Eq. (10.9) are the first direct measurements of the strength behavior of the C-S-H phases. To the best of our knowledge, no other experimental data of the strength of C-S-H exists in the literature. Some estimates by extrapolation will be discussed.

10.1.3 Discussion of Results

The dual indentation technique provides first order estimates of the cohesion and angle of friction of the two types of C-S-H. The accuracy of the values, however, reflects the assumptions made in the process. We recall that the method excludes any hardening phenomena and is also subjected to possible errors from the exclusion of indenter-material friction. It can be stated however that both assumptions in the model tend to underestimate the angle of friction and overestimate the cohesion. These can be considered as upper bound values of the cohesion and as lower bound values of the angle of friction [93].

Given the Berkovich indentation hardness values presented in Tab. 10.2, the maximum cohesion that the two types of C-S-H can obtain are for a frictionless material , $\varphi \rightarrow 0$, where

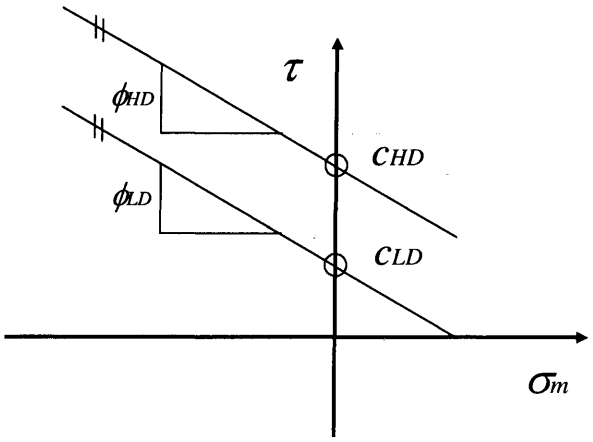

Figure 10-4: Representation in the $\tau - \sigma_m$ plane of the Mohr-Coulomb failure envelope of the two types of C-S-H.

the relation between hardness and cohesion reduces to (see Eq. (2.18)):

$$\frac{H}{c} \simeq 5.6 \Longleftrightarrow \left\{ \begin{array}{l} c_{LD} = 84\,\text{MPa} \\ c_{HD} = 155\,\text{MPa} \end{array} \right\} \tag{10.10}$$

These values provide an upper bound solution to the two C-S-H cohesions. The values obtained from indentation analysis of the dual indentation technique (see Eq. 10.9) constitute a significant improvement. Unfortunately there is no alternative technique to validate or invalidate the experimentally obtained values. In the absence of any other estimate, we will assume their validity, returning to this subject in Chapter 12.

Given the Berkovich indentation data for the two types of C-S-H (see Tab. 10.2) and the $\frac{H}{c} = \mathcal{H}(\varphi)$ given in Eq. (2.38), one can calculate the evolution of the C-S-H cohesions as a function of the angle of friction. This is shown in Fig. 10-5. It is readily observed that as the angle of friction increases, the cohesion of the two types of C-S-H decreases. Similar behavior is observed for the equivalent uniaxial compressive strengths of these two phases. Figure 10-6 shows in addition that the ratios of the cohesions and uniaxial compression values for different angle of friction. It is impressive to see that while the properties of both phases evolve with

internal friction, their ratios of cohesion and strength remain almost unaffected. The values reported in Eq. (10.9) require further attention.

C-S-H Frictional Behavior

The results testify towards the frictional behavior of the C-S-H. The difference between Berkovich and Cube Corner hardness validates the assumption of the pressure dependency of the C-S-H phases made *a priori*. This further suggests that the frictional dependency of the material at larger scales is a consequence of the C-S-H phase. It is impressive to see that the material at the $100 - 300$ nm scale can be described by a Mohr-Coulomb frictional law. The observed pressure sensitivity, even at that length-scale, is a remarkable observation. It goes against dislocation mechanisms, commonly observed in metallic materials, and hints towards other forms of deformation, driven by surface effects where local hydrostatic pressure becomes an important parameter.

The experimental observation that the pressure dependency of the two C-S-H phases is the same - that is the angle of friction does not scale with the porosity of the C-S-H phase - is in contradiction with knowledge in soil mechanics. This hints towards a different origin of the frictional response. While in clays and sands the frictional behavior is primarily due to the frictional contact and interlocking of adjacent solid particles, this might not be the case for the C-S-H phase. The high values of cohesion (compared to clays and sands) obtained above suggest that there is a chemical bond between the colloidal particles. Macroscopic failure of the material will involve deformation within those interfaces and slippage along planes defined by the nature of the chemical/secondary bonding. In such a scenario where the amorphous interface dominates microscopic response, the angle of friction may indeed not be a function of the particle packing. Furthermore, the same pressure dependency suggests that the nature of the bonding is the same for LD and HD C-S-H, the difference in strength lying in the number of bonds rather than the nature of it.

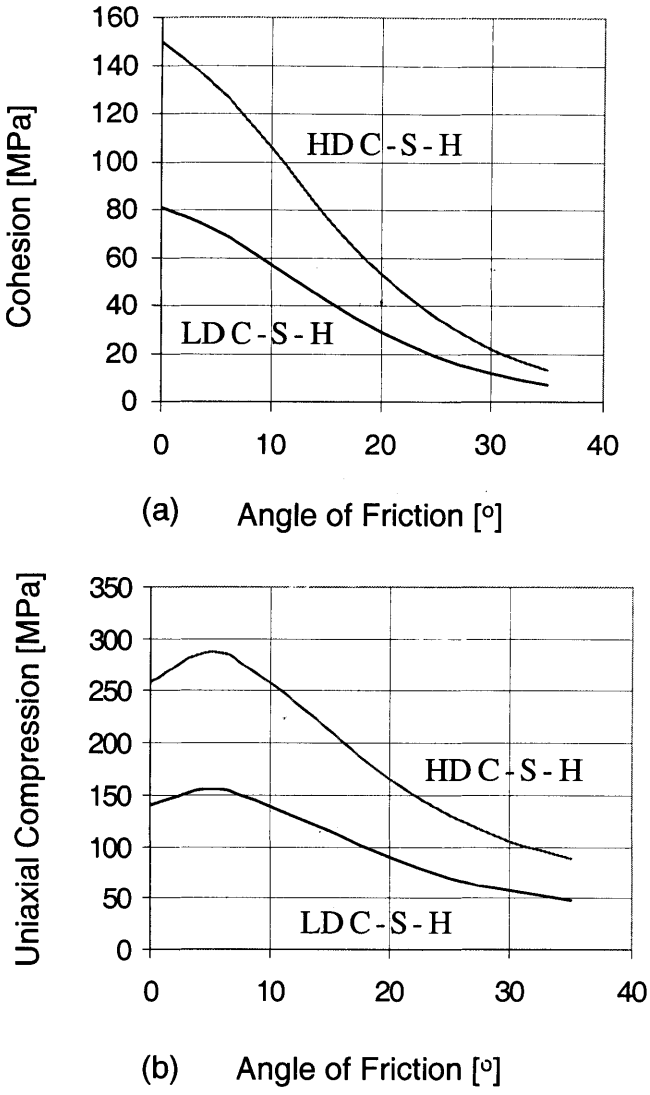

Figure 10-5: Scaling of HD to LD C-S-H ratio of cohesions (a) and uniaxial compression values (b) as a function of the internal friction of angle. Berkovich indentation hardnesses are used.

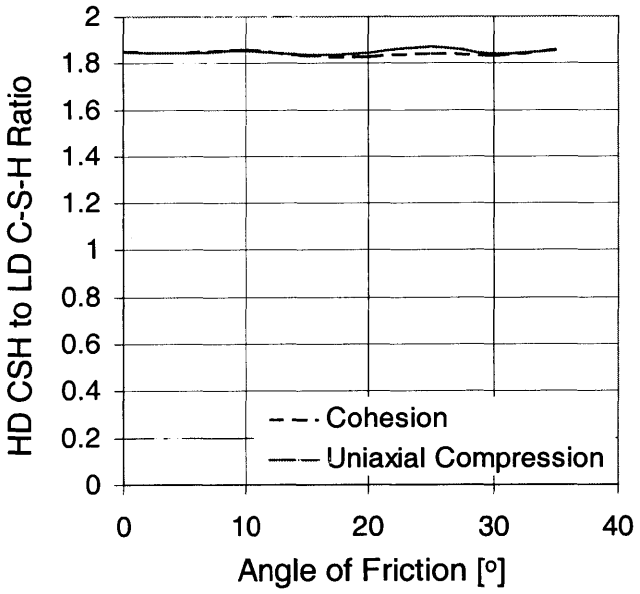

Figure 10-6: Scaling of HD to LD C-S-H cohesions and uniaxial compresive strength ratios as a function of the internal angle of friction.

Equivalent Uniaxial Compression

Using the measured cohesions and angle of friction, the (currently non-accessible) uniaxial compression strength of these two phases can be calculated:

$$\Sigma_c^{HD} = \frac{2c_{HD}\cos\varphi_{HD}}{(1-\sin\varphi_{HD})} = 244\text{MPa} \tag{10.11}$$

$$\Sigma_c^{LD} = \frac{2c_{LD}\cos\varphi_{LD}}{(1-\sin\varphi_{LD})} = 128\text{MPa} \tag{10.12}$$

The ratio of the uniaxial compression, $\frac{\Sigma_{HD}}{\Sigma_{LD}} = \frac{244}{128} = 1.91$, follows closely the ratios of cohesion, hardness, and creep intensity parameter A, suggesting that all these properties depend on the same factors; probably on the number and nature of bonding in the nanogranular assembly. While it is tempting to extend the estimates to the tensile regime, we suggest that the results indicated in Fig. 10-4 are restricted to the compressive regime where most input data was obtained[1]. Failure in the tensile regime involves localized phenomena around stress concentration and scaling with the defect size that needs to be taken into account.

Inverse Analysis of C-S-H Solid Cohesion

It is readily understood that the primary difference between the C-S-H phases lies in the cohesive strength of the material, which clearly scales with the porosity. In fact the ratio of the two cohesions is on the same order as the hardness and creep parameters, $\frac{c_{HD}}{c_{LD}} = \frac{97}{50} = 1.94$. This hints towards the relation of all these parameters with the number of bonds, which in turn scales the dissipation capacity of the system. In order to get first order estimates of the C-S-H solid (0 porosity material) cohesion, c_s, we take advantage of the LD and HD C-S-H which provide two points on the $c/c_s = \mathcal{C}(\phi)$ scaling relation. We assume in addition that a percolation threshold exists for $\phi = 0.5$. This is motivated by the self-consistent scheme which predicts zero cohesion at a porosity fraction of 0.5 and which it was found in Section 7.3.1 to be the preferred scheme for the given morphology at that scale. The data point and the best fitted straight line is shown in Fig. 10-7. While there are no theoretical arguments that a straight line should fit the behavior for small porosities, the extrapolation of a linear fit to zero porosity

[1] During an indentation test the material is subjected to a highly compressive triaxial stress state.

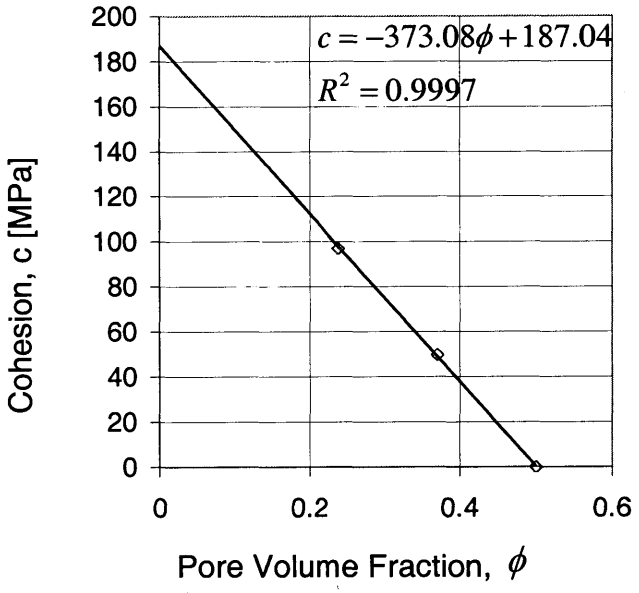

Figure 10-7: Extrapolation of the C-S-H solid cohesion based on the LD and HD C-S-H results. A percolation threshold of $\phi = 0.5$, which is embedded in the self-consistent scheme, is employed in the fitting process.

provides convenient first order estimates of the C-S-H cohesion: $c_s = 187$ MPa. The very origin of this cohesion is still a matter of intense research. In particular, colloid chemists have found that many if not most colloids consist of crystalline particles but, these being extremely small, have a large surface area which give them what appears to be different properties from the usual solids. Thus colloidal behavior is essentially driven by the surface area rather than by the non-regularity of the internal structure of the particles involved. It is therefore expected that the estimated C-S-H cohesion is representative of the nature of the bond in between solid particles rather than the ionic-covalent bonding binding the crystal structure itself. A refined analysis of this estimated cohesion is given in Appendix F.

The measurement of the cohesion and angle of friction of the two types of C-S-H completes the mechanical characterization of these two phases. Elastic, poroelastic, strength, creep and physical parameters (porosity, density, surface area) where obtained for these two phases that appear to be intrinsic in nature.

10.2 Chapter Summary

We have presented in this chapter the first estimates of the strength behavior of the C-S-H matrix. We have shown experimentally, with the use of the newly developed dual indentation technique, that the two types of C-S-H exhibit pressure sensitivity that can be well described by the Mohr-Coulomb failure criterion. The strength properties of the two types of C-S-H are summarized in Tab. 10.3. These first order indentation estimates of the C-S-H strength rely on several assumptions that were included during the development of the dual indentation technique: The technique neglects the effect of friction between indenter and indented material on the $P - h$ response and the effect of any hardening/softening or dilating/contracting phenomena that the material might exhibit. These values will serve as input data to the micro-poromechanical model for strength that is presented in the following chapter. Their accuracy remains to be determined through the macroscopic performance of the micromechanical models.

	c	φ	Σ_c
	[MPa]	[°]	[MPa]
LD C-S-H	50	12	128
HD C-S-H	97	12	244
C-S-H solid	187	N/A	N/A

Table 10.3: Indentation estimates of the strength behavior of the two types of C-S-H.

Chapter 11

Multi-scale Modeling of CBM Strength

This chapter is devoted to the development of a microporomechanics model for the strength behavior of cement-based materials. The multi-scale structure presented in Chapter 4 and the indentation results of Chapter 10 make it possible now to upscale strength properties from very fine scales of CBM materials, where cementitious materials do no more change – in a statistical sense – from one mix proportion to another. Following our poroelastic developments in Chapter 7, we start our modeling at the level of the two types of C-S-H, where the morphology and the mechanical properties are intrinsic, being determined by the chemical formation process. With this scale in mind, it becomes possible to employ advanced non-linear homogenization techniques of microporomechanics [218, 14, 253], and adapt them to meet the requirements of the multiscale microstructure of cementitious materials, starting at the scale where physical chemistry meets mechanics. The results of this challenging endeavor are estimates of the strength properties of cementitious materials at multiple scales. This is in short the focus of this chapter. With such a tool in hand, one can quantify the relative contribution of each constituent on the macroscopic strength performance and in knowledge of the volumetric proportions of the different constituents present in the microstructure one can translate chemical properties into mechanical behavior.

11.1 Existing Literature: Empirical Models

Some of the factors that determine the macroscopic compressive strength of cement paste include: a) cement composition, b) $w/c-$ratio and air content, c) mixing and curing conditions (especially temperature and relative humidity) d) the age or degree of hydration, etc. Careful consideration of the aforementioned variables affecting macroscopic behavior indicates that they all have a particular impact on the microstructural development during hydration. It is therefore expected that a chemistry model that can predict the microstructure (in particular the volumetric proportions of all constituents) for all scenarios presented above can serve as input for our micromechanical model. In what follows, we will concentrate our effort on developing a micromechanical model for strength assuming that the volumetric proportions of all constituents are known. We will return to the evaluation of the chemical constituents in the validation of the strength model in Chapter 12.

11.1.1 Strength-Porosity Models

The majority of the models reported in the literature concentrate on the effect of porosity on the macroscopic mechanical behavior. Several researchers attempted to relate functions obtained on other porous materials to cement-based systems. The majority of the models, however, involve empirical constants and data fitting. In particular we acknowledge the work of Balshin [10], Ryshwekitch [201], and Hasselman [110] who proposed relations linking the residual strength capacity of a variety of porous materials $s = \Sigma_c(\phi)/\Sigma_c(\phi = 0)$ to the volume fractions of the pore spaces ϕ :

$$\text{Balshin} \quad s = (1-\phi)^A \tag{11.1a}$$

$$\text{Ryshkewitch} \quad s = \exp(-A\phi) \tag{11.1b}$$

$$\text{Hasselman} \quad s = 1 - A\phi \tag{11.1c}$$

As should be expected, Eqs. (11.1) are all inversely proportional to the volume fractions of the porosity. Figure (11-1) shows the evolution of the normalized strength s with porosity ϕ, as predicted by the three different models for several values of the empirical constants A. Balshin's relation of Eq. (11.1a) seems to us the most reasonable representation of reality. The relation

satisfies the two asymptotic conditions:

$$\begin{aligned} s &\rightarrow 1 \text{ as } \phi \rightarrow 0 \\ s &\rightarrow 0 \text{ for } \phi \rightarrow 1 \end{aligned} \tag{11.2}$$

for all values of the empirical constant, A. In addition, the parabolic evolution of the composite strength (see Fig. 11-1) is typical to that observed in most experiments [180]. Equation (11.1a) was obtained on an experimental investigation of a porous metal-ceramic material. Similarly, Ryshkewitch equation was the result of an experimental investigation on a porous sintered alumina and zirconia [201]. While Eq. (11.1b) follows similar trends to Balshin's function, Eq. (11.1a), it tends to overestimate experimental results for high volume fractions of porosity. In fact, the proposed exponential decay, asymptotically approaches a zero strength as the volumetric proportions of porosity goes to infinity. While a volume fraction of porosity greater than 1 has no physical significance, an empirical relation of this form was found to fit the experimental CBM data (which usually ranges in $\phi = 0.1 - 0.4$) with significant accuracy. Finally, Hasselman [110] suggested the existence of a linear relationship between strength and pore volume. His investigations were concentrating on polycrystalline refractory materials. For values of the empirical constant less than $A < 1$, Eq. (11.1c) satisfies the asymptotic conditions of Eq. (11.2). In fact, for values of $A < 1$ the proposed relationship predicts a percolation threshold for porosity values less than 1. Such a phenomenon is commonly observed in many materials, in particular in materials of granular nature.

11.1.2 Power's Model: Gel/Space Ratio

All of the empirical relationships presented in Eq. (11.1) that were originally found to hold for other porous materials have been applied to cement-based systems (for a review see Ref. [200]). The most well known example is the model of Powers and Brownyard (PB). As it will be later discussed in Section 12.2.2, the PB model can be considered as an application of Balshin's equation. In their classic work published in 1946-47, Powers and Brownyard attempted to relate the strength of CBM to the concentration of the solid products of hydration. In particular, they stated that the increase in compressive strength in Portland cements is "directly proportional to the increase in the gel/space ratio regardless of age, original $w/c-$ratio, or identity of cement."

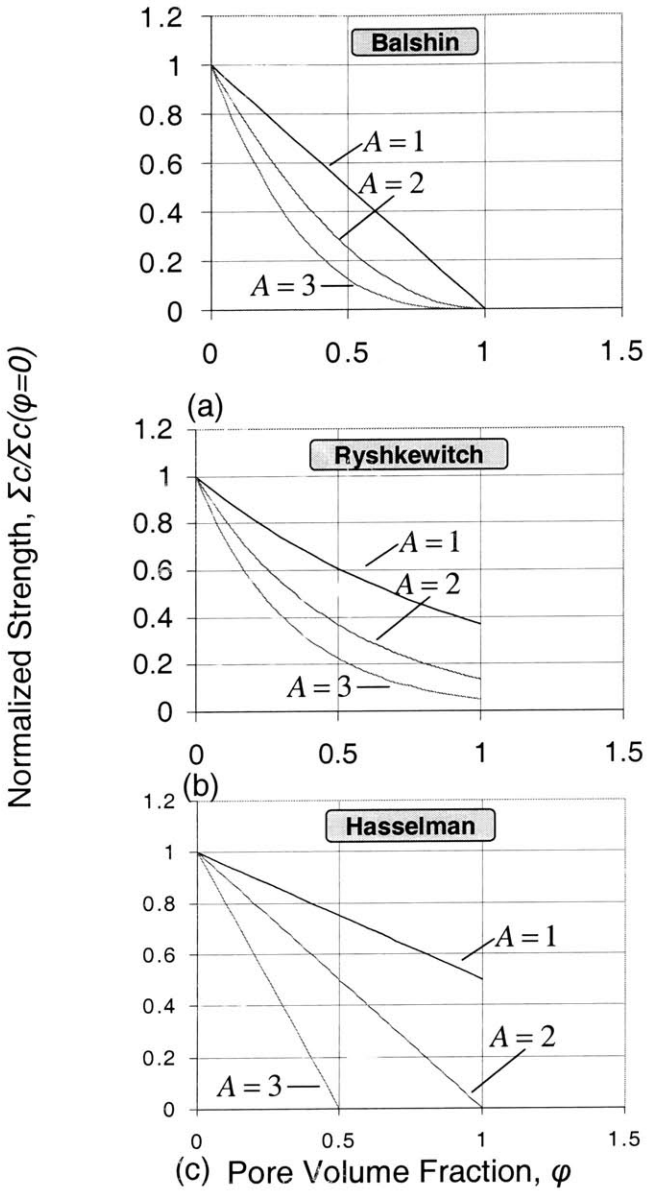

Figure 11-1: Empirical relationships linking normalized uniaxial compressive strength $s = \Sigma_c(\phi)/\Sigma_c(\phi = 0)$, to the volume fractions of porosity ϕ.

The gel/space ratio was defined as the ratio of the volume of the solid hydration products to the volume of the available for these products to reside:

$$r = \frac{\text{Volume of Gel}}{\text{Volume of Gel + Volume of Capillary Pore}} \tag{11.3}$$

all quantities being defined as in Section 4.5.1. In other words, the gel/space ratio is representative of the capillary porosity in the system. Before hydration begins, the gel/space ratio equals to zero, and according to Powers, hydration stops once there is no more space for hydration products to precipitate, i.e., the gel/space ratio approaches 1. Given the empirical microstructural chemistry model proposed by Powers (see Section 4.5.1) the gel/space ratio can be expressed in terms of the $w/c-$ratio and degree of hydration, ξ:

$$r = \frac{0.68\xi}{0.32\xi + \frac{w}{c}} \tag{11.4}$$

Experimental data presented by Powers and Brownyard [194] indicates a strength to gel/space-ratio relationship of the form:

$$\Sigma_c = Ar^m \tag{11.5}$$

where A is a constant representing the intrinsic strength of the cement gel, (i.e., the strength at $r = 1$) and m is a constant that it was experimentally found to have values between $2.6 - 3$. Estimated values of the empirical constant A show significant scatter varying in the range $A = 110 - 235$ MPa. It is interesting to note that the range of experimentally obtained values of the uniaxial compressive strength of the C-S-H is consistent with the bounds provided by the two C-S-H phases: $\Sigma_c^{LD} = 128$ MPa $\leq \Sigma_c^{csh} \leq \Sigma_c^{HD} = 244$ MPa. Constants extracted by fitting Eq. (11.5) to the experimental data presented in [194] yield:

$$\Sigma_c = 235r^3 \tag{11.6}$$

There is a question remaining however: What is the origin and physical relevance of such empirical constants: A and m ?

The model of Powers and Brownyard is regarded as the best representation of reality and is generally accepted among the cement research community. Closer consideration of Eq. (11.5)

reveals that:

1. The macroscopic strength of the material is intimately related to the volume fraction of the pore spaces, in particular the capillary porosity. The volume fraction of the gel porosity is considered as an integrate part of the gel which gives its unique/intrinsic mechanical performance A. Experimental data show a significant scatter for A (see Fig. 11-2) indicating that this empirical "constant" might itself be a function of the $w/c-$ratio and/or degree of hydration ξ.

2. The effect of residual clinker is not explicitly considered. In fact, the Powers and Brownyard model suggests that once the capillary porosity is eliminated then there should be no change in the macroscopic mechanical response. This is shown in Fig. 11-2 where the PB model is plotted versus the $w/c-$ratio for the two extreme values of A, 110 MPa and 235 MPa. It can be seen that for $w/c < 0.38$ the strength predictions remain constant due to the fact that the capillary porosity is consumed in that range. This is in contradiction with experimental data which suggest that the strength of the material even below $w/c < 0.38$ continues to increase even though some of the cement does not hydrate [226].

It therefore becomes apparent that even the most well accepted model in the literature suffers from a few limitations and relies on empirical constants and fitted relations. In what follows, we will attempt to give a micromechanical interpretation of Eq. (11.5) and eventually propose a multi-scale model that does not rely on empirical constants but on material (invariant) properties. But first an extension of the linear micromechanics tools to the non-linear case is in order.

11.2 Micromechanical Approach to Strength of Composites: Non-Linear Homogenization

The micromechanical approach to linear elastic systems has been presented in Chapter 7 and employed in the upscaling of CBM systems, with significant success, in Chapter 8. While the elastic approach appears as a well established area, the application in the non-linear domains is a more recent attempt and several important issues are still under development [218]. We aim

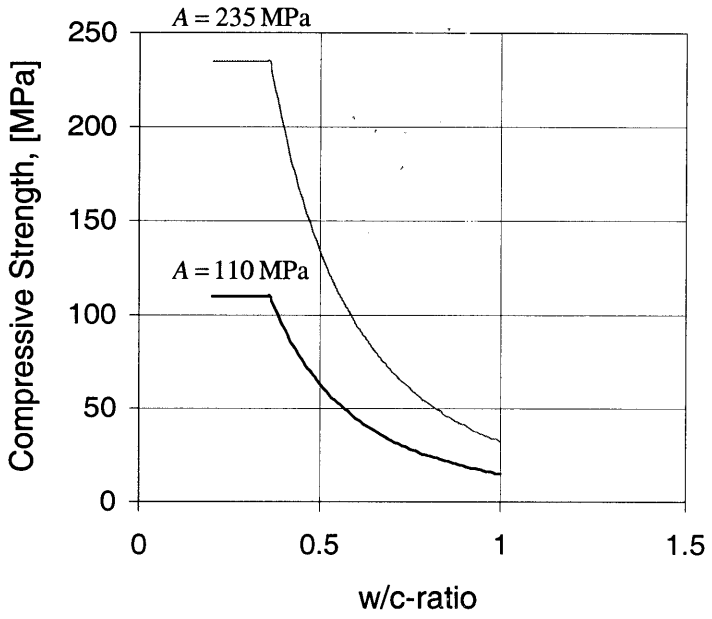

Figure 11-2: Powers-Brownyard model predictions for strength as a function of the $w/c-$ratio. Equation (11.5) has been evaluated for the the two extreme $A-$values reported in the literature. The exponent m was assumed constant at 3.

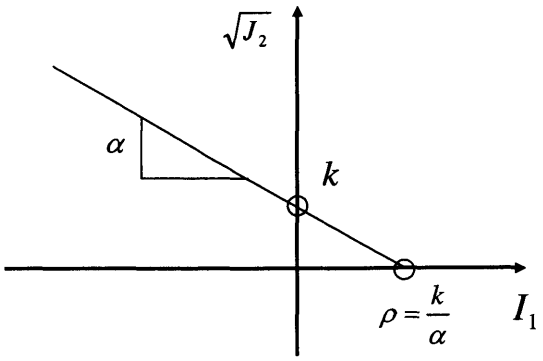

Figure 11-3: Graphical representation of a Drucker-Prager failure envelope in the $\sqrt{J_2} - I_1$ plane. The geometrical parameters characterizing the response are shown.

in this section to present the necessary changes required to apply the linear micromechanics approach to the strength of composites which is simplified as a non-linear elastic behavior. The three step approach discussed in Section (7.1.2) will continue to serve as a framework: representation, localization and homogenization. The presentation below is inspired by the recent developments of Dormieux and coworkers [73,74,13,75].

11.2.1 Representation

For the homogenization of strength properties, the representation of the phases has to include, in addition to the volume fractions, geometry and elastic properties, information about the strength. For each phase a microscopic strength criterion is applied:

$$f(\boldsymbol{\sigma}_\chi) \leq 0 \tag{11.7}$$

For the cement-based materials considered in this study, this local strength criterion is approximated by the Drucker-Prager frictional law. The Drucker-Prager criterion of a phase, χ, reads:

$$\begin{aligned} f(\boldsymbol{\sigma}_\chi) &= \sqrt{j_2} + \delta_\chi \sigma_M^\chi - c_\chi \leq 0 \\ f(\boldsymbol{\sigma}_\chi) &= \sqrt{j_2} + \delta_\chi \left(\sigma_M^\chi - \rho_\chi\right) \leq 0 \end{aligned} \tag{11.8}$$

where $j_2 = \frac{1}{2}\mathbf{s}_\chi : \mathbf{s}_\chi$ is the second invariant of the deviatoric stress $\mathbf{s}_\chi = \boldsymbol{\sigma}_\chi - \sigma_M^\chi \mathbf{1}$, with σ_M^χ the microscopic mean stress; δ_χ and c_χ are the friction coefficient and cohesion; ρ_χ is the cohesion pressure defined as $\rho_\chi = c_\chi/\delta_\chi$. A graphic representation of the Drucker-Prager criterion in the $\sqrt{j_2} - \sigma_M$ plane is shown in Fig. 11-3. Moreover, microscopic nonlinear stress-strain relations need to be specified. A common way of describing local nonlinear behavior in the context of strength homogenization is the nonlinear elastic representation [218]:

$$\boldsymbol{\sigma}_\chi = k_\chi\left(\epsilon_\chi, \varepsilon_\chi^v\right)\varepsilon_\chi^v \mathbf{1} + 2\mu_\chi\left(\epsilon_\chi, \varepsilon_\chi^v\right)\boldsymbol{\epsilon}_\chi \tag{11.9}$$

where $\varepsilon_\chi^v = \mathrm{tr}\boldsymbol{\varepsilon}_\chi$ is the volumetric microscopic strain, $\boldsymbol{\epsilon}_\chi = \boldsymbol{\varepsilon}_\chi - \frac{1}{3}\varepsilon_\chi^v \mathbf{1}$ is the microscopic deviatoric strain tensor and $\epsilon_\chi = \sqrt{\boldsymbol{\epsilon}_\chi : \boldsymbol{\epsilon}_\chi}$ is the invariant of the deviatoric strain tensor. $g_\chi\left(\epsilon_\chi, \varepsilon_\chi^v\right)$ and $k_\chi\left(\epsilon_\chi, \varepsilon_\chi^v\right)$ are strain dependent shear and bulk secant moduli which give this approach the name "secant method" [218]. The non-linearity of the stress strain relationship is taken into account through the dependence of $g_\chi\left(\epsilon_\chi, \varepsilon_\chi^v\right)$ and $k_\chi\left(\epsilon_\chi, \varepsilon_\chi^v\right)$ on ϵ_χ and ε_χ^v. For this reason the classical homogenization schemes cannot be directly applied because they only deal with homogeneous phases. The idea consists of reducing the problem to an equivalent linear one that can take advantage of the homogenization schemes presented in Chapter 7.

11.2.2 Localization and Homogenization

The general idea of the localization, that is, determining the microscopic stresses and strains as a response to the macroscopic load, remains unchanged. However, the material representation with a nonlinear stress-strain relation changes the determination of the local strains. The boundary conditions to which the R.E.V. is subjected, induce a nonhomogeneous strain field in the matrix phase. Given the secant representation of the solid phase, the matrix now appears as a heterogenous material. Phases, however, as defined in linear micromechanics are domains of constant mechanical properties. This poses a difficulty in the application of linear homogenization schemes. The problem can therefore be addressed in a two-stage approach:

1. A common way to account for locally varying strains, $\boldsymbol{\varepsilon}_\chi\left(\epsilon_\chi, \varepsilon_\chi^v\right)$, is to replace them by an equivalent homogenous strain, the so called effective strains, $\boldsymbol{\varepsilon}_{eff}$, a concept due to Suquet [218]. This will allow us to replace the spatially variable $g_\chi\left(\epsilon_\chi, \varepsilon_\chi^v\right)$ and $k_\chi\left(\epsilon_\chi, \varepsilon_\chi^v\right)$

with an equivalent value which will be assumed constant within the matrix:

$$k_{eq} = k_{eq}\left(\epsilon_{eff}, \varepsilon^{v}_{eff}\right); g_{eq} = g_{eq}\left(\epsilon_{eff}, \varepsilon^{v}_{eff}\right) \tag{11.10}$$

The effective strain invariants, ϵ_{eff} and ε^{v}_{eff}, are defined as moments of the microscopic strains per phase, and are expected to give a realistic approximation of the strain energy prevailing in the matrix.

2. With the definition of the equivalent modulus in place via Eq. (11.10) one can readily employ the schemes of linear micromechanics presented in Section 7.1 to get an estimate of the overall non-linear response, g_{hom} and k_{hom} as a function of the equivalent linear elastic ones:

$$k_{\text{hom}} = k_{\text{hom}}\left(k_{eq}, g_{eq}\right); g_{\text{hom}} = g_{\text{hom}}\left(k_{eq}, g_{eq}\right) \tag{11.11}$$

Homogenized values of the overall response can be obtained with any of the micromechanical schemes presented in Section 7.1.2. Given the morphological arrangement of the microstructure, application of the Mori-Tanaka (matrix-inclusion geometry) or Self-Consistent (polycrystal geometry) scheme can provide reliable links between macroscopic and microscopic constants.

While the application of linear homogenization is a straight forward procedure, the key to a successful non-linear homogenization lies in the choice of effective strains. This is an arbitrary selection and several possibilities exist. The most natural choice corresponds to the first moment, which is the strain localization used in the classical linear homogenization of elastic properties, that is:

$$\varepsilon^{eff}_{\chi} = \langle \boldsymbol{\varepsilon}_{\chi} \rangle_{V_{\chi}} = \frac{1}{V_{\chi}} \int_{V_{\chi}} \boldsymbol{\varepsilon}_{\chi}\left(\mathbf{x}\right) d\Omega \tag{11.12}$$

where V_{χ} is the volume of phase χ. This first-order moment definition carries the name "classical" method. Definition (11.12) leads to the following invariants of the "effective" strains:

$$\epsilon^{eff}_{\chi} \equiv \bar{\epsilon}_{\chi} = \sqrt{\langle \boldsymbol{\epsilon}_{\chi} \rangle_{V_{\chi}} : \langle \boldsymbol{\epsilon}_{\chi} \rangle_{V_{\chi}}} \tag{11.13}$$

$$\varepsilon^{eff}_{\chi} \equiv \bar{\varepsilon}^{v}_{\chi} = \langle tr\left(\boldsymbol{\varepsilon}_{\chi}\right) \rangle_{V_i} \tag{11.14}$$

For isotropic materials, Eqs. (11.13) and (11.14) can be expressed as functions of the localization factors:

$$\overline{\epsilon}_\chi = \overline{A}^d_\chi E_d \tag{11.15}$$

$$\overline{\boldsymbol{\varepsilon}}^v_\chi = \overline{A}^v_\chi E_v \tag{11.16}$$

where $E_d = \sqrt{\mathbf{E}_d : \mathbf{E}_d}$ is the macroscopic deviatoric invariant $\mathbf{E}_d = \mathbf{E} - \frac{1}{3}E_v\mathbf{1}$, and $E_v = \mathrm{tr}\mathbf{E}$ is the macroscopic volumetric strain. The single horizontal bar indicates the first moment definition[1]. The localization coefficients then need to be specified for a given scheme, given in Chapter 7. The use of effective strains has been questioned in the literature as it was generally considered as a crude approximation due to its inability to capture strong variations in the real strain domain. A first refinement of the "classical" theory consists in considering a second moment definition for the effective strains which is referred to as the modified secant method [218]. The effective shear strain invariant reads in the second moment definition:

$$\epsilon^{eff}_\chi \equiv \overline{\overline{\epsilon_\chi}} = \sqrt{\left\langle (\boldsymbol{\epsilon}_\chi)^2 \right\rangle_{V_\chi}} = \sqrt{\langle \boldsymbol{\epsilon}_\chi : \boldsymbol{\epsilon}_\chi \rangle_{V_i}} \tag{11.17}$$

or, equivalently:

$$\overline{\overline{\epsilon_\chi}}^2 = \left(\overline{\overline{A}}^{dd}_\chi\right)^2 E_d^2 + \left(\overline{\overline{A}}^{dv}_\chi\right)^2 E_v^2 \tag{11.18}$$

where $\overline{\overline{A}}_\chi$ stands for concentration factors. In contrast to the classical method, the modified method involves a priori a coupling in the localization between shear and volume strain. The use of of second order moments for the estimation of effective strains has been considered as a considerable improvement [218]. In homogenization solutions of different problems, it is not unusual to use a combination of the classical and modified approaches, the so-called mixed

[1] The localization factors in the "classical" method obey the consistency condition: $\sum_\theta f_\theta \overline{A}^v_\theta = \sum_\theta f_\theta \overline{A}^d_\theta$.

approach [149]. A summary of the effective strain approaches is given below:

$$\text{Classical} \quad \epsilon_\chi^{eff} \equiv \overline{\epsilon}_\chi \quad \varepsilon_\chi^{eff} \equiv \overline{\varepsilon}_\chi^v \tag{11.19}$$

$$\text{Modified} \quad \epsilon_\chi^{eff} \equiv \overline{\overline{\epsilon}}_\chi \quad \varepsilon_\chi^{eff} \equiv \overline{\overline{\varepsilon}}_\chi^v \tag{11.20}$$

$$\text{Mixed} \quad \epsilon_\chi^{eff} \equiv \overline{\overline{\epsilon}}_\chi \quad \varepsilon_\chi^{eff} \equiv \overline{\varepsilon}_\chi^v \tag{11.21}$$

With the effective strain concept in hand, the linear localization schemes can be used and the strength properties can be upscaled. The non-linear elastic representation of the real behavior of the material allows to link the macroscopic deviatoric Σ_d and hydrostatic stress Σ_M of the composite to E_d and E_v by:

$$\Sigma_d = 2g_{\text{hom}}E_d \quad ; \quad \Sigma_M = k_{\text{hom}}E_v \tag{11.22}$$

where g_{hom} and k_{hom} are the macroscopic secant moduli (i.e., the one of the cement paste) estimated by homogenization theory. Finally, the shear strength can be seen as an asymptotic value in a deviatoric compression stress. Such an approach allows the macroscopic strength properties to be linked to microscopic phase quantities.

11.3 Multi-scale Strength Model for CBM Systems

This section is devoted to the development of a novel multi-scale micromechanics model for mature cement based materials. The model will be developed within the non-linear micromechanical framework presented above. By considering mature CBM systems we set aside the effect of hydration degree (and time) which is now purely defined by the initial water/cement ratio. We have shown in Section 9.1.1 that mature cement pastes can be divided into two regimes:

1. $w/c < 0.42$: The initial water provided to the system is insufficient to hydrate all cement particles leaving some residual clinker in the microstructure. Such a microstructure can be considered as a matrix with rigid inclusions from a micromechanical point of view.

2. $w/c > 0.42$: For such high water/cement ratios complete hydration is always possible.

In fact, the volume of hydration products is insufficient to fill the whole available space leaving behind some residual capillary porosity. A micromechanical representation of such a system can be considered as a matrix with pore inclusions.

These two cases will be separately considered below. The homogenization behavior of these two cases has been recently addressed by Barthelemy and Dormieux [13,14]. Their results, which are essential for our micromechanical model development, will be detailed below.

11.3.1 Level 0: LD and HD C-S-H Strength

The mechanical behavior of the two types of C-S-H has been experimentally obtained in Section 10.1.2 of this part. The analysis was based on the premise that the two phases obey to the Mohr-Coulomb frictional criterion. For further developments we will use the Drucker-Prager criterion which offers better mathematical tractability for upscaling operations. The two criteria are essentially the same differing in minor points. The main feature which is the dependency of the shear strength on the pressure is present in both criteria. In the case of the Mohr-Coulomb criterion, the pressure is the one on any material surface, which in the Drucker-Praguer criterion, the pressure is the hydrostatic pressure. In this way, the Drucker-Prager criterion can be viewed as a smooth approximation to the Mohr-Coulomb criterion. As a consequence, the two can be made to match in specific regions by adjusting the size of the cone (see Fig. 11-4). Given the fact that our modeling attempt relies on highly compressive input data (indentation tests) we make the Drucker-Prager circle to match the outer apices of the Mohr-Coulomb hexagon, i.e., the two surfaces are made to coincide along the compression meridian. Then the constants δ and c^{DP} are related to the constants φ and c^{MC}; see i.e., [42]:

$$\delta = \frac{2\sin\varphi}{\sqrt{3}\,(3-\sin\varphi)}; \qquad c^{DP} = \frac{6c^{MC}\cos\varphi}{\sqrt{3}\,(3-\sin\varphi)} \tag{11.23}$$

Using Eq. (11.23) one can translate the Mohr-Coulomb failure envelope of the two types of C-S-H to their Drucker-Prager counterparts:

$$\text{LD C-S-H} \;:\; f(\boldsymbol{\sigma}_{LD}) = \sqrt{j_2} + 0.094\,\sigma_M^{LD} - 61 \leq 0 \tag{11.24a}$$

$$\text{HD C-S-H} \;:\; f(\boldsymbol{\sigma}_{HD}) = \sqrt{j_2} + 0.094\,\sigma_M^{HD} - 118 \leq 0 \tag{11.24b}$$

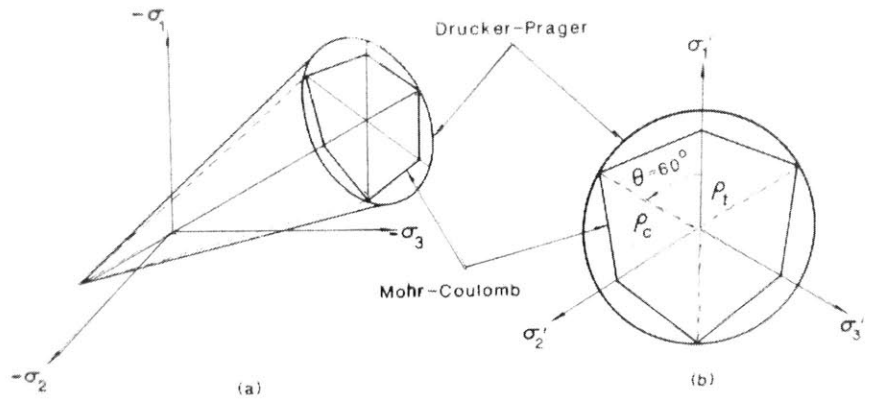

Figure 11-4: Equivalence between Mohr-Coulomb and Drucker-Prager criteria when matched along the compressive meridian. (a) Principal stress space; (b) Deviatoric plane (image from Ref. [42]).

where $[c_{LD}^{DP} = 61 \text{ MPa}; \delta_{LD} = 0.094]$ and $[c_{HD}^{DP} = 118 \text{ MPa}; \delta_{HD} = 0.094]$ are the Drucker-Prager parameters of the LD C-S-H and the HD C-S-H respectively. For the rest of this thesis the symbol c will correspond to the cohesion of a material as defined by the Drucker-Prager criterion shown in Eq. (11.8) dropping the superscript of DP.

11.3.2 Level I: Voigt-Reuss estimates of C-S-H matrix

The homogenization of a frictional matrix with frictional inclusions is a very complicated problem that prohibits detailed analytical solutions. We therefore attempt in this section to bound the exact behavior with simple lower and upper bound solutions using the bounding theorems of limit analysis (see i.e., Ref. [119]). In following developments we will be concerned with the uniaxial strength that CBM materials can obtain. To this end we consider a fictitious uniaxial compression test performed on Level I, for which:

$$\Sigma = -\Sigma e_3 \otimes e_3 \tag{11.25}$$

where $\Sigma > 0$ is the uniaxial compression strength. We consider an R.E.V. composed of the two types of C-S-H that both obey to a Drucker-Prager strength criterion of the form presented in

Eqs. (11.24). The dissipation function of a Drucker-Prager material is [204]:

$$\text{in } \Omega : \pi(\mathbf{d}) = \left\{ \begin{array}{ccc} +\infty & \text{if} & \text{tr}\mathbf{d} < \sqrt{2}\delta\sqrt{\mathbf{d}:\mathbf{d} - \frac{1}{3}(\text{tr}\mathbf{d})^2} \\ \rho(z)\,\text{tr}\mathbf{d} & \text{if} & \text{tr}\mathbf{d} \geq \sqrt{2}\delta\sqrt{\mathbf{d}:\mathbf{d} - \frac{1}{3}(\text{tr}\mathbf{d})^2} \end{array} \right\} \tag{11.26}$$

where $\rho(z) = c(z)/a(z)$ is the cohesion pressure.

The simplest lower bound consists in considering a uniform microstress throughout the heterogeneous microstructure. Such a simplified stress field, $\boldsymbol{\sigma}'$ satisfies the equilibrium conditions:

$$\forall \underline{z} \in \Omega : \left\{ \begin{array}{c} \boldsymbol{\sigma}(\underline{z}) = {}^t\boldsymbol{\sigma}(\underline{z}) \\ \text{div}\,\boldsymbol{\sigma}(\underline{z}) = 0 \\ [[\boldsymbol{\sigma}(\underline{z}) \cdot n(\underline{z})]] = 0 \end{array} \right\} \tag{11.27}$$

Use of this statically admissible stress field in Eq. (11.8) yields:

$$f(\boldsymbol{\sigma}', \underline{z}) \leq 0 \Longleftrightarrow \Sigma \leq \frac{3c(\underline{z})}{\sqrt{3} - \delta(\underline{z})} = \Sigma_c(\underline{z}) \tag{11.28}$$

The simplest upper bound consists in considering a uniform strain field throughout the heterogeneous microstructure, $\mathbf{D}' = \mathbf{d}'$:

$$\left(D'_{ij}\right) = \left[\begin{array}{ccc} D'_1 & & \\ & D'_2 & \\ & & D'_3 = \frac{\beta - \sqrt{3}}{\beta - \sqrt{3}/2} D'_1 \end{array} \right] \tag{11.29}$$

where $0 \leq \beta \leq \sqrt{3}$ can be seen as a macroscopic dilatation coefficient. In order to ensure the finiteness of the dissipation in Eq. (11.26) it must be:

$$0 \leq \delta(\underline{z}) \leq \beta \leq \sqrt{3} \tag{11.30}$$

The local dissipation capacity reads:

$$\pi(\mathbf{d}') = -\rho(\underline{z}) \frac{3\beta}{\sqrt{3} - \beta} D'_3 \tag{11.31}$$

Within the limits of Eq. (11.30) we realize that $\pi(\mathbf{d}') = -\rho(\underline{z})\,\Sigma_c(\underline{z})\,D_3'$ where $\delta(\underline{z}) = \beta$, while $\pi(\mathbf{d}') \geq -\rho(\underline{z})\,\Sigma_c(\underline{z})\,D_3'$ for any $\delta(\underline{z}) \leq \beta$. The maximum local dissipation capacity, which satisfies Eq. (11.30) is obtained for $\beta = \max\delta(\underline{z})$, and yields after integration the following upper bound:

$$-\Sigma D_3' \leq \sup\pi(\mathbf{d}') = -\overline{\rho(\underline{z})}\sup\frac{\Sigma_c(\underline{z})}{\rho(\underline{z})}D_3' \tag{11.32}$$

Finally, a combination of the lower bound, (11.28), and the upper bound, (11.32), yields the following Voigt-Reuss bounds for the effective uniaxial compressive strength of the C-S-H matrix composed of the two Drucker-Prager microhomogeneous C-S-H phases:

$$\min\Sigma_c(\underline{z}) \leq \Sigma \leq \overline{\rho(\underline{z})}\max\frac{\Sigma_c(\underline{z})}{\rho(\underline{z})} \tag{11.33}$$

Equation (11.33) provides first order bounds which a) are consistent with asymptotic values, $f_{LD} \to 1; \Sigma_c^{CSH} \to \Sigma_c^{LD}, f_{HD} \to 1; \Sigma_c^{CSH} \to \Sigma_c^{HD}$, and b) provide convenient first order means for interpolating the homogenized strength for a given mixture. To summarize, the homogenized failure envelope of the C-S-H matrix continues to be a Drucker-Prager matrix which can be represented by the following parameters:

$$c^I = \begin{cases} \min\left[c_{LD}^0, c_{HD}^0\right] & \text{Lower Bound} \\ f_{LD}\,c_{LD}^0 + f_{HD}c_{HD}^0 & \text{Upper Bound} \end{cases} \tag{11.34a}$$

$$\delta^I = \delta_{LD}^0 = \delta_{HD}^0 \tag{11.34b}$$

The homogenized C-S-H values will serve as input information for our next homogenization step.

11.3.3 Level II-($w/c > 0.42$) : Effect of Capillary Pores

For $w/c > 0.42$ the hydration products do not fill the whole available space and a residual pore volume is retained in the system. We consider an R.E.V. V composed of two phases: a C-S-H solid, s, surrounding some capillary pore spaces, p (see Fig. 11-5). In what follows, ϕ denotes the volume fractions of the porosity, $\phi = \frac{V_p}{V}$, and $1-\phi$ the volume fraction of the solid phase. The strength in the C-S-H matrix is characterized by a Drucker-Prager criterion of the form of

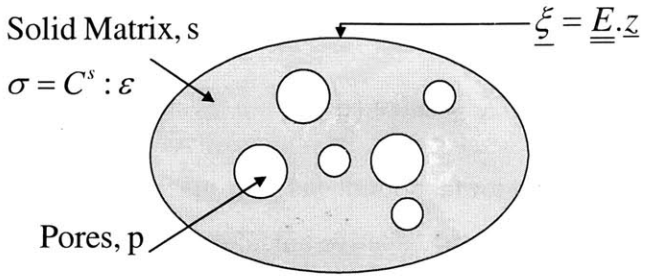

Figure 11-5: Representative element volume (R.E.V.) of a solid matrix containing some pore inclusions.

Eq. (11.8):

$$f(\boldsymbol{\sigma}_s) = \sqrt{j_2} + \delta_s \sigma_M^s - c_s \leq 0 \tag{11.35}$$

where δ_s is the pressure sensitivity coefficient and c_s is the cohesion of the solid matrix, as defined by the Drucker-Prager criterion. The non-linear boundary value problem on the R.E.V. then becomes:

$$\begin{aligned} \text{div } \boldsymbol{\sigma} &= 0 \\ \boldsymbol{\sigma} &= \mathbb{C}(\underline{z}) : \boldsymbol{\varepsilon} \\ \underline{\boldsymbol{\xi}} &= \mathbf{E} \cdot \underline{z} \quad (\partial V) \end{aligned} \tag{11.36}$$

where the homogeneous displacement boundary condition has been imposed and the spatial variation of the stiffness tensor is described by:

$$\mathbb{C}(\underline{z}) = \begin{cases} 0 & \text{in } \mathrm{V}_p \\ \mathbb{C}^s(\varepsilon(\underline{z})) & \text{in } \mathrm{V}_s \end{cases} \tag{11.37}$$

The non-linear homogenization problem posed in Eq. (11.36) has been recently solved by Barthelemy and Dormieux [13]. We briefly recall their result. Following the tools of non-linear homogenization we make use of the secant representation of the elastic tensor of the solid phase

(11.8):

$$\mathbb{C}^s(\varepsilon) = 3k^s\left(\epsilon_s, \varepsilon_s^v\right)\mathbb{J} + 2\mu^s\left(\epsilon_s, \varepsilon_s^v\right)\mathbb{K} \tag{11.38}$$

Using Eqs. (11.38) and (11.36) yields:

$$\boldsymbol{\sigma}_s = k^s\left(\epsilon_s, \varepsilon_s^v\right)\varepsilon_s^v\mathbf{1} + 2\mu^s\left(\epsilon_s, \varepsilon_s^v\right)\boldsymbol{\epsilon}_s \tag{11.39}$$

where $\frac{1}{3}\mathrm{tr}\boldsymbol{\sigma} = k^s\left(\epsilon_s, \varepsilon_s^v\right)\varepsilon_s^v$ and $\sqrt{j_2} = 2\mu^s\left(\epsilon_s, \varepsilon_s^v\right)\epsilon_s$. We now introduce the effective strain invariants which allow one to translate the non-linear representation of the local stress tensor into an equivalent linear one:

$$\boldsymbol{\sigma}_s = k_{eq}^s\left(\varepsilon_s^{eff}, \epsilon_s^{eff}\right)\varepsilon_s^v\mathbf{1} + 2\mu_{eq}^s\left(\varepsilon_s^{eff}, \epsilon_s^{eff}\right)\boldsymbol{\epsilon}_s \tag{11.40}$$

In the presence of such an effective strain in the matrix, we can now employ the linear homogenization step and relate the macroscopic elastic properties to local quantities:

$$\mathbb{C}^{\mathrm{hom}} = 3k^{\mathrm{hom}}\mathbb{J} + 2\mu^{\mathrm{hom}}\mathbb{K} \tag{11.41}$$

$$k^{\mathrm{hom}} = \mathcal{F}_1(\phi)\, g_{eq}^s\left(\epsilon_s, \varepsilon_s^v\right) \tag{11.42}$$

$$g^{\mathrm{hom}} = \mathcal{F}_2(\phi)\, g_{eq}^s\left(\epsilon_s, \varepsilon_s^v\right) \tag{11.43}$$

Estimates of the coefficients $\mathcal{F}_1(\phi)$ and $\mathcal{F}_2(\phi)$ can be given for different localization schemes:

$$\begin{array}{lll} \text{Mori-Tanaka:} & \mathcal{F}_1^{MT} = \frac{4(1-\phi)}{3\phi} & \mathcal{F}_2^{MT} = \frac{(1-\phi)}{1+2/3\phi} \\ \text{Self-Consistent:} & \mathcal{F}_1^{SC} = \frac{4(1-\phi)(1-2\phi)}{\phi(3-\phi)} & \mathcal{F}_2^{SC} = \frac{3(1-2\phi)}{(3-\phi)} \end{array} \tag{11.44a}$$

where the incompressibility condition, $g^s/k^s \ll 1$, was used. We recall that in the non-linear homogenization approach the strength is asymptotically reached for large deviatoric strains, such that:

$$\underset{\epsilon_s \to \infty}{f^s}\left(\lim \boldsymbol{\sigma}\right) = 0 \tag{11.45}$$

Equation (11.35) together with Eq. (11.45) yields:

$$g_{eq}^{s}\left(\varepsilon_{s}^{eff},\epsilon_{s}^{eff}\right)\simeq\delta\frac{\rho-k_{eq}^{s}\left(\varepsilon_{s}^{eff},\epsilon_{s}^{eff}\right)\varepsilon_{s}^{eff}}{2\sqrt{\epsilon_{s}^{eff}}} \tag{11.46}$$

Finally one needs to relate the effective strain in the matrix with macroscopic quantities. We start our discussion of effective strains considering a secant approximation to the effective strains defined by Eq. (11.12). Using the microscopic state equation, we can calculate the average strain field in the solid phase:

$$\overline{\boldsymbol{\varepsilon}}^{s}=\mathbb{C}^{s-1}:\overline{\boldsymbol{\sigma}}^{s} \tag{11.47}$$

Combining Eq. (11.47) with the stress average rule, $\Sigma=(1-\phi)\,\overline{\boldsymbol{\sigma}}^{s}$, we relate the strain function in the solid phase with the macroscopic stress and strain:

$$(1-\phi)\,\overline{\varepsilon}_{v}^{s} = \mathbb{C}^{s-1}:\Sigma \tag{11.48a}$$

$$(1-\phi)\,\overline{\boldsymbol{\varepsilon}}^{s} = \mathbb{C}^{s-1}:\mathbb{C}_{\text{hom}}:\mathbf{E} \tag{11.48b}$$

Given the isotropic nature of the solid phase and the absence of any morphological anisotropy, Eq. (11.48) can be decomposed into its deviatoric and volumetric components:

$$(1-\phi)\,\overline{\varepsilon}_{v}^{s} = \frac{k_{\text{hom}}}{k_{s}}\text{tr}\mathbf{E} \tag{11.49}$$

$$(1-\phi)\,\overline{\epsilon}^{s} = \frac{g_{\text{hom}}}{g_{s}}E_{d} \tag{11.50}$$

We have commented in Section 11.2 that the first order moment estimates of the effective strains are a crude approximation to reality. For additional accuracy we consider the higher moment definition presented in Section 11.2 which is based on an energy approach in which the effective strains are obtained as the derivatives of the macroscopic elastic strain energy [140,14]. The elastic energy of the R.E.V. is:

$$2\mathcal{E}=\langle\boldsymbol{\varepsilon}:\mathbb{C}:\boldsymbol{\varepsilon}\rangle_{\Omega}=\mathbf{E}:\mathbb{C}_{\text{hom}}:\mathbf{E} \tag{11.51}$$

Assuming isotropic behavior of the phases we have:

$$\mathcal{E} = \left\langle \frac{1}{2} k (\varepsilon^v)^2 + g \boldsymbol{\varepsilon} : \boldsymbol{\varepsilon} \right\rangle_\Omega \tag{11.52}$$

Following Kreher [140] displacements $\boldsymbol{\xi}$ and strains are considered functions of the elastic moduli. This leads to expressing the derivatives of the elastic energy in the form:

$$\frac{\partial \mathcal{E}}{\partial k_s} = (1-\phi)\left(\frac{1}{2}\overline{\overline{\varepsilon_s}}^2 + \left\langle \boldsymbol{\sigma} : \frac{\partial \varepsilon}{\partial k_s} \right\rangle_V\right) \tag{11.53a}$$

$$\frac{\partial \mathcal{E}}{\partial g_s} = (1-\phi)\left(\frac{1}{2}\overline{\overline{\epsilon_s}}^2 + \left\langle \boldsymbol{\sigma} : \frac{\partial \varepsilon}{\partial g_s} \right\rangle_V\right) \tag{11.53b}$$

where $V = \Omega - \omega_s$. This expression serves as a definition for $\overline{\overline{\varepsilon_s}}^2$ and $\overline{\overline{\epsilon_s}}^2$. In the case of our two phase system Eq. (11.53) reduce to:

$$\frac{1}{2}(1-\phi)\overline{\overline{\varepsilon_s}}^2 = \frac{\partial k_{\text{hom}}}{\partial k_s} E_v^2 + \frac{1}{2}\frac{\partial g_{\text{hom}}}{\partial k_s} E_d^2 \tag{11.54}$$

$$(1-\phi)\overline{\overline{\epsilon_s}}^2 = \frac{\partial k_{\text{hom}}}{\partial g_s} E_v^2 + \frac{1}{2}\frac{\partial g_{\text{hom}}}{\partial g_s} E_d^2 \tag{11.55}$$

or in terms of the macroscopic stress invariants:

$$2(1-\phi)\overline{\overline{\varepsilon_s}}^2 = -\frac{\partial}{\partial k_s}\left(\frac{1}{k_{\text{hom}}}\right)\Sigma_m^2 - \frac{\partial}{\partial g_s}\left(\frac{1}{g_{\text{hom}}}\right)\Sigma_d^2 \tag{11.56}$$

$$4(1-\phi)\overline{\overline{\epsilon_s}}^2 = -\frac{\partial}{\partial g_s}\left(\frac{1}{k_{\text{hom}}}\right)\Sigma_m^2 - \frac{\partial}{\partial g_s}\left(\frac{1}{g_{\text{hom}}}\right)\Sigma_d^2 \tag{11.57}$$

In solving the non-linear problem posed in Eq. (11.36) we will use a mixed formulation of the secant effective strains where the volumetric component is related to the first moment, $\varepsilon_\chi^{eff} \equiv \overline{\varepsilon}_\chi^v$, and the deviatoric component to the second moment, $\epsilon_\chi^{eff} \equiv \overline{\overline{\epsilon_\chi}}$. To summarize, the

following relations form a closed set of equations that have to be solved for the $\Sigma_m - \Sigma_d$ space:

$$(1-\phi)\,\overline{\varepsilon}_s^2 = \frac{\Sigma_m}{k_s} \tag{11.58a}$$

$$4\,(1-\phi)\,\overline{\overline{\epsilon}}_s^2 = -\frac{\partial}{\partial g_s}\left(\frac{1}{k_{\text{hom}}}\right)\Sigma_m^2 - \frac{\partial}{\partial g_s}\left(\frac{1}{g_{\text{hom}}}\right)\Sigma_d^2 \tag{11.58b}$$

$$k^{\text{hom}} = \mathcal{F}_1(\phi)\, g^s(\epsilon_s, \varepsilon_s^v) \tag{11.58c}$$

$$g^{\text{hom}} = \mathcal{F}_2(\phi)\, g^s(\epsilon_s, \varepsilon_s^v) \tag{11.58d}$$

$$g_{eq}^s\left(\varepsilon_s^{eff}, \epsilon_s^{eff}\right) \simeq \delta\frac{\rho - k_{eq}^s\left(\varepsilon_s^{eff}, \epsilon_s^{eff}\right)\varepsilon_s^{eff}}{2\sqrt{\epsilon_s^{eff}}} \tag{11.58e}$$

Finally Eqs. (11.58) yield an estimate of the homogenized yield criterion:

$$F(\Sigma_m, \Sigma_d) \;:\; (\Sigma_m - \Sigma_m^c)^2\left(\frac{1}{\mathcal{F}_1(\phi)} - \frac{\delta^2}{(1-\phi)}\right) + \Sigma_d^2\frac{1}{\mathcal{F}_2(\phi)} - \frac{\delta^2\rho^2(1-\phi)^2}{1-\phi-\delta^2\mathcal{F}_1(\phi)} \leq 0 \tag{11.59}$$

$$: \; \Sigma_m^c = \frac{\delta^2\rho}{\left(\frac{1}{\mathcal{F}_1(\phi)} - \frac{\delta^2}{(1-\phi)}\right)} \tag{11.60}$$

It is impressive to see that the plastic envelope of macroscopic stress states is now an ellipse which provides a boundary closed on the hydrostatic axis (see Fig. 11-6). The ellipse which is non-symmetric, has its center around $(\Sigma_m^c, 0)$ in the (Σ_m, Σ_d) −plane. The uniaxial compressive capacity Σ_c of a porous material characterized by Eq. (11.59) can be evaluated by considering a uniaxial compression test in which the maximum capacity is obtained at the limit:

$$\left(\frac{\Sigma_c}{3} - \frac{\left(\delta^I\right)^2\rho^I}{\left(\frac{1}{\mathcal{F}_1(\phi)} - \frac{\left(\delta^I\right)^2}{(1-\phi)}\right)}\right)^2\left(\frac{1}{\mathcal{F}_1(\phi)} - \frac{\left(\delta^I\right)^2}{(1-\phi)}\right) + \frac{\Sigma_c^2}{3}\frac{1}{\mathcal{F}_2(\phi)} \tag{11.61}$$

$$= \frac{\left(\delta^I\rho^I\right)^2(1-\phi)^2}{1-\phi-\left(\delta^I\right)^2\mathcal{F}_1(\phi)} \tag{11.62}$$

where the functions $\mathcal{F}_1(\phi), \mathcal{F}_2(\phi)$ depend on the chosen localization scheme. The Mori-Tanaka and self-consistent estimates are given in Eq. (11.44). Figure 11-7 shows the normalized uniaxial compressive strength of a Drucker-Prager solid as a function of the volume fraction of the pore spaces, and this for the two localization schemes presented in Eq. (11.44). It is

readily observed that the macroscopic strength vanishes for $\phi \rightarrow 1$ in the Mori-Tanaka scheme and for $\phi \rightarrow 0.5$ in the self-consistent scheme. The choice of the localization scheme is therefore of crucial importance and relates to the morphological details of the microstructure. It has to be carefully specified for all level considered in our analysis.

11.3.4 Level II-($w/c < 0.42$): Effect of Rigid Inclusions

In cases where the $w/c-$ratio is less than $w/c < 0.42$, cement-paste is composed from a C-S-H material surrounding some clinker phases. From a micromechanical point of view we consider cement paste ($w/c < 0.42$) as an R.E.V. V composed of two phases: a C-S-H solid matrix s surrounding some clinker particles cl (see Fig. 11-5). The clinker phases are approximated as rigid spheres. Given their elasticity and hardness values which are one order of magnitude higher than the C-S-H matrix the rigid inclusion approximation is a fair assumption. In what follows, f_{cl} denotes the volume fractions of the clinker, $f_{cl} = \frac{V_{cl}}{V}$, and $1 - f_{cl}$ the volume fraction of the solid phase. The strength in the C-S-H matrix is characterized by a Drucker-Prager criterion of the form of Eq. (11.8):

$$f(\boldsymbol{\sigma}_s) = \sqrt{j_2} + \delta_s \, \sigma_M^s - c_s \leq 0 \tag{11.63}$$

The non-linear boundary value problem on the R.E.V. then reads:

$$\begin{aligned} \text{div } \boldsymbol{\sigma} &= 0 \\ \boldsymbol{\varepsilon} &= \mathbb{S}(\underline{z}) : \boldsymbol{\sigma} \\ \underline{\mathbf{t}} &= \boldsymbol{\Sigma} \cdot \underline{n} \quad (\partial V) \end{aligned} \tag{11.64}$$

where the homogeneous traction boundary condition has been imposed and the spatial variation of the compliance tensor is described by:

$$\mathbb{S}(\underline{z}) = \begin{cases} 0 & \text{in } \mathrm{V}_{cl} \\ \mathbb{S}^s(\varepsilon(\underline{z})) & \text{in } \mathrm{V}_s \end{cases} \tag{11.65}$$

The non-linear homogenization technique presented in Section ?? has also been employed to the case of a Drucker-Prager matrix reinforced by rigid inclusions (see Ref. [149]). It has been

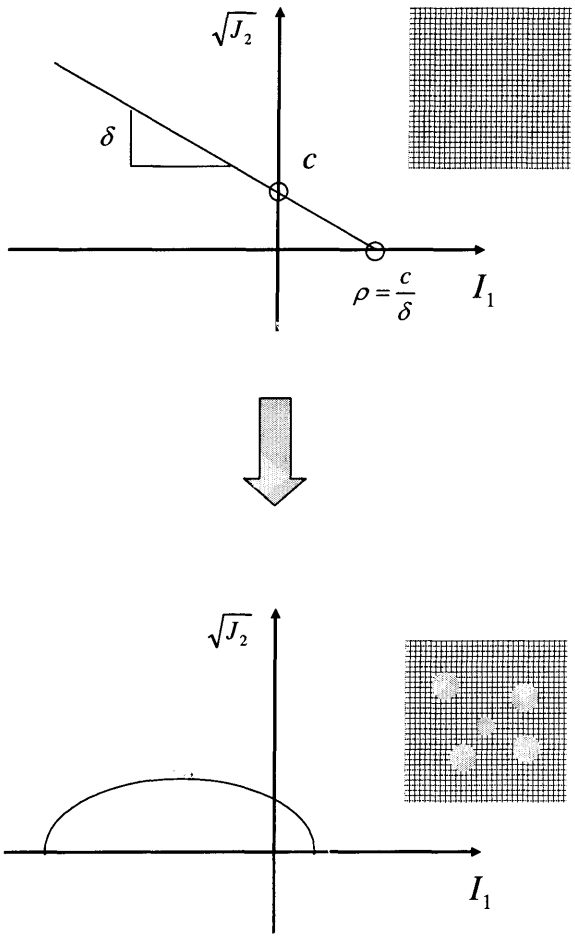

Figure 11-6: The Drucker-Prager criterion characterizing the solid failure envelope is transformed into an elliptical domain through the introduction of pores.

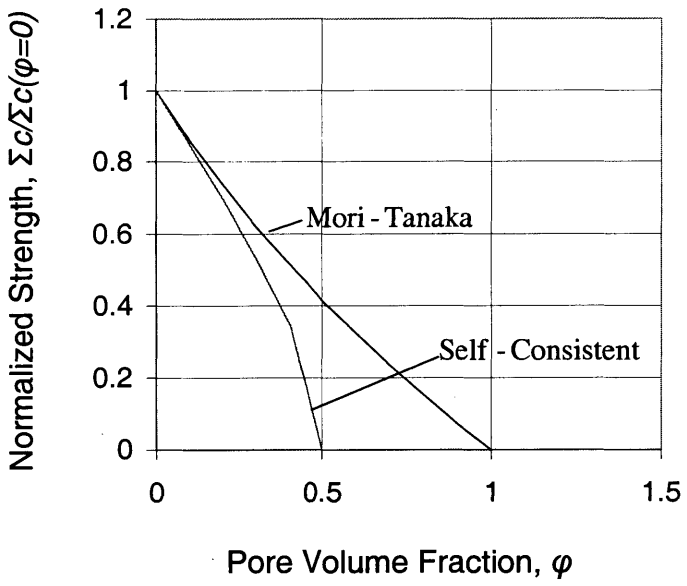

Figure 11-7: Scaling of normalized uniaxial compressive strength ($\Sigma_c(\phi)/\Sigma_c(\phi = 0)$) with volume fractions of porosity ϕ, for two localization schemes.

argued however that such an approach applied to this system does not satisfy the normality rule with respect to the matrix strength criterion [14]. To overcome this limitation, Barthelemy and Dormieux [14] used the mathematical equivalence between the limit analysis problem to be solved and a fictitious non-linear viscous problem. In their derivation presented in Ref. [14], two mechanical models have been considered for the matrix/inclusion interfaces, namely perfect bonding and non-frictional contact. For both types of interfaces, the macroscopic strength criterion takes the form of a Drucker– Prager criterion with scaled strength properties (see also Fig. 11-8):

$$\sqrt{J_2} + \overbrace{\sqrt{\frac{1+3/2f_{cl}}{1-2/3f_{cl}\left(\delta_s\right)^2}}}^{\Delta^{pb}} \delta_s \left(\Sigma_m - \rho_s\right) \leq 0 \tag{11.66a}$$

$$\sqrt{J_2} + \overbrace{\sqrt{\frac{\left(1+3/5f_{cl}\right)\left(1-f_{cl}\right)}{\left(1-2/3f_{cl}\left(\delta_s\right)^2\right)\left(1-2/5f_{cl}\right)}}}^{\Delta^{fr}} \delta_s \left(\Sigma_m - \rho_s\right) \leq 0 \tag{11.66b}$$

It is impressive to see that the micromechanical model predicts that the macroscopic strength criterion of a Drucker-Prager matrix reinforced by rigid inclusions continues to be a Drucker-Prager material with enhanced friction angle (and cohesion) but unchanged cohesive pressure, ρ_s. In fact, the predicted homogenized yield envelope rotates around the tensile pressure point. The amplification of the frictional capacity is both a function of the volume of inclusions and the nature of the interfacial properties. To further demonstrate this point we consider the uniaxial compressive strength of the homogenized material. This can be evaluated by considering $\Sigma_d = \Sigma_c/\sqrt{3}, \Sigma_m = -\Sigma_c/3$ in Eqs. (11.66):

$$\Sigma_c = \frac{3\Delta\rho_s}{\left(\sqrt{3}-\Delta\right)} \tag{11.67}$$

where Δ is the macroscopic pressure dependency coefficient which depends on the interface conditions. For a perfectly bonded (pb) and frictionless (fr) response the homogenized properties

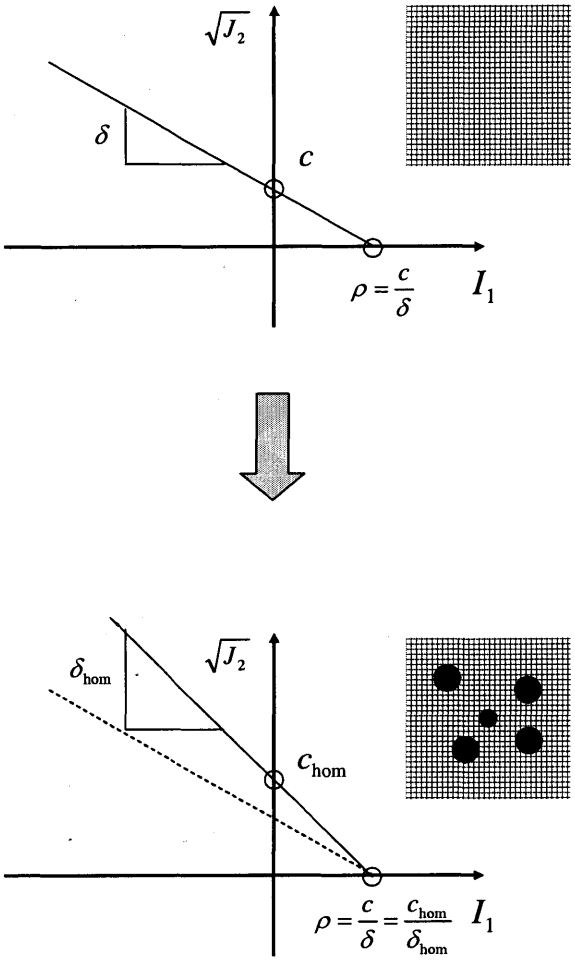

Figure 11-8: The Drucker-Prager criterion characterizing the solid failure envelope is transformed into a Drucker-Prager domain with scaled coefficients through the introduction of rigid inclusions.

are:

$$\Delta^{pb} = \sqrt{\frac{1+3/2f_{cl}}{1-2/3f_{cl}\left(\delta_s\right)^2}}\delta_s \tag{11.68}$$

$$\Delta^{fr} = \sqrt{\frac{\left(1+3/5f_{cl}\right)\left(1-f_{cl}\right)}{\left(1-2/3f_{cl}\left(\delta_s\right)^2\right)\left(1-2/5f_{cl}\right)}}\delta_s \tag{11.69}$$

Figure 11-9 shows the uniaxial compressive strength evolution as a function of the volume fractions of the inclusions for the two cases of interface conditions. The results were evaluated for two sets of solid material properties: ($\delta_s = 0.1; c_s^{DP} = 100$ MPa) and ($\delta_s = 0.7, c_s^{DP} = 100$ MPa). In the case of perfect bonding between matrix and inclusions, rigid inclusions lead to a reinforcement of the matrix. This phenomenon is further amplified with increasing volume of clinkers. The reinforcing effect is significantly lower and, in some cases, the strength of the material can even decrease if the interface is non-frictional (i.e., the matrix cannot transfer shear stresses to the inclusions). The result, which might seem surprising at first, is a phenomenon commonly observed in practice where the incorporation of inhomogeneities in uniform matrices introduces interfaces that constitute weak links in the systems. Furthermore, the reinforcing effect appears to be a function of the frictional capity of the matrix, with higher values of δ giving a higher amplification effect. It should be noted, however, that in the range of 0-40% of inclusion, the range for most CBM systems, and for small δ ($\delta \simeq 0.1$) the effect of rigid inclusions (clinker phases in Level II) is expected to be of secondary importance as the uniaxial compressive strength is only slightly modified. Figure 11-9 shows that the uniaxial compressive strength of all volume fractions of inclusions is within 25% of the uniaxial compressive strength of the matrix.

Given that estimates of δ_s and ρ_s are suggested by the previous homogenization level, the homogenized quantities at Level II can now be summarized:

$$\rho^{II} = \rho^{I} \tag{11.70a}$$

$$\delta^{II} = \begin{cases} \sqrt{\frac{1+3/2f_{cl}}{1-2/3f_{cl}\left(\delta^I\right)^2}}\delta^I & = \delta_{pb}^{II} \\ \sqrt{\frac{\left(1+3/5f_{cl}\right)\left(1-f_{cl}\right)}{\left(1-2/3f_{cl}\left(\delta^I\right)^2\right)\left(1-2/5f_{cl}\right)}}\delta^I & = \delta_{nb}^{II} \end{cases} \tag{11.70b}$$

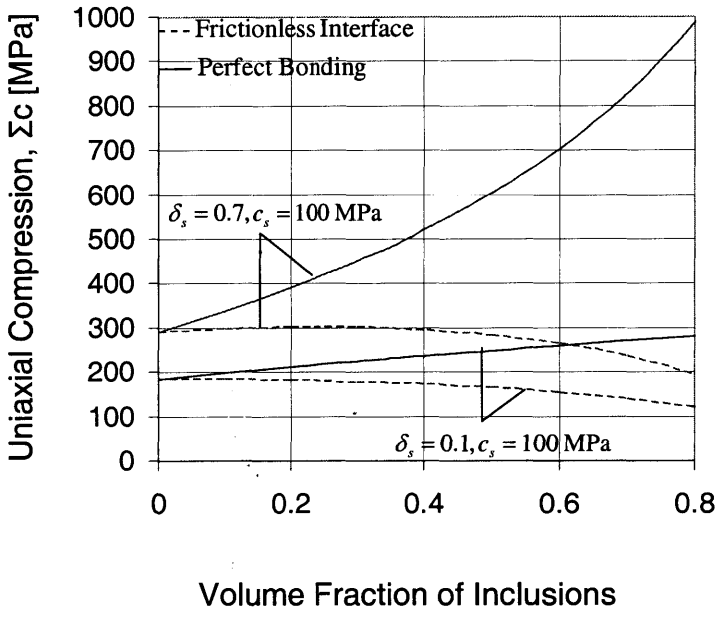

Figure 11-9: Scaling of uniaxial compressive strength with volume fractions of inclusions as predicted by equation (11.66) and (11.67). The case of a perfectly bonded interface and a frictionless interface is shown for two sets of solid parameters: ($\delta_s = 0.1, c_s = 100$ MPa) and ($\delta_s = 0.7, c_s = 100$ MPa)

The uniaxial compression can then be evaluated with:

$$\Sigma_c^{II} = \frac{3\delta^{II}\rho^{II}}{\sqrt{3} - \delta^{II}} \tag{11.71}$$

11.4 Chapter Summary

We have shown in this chapter that current strength models for CBM systems pose several limitation and rely on empirical constants and data fitting. Motivated by this observation, we have proposed a new multi-scale model for the strength behavior of CBM systems within the framework of nonlinear microporomechanics. The model presented in Section 11.3 provides strength estimates of CBM at multiple scales, provided the knowledge of the intrinsic properties of the individual components and their volumetric proportions. The intrinsic strength properties of the two types of C-S-H (LD and HD C-S-H) have been obtained through indentation testing (see Chapter 10). With this material invariant properties in hand one can calculate the strength response of any cement-based material system independent of initial mix proportions:

1. The estimated cohesion and angle of friction of the two types of C-S-H along with their volumetric proportions are incorporated in Eq. (11.34) that predicts the strength of the C-S-H matrix.

2. The homogenized values of the C-S-H matrix are incorporated in Level II (Eq. (11.70) or (11.61)) which yields, with the help of volumetric proportions of the clinker and capillary porosity the strength of Level II (cement paste). In the case were aggregates are present in the system one can use the micromechanical developments of Section 11.3.4 to provide homogenized values for concrete.

Figure 11-10 summarizes the multi-step microporoplastic model now in place. The proposed model reduces the complexity of cement-based materials to 10 parameters. These are the strength properties of the C-S-H solid phase (c_s, δ_s) - (the clinker phase and aggregate phases being considered as rigid particles with infinite strength), the volume fractions of the two types of C-S-H, (f_{LD}, f_{HD}), the volume fractions of the C-S-H matrix, (f_{CSH}), the volume fractions of the clinker phase, (f_{cl}), the volume fraction of the aggregate phase (f_g) and the pore space

at each level, $\phi^0_{LD}, \phi^0_{HD}, f_{cp}$. Consistent with the poroelastic model, the strength properties of the C-S-H solid phase, together with the porosities of the two types of C-S-H are assumed to be constant. Thus for each cement-based material of given mix proportions only the four parameters describing the volumetric proportions at each level are required: f_{LD} for Level I, f_{CSH} and f_{cl} for Level II, and f_g for Level III. The remaining volume fractions of the HD C-S-H, the capillary pore space, and cement paste matrix are obtained by employing the compatibility conditions, $\sum f_i = 1$, at each level: $f_{HD} = 1 - f_{LD}$, and $f_{cp} = 1 - f_{CSH} - f_{cl}$, $f_m = 1 - f_g$.

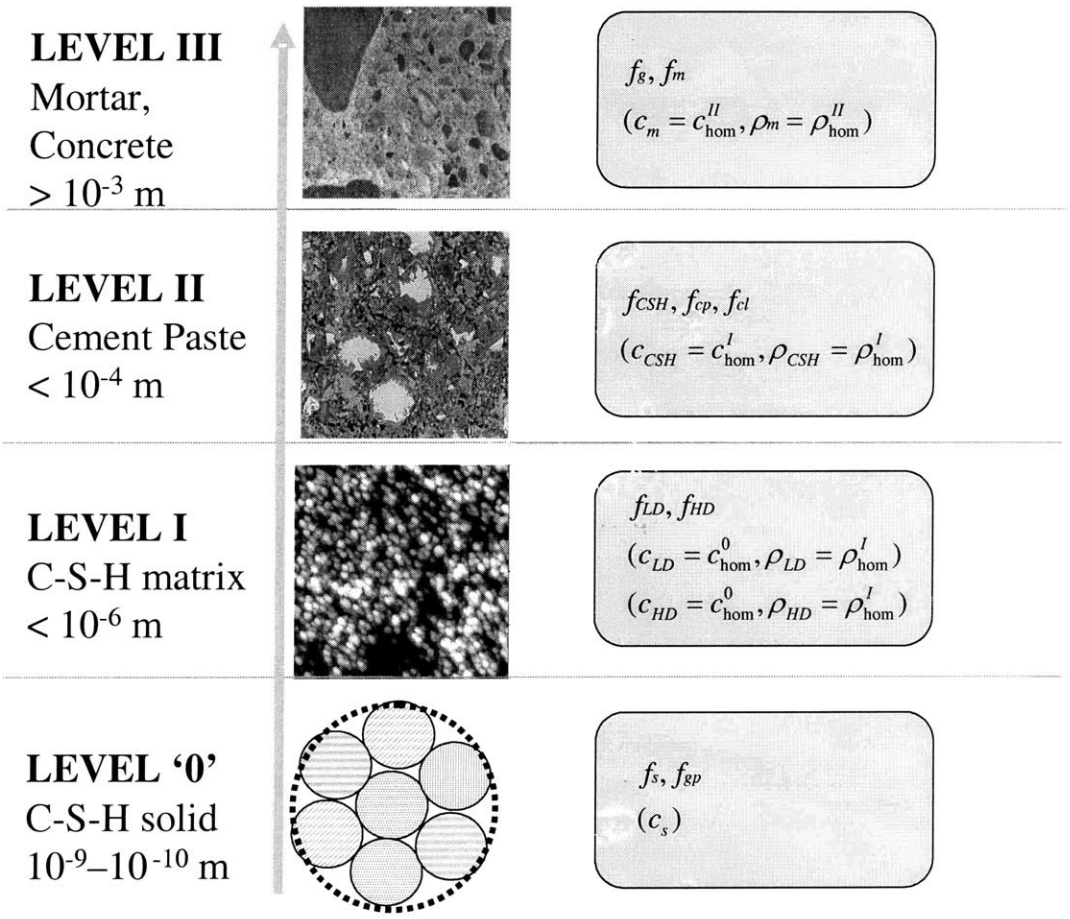

Figure 11-10: Summary of model parameters required for upscaling of CBM strength.

Chapter 12

Model Calibration, Validation and Application

This chapter presents details about the calibration and validation of the four-parameter model summarized in Section 11.4. Theoretical developments presented in Chapter 11 suggest that the macroscopic strength behavior relies on the exact nature of the bonding between cement particles and cement hydrates. Experimental data is compared with micromechanical predictions of Section 11.3 in an attempt to quantify the nature of C-S-H−clinker bonding in CBM systems. Following this calibration procedure, the model is validated on a set of macroscopic uniaxial compressive strength data found in the literature. The investigated cement pastes had different water/cement ratios ranging within $w/c = 0.17 - 1.0$. Finally, with this powerful tool in hand we move forward in optimizing the material response and provide an estimate for the maximum strength capacity that CBM systems can develop.

12.1 Input Parameters: Volumetric Proportions

The major conclusion of Chapter 11 is that the macroscopic mechanical performance of any CBM system can be estimated with the help of the micromechanical model presented in Section 11.3 provided the volumetric proportions of the different constituents present in the four-level think-model are known. Over the past few chapters, we have outlined several possible approaches for such an endeavour. In particular, the volumetric proportions of all constituents

can be calculated either experimentally (with the help of nanoindentation and the deconvolution technique presented in Chapter 5) or theoretically (by modeling the chemical reactions between the different cement constituents; see Section 4.5). In what follows we will make use of the chemistry models (theoretical approach) presented in Chapter 4. In particular, we will use the simplified microstructural representation of Powers in which cement paste is composed of a C-S-H matrix with some capillary porosity and residual clinker phases. An estimate of the volume fractions of these phases is provided by Powers model for a given $w/c-$ratio and degree of hydration ξ:

$$f_{cp} = \frac{\frac{w}{c} - 0.36\xi}{\frac{w}{c} + 0.32} \tag{12.1a}$$

$$f_{uc} = \frac{0.32\,(1-\xi)}{\frac{w}{c} + 0.32} \tag{12.1b}$$

$$f_{CSH} = 1 - f_{cp} - f_{uc} \tag{12.1c}$$

The decomposition of the two types of C-S-H will then be approximated with the Jennings and Tennis model:

$$f_{LD} = \frac{\mathcal{M}_r}{\mathcal{M}_r + (1-\mathcal{M}_r)\frac{\rho_{LD}}{\rho_{HD}}} \tag{12.2a}$$

$$f_{HD} = 1 - f_{LD} \tag{12.2b}$$

where we recall that $\mathcal{M}_r$ is the mass of LD C-S-H over the total C-S-H mass and is given by:

$$\mathcal{M}_r = 3.017\frac{w}{c}\xi - 1.347\xi + 0.538 \tag{12.3}$$

The output of this combination of Powers and J-T models are estimates of the volumetric proportions of all constituents which are allocated throughout the four-level microstructural think model, depending on length scale. With this knowledge in hand, we can then employ the micromechanical model of Chapter 11, summarized in Section 11.4, to provide predictions of the mechanical behavior of any CBM system. The procedure which will be detailed below is shown schematically in Fig. 12-1.

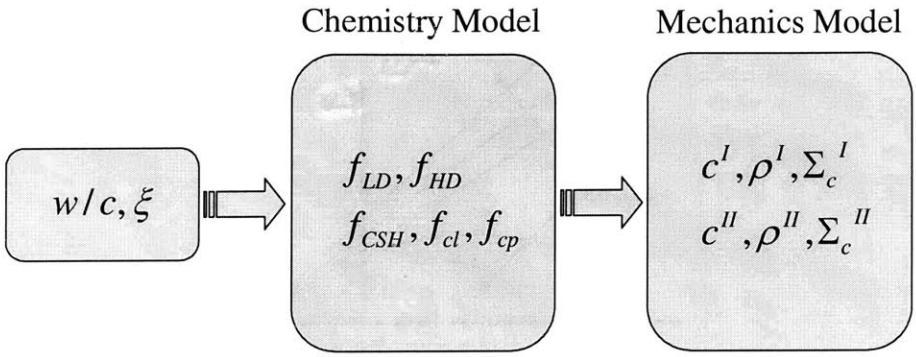

Figure 12-1: Schematic representation of the input-output procedure used for the prediction of macroscopic strength.

12.2 Model Calibration

12.2.1 Micromechanical Bounds for Mature Cement Pastes Strength

In order to demonstrate the predictive capabilities of the proposed strength model, we consider the mechanical behavior of mature cement pastes. By considering mature cement paste we assume that the material is at a state of chemical equilibrium at which the microstructure remains constant with time (we exclude here any aging effects) and the degree of hydration has achieved the maximum possible value, $\xi = \xi_{\max}$. The major parameter controlling the maximum degree of hydration is the initial water/cement ratio, $\xi_{\max} \simeq \xi_{\max}(w/c)$. An empirical relation relating $\xi_{\max}$ to w/c has been proposed in Section 9.1 (see Eq. (9.3)) and will also be used below.

Given the $w/c-$ratio and the maximum degree of hydration, the volumetric proportions of all constituents can be calculated from Eqs. (12.1)-(12.3). The volume fractions together with the intrinsic plastic properties of the two types of C-S-H are inserted in Eqs. (11.34) and (11.61) which yield the macroscopic strength properties of cement pastes. The procedure is shown schematically in Fig. 12-1. Figure 12-2 illustrates the evolution of the failure envelope of mature cement pastes as a function of the $w/c-$ratio. For $w/c-$ratio<0.42 the macroscopic

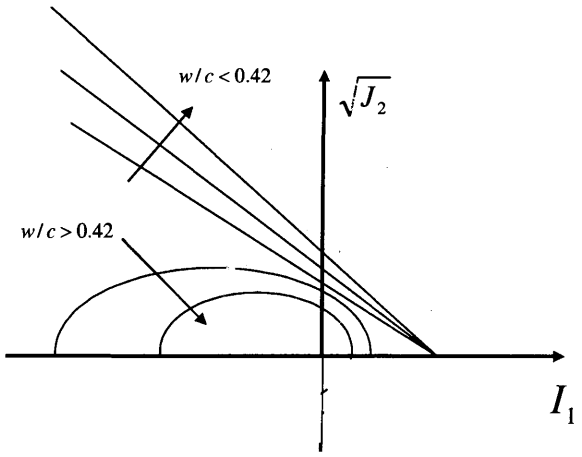

Figure 12-2: Schematic of the evolution of the failure envelope with the $w/c-$ratio.

strength envelope continues to be of the Drucker-Prager type with enhanced frictional behavior. This is attributed to the residual clinker phases retained is the system. For $w/c-$ratios$>$ 0.42, there will always be a certain amount of capillary porosity which gives cementitious materials a yield envelopes closed on the hydrostatic axis. The yield envelopes provide estimates of the limiting stress states in the three dimensional domain that any CBM material can obtain. Of particular interest is the uniaxial compressive strength which is commonly employed in practice. The micromechanical predictions of the uniaxial compressive strength as a function of the $w/c-$ratios is shown in Fig. 12-3. The upper bound consist of the combination of upper bounds in the Level I and Level II, respectively the lower bound consists of the combination of lower bounds in Level I and Level II. While the bounds in Level I results from the theorems of yield design, the bounds in Level II are a consequence of the state of bonding between C-S-H and clinker phases.

It becomes apparent that for small values of $w/c-$ratios, the model predictive capabilities are restricted within a range of values rather than a single absolute value. To refine our bounds, we will attempt to determine with the help of experimental data the nature of bonding between C-S-H matrix and the residual clinker phases.

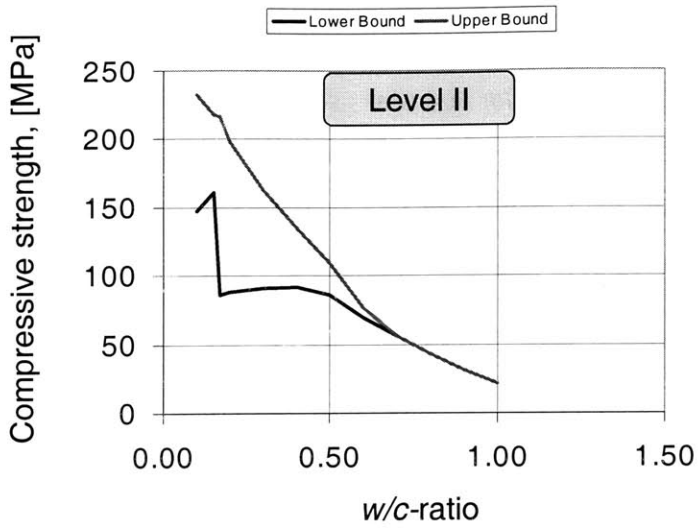

Figure 12-3: Micromechanical bounds for the uniaxial compressive strength of cement pastes. The results are for mature cement pastes plotted as a function of the initial $w/c-$ratios.

12.2.2 C-S-H−Clinker Bonding: Interface Effect

In what follows, we propose a series of arguments that the clinker phases present in the microstructure of cement-based materials do not contribute to the macroscopic strength capacity of the considered system. The physical mechanism behind this observation is not clear and potential sources will be discussed below.

Compressive Strength of Ductal^{TM}

To answer the question regarding the nature of bonding in the interface between C-S-H matrix and clinker inclusions, we consider a highly filled cement-based material with known microstructure and known macroscopic mechanical properties, Ductal^{TM}. Ductal^{TM} is an ultra high performance cementitious material with exceptionally high mechanical properties: a macroscopic uniaxial compressive strength of $\Sigma^{\text{exp}}_{\text{Ductal}} = 190$ MPa and a Young's modulus of $E^{\text{exp}}_{\text{Ductal}} = 50$ GPa. From a microstructural point of view the material has almost zero capillary porosity and a significant amount of residual clinker [2]. Experimental measurements indicate a degree of hydration of $\xi = 43\%$ [2] which translates with the use of Powers model (see Eq.

(12.1b)) into a volume fraction of clinker of $f_{cl} = 0.37$ and a volume fraction of C-S-H matrix of $f_{CSH} = 1 - f_{cl} = 0.63$. In order to eliminate the capillary porosity and maintain such a high proportion of residual clinker, the material uses very little initial water. Typical mix designs operate at a $w/c \simeq 0.19$. Use of this $w/c-$ratio in Eq. (9.7) gives an estimate of the volumetric proportions of LD and HD C-S-H in the C-S-H matrix: $f_{LD} = 0.04$, $f_{HD} = 1 - f_{LD} = 0.96$. Use of these volumetric proportions in equations (11.34) yield bounds for the macroscopic uniaxial compressive strength:

$$\text{LEVEL I:} \qquad \Sigma^{I}_{CSH} = 188 \text{ MPa} \tag{12.4}$$

$$\text{LEVEL II:} \qquad 161 \text{ MPa} \leq \Sigma_{\text{Ductal}} \leq 208 \text{ MPa} \tag{12.5}$$

Equation (12.4) assumes that the mechanical behavior of the C-S-H composite matrix is characterized by the upper bound estimate proposed in Eq. (11.33). This is a fair assumption, as the high volume fractions of the HD C-S-H phase suggest that the strength of the composite it is very close to the one proposed in HD C-S-H phase. It is impressive to see that the experimentally obtained value of Ductal$^{\text{TM}}$, which is on the order of $\Sigma_{\text{Ductal}} = 190$ MPa lies within the two bounds proposed by the micromechanical model, (12.5). We recall that the upper bound estimate was calculated on the premise that the C-S-H–clinker interface is perfectly bonded, in the sense that there is continuity of the stress vectors. On the contrary the lower bound allows for an imperfect interface, i.e., with no transfer of shear stress in the interface which allows eventually a discontinuity on the displacement field. The experimentally obtained value of Ductal$^{\text{TM}}$ suggests an average performance in terms of the interface bonding and stress continuity. It can therefore be concluded that the nature of bonding between hydration products and the clinker phases allows partial transfer of the shear stresses in the interface, part of them contributing to local discontinuities of the displacement fields. From a micromechanical modeling point of view, it is worth noticing that the estimate of the C-S-H matrix at Level I, $\Sigma^{I}_{CSH} = 188$ MPa is in fact in close agreement (within 1%) with the Ductal strength value, $\Sigma^{\text{exp}}_{\text{Ductal}} = 190$ MPa, suggesting that the 37% of residual clinker present at Level II has little influence on the macroscopic uniaxial compressive strength.

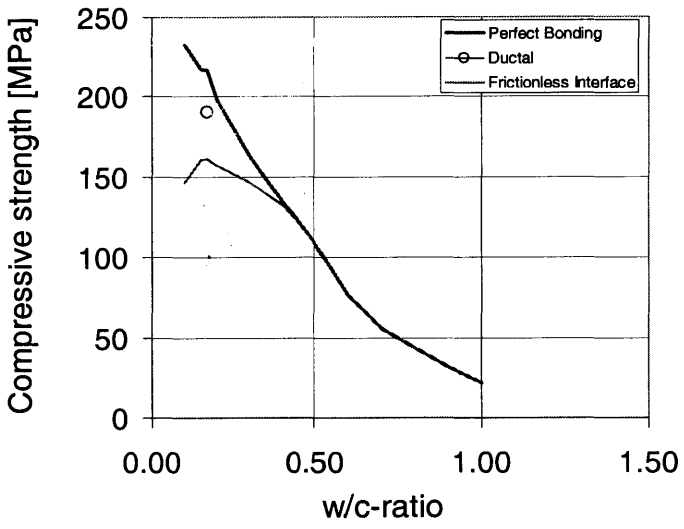

Figure 12-4: Experimental data on Ductal^{TM} lies within the two micromechanical bounds (perfectly bonded vs. frictionless interface).

Microhardness Data of Igarashi *et al.*: H/Σ_c vs. $(\xi, w/c)$

Experimental evidence presented by Igarashi *et al.* [125] suggest that the ratio of hardness to uniaxial compression is independent of the initial water/cement ratio and degree of hydration. Recall that the volumetric proportions of the clinker phases and pore volumes are strong functions of these two variables, $(w/c, \xi)$. Given the fact that the normalized strength to cohesion and hardness to cohesion are functions of the angle of friction:

$$H/c = \mathcal{H}_1(\varphi) \tag{12.6}$$

$$\Sigma_c/c = \mathcal{H}_2(\varphi) \tag{12.7}$$

it becomes apparent that their ratio, H/Σ_c, is a unique function of the angle of friction, $H/\Sigma_c = \mathcal{H}_3(\varphi)$. The experimental observation that H/Σ_c is a constant leads to two important conclusions:

1. The angle of friction is unaffected by the volume of clinkers present in the system. This supports our hypothesis that the volumetric proportions of the residual clinker phases do not contribute to macroscopic strength response;

2. The angle of friction is independent of the pore volume. This further supports our initial observation, stated in Section 10.1.2, that the angle of friction does not scale with the volume of porosity.

Regression Analysis

A multi-regression linear analysis of the factors influencing the strength behavior of concrete was reviewed in [144]. It was concluded that the volume fractions of porosity shows the strongest correlation with macroscopic mechanical performance rendering the effect of other components, including the volumetric proportions of residual clinker of secondary importance.

A Reinterpretation of Powers-Brownyard Model

A final argument towards the inert mechanical nature (in terms of uniaxial compressive strength) of residual clinker phases is the predictive capability of the PB model. It is clear from experi-

mental data presented in Ref. [194] that the PB model can predict with significant accuracy the macroscopic mechanical behavior of any cement based material, which was found to scale with the gel/solid ratio, r. A closer look on the definition of this gel/solid ratio reveals that the effect of clinker phases is excluded from the analysis. In fact, the definition of a representative element volume used in the PB model is one which excludes the volume fractions of the clinker phases, $\Omega^{PB} = 1 - f_{cl}$. Such an R.E.V. definition does not respect the compatibility condition, $\Sigma f_i = 1$, $f_{CSH} + f_{cp} = 1 - f_{cl} \neq 1$. For consistency with micromechanical representation we will consider an R.E.V. composed of the C-S-H matrix and capillary porosity. In such a case the volume fractions of C-S-H is consistent with the gel/space ratio, r, defined in (11.3). Respectively the volume fractions of the pore space, ϕ, is equal to $\phi = V_{cp}/(V_{cp} + V_{cl}) = 1 - r$. In such a case the PB model takes the form of the Balshin Eq. (11.1a):

$$\Sigma_c = Ar^m = A\,(1 - \phi)^m \tag{12.8}$$

Such a definition excludes the mechanical contribution of the clinker phases in the macroscopic strength response. The excellent predictive capabilities of the PB model suggest that the clinker particles do not significantly contribute to the uniaxial compressive strength.

Summary of Model Calibration

From the above discussion, it can be concluded that the presence of clinker does not significantly affect the uniaxial compressive strength of cementitious materials. To model this phenomenon we will make use of the micromechanical interpretation of the PB model, which is equivalent of a two-step homogenization process:

1. We first consider an R.E.V. composed of C-S-H matrix and capillary porosity. The homogenized response of such a system is treated in Section ?? and the resulting homogenized yield envelope is described by Eq. (11.61). The volumetric proportions of the two phases can be estimated from the Powers-Brownyard model after excluding the clinker phases:

$$f'_{CSH} = \frac{V_{CSH}}{V_{CSH} + V_{CP}}; f'_{CP} = \frac{V_{CP}}{V_{CSH} + V_{CP}} = 1 - f'_{CSH} \tag{12.9}$$

2. The homogenized material then serves as a matrix for the rigid cement particles. Although an analytical solution to such a problem does not exist the experimental data of Powers and Brownyard suggest that the yield envelope (or at least the uniaxial compressive strength) changes little (if any). This suggests that the contribution of the clinker phases to macroscopic strength response is insignificant and can be excluded from our analysis. The homogenized value from step 1 can be equated to the macroscopic response.

12.3 Model Validation

This section investigates the predictive capabilities of the calibrated micromechanical model. The predictions are compared with the experimental data of Alexander et al. [5], Pann et al. [186], and Rössler and Odler [200].

12.3.1 Data of Alexander et al. [5]

Alexander et al. [5] considered the uniaxial compressive strength of cement paste specimens hydrated for 28 days with different $w/c-$ratios ranging within $w/c = 0.3 - 0.9$. Unfortunately, the degrees of hydration were not measured experimentally. One can get an estimate of the degree of hydration by considering the kinetics of the chemical reactions. An empirical estimate which circumvents the complicate calculations of the different forms of kinetic reactions was proposed in Ref. [186]. The experimentally obtained degree of hydration was correlated with initial water/cement ratio using a non-linear regression analysis. The experimental data which has been presented in Ref. [186] are shown as a function of both the $w/c-$ratio and time elapsed after mixing. The recommended best fitted relation for the 28-day specimen is:

$$\xi = -44.028 + 621.42\,(w/c) - 1144.053\,(w/c)^2 + 696.890\,(w/c)^3 \tag{12.10}$$

The third column in Tab. 12.1 was calculated by considering the initial $w/c-$ratio of each specimen in Eq. (12.10). Given the $w/c-$ratio and degree of hydration one can calculate the volumetric proportions of the different phases and eventually obtain an estimate of the macroscopic mechanical response (see Fig. 12-1). The results as a function of the $w/c-$ratio are shown in Fig. 12-5. In the range of $0.4 < w/c < 0.6$, the experimental data is in very good

			Measured
Age	w/c	ξ	Σ_c^{mea}
[days]	[-]	[-]	[MPa]
28	0.3	0.58	100
28	0.4	0.66	63
28	0.5	0.68	42
28	0.6	0.67	31
28	0.7	0.69	21
28	0.8	0.78	14
28	0.9	0.97	10

Table 12.1: Experimental data of Alexander et al. vs. micromechanical predictions for various $w/c-$ratios.

agreement with the lower bound micromechanical estimate, suggesting that the LD C-S-H phase dominates the mechanical response of the C-S-H matrix in that particular range. Consistent with the theorems of yield design, the experimental value of uniaxial compression for $w/c < 0.4$ lies in between the two bounds. In contrast, for $w/c > 0.6$ the values lie ahead. In fact, the two bounds collapse to a single curve as the $w/c-$ratio gets higher than $w/c = 0.62$: the C-S-H phase is now purely composed of LD C-S-H. The underestimation of the micromechanical predictions in this range can be attributed to the localization scheme used. The self-consistent estimate predicts a percolation threshold for porosities of 0.5, while it seems that materials retain the strengths up to porosities of 0.6.

12.3.2 Data of Pann et al. [186]

A compilation of 28 data sets found in the literature is presented in Pann et al. [186]. The chosen data was for specimens that were 28 days old and their $w/c-$ratios ranged within $0.30 - 0.80$. Details of the experimental data is provided in Tab. 12.2. The degree of hydration for each specimen was once again estimated from Eq. (12.10). The predictions which are shown in Fig. 12-5 testify towards the relevance of the lower bound estimate in modeling the macroscopic strength response. The micromechanical predictions are in close agreement with the experimental data with deviation getting greater for high values of $w/c-$ratios (see Section 12.3.1).

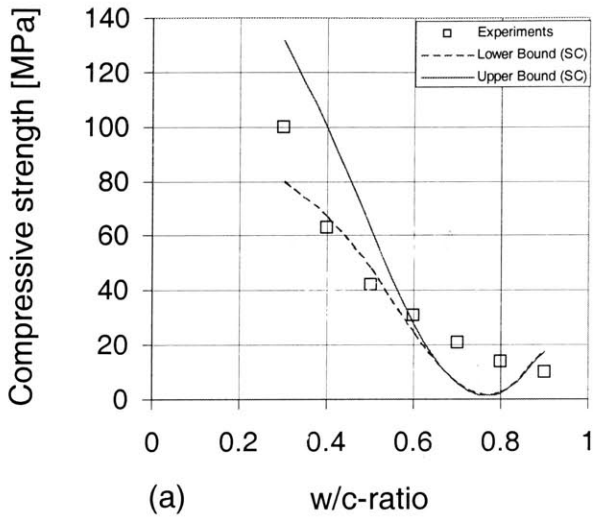

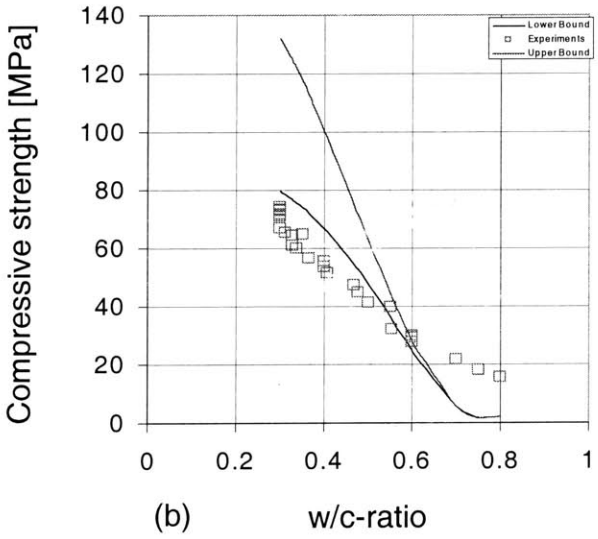

Figure 12-5: Micromechanical estimates vs. experimental data of uniaxial compressive strengths of cement paste specimens of different $w/c-$ratios. (a) Experimental data of Alexander et al. [5]. (b) Experimental data compiled by Pann et al. [186].

			Measured				Measured
Age	w/c	ξ	Σ_c^{mea}	Age	w/c	ξ	Σ_c^{mea}
[days]	[-]	[-]	[MPa]	[days]	[-]	[-]	[MPa]
28	0.30	0.58	67	28	0.40	0.66	56
28	0.30	0.58	71	28	0.41	0.66	52
28	0.30	0.58	74	28	0.47	0.68	47
28	0.30	0.58	73	28	0.48	0.68	45
28	0.30	0.58	72	28	0.50	0.68	41
28	0.30	0.58	73	28	0.55	0.68	40
28	0.31	0.60	66	28	0.55	0.68	32
28	0.33	0.61	65	28	0.60	0.67	28
28	0.33	0.61	61	28	0.60	0.67	30
28	0.34	0.62	60	28	0.60	0.67	29
28	0.35	0.63	65	28	0.70	0.69	22
28	0.36	0.64	57	28	0.75	0.73	18
28	0.40	0.66	54	28	0.75	0.73	18
28	0.40	0.66	54	28	0.80	0.78	16

Table 12.2: Experimental data of Pann et al. vs. micromechanical predictions for various $w/c-$ratios.

12.3.3 Data of Rössler and Odler [200]

A series of experiments has been presented by Rössler and Odler [200] in which they systematically changed the $w/c-$ratio and measured the uniaxial compressive strength for 2 different specimen age, 28 days and 180 days. The volume fractions of the capillary porosity was measured by Mercury Intrusion Porosimetry (MIP). The experimental values of the capillary porosity and uniaxial compressive strength for the different specimens are presented in Tab. 12.3. It is evident that the more mature specimens have a reduced capillary porosity and an increased compressive strength. This might be attributed to the continued hydration which continues long after mixing and has the tendency to fill space and reduce porosity. The micromechanical predictions of the lower bound estimates are also shown for comparison. The experimental and micromechanical strength values are plotted in Fig. 12-6 as a function of the capillary porosity. In order to quantify the accuracy of our model we computed the error between measured and predicted values: $e = \left(\Sigma_c^{pre} - \Sigma_c^{mea}\right)/\Sigma_c^{mea} \times 100$. The percentage errors which are shown in the last column of Tab. 12.3 verify the predictive capabilities of the model. Individual errors

			Measured	Predicted	Error
Age	w/c	f'_{cp}	Σ_c^{mea}	Σ_c^{pre}	e
[days]	[-]	[-]	[MPa]	[MPa]	[%]
28	0.22	0.10	101	93	−8
28	0.27	0.10	117	93	−20
28	0.32	0.09	108	94	−13
28	0.37	0.13	108	89	−18
28	0.42	0.16	87	84	−4
28	0.47	0.15	71	85	+20
28	0.52	0.14	84	87	+4
180	0.22	0.04	102	103	+1
180	0.27	0.05	118	102	−13
180	0.32	0.06	110	100	−8
180	0.37	0.09	113	95	−15
180	0.42	0.10	89	94	+6
180	0.47	0.09	90	94	+5
180	0.52	0.10	105	94	−11

Table 12.3: Experimental data of Rossler and Odler vs. micromechanical predictions for various $w/c-$ratios.

vary from +20% to −20%, with an average value of 10%[1].

12.4 Model Application

The strength model developed so far quantifies the relative contribution of each constituents present in CBM microstructure. This is a powerful tool for modeling any CBM system, provided knowledge of the volumetric proportions of each constituent. For demonstration purposes, we apply the model to two cases of industrial interest: a) The mechanical response of the thermally affected systems considered in Chapter 6; and b) The optimization of cementitious composites.

12.4.1 Thermally Treated Systems

Given our microporomechanics model, we can now estimate the macroscopic mechanical response of the thermally cured and thermally treated cement-based materials studied in Chapter

[1] This is the average value of the absolute values of the errors, computed as: $\sum \sqrt{(\Sigma_c^{mea} - \Sigma_c^{pre})^2}/N$, where N is the number of tests.

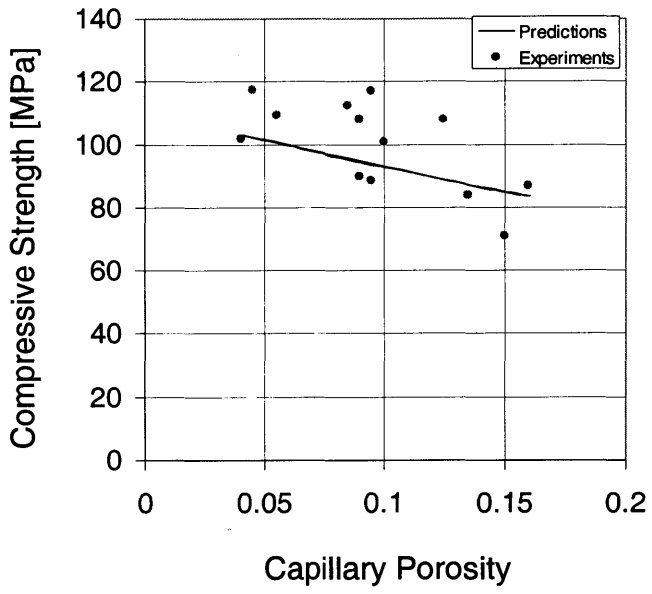

Figure 12-6: Micromechanical predictions vs. experimental measurements of uniaxial compressive strength of cement pastes with different capillary porosities.

6 of this thesis. The volumetric proportions of the individual constituents are summarized in Tab. 8.4 and the micromechanical predictions are now given:

$$\begin{pmatrix} \Sigma_c^{II} & \left(\Sigma_c^{II}\right)^J / \left(\Sigma_c^{II}\right)^{\text{'C'}} & J \\ \text{[MPa]} & \text{[\%]} & \text{[-]} \\ 96 & 0 & \text{'C'} \\ 107 & +4 & \text{'HC-1'} \\ 83 & -14 & \text{'HC-28'} \\ 101 & +5 & \text{'HT'} \end{pmatrix} \tag{12.11}$$

The estimates given in Eq. (12.11) are based on the lower bound scheme which has been found to be in excellent agreement with experimental data. The predicted values are in compliance with the trends observed in practice. That is, the heat cured specimen (HC-28) shows a reduced mechanical performance compared with the control specimen. The micromechanical model which can capture this behavior suggests that the macroscopic drop in strength is due to the increase in the volume of the capillary porosity. Any densification of the C-S-H matrix contributes little to the macroscopic strength given the fact that the LD C-S-H (lower bound) generally dominates. In the case of heat-treated specimens, the results remain relatively unaffected, given the limited change of the microstructure.

12.4.2 Strength Capacity of CBM Systems and Material Optimization

In this section, we consider an optimized version of CBM materials in order to evaluate the efficiency of existing cement based composites and propose ways of improving their performance. We consider the case of a matrix that is composed of only HD C-S-H and a significant proportion of unhydrated clinker phases. Such a scenario represents the cases of extremely low $w/c-$ratio on the order of $0.1-0.2$. Ductal$^{\text{TM}}$ which is a high performance concrete operates in this regime, and will serve as means of monitoring the relevance of the model. The mechanical properties of the two types of C-S-H will serve as input data to the model and as a consequence Level 0 of the multi-scale model can be neglected.

Level I: C-S-H Matrix

As the water/cement ratio decreases, there is a significant increase in the volumetric proportions of HD C-S-H. Coupled with temperature treatment techniques the material at Level I can be considered as a purely densified matrix in which only HD C-S-H exists. In fact, we have shown in Section 9.1.1 and Fig. 9-5, that a $w/c-$ratio of $w/c < 0.17$ is sufficient to completely densify the C-S-H matrix. Therefore the mechanical performance of an optimized version of CBM material at this level will be driven by the mechanical response of the HD C-S-H phase:

$$f_{HD} \rightarrow 1; c^I \rightarrow c^0_{HD}; \delta^I = \delta^0_{HD} \tag{12.12}$$

Level II: Cement Paste

Level II is the level where the C-S-H matrix is reinforced by the rigid inclusions present in the system. At such low $w/c-$ratios, an extremely low hydration degree is achieved and a significant portion of clinker phases is left in the system. In fact for a $w/c-$ratio of 0.19 (Ductal^{TM}) $f_{cl} = 0.37$ of clinker phases is left unhydrated (see Section 12.2.2). Theoretically, the maximum amount of clinker phases that can exist in the C-S-H matrix is the value for which the C-S-H matrix remains percolated, since this is the only phase that has cohesive properties[2]. Percolation thresholds for spherical particles are on the order of $f_{cl} \simeq 0.50$ and will be considered for our simplified analysis. The effect of rigid inclusions on the macroscopic strength of a Drucker-Prager material can be calculated from Eq. (11.66). The micromechanical estimates for the two particular cases of a perfect bonding and a non frictional contact between inclusions are:

$$c^{II}_{nf} = 106 \text{ MPa} < c^{II} < c^{II}_{pb} = 156 \text{ MPa} \tag{12.13}$$

$$\delta^{II}_{nf} = 0.085 < \delta^{II} < \delta^{II}_{pb} = 0.125 \tag{12.14}$$

[2] We exclude here any sintering phenomena and we restrict ourselves to the simple scenario of matrix with spherical inclusions.

The uniaxial compressive strength can then be calculated as:

$$\Sigma_{pb}^{II} = 166\text{MPa} < \Sigma^{II} = \frac{3k^{II}}{\sqrt{3} - \delta^{II}} < \Sigma_{nf}^{II} = 262 \text{ MPa}$$

The consideration of the two extreme cases, the one of perfect bonding and the one of non-frictional contact provide the means of estimating an upper bound to the strength of CBM systems ($\Sigma_{nf}^{II} = 262\text{MPa}$) and a measure of the effective bonding between the phases respectively. There are several conclusions to be drawn from this analysis:

- The upper bound to the strength is an estimate of the maximum allowable strength that a CBM system can obtain provided that the globular structure is respected, i.e., there is no chemical change of the intrinsic globule by the application of chemicals, pressure or high temperatures. This upper bound can therefore serve as a means of estimating the efficiency of a given mix and further optimizing our material. It is impressive to note that Ductal$^{\text{TM}}$ is within $190/262 = 73\%$ of the maximum capacity of the system. The remaining improvement will probably rely on the imperfect bonding and may be due to the possibility that not 100% of the matrix is HD C-S-H. It should be noted, however, that this is a significant improvement in contrast to normal cement pastes that operate at $10 - 15\%$ of material efficiency (in terms of strength).

- It is impressive to note that empirical approaches have enabled significant optimization of the material. A moderate improvement is to be expected from optimizing the C-S-H matrix. Further improvement should require influence of the cement chemistry at the level of the C-S-H globule. We have in fact shown in Section 10.1.2 that eliminating the gel porosity is one means of further improving the mechanical response.

12.5 Chapter Summary

In this chapter the micromechanical model developed in Chapter 11 has been calibrated and validated on a set of uniaxial compressive strength specimens reported in the literature. The main conclusions are summarized:

- A series of arguments put forward in Section 12.2.2 suggests that the macroscopic uniaxial

compressive behavior of CBM materials is relatively unaffected by the volume fractions of the residual clinker present at any time in the system. This phenomenon may be attributed to a poor bonding between clinker and hydration products.

- The LD C-S-H phase was found to dominate the strength behavior of the C-S-H matrix. This phenomenon may be related to the fact that the LD C-S-H surrounds most of the capillary porosity, and as a consequence is subjected to stress concentrations which eventually induce failure. This observation is also in line with the weakest link theory.

These two observations/calibrations have been incorporated in our micromechanical model, which was found to predict macroscopic experimental data with high accuracy. In fact, the lower bound estimate of the C-S-H matrix was found to comply best with macroscopic data. The lower bound micromechanical predictions which are summarized in Fig. 12-7 underscore this agreement. The model was then used for design purposes in optimizing the material response and provide an estimate of the strength capacity that CBM materials can theoretically achieve. It has been found that existing cement-based materials operate at the 10-60% of material efficiency and that there is still room for improvement. While additional contributions are to be expected by eliminating the LD C-S-H phase and maximizing the clinker proportions in the matrix, significant impact is expected from the elimination of the gel porosity by manipulating C-S-H phases at the nanometer level and breaking down the globular structure.

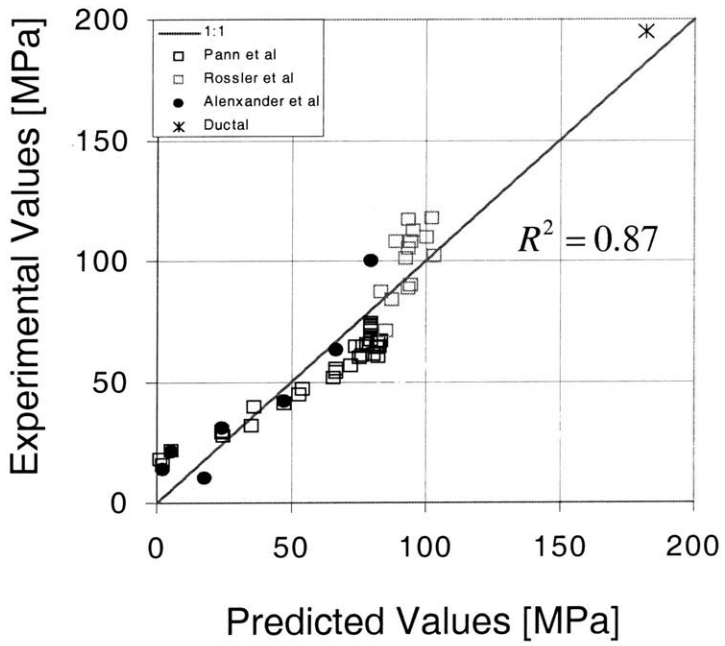

Figure 12-7: Micromechanical predictions vs. experiments for the uniaxial compressive strength of CBM with different $w/c-$ratio and degree of hydration ξ. The correlation coefficient between micromechanical predictions and experiments is also shown.

Part VI

CONCLUSIONS AND PERSPECTIVES

Chapter 13

Summary of Results and Future Perspectives

We asked at the outset of this thesis if it was possible to break our understanding of cement-based materials down to a scale where constituent material properties do not change from one sample to another and if we could then upscale the behavior from the nanoscale to the macroscale. The experimental data, analysis, and interpretation, along with the theoretical modeling and prediction developed in this thesis, provide an affirmative answer to these questions. This chapter presents a summary of the multi-scale investigation of cement-based materials. Based on these findings, some future research is proposed and perspectives on the micromechanical modeling of CBM are given.

13.1 Summary of Main Findings

Continuum micromechanics coupled with advanced experimental techniques provide a reliable framework for modeling the macroscopic mechanical behavior of cement-based-materials, while incorporating their large heterogeneity in the model. Models are predictive over several orders of magnitude and for a variety of compositions, chemical conditions etc. The following conjectures are made:

Conjecture 1 *Level 0: There exists a unique C-S-H solid phase at level '0' (the 'globules' in Fig. 4-8) composed of several C-S-H sheets of a characteristic size in the nanometer range, and*

a nanoporosity of 18%. The 18% hints towards a very dense packing of the sheets, which could be a consequence of the chemophysical nature of the interlayer structural water. Estimates of the mechanical properties of this phase were estimated by inverse analysis of the indentation data: $E^{CSH} = 61$ *GPa,* $c^{CSH} = 187$ *MPa. The nanoindentation creep results allow us to identify this scale as the scale of the rate determining mechanism of the time dependent deformation of cementitious materials. Application of moderate heat (60° C) tends to polymerize the chains within this solid releasing water in the process which appears to reinforce the material against creep and shrinkage deformations. The packing density of LD and HD C-S-H is associated with the random packing limit and the cubic or hexagonal close packing, respectively. The strength of this solid phase, which is most probably governed by attractive correlations forces at very short separation distances* [101]*, should be some order of magnitude greater than any strength at larger scales. Further work from the atomistic modeling point of view is required to reinforce our understanding at this scale.*

The question remains about the physical state of the water in the structural porosity, and related surface properties at the scale of the C-S-H sheets forming the C-S-H solid phase. They appear to be of great importance for the creep behavior.

Conjecture 2 *Level I: The diversity of cementitious materials starts at the scale where the solid phases form two different characteristic packing patterns that are present in different volumetric proportions in different cementitious materials. While the two packing patterns are still universal, their respective volume proportions depend on mix proportions, thermal curing, aging, etc. The difference in packing density per se suffices to explain intensive material properties that govern the deformation behavior of cementitious materials: elastic properties and strength properties. Estimates of these properties were provided by the grid indentation and dual indentation techniques developed in this thesis:* $[E^{LD} = 21$ *GPa,* $c^{LD} = 50$ *MPa,* $\varphi^{LD} = 12°$, $\Sigma_c^{LD} = 128$ *MPa],* $[E^{LD} = 31$ *GPa,* $c^{LD} = 97$ *MPa,* $\varphi^{LD} = 12°$, $\Sigma_c^{LD} = 224$ *MPa]. It is most likely that the individual properties are a mere consequence of the number and nature of contact points between solid phases, 6 vs. 12 in LD C-S-H and HD C-S-H. The higher the number of contact points the more degrees of freedom to restrain the deformation and to dissipate energy. When it comes to creep intensity, one needs to acquire information from a length scale sepa-*

rated by (at least) one order of magnitude. The creep mechanism which has been identified to lie within the globule (or layered) structure has been found to be sensitive to the heat application and duration. A correlation between the silicate polymerization and creep intensity appears to be consistent.

The question remains as to what triggers the creation of a highly ordered or disordered structure, and why thermal curing leads to the creation of more ordered elements in the material system. A mechanical explanation would be a thermal compaction: shaking up randomly distributed spheres leads to a higher probability of formation of ordered structure. On the other hand, the observation that the degree of silicate polymerization increases hints towards a chemical origin of this orientation.

Conjecture 3 *Level II: The macroscopic behavior at Level II is an amalgamation of all the phenomena taking place below. For the heat-cured specimens, two competing mechanisms are at work at the scale of a cement paste: One is creation of a net macroporosity as a result of the conversion of LD-C-S-H into HD-C-S-H in the course of heat curing. The second is the change of percolation of the governing C-S-H phase in the material system: the percolated C-S-H phase in normal cementitious materials is the LD-C-S-H phase, while it is the HD-C-S-H phase that is percolated in heat cured specimen. The creation of the macroporosity is detrimental for macroscopic strength properties of cementitious materials; while the change in percolation may well explain the lower creep intensity (but not the rate) of the heat-cured specimens. The loss in elasticity can be partly compensated by a) residual clinker phases reinforcing the cement paste and b) densification of the C-S-H matrix. In contrast, those compensating mechanisms do not productively work for strength. An 18% reduction in strength is observed in the case of heat cured specimens. Heat treatment offers a convenient framework were the benefits of time dependent deformation can be acquired without the drawbacks of the reduction of strength. Heat treatment operates at Level 0 only, without any detrimental effects for strength and elasticity.*

13.2 Research Contributions

Several new elements have been developed in this study, which are listed below:

1. Indentation testing has been extended to cohesive-frictional materials. A novel way of extracting strength properties of cohesive-frictional materials is proposed. The dual indentation technique which has been presented in Section 2.3.4 and Ref. [92] is the first of its kind. It takes advantage of the hardness dependency on indenter geometry to back calculate the cohesion and angle of friction of the material. The tools of indentation analysis on cohesive-frictional materials, together with the dual indentation technique have been validated in Section 3.4.3 on a Bulk Metallic Glass. We have proposed in addition a new way for accounting for the pile-up present in most cube-corner indentations (Elasticity corrector method, Section 2.5.4).

2. The multi-scale structure of CBM has been reconstructed in Chapter 4 (see also Ref. [58]). This has been done using the extensive data reported in the literature, i.e., microscopy investigations (SEM, ESEM, AFM etc.), porosity measurements, X-ray diffraction techniques etc., and the experimental investigations reported in this thesis. The resulting four-scale think-model forms the backbone for experimental and modeling attempts that followed in the rest of this thesis.

3. A way to extend indentation methods to multiphase composite systems has been presented in Chapter 5. The proposed grid indentation technique, which has been validated in Section 5.3 and Appendix D, provides easy access to the intrinsic mechanical properties of all involved phases, their volumetric proportions and morphological arrangement in space. These are all input requirements for any micromechanical modeling attempt.

4. We have identified two intrinsic packing modes of the C-S-H elementary block with corresponding intrinsic mechanical behavior. The elastic, poroelastic, creep and strength estimates of the two C-S-H phases have been measured experimentally for the first time. We have also provided intrinsic estimates for the rest of the individual phases present in cement-based systems. A summary of the results is reported in Tab. 13.1.

5. The multi-scale mechanical behavior of heat cured and heat treated specimens has been studied in detail. Results presented in Chapter 6 are in favour of a densification process that takes place at the C-S-H level as a consequence of early heat application during

		C-S-H$_{LD}$	C-S-H$_{HD}$	Globule
Physical				
Porosity-ϕ	[%]	37	24	18
Density (Sat/Dry) -ρ_{sat}/ρ_{dry}	[kg/m^3]	1,930/1440	2,130/1750	2,800
Poroelasticity				
Skempton coefficient-B	[-]	0.25	0.24	–
Biot coefficient-b	[-]	0.72	0.54	–
Biot skeleton modulus-N	[GPa]	114	133	–
Biot Modulus-M	[GPa]	5.9	6.0	–
Elasticity				
Elastic Modulus-E	[GPa]	21	31	61
Poisson's Ratio-ν	[-]	0.24	0.24	0.25
Strength				
Cohesion-c	[MPa]	50	97	187
Angle of Friction-φ	[-]	12	12	–
Uniaxial Compression-Σ_c	[MPa]	128	224	–
Creep				
A	[nm]	10	5	–
B	[s]	1.3 – 1.5	1.3 – 1.5	–

Table 13.1: Summmary of intrinsic mechanical properties of C-S-H phases.

curing. The resulting material is one of reduced gel porosity but increased macroporosity, giving heat cured specimens their reduced macroscopic strength performance and increased permeability.

6. The material invariant properties proposed in Chapter 5 were used in a novel microporoelastic model that can deliver the poroelastic properties of a variety of cement-based materials over several orders of magnitude in length scales (Chapters 7 to 9).

7. The dual indentation technique was applied in Chapter 10 on a white cement paste to provide the first experimental estimates of C-S-H strength.

8. A novel micromechanical model for CBM strength is developed in Chapter 11. It provides a physical interpretation to the link between compressive strength and w/c–ratio and investigates the effect of porosity and clinker phases on the macroscopic mechanical performance.

9. The materials science approach developed in this thesis is general and can be equally

applied to any other natural composite, whether geological or biological. The approach which has its origin at the level of the individual components, provides a direct link between physical chemistry and mechanics.

13.3 Current Limitations and Future Perspectives

The experimental and analytical developments presented in this thesis exposed areas of future scientific interest and industrial importance. The following are possible extensions for future research:

13.3.1 Continuum vs. Discrete

Modeling of CBM has been performed within the framework of continuum micromechanics. Their discrete nature has been ignored and their colloidal matrices have been replaced by an equivalent continuum medium. This representation has provided the means for mechanistic models, but a more rigorous approach that takes the discrete nature of the material into account may prove to be useful in the future. The analysis presented in this thesis has stretched the limits of continuum mechanics and reached length scales low enough allowing researchers from atomistic simulations and quantum mechanics to bridge to the CBM continuum.

13.3.2 Nature of Globule and Origin of Cohesion

Much of our discussion in this thesis culminated in a few material invariant properties which are intrinsic for a given a material system, with our starting point being the single particle level. It becomes apparent that the individual solid units considered in this thesis are not the individual C-S-H sheets but crystallites thereof. Some fundamental questions of extreme scientific and industrial interest remains: What determines the exact shape and morphology of the individual solid particles? What is the nature of their bonding and the origin of the cohesion with neighboring particles? The physicochemical processes that define these features are still at embryonic stages. To emphasize the importance of these questions on the mechanics side it suffices to note that the exact shape and size is intimately related with the surface forces and packing arrangement (therefore porosity) that is at the heart of the macroscopic mechanical

behavior. Much of the advancement in the last 50 years has been concentrating on improving the packing arrangement of cement particles at the level of a few micrometers eliminating in the process the capillary porosity. We dare to forecast that future improvements will be at the level of the individual globules, with significant consequences for material development.

13.3.3 C-S-H Creep

The C-S-H phases in CBM materials have been shown to exhibit some time dependent deformation. As a consequence a portion of the displacement recorded during an indentation test is due to the creep phenomena which has not been explicitly considered into our analysis. We have demonstrated in Chapter 6 that a measure of the time dependent deformation behavior of a material at the nanoscale can be obtained from nanoindentation by employing a soaking period at maximum load, as any increase in indentation depth at constant load will be a result of creep. We have so far provided first order estimates of the creeping process of the material by fitting the time dependent deformation during the swelling period to a logarithmic function, see Eq. (6.2). A more rigorous approach would be to consider analytical models of indentation on a viscoelastic or viscoplastic solid [50]. One such model has been proposed by Vandamme and Ulm [237] and its application to cementitious materials is the matter of current research. While the analysis of creep data obtained by indentation is still in its infancy, the technique holds great promise for shedding some light on the mechanisms of creep deformations.

13.3.4 Indentation on Cohesive-Frictional Material and Dual Indentation Technique

The extension of indentation analysis to cohesive-frictional materials presented in Chapters 2 and 5 has been performed within the framework of yield design approaches. This reductionist approach offers easy determination of the angle of friction and cohesion of the indented material through the dual indentation technique. A refined analysis through finite element simulation can incorporate the effects of elasticity, friction between indenter and indented material, hardening phenomena, time dependent phenomena, and provide additional information about the indentation response of such a system. Potential master curves of dimensional quantities can provide a similar framework to our dual indentation technique which will also incorporate the

effect of friction, and the non-associative flow rule and will reduce by design the sensitivity of the inverse analysis procedure on the input data.

13.3.5 C-S-H and Concrete Strength

From the analysis of the material properties at the three levels of microstructure, it emerged that the description of strength at Level 0 can be improved. The first order indentation estimates of strength at Level I are limited by the assumptions involved in the computational yield design approach presented in Chapter 2: time dependent and hardening phenomena have been neglected from our analysis. It remains uncertain whether the concept of hardness will remain to be valid in the presence of such phenomena. Further work in clarifying these issues and refining the first order indentation estimates of the C-S-H phases is required. In the absence of any other experimental determination the indentation strength estimates of C-S-H phases cannot be directly validated/invalidated but they can be tested against macroscopic experimental data. Alternative means of measuring their mechanical response can be of intense interest. The C-S-H strength was linked to macroscopic mechanical behavior with the use of analytical micromechanical schemes. Localized deformations such as fracture and damage that might take process during the loading to failure have not been explicitly considered in our analysis. At present, clearly the non-consideration of fracture is a limiting factor for the application of the model. This challenging endeavour needs to be accompanied with careful fracture experiments that will provide measurements for the C-S-H phases. Fracture testing at small scales has not been extensively discussed in the literature, but it would certainly prove to be of immense interest to analysis of this materials once developed.

13.4 Concluding Remarks

We have presented in this thesis a systematic procedure for upscaling mechanical properties of cement-based materials. We have verified the existence of a few material invariant properties that exist in all CBM systems, and shown through micromechanical modeling that the macroscopic diversity is essentially a consequence of volumetric mismatches between specimens composed of the same species. Modeling attempts initiated at the level of the individual con-

stituents essentially provide a direct link with physical chemistry. It is our hope that the current developments provide a refined understanding of the most widely used material on Earth, and a bridge between the cement-chemistry and mechanics communities, and serve as a showcase for modelling other complicated porous composites. Finally it is our hope that the results presented in this thesis will stimulate the interest for research to follow. The influx of new nanoscale information that become available through experimentation and advanced modeling are about to revolutionize our understanding of CBM and natural composites.

Appendix A

Bibliography

1. Aboudi J, (1991) 'Mechanics of composite materials: A unified micromechanical approach', Elsevier.

2. Acker, P., (2001) 'Micromechanical analysis of creep and shrinkage mechanisms', *In F.-J. Ulm, Z.P. Bazant, and F.H. Wittmann, editors, Creep, Shrinkage and Durability Mechanics of Concrete and other quasi-brittle Materials,* (Proc. Int. Conf. CONCREEP-6@MIT, Cambridge, MA, August 2001), Elsevier, Oxford UK, *15–25.*

3. Acker, P., and Ulm, F.-J., (2001) 'Creep and shrinkage of concrete: physical origins, practical measurements', *Nuclear Engineering and Design*, Vol. 203(2–3), 143—158.

4. Aitcin P.C., (2000) 'Cements of yesterday and today - Concrete of tomorrow', *Cement and Concrete Research*, 30(9):1349-1359.

5. Alexander K.M., Wardlaw J., and Gilbert D.J., (1968) 'Aggregate-cement bond, cement paste strength and the strength of concrete' in Proceedings of an international conference 'Structure of Concrete' edited by Brooks A.E., and Newman K., London.

6. Anderheggen, E., Knopfel, H. (1972) 'Finite element limit analysis using linear programming' *International Journal of Solids and Structures*, 8, 1413-1431.

7. Ang, A.H-S., and Tang. H.W., (1975) '*Probability concepts in engineering planning and design*' New York, Wiley.

8. Ashby, M. F. (1999) 'Materials selection in mechanical design', Oxford, Boston : Butterworth-Heinemann.

9. Atri R.R., Ravichandran K.S., and Jha S.K., (1999), 'Elastic properties of in-situ processed Ti-TiB composites measured by impulse excitation of vibration', *Materials Science and Engineering* A271, 150-159.

10. Balshin, M.Y. (1949), 'Dependence of mechanical properties of metal powders on porosity and limiting properties of metal – ceramic materials (in Russian)', Dokl. Akad. Nauk UzSSR 67 (5) 831– 834.

11. Barenblatt, G. I. (1996). 'Scaling, Self-Similarity and Intermediate Asymptotics', Cambridge, Cambridge University Press.

12. Barenblatt, G. I. (2003) 'Scaling' Cambridge University Press.

13. Barthelemy J.F., Dormieux L., (2003), 'Determination of the macroscopic strength criterion of a porous medium by nonlinear homogenization ' *IComptes Rendus Mecanique* 331 (4): 271-276.3

14. Barthelemy J.F., Dormieux L., (2004), 'A micromechanical approach to the strength criterion of Drucker-Prager materials reinforced by rigid inclusions' *International Journal for Numerical and Analytical Methods in Geomechanics* 28 (7-8): 565-582.

15. Bary, B., Bournazel, J.-P., and Bourdarot, E., (2000) 'Porodamage approach applied to hydrofracture analysis of concrete', *Journal of Engineering Mechanics*, 126(**9**), 937–943, 2000.

16. Bathe, K.J., (1996) 'Finite element procedures', Prentice Hall, Upper Saddle River, NJ.

17. Bazant, Z.P. (1972), 'Thermodynamics of interacting continua with surfaces and creep analysis of concrete structures', *Nuclear Engrg. and Design*, **20**, 477–505, 1972.

18. Bažant, Z.P., Hauggaard, A.B, Baweja, S., and Ulm, F.-J., (1997) 'Microprestress-solidification theory for concrete creep. I: Aging and drying effects', *Journal of Engineering Mechanics*, ASCE, 123(11), 1188–1194.

19. BBC News, http://www.che.utexas.edu/~truskett/news-items/bbc.htm.

20. Beaudoin J.J., (1983), 'Comparison of mechanical properties of compacted calcium hydroxide and portland cement paste systems', *Cement and Concrete Research*, 13:319-324.

21. Bentur, A., (1980) 'Effect of curing temperature on the pore structure of tricalcium silicate pastes', *Journal of Colloid and Interface Science*, Vol. 74 (2), 549—560.

22. Bernard, O., Ulm, F.-J., Germaine, J.T., (2003) "Volume and Deviator Basic Creep of Calcium Leached Cement-Based Materials", *Cement & Concrete Research*, Vol. **33**(8), 1155—1173,.

23. Bernard, O., Ulm, F.-J., Lemarchand, E., (2003) 'A multiscale micromechanics–hydration model for the early-age elastic properties of cement-based materials', *Cement & Concrete Research*, Vol. 33(9), 1293-1309.

24. Berryman, J.G., (2002) 'Extension of Poroelastic Analysis to Double-Porosity Materials: New Technique in Microgeomechanics', *Journal of Engineering Mechanics*, 128(**8**), 840–847.

25. Bhattacharya A. K. and Nix W. D., (1988) 'Analysis of elastic and plastic deformation associated with indentation testing of thin films on substrates' *International Journal of Solids and Structures*, 24(12), 1287-1298.

26. Biot, M.A., (1941) 'General theory of three dimensional consolidation." *Journal of Applied Physics*, **12**, 155—164.

27. Birchall J.D., Howard A.J., and Kendall K., (1981) 'Flexural strength and porosity of cements', *Nature,* **289**, 388–390.

28. Bishop, R.F., Hill R., and Mott N.F. (1945), 'The theory of indentation and hardness tests', *Proceedings Physics Society*, 57 (147), 172.

29. Bonaccorsi E., Merlino S., and Taylor H.F.W., (2004) 'The crystal structure of jennite, $Ca_9Si_6O_{18}(OH)_6.8H_2O$.' *Cement and Concrete Research* 34:1481-1488, 2004.

30. Borodich F. M., Keer L. M. and Korach C.S. (2003). 'Analytical Study of Fundamental Nanoindentation Test Relations for Indenters of Non-Ideal Shapes'. *Nanotechnology* 14, 803-808.

31. Borodich F. M. and Keer L. M. (2004). 'Evaluation of elastic modulus of materials by adhesive (no-slip) nano-indentation'. *Proc. R. Soc. Lond. A*, 460, 507-514.

32. Bottero, A., Negre, R., Pastor, J., Turgeman, S. (1980) 'Finite element method and limit analysis theory for soil mechanics problems', *Computer methods in applied mechans and engineering*, 22, 131-149.

33. Boussinesq, J. (1885) 'Applications des potentials a l' étudede l' equilibre et du mouvement des solides elastiques' *Gauthier-Villars.*

34. Brown, R. J. S., and Korringa, J., (1975) 'On the dependence of the elastic properties of a porous rock on the compressibility of a pore fluid', *Geophysics*, **40**, 608–616.

35. Bruck HA, Christman T, Rosakis AJ, Johnson WL. (1994) Quasi-static constitutive behavior of Zr41.25Ti13.75Ni10Cu12.5Be22.5 bulk amorphous alloys' *Scripta Metallurgica et Materialia* 30 (4): 429-434.

36. Brinell, J. A. (1901). 'Memoire sur les epreuves a bille en acier'. In *Congres International des Methodes d Essai des Materiaux de Construction*, Paris, Tome 2, 83-94.

37. Bucaille J.L, Stauss S., Felder E. ,Michler J. (2003) 'Determination of plastic properties of metals by instrumented indentation using different sharp indenters', *Acta Materialia*, **51**:1663-1678, 2003.

38. Buckle H in Westbrook J.W. and Conrad H., eds (1973) 'The Science of Hardness Testing and its Applications', American Society for Metals, Metal Park OH, pp. 453-491.

39. Bulychev, S.I., Alekhin, V. P., Shorshorov, M. Kh., Ternovskii, A. P. and Shnyrev, G. D., (1975) 'Determination of Youngs modulus according to an indentation diagram' Ind. Lab. , Transl: Zavodskaya Laboratoria) 41, 1409-1412, cited from [30].

40. Chateau, X. and Dormieux, L., (2002) 'Micromechanics of saturated and unsaturated porous media', *International Journal of Numerical Analysis Methods in Geomechanics*, **26**, 830–844.

41. Chen J.J., Thomas J.J., Taylor H.F.W., and Jennings H.M., (2004) 'Solubility and structure of calcium silicate hydrate.' *Cement and Concrete Research* 34:1499-1519.

42. Chen W.F., and Han D.J., (1988) '*Plasticity for Structural Engineers*', Springer-Verlag, New York.

43. Chen X., Vlassak J.J., (2001) 'Numerical study on the measurement of thin film mechanical properties by means of nanoindentation' *Journal of Materials Research* 16 (10): 2974-2982.

44. Cheng, L., Xia, X., Yu, W., Scriven, L. E. and Gerberich, W. W. (2000). 'Flat-Punch Indentation of Viscoelastic Material.' *Journal of Polymer Science Part B: Polymer Physics* 38, 10-22.

45. Cheng, L., Xia, X., Scriven, L. E. and Gerberich, W. W. (2004). 'Spherical-tip indentation of viscoelastic material.' *Mechanics of Materials.* In press.

46. Cheng C.M., Cheng Y.T., (1997). 'On the initial unloading slope in indentation of elastic-plastic solids by an indenter with an axisymmetric smooth profile', *Applied Physics Letters* 71 (18): 2623-2625, 1997

47. Cheng, Y.-T. and Cheng, C.-M. (1998). 'Relationships between hardness, elastic modulus, and the work of indentation.' *Applied Physics Letters* 73(5), 614–616.

48. Cheng, Y.-T. and Cheng, C.-M. (1998). 'Scaling relationships in conical indentation of elastic-perfectly plastic solids.' *International Journal Solids Struct.* 36(8), 1231–1243.

49. Cheng, Y. T. and Cheng, C. M. (2000). 'What is indentation hardness?', *Surface and Coatings Technology* 133-134, 417-424.

50. Cheng, Y. T. and Cheng, C. M. (2004).'Scaling, dimensional analysis, and indentation measurements.' *Materials Science. and Engineering* R44, 91-149.

51. Chitkara, N.R., and Butt, M.A. (1992) 'Numerical Construction of axisymmetric slip-line fields for indentation of thick blocks by rigid conical indenters and friction at the tool-metal interface', *International Journal of Mechanical Science*, **34(11)**:849-862.

52. Chollacoop, N., Dao, M. and Suresh, S. (2003). 'Depth sensing instrumented indentation with dual sharp indenters', *Acta Materialia*, 51, 3713-3729.

53. Christensen R.M., (1979), '*Mechanics of composite materials*', John Wiley and sons, New York.

54. Christensen R.M., (1990), 'A critical evaluation for a class of micromechanics models.' *Journal of the Mechanics and Physics of Solids* 38(3):379-404.

55. Conner RD, Dandliker RB, Johnson WL (1998) 'Mechanical properties of tungsten and steel fiber reinforced Zr41.25Ti13.75Cu12.5Ni10Be22.5 metallic glass matrix composites', *Acta Materialia* 46 (17): 6089-6102.

56. Cong X., Kirkpatrick R.J., (1995) 'Effects of the temperature and relative humidity on the structure of the CSH gel' *Cement and Concrete Research* 25(6):1237-1245.

57. Cong X., Kirkpatrick R.J., (1996) '^{29}Si MAS NMR study of the structure of calcium silicate hydrate' *Advanced Cement Based Materials* 3:144-156.

58. Constantinides, G. and Ulm, F.-J., (2002) 'The elastic properties of calcium-leached cement pastes and mortars:a multi-scale investigation', *MIT CEE Report* R02-01, (MS Thesis), Cambridge, MA.

59. Constantinides, G., Ulm, F.-J., and van Vliet, K.J. (2003). 'On the use of nanoindentation for cementitious materials', *Materials and Structures* 205 (Special issue of Concrete Science and Engineering) RILEM, 191–196.

60. Constantinides, G., and Ulm, F.-J. (2004). 'The effect of two types of C–S–H on the elasticity of cement-based materials: Results from nanoindentation and micromechanical modeling.' *Cement and Concrete Research*, Vol. 34 (1), 67–80.

61. Constantinides, G. and Ulm, F.-J. (2004). 'Stiffness, strength and creep behavior of heat-cured cement pastes: a multiscale indentation investigation.' MIT Research Report to Lafarge, Cambridge, MA, June 2004.

62. Coussy, O., (1995) 'Mechanics of porous continua', J. Wiley & Sons, Chichester, UK.

63. Coussy, O., Eymard, R., Lassabatère, T., (1998) 'Constitutive modelling of unsaturated drying deformable materials', *Journal of Engineering Mechanics*, 124(**6**), 658–667.

64. Coussy, O. (2004). 'Poromechanics', J. Wiley & Sons, Chichester, UK.

65. Dalgleish B.J. and Ibe K., (1981) 'Thin foil studies of hydrated cements', *Cement and Concrete Research* 11:729-739.

66. Dao, M., Chollacoop, N.,Van Vliet, K.J.,Venkatesh, T.A. and Suresh, S. (2001) 'Computational modeling of the forward and reverse problems in instrumented sharp indentation', *Acta Materialia* **49**, (19): 3899-3918

67. Delafargue, A. and Ulm, F.-J. (2004). 'Material invariant properties of shales: Nanoindentation and microporoelastic analysis.' MIT-CEE Research Report (SM-Thesis).

68. Diamond S. and Bonen D., (1993) 'Micostructure of hardened cement paste - A new interpretation', *Journal of American Ceramic Society*, 76 (12), 2993–2999.

69. Diamond S., (1999) 'Aspects of concrete porosity revesited', *Cement and Concrete Research* 29(8):1181-1188.

70. Doerner M. F. and Nix W. D. (1986). 'A Method for Interpreting the Data from Depth-Sensing Indentation Instruments. *Journal of Materials Research* 1, 601-609.

71. Donev, A., Cisse, I. Sachs, D., Variano, E.A., Stillinger, F.H., Connely, R., Torquato, S., Chaikin, P.M., (2004) 'Improving the density of jammed disordered packings using ellipsoids', *Science*, Vol. 303, 990–993.

72. Donovan P.E. (1989) 'Plastic-flow and fracture of $Pd_{40}Ni_{40}P_{20}$ metallic-glass under an indentor.' *Journal of materials science* (2): 523-535.

73. Dormieux, L., Molinari, A. and Kondo, D., (2002) 'Micromechanical approach to the behaviour of poroelastic materials', *Journ. Mechanics and Physics of Solids*, **50**, 2203–2231.

74. Dormieux, L. and Bourgeois, E., (2003) 'Introduction à la micromécanique des milieux poreux, *Presses de l'Ecole nationale des ponts et chaussees*, Paris, France.

75. Dormieux, L., Kondo, D., Ulm, F.-J., '*Microporomechanics*' in preparation.

76. Dotelli, G., and Mari, C.M., (2001) 'The evolution of cement paste hydration process by impedence spectroscopy', *Materials Science and Engineering*, A303, 54-59.

77. Durst K, Goken M, Vehoff H, (2004) 'Finite element study for nanoindentation measurements on two-phase materials' *Journal of Materials Research* 19 (1): 85-93.

78. Escalante-Garcia, J.I., and Sharp J.H., (1998) 'Effect of temperature on the hydration of the main clinker phases in portland cements: Part I, Neat Cements', *Cement and Concrete Research*, Vol. 38 (9), 1245—1257.

79. Escalante-Garcia, J.I., and Sharp J.H., (2001) 'The microstructure and mechanical properties of blended cements hydrated at various temperatures', *Cement and Concrete Research*, Vol. 31, 695—702.

80. Eshelby, J.D., (1957) 'The determination of the elastic field in an ellipsoidal inclusion', *Proceedings of the Royal Society of London*, **A 241**, 376–392.

81. Evans A., San Marchi C., and Mortensen A., (2003) *'Metal matrix composites. An introduction and a survey'*, Kluwer Academic Publisher.

82. Famy C., Scrivener K.L., Atkinson A., Brough A.R., (2002) 'Effect of an eraly and late heat treatment on the microstructure and composition of inner CSH product of Portland cement mortars', *Cement and Concrete Research* 32:269-278.

83. Faucon P., Delagrave A., Petit J.C., Richet C., Marchand J.M., and Zanni H., (1999) 'Aluminum incoporation in calcium silicate hydrates (C-S-H) depending on their Ca/Si ratio.' *Journal of Physical Chemistry B*, 103:7796-7802.

84. Fauchet, B., Coussy, O., Carrère, A., Tardieu, B., (1991) 'Poroplastic analysis of concrete dams and their foundations', *Dam Engineering* , Vol. II(**3**), 165-192.

85. Feldman R.F. and Sereda P.J., (1970) "A new model of hydrated cement and its practical implications," Engineering Journal Canada 53, pp. 53-59.

86. Fischer-Cripps, A. C. (2002). 'Nanoindentation'. Springer Verlag, New-York.

87. Fremond, M., and Salencon J. (1973) 'Limit analysis by finite elemnt methods' In A.C. Palmer, editor, Proceedings of teh symposium on role of plasticity in soil mechanics, Cambridge, UK.

88. Futakawa M, Wakui T, Tanabe Y, Ioka I (2001) 'Identification of the constitutive equation by the indentation technique using plural indenters with different apex angles', Journal of Materials Reserach 16 (8): 2283-2292.

89. Galin, L. A. (1951). 'Contact Problems in Theory of Elasticity', translated by H. Moss. In: Sneddon, I. N. (Ed.), North Carolina State College.

90. Garboczi, E.J., (1993) 'Computational materials science of cement-based materials', *Materials and Structures*, **26**(2), 191–195.

91. Gatty L., Bonnamy S., Feylessoufi A., Clinard C., Richard P., Van Damme H., (2001) 'A transmission electron microscopy study of interfaces and matrix homogeneity in ultra-high-performance cement-based materials' *Journal of Materials Science* 36:4013-4026.

92. Ganneau, F.P., Constantinides G., and Ulm, F.-J. (2004). 'Dual-Indentation technique for the assesment of strength properties of cohesive-frictional material',will submited to *International Journal of Solids and Structures* (in press).

93. Ganneau, F.P. and Ulm, F.-J. (2004). 'From nanohardness to strength properties of cohesive-frictional Materials — Application to shale materials', MIT-CEE Research Report (SM-Thesis).

94. Gao H.J., Chiu C.H., Lee J., (1992) 'Elastic contact versus indentation modeling of multilayered materials' *International Journal of Solids and Structures* 29 (20): 2471-2492.

95. Gartner E., (2004), 'Industrially interesting approaches to "low-CO2" cements', *Cement and Concrete Research*, **34**(9), 1489–1498.

96. Gassmann, F., (1951) 'Über die elastizität poröser medien', *Vierteljahrsschrift der Naturforschenden Gesellschaft in Zürich*, **96**, 1–23 (in German).

97. Giannakopoulos, A.E. and Larsson, P. L. and Vestergaard, R. (1994) 'Analysis of vickers indentation', *International Journal of Solids and Structures*, 31(19):2679–2708.

98. Giannakopoulos, A.E. and Suresh, S. (1999) 'Determination of elastoplastic properties by instrumented sharp indentation', *Scripta Materialia*, **40**(10):1191–1198.

99. Gibson, L.J. and Ashby, M.F., 'Cellular Solids: Structure and Properties', Second Edition, Cambridge University Press, Cambridge, U.K, 1997.

100. Gilbert CJ, Schroeder V, Ritchie R.O., (1996) 'Mechanisms for fracture and fatigue-crack propagation in a bulk metallic glass' Mettalurgical and materials Transactions APhysical Metallurgy and Materials Science 30 (7): 1739-1753.

101. Gmira, A., Zabat, M., Pellenq, R.J.-M., and Van Damme, H., (2004) 'Microscopic physical basis of the poromechanical behavior of cement-based materials', *Materials and Structures (Special issue of Concrete Science and Engineering)*, Vol. 37 (265), 3–14.

102. Goodman L.E. (1962) 'Contact stress analysis of normally loaded rough spheres', Journal of Aplied Mechanics 29, 512-522.

103. Gorsse S., Le Petitcorps Y., Matar S., and Rebillat F., (2003) 'Investigation of the Young's modulus of TiB needles in situ produced in titanium matrix composite' *Materials Science and Engineering A-Structural Materials Properties Microstructure and Processing* 340 (1-2): 80-87

104. Gregory, J.R. and Spearing, S.M., (2005), 'Nanoindentation of neat and in situ polymers in polymer matrix composites.' *Composite Science and Technology*, 65, 595-607.

105. Groves G.W., (1987) 'TEM studies of cement hydration', *Materials Reserach Society Symposium Proceedings*, 85:3-12.

106. Hamid S.A., (1981) 'The crystal structure of 11 Å natural tobermorite, $Ca_{2.25}[Si_3O_{7.5}(OH)_{1.5}].1H_2O$.' *Z. Kristallogr.* 154:189.

107. Harding, J. W. and Sneddon, I. N. (1945). 'The elastic stress field produced by the indentation of the plane surface of a semi-infinite elastic solid by a rigid punch'. *Proc. Cambridge Phil. Soc.* 41, 16-26.

108. Hansen T.C., (1986) 'Physical structure of hardened cement paste. A classical approach.' *Materials and Structures*, **19**(114):423-436.

109. Hashin, Z., and Monteiro, P.J.M., (2002) 'An inverse method to determine the elastic properties of the interphase between the aggregate and the cement paste', *Cement and Concrete Research*, **32**(8), 1291–1300.

110. Hasselman, D.P.H., (1963) 'Relation between effects of porosity on strength and on young's modulus of elasticity of polycrystalline materials, *Journal of the American Ceramic Society* 46 (11) 564–565.

111. Hay J.C, Bolshakov A, Pharr GM, (1999) 'A critical examination of the fundamental relations used in the analysis of nanoindentation data' *Journal of Materials Research* 14 (6): 2296-2305.

112. He Y, Schwarz RB, Mandrus D, and Jacobson L. (1996) 'Elastic moduli, density, and structural relaxation in bulk amorphous Zr41.2Ti13.8Cu12.5Ni10Be22.5 alloy', Journal of non-crystalline solids 207: 602-606 Part 2.

113. Helmuth R.A., and Turk D.H., (1966) 'Elastic moduli of hardened portland cement and tricalcium silicate pastes: effect of porosity', Symposium on structure of portland cement paste and concrete (special report 90), Highway research board, Washington DC.

114. Hertz, H. (1881) 'On the contact of elastic solids (in german), zeitschrift fur die reine und angewandte mathematik', *English translation in miscellaneous papers (translated by D.E. Jones and G.A. Schott):***99**.146-62. Macmillan, London, UK, 1986, **92**:156–71.

115. Heukamp, F. H., Ulm, F. J. and Germaine, J. T., (2001) 'Mechanical properties of calcium-leached cement pastes: Triaxial stress states and the influence of the pore pressures', *Cement and Concrete Research*, **31**(5), 767–774.

116. Heukamp, F.H., Ulm, F.-J., (2002) 'Chemomechanics of calcium leaching of cement-based materials at different scales: The role of CH-dissolution and C-S-H degradation on strength and durability performance of materials and structures', MIT-CEE Report R02-03 (D.Sc.-Dissertation), Cambridge, MA.

117. Heukamp, F.H., Ulm, F,-J., Germaine, J.T., (2003) 'Poroplastic properties of calcium leached cement-based materials", *Cement & Concrete Research*, Vol. **33**(8), 1127—1136.

118. Heukamp F.H., Lemarchand E., Ulm F-J., (2005) 'The effect of interfacial properties on the cohesion of highly filled composite materials' *International Journal of Solids and Structures* 42 (1): 287-305.

119. Hill R. (1950), '*The Mathematical Theory of Plasticity*', Oxford University Press, Oxford,

120. Hill R., (1952) 'The Elastic Behavior of a Crystalline Aggregate', Proceedings of the Physical Society of London A, 65, 349-354.

121. Hopkins, H.G., Cox A.D., Eason, G. (1961) 'Axially symmetric plastic deformation in soils', Philosophical Transactions, Royal Society, A264, 1-45.

122. Houlsby, G.T., Wroth,C.P. (1982) 'Determination of undrained strengths by cone penetration tests. In Proc. 2nd Europena Symposium on Penetration Testing, Amsterdam, NL.

123. Hutchinson J.W. (2000) 'Plasticity at the micron scale' *International Journal of Solids and Structures*, **37(1-2)**:2225-2238.

124. Hysitron Inc (2001) 'Triboindenter users manual', Minneapolis, MN.

125. Igarashi, S., Bentur, A. and Mindess, S., (1996) 'Characterization of the microstructure and strength of cement paste by microhardness testing' *Advances in cement research*, **8**(30):877–92.

126. Ishida, H., Sasaki, K., Okada, Y., and Mitsuda, T., (1992) 'Highly reactive b-Dicalcium silicate: III, Hydration behavior at 40-80 °C', *Journal of the American Ceramic Society*, 75 (9), 2541—2546.

127. ISO 14577 (2002)'Metallic Materials - Instrumented indentation test for hardness and materials parameters'

128. Jaeger, H.M., and Nagel, S. R., (1992) 'Physics of granular state', *Science*, Vol. 255, No. 5051, 1523–1531.

129. Jennings, H. M., and Tennis P.D., (1994) 'A model for the developing microstructure in portland cement pastes', *Journal of American Ceramic Society*, 77 (12), 3161–72.

130. Jennings, H. M., (2000) 'A model for the microstructure of calcium silicate hydrate in cement paste', *Cement and Concrete Research*, 30 (1), 101–116.

131. Jennings, H. M., (2004) 'Colloid model of C-S-H and implications to the problem of creep and shrinkage', *Materials and Structures (Special issue of Concrete Science and Engineering)*, Vol. 37 (265), 59–70,.

132. Johnson, K. L. (1985) 'Contact mechanics', Cambridge University Press.

133. Jonsson B., Wennerstrom H., Nonat A., amd Cabane B., (2004) 'Onset of cohesion in cement paste', *Langmuir* 20:6702-6709.

134. Kaplan, M. F. (1989) '*Concrete Radiation Shielding*', Longman Scientific and Technical, Concrete Design and Construction, New York.

135. Kawamura Y., Kato H., Inoue A., and Masumoto T., (1996) 'Effects of extrusion conditions on mechanical properties in Zr-Al-Ni-Cu glassy powder compacts', Journal of Materials Science and Engineering, A219, 39-43.

136. Kholmyansky, M., Kogan, E. and Kovler, K., (1994) 'On the hardness determination of fine-grained concrete', *Materials and Structures*, **27**(174):584-587.

137. King, R.B, (1987) 'Elastic analysis of some punch problems for a layered medium', *International Journal of Solids and Structures*, **23**:1657-1664.

138. Kjellsen, K. O., (1996) 'Heat curing and post-heat curing regimes of high performance concrete: influence on microstructure and C-S-H composition', *Cement and Concrete Research*, Vol. 26 (2), 297—307.

139. Kozola BD, Shen YL, (2003) 'A mechanistic analysis of the correlation between overall strength and indentation hardness in discontinuously reinforced aluminum' *Journal of Materials Science* 38 (5): 901-907

140. Kreher W. (1990), 'Residual stresses and stored elastic energy of composites and polycrystals' Journal of the mechanics and physics of solids 38 (1): 115-128.

141. Kroner E., (1971) 'Statistical continuum mechanics', CISM, Courses and Lectures - No 92.

142. Lambe W.T., and Whitman R.V., 'Soil mechanics', Series in soil engineering, John Wiley, New York, 1969.

143. Landau, D. (1943) "Hardness", The nitralloy corporation, New York.

144. Hewlett P.C., editor (1998) '*Lea's chemistry of cement and concrete*' John Wiley & Sons Inc., Ney York.

145. Le Bellego, C., (2001) 'Couplage chimie-mecanique dans les structures en beton attaquees par l'eau: etude experimentale et analyse numerique', *PhD.-Dissertation*, ENS de Cachan, France.

146. Lee, E.H., (1955). 'Stress analysis in visco-elastic bodies'. *Quarterly Applied Mathematics* 13, 183–190.

147. Lee, E.H., Radok, J.R.M., (1960). 'The contact problem for viscoelastic bodies'. *Jounal of Applied Mechanics* 27, 438–444.

148. Leggoe JW, (2004) 'Determination of the elastic modulus of microscale ceramic particles via nanoindentation' *Journal of Materials Research* 19 (8): 2437-2447.

149. Lemarchand, E., Ulm, F.-J., and Dormieux, L., (2002) 'Effect of inclusions on friction coefficient of highly filled composite materials, *Journal of Engineering Mechanics*, ASCE, Vol. 128(8), 876—884, 2002.

150. Lesko S., Lesniewska E., Nonat A., Mutin J.C., Goudonnet J.P., (2001) 'Investigation by atomic force microscopy of forces at the origin of cement cohesion' Ultramicroscopy 86 (1-2).

151. Lewandowski J.J., Lowhaphandu P. (2002) 'Effects of hydrostatic pressure on the flow and fracture of a bulk amorphous metal.', *Philosophical Magazine A* 82 (17-18): 3427-3441.

152. Li, G.Q., Zhao, Y., Pang, S.S. and Li, Y.Q., (1999) 'Effective Young's modulus estimation of concrete", *Cement & Concrete Research*, **29**(9), 1455–1462.

153. Li, G.Q., Zhao, Y., and Pang, S.S., (1999) 'Four-phase Sphere Modeling of Effective Bulk Modulus of Concrete', *Cement & Concrete Research*, **29**(6), 839–845.

154. Liu CT, Heatherly L, Easton DS, Carmichael CA, Schneibel JH, Chen CH, Wright JL, Yoo MH, Horton JA, Inoue A (1998) 'Test environments and mechanical properties of Zr-base bulk amorphous alloys' Metallurgical and Materials Transactions A-Physical Metallurgy and Materials Science 29 (7): 1811-1820.

155. Li J, Chou TW, (1997) 'Elastic field of a thin-film/substrate system under an axisymmetric loading' *International Journal of Solids and Structures* 34 (35-36): 4463-4478.

156. Locket F.J. (1963) 'Indentation of a rigid/plastic material by a conical indenter', *Journal of the Mechanics and Physics of Solids*, 11(5), 345-355.

157. Love, A.E.H. (1939). 'Boussinesq's problem for a rigid cone'. *Quart. Journal Math.*, 10, 161-175.

158. Lu J. and Ravichandran G. (2003) 'Pressure-dependent flow behavior of $Zr_{41.2}Ti_{13.8}Cu_{12.5}Ni_{10}Be_{22.5}$ bulk metallic glass' *Journal of Materials Research* 18(9), 2039–2049.

159. Lund A.C., Schuh C.A. (2003) 'Yield surface of a simulated metallic glass.', *Acta Materialia* 51 (18): 5399-5411.

160. Lyamin, A.V., Sloan, S.W., (2002), 'Lower bound limit analysis using non-linear programming.' *International Journal of Numerical Analysis Methods in Geomechanics*, 26, 181–216.

161. Lyamin, A.V., Sloan, S.W., (2002), 'Upper bound limit analysis using linear finite elements and non-linear programming.' *International Journal of Numerical Methods in Engineering*, 55, 573–611.

162. Lysmer, L. (1970) 'Limit analysis of plane problems in soil mechanics.' ASCE Journal of the soil mechanics and foundation division, 96, 1311-1334, 1970.

163. Martin B.R., Burr D.B., and Sharkey N.A., "Skeletal tissue mechanics", Springer, New York, 1998.

164. Maso J.C., (1996) '*Intrefacial transition zone in concrete*', Report 11, RILEM.

165. Matar, M. and Salençon, J. (1982). 'Capacité portante des fondations superficielles circulaires.' Journal de Mechanique Théorique et Appliquée, 1(2), 237—267. Available in English in 'Foundation Engineering, Volume 1, Soil properties-Foundation design and construction', Presse de l'Ecole Nationale des Ponts et Chaussées, France.

166. Mayo, M. J., Siegel, R. W., Narayanasamy, A., and Nix, A. D., (1990) 'Mechanical properties of nanophase TiO as determined by nanoindentation', *Journal of Materials Research*, 5(5), 1073–1082.

167. Mehta P.K. and Monteiro P.J.M., (1993) 'Concrete: structures, properties and materials' Prentice Hall, 2nd edition.

168. Meschke, G., and Grasberger, S., (2003) 'Numerical modeling of coupled hygromechanical degradation of cementitious materials', *Journal of Engineering Mechanics*, 129(**4**), 383–392.

169. Mindess S., Young J.F., and Darwin D., (2002) ' *Concrete*', 2nd Edition, Prentice Hall, Upper Saddle River, NJ, USA.

170. Micromaterials Ltd. (2002) 'Micromaterials nanotest user manual', Wrexham U.K.

171. Monteiro, P.J.M., and Chang, C.T., (1995) 'The elastic moduli of calcium hydroxide', *Cement and Concrete Research*, **25**(8), 1605–1609.

172. Mori, T. and Tanaka, K., (1973) 'Average stress in matrix and average elastic energy of materials with misfitting inclusions', *Acta Metallurgica*, **21**(5), 1605–1609.

173. Moser B., (2004) Personal Communication.

174. Mossakovskii V.I. (1954) 'The fundamental mixed problem of the theory of elasticity for a half-space with a circular line seperating the boundary conditions' Jornal of Applied Mathematics and Mechanics 18, 187-196 (in Russian).

175. Mossakovskii V.I. (1963) 'Compression of elastic bodies under conditions of adhesion (axisymmetric case)' Jornal of Applied Mathematics and Mechanics 27, 630-643 (in Russian).

176. Mukai T., Nieh T.G., Kawamura Y., Inoue A., and Higashi K., (2002) 'Dynamic response of a Pd40Ni40P20 bulk metallic glass in tension', Scripta Materialia, 46(1), 43-47.

177. Munro, R.G., (2000) 'Material Properties of Titanium Diboride', *J. Res. Natl. Inst. Stand. Technol.* 105, 709-720 (2000)]

178. Mura, T.(1982) 'Micromechanics of Defects in Solids', Martinus Nijhoff, Publishers.

179. 'The concrete microscopy library', http://sftp.cee.uiuc.edu/research/dlange/micro/

180. Neville A.M., (1995) 'Properties of Concrete', 4th Edition, Longman Group Limited, Essex, England.

181. Nix WD, Gao HJ (1998) 'Indentation size effects in crystalline materials: A law for strain gradient plasticity' *Journal of the Mechanics and Physics of Solids* 46 (3): 411-425.

182. Nonat A., and Lecoq X., 'The structure, stochiometry and properties of C-S-H prepared by C3S hydration under controlled solution.' in: P.Colombet, A.R. Grimmer, H. Zanni, P.Sozzani (Eds), *Nuclear Magnetic Resonance Spectroscopy of Cement Based Materials*, Springler, Berlin, 1996, 197-207.

183. Nonat A., 'The structure and stochiometry of C-S-H.' *Cement and Concrete Research* 34:1521-1528, 2004.

184. Oliver, W.C. and Pharr, G.M. (1992). 'An improved technique for determining hardness and elastic modulus using load and displacement sensing indentation experiments.' *Journal Mater.* Research, 7(6), 1564–1583.

185. Oliver, W.C. and Pharr, G.M. (2004). 'Measurement of hardness and elastic modulus by instrumented indentation: Advances in understanding and refinements to methodology.' *Journal Mater.* Research, 19(1), 3–20.

186. Pann K.S., Yen T., Tang C-W, and Lin T.D., (2003), 'New strength model based on water-cement ratio and capillary porosity' *ACI Materials Journal, Technical Paper,* 311-317.

187. Parrott L.J., (1977). 'Basic creep, drying creep and shrinkage of a mature cement paste after a heat cycle' *Cement and Concrete Research*, 7:597-604.

188. Pastor J. (1976) 'Application de l'analyse limite a l'etude de la stabilite des pentes et des talus' Ph.D. Dissirtation, USMG, Grenoble, France.

189. Pellenq R.J.M., Van Damme H., (2004) 'Why does concrete set?: The nature of cohesion forces in hardened cement-based materials' *MRS Bulletin* 29 (5): 319-323.

190. Perriot A, Barthel E, (2004) 'Elastic contact to a coated half-space: Effective elastic modulus and real penetration' *Journal of Materials* Research, 19 (2): 600-608.

191. Pharr, G. M., Oliver, W. C. and Brotzen, F. R. (1992). 'On the generality of the relationship among contact stiffness, contact area, and elastic modulus during indentation'. *Journal Materials* Research, 7(3), 613-617.

192. Plassard C, Lesniewska E, Pochard I, Nonat A., (2004) 'Investigation of the surface structure and elastic properties of calcium silicate hydrates at the nanoscale.', Ultramicroscopy 100 (3-4): 331-338.

193. Porteneuve, C. (2001) 'Characterisation des betons par resonance magnetique nucleaire: application a l"etude de l'alteration par l'eau' PhD thesis, Universite Paris VI, France, (in French).

194. Powers T.C. and Brownyard T.L., (1948) 'Studies of the Physical Properties of Hardened Portland Cement Paste', *PCA Bulletin* **22.**

195. Rice, J. R., (1975) 'On the stability of dilatant hardening for saturated rock masses', *Journal of Geophysics Research*, **80**, 1531–1536.

196. Richardson I.G., Rodger S.A., Groves G.W., (1989) 'The porosity and pores structure of cement paste as revealed by electron microscopy', *Materials Reserach Society Symposium Proceedings*, 137:313-318.

197. Richardson I.G. and Groves G.W., (1992)'Models for the composition and structure of calcium silicate hydrate (C-S-H) gel in hardened tricalcium silicate pastes' *Cement and Concrete Research*, 22:1001-1010.

198. Richardson I.G., (1999) 'The nature of C-S-H in hardened cements' *Cement and Concrete Research*, 29:1131-1147.

199. Richardson I.G., (2004) 'Tobermorite/jennite- and tobermorite/calcium hydroxide-based models for the structure of C-S-H:applicability to hardened pastes of tricalcium silicate,β-dicalium silicate, Portland cement, and blends of Portland cement with blast-furnace slag, metakaolin, or silica fume.' *Cement and Concrete Research*, 34:1733-1777.

200. Rösler M. and Odler I., (1985) 'Investigations on the relationship between porosity, structure and strength of hydrated portland cement pastes I: Effect of porosity', *Cement and Concrete Research* 15:320-330.

201. Ryshkewitch, E. (1953) 'Compression strength of porous sintered alumina and zirconia', *Journal of the American Ceramic Society*, 36 (2) 65– 68.

202. Sahay S.S., Ravichandran K.S., Atri R.R., Chen B., and Rubin J., (1999), 'Evolution of microstructure and phases in *in situ* processed Ti-TiB composites containing high volume of whiskers' *Journal of Materials Research* 14(11) 4214-4223.

203. Saito T., Furuta T., Yamaguchi T., 'Development of low cost titanium matrix composite' in: 'Recent advances in titanium metal matrix composites': proceedings of a symposium held during Materials Week, (1994), in Rosemont, Illinois, edited by F.H. Froes, J. Storer.

204. Salençon, J. (1983) Calcul à la rupture et analyse limite. Presses de l'Ecole nationale des ponts et chaussées, Paris, France.

205. Scherer G.W. (1999), 'Structure and properties of gels', *Cement and Concrete Research* 29:1149-1157.

206. Schuh C.A. and Nieh T.G., (2004). 'A survey of intrumented indentation studies on metallic glasses' *Journal of Materials Research* 19(1), 46–57.

207. Scrivener K.L., Patell H.H., Pratt P.L., and Parrott L.J. (1985), 'Analysis of phases in cement paste using backscattered electron images, methanol adsorption, and thermogravimetric analysis', *Materials Reserach Society Symposium Proceedings*, 85:67-76.

208. 'Construction materials: From innovation to conservation', Editors: Scrivener K. and Van Damme H.V., MRS Bulletin, 2004

209. Sloane, N. J. A. (1998), 'Kepler's conjecture confirmed', *Nature*, Vol. 395, 435–436.

210. Sloan, S.W., (1988), 'Lower bound limit analysis using finite elements and linear programming' *International Journal of Numerical Analysis Methods in Geomechanics*, 12, 61–77.

211. Sloan, S.W., (1988), 'A steepest edge active set algorithm for solving sparse linear programming problems' *International Journal of Numerical Analysis Methods in Geomechanics*, 12, 2671-2685.

212. Sloan, S.W., Kleeman, P.W., (1995), 'Upper bound limit analysis with discontinuous velocity fields' *Computational Methods in Applied Mechanics and Engninnering*, 127, 293–314.

213. Sneddon, I. (1965) 'The relation between load and penetration in the axisymmetric boussinesq problem for a punch of arbitrary profile', *International Journal of Engineering Science*, **3**:47-57.

214. Sneddon, I. editor (1977). 'Application of Integral Transforms in the Theory of Elasticity.' Springer Verlag, Wien-New York.

215. Spence, D.A. (1968) 'Self similar solutions to adhesive contact problems with increamental loading' *Proceeedings of Royal Society of London A* 305, 55-80.

216. Stillwell, N.A., and Tabor D. (1961), 'Elastic recovery of conical indentations', *Proceedings of Physical Society*, 78 169-179.

217. Subhash G, Dowding RJ, Kecskes LJ. (2002) 'Characterization of uniaxial compressive response of bulk amorphous Zr-Ti-Cu-Ni-Be alloy', *Materials Science and Engineering A-Structural Materials Properties Microstructure and Processing* 334 (1-2): 33-40.

218. Suquet, P., (1997) 'Effective properties of non-linear composites' In: Suquet, P., Editor, *Continuum Micromechanics*, number 377 in CISM Courses and Lectures, pages 197-264, New York, Springer.

219. Suresh, S. and Giannakopoulos, A.E. (1998) 'Report Inst 2/98', *Massachusetts Institute of Technology.*

220. Suresh, S., Giannakopoulos, A.E. and Alcala, J. (1997) 'Spherical indentation of compositionally graded materials: Theory and experiments', *Acta Materialia*, **45**(4):1307–1321.

221. Swaddiwudhipong S, Tho KK, Liu ZS, Zeng K. (2005) 'Material characterization based on dual indenters', *International Journal of Solids and Structures* 42 (1): 69-83.

222. Swadener, J. G. and Pharr, G. M., (2001). 'Indentation Modulus of Elastically Anisotropic Half-Spaces by Cones and Parabolae of Revolution.' *Philosophical Magazine A,* 81, 447-466.

223. Tabor, D. (2000) 'The hardness of metals'. Oxford classical texts in the physical sciences-First published 1951.

224. Taplin J.H., (1959) 'A method for following the hydration reaction in Portald cement pastes', *Australian Journal of Applied Sciences*, 10:329-345.

225. Taylor, H.F.W., (1984) 'Studies on the chemistry and microstructure of cement pastes' *Proceedings of British Ceramic Society*, 35:65-82.

226. Taylor, H.F.W., (1997) '*Cement Chemistry'*, 2nd Edition, Thomas Telford, London.

227. Tennis, P.D. and Jennings, H.M., (2000) 'A model for two types of calcium silicate hydrate in the microstructure of portland cement pastes', *Cement and Concrete Research*, **30**(6), 855–863.

228. Terzaghi, K., (1925) 'Principles of soil mechanics. A summary of experimental results of clay and sand', *Eng. News Rec.*, 3—98.

229. Thomas J.J, Jennings H.M., and Allen A.J., (1998) 'The surface area of cement paste as measured by neutron scattering: Evidence for two C-S-H morphologies', *Cement and Concrete Research* 28(6):897-905.

230. Thomas, J.J., and Jennings, H.M., (2002) 'Effect of heat treatment on the pore structure and drying shrinkage behavior of hydrated cement paste', *Journal of the American Ceramic Society*, 85 (9), 2293—2298.

231. Troczynski, T., (2004) 'Bioceramics - A concrete solution', *Nature Materials* 3 (1): 13-14.

232. Ulm, F.-J. and Coussy, O. (2003). Mechanics and durability of solids. Vol. I: Solid Mechanics. Prentice Hall, Upper Saddle River, New Jersey.

233. Ulm, F.-J., Heukamp, F.H., Germaine, J.T., (2002) 'Residual design strength of cement-based materials for nuclear waste storage systems', *Nuclear Engineering and Design*, Vol. **211**(1), 51–60.

234. Ulm, F.-J., (2003) 'Chemomechanics of concrete at finer scales', Materials and Structures, Vol. **36**, 426–438.

235. Ulm, F.-J., Constantinides, G. and Heukamp, F.H., (2004) 'Is concrete a poromechanics material? – A multiscale investigation of poroelastic properties', *Materials and Structures (Special issue of Concrete Science and Engineering)*, Vol. 37 (265), 43–58.

236. Vaidyanathan R., Dao. M., Ravichandran G., and Suresh S., (2001). 'Study of the mechanical deformation in bulk metallic glass through instrumented indentation' *Acta Materialia* 49(18), 3781–3789.

237. Vandamme, M. and Ulm, F-J., (2005) 'Viscoelastic solutions for conical indentation' *accepted for publication in International Journal of Solids and Structures.*

238. Van Vliet, K.J., Prchlik, L., and Smith J.F. (2004), 'Direct measurement of indentation frame compliance', *Journal of Materials Research*, 19(1) 325-331.

239. Velez, K.,Maximilien, S., Damidot, D., Fantozzi, G. and Sorrentino, F., (2001) 'Determination by nanoindentation of elastic modulus and hardness of pure constituents of portland cement clinker', *Cement and Concrete Research*, 31 (4), 555–561.

240. Vichit-Vadakan W., and Scherer G.W., (2002) 'Measuring Permeability of Rigid Materials by a Beam-Bending Method: III. Cement Paste', *Journal American Ceramic Society* **85**(6), 1537–1544.

241. Wegst U.G.K. and Ashby M.F., "The mechanical efficiency of natural materials", Philosophical Magazine,Vol. 84 (21), 2167-2181, July 2004.

242. Wei Y. and Hutchinson J.W (2003) 'Hardness trends in micron scale indentation' *Journal of the Mechanics and Physics of Solids*, 51(11-12), 2037-2056.

243. Weitz, D.A., (2004), "Packing in the Spheres", *Science*, vol 303, 968-969.

244. Weisstein, E.W., 'Packing Density', From MathWorld–A Wolfram Web Resource. *http://mathworld.wolfram.com/PackingDensity.html*

245. Williams, S.R. (1942) 'Hardness and hardness measurements', American society of metals, Cleveland, Ohio.

246. Wittmann, F.H., (1974) 'Bestimmung physikalischer Eigenschaften des Zementsteins', *Deutscher Ausschuss fuer Stahlbeton*, Heft **232**, W. Ernst & Sohn, Berlin, Germany, 1–63 (in German).

247. Wittmann, F.H., (1986) 'Estimation of the modulus of elasticity of calcium hydroxide' *Cement and Concrete Research* 16(6):971-972.

248. Wittmann, F.H., (1988) 'Creep and shrinkage mechanisms in concrete', *In Z.P. Bazant and F.H. Wittmann, editors, Creep & Shrinkage of Concrete, J. Wiley & Sons, New York.*

249. Wright, W.J., Saha, J., and Nix W.D. (2001) 'Deformation mechanics of the $Zr_{40}Ti_{14}Cu_{12}Bi_{24}Ni_{10}$ bulk metallic glass', Materials Transactions, 42(4):642-649.

250. Yang C.C., and Hunag R., (1996) 'Double inclusion model for approximate elastic moduli of concrete material' *Cement & Concrete Research*, **26**(1), 83–91.

251. Young, J. F., (1988) 'Investigations of calcium silicate hydrate structure using silicon-29 nuclear magnetic resonance spectroscopy', *Journal of the American Ceramic Society*, 71 (3), C-118—C120.

252. Yu H.Y., Sanday S.C., Rath B.B., (1990) 'The effect of substrate in the elastic properties of films determined by the indentation test - Axisymmetric Boussinesq problem' *Journal of the Mechanics and Physics of Solids* 38 (6): 745-764.

253. Zaoui, A., (2002) 'Continuum micromechanics: survey', *Journal of Engineering Mechanics*, **128**(8), 808–816.

254. Zhang ZF, Eckert J, Schultz L. (2003) 'Difference in compressive and tensile fracture mechanisms of $Zr_{59}Cu_{20}Al_{10}Ni_8Ti_3$ bulk metallic glass.' *Acta Materialia* 51 (4): 1167-1179.

255. Zimmerman R.W., King M.S., and Monteiro P.J.M, (1986) 'The elastic moduli of mortar as a porous granular material', *Cement & Concrete Research*, Vol. **16**, 239-245.

256. Zohdi T.I., Monteiro P.J.M., and Lamour V., (2002) ' Extraction of elastic moduli from granular compacts', *International Journal of Fracture* 115:L49-L54.

257. Technical Library of Lafarge: http://www.ductal-lafarge.com/

Appendix B

Notations

In this chapter we introduce the notations that we use throughout this thesis.

B.1 Tensor Notations

$\underline{z}$ = Vector.

$\boldsymbol{\sigma}$ = Second order tensor.

$\mathbf{E}$ = Uniform second order tensor.

$\mathbf{1}$ = Second order identity tensor.

E_{ij}, σ_{ij} = Second order tensor components. $i, j \in \{1, 3\}$.

$\mathbb{C}$ = forth order tensor.

$\mathbb{I}$ = Forth order identity tensor.

C_{ijkl} = forth order tensor components. $i, j, k, l \in \{1, 3\}$.

'$\cdot$' refers to scalar products, and single tensorial contractions.

':' refers to tensorial double contractions.

For operations on tensors written with the index notation, summation is performed on repeated indices, i.e., $a_{ij}b_{jk} = c_{ik}$.

B.2 Average Operators

The volume average of the field quantity $A(\underline{z})$ defined in a domain Ω of volume V_Ω reads:

$$\langle A \rangle_\Omega = \frac{1}{V_\Omega} \int_\Omega A(\underline{z}) d\Omega \tag{B.1}$$

The mean value of a quantity B defined in a statistical sense will be denoted by μ_B:

$$\mu_B = \frac{1}{N} \sum_{i=1}^{N} B_i \tag{B.2}$$

where N is the number of tests.

B.3 Levels of Material Representation

For purposes of material modeling we break the cement-based microstructure representation into four characteristic levels which are separated by at least one order of magnitude in length scale.

- Level 0: This is the atomic scale level characterizing the crystal structure of individual components composing the heterogeneous material. In the case of the C-S-H, this is the level were the crystal structure characterizes the response of the individual particles. Homogenization of colloidal particles with porosity yields estimates of the two types of C-S-H.

- Level I: This is the level where the individual colloidal particles agglomerate to form two distinct types of C-S-H. Homogenization of this level yields the C-S-H matrix.

- Level II: This is the level where the C-S-H matrix accommodates the capillary pores and residues of unhydrated cement. Homogenization of this level yields properties of cement paste.

- Level II: This is the level were cement paste is reinforced by sand or aggregates. Homogenization of this level yields mortar or concrete.

Appendix C

Eshelby's Solution

Eshelby in a series of papers (see Ref. [80] and citations in Ref. [178]) set the foundations for what is now known as micromechanics. An ellipsoidal inclusion is considered in an isotropic infinite body subjected to a uniform strain at infinity. It is remarkable to see that his solutions suggests that the strain and stress fields inside the inclusion are uniform. Through his analysis he managed to link microscopic strains within the inclusion, $\boldsymbol{\varepsilon}_p$, with macroscopic strains applied in the boundary, $\mathbf{E}^0$, in the form[1]:

$$\boldsymbol{\varepsilon}_p = \left[\mathbb{I} + \mathbb{P}_p^0 : (\mathbb{C}_p - \mathbb{C}^0)\right]^{-1} : \mathbf{E}^0 \tag{C.1}$$

where $\mathbb{I}, I_{ijkl} = 1/2\left(\delta_{ik}\delta_{jl} + \delta_{il}\delta_{kj}\right)$, is the fourth-order unity tensor, δ_{ij} is the Kronecker delta, $\mathbb{C}_p$ is the stiffness of the inclusion, and $\mathbb{C}^0$ the one of the matrix. The fourth order tensor, $\mathbb{P}_p^0$, defined by Eshelby characterizing the interaction between the inclusion and the matrix. depends on the shape of the inclusion, and on the stiffness properties of the matrix, and can be obtained from the matrix Green's function G^0:

$$P^0_{p,ijkl} = -\left(\partial^2 \left(\int_V G^0_{ik}(\underline{z} - \underline{z}')dV\right)/\partial x_j \partial x_l\right)_{(ij)(kl)} \tag{C.2}$$

[1]Expressions for the solution are different for points inside the inclusion and points outside. For purposes of micromechanical analysis we are particularly interested in the strain and energy stored within the inclusion/inhomogeneity.

where $(ij)(kl)$ stands for the symmetrization with respect to (ij) and (kl). The Green's function $G^0_{ik}(\underline{z}-\underline{z}')$ expresses the displacement at point $\underline{z}$ in the direction i in a linear elastic solid of stiffness $\mathbb{C}^0$ subjected to a unit force $\delta(\underline{z}-\underline{z}')$ applied in direction k at point $\underline{z}'$. $\delta(\underline{z}-\underline{z}')$ is such that $\delta(0)=\infty$, $\delta(\underline{z}\neq\underline{z}')=0$ and $\int_V \delta(\underline{z}-\underline{z}')dV(\underline{z})=1$. The analytical expressions of tensor $\mathbb{P}^0_p$ and the Eshelby tensor are defined by:

$$\mathbb{S}^0_p = \mathbb{P}^0_p : \mathbb{C}^{0,-1} \tag{C.3}$$

where $\mathbb{C}^{0,-1}$ is the inverse of the matrix stiffness tensor. Analytical forms of $\mathbb{P}^0_p$ and $\mathbb{S}^0_p$ were given for ellipsoidal inhomogeneities lying in an isotropic medium subjected to homogeneous boundary conditions at infinity (see Eshelby, 1957 [80], and Mura, 1982 [178]):

$$S_{ijkl} = S_{jikl} = S_{ijlk} \tag{C.4}$$

$$\begin{aligned}
S_{1111} &= \frac{3}{8\pi(1-\nu)}a_1^2 I_{11} + \frac{1-2\nu}{8\pi(1-\nu)}I_1 = S_{2222} \\
S_{1122} &= \frac{1}{8\pi(1-\nu)}a_2^2 I_{12} + \frac{1-2\nu}{8\pi(1-\nu)}I_1 = S_{2211} \\
S_{1133} &= \frac{1}{8\pi(1-\nu)}a_3^2 I_{13} + \frac{1-2\nu}{8\pi(1-\nu)}I_1 \\
S_{3311} &= \frac{1}{8\pi(1-\nu)}I_{13} + \frac{1-2\nu}{8\pi(1-\nu)}I_3 = S_{3322} \\
S_{1212} &= \frac{1}{8\pi(1-\nu)}I_{12} + \frac{1-2\nu}{16\pi(1-\nu)}(I_1+I_2) \\
S_{2323} &= \frac{a_1^2+a_2^2}{16\pi(1-\nu)}I_{13} + \frac{1-2\nu}{16\pi(1-\nu)}(I_1+I_3)
\end{aligned} \tag{C.5}$$

The integrals in $(C.5)$ are expressed in their elliptical form and for $\alpha_1>\alpha_2>\alpha_3$,

$$\begin{aligned}
I_1 &= \frac{4\pi\alpha_1\alpha_2\alpha_3}{\left(\alpha_2^2-\alpha_3^2\right)\left(\alpha_1^2-\alpha_3^2\right)^{1/2}}\left\{F(\theta,k)-E(\theta,k)\right\}, \\
I_3 &= \frac{4\pi\alpha_1\alpha_2\alpha_3}{\left(\alpha_2^2-\alpha_3^2\right)\left(\alpha_1^2-\alpha_3^2\right)^{1/2}}\left\{\frac{\alpha_2\left(\alpha_1^2-\alpha_3^2\right)^{1/2}}{\alpha_1\alpha_3}-E(\theta,k)\right\}
\end{aligned} \tag{C.6}$$

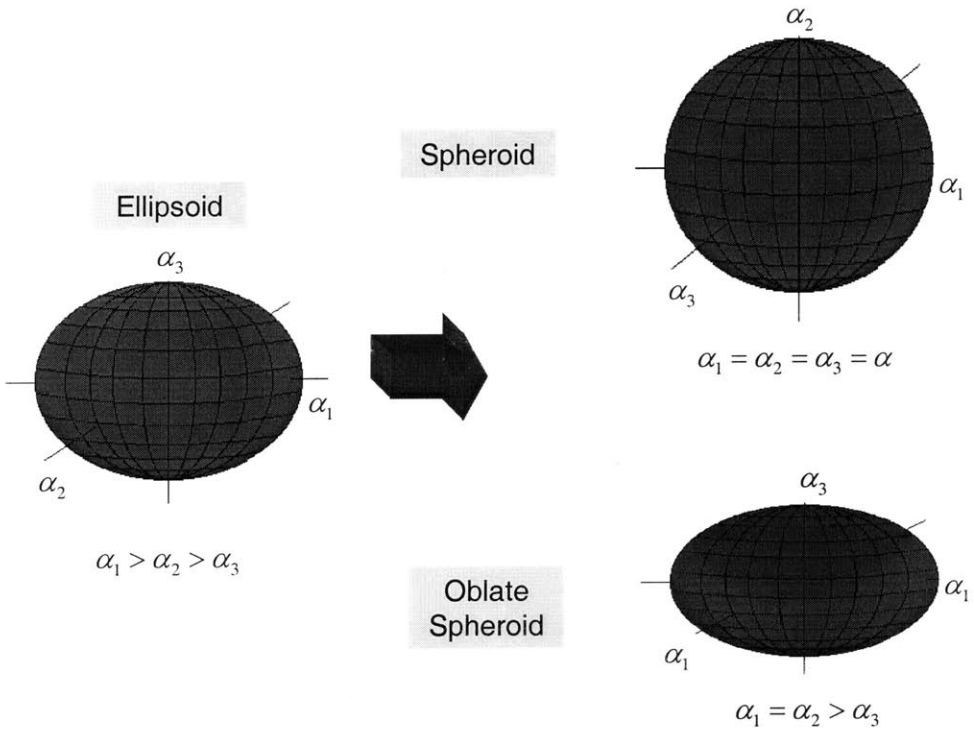

Figure C-1: Geometrical characterstics of particles for which the ellipsoidal shape considered in eshelby's solution can converge. The general mathematical expression of ellipsoid yield the spheroid and oblate spheroid for two special cases. Other limiting geometrical cases of interest are also possible.

where

$$F(\theta,k) = \int_0^{\theta} \frac{dw}{\left(1-k^2\sin^2 w\right)^{1/2}}, E(\theta,k) = \int_0^{\theta} \left(1-k^2\sin^2 w\right)^{1/2} dw \qquad (C.7)$$

$$\theta = \sin^{-1}\left(1-\frac{\alpha_3^2}{\alpha_1^2}\right)^{1/2}, k = \left\{\frac{(\alpha_1^2-\alpha_2^2)}{(\alpha_1^2-\alpha_3^2)}\right\}^{1/2}$$

The integrals of Eq. $(C.6)$ become elementary functions for special shapes of inclusions. The ellipsoidal shape can take several convenient forms for specific limited cases (prolate spheroid, oblate spheroid, cylinder, sphere). The spherical one which is of interest is detailed below:

- Sphere ($a_1 = a_2 = a_3 = a$): In the case of a spherical inclusion embedded in an isotropic matrix the elliptical integrals and the Eshelby tensor reduce to:

$$\begin{aligned} I_1 &= I_2 = I_3 = \frac{4\pi}{3} \\ I_{11} &= I_{22} = I_{33} = I_{12} = I_{23} = I_{31} = \frac{4\pi}{5}a^2 \end{aligned} \tag{C.8}$$

$$S_{1111} = S_{2222} = S_{3333} = \frac{7-5\nu}{15(1-\nu)} \tag{C.9}$$

$$S_{1122} = S_{2233} = S_{3311} = S_{1133} = S_{2211} = S_{3322} = \frac{5\nu-1}{15(1-\nu)} \tag{C.10}$$

$$S_{1212} = S_{2323} = S_{3131} = \frac{4-5\nu}{15(1-\nu)} \tag{C.11}$$

In tensorial format the Eshelby solution for spherical articles reads:

$$\mathbb{S}_r^{Esh} = \alpha_0^{est}\mathbb{J} + \beta_0^{est}\mathbb{K} \tag{C.12}$$

with

$$\alpha_0^{est} = \frac{3k_0}{3k_0 + 4g_0}; \quad \beta_0^{est} = \frac{6\,(k_0 + 2g_0)}{5\,(3k_0 + 4g_0)} \tag{C.13}$$

In this case, the localization tensors presented in Section 7.1.2 reduces to[2]:

$$\langle \mathbb{A}(\mathbf{x}) \rangle_{V_r} = A_r^v\mathbb{J} + A_r^d\mathbb{K} \tag{C.14}$$

in which the volumetric, A_r^v, and deviatoric, A_r^d, strain localization coefficients are estimated

[2] We recall that J_{ijkl}=1/3 $(\delta_{ij}\delta_{kl})$ and $\mathbb{K} = \mathbb{I} - \mathbb{J}$ are the spherical and deviatoric projections of the forth order identity tensor $I_{ijkl} = \frac{1}{2}(\delta_{ik}\delta_{jl} + \delta_{il}\delta_{jk})$, and δ_{ij} is the Kronecker delta.

by:

$$A_r^{v,est} = \left(1+\alpha_0^{est}\left(\frac{k_r}{k_0}-1\right)\right)^{-1}\left[\sum_r f_r\left(1+\alpha_0^{est}\left(\frac{k_r}{k_0}-1\right)\right)^{-1}\right]^{-1} \quad \text{(C.15)}$$

$$A_r^{d,est} = \left(1+\beta_0^{est}\left(\frac{g_r}{g_0}-1\right)\right)^{-1}\left[\sum_r f_r\left(1+\beta_0^{est}\left(\frac{g_r}{g_0}-1\right)\right)^{-1}\right]^{-1} \quad \text{(C.16)}$$

For Mori-Tanaka estimates we let $k_0 = k_M$ and $g_0 = g_M$ whereas for Self-Consistent estimates we let $k_0 = k_{\text{hom}}$ and $g_0 = g_{\text{hom}}$ in (C.13), (C.15) and (C.16). For purpose of clarity we illustrate the approach in the case of a solid matrix of elastic properties (k_s, g_s) and a certain fraction of pore spaces, ϕ. The homogenized properties are:

$$k_{\text{hom}} = (1-\phi)k_s A_s^{v,est} \quad \text{(C.17a)}$$

$$g_{\text{hom}} = (1-\phi)g_s A_s^{d,est} \quad \text{(C.17b)}$$

where $A_s^{v,est}, A_s^{d,est}$ are given by (C.15) and (C.16). Using a Mori-Tanaka estimate of the localization factors, the homogenized bulk and shear properties reduce to:

$$k_{\text{hom}} = \frac{\left(1-\alpha^{MT}\right)(1-\phi)\,k_s}{\left(1-\alpha^{MT}+\alpha^{MT}\phi\right)};\ \alpha^{MT} = \frac{3k_s}{3k_s+4g_s} \quad \text{(C.18)}$$

$$g_{\text{hom}} = \frac{\left(1-\beta^{MT}\right)(1-\phi)\,g_s}{\left(1-\beta^{MT}+\beta^{MT}\phi\right)};\ \beta^{MT} = \frac{6\left(k_s+2g_s\right)}{5\left(3k_s+4g_s\right)} \quad \text{(C.19)}$$

Similarly, using a self-consistent estimate of the localization factors relations in Eq. (C.17) now give:

$$k_{\text{hom}} = \frac{(1-\phi)\,k_s}{1+\alpha^{SC}\left(k^s-k_{\text{hom}}\right)/k_{\text{hom}}};\ \alpha^{SC} = \frac{3k_{\text{hom}}}{3k_{\text{hom}}+4g_s} \quad \text{(C.20)}$$

$$g_{\text{hom}} = \frac{(1-\beta)\,(1-\phi)\,g_s}{(1-\beta+\beta\phi)};\ \beta^{SC} = \frac{6\left(k_{\text{hom}}+2g_{\text{hom}}\right)}{5\left(3k_{\text{hom}}+4g_{\text{hom}}\right)} \quad \text{(C.21)}$$

It is interesting to observe that the homogenized bulk and shear moduli estimated by both localization schemes are coupled as both localization coefficients depend on k and g accordingly.

Appendix D

Experimental Validation of Grid Indentation

This chapter is devoted to a further validation of the grid indentation approach proposed in Chapter 5. To this end, we investigate a series of discontinuously reinforced titanium alloys containing titanium boride (TiB) whiskers in different distributions. The microstructural details and volume fractions of the different phases have been studied in detail in Refs. [202] and [9], respectively.

D.1 Materials and methods

D.1.1 Specimen preparation

In situ Ti–TiB composite plates with various volume fractions of TiB (see Tab. D.1) reinforcements were fabricated by hot pressing Ti and TiB_2 powders. The specimens were fabricated in the Department of Metallurgy, University of Utah, by the group of Prof. RaviChandran and delivered polished to M.I.T. Details of the specimen preparation and microstructural investigations are presented in Refs. [202] and [9].

Powder Mixture [%]	Composite [%]		
Ti/TiB_2	**Ti**	TiB	TiB_2
1.000/0.000	1.00	0.00	0.00
0.882/0.118	0.70	0.30	0.00
0.763/0.237	0.45	0.55	0.00
0.526/0.474	0.08	0.86	0.06

Table D.1: Volumetric proportions of power mixture and resulting composite solid composition.

D.1.2 Indentation parameters

We have suggested in Section 5.1.2 that the elastic properties of the individual components can be accessed by indentation experiments with maximum indentation depths $h_{\max}/D \leq 1/10$, where D stands for the characteristic size of individual phases or microstructural elements:

$$d_0 << h_{\max} \leq D/10. \tag{D.1}$$

Hence, in order to obtain the properties of Ti and TiB, d_0 and D represent the characteristic sizes of respectively the heterogeneity within Ti and TiB, and D the microstructure of TiB. The crystalline nature of titanium and titanium boride imply d_0 on the order the lattice parameters of the underlying crystal structures (Angstroms). Certainly, the characteristic size of the microstructure D is more difficult to estimate, as the size and shape of the TiB whiskers depend directly on initial composition and heat treatment (temperature, duration, etc.). Scanning electron microscopy images of Ti-TiB [202],[103] suggest that a length scale of $D_I \sim 1 - 3\,\mu$m is characteristic of the TiB whiskers; we adopt this limit herein. Hence, an appropriate indentation depth that allows access to the Ti and TiB phases by nanoindentation is:

$$h_{\max} \in [100, 300] \text{ nm} \tag{D.2}$$

In the case of 45Ti-55TiB specimen, the TiB whiskers exhibited a refined morphology and the indentation depth was reduced further to access the individual constituents, $h_{\max} \simeq 40\,$nm.For smaller depths, issues related to imperfect geometry at the indenter apex may become significant (see Section 2.2.3 and Ref. [86]), and for larger depths the "substrate effect" related to the proximity of other phases will prohibit access to intrinsic properties of the TiB (see Section

		100Ti	70Ti-30TiB	45Ti-55TiB	8Ti-86TiB-6TiB_2
	#	1×100	2×100	2×100	2×100
$P^*_{\max}$	[μN]	$3,481 \pm 2$	$3,484 \pm 2$	493 ± 2	$3,995 \pm 1$
$h_{\max}$	[nm]	179 ± 18	137 ± 33	40 ± 11	89 ± 8
S	[μN/ nm]	79.94 ± 10.38	81.69 ± 55.82	47.11 ± 5.52	142.25 ± 7.36
$\tau_L/\tau_H/\tau_U$	[s]	10/5/10	10/5/10	10/5/10	10/5/10

Table D.2: Experimental program and mean $\pm$ standard deviation of indentation results: (*) The deviation of the maximum force from the applied number is due to the spring force correction (see [124]).

5.1.2). We should emphasize, however, that Eq. (D.1) is only satisfied in an average sense, and that the presence of experiments within a massive array that violate these conditions is inevitable. For instance, the length and width of TiB whiskers has been determined previously to vary within a specimen, with a fraction of the whisker population exhibiting widths $D < 1$ μm [103]. The error induced by indentation on such phases that do not satisfy Eq. (D.1) is expected to be random in nature, and should be captured by the statistical analysis method (see Section 5.2.2).

Finally, we must relate the target indentation depths to the massive array of identical experiments (or grid indentation) conducted on a highly heterogeneous material (see Fig. 5-6). A convenient way to achieve on-average indentation depths of the magnitude specified by Eq. (D.2) is to employ a series of load-controlled indentation experiments. This requires some experimental iteration. For the present material system, we found that a maximum load of $P_{\max} = 3,500\,\mu$N yields an average maximum indentation depth of $h_{\max} \in [80, 170]$ nm. Experiments were conducted using the Hysitron, Triboindenter described in Section 3.1. In all indentation experiments within an array, a trapezoidal load history was prescribed, defined by a loading segment duration $\tau_L = 10$ s, a holding period at P_{max} of $\tau_H = 5$ s, and an unloading segment duration $\tau_U = 10$ s. In addition, a holding period of 10 s subsequent to the initiation of contact facilitated correction for thermal drift within the load train of the instrumented indenter. Table D.2 summarizes the details of the experimental program.

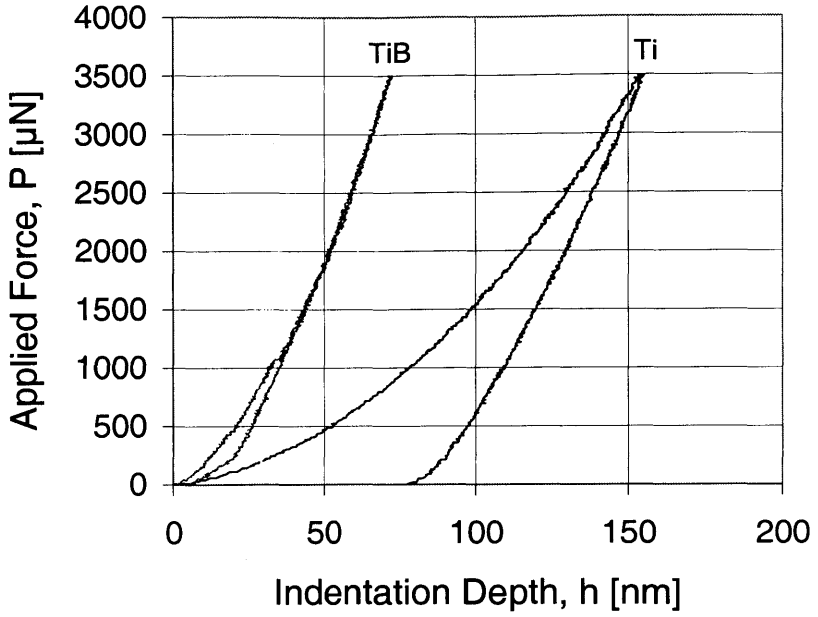

Figure D-1: Typical $P-h$ curves of indentations on Ti and TiB. Indents span within this range depending on the degree of ineteraction between the two phases.

D.2 Indentation Results and Statistical analysis

Indentation results were analyzed both individually and globally according to the procedure described in Chapter 5: An individual test gives access to mechanical information of the indented region, and a series of tests describes the composite material behavior. Typical load - depth ($P-h$) responses for indentation on the two phases (Ti and TiB) are illustrated in Fig. D-1. The complete set of indentations varied in terms of the maximum indentation depths all across the region defined by these two extreme scenarios, depending on the degree of interaction between the two phases. The majority of the responses, however, were centered around these two mean values. This will be further exemplified through the statistical analysis of the indentation moduli presented below. Individual tests were analyzed based on the methodology presented by Oliver and Pharr [184], also outlined in Section 2.5. Scanning probe microscopy images of residual indentations (Fig. D-2) demonstrate that there is no visible pile-up in the Berkovich indentation of the Ti-TiB composites, suggesting that the Oliver and Pharr method would yield reliable estimates of the area of contact. The large amount of analyzed indentation

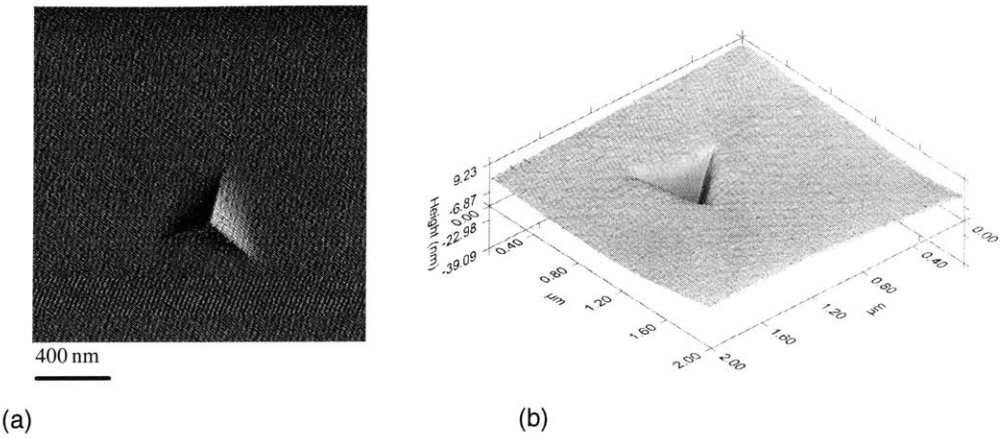

Figure D-2: An atomic resolution scanning probe microcopy image of a residual indent on a Ti-TiB-TiB_2 specimen in a gradient (a) and three-dimensional (b) mode.

data was then treated in a statistical fashion:

D.2.1 Mechanical Response Distributions

Mechanical response distributions represented as frequency plots are used to analyze indentation data on a composite material. For small indentation depths, $h << D$, such plots give rise to multimode distributions, each peak corresponding to the mechanical manifestation of a phase[1]. In order to extract elastic properties of the relevant phases, the deconvolution technique presented in Section 5.2.2 is employed. For indentation depths much greater than the largest characteristic length scale of heterogeneities, $h >> D$, the mechanically distinct phases tend towards a single peak value, which is the mechanical manifestation of the composite material (here Ti-TiB alloys).

Figure D-3(a) shows the distribution of indentation modulus on a pure titanium matrix, 100Ti. In this case, $n = 1$ and the data can be fitted by a normal distribution of the form (5.9), where the mean value and the standard deviation are $M_{100\mathrm{Ti}} = 134 \pm 5$ GPa (see Eq.

[1]In the case of nanoindentation on Ti-TiB systems, the mechanical phases coincide with a chemical phase. Such a scenario provides a direct link between physical chemistry and mechanics.

(5.10)). The resulting frequency plot shows a relatively small scatter and high repeatability, underscoring the microstructural and mechanical homogeneity of this elemental matrix and the robustness of the indentation experiments and analysis. Figures D-3(b)−(d) depict the frequency plots of M for three Ti-TiB alloys; 70Ti-30TiB ($n = 2$), 46Ti-54TiB ($n = 2$), 8Ti-86TiB-6TiB_2 ($n = 3$). It is evident from the results that a second peak increases in intensity as the boron content increases, indicating the presence of a new phase, TiB. In the case of 8Ti-86TiB-6TiB_2 a small percentage of residual, unreacted TiB_2 remained in the matrix. This was detected by our indentation results and is manifested as a peak in the frequency plot of Fig. D-3(d) with an indentation modulus of: $M_{TiB_2} = 394 \pm 13$. The extracted indentation moduli and volumetric proportions of the different phases are summarized in Tab. D.3. In order to quantify the effect of the phases surrounding the RVE of indentation on the calculated M of each phase, we will use as reference for M_{Ti} and M_{TiB} the results obtained on 100% Ti and Ti-86TiB-6TiB_2 specimens accordingly. The indentation moduli obtained for Ti and TiB in the two intermediate-volume specimens, Ti-30%TiB ($M_{Ti} = 144 \pm 12$ GPa, $M_{TiB} = 330 \pm 147$ GPa) and Ti-54%TiB ($M_{Ti} = 141 \pm 10$ GPa, $M_{TiB} = 280 \pm 70$ GPa) are within 10 % of the independently measured values reported in the literature ($M_{Ti} = 134 \pm 5$ GPa) and $M_{Ti-86TiB-6TiB_2} = 306 \pm 22$ GPa). This is in line with the restrictions posed by finite element calculations for the specific choice of indentation depth (see Fig. 5-2). Furthermore, this agreement with independent measures or computationally simulated estimates of M for these phases supports the accuracy of the current approach in composite analysis. That is, given a careful choice of the indentation depth and a large number of well-designed indentation experiments, the intrinsic elastic properties of individual phases can be extracted. This is a consequence of the choice of the indentation depth h, which was deliberately chosen to be small enough compared to the characteristic length of the heterogeneities D, such that an indentation test that is situated on an inclusion phase satisfies the $h/D << 1$.

The relatively high standard deviation observed for the TiB phase should be noted. This is a consequence of the "substrate effect" due to proximity of non-TiB phases in close proximity to the RVE that includes TiB. It is in fact evident from Fig. 5-2 that this hard-on-soft material scenario is more vulnerable to proximity effects than the reverse case. Since the whisker width varies significantly, the condition $h/D << 1$ is likely violated in a significant number of

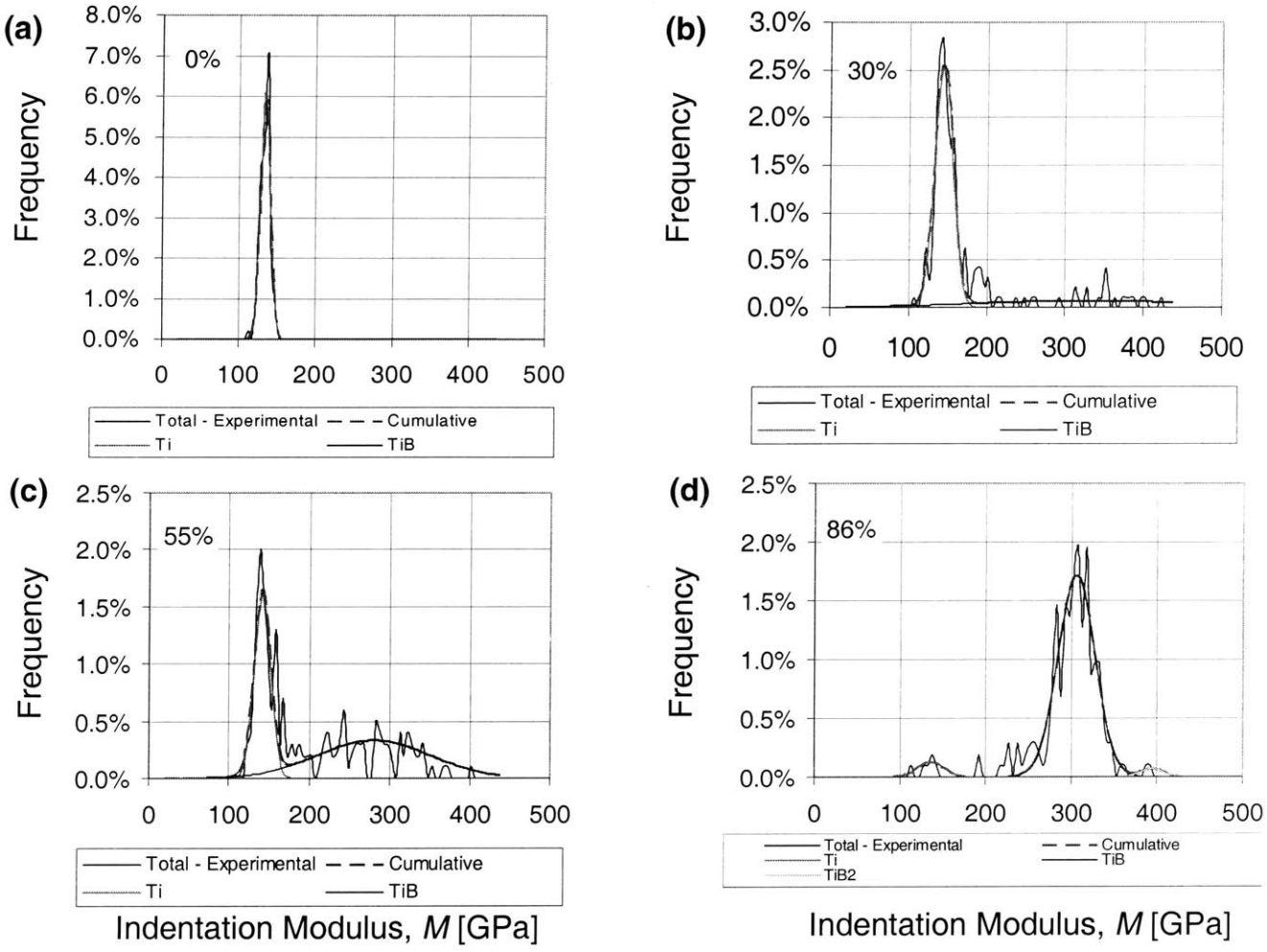

Figure D-3: Frequency plots of the indentation modulus for the four specimens: 100Ti, 70Ti-30TiB, 45Ti-55TiB, and 8Ti-86TiB-6TiB_2.

	Indentation Modulus, M [GPa]			*Volume Fraction, f* [%]		
	Ti	TiB	TiB_2	**Ti**	TiB	TiB_2
100Ti	134 ± 5	–	–	100	0	0
70Ti-30TiB	144 ± 12	330 ± 147	–	74	26	0
46Ti-54TiB	141 ± 10	280 ± 70	–	44	56	0
8Ti-86TiB-6TiB_2	136 ± 15	306 ± 22	394 ± 13	5	92	3

Table D.3: Indentation Moduli and Volumetric Proportions of the different phases (Ti and TIB) obtained from the deconvolution of the experimentally obtained frequency plots.

individual experiments within the massive array. In principle, this experimental obstacle could be overcome by further reducing the maximum indentation depth, but was beyond the limits of the current experimental capabilities due to geometric imperfections at the indenter apex for $h < 40nm$. The proximity effect is also demonstrated by the decrease in the standard deviation with increasing volumetric proportions of TiB. It has been shown that the characteristic size of the TiB, D, increases with increasing volumetric proportions of the phase [9], and thus the condition h/D is better satisfied as f_{TiB} increases.

D.2.2 Volumetric proportions

The volumetric proportions of the two phases Ti and TiB have been measured previously in Ref. [9] by quantitative X-ray diffraction analysis and are reported in Tab. D.1. These values are to be compared with the volumetric proportions estimated from the deconvolution procedure of the cumulative frequency plot (see Section 5.2.2 and Eq. (5.11)). The resulting values after deconvolution of the four alloys are provided in Tab. D.3, and demonstrate the capacity of massive array indentation to quantify the relative presence of different phases. Importantly, herein these volume fractions are determined not by the differential chemical composition of these phases, but by the differential mechanical properties of these phases. It should be noted that this criterion immediately implies that the volume fractions estimated by the indentation approach increase in accuracy as the mechanical dissimilarity between any two phases increases.

D.2.3 Mechanical Mapping of Microstructure

Instrumented indentation facilitates controlled spatial distribution among indents in patterns such as regularly spaced arrays. In the nanoindentation arrays employed herein, a square grid of 10 μm inter-indentation spacing was chosen. The analysis of each indentation $P-h$ response provides information about the mechanical properties such as M at each array coordinate (x, y). These properties are, strictly speaking, representative of a material domain of characteristic length scale $\max(h, a)$ that defines the R.E.V. Hence, provided that the array spacing is larger than the characteristic length scale of the material sampled in each experiment, mapping of the properties over the grid region indicates the morphological arrangement of the phases comprising the microstructure. This is a second result of the proposed grid indentation approach. A convenient and simple way to generate these maps is by transforming the discrete data system into a continuous distribution of mechanical properties by linearly interpolating the grid point values over the grid region. The result of this mapping can be displayed as contour plots in plan view (see Fig. D-4). Such a contour depiction of mechanical properties requires the selection of minima-maxima limits between different phases. As the frequency plots in Figs. D-3(b) to (d) show, there is some overlap in the distribution between different phases, which complicates the definition of clear boundaries between phases. As a first order approach we choose equal size domains centered around the mean values of each phase:

1. 0 – 200 GPa: Values situated in this range are associated with regions for which the mechanical response is dominated by the titanium matrix.

2. 200 – 400 GPa: Values situated in this range are contained within the second peak in the frequency plots of Figs. D-3(b) to (d), and are associated with regions in which the mechanical response is dominated by the TiB whiskers.

Figure D-4 shows plan views of contour plots of the indentation modulus for the Ti-30%TiB specimen. An SEM image from Ref. [9] is also shown in Fig. D-4, and demonstrates the correlation of these mechanical maps with electron microscopy images of the microstructure. Hence, the mechanical maps provide a means to characterize the morphology of the microstructure at the scale defined by the chosen indentation depth, and enables visualization of the mechanically distinct features. In particular, for the Ti-TiB composite, the contour plots provide a snapshot

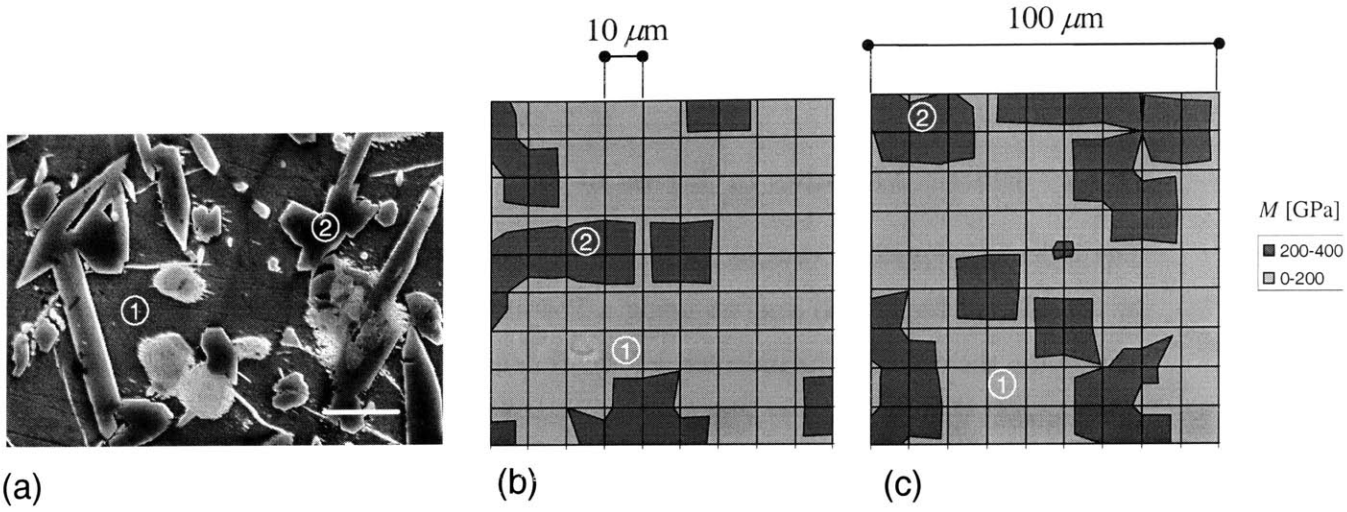

Figure D-4: Mechanical mapping of the indentation results on 70Ti-30TiB (b-c) as compared with an SEM image (a) of an etched mirostucture at a similar magnification. 1 = Titanium (Ti), 2 = Titanium monoboride (TiB)

of the formation process of the composite: TiB whiskers and particles are embedded in a percolated matrix of Ti (see Fig. D-4). The morphological characterization of the microstructure provided by this mechanical mapping completes the characterization of the properties and morphological arrangement in space. As it will be further discussed in Section D.3.2, these data is a piece of the puzzle for the development of micromechanical models for upscaling of composite mechanical performance.

D.3 Elastic properties of Ti, TiB, and TiB_2

The indentation moduli M determined from the grid indentation experiments for the Ti, TiB, and TiB_2 phases are insensitive to spatial location, number of experiments, and specimen preparation procedure. The extracted values can therefore be considered as mechanical properties characteristic of each phase. To further investigate the intrinsic nature of these properties, we compare our results with values reported in the literature. Since the TiB phase cannot be reproduced in macroscale physical dimensions, data on the elastic constants of this phase are

scarce. In fact, the only information regarding E of this phase is provided by atomistic simulations [103] or by extrapolating macroscopic experiments on composites comprising different volumetric proportions of TiB, f_{TiB}, to $f_{\mathrm{TiB}} = 1$ [9].

D.3.1 Elastic Modulus in Terms of M

The indentation moduli can be converted to the elastic properties of the individual phases by considering Eq. (2.68) and assuming a Poisson's ratio for each phase. It is interesting to decompose the effect of the indenter deformation and the Poisson's effect on the magnitude of E calculated from a given M. To this end, we start by calculating the material plane-stress elastic modulus M_s, which does not include any assumption on the Poisson's ratio. Figure D-5 shows the contribution of the indenter deformation on the elastic properties extracted thereby. The horizontal axis corresponds to the measured (composite) M which implicitly includes the deformation of the indenter, and the vertical axis quantifies the effect of indenter deformation on M_s calculated as a function of M for a given indenter stiffness. It is impressive to note that as the stiffness of the indented material increases, the indenter deformation becomes more significant and should be accounted in our analysis. In the following calculations, we will rely on the Hertz solution of the contact between two isotropic solids of Eq. (2.68), and the isotropic assumption of the diamond indenter suggested by ISO [127].

Given the plain-stress elastic modulus of the indented material, the Young's or uniaxial elastic modulus, $E_s = M_s \times (1 - \nu^2)$ can be determined, provided a reasonable estimate of the Poisson's ratio. However, it is not necessary to know the value of the Poisson's ratio with great precision to obtain a reasonable estimate of the Young's modulus. In fact, a Poisson's ratio of $0.1 - 0.4$, representative of the range including most engineering metals and ceramics, induces an error on E of less than 10%. Assuming a value of $\nu = 0.32$ [81], 0.16 [9], 0.17 [177] for Ti ,

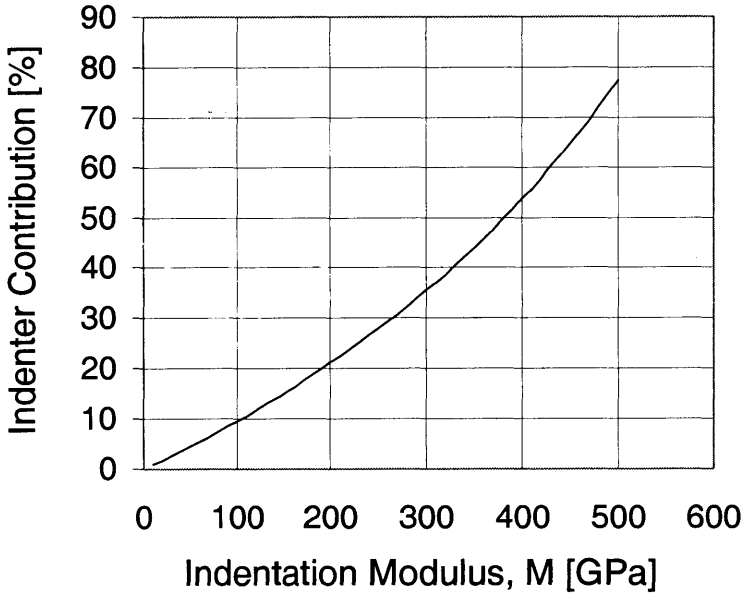

Figure D-5: Error induced by the deformation of the indenter, defined as $(M_s - M)/M \times 100$.

TiB, and TiB_2, respectively, the elastic moduli of the three phases can be calculated:

$$M = \left\{ \begin{array}{ccccc} M & M_s & (M_s - M)/M_s & E_s & \\ \text{[GPa]} & \text{[GPa]} & \text{[\%]} & \text{[GPa]} & \\ 140 & 159 & 14 & 138 & \text{Ti} \\ 305 & 416 & 36 & 406 & \text{TiB} \\ 394 & 600 & 52 & 585 & \text{TiB}_2 \end{array} \right.$$

The elastic moduli of Ti and TiB ($E_{\text{Ti}} = 138$ GPa, $E_{\text{TiB}_2} = 585$ GPa) are in excellent agreement with macroscopic properties reported in the literature: $E^{\text{lit}}_{\text{Ti}} = 110 - 120$ GPa [81], $E^{\text{lit}}_{\text{TiB}_2} = 565$ GPa [177]. The elastic properties of the TiB, however, remain a matter of current debate. This material exhibits crystalline anisotropy (orthotropic unit cell), but the 9 elastic constants required to describe the stiffness tensor have never been measured experimentally, due chiefly to the inability to prepare appropriate samples. Estimates of E_{TiB} that assume isotropic behavior vary widely ($E^{\text{lit}}_{\text{TiB}} = 232 - 622$ GPa). A value of $E^{\text{lit}}_{\text{TiB}}$ =371 GPa was suggested from inverse analysis of the composite elastic modulus [9], whereas a value of $E^{\text{lit}}_{\text{TiB}} = 485$ GPa was estimated from *ab-initio* atomistic simulations [103]. Some estimates from indentation experiments have also been reported [103], but the experimental scatter was quite significant. Thus, validation of the magnitude of E_{TiB} obtained herein by recourse to existing data is difficult.

D.3.2 Micromechanical Modeling and Macroscopic Composite Behavior

To investigate the accuracy of our extracted E_{TiB}, we will use $E^{\text{exp}}_{\text{TiB}} = 406$ GPa as input in a composite model that predicts the macroscopic (homogenized) response, and compare this prediction with reported macroscopic data. The Ti-TiB composite can be conveniently modeled with the Mori-Tanaka micromechanical scheme, which is suitably applied for matrix-inclusion geometries [172] (see Section 7.1.2). In the case of a titanium matrix with isotropic spherical inclusions of TiB, the Mori-Tanaka scheme yields the following homogenized response

$(K_{\text{hom}}, G_{\text{hom}})$:

$$K_{\text{hom}} = K_{\text{Ti}} + \frac{(K_{\text{TiB}} - K_{\text{Ti}}) f_{\text{TiB}}}{1 + a(1 - f_{\text{TiB}}) \left(\frac{K_{\text{TiB}}}{K_{\text{Ti}}} - 1\right)} \tag{D.3}$$

$$G_{\text{hom}} = G_{\text{Ti}} + \frac{(G_{\text{TiB}} - G_{\text{Ti}}) f_{\text{TiB}}}{1 + b(1 - f_{\text{TiB}}) \left(\frac{G_{\text{TiB}}}{G_{\text{Ti}}} - 1\right)} \tag{D.4}$$

where K_{Ti} and K_{TiB}) are the bulk modulus of the titanium matrix and TiB inclusion, respectively, and G_{Ti} and G_{TiB} are the shear modulus of the titanium matrix and titanium boride inclusion, respectively. The variables a and b in Eqs. (D.3) and (D.4) are stated as:

$$a = \frac{3K_{\text{Ti}}}{3K_{\text{Ti}} + 4G_{\text{Ti}}}; b = \frac{6}{5} \frac{K_{\text{Ti}} + 2G_{\text{Ti}}}{3K_{\text{Ti}} + 4G_{\text{Ti}}} \tag{D.5}$$

Equations (D.3) and (D.4) simplify the elongated whisker morphology of the titanium composite by equivalent isotropic spheres. It has been found however that, given the random orientation of the fibers in the matrix, the experimentally observed isotropic behavior of a macroscopic composite can be well approximated by a spherical assumption [54],[9]. Finally, given the homogenized values of the bulk and shear moduli, the Young's modulus and the Poisson's ratio can be calculated using standard relations of elasticity theory:

$$E_{\text{hom}} = (9K_{\text{hom}}G_{\text{hom}}) / (3K_{\text{hom}} + G_{\text{hom}}); \qquad \nu_{\text{hom}} = (3K_{\text{hom}} - 2G_{\text{hom}}) / (6K_{\text{hom}} + 2G_{\text{hom}}) \tag{D.6}$$

The mean elastic values of titanium boride ($E_{\text{TiB}} = 406$ GPa, $\nu_{\text{TiB}} = 0.16$) and volumetric proportions thereof, as extracted from the indentation analysis (see Tab. D.3), are incorporated in Eqs. (D.3)−(D.4) to calculate the micromechanical predictions of E for a series of f_{TiB}. The micromechanical predictions of the E and G, together with experimental data found in the literature (Refs. [9],[103],[81]), are reported in Fig. D-6. The accuracy of the predictions validates the extracted elastic modulus of the TiB phase, as well as the use of the Mori-Tanaka scheme to capture the strain localization within TiB inclusions.

This verification of E_{TiB} completes the validation of the proposed massive array or grid indentation approach. This methodology is of particular importance for materials for which the properties of constituent phases are measurable only *in situ*. As such, grid indentation rep-

resents the only currently available approach for measuring the intrinsic mechanical properties of phases as required for micromechanical modeling of composite response. Application of this approach to cementitious composite is detailed in Chapters 5 and 6.

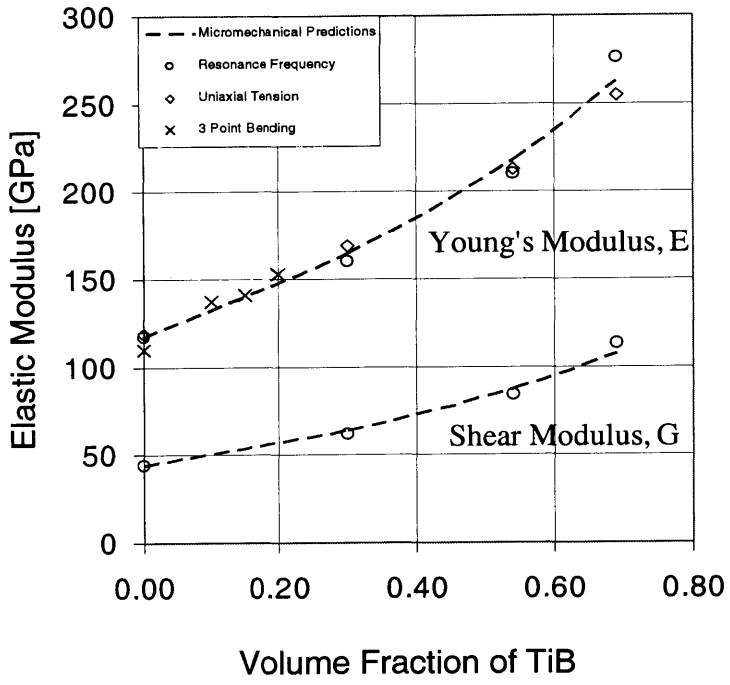

Figure D-6: Experimental data and micromechanical predictions of composite modulus versus the volume fractions of the reinforcing TiB. Source of Macroscopic data: Resosnance Frequency, [9]; Uniaxial Tension, [9]; 3 Point Bending, [103].

Appendix E

Packing of Monosize Spheres

This chapter gives a short overview of the extensive literature on the packing of particles. We restrict ourselves to the simplest geometrical representation of three dimensional geometries, the sphere, returning to geometries issues at the end of our discussion. The presentation given below follows in parts the short reviews given in [243] and [19].

E.1 Random Close Packing

Packing of particles has been of great interest for shippers, packagers, merchants, grocery stores, and more recently physicists, mathematicians and materials scientists. There is a broad range of problems that involve the geometrical arrangement in space of discrete three dimensional particles, ranging from atomic structure of solid materials to packaging of oranges and candies. Even though the problem might seem trivial our understanding is limited to the simple geometrical case of sphere. It is commonly accepted by researchers in the field that, given enough stirring and shaking, a random collection of particles will always settle to a maximum packing density of, $\varrho \simeq 0.64$, a state known as Random Close Packing (RCP). This is the highest volumetric solid fraction that spheres can pack while retaining a random configuration. The definition of random configuration is ill-defined and is currently the topic of intense research. In the RCP state all particles are jammed in space and cannot move under gravity. The RCP state has been verified by several researchers experimentally and by numerical simulations using several different algorithms, all yielding the same value $\varrho \simeq 0.64$ (see refs in [243]). While this value

was long believed to be universal, there are no analytical derivations to this problem. The RCP is not the only packing arrangement that solid spheres can achieve and two more packing states that are of extreme interest for our work will be discussed below.

E.2 Face Centered Cubic Packing

Scientists and researchers have long been concluded that the most efficient way to put particles in packages in not to randomly throw them in cases but rather to pack them in order in a non-random way. In fact if we take a jar of randomly distributed candies and start shaking it hard, allowing particles to loose contact slightly and rearrange themselves in space, '*...then they begin to order, forming layers of spheres packed in a hexagonal lattice, with each layer nested in the hollows formed by the layer beneath it.*' cited from [243]. This kind of arrangement corresponds to the crystalline structure taken by the atoms in many metals, and forms the highest volume fraction packing of spheres, with $\varrho \simeq 0.74$. An analytical derivation of this problem, also known as Kepler's conjecture became only recently available and the FCC packing can now be considered as a well established fact, $\varrho = \pi/\sqrt{18} = 0.74048$.

E.3 Random Loose Packing

Another important configuration that spheres can achieve when they are gently packed, is an arrangement even looser than the RCP. Such a scenario can be obtained when particles precipitate from a fluid suspension where gravitational forces are minimal. Particles have been reported to have densities as low as $\varrho \simeq 0.56$. Such an arrangement is called the Random Loose Packing (RLP) and corresponds to the loosest mechanically stable arrangement that an agglomerate network can exist. However as it was reported by Weitz [243], this form of packing is somewhat controversial and a consensus on an absolute values does not exist!

So far we have been discussing the packing arrangement of spheres which is the simplest geometrical representation and the one used in the colloidal model for the C-S-H employed in this thesis [130]. However other geometrical shapes can significantly change the packing arrangements reported above and their link with cementitious materials may require reinterpretation once a definite shape is reported for the single C-S-H colloidal particle.

Appendix F

Micromechanical Estimates of C-S-H Cohesion

Level '0' is the scale where the C-S-H particles form porous spaces of varying proportions (LD and HD C-S-H). The cohesion and angle of friction of such systems was experimentally obtained with the dual indentation technique (see Chapter 2). An estimate of the C-S-H solid cohesion was given using an interpolation to zero porosity values. We attempt in this section to provide a better estimate of the C-S-H cohesion based on micromechanical modeling.

F.1 Von-Mises Assumption

It is unclear a priori whether the C-S-H solid exhibits a cohesive-frictional behavior of the Drucker-Prager type or whether it can be considered as a crystalline solid following Von-Mises yield criterion. We here make the assumption that the material follows a Von-Mises yield criterion of the form:

$$j_2 - k_s^2 \leq 0 \tag{F.1}$$

In such a case the secant formulation of the nonlinear problem for large deviatoric strains yields:

$$g^s\left(\epsilon_s, \varepsilon_s^v\right) \simeq k/2\sqrt{\epsilon_s} \tag{F.2}$$

Following the same procedure as in Section 11.3.3 one can calculate the homogenized yield

envelope [13]:

$$(1-\phi) = \frac{1}{\mathcal{F}_1(\phi)}\left(\frac{\Sigma_m}{c}\right)^2 + \frac{1}{\mathcal{F}_2(\phi)}\left(\frac{\Sigma_d}{c}\right)^2 \tag{F.3}$$

where $\mathcal{F}_1(\phi)$ and $\mathcal{F}_2(\phi)$ are defined in Eq. (11.44) [75]. In the case of a Mori-Tanaka and Self-consistent estimates of the localization relations we have:

$$\text{MT Estimate} \qquad (1-\phi)^2 c^2 = \frac{3\phi}{4}\Sigma_m^2 + \left(1+\frac{2\phi}{3}\right)\Sigma_d^2 \tag{F.4}$$

$$\text{SC Estimate} \quad (1-2\phi)(1-\phi)c^2 = \frac{\phi(3-\phi)}{4(1-\phi)}\Sigma_m^2 + \left(1-\frac{\phi}{3}\right)\Sigma_d^2 \tag{F.5}$$

The two surfaces are elliptic in nature and closed on the hydrostatic axis which is different from the assumption we made in evaluating the LD and HD C-S-H in Section 10.1.2. In order to get an estimate however of the C-S-H solid strength we make the two criteria match for uniaxial compressive strength. In fact the uniaxial compressive strength of the two yield envelopes can be calculated by substituting $\Sigma_d = \Sigma_c/\sqrt{3}, \Sigma_m = \Sigma_c/3$ in Eqs. (F.4) and (F.5):

$$\text{MT Estimate} \qquad \Sigma_c/c = \sqrt{36(1-\phi)^2/(12+11\phi)} \tag{F.6}$$

$$\text{SC Estimate} \qquad \Sigma_c/c = \sqrt{36(1-2\phi)(1-\phi)^2/(4\phi^2-9\phi+7)} \tag{F.7}$$

The LD and HD C-S-H phases have an intrinsic porosity of $\phi_{LD} = 37.3\%$ and $\phi_{HD} = 23.7\%$ which yield for the Von-Mises model with porosity a uniaxial compression to cohesion ratio of:

$$\text{MT Estimate} \quad \begin{array}{l} [\Sigma_c/c]_{LD} = 0.69 \Longleftrightarrow c_s = 137 \text{ MPa} \quad \Sigma_s = 237 \text{ MPa} \\ [\Sigma_c/c]_{HD} = 1.10 \Longleftrightarrow c_s = 204 \text{ MPa} \quad \Sigma_s = 353 \text{ MPa} \end{array} \tag{F.8}$$

$$\text{SC Estimate} \quad \begin{array}{l} [\Sigma_c/c]_{LD} = 0.69 \Longleftrightarrow c_s = 138 \text{ MPa} \quad \Sigma_s = 240 \text{ MPa} \\ [\Sigma_c/c]_{HD} = 1.10 \Longleftrightarrow c_s = 166 \text{ MPa} \quad \Sigma_s = 287 \text{ MPa} \end{array} \tag{F.9}$$

The two values (for the Self-consistent scheme) differ by 17% further enforcing what was earlier suggested, that the nature of the bonding between C-S-H particles is the same for both LD and HD C-S-H. What appears to differ between the two phases is their internal porosity (or packing

density) which in turn defines the number of bonds (or bond sites) in the agglomerate network.

F.2 Drucker-Prager Assumption

In this section we assume that the C-S-H solid phase is characterized by a Drucker-Prager criterion of the form (11.35). We will be using the uniaxial compression estimates for the two types of C-S-H in an attempt to get an estimate of the cohesive-frictional properties of the C-S-H solid phase. In particular we pay special attention to the pressure dependency coefficient in attempt to evaluate whether the C-S-H solid at the scale of a few nanometers can be regarded as a pressure dependent material. The uniaxial compression of porous Drucker-Prager matrix is given by (11.59):

$$\frac{\delta^2\rho^2(1-\phi)^2}{1-\phi-\delta^2\mathcal{F}_1(\phi)} = \left(\frac{\Sigma_c}{3}-\Sigma_m^c\right)^2\left(\frac{1}{\mathcal{F}_1(\phi)}-\frac{\delta^2}{(1-\phi)}\right)+\frac{\Sigma_c^2}{3}\frac{1}{\mathcal{F}_2(\phi)} \tag{F.10a}$$

$$\Sigma_m^c = \frac{\delta^2\rho}{\left(\frac{1}{\mathcal{F}_1(\phi)}-\frac{\delta^2}{(1-\phi)}\right)} \tag{F.10b}$$

We intend to calculate the cohesive-frictional behavior of the solid matrix by evaluating the yield criterion (F.10) for the two types of C-S-H at their uniaxial compression points:

$$\begin{aligned}\Sigma_{LD} &= 128 \quad \phi_{LD} = 37.3\% \\ \Sigma_{HD} &= 244 \quad \phi_{HD} = 23.7\%\end{aligned} \tag{F.11}$$

and solve the system for the two unknowns (δ, ρ):

$$\text{MT Estimate } \delta = 0.0005 \quad ;\rho = 46,667\text{MPa} \tag{F.12}$$

$$\text{SC Estimate } \delta = 1.6\times10^{-5};\rho = 46,667\text{MPa} \tag{F.13}$$

The problem had to be solved using the solver function in Excel. It is interesting to note that the solutions were converging towards very small values of δ suggesting that the C-S-H phase at the nanometer scale has limited pressure dependency. A more detailed investigation is required to test this hypothesis. For the moment being, the above observation comes to suggest that a

pressure independent criterion like Von-Mises better describes the C-S-H solid phase. Strength properties estimated using the Von-Mises assumption are therefore retained.